UNIVERSITÉ DE STRASBOURG

ÉCOLE DOCTORALE de Physique et Chimie-Physique (ED182)

IPCMS (UMR 7504 CNRS – Unistra)

Synchrotron SOLEIL

Laboratoire Léon Brillouin (UMR 12 CEA – CNRS)

THÈSE

présentée par :

Kevin SARTORI

soutenue le : **7 novembre 2019**

pour obtenir le grade de : **Docteur de l'université de Strasbourg**

Discipline/ Spécialité : Science des matériaux

Etude du couplage d'échange interfacial au sein de nanoparticules magnétiques à base de ferrite préparées via une succession de synthèses par décomposition thermique

THÈSE dirigée par :

M. PICHON Benoît	Maître de conférences, IPCMS, Université de Strasbourg
M. CHOUEIKANI Fadi	Chercheur, Synchrotron SOLEIL

RAPPORTEURS :

Mme CHANEAC Corinne	Professeur, INSP, Université Pierre et Marie-Curie
M. SAINCTAVIT Philippe	Directeur de recherche, IMPMC, Université Pierre et Marie-Curie

---

AUTRES MEMBRES DU JURY :

Mme VIART Nathalie	Professeur, IPCMS, Université de Strasbourg
M. CHAUDRET Bruno	Directeur de recherches, LPCNO, INSA, Université Paul Sabatier
M. CHABOUSSANT Grégory	Directeur de recherches, LLB, UMR12 CEA-CNRS, Gif-sur-Yvette
M. TOURNUS Florent	Chargé de recherches, ILM, Université Claude Bernard Lyon 1

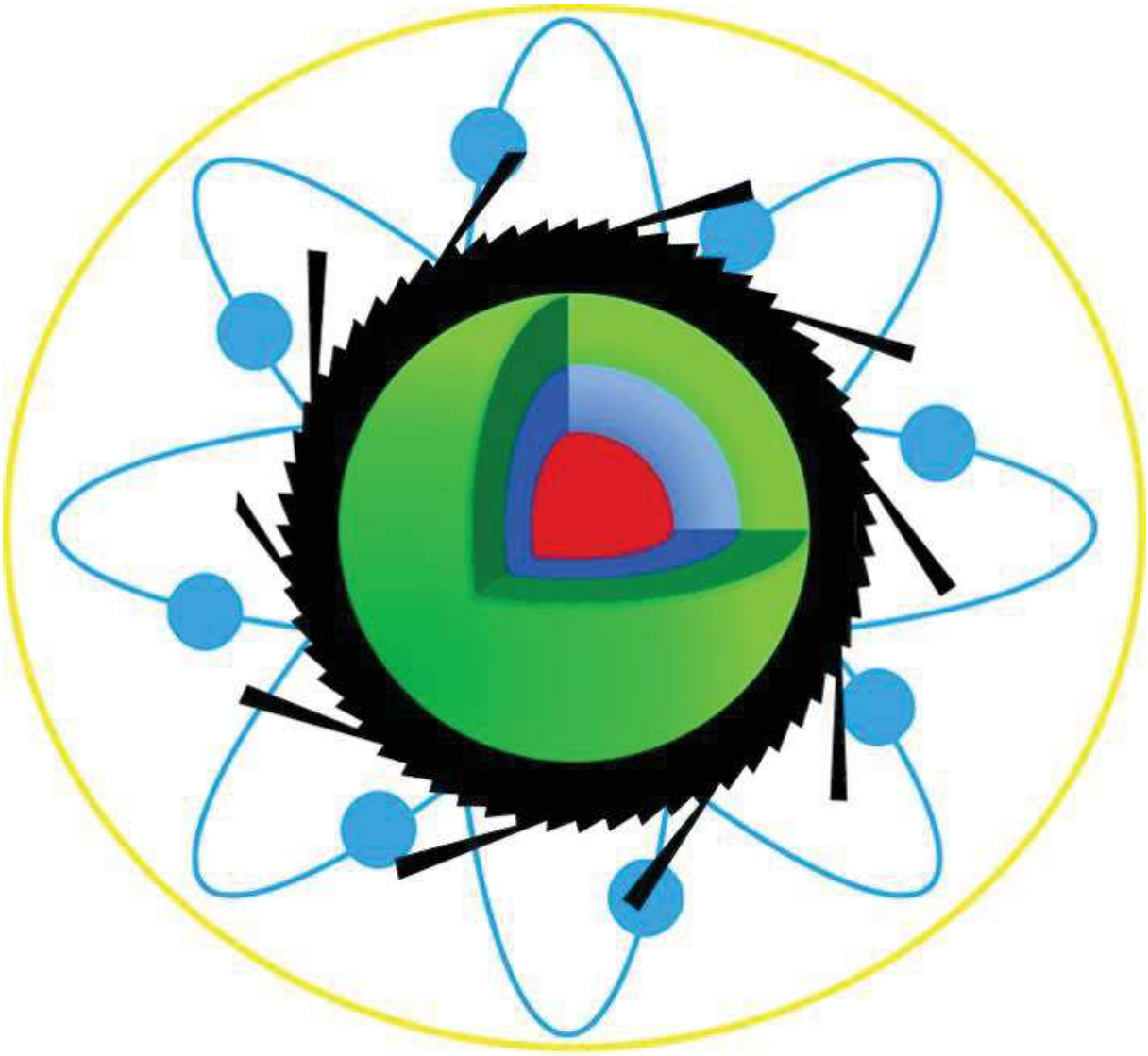

Illustration of a core@shell@shell nanoparticle which structure and magnetic properties were investigated by the use of a wide panel of analysis techniques.

Content

CHAPTER I

Increasing the size of $Fe_{3-d}O_4$ nanoparticles by performing a multistep seed-mediated growth approach

$Fe_{3-d}O_4$(@$Fe_{3-d}O_4$)n

Chapter II

Strong interfacial coupling through exchange interactions in soft/hard core-shell nanoparticles as function of cationic distribution

$Fe_{3-d}O_4$ – Co doped, $Fe_{3-d}O_4$@$CoFe_2O_4$, $Fe_{3-d}O_4$@CoO

CHAPTER III

Exchange-biased hybrid magnetic nanoparticles

$Fe_{3-d}O_4$@CoO@$Fe_{3-d}O_4$

CHAPTER IV

Exchange-coupled nanomagnet

$Fe_{3-d}O_4@CoFe_2O_4@Fe_{3-d}O_4$

Chapter V

AFM proximity effect of NiO on $Fe_{3-d}O_4$@CoO nanoparticles

$Fe_{3-d}O_4$@CoO@NiO

General introduction

Owing to their size and shape dependent properties, magnetic nanoparticles have gained tremendous interest since the past two decades. Size reduction down to the nanoscale may disturbs the magnetic order and produce unblocked magnetic moment at room temperature. Indeed, the magnetic stability ordering versus temperature (k_BT) depends on the volume of the nanoparticles (V) but also on their magnetic anisotropy constant (K). Thus, for small size, $KV < k_BT$ the magnetic ordering vanishes. Such property has found interest in biomedicine application. However, some other application such as data storage requires to get blocked magnetic moment over room temperature i.e. to get $KV > k_BT$. In order to increase the magnetic stability of small nanoparticles against temperature, it is possible to tune their magnetic anisotropy constant by tuning their chemical composition.

In this thesis, we are interesting to use iron oxide based magnetic nanoparticles which are made of a costless, abundant and natural material contrary to other commonly used rare earth based magnetic nanoparticles. However, small iron oxide magnetic nanoparticles of size of 10 ± 3 nm do not display magnetic ordering at room temperature. To increase their effective magnetic anisotropy constant, it is possible to synthesize bi-magnetic nanoparticles according to a core@shell model. Two different type of bi-magnetic coupling were investigated in this thesis: the exchange-bias coupling and the hard-soft coupling. The first one occurs between a ferrimagnetic phase and an antiferromagnetic phase and is further described in the general introduction. The second consists to benefit of a sufficient anisotropy difference between a hard and a soft magnetic phase and is described later.

Besides the requirements needed to generate strong magnetic couplings (exchange coupling or hard-soft coupling), the synthesis of bi-magnetic nanoparticles requires the two magnetic phases to display good epitaxial relationship i.e. crystallisation in similar space groups with close cell parameters. Three different compounds were selected: Fe_3O_4, $CoFe_2O_4$, CoO and NiO.

Previous studies on $Fe_{3-d}O_4$@CoO nanoparticles has showed that the growth of a CoO shell on the iron oxide core allows to increase the magnetic properties of iron oxide-based nanoparticles. This increase was attributed to a strong exchange magnetic coupling between the ferrimagnetic iron oxide core and the antiferromagnetic CoO shell which was favour thanks to the possible presence of interfacial diffusion. In this thesis, we have thus firstly investigated the diffusion mecanisms involved in bi-magnetic core@shell nanoparticles based on an iron oxide core.

Then, as the $Fe_{3-d}O_4$@CoO nanoparticles do not show a magnetic ordering at room temperature, the $Fe_{3-d}O_4$@CoO interface has been doubled in attempt to synthesize $Fe_{3-d}O_4$@CoO@$Fe_{3-d}O_4$ nanoparticles. It is expected here that the two ferrimagnetic/antiferromagnetic interfaces would increase the magnetic anisotropy constant further. To get rid of diffusion processes that may occur at both interfaces, $Fe_{3-d}O_4$@$CoFe_2O_4$@$Fe_{3-d}O_4$ nanoparticles were synthesized and their magnetic properties were compared to the previous $Fe_{3-d}O_4$@CoO@$Fe_{3-d}O_4$ nanoparticles. Finally, in order to benefit of the high magnetic ordering versus temperature of NiO, $Fe_{3-d}O_4$@CoO@NiO nanoparticles were synthesized.

The exponential development of devices for applications dealing with communications (data and motion) was allowed by the use of permanent magnets that are mostly composed of rare earth materials. In 2018, the world production of rare earth reached 170 000 tons, where China produced 71 % of it. The extraction of rare earth components requires to dig mines which adulterate and pollute the subsoil. Moreover, after extraction, their purification rejects a high volume of acids, bases, solvents, heavy metal and even radioactive materials. The purification processes also requires around 200 cubic meters of water which is at the end of the process, full of pollutants and often simply rejected. On top of that, the production of rare earth components emits a large amount of carbon dioxide which have to be decreased to limit the global warming according to the Paris agreements. Thus an alternative to produce new permanent magnets which are rare earths free has to be found.
Owing to their unique structure, magnetic properties and low cost, spinel ferrites have already gained tremendous interest in different applications such as microwave,[1] biomedical,[2,3,3,4] sensors,[5,6] high-frequency components,[7] supercapacitors[8,9] and photocatalytic activity.[10,11] Ferrites crystallize in the Fd-3m cubic face centered AB_2O_4 structure where the 32 O^{2-} anions form the cubic close-packed lattice, defining 64 tetrahedral (Td) sites and 32 octahedral (Oh) sites. However, only 8 Td sites and 16 Oh sites are occupied by cations. In a normal or direct spinel structure, the divalent transition metal cations (M^{2+}) are located in Td sites while the trivalent Fe cations are in the Oh sites. The general formula is thus written $(M^{2+})[Fe_2^{3+}]O_4$. At the opposite, in an inverse spinel structure the M^{2+} share the Oh sites with half of the Fe^{3+} while Td sites are occupied by the rest of the Fe^{3+} cations according to $(Fe^{3+})[M^{2+}Fe^{3+}]O_4$. Ferrites may also display an intermediate structure as $(M_{1-x}^{2+}Fe_x^{3+})[M_x^{2+}Fe_{2-x}^{3+}]O_4$ where x is the inversion parameter. It is called partially inverse structure.

In the spinel structure, the magnetic moments supported by cations in Oh sites are parallel coupled one to the other through superexchange interactions via the oxygen anions. Such interactions is favored by the direct overlap of the d orbitals of the metal cations with the anion. The magnetic moment of cations in Td sites are opposed in sign to the magnetic moment of cations in Oh sites. Thus spinel ferrite are ferrimagnet. Therefore, the net magnetization is governed by the type of cations and their distribution in the crystallographic sites.

The most common spinel ferrites are composed of M^{2+} = Mn, Fe, Co, Ni, Cu and Zn. They are all in an inverse spinel structure except for $ZnFe_2O_4$ which displays a direct spinel structure. Their main characteristics are presented in

Table 1. According to this, they all present advantages and disadvantages:

Except $ZnFe_2O_4$, all Ferrites display very high Curie temperatures (T_C) which corresponds to the transition temperature above which the ferrimagnetic order vanishes. Therefore, ferrites display permanent magnetization far above the room temperature. Due to a 4.6 μ_B magnetic moment, $MnFe_2O_4$ has the highest saturation magnetization (M_S) of 111 emu/g. M_S corresponds to the highest magnetic moment reached for a material submitted to an external induction due to the orientation of the spins along this induction. High M_S are suitable for biomedical[12–14] or permanent magnet applications.[15,16] In contrast, Zn and Cu ferrite are not interesting from this point of view. $CoFe_2O_4$ displays the highest magnetic anisotropy constant (K) which is a critical parameter for permanent magnets. However its cytotoxicity avoids biomedical applications and in this way, its use should be limited for every days devices. Although $NiFe_2O_4$ and Fe_3O_4 display the highest T_C (858 K), Fe_3O_4 is usually preferred because of its higher magnetization saturation (M_S) which is suitable for biomedical and permanent magnet applications. Furthermore, owing to its natural abundance, iron oxide is very cheap and can be produced with eco-friendly pathways. Iron oxide for advanced and day-life applications should be spread out.

Table 1. Structural and magnetic characteristics of principal spinel ferrites. a, T_C, T_N and μ_B stands for lattice parameters, Curie temperature, Néel temperature and Bohr magneton, respectively.

	a (Å)	T_C (K)	Theoretical μ_B (0 K)	Calculated μ_B (0 K)	Experimental μ_B (0 K)	M_S bulk (0 K) (emu/g)	K bulk (kJ/m^3)
$MnFe_2O_4$	8.513	585	5	4.6	4.6	111	-4
Fe_3O_4	8.396	858	4	4.1	4.1	98	20
$CoFe_2O_4$	8.392	790	3	3.7	3.7	94	220
$NiFe_2O_4$	8.337	858	2	2.2	2.2	56	-6.7
$CuFe_2O_4$	5.844	720	1	1.3	1.3	29	-6
$ZnFe_2O_4$	8.46	9 (T_N)	0	0	0	-	0

Spinel ferrites crystallize in the MFe_2O_4 structure with trivalent Fe cations and M a divalent transition metal. If the divalent metal is in the Td sites, the spinel structure is called direct while if the divalent metal is in an Oh site, the spinel structure is called invert. A mixed structure is characterized by an inversion parameter which has a high impact on the magnetic properties of the spinel. Moreover, the nature of the metal also modify the magnetic properties of the resulting spinel ferrite material.

$Fe_{3-d}O_4$ structure

Crystallographic structure

The iron oxide ($Fe_{3-d}O_4$) spinel structure consists of iron cations with several oxidation states (Fe^{3+} and Fe^{2+}) where non-oxidized Fe_3O_4 material is called magnetite with d=0 while the fully oxidized state with d=1, is called maghemite and displays the γ-Fe_2O_3 general chemical formula. Magnetite crystallizes in the inverse spinel structure defined previously. Its' primitive cell, shown in Figure 1, is composed of 56 atoms with 32 oxygen atoms with 8 Fe^{3+} in Td sites, 8 Fe^{3+} and 8 Fe^{2+} in Oh sites.[17]

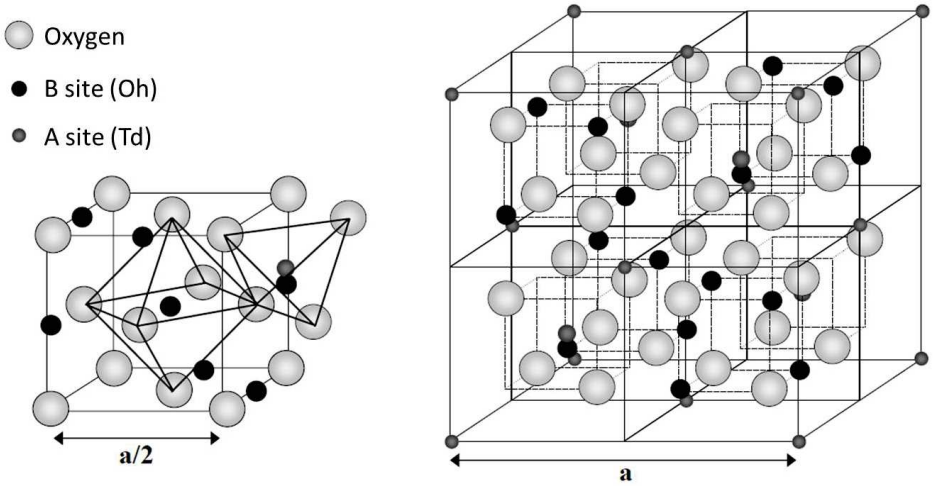

Figure 1. Scheme of a primitive cell of the inverse spinel structure. From ref.[18]

The developed formula for magnetite is $(Fe^{3+})_{Td}[Fe^{3+}Fe^{2+}]_{Oh}(O^{2-})_{Td}$ while maghemite, which can be considered as a Fe^{2+} deficient magnetite, displays no Fe^{2+} cations leading to the apparition of vacancies denoted □. Contrary to the magnetite, three different structures of maghemite have been reported in the literature according to the disposition of the vacancies:

- within the same Fd-3m space group as magnetite and without any cell deformation, with a general formula $(Fe^{3+})_{Td}\left[Fe^{3+}_{5/3}\square_{1/3}\right]_{Oh}(O^{2-})_4$. This structure is favored by a similar occupation rate of 5/6[19] and is the major compound formed after the oxidation of magnetite.

- In the $P4_132$ space group without any cell deformation, with a general formula $(Fe^{3+}_8)_{Td}\left[Fe^{3+}_{4/3}\square_{8/3}Fe^{3+}_{12}\right]_{Oh}(O^{2-})_{32}$ favored by a partial order on the O_h sites.[19,20]

- In the $P4_32_12$ space group where the cubic cell becomes tetragonal.[19,21]

Magnetite is an abundant material which crystallizes in the inverse spinel structure. This material easily oxidize upon exposure to air to produce maghemite, leaving room to the apparition of vacancies instead of the originals Fe^{2+}.

Magnetic structure

Fe^{26} displays a [Ar] $3d^64s^2$ electronic structure with 8 electrons in the external electronic layer. Hence, Fe^{2+} and Fe^{3+} are featured by 6 and 5 electrons in their external electronic layer represented in Figure 2. According to this, Fe^{2+} and Fe^{3+} cations support respectively 4 and 5 μ_B of electronic moment.

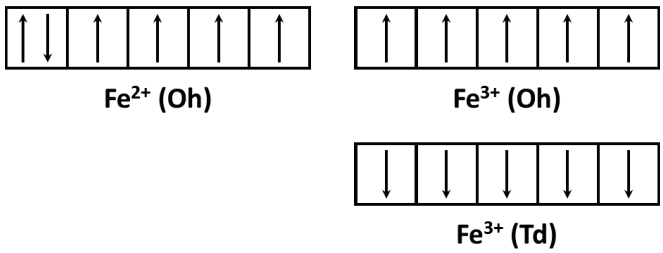

Figure 2. Scheme of the electronic configuration of Fe^{2+} and Fe^{3+} in the magnetite.

As in the inverse spinel structure, the spins present in Td sites are opposed in sign to the ones in Oh sites. Fe^{2+} and Fe^{3+} in Oh sites are antiparallel coupled through double exchange interactions. Hence, in the magnetite structure, the magnetic moments of Fe^{3+} cations cancelled each other's. The net magnetic moment of 4 μ_B is only given by the Fe^{2+}. Thus, magnetite displays a ferrimagnetic (F(i)M) magnetic behavior.

The same ferrimagnetic behavior is observed in the $(Fe^{3+})_{Td}\left[Fe^{3+}_{5/3}\square_{1/3}\right]_{Oh}(O^{2-})_4$ maghemite where the magnetic moment of one Fe^{3+} in Td sites is opposed to five third of the magnetic moment supported by Fe^{3+} in Oh sites, leading to a net magnetic moment of 3.33 μ_B for the maghemite.

Due to the invert spinel structure, magnetite displays a ferrimagnetic behavior leading to a net magnetic moment of 4 μ_B. While in maghemite the net magnetic moment decreases to 3.33 μ_B with the disappearance of Fe^{2+} and the apparition of vacancies.

Size reduction to the nanoscale

In order to be incorporated into devices such as computers, smartphones and so on, the size of iron oxide based magnet has to be very tiny. Size reduction to the nanoscale allows to open new frontiers. At the nanoscale, the effect of oxidation on the magnetite structure is spontaneous and has a higher impact than in the bulk form.[14,22–24] Indeed, it has been proved that below a size of 8 nm, an iron oxide nanoparticle is only composed of maghemite. For sizes higher than 12 nm, it displays a magnetite structure with a maghemite shell according to a core@shell structure with a gradient of maghemite composition from the surface. For intermediate sizes, the composition of the nanoparticle is a mixture of both magnetite and maghemite, according to a general structure of $Fe_{3-d}O_4$.[25] Such behavior modifies the magnetic properties of the nanoparticles.[26]

Magnetic domains size

Size reduction down to the nanoscale increases the surface over volume ratio which has the disadvantage to decrease the magnetic stability for increasing temperatures.
Indeed, in the bulk state, a magnetic material is composed of several magnetic domains called Weiss domains, which minimize the magnetostatic energy and are delimited by the Bloch walls. Inside each magnetic domain, there is a single magnetic orientation while the domains have different magnetic orientations between them. This magnetic structure leads to the absence of a spontaneous magnetization. However, under a critical radius, r_C, which varies according to the chemical structure of the material, the material shows a single magnetic domain with a spontaneous magnetization.

$$r_C = \frac{9\sqrt{AK}}{\mu_0 M_S^2}$$

with A the exchange constant, K the magnetic anisotropy constant, μ_0 the magnetic permeability and M_S the saturation magnetization.

If the size is even more reduced under a critical radius r_0, the spontaneous magnetization at room temperature disappears, living room to the superparamagnetic state where the overall magnetic moment of the particle fluctuates over short times.

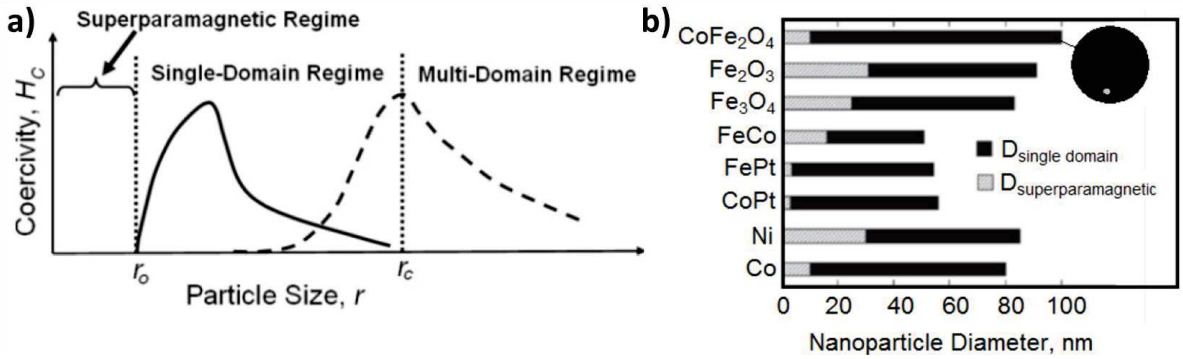

Figure 3. a) Magnetic behavior as a function of the size of the nanoparticles.[27] b) Maximum sizes of nanoparticles for single magnetic domains (r_c) and superparamagnetic (r_O) behavior according the chemical composition.[28]

In the bulk form, a material has no spontaneous magnetization due to the presence of several Weiss domain. Decreasing the size under a critical r_c radius lead to the apparition of a single magnetic domain. If the size is decreased further under r_0, the spontaneous magnetization disappears, and the magnetic moment fluctuates rapidly, it is the superparamagnetic state.

Superparamagnetism

According to the Stoner-Wohlfarth model, size reduction below a critical volume (V) depending on r_0, lead to the overall decrease of E_a defined as $E_a = KV \sin^2 \theta$ with K the magnetic anisotropy constant of the material and θ the angle between the magnetization direction and the easy axis. Thus, if the thermal energy $25k_BT$ is higher than E_a, the magnetic moment of the nanoparticles will easily shift from the spin up to the spin down configuration over time.[29] This regime is called superparamagnetism and was predicted by Frenkel and Dorfman.[30] Such properties has found applications in biomedicine for MRI contrast agents as an example[31] while they are not suited for others such as data storage where blocked magnetic moment above room temperature are required. For nanoparticles, the transition temperature between the blocked magnetic state and the superparamagnetic state is called blocking temperature (T_B) defined as

$$T_B = \frac{KV}{\left(k_B ln\left(\frac{\tau_m}{\tau_0}\right)\right)}$$

where the KV product corresponds to the magnetic anisotropy energy of the material, k_B is the Boltzman constant and τ_m and τ_0 are the time of measurements and the reversal attempt time (usually in the range of 10^{-9} to 10^{-12} s) respectively. Hence, it shows that the superparamagnetic state is not only proper to the material but also depends on the magnetic measurement technique where τ_m is in the order of 100 s for SQUID measurements in DC mode and in the range 10^{-7} to 10^{-10} s for Mössbauer measurements. Where SQUID refers to super quantum interference device and is a magnetometry measurement technique. For SQUID measurements, the typical times used are $\tau_m = 100$ s and $\tau_0 = 10^{-9}$ s, thus the equation becomes

$$KV = 25k_BT_B$$

When the nanoparticles display a size distribution, it leads to a large volume (V) of distribution and thus the determination of T_B is often challenging. Thus, in the literature, the T_{max} is better compared than T_B. T_{max} is ascribed to be the maximum of the zero field cooled curve (ZFC) from magnetization versus temperature measurements. The width of this curve depending on the size distribution of the nanoparticles, T_{max} corresponds to a distribution of blocking temperatures.

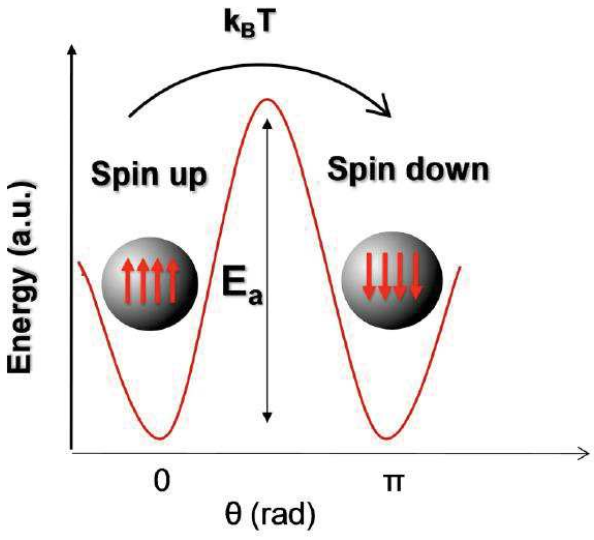

Figure 4. Anisotropy energy profile as a function of the angle between the magnetic moment and the easy axis for a single domain NP with pure uniaxial symmetry.[32]

More specifically, iron oxide displays superparamagnetic properties at room temperature for size smaller than 30 nm.[33] Such properties are evidenced by recording magnetization as a function of the temperature (Figure 5) which also shows that the size reduction of the nanoparticles results in the decrease of T_{max}.

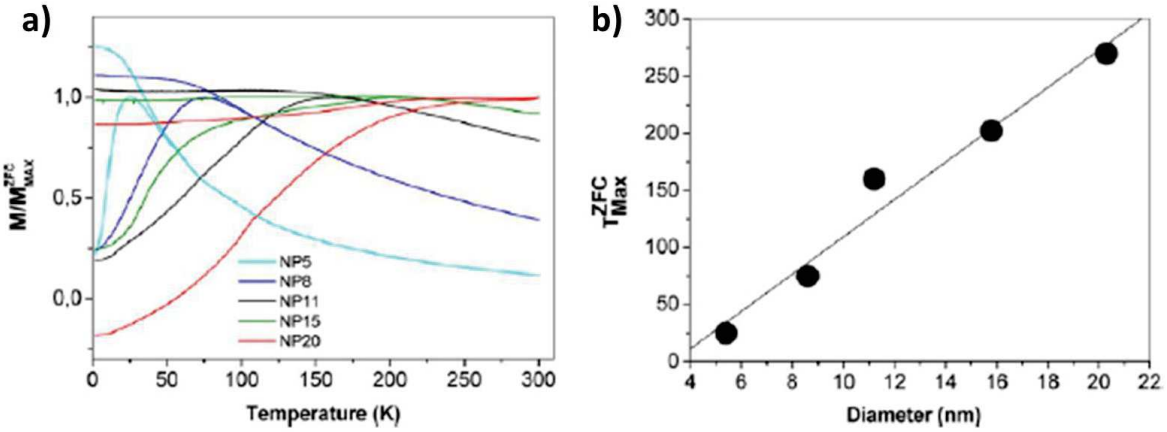

Figure 5. a) Magnetization versus temperature curves for different size of iron oxide nanoparticles. b) T_{max} as a function of the size of iron oxide nanoparticles. ***[Baaziz reproducible tuning]***

If a material is in a superparamagnetic state, the measure of its magnetization curve subjected to a reversing applied magnetic field, evidences a single and closed curve called hysteresis (Figure 6a) i.e. which does not have any coercive field.
Indeed, a hysteresis is characterized by three factors:

- A saturation magnetization (M_S) (defined in the general introduction)
- A remanent magnetization (M_R) which is the natural magnetization of the material without any applied magnetic field,
- And a coercive field (H_C) corresponding to the reverse magnetic field needed to cancel the magnetization of the material.

According to this, a nanoparticle with a blocked magnetic domain shows an open hysteresis with a coercive field which at T = 0 K can be calculated according to the Stoner-Wohlfarth model:[34]

$$H_C \approx \frac{K_a}{\mu_0 M_S}$$

Showing that this coercive field is proportional to the anisotropy constant of the material and to its saturation magnetization. According to this observation, a material featured by a low anisotropy constant and a high saturation magnetization, also called soft magnetic material, display a hysteresis which has a small coercive field. While a hard magnetic material featured by a high anisotropy constant and a low saturation magnetization displays a hysteresis curve that has a large coercive field (Figure 6b).

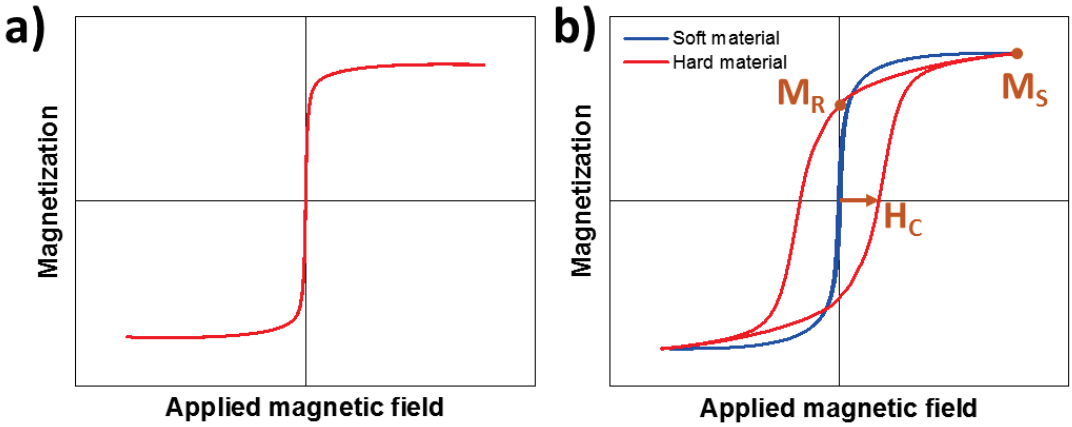

Figure 6. a) Magnetization curve of a superparamagnetic material. b) Magnetization curve of a hard and soft blocked material with the characteristics features of a hysteresis curves (M_S, M_R and H_C).

Superparamagnetic properties are the results of a higher thermal energy than the intrinsic magnetic anisotropy energy of the considered material. The transition temperature between the blocked magnetic state and the superparamagnetic state of a nanoparticle is called blocking temperature. However, the superparamagnetic state is time-dependent and the determination of T_B depends also on the time of measurements of the analysis technic used to probe the magnetic properties of the material. In M(T) curves, T_{max} is generally better used than T_B as it is easier extracted. The close hysteresis in a M(H) curve of a material evidences the presence of superparamagnetic properties.

Dipolar interactions

It is important to note that in this manuscript, the magnetic properties of the nanoparticles are recorded on powders (unless otherwise stated). Hence nanoparticles supporting a net magnetic moment are influenced by the presence of dipolar interactions which depend on the distance between the nanoparticles (d) and on their magnetic moment (μ). For spheres of radius r, the dipolar interaction energy depends thus on the saturation magnetization of the nanoparticles and on the separating edge-to-edge distance (s), which according to the 2-dipole approximation model gives:[35]

$$E_d = \frac{\mu^2}{d^3} = \frac{(M_S \times 4/3\,\pi r^3)^2}{(2r+s)^3}$$

It shows that dipolar interactions can be avoided by increasing sufficiently the distance between the nanoparticles, i.e. by diluting the nanoparticles in a matrix such as eicosane[17] or in a solvent or by carefully assemble isolated nanoparticles on a substrate.[36]
Dipolar interactions correspond to the magnetostatic interaction between the magnetic moment of each nanoparticle. Thus according to interactions in a triangular lattices which is a more reasonable model than the 2-dipole approximation for nanoparticles in the powder state,[35,37] it results that:

$$E_d = 2.8 \times 10^{-7}\,\frac{\mu^2}{d^3}$$

In consequence, dipolar interactions modify significantly the magnetic properties compared to isolated nanoparticles. Dipolar interactions results in the enhancement of the blocking temperature.[38,39] They are also expected to decrease H_C and the M_R/M_S ratio because of the collective properties which favor the easier reversal of magnetization.[38,40]

Although dipolar interactions markedly modify the magnetic properties of nanoparticles, it is difficult to rationalize their effect. Indeed the precise control of the spatial arrangement of nanoparticles (interparticle distance and the dimensionality of their assembly) over large areas is very challenging.

Magnetic nanoparticles can be subjected to dipolar interactions whose strength depends on the distance between the nanoparticles. Such interaction may affect the magnetic properties of the nanoparticles assembly. Thus, a precise control on the distance between the nanoparticles allow to better understand the magnetic properties of a unique nanoparticles or of a packed arrays of nanoparticles. Nevertheless, the control of the distance between nanoparticles over large area is often challenging.

Small iron oxide nanoparticles

For permanent magnet applications in data storage, very small iron oxide nanoparticles should be used in order to store a high density of information in the smallest space as possible. However, it was shown that for size smaller than 30 nm, these nanoparticles are superparamagnetic at room temperature. Thus, an alternative has to be found in order to increase the magnetic anisotropy energy of such nanoparticles.

Exchange-bias coupling in nanoparticles

Definition and characteristics

The interfacial exchange anisotropy mostly known as exchange-bias coupling has been discovered by Meiklejohn and Bean in 1956.[41] They studied the magnetic properties of ferrimagnetic (FiM) cobalt nanoparticles surrounded by an antiferromagnetic (AFM) cobalt oxide shell. They noticed that for $T > T_N$, where T_N is the Néel temperature of CoO, the nanoparticles displayed typical properties of Co nanoparticles. In contrast, for $T < T_N$, FiM-AFM spins interactions modify the magnetic properties of the Co@CoO nanoparticles.
Indeed, ferro(i)magnetic F(i)M nanoparticles generally evidence a uniaxial anisotropy with a nice sinusoidal applied magnetic field angular (φ) dependence behavior of their torque magnetic curve (Figure 7 a, b, c). When they are in contact with an AFM, for $T > T_N$ (Figure 7a), the magnetic torque curve evidences an increase in amplitude, and for $T < T_N$, the torque curve displays a different number of stable positions (magnetic torque = 0) with variations of the amplitude.[42,43]

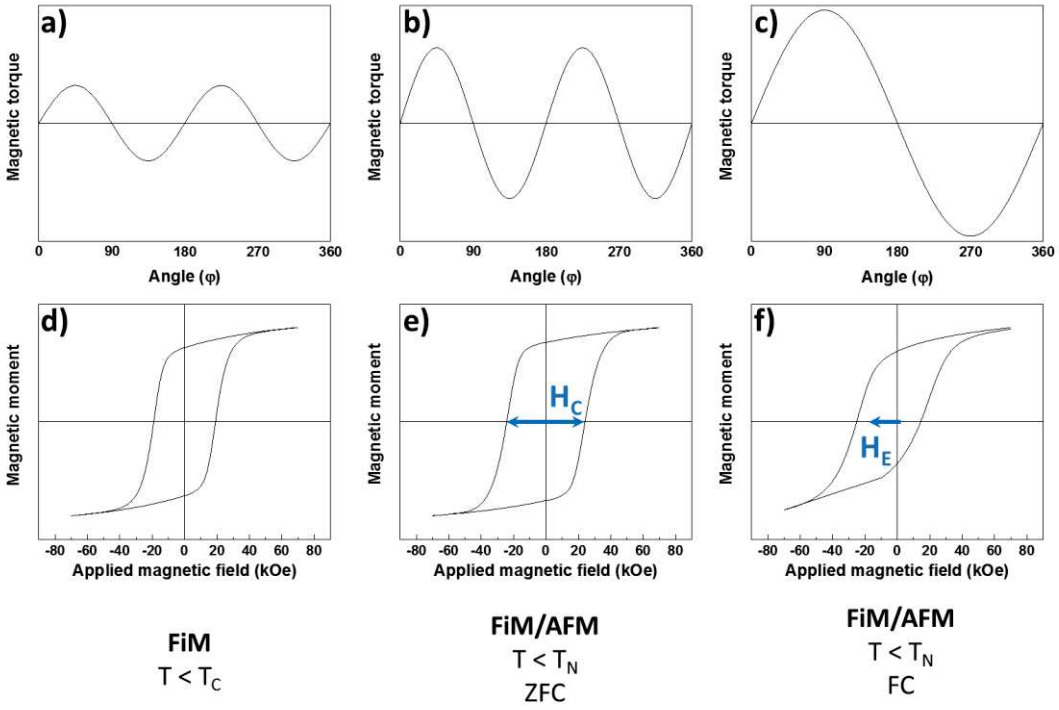

Figure 7. a, b, c) Magnetic torque as a function of φ angle where φ is the angle between magnetization and applied magnetic field, d, e, f) magnetic moment versus an applied magnetic field (M(H)) curves of a, d) a ferrimagnet below T_C, a ferrimagnetic in contact with an antiferromagnet at T<T_N b, e) after ZFC, c, f) after FC. Adapted from ref.[42,43]

Moreover, considering a ferro(i)magnet and an antiferromagnet with T_C>T_N as it is generally the case, a M(H) hysteresis cycle of a ferro(i)magnet in direct contact with an antiferromagnet recorded at T<T_N after zero field cooling (ZFC) evidence an increase of the coercive field (H_C) due to the pinning of the ferro(i)magnetic spins by the antiferromagnet (Figure 7 d, e). In contrast, after field cooling, the hysteresis curve is shifted to negative magnetic field which corresponds to the so-called exchange-field (H_E) and is typical of exchange-bias coupling (Figure 7 f).

Such a phenomenon is allowed by the coupling of interfacial AFM spins with the interfacial F(i)M spins during the field cooling procedure. The F(i)M interfacial spins are pinned by the AFM spins if $K_{AFM}V_{AFM}$ > $K_{F(i)M}V_{F(i)M}$, the AFM exerts a torque on the ferro(i)magnet resulting in the apparition of H_E. However, if $K_{AFM}V_{AFM}$ < $K_{F(i)M}V_{F(i)M}$, the AFM does not exert a sufficient torque on the ferro(i)magnet to pin the interfacial spins resulting in the solely increase of H_C without any H_E. A second condition to allow the presence of an exchange-bias interaction is that $K_{AFM}V_{AFM}$ has to be superior to the interfacial coupling energy J_{int} defined as $J_{int} = (H_E M_S D)/6$, where D is the size of the FiM core.[42]

In order to universally compare the strength of exchange-couplings between different materials, it is possible to calculate the coupling energy $E=H_E M_S V_{F(i)M}$ with M_S the saturation magnetization and V the volume. It becomes $E=H_E M_S d_{F(i)M}/6$ in the case of spherical core-shell nanoparticles.[42] However, this is not a very accurate consideration as small variation of the initial spherical shape model has a strong influence on the physical properties. Furthermore, in this manuscript we are more interested in the direct comparison of the exchange-bias strength. Thus we will compare the values of H_E which are directly proportional to the interface exchange anisotropy.[44]

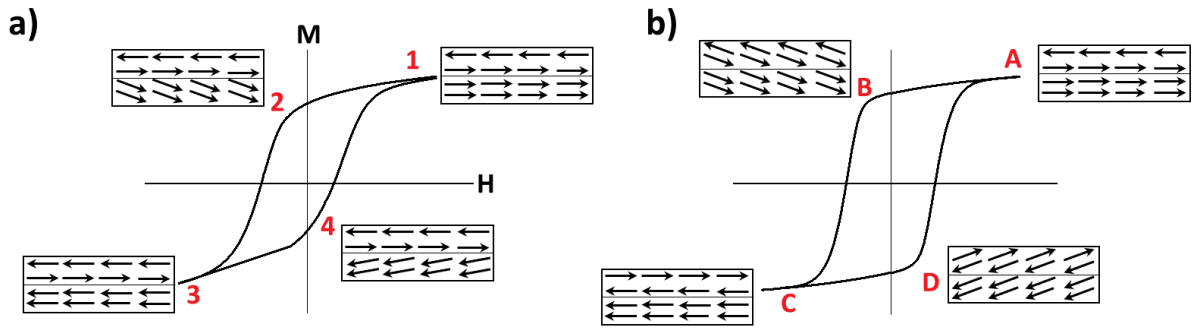

Figure 8. Scheme of the spins configuration during the recording of the magnetic moment versus an applied magnetic field after field cooling at a FM/AFM interface a) with $K_{AFM}V_{AFM}>K_{FM}V_{FM}$, b) with $K_{AFM}V_{AFM}<K_{FM}V_{FM}$. Adapted from ref.[42]

Figure 8a presents the spin configuration at the FM/AFM interface during the recording of the M(H) hysteresis cycle after FC for a ferromagnetic interfacial exchange coupling. For $K_{AFM}V_{AFM} > K_{FM}V_{FM}$, it evidences that:

- 1/ The FM and AFM spins display a parallel configuration.
- 2/ The spins of the FM phase follow the applied magnetic field as it is reversed with some difficulties due to the torque exerted by the AFM.
- 3/ The FM spins display an antiparallel configuration compared to the AFM spins.
- 4/ The FM spins easier follow the reversing of the applied magnetic field than in (1) thanks to the help of the interfacial spins of the AFM which are this time oriented in the same direction as the applied magnetic field (1). Thus the spins configuration get back to their initial and lower magnetic configuration.

The exchange-bias is usually characterized by a negative shift of the hysteresis toward the applied magnetic field axis which allows to reach the saturation magnetization with lower applied magnetic field. However, a positive shift was also attributed to an antiferromagnetic interfacial coupling.[45] At the opposite, for $K_{AFM}V_{AFM} < K_{FM}V_{FM}$ (Figure 8b), after FC,

- A, C/ the spins are oriented in the same directions as in the previous case.
- B, D/ Then the spins in the FM phase follow the applied magnetic field reverse and exert a torque on the AFM spins' which will follow the field reversing due to its' lower magnetic anisotropy.

In this case, no exchange field is observed as the FM and AFM phases rotate coherently with the applied magnetic field.

The exchange-bias properties is the result of the spin pinning of ferromagnetic or ferrimagnetic phase by an antiferromagnetic counterpart. Such magnetic exchange coupling is observed if $K_{AFM}V_{AFM} > K_{FiM}V_{FiM}$ and if $K_{AFM}V_{AFM} > J_{int}$. It results in the increase of the overall magnetic anisotropy of the material and allows to increase the T_B of the ferrimagnet. The exchange-bias properties is characterized by a shift of the hysteresis on the applied magnetic field axis in M(H) curves due to a resistance of the FiM spins to follow magnetic field reversal.

Limitations of the exchange-bias coupling

Effect of temperature

The exchange-bias coupling is the result of the interfacial spin pinning of the F(i)M phase by the AFM one. Hence when $T>T_N$, the AFM phase loses its' magnetic stability and displays paramagnetic properties. Thus the AFM is no longer able to drive the interfacial pinning and the exchange-bias coupling becomes absent.
According to this consideration, from low temperature, H_E and H_C are expected to decrease when T approaches T_N. It is observed that H_E vanishes before reaching T_N while H_C can be present up to $T=T_N$.[46,47] The temperature at which H_E vanishes is also called T_B in the literature and needs to be differentiate to the T_B representing the limit between an overall blocked magnetic state and a superparamagnetic state. Nevertheless, the disappearance of H_E before the one of H_C can be attributed to the eventual presence of small AFM crystallite which are in a superparamagnetic state phase for $T<T_N$.[48]

Volume effect

The exchange-bias coupling depends on the volume of the AFM and F(i)M materials as it is an interface effect. Indeed, considering $K_{AFM}>K_{F(i)M}$, there exists a maximum and a minimum volume of the F(i)M where H_E vanishes. The maximum volume of F(i)M is reached for volumes that are equals to the F(i)M domain wall volumes. And the minimal volume may be reached if the F(i)M phase displays a discontinuity.[49] In between, H_E is proportional to $1/V_{F(i)M}$ and is enhanced for small volume of F(i)M such as H_C which follows the same evolution as H_E.[50]

Moreover, there also exists a minimal volume of AFM for which $K_{AFM}V_{AFM}$ is inferior to the interfacial energy coupling J_{FM-AFM} resulting in the vanishing of H_E. This minimal volume is defined as $V_{AFM}=J_{FM-AFM}/K_{AFM}$.[51,52]

Training effect

Training effects have been observed in thin films[53–55] and in nanoparticles[56,57] and correspond to a decrease of H_E and H_C for a successive repetition of M(H) loops. This is attributed to a deviation of the interfacial spins from their equilibrium configurations due to a relaxation phenomenon of the interfacial frozen spins along the field cooling direction.[50] Larger training effects are generally observed for thin AFM thicknesses.[53,54]

Field cooling effect

Different behavior of H_E towards the increase of the cooling field were reported.
In core@shell cobalt ferrite nanoparticles, it is possible that H_E increases up to 1.5 kOe with the increase of the field cooling to 5.0 kOe and decreases for higher fields.[58] The increase of H_E arises from an increase of the number of FiM spins aligned with the applied magnetic field. While the decrease is attributed to a decorrelation of the interfacial AFM spins that tend to align with the applied magnetic field.
Moreover, in FeF_2-Fe bilayers, Nogués and *al.* have reported a negative exchange field for small cooling fields while for cooling fields higher than 20 kOe, they reported a positive exchange-bias which arise from an AFM interface coupling.[45] The same behavior has been reported for iron and manganese oxide based core@shell nanoparticles.[46] Thus field cooling has an effect on the measured H_E and it is necessary to record the H_E in the exact same condition.

Asymmetry

Hysteresis curves can display some asymmetry related to the presence of differences in the magnetic reversal process between the two branches.[50] Different mechanisms can occur in such conditions:

- A uniform spin rotation appears for the reversal in the decreasing field branch while in the increasing field branch, the spins' reversal are subjected to nucleation and propagation of domains wall
- It can also be produced by a competition between the ferromagnet and the interfacial FM-AFM interfacial anisotropies.

Spins orientation

Exchange-bias results from the parallel coupling of interfacial F(i)M-AFM spins. However, it is also possible that the spins display a different orientation with a perpendicular direction of the AFM toward the F(i)M.[59,60] It results from the rotation of the AFM or F(i)M during the field cooling procedure and was predicted to occur for systems with a low F(i)M magnetic anisotropy.[61] It induces a minimal value of the interfacial energy for perfectly compensated surface and can thus increase the exchange bias.[61]

Vertical shift

Hysteresis loop may also show a shift along the magnetization axis called vertical shift (H_V). It has been proved that the vertical shift is influenced by the field cooling where it is negative for low field cooling, positive for high field cooling and arises from uncompensated spins momentum in the AFM.[62] Hence the vertical shift is proportional to the number of uncompensated spins.[50]

Interface disorder

Roughness

The increase of interfacial roughness induces some magnetic interfacial defects that generally decrease the exchange field due to the presence of magnetic frustration as shown by Figure 9.

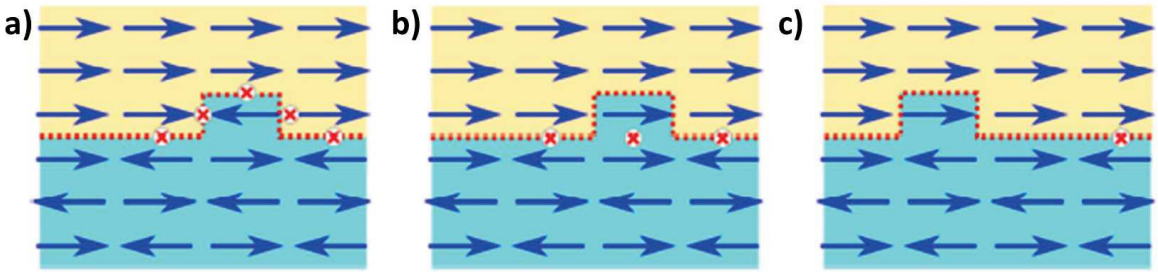

Figure 9. Schematic representation of the interfacial spin configurations with magnetic defects. Adapted from ref.[63]

However, it has also been reported that some systems are not influenced by the increase of interfacial roughness.[64] Or that the exchange bias coupling increased with the increase of the interfacial roughness due to the pinning of the propagating domain walls in the ferromagnet.[65]

Diffusion

Interfacial atomic graded composed interfaces,[66] mixed interfaces[67] and diffusion,[68] have shown the enhancement of coercive field while the exchange field and so the exchange coupling was reduced. The role of the interfacial diffusion is further studied in **Chapter II**.

The exchange-bias coupling finds numerous parameters where their control allows to finely tune the resulting properties in order to use it for different magnetic applications.

Applications

The exchange-bias property finds applications for read head,[69] giant magneto-resistance[69] and MRAM.[70] Moreover, in the past years, this property has also found interest in permanent magnets[71] and data storage[72] thanks to the enhancement of the coercive field and blocking temperature.[49] Owing to the improvement of the digital technology and the exponential increase of the numerical tools used by the world population, the need to extend the data storage capability is crucial. A solution could be the use of magnetic nanoparticles. However, most of them are based on rare-earth materials which on top of that display low energy product $(BH)_{max}$.[73] A high energy product in the hysteresis ensures the magnetic stability of the nanoparticles over time allowing to store the information for long time. Thus, the development of rare-earth free small nanoparticles with a stable magnetic moment above room temperature and a high energy product is of interest.

Exchange-biased iron oxide based magnetic nanoparticles

Iron oxide nanoparticles are particularly attractive due to their biocompatibility and abundance. They display a ferrimagnetic order which, coupled to an antiferromagnet, is expected to produce exchange bias coupling. Thus the magnetic properties or iron oxide based nanoparticles can be tuned with this exchange coupling property.

As the exchange-bias is an interfacial coupling effect, it is required to get an intimate contact between the iron oxide nanoparticles and the AFM material. According to this, it is possible to insert the F(i)M nanoparticles in an AFM matrix[74] or to synthesize FiM@AFM core@shell nanoparticles which have the advantage to be more modular. Indeed, with core@shell nanoparticles, it is possible to tune the core size, the shell thickness, and the distances between the nanoparticles which all have a high impact on the magnetic properties.

In order to get a smooth FiM/AFM interface in iron oxide@AFM core@shell nanoparticles, the AFM phase needs to be cautiously selected. Indeed, to grow the shell on the core, a good epitaxial relationship is required: the AFM also has to crystallize according to a cubic structure with a cell parameter displaying the lowest lattice mismatch as possible. Moreover, to display exchange-bias property, the effective magnetic anisotropy energy of the AFM phase has to be so that $K_{AFM}V_{AFM}>J_{FiM-AFM}$ and that $K_{AFM}V_{AFM}>K_{F(i)M}V_{F(i)M}$. On top of that, the AFM should display a high T_N as the blocking temperature in such system is generally equal to T_N because above T_N, the AFM order vanishes, and consequently the exchange bias.

According to the previous paragraphs, iron oxide based nanoparticles featuring exchange-bias properties are listed in Table 4.

Surface anisotropy

Surprisingly, it was found that simple FiM nanoparticles of γ-Fe_2O_3,[75–77] $Fe_{3-d}O_4$[25] and $CoFe_2O_4$[58] are also able to display an exchange field without the need to be in contact with an antiferromagnet. So does with iron oxide nanoparticles subjected to a 5 GPa pressure.[78] The origin of their exchange bias property lies in the presence of disordered spins at their surface, resulting in spin canting effects. They are the result of a break of magnetic symmetry at the surface of the nanoparticles. Canted surface spins align then with the external field during the field cooling procedure creating a magnetic core@shell structure. The surface spins exert then a magnetic torque on the interfacial internals spins leading to a small exchange field. However, even if the presence of exchange-bias in these nanoparticles increase their coercive field, it does not have any significant impact on their blocking temperature which remains very low.

Exchange-bias coupling were observed in simple material nanoparticles that results from spin canting effect which generate a magnetic core@shell structure.

Phase oxidation

Most of the studied systems that display an exchange field are based on the spontaneous or forced oxidation of the native material as first reported for the Co@CoO nanoparticles studied by Meiklejohn and bean.[41]
Interestingly, FeO is an AFM material that spontaneously oxidized into FiM $Fe_{3-d}O_4$. According to the size of the native FeO nanoparticles, it is possible to form a stable FeO@$Fe_{3-d}O_4$ system. It has been reported that small FeO@$Fe_{3-d}O_4$ nanoparticles with a core size of 7 nm and a core@shell size of 14 nm, display low H_C, H_E and T_B of 0.7 kOe, 0.5 kOe and 100 K respectively.[79] The increase of the size to 16.2 nm of cubic FeO@$Fe_{3-d}O_4$ nanoparticles evidenced an increase of H_C, H_E and T_B to 1.9 kOe, 0.6 kOe and 209 K respectively.[80] In the previously cited nanoparticles, it is possible that the cubic shape of the nanoparticles has tuned the magnetic properties of the FeO@$Fe_{3-d}O_4$ nanoparticles compared to a spherical morphology of the same volume.[81] Bigger spherical FeO@$Fe_{3-d}O_4$ nanoparticles with a core size of 10 nm and a core@shell size of 23.2 nm show a further increase of H_C and H_E to 2.3 kOe and 1.6 kOe and of T_B over 275 K.[82] However, the last nanoparticles do not show a significant improvement of the magnetic stability with respect to temperature compared to pure $Fe_{3-d}O_4$ nanoparticles of 21 nm which display a T_B of 248 K.[25] As the T_N of FeO is 198 K, it is not expected that FeO still pin the spins of the $Fe_{3-d}O_4$ FiM shell above this temperature. Thus the high T_B of the two last mentioned nanoparticles is more related to volume effects than to an efficient exchange-bias coupling.

Fe is a ferromagnet (FM) which easily oxidized into $Fe_{3-d}O_4$. Thus Fe@$Fe_{3-d}O_4$ nanoparticles which consists of a FM@FiM material can be synthesized. Hence no exchange bias property are expected while some rather high H_E in the order of the 1-6 kOe were measured for core@shell sizes of 11 to 13.8 nm.[56,83] The same behavior was observed in FiM@FiM Fe_3O_4@γ-Fe_2O_3 nanoparticles. Indeed, as magnetite also spontaneously oxidized into maghemite, it has been reported that Fe_3O_4@γ-Fe_2O_3 nanoparticles with a size of 12 nm evidence a low H_E of 0.1 kOe with a low T_B of 180 K.[84] Moreover, it was reported that ultrasmall $MnFe_2O_4$@γ-Fe_2O_3 and $CoFe_2O_4$@γ-Fe_2O_3 with a size of 3.6 and 4.3 nm also display small H_E of 0.09 and 0.12 kOe respectively.[85] The intriguing presence of exchange-bias in such F(i)M@FiM nanoparticles was attributed to spin-glass-like phase which has a higher magnetic anisotropy energy than the rest of the FiM phase in the nanoparticles. The spin glass like phase orientates with the external field during the field cooling process and acts then as the pinning layer.[56] Even if this property is very interesting in such system, the T_B of such nanoparticles remains well below room temperature.

The natural oxidation of a magnetic material alters its chemical structure but also its magnetic structure. Hence it is possible that a native AFM material oxidized into a ferrimagnet, and generates an AFM/FiM interface resulting in the appearance of exchange-bias coupling.

Synthesis of iron oxide nanoparticles

Besides the oxidation of a magnetic phase, recent advances in synthesis techniques has allowed to go deeper by controlling the formation of a shell with different chemical compositions and with a good epitaxial relationship. The variety of combination between a hard AFM and a soft FiM phases has opened huge perspectives towards the enhancement of the magnetic properties of nanoparticles through exchange bias coupling. Seed-mediated growth methods were developed in order to synthesize iron oxide based core@shell nanoparticles that does not result from the oxidation and are grown at the surface of a ferrite spinel structure.
The seeds nanoparticles can be synthesized according to various techniques which are presented in Table 2. Each one has its own pro and cons. In this thesis, the nanoparticles have a size smaller than 20 nm with a high control of their size and size distribution. Furthermore, their morphology should be controlled as well and the synthesis should produce nanoparticles with a yield as high as possible in order to use them for potential applications. Thus the thermal decomposition appears to be a technique of choice.

Table 2. Summary of the different synthesis conditions for inorganic nanoparticles.[17]

Synthesis method	Synthesis conditions	T (°C)	Reaction time	Solvent type	Size (nm)	Size control	Morphology control	Yield
Coprecipitation	Very simple	20-90	Very short	aqueous	< 20	Not well controlled	Medium	High
Microemulsion	Difficult	20-50	Short	aqueous/ organic	< 50	Narrow	Good	Low
Polyol	Very simple	> 180	Short	organic	< 10	Narrow	Very good	Medium
Hydrothermal	Simple	> 200	Hours	aqueous / ethanol	< 1000	Narrow	Very good	Medium
Thermal decomposition	Difficult	200-350	Hours	organic	< 40	Highly controlled	Very good	High

Thermal decomposition method

The thermal decomposition method is based on the decomposition of an organic metallic precursor in a solvent at high temperature, typically from 290 to 350 °C. Thus organic solvents with high boiling temperatures are considered. The principle of this synthesis is governed by the LaMer theory[86] described in Figure 10 which was directly observed in solution thanks to in situ small-angle scattering.[87] When the solution containing the metallic precursor is heated to high temperature, the precursor starts to decompose and to form monomers which are the smallest building units. The concentration of the monomers then increase gradually in solution up to a critical supersaturation concentration (S_C) where the energy is high enough to overcome the energy barrier of the burst of nucleation. The monomers aggregate forming nucleus and their concentration in solution rapidly drops down to S_C, where the homogeneous nucleation of the monomers stop and the growth step starts. This last is favored by the fact that the energy barrier of growth is much lower than the energy barrier of nucleation. As the nucleus were formed simultaneously and rapidly, they all display the same size which allow the nuclei to grow at the same time, thus giving rise to the narrow size distribution of the nanoparticles.[88,89] If the reaction time is continued during the growth step, the nanoparticles are subjected to a new process called Ostwald-Ripening where the smallest nanoparticles are resolubilized in solution in order to grow on the biggest ones.

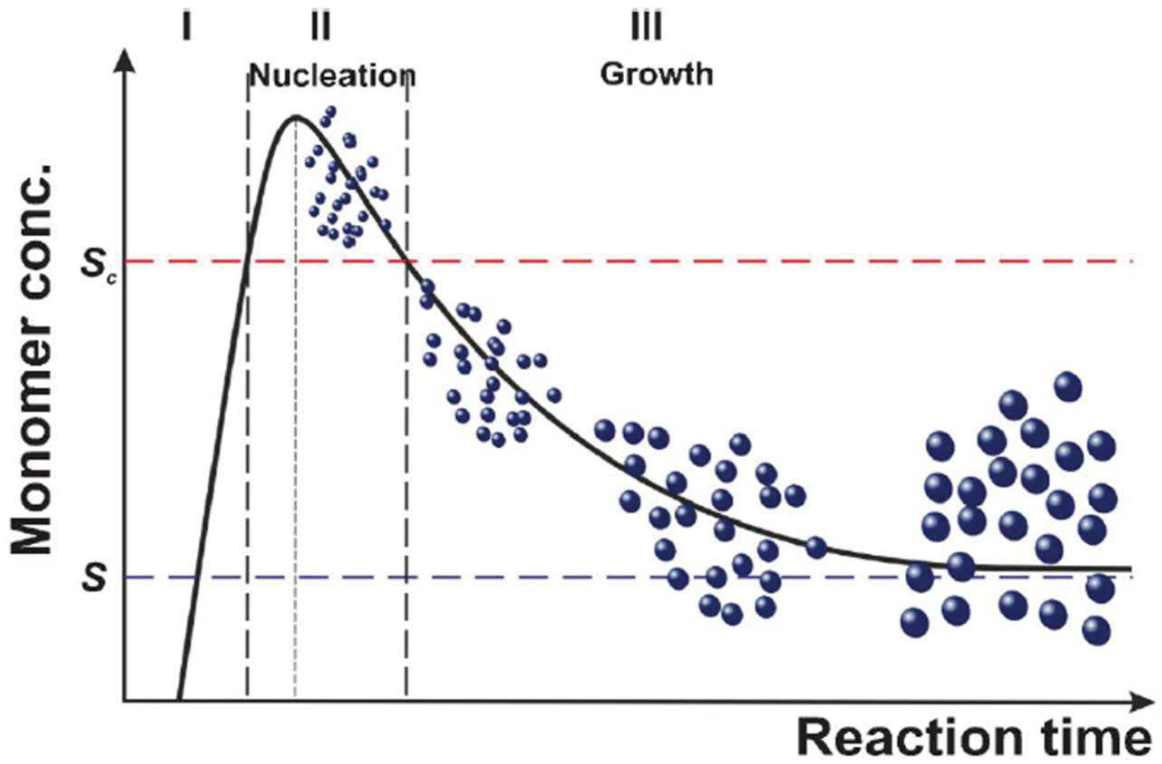

Figure 10. Schematic representation of the LaMer theory governing the synthesis of nanoparticles in solution.[88]

The thermal decomposition method allows to produce a large quantity of controlled size nanoparticles in a few hours. It consists in decomposing an organo metallic precursor in a high boiling point solvent with the eventual presence of a surfactant. This synthesis is ruled by the LaMer theory where the monomer concentration in solution allows to control the nucleation and growth step and de facto the structure of the resulting nanoparticles.

Seed-mediated growth synthesis by thermal decomposition

The synthesis conditions of the thermal decomposition may be modified by the presence of seeds in the reaction medium. According to ref,[90] the seed-mediated growth in solution occurs in three stages (Figure 11):

1/ The heating of a solution containing seeds and metallic precursors generates monomers, leading to a first burst of nucleation. This heterogeneous nucleation allows to block the seed from a rapid growth and will later act as a monomer tank for the growth of the nanoparticles. The primary nucleation is then followed by a second burst of nucleation located at the surface of the seeds.

2/ An intraparticle ripening process occurs which is different from Ostwald ripening. There, the smallest particles synthesized from the first burst of nucleation dissolve. The size-dependent dissolution of the nanoparticles is proportional to 1/(exp(diameter)) according to the Gibbs-Thomson equation.[91] Their dissolution participates to a dynamic equilibrium of the monomer concentration which is mainly governed by their diffusion and allows the growth of the remaining nanoparticles.

3/ Once the monomers are entirely consumed, the small nanoparticles dissolve at the expense of the larger ones, according to the Ostwald ripening process.

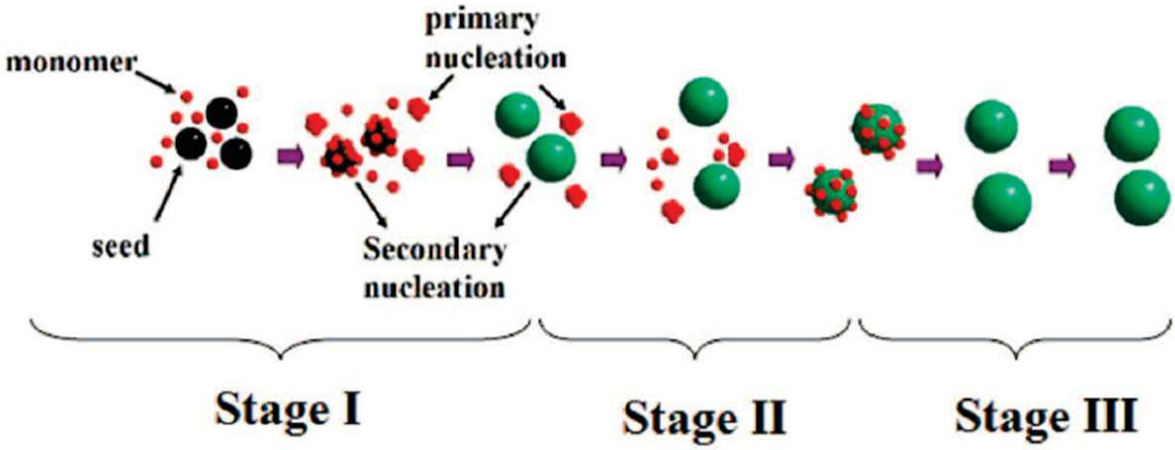

Figure 11. Schematic representation of a seed-mediated growth synthesis. From ref.[90]

In thermal decomposition, the seed-mediated growth synthesis lowers the energy barrier of nucleation and helps to decompose an organo-metallic precursor.

MnO, CoO and NiO wüstite phases as shells

Thus the thermal decomposition method allows to finely control the structure of the nanoparticles. However, in order to synthesize hybrid exchange-biased core@shell nanoparticles, the shell has to display good epitaxial relationship with the $Fe_{3-d}O_4$ core. In the literature, three components were mainly reported: MnO, CoO and NiO.

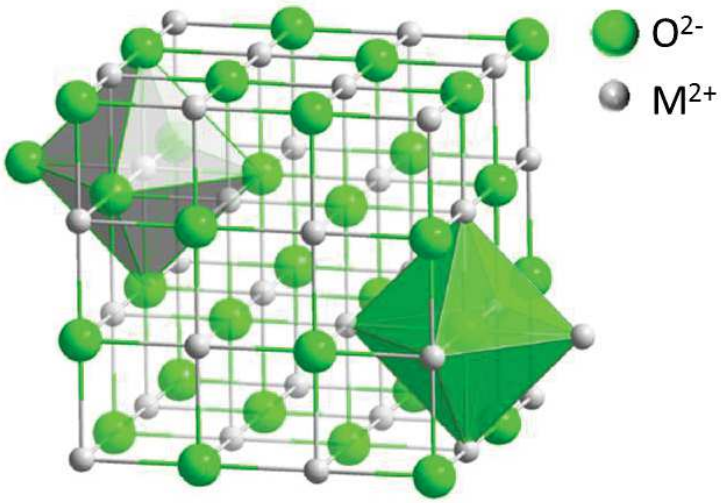

Figure 12. Representation of the primitive cell of a NaCl type structure in the case of MnO, CoO or NiO.

They all crystallize in the cubic Fm-3m space group according to the cubic centered face NaCl structure. The oxygens and metallic ions both form two networks that are nested one into the other. Hence, oxygens and metal ions are all in Oh sites. MnO, CoO and NiO are featured by cell parameters of 4.446 Å (JCPDS card n°04-005-4310), 4.2612 Å (JCPDS card n° 70-2856) and 4.1771 Å (JCPDS card n° 47-1049) respectively. As they crystallize in a similar space group as magnetite (Fd-3m) and their cells parameters match well with the 8.396 Å of magnetite nanoparticles, good epitaxial relationships between $Fe_{3-d}O_4$, MnO, CoO and NiO are expected.

Table 3. Main structural and magnetic characteristics of MnO, CoO and NiO.

	Cell parameter (Å)	K (kJ/m^3)	T_N (K)
MnO	4.4460	$2.8\ 10^{-2}$	118
CoO	4.2612	$5.0\ 10^{2}$	525
NiO	4.1771	8.0	290

In the MnO, CoO and NiO structures, the oxygens and metal cations, which are first neighbors, are ferromagnetically coupled. While two atoms that are second neighbors are antiferromagnetically coupled through super-exchange interactions. Thus MnO, CoO and NiO are antiferromagnets.
Moreover, the magnetic anisotropy constants are 0.028, 500 and 8 kJ/m^3 for MnO,[92] CoO[41] and NiO[93] respectively.
Concerning magnetite and maghemite, $K_{magnetite}$ = 11-13 kJ/m^3 [94] and $K_{maghemite}$ = 5-15 kJ/m^3 [76,95] in the bulk form. Thus, $K_{MnO} << K_{NiO} < K_{magnetite/maghemite} << K_{CoO}$. And, T_N of bulk MnO, NiO and CoO is 118, 525 and 290 K respectively while small iron oxide nanoparticles of 10 nm diameter display a T_B of 150 K.[25] Thus, T_N (MnO) < T_B ($Fe_{3-d}O_4$, 10 nm) < T_N (CoO) << T_N (NiO).

Wüstite MnO, CoO and NiO phases all crystallise in a similar space group as $Fe_{3-d}O_4$ with a good matching of their cell parameters. This should allow to get good epitaxial relationship between the phases in core@shell nanoparticles based on $Fe_{3-d}O_4$ nanoparticles. Furthermore, thanks to their AFM property, it is expected that the core@shell nanoparticles display exchange-bias properties in order to increase their magnetic order with respect to temperature.

$Fe_{3-d}O_4$@MnO nanoparticles

According to this, $Fe_{3-d}O_4$@MnO nanoparticles were synthesized.[67,96] In such nanoparticles, the exchange field can be very low (0.07 kOe[67]) or very high (5.9 kOe[96]) that we attribute to the structure of the core@shell nanoparticles. However, in both cases the exchange-bias coupling does not have a real impact on the blocking temperature of the nanoparticles were the maximum reaches 70 K.[96] Such consideration is attributed to the low magnetic anisotropy energies of MnO and magnetite and to the low T_N of MnO. Indeed, for an efficient exchange-bias coupling, $K_{AFM}V_{AFM}$ should be superior to $K_{FiM}V_{FiM}$ and to J_{int} and, T_B generally reaches a maximum which corresponds to T_N. Thus, they do not allow to increase so far the magnetic anisotropy energy of such core@shell nanoparticles.

The low magnetic anisotropy of $Fe_{3-d}O_4$ and MnO and the low T_N of MnO does not allow to increase the magnetic properties of the native iron oxide nanoparticles.

$Fe_{3-d}O_4$@NiO nanoparticles

Owing to the high T_N of NiO, $Fe_{3-d}O_4$@NiO nanoparticles were expected to display high T_B.[67,97,98] It appears that the core@shell nanoparticles all display very low exchange field arising from weak exchange bias coupling. This is attributed to the anisotropy constant of magnetite and NiO that are very close and that the condition $K_{AFM}V_{AFM} > J_{FiM\text{-}AFM}$ is not respected. Although T_N of NiO is much higher than room temperature, the T_B of the native iron oxide nanoparticles was not increased by the core@shell structure.[67,97]

Due to similar magnetic anisotropy of NiO and $Fe_{3-d}O_4$, the $K_{AFM}V_{AFM} > J_{int}$ condition is not satisfied, resulting in a very weak exchange-bias coupling in the $Fe_{3-d}O_4$@NiO nanoparticles.

$Fe_{3-d}O_4$@CoO nanoparticles

According to the very high magnetic anisotropy of CoO (500 kJ/m^3) compared to magnetite (11-13 kJ/m^3), $Fe_{3-d}O_4$@CoO nanoparticles evidenced the highest exchange field of the iron oxide based core@shell nanoparticles. Indeed, H_E reaches 4.3 kOe for a core size of 9.6 nm and a 1.5 nm thick shell.[52] Moreover, due to a high exchange coupling effect, the H_C of the native iron oxide nanoparticles has been drastically increased from 0.4 to 12.7 kOe for the best structure which consists in a core with a size of 8.2 nm and a shell thickness of 1.0 nm.[52] This coupling also allowed to increase T_B from 150 K for the 10 nm iron oxide nanoparticles up to 290-300 K for the $Fe_{3-d}O_4$@CoO nanoparticles.[47,67] Such improvements are attributed to the high pinning effect of the CoO shell with $K_{AFM}V_{AFM} >> J_{FiM-AFM}$ and also to a good crystallinity of the interface favored by the good epitaxial relationships.

Thanks to the high magnetic anisotropy and high T_N of CoO compared to $Fe_{3-d}O_4$, the T_B of $Fe_{3-d}O_4$@CoO nanoparticles was successfully increased up to 290 K as for H_C and H_E which appears to reach very high values.

AFM@FiM core@shell nanoparticles

Even if this thesis aims at studying the structure – magnetic properties relationship of FiM@AFM exchange-biased core@shell nanoparticles, exchange bias property were of course observed in inverted AFM@FiM ferrite based nanoparticles. Indeed, we have already discussed on the presence of exchange-bias properties in FeO@$Fe_{3-d}O_4$ nanoparticles (Table 4) which were synthesized thanks to the natural oxidation of the native AFM FeO nanoparticles. However, the main disadvantage of these nanoparticles is that the FeO phase is unstable and turns to the $Fe_{3-d}O_4$ when exposed to air.

Panagiotopoulos and al.[99] reported on the direct comparison of the magnetic properties of γ-Fe_2O_3@CoO (FiM@AFM) and CoO@γ-Fe_2O_3 (AFM@FiM) synthesized by thermal decomposition. They showed that in both cases, the dependence of H_E and H_C with respect to temperature is similar, describing an exponential decay. Unfortunately, due to the size difference between the two systems and to different dipolar interactions in the sample, they were not able to give a clear comment on the T_B properties.

In CoO@$CoFe_2O_4$ nanoparticles, no exchange field has been reported.[100–102] Such observation has been attributed to the higher interfacial coupling energy (J_{int}) than the magnetic anisotropy energy of the antiferromagnetic core ($K_{AFM}V_{AFM}$) and to similar magnetic anisotropy energy between both counterparts ($K_{AFM}V_{AFM} \simeq K_{FiM}V_{FiM}$). It was also observed that the T_B of the CoO@$CoFe_2O_4$ nanoparticles was higher than room temperature. It is worth noting that the ZFC M(T) curve evidenced a kink at 300 K which was attributed to the losse of the magnetic stability of the AFM CoO phase (T_N = 293 K). However, the absence of exchange bias coupling (no H_E and $T_B > T_N$) was not concomitant with the absence of magnetic coupling within the core@shell nanoparticles. Indeed, CoO@$CoFe_2O_4$ nanoparticles evidenced very high H_C in the order of 28 kOe at 5 K for a total diameter of 7 nm and a 2-3 nm thick shell.[100] The authors attributed such high H_C and T_B to the strong magnetic exchange coupling between the AFM core and the FiM shell. Such a result is supported by a study on size effects on CoO@$CoFe_2O_4$ nanoparticles.[101] The core size was tuned between 2.6 and 6.0 nm while the shell thickness was increased from 1.3 to 2.7 nm. While no H_E was measured whatever the core size of the nanoparticles and their shell thicknesses, H_C decreased from 30.8 to 21.5 kOe (at 5 K), and T_B increased from 167 to 388 K with the nanoparticle size. They also attributed this behavior to arise from a very strong magnetic exchange coupling between both phases, even for $T>T_N$, and to "the formation of a highly crystalline magnetic phase, which improves the coupling at the interface".
The gradual replacement of some Co atoms from the $CoFe_2O_4$ shell in the CoO@$CoFe_2O_4$ nanoparticles according to CoO@$Zn_xCo_{1-x}Fe_2O_4$ nanoparticles with x = 0, 0.25, 0.5, 0.75 and 1.0 [102] showed very high

H_C for x = 0 with the absence of H_E. Such behavior was also attributed to both conditions where $K_{AFM}V_{AFM} \simeq K_{FiM}V_{FiM}$ and $J_{int} > K_{AFM}V_{AFM}$. However, the increase of x to 0.25 led to the appearance of H_E but to the decrease of H_C ; and the further gradual increase of x was concomitant with the gradual decrease of H_C and H_E. The authors attributed this behavior to the gradual decrease of J_{int} and to the decrease of the exchange bias coupling where $ZnFe_2O_4$ has 0 μ_B of magnetic moment compared to $CoFe_2O_4$ which displays 3.7 μ_B.
Lavorato and al.[103] has synthesized inverted ZnO@$CoFe_2O_4$ (diamagnetic@FiM) and CoO@$CoFe_2O_4$ core with similar core diameters of 4.0 nm and shell thicknesses of 2.0 nm. Such considerations allow to directly compare the magnetic properties of both systems. Hence, they showed that the magnetic properties recorded for ZnO@$CoFe_2O_4$ nanoparticles arise mostly from surface effects. However, the replacement of the diamagnetic ZnO by an AFM CoO core allowed to reduce the magnetic surface disorders and to increase thus H_C from 7.8 to 27.8 Koe (at 5K) and T_B from 106 to 276 K.

Even if this thesis studies the exchange bias coupling in FiM@AFM nanoparticles, the presence of exchange-bias properties were also reported in AFM@FiM nanoparticles of diverse chemical composition. Different examples are listed above.

Table 4. Principal characteristics of iron oxide based nanoparticles displaying exchange-bias properties.

		Core				CS				Ref
	Type of interfacial coupling	**Size (nm)**	**H_C (kOe)**	**H_E (kOe)**	**T_B (K)**	**Size (nm)**	**H_C (kOe)**	**H_E (kOe)**	**T_B (K)**	
$Fe_{3-d}O_4$ under 5 GPa pressure	FiM	20	0.9	0.8	100					78
γ-Fe_2O_3	FiM	4	1.2	0.8	7					75
		7	0.3	0.03	20					76
		9.5	1.9	1.3	75					77
$CoFe_2O_4$	FiM	21	0.8	0.3	263					58
$Fe_{3-d}O_4$@CoO	FiM/AFM	6.6	0.3	0.04	150	7.9	2.98	0.2	300	67
		8	0.4	8.1	150	8.6	18.0	0.23	225	52
		8.9	-	-	-	10.6	20.6	1.4	264	
		8.2	-	-	-	10.1	12.7	5.1	256	
		9.6	-	-	-	12.6	8.4	4.3	254	
		8.3	-	-	-	13.4	6.1	1.9	225 K	
		11.2	0.4	-	150	14.2	15.2	4.1	290	47
		10	0.2	-	138	20	8.2	0.9	285	104
		5	-	-	-	7.5	10	1.1	150	99
$Fe_{3-d}O_4$@NiO	FiM/AFM	6.6	0.3	0.04	150	7.9	0.6	0	150	67
		6.6	0.3	0.05	75	2.3&6.5	600	15	75	97
		17.1	-	-	-	-	0.2	0.05	-	98
		18.2	-	-	-	-	0.1	0.06	-	98
$Fe_{3-d}O_4$@MnO	FiM/AFM	6.6	0.3	0.04	150	7.9	0.5	0.07	150	67
		6	0.3	0.2	35	19	5.1	5.9	70	96
γ-Fe_2O_3@CuO@Cu	FiM/AFM	6.5	0.4	0.04	50	7.5	0.5	0.02	50	105
$CoFe_2O_4$@MnO	FiM/AFM	4.5	16	-	200	8	2.5	0.6	100	106
CoO@γ-Fe_2O_3	AFM/FiM	-	-	-	-	-	9.1	2	50	99

		Core				CS				Ref
	Type of interfacial coupling	Size (nm)	H_C (kOe)	H_E (kOe)	T_B (K)	Size (nm)	H_C (kOe)	H_E (kOe)	T_B (K)	
$CoO@CoFe_2O_4$	AFM/FiM	2	-	-	-	7	27.8	0	$\simeq$ 325	100
		2.6	-	-	-	5.1	30.8	0	167	101
		3.8	-	-	-	8.2	27.8	0	271	
		6	-	-	-	11.3	21.5	0	388	
		4	-	-	-	8.2	27.8	0	$\simeq$ 320	103
		3	-	-	-	12	21.5	0	>300	102
$CoO@Co_{0.75}Zn_{0.25}Fe_2O_4$		3	-	-	-	10	14.6	1.44	122	
$CoO@Co_{0.5}Zn_{0.5}Fe_2O_4$		3	-	-	-	10.5	11.3	1.11	112	
$CoO@Co_{0.25}Zn_{0.75}Fe_2O_4$		3	-	-	-	11.7	8.5	0.83	137	
$CoO@ZnFe_2O_4$		3	-	-	-	10.4	7.1	0.3	123	
$ZnO@CoFe_2O_4$		4	-	-	-	8.1	7.8	0	200	103
$FeO@Fe_{3-d}O_4$	AFM/FiM	7	-	-	-	14	0.7	0.5	Approx 100 K	79
		27	-	-	-	35	0.9	2.3	270	107
		18	-	-	-	24	0.8	3.7	220	108
		1	-	-	-	18	2.1	1	-	
		-	-	-	-	10.1	-	1.7	220	109
		10	-	-	-	23.2	2.3	1.6	>275	82
		7	-	-	-	-	1	0.4	270	
$Fe_{3-d}O_4@CoFe_2O_4$	FiM/FiM	21	1.6	-	250	-	4	-	310	110
		9	837	-	130	-	4.7	-	210	
$Fe_{3-d}O_4@\gamma\text{-}Fe_2O_3$	FiM/FiM	-	-	-	-	12	-	0.1	180	84
$MnFe_2O_4@\gamma\text{-}Fe_2O_3$	FiM/FiM	2.8	-	-	-	3.6	-	0.09	-	85
$CoFe_2O_4@\gamma\text{-}Fe_2O_3$	FiM/FiM	3.3	-	-	-	4.3	-	0.12	-	

FiM@FiM hard-soft magnetic exchange coupled core@shell nanoparticles

Core@shell nanoparticles composed of only FiM materials which are featured by a difference of magnetic anisotropy energy of at least one order of magnitude can also show a global increase of the magnetic anisotropy energy. Such behavior is due to a strong magnetic coupling between a hard (low saturation magnetization and high H_C) and a soft (high saturation magnetization, low H_C) phase and was reported for magnetic bilayers[111] and also for core@shell nanoparticles.[73]

According to the thickness of the soft phase compared to the hard phase, the magnetic properties of the hybrid material can be modified. Indeed, for a thickness lower than twice the width of a domain wall defined by $\delta_H = \pi(A_{hard}/K_{hard})^{1/2}$ with A_{hard} the exchange stiffness, the soft and hard phases are strongly exchanged coupled. It results that their magnetizations reversed coherently with the application of an external magnetic field, leading to a rectangular shape of the hysteresis curve. However if the thickness of the soft materials is higher than twice the width of a domain wall, the soft phase nucleates the reversal of magnetic moments at much lower field than the hard phase. It causes an inhomogeneous magnetic reversal characterized by steps in the hysteresis curve. This phenomenon is called exchange spring magnet.

Strongly exchange coupled FiM/FiM core@shell nanoparticles such as $Fe_{3-d}O_4$@$CoFe_2O_4$ nanoparticles allowed to show high H_C of 4.7-4 kOe and high T_B of 210-310 K for size small of 9-21 nm.[110] A similar behavior was reported for Co@γ-Fe_2O_3 FM@FiM nanoparticles of 15 nm which display a T_B higher than 350 K but a low H_C of 0.8 kOe.[112]

Interestingly, the order of the phases has an effect on the resulting magnetic properties of the core-shell nanoparticles. For core@shell nanoparticles featured by a hard core and a soft shell which is the conventional system, the resulting hysteresis shows an enhancement of M_S and a reduction of H_C.[113–117] While for inverted systems with a soft core and a hard shell, the inverse effect has been reported. If M_S of the two phases are identical, the resulting M_S remains constant with an increase of H_C which depends on the hard/soft volume ratio.[46,117–120] These results agree with the magnetic characteristics of hard and soft phases as mentioned in the first paragraph of this section.
Some studies are also focusing on the gradual increase of the hard (or soft) magnetic shell on the soft (or hard respectively) counterpart and evidenced an almost linear evolution of H_C according to the hard/soft volume ratio.[113,116,117,120,121]
The hard-soft coupling also has an influence on the blocking temperature. As T_B depends on the KV product, in a strongly exchange coupled system, it will depend on the hard/soft volume ratio.[73,117] Indeed, considering similar core size and similar shell thickness, T_B of a soft@hard system will increase faster than for a hard@soft system, owing to the higher K of the hard phase than for the soft counterpart.[117] In contrast, as in a spring magnet, the hard and soft layers are not magnetically coupled, two blocking temperatures can be measured which correspond to the T_B of each counterpart.

FiM@FiM magnetic nanoparticles can evidence an exchange magnetic coupling if the magnetic anisotropy constant of the core and the shell is different of at least one order of magnitude. If the phases evidence a good magnetic coupling, the resulting magnetic properties of the core@shell nanoparticles will display an intermediate behavior between the magnetic properties of the hard and soft phases. While if the magnetic coupling of both phases is not efficient, the magnetic properties of the core@shell nanoparticles will result in the addition of the magnetic properties of both counterparts. In a strongly exchange coupled core@shell nanoparticles, the order of the soft and hard phase has an impact on the resulting magnetic properties. Indeed, using a hard core and a soft shell leads to the enhancement of M_S and to the reduction of H_C, while for an inverted system (soft core and hard shell), M_S decreases and H_C increases.

Onion-type magnetic nanoparticles

As shown in Table 4, ferrite based exchange biased core-shell nanoparticles display maximum T_B around room temperature which is not suitable for applications dealing with data storage. To increase further the overall magnetic anisotropy energy of exchange biased core-shell nanoparticles, the doubling the FiM/AFM interface may solve this issue. Only a few articles reports the synthesis of onion-type magnetic nanoparticles which consist of one or two extra shells grown at the surface of core-shell nanoparticles.
FeO@Fe_3O_4@MnO@Mn_3O_4 nanoparticles were synthesized by Salazar-Alvarez and al.[122] with three FiM/AFM interfaces (AFM/FiM/AFM/FiM). The FeO core was first synthesized and exposed to air to form the FeO@Fe_3O_4 nanoparticles. The core@shell nanoparticles were used as seeds to synthesize FeO@Fe_3O_4@MnO nanoparticles where upon exposure to air, MnO has been partially oxidized into Mn_3O_4 resulting in the creation of the FeO@Fe_3O_4@MnO@Mn_3O_4 nanoparticles. The seeds consist of truncated cubes with edge length of 11 nm while the final nanoparticles display a cuboctahedron or truncated cuboctahedron shape with a size of around 34 nm. They have also synthesized smaller nanoparticles of final size of 14 nm which resulted in a solely FeO@Fe_3O_4@Mn_3O_4 (core@2-shell) structure where, all the native MnO were oxidized into Mn_3O_4. The FeO@Fe_3O_4 seed displays a T_B of 120 K which is increased to 200 K when the seeds are covered by a thin Mn_3O_4 shell. This is due to a

strong exchange coupling between the Fe_3O_4 and Mn_3O_4 components that have magnetic anisotropy constants of 2.0 10^4 J/m^3 [123] and 1.4 10^5 J/m^3 [124,125] respectively. At the opposite, the core@3-shell nanoparticles evidence several T_B of 40, 120 and 130 K corresponding to the magnetic order transition temperature of MnO, Mn_3O_4 and FeO@Fe_3O_4 respectively. Despite a higher exchange field in the core@3-shell nanoparticles than in the core@2-shell nanoparticles, the presence of three different T_B suggests a weak coupling effect in the overall nanoparticle. Finally, the author attributes the magnetic properties in the core@2-shell nanoparticles to be dominated by interfacial effects while MnO dominates the magnetic properties of the core@3-shell nanoparticles.

Krycka and al.[126] synthesized 6 nm magnetite nanoparticles surrounded by a 30 nm thick MnO shell which upon exposure to air were partially oxidized into 5 nm thick γ-Mn_2O_3. They compared the magnetic properties of this core@2-shell nanoparticle to the ones of a Fe_3O_4@γ-Mn_2O_3 core@shell nanoparticles with a core of 3 nm of diameter and a 2.5 nm thick shell. The magnetic properties of Fe_3O_4@MnO@γ-Mn_2O_3 FiM@AFM@FiM and Fe_3O_4@γ-Mn_2O_3 FiM@FiM nanoparticles were probed with polarized small angle neutron scattering. They showed that the spins within the core and the shell in the core@shell nanoparticles rotate together as expected from a strong exchange coupling. And that there exists a magnetic proximity effect between MnO and γ-Mn_2O_3 in the core@2-shell nanoparticles where the spins in γ-Mn_2O_3 remain magnetically ordered above T_C of γ-Mn_2O_3

In another system, a succession of three thermal decompositions was performed to synthesize $MnFe_2O_4$@$CoFe_2O_4$@$NiFe_2O_4$ nanoparticles.[127] The core@shell@shell nanoparticle consists of a core of size of 5.5 nm surrounded by 1.2 nm thick $CoFe_2O_4$ and 2.0 nm thick $NiFe_2O_4$ shells. Thanks to this, T_B was increased from 20 K to 190 and 220 K for the core, core@shell and core@shell@shell nanoparticles respectively. Only one T_B was measured for each sample, showing the strong magnetic exchange coupling between the different phases of the trimagnetic nanoparticles. Furthermore, H_C has been increased from 0.07 to 10.6 kOe from the core to the core@shell. However, it decreases to 7.7 kOe for the core@shell@shell nanoparticles which is concomitant with the addition of the soft $NiFe_2O_4$ shell with respect to the hard $CoFe_2O_4$ counterpart.

Only a few articles report on the synthesis of core@shell@shell magnetic nanoparticles. They show that such strategy allows to tune the magnetic properties of the system and more precisely to increase the mean T_B of the system. Nevertheless, they also show that the control of the structure of such material is crucial in order to produce a strong magnetic coupling between each phase.

Conclusion of the introduction

According to the literature, it is possible to tune the magnetic properties of nanoparticles by designing core-shell structures. However the combination of different magnetic crystal phases is restricted to chemical structures with low lattice mismatch in order to allow good epitaxial relationship. Furthermore, the fine tuning of the magnetic properties through interfacial exchange coupling requires several prerequisites (adaptation of K and T_N between the counterparts). This field of research can be further investigated by designing onion-type nanoparticles with multiple interfaces. Although these structures are very promising, they remain scarcely explored. In this frame, this thesis divided in 5 chapters, explores the strategy from the bottom to the top to design ferrite based nanoparticles with enhanced magnetic properties.

I/ Iron oxide magnetic nanoparticles were grown according to a multi-seed mediated growth approach which consists in a succession of five thermal decompositions. It is the first time that so many thermal decomposition were proceeded one after the other. This study allowed us to investigate the oxidation behavior in core(@shell)n iron oxide nanoparticles. Furthermore, it has also demonstrated that it is possible to grow more than three shells on a nanoparticle by preserving the fine control of shape, size and size distribution.

II/ Bi-magnetic core@shell nanoparticles were synthesized via the seed-mediated growth approach. The fine tuning of the experimental conditions resulted in the growth of CoO or $CoFe_2O_4$ as shells at the surface of $Fe_{3-d}O_4$ nanoparticles. The fine study of their structure revealed that the interface and the nature of the shell play a huge role on the exchange coupling between a soft core and a hard shell. This chapter has also proved the formation of an interfacial Co-doped layer within the $Fe_{3-d}O_4$@CoO nanoparticles which contribute to the enhancement of the magnetic properties.

III/ Above a maximum temperature of 290 K, the AFM CoO loses its magnetic order and thus its ability to pin the FiM of iron oxide. In consequence, the T_B of $Fe_{3-d}O_4$@CoO nanoparticles cannot reach a temperature higher than 290 K. However, as exchange-bias properties were reported to increase the magnetic stability toward room temperature, $Fe_{3-d}O_4$@CoO@$Fe_{3-d}O_4$ nanoparticles were synthesized in order to benefit of a double FiM/AFM interface. It is expected that such structures would increase further the effective magnetic anisotropy compared to simple $Fe_{3-d}O_4$@CoO nanoparticles. The use of a large range of analytic techniques has shown that the structure is more complicated than the expected $Fe_{3-d}O_4$@CoO@$Fe_{3-d}O_4$. Indeed, the presence of interfacial layers resulting from atomic diffusion has a high impact on the resulting magnetic properties of the onion type magnetic nanoparticles.

IV/ The synthesis of $Fe_{3-d}O_4$@$CoFe_2O_4$@$Fe_{3-d}O_4$ nanoparticles was expected to further increase the effective magnetic anisotropy energy of the iron oxide based nanoparticles through a double soft@hard and hard@soft magnetic coupling. Selective hysteresis measurements have shown strong magnetic coupling between each phases of the nanoparticles. However, all analysis techniques agree on the increase of the cobalt ferrite shell during the synthesis of the core@shell@shell nanoparticles. Thanks to the concomitant use of the different analytical techniques, it was possible to determine the real composition of the final nanoparticles and the true size and thicknesses of each phase. SQUID magnetometry measurements agrees with this model and evidenced further the complexe structure of the $Fe_{3-d}O_4$@$CoFe_2O_4$@$Fe_{3-d}O_4$ nanoparticles that has been studied in details.

V/ Onion type nanoparticles have shown their efficiency in the two previous chapters. Hence, in this chapter, onion type magnetic nanoparticles were synthesized with a NiO shell. It is expected through proximity effects that $Fe_{3-d}O_4$@CoO nanoparticles would benefit of the high T_N of NiO (525 K), in synthesizing $Fe_{3-d}O_4$@CoO@NiO nanoparticles. Indeed, De Toro and *al.*[128] have shown the drastic

increase of the magnetic stability toward room temperature of Co@CoO nanoparticles thanks to their deposition in a NiO matrix. However the decomposition of Ni based organo metallic precursor is scarcely reported in the literature. Thus the first approach consisted in studying the decomposition of Ni based precursor and synthesizing a precursor that meets the standard decompositions required for the thermal decomposition method. Afterwards, the growth of a NiO shell according to a seed-mediated growth approach has been studied. These preliminary studies required for the synthesizing of onion type nanoparticles containing NiO are presented in annexes. During the preliminary studies, we have evidenced that the shape of the core@shell nanoparticles have an effect on the growth of the NiO shell. According to this, chapter V reports on the synthesis of two different series of $Fe_{3-d}O_4$@CoO@NiO nanoparticles, a cubic one and a spherical one. They both show different magnetic behavior. In order to find their origin, we have investigated the structure and growth mechanisms of these cubic and spherical $Fe_{3-d}O_4$@CoO@NiO nanoparticles.

Complementarity of analysis techniques

The main purpose of this manuscript is to study the structural – physical properties relationship of each synthesized core@shell and core@shell@shell nanoparticles. The precise understanding of the origin of the magnetic properties in such complex nanoparticles requiring the deep investigation of their structure. In consequence, a wide set of experimental techniques with high complementarity was used.

Transmission electron microscopy

Due to high surface over volume ratio on the magnetic properties, the fine control of narrow size distribution and well defined shape is critical. Transmission electron microscopy (TEM) is a very local analysis which allows to calculate the mean size of a batch of nanoparticles with a standard deviation, in measuring a large number of nanoparticles (more than 300 in this manuscript). However, according to the very small size of our nanoparticles (< 20 nm), TEM only allows to record 2D micrographs while the nanoparticles display a 3D shape. The chemical composition can also be investigated with energy dispersive spectroscopy (EDS). This technique records the emission of a X photon following the relaxation of an atom after the removal of a core electron. While more local analysis such as energy filtered TEM (EFTEM) and electron energy loss spectroscopy or spectrum imaging (EELS-SI) mode allow to directly measure the atomic distribution on a single nanoparticle and thus to have a real overview of the structure of a core@multi-shell nanoparticle in displaying a chemical map.
Moreover, with the TEM, it is also possible to look at the crystalline structure of the nanoparticles by recording high-resolution micrographs (HR-TEM). Hence, it is possible to observe the lattice fringes of single crystal nanoparticles. If the different layers in a core@multi-shell nanoparticle display good epitaxial relationship, the fringes will appear periodic and continuous all across the nanoparticle without any defect. This is a good indication on the absence of multi crystal domain and crystal defects.

X-ray diffraction

The first use of XRD is generally to identify the chemical structure via the position and intensity of the peaks present in the diffractogram. Indeed, each peak arises from a specific reflection of a Bragg plan of the probed crystal which obey the Bragg law $2d_{hkl}sin\theta = \lambda n$, with d_{hkl} the inter-reticular distance, θ the Bragg angle or half-angle deviation and n the diffraction order. In a classical laboratory x-ray diffractometer, the wavelength λ corresponds to the cupper Kα edge of 1.5406 Å.
The crystal structure of the nanoparticles was also investigated by X-ray diffraction (XRD) where the evolution of the broadness of the peaks is an indication of a good epitaxial relationship. Indeed, the width of a peak reflects the crystal size and its narrowing is a consequence of a larger crystal size. According to the Debye-Scherrer equation, it is possible to calculate this size (t) from the full-width at half maximum of a peak (H)

$$t = \frac{k\lambda}{(H - s)cos\theta}$$

With λ, s and θ being the incoming beam wavelength, an instrumental error factor and the angle respectively. X-ray diffraction is also used to determine the mean cell parameter which is inherent to the structure of each material.
It is also possible to determine the cell parameter (a) of a cubic system according to the inter-reticular distance and the index of the h, k and l plans.

$$a = d_{hkl}\sqrt{h^2 + k^2 + l^2}$$

The cell parameter is inherent to each structure and can also give information on the stoichiometry and oxidation of a chemical compound. For example, magnetite displays a cell parameter of 8.396 Å (JCPDS card n° 19-062) while its oxidized phase, maghemite, evidence a cell parameter of 8.338 Å 5JCPDS card n° 39-1346). Due to very close cell parameter, the resolution of XRD does not allow to get a precise oxidation state of the nanoparticles.

Fourier transform infrared

Fourier transform infrared (FT-IR) is used to determine the chemical composition of the nanoparticles and the interaction mode between the nanoparticles and their stabilizing agents and also between the metallic ions and the ligands in the precursor. It is also possible to evidence the presence of impurities and side products resulting from the synthesis of precursors and of nanoparticles. Moreover, after the synthesis of the nanoparticles by thermal decomposition, this technique allows to follow the good cleaning of the nanoparticles thanks to the decrease of the $\nu_{s\text{-}as}/\nu_{M\text{-}O}$ ratio where $\nu_{s\text{-}as}$ is the symmetric (s) and antisymmetric (as) vibration of C-H bonds from CH_2 group between 2 925 and 2 855 cm^{-1} and $\nu_{M\text{-}O}$ is the vibration of the metal-oxygen bond centered around 570 cm^{-1} for Fe_3O_4. The nanoparticles are considered clean when this ratio reaches 1 as some oleic acid ligands grafted at the surface of the nanoparticles are still present, allowing their colloidal stability. If the $\nu_{s\text{-}as}/\nu_{M\text{-}O}$ ratio is lower than 1, it can result in the appearance of aggregates due to the fact that the quantity of oleic acid surfactant grafted at the surface of the nanoparticles is not sufficient to induce steric repulsions between the nanoparticles. Furthermore, FT-IR also evidences the good removal of the free stearate and free oleic acid surfactant in the case of nanoparticles.

Granulometry

Besides the control of the structure of the nanoparticles, stable suspensions are prerequisite for biomedical applications and applications based on nanoparticles assemblies as high ordered arrays. The thermal decomposition method allows the nanoparticles to have surfactant grafted at the surface of the nanoparticles which ensure their stability in suspensions. A first indication of the size of the nanoparticles is given by granulometry measurements also called dynamic light scattering (DLS) or photon correlation spectroscopy (PCS). It consists in recording the intensity of an incident scattered beam by the nanoparticles as a function of the time. The nanoparticles in solution are subjected to Brownian motion due to the thermal agitation. A fit of the light intensity in function of the time according to the Stokes-Einstein equation allow to determine the hydrodynamic diameter (D_h) which depends on the temperature (T), the carrier liquid viscosity (η) and the diffusion coefficient (D_t):

$$D_h = \frac{k_B T}{3\pi\eta D_t}$$

The hydrodynamic diameter includes the size of the inorganic nanoparticles coated by the ligands grafted at their surface. Granulometry allows to determine the number of particles in solution, their hydrodynamic volume or intensity.

Small-angle X-ray scattering

Thanks to the high penetration of X-rays in matter, it is possible with SAXS to probe nanoparticles in suspension in solutions and to determine the volume of the nanoparticles, their size distribution, their shape and their aggregation rate in solution. Hence this technique is complementary to granulometry and even more precise and performant. Small-angle X-ray scattering (SAXS) is very similar to small-angle neutron scattering (SANS), which is described latter, as they are both small angle scattering analysis. However they are highly complementary because the probing particle is different: while neutrons probe the nucleus, X photons probe the electrons.

^{57}Fe Mössbauer

Mössbauer is a spectroscopic technique discovered in 1958 by Rudolf Mössbauer. ^{57}Fe Mössbauer requires the use of a ^{57}Co source that emits a γ beam which interacts with the ^{57}Fe atoms in order to investigate the interactions between nucleus and electron of ^{57}Fe atoms. Hence it is at the frontier between SANS and XMCD technics. A fit of the intensity in function of the velocity (mm/s) spectra allows to determine:

- the isomer shift which is influenced by the interactions between the electron and the nucleus of an atom, it is used to describe the valence state of the iron atoms
- the quadrupole shift depends on the interaction between the quadrupole moment of the nucleus and an electrical gradient field which may lead to a splitting of the nuclear energy levels
- the hyperfine field which is influenced by the magnetic dipole moment – nucleus interactions. Moreover, the application of an external magnetic induction may induce a degeneracy of the energy levels and split the orbitals according to a Zeeman effect
- The relative subspectral area allows to determine the proportion of each component

Mössbauer, contrary to XMCD, is sensitive to the whole volume of the probed material and is thus complementary to this technique. Moreover, ^{57}Fe Mössbauer spectroscopy allows to bring additional information on the oxidation state and atomic nearest neighbors which comfort the complementarity with XAS analysis.

Big instruments

In exchange-biased and exchange coupled nanoparticles, the magnetic properties are governed by the interfacial structure. In order to probe such a small volume in the nanoparticles, it is required to use highly structurally, spatially and energy resolved instruments. This is only possible with instruments at large scale facilities such as synchrotron and neutrons beam.

X-ray absorption (XAS, XMCD)

Another technique which uses X-ray is the X-ray absorption spectroscopy (XAS). This technique has the ability to be chemical and spin selective, and to probe the environment of specific atoms contrary to Mössbauer spectroscopy which only probes the ^{57}Fe nucleus. Hence XAS brings additional information on the site occupancy and oxidation degree of each type of atoms.

Thanks to it, Brice-Profeta and *al.*[129] have investigated the effect of the oxidation rate of $Fe_{3-d}O_4$ for $0 < d < 1$ in the XAS-XMCD spectra recorded at the Fe edge. Owing to the chemical selectivity of x-ray absorption spectroscopy, Byrne and *al.*[130] have evidenced that the increase of Co content based precursor for an equivalent content of Fe based precursor led to the synthesis of $Co_{1-x}Fe_{2+x}O_4$ nanoparticles where Co atoms mostly substitute in Oh sites while a small fraction (likely 17 %) of Co atoms surprisingly substitutes in Td sites. Such structural properties are responsible of the recorded

magnetic properties showing the drastic increase of H_C as long as the Co content is increased, followed by a decrease of this parameter for very high Co content. Skoropata and *al.*[97] has studied the effect of a NiO shell on a maghemite core of 6.6 nm of size. They showed a strong magnetic coupling between the iron oxide core and the NiO shell favored by the presence of an interfacial Ni-ferrite, leading to an increase of H_C in the core@shell compared to the core nanoparticles. In ref,[67] XAS and XMCD were used in order to probe the magnetic interface in g-Fe_2O_3@wüstite (with wüstite = CoO, MnO or NiO). It has thus been showed that the magnetic properties are mostly due to an interfacial doped layer synthesized by the migration of the metals of the wüstite shell in the maghemite core.

Hence, XAS-XMCD appears to be a unique tool to separately probe the electronic properties of 3d transition element in complex structured nanoparticles. It allows to investigate the interfacial structure in core@shell nanoparticles. The physical principle of the XAS and XMCD techniques is described in annexe.

Small-angle neutron scattering

Small-angle neutron scattering (SANS) is a very powerful analysis method, complementary to XAS, XMCD as the probing particles, the neutrons, have the ability to interact with the nucleus of the atoms and not with the electrons as for Mössbauer spectroscopy. Contrary to Mössbauer spectroscopy, the neutrons interact which each type of atoms. The physical principle of this technique is described in annexe. Hence SANS was used in nanoparticles in order to determine their size, size distribution, shape, aggregation state and chemical composition.[131–133]
However, the major interest in this technic lies in the fact that polarized neutrons interact differently according to the magnetic properties of a sample. Hence polarized small-angle neutron scattering (p-SANS) was used in order to determine the spin configuration in nanoparticles. It evidenced in most cases the presence of spin canting effect[133] and allows to determine the spin direction of the magnetic shells compared to the spins of the magnetic core.[134,135] Owing to the high penetration depth of neutrons, p-SANS was also used to determine the spin configuration in more complex structures such as chemical core@shell structures.[126,136]

Magnetometry measurements

Magnetometry measurements were performed with a super conductive quantum interference device (SQUID) which allows to record the magnetic response of a sample subjected to different conditions such as a change of temperature or external magnetic induction. In both cases, it can be recorded before (ZFC) or after field cooling (FC). Cooling a sample with an applied magnetic induction allows to orient the spins in the field direction while a ZFC favors unoriented spins directions.
SQUID magnetometry is sensitive to the whole material and do not discriminate the origin of the magnetic answer as in XMCD or p-SANS. It is useful to know the bulk magnetic properties in order to compare it to other systems in the literature but also for any further eventual applications such as recording media.
In SQUID measurements, it is possible to measure the magnetization by reversing the applied magnetic field. M(H) curves allow to determine the magnetic parameters of nanoparticles such as the coercive field, the remanent magnetization, the saturation magnetization and the exchange field. Hence, to study interfacial exchange coupling in nanoparticles and its consequence on the magnetic properties.
SQUID measurements can also probe the magnetization as a function of the temperature. M(T) curves gives precious information on the magnetic thermal stability of the nanoparticles through the blocking temperature as wall as the presence of exchange coupling.

Conclusion on the complementarity of analysis technics

The tuning of the magnetic properties of iron oxide based nanoparticles is at the heart of this thesis. However, as the magnetic properties come out from the structure of the probed material and as the structure of the newly designed core@shell and core@shell@shell nanoparticles is very complex, a wide panel of different and complementary analytic techniques has to be used.

References

(1) Pardavi-Horvath, M. Microwave Applications of Soft Ferrites. *J. Magn. Magn. Mater.* **2000**, *215–216*, 171–183. https://doi.org/10.1016/S0304-8853(00)00106-2.

(2) Tanaka, T.; Shimazu, R.; Nagai, H.; Tada, M.; Nakagawa, T.; Sandhu, A.; Handa, H.; Abe, M. Preparation of Spherical and Uniform-Sized Ferrite Nanoparticles with Diameters between 50 and 150nm for Biomedical Applications. *J. Magn. Magn. Mater.* **2009**, *321* (10), 1417–1420. https://doi.org/10.1016/j.jmmm.2009.02.054.

(3) Bender, P.; Fock, J.; Frandsen, C.; Hansen, M. F.; Balceris, C.; Ludwig, F.; Posth, O.; Wetterskog, E.; Bogart, L. K.; Southern, P.; et al. Relating Magnetic Properties and High Hyperthermia Performance of Iron Oxide Nanoflowers. *J. Phys. Chem. C* **2018**, *122* (5), 3068–3077. https://doi.org/10.1021/acs.jpcc.7b11255.

(4) Levy, M.; Quarta, A.; Espinosa, A.; Figuerola, A.; Wilhelm, C.; García-Hernández, M.; Genovese, A.; Falqui, A.; Alloyeau, D.; Buonsanti, R.; et al. Correlating Magneto-Structural Properties to Hyperthermia Performance of Highly Monodisperse Iron Oxide Nanoparticles Prepared by a Seeded-Growth Route. *Chem. Mater.* **2011**, *23* (18), 4170–4180. https://doi.org/10.1021/cm201078f.

(5) Sandu, I.; Presmanes, L.; Alphonse, P.; Tailhades, P. Nanostructured Cobalt Manganese Ferrite Thin Films for Gas Sensor Application. *Thin Solid Films* **2006**, *495* (1–2), 130–133. https://doi.org/10.1016/j.tsf.2005.08.318.

(6) Falsafi, F.; Hashemi, B.; Mirzaei, A.; Fazio, E.; Neri, F.; Donato, N.; Leonardi, S. G.; Neri, G. Sm-Doped Cobalt Ferrite Nanoparticles: A Novel Sensing Material for Conductometric Hydrogen Leak Sensor. *Ceram. Int.* **2017**, *43* (1), 1029–1037. https://doi.org/10.1016/j.ceramint.2016.10.035.

(7) Praveena, K.; Chen, H.-W.; Liu, H.-L.; Sadhana, K.; Murthy, S. R. Enhanced Magnetic Domain Relaxation Frequency and Low Power Losses in Zn2+ Substituted Manganese Ferrites Potential for High Frequency Applications. *J. Magn. Magn. Mater.* **2016**, *420*, 129–142. https://doi.org/10.1016/j.jmmm.2016.07.011.

(8) Kumbhar, V. S.; Jagadale, A. D.; Shinde, N. M.; Lokhande, C. D. Chemical Synthesis of Spinel Cobalt Ferrite (CoFe2O4) Nano-Flakes for Supercapacitor Application. *Appl. Surf. Sci.* **2012**, *259*, 39–43. https://doi.org/10.1016/j.apsusc.2012.06.034.

(9) Bashir, B.; Shaheen, W.; Asghar, M.; Warsi, M. F.; Khan, M. A.; Haider, S.; Shakir, I.; Shahid, M. Copper Doped Manganese Ferrites Nanoparticles Anchored on Graphene Nano-Sheets for High Performance Energy Storage Applications. *J. Alloys Compd.* **2017**, *695*, 881–887. https://doi.org/10.1016/j.jallcom.2016.10.183.

(10) Casbeer, E.; Sharma, V. K.; Li, X.-Z. Synthesis and Photocatalytic Activity of Ferrites under Visible Light: A Review. *Sep. Purif. Technol.* **2012**, *87*, 1–14. https://doi.org/10.1016/j.seppur.2011.11.034.

(11) Valero-Luna, C.; Palomares-Sanchéz, S. A.; Ruíz, F. Catalytic Activity of the Barium Hexaferrite with H 2 O 2 /Visible Light Irradiation for Degradation of Methylene Blue. *Catal. Today* **2016**, *266*, 110–119. https://doi.org/10.1016/j.cattod.2015.08.049.

(12) Hao, R.; Xing, R.; Xu, Z.; Hou, Y.; Gao, S.; Sun, S. Synthesis, Functionalization, and Biomedical Applications of Multifunctional Magnetic Nanoparticles. *Adv. Mater.* **2010**, *22* (25), 2729–2742. https://doi.org/10.1002/adma.201000260.

(13) Kim, D.; Shin, K.; Kwon, S. G.; Hyeon, T. Synthesis and Biomedical Applications of Multifunctional Nanoparticles. *Adv. Mater.* **2018**, *30* (49), 1802309. https://doi.org/10.1002/adma.201802309.

(14) Nemati, Z.; Alonso, J.; Rodrigo, I.; Das, R.; Garaio, E.; García, J. Á.; Orue, I.; Phan, M.-H.; Srikanth, H. Improving the Heating Efficiency of Iron Oxide Nanoparticles by Tuning Their Shape and Size. *J. Phys. Chem. C* **2018**, *122* (4), 2367–2381. https://doi.org/10.1021/acs.jpcc.7b10528.

(15) Lottini, E.; López-Ortega, A.; Bertoni, G.; Turner, S.; Meledina, M.; Van Tendeloo, G.; de Julián Fernández, C.; Sangregorio, C. Strongly Exchange Coupled Core|Shell Nanoparticles with High Magnetic Anisotropy: A Strategy toward Rare-Earth-Free Permanent Magnets. *Chem. Mater.* **2016**, *28* (12), 4214–4222. https://doi.org/10.1021/acs.chemmater.6b00623.
(16) Coey, J. M. D. Permanent Magnet Applications. *J. Magn. Magn. Mater.* **2002**, 16.
(17) Matthias, P. Structuration de nanoparticules magnétiques d'oxyde de fer en films et étude de leurs propriétés magnétiques et de magnétotransport, 2010.
(18) Mornet, S. Synthèse et Modification Chimique de La Surface de Nanoparticules de Maghémite à Des Fins d'applications Biomédicales, Bordeaux I, 2002.
(19) Morales, M. P.; Pecharroman, C.; Gonzalez-Carreño; Serna, C. J. Structural Characteristics of Uniform Y-Fe2O3 Particles with Different Axial (Length/Width) Ratios. *J. Solid State Chem.* **1994**, *108*, 158–163.
(20) Shmakov, A. N.; Krvukova, G. N.; Tsvbulva, S. V. Vacancy Ordering in Y-Fe203: Synchrotron X-Ray Powder Diffraction and High-Resolution Electron Microscopy Studies. 5.
(21) Morales, M. P.; Andres-Verges, M.; Veintemillas-Verdaguer; Montero, M. I.; Serna, C. J. Structural Effects on the Magnetic Properties of Y-Fe2O3 Nanoparticles. *J. Magn. Magn. Mater.* **1999**, *203*, 146–148.
(22) Park, J.; Lee, E.; Hwang, N.-M.; Kang, M.; Kim, S. C.; Hwang, Y.; Park, J.-G.; Noh, H.-J.; Kim, J.-Y.; Park, J.-H.; et al. One-Nanometer-Scale Size-Controlled Synthesis of Monodisperse Magnetic Iron Oxide Nanoparticles. *Angew. Chem. Int. Ed.* **2005**, *44* (19), 2872–2877. https://doi.org/10.1002/anie.200461665.
(23) Guardia, P.; Labarta, A.; Batlle, X. Tuning the Size, the Shape, and the Magnetic Properties of Iron Oxide Nanoparticles. *J. Phys. Chem. C* **2011**, *115* (2), 390–396. https://doi.org/10.1021/jp1084982.
(24) Demortière, A.; Panissod, P.; Pichon, B. P.; Pourroy, G.; Guillon, D.; Donnio, B.; Bégin-Colin, S. Size-Dependent Properties of Magnetic Iron Oxidenanocrystals. *Nanoscale* **2011**, *3* (1), 225–232. https://doi.org/10.1039/C0NR00521E.
(25) Baaziz, W.; Pichon, B. P.; Fleutot, S.; Liu, Y.; Lefevre, C.; Greneche, J.-M.; Toumi, M.; Mhiri, T.; Begin-Colin, S. Magnetic Iron Oxide Nanoparticles: Reproducible Tuning of the Size and Nanosized-Dependent Composition, Defects, and Spin Canting. *J. Phys. Chem. C* **2014**, *118* (7), 3795–3810. https://doi.org/10.1021/jp411481p.
(26) Dehsari, H. S.; Kasenofontov, V.; Möller, A.; Jakob, G.; Asadi, K. Determining Magnetite/Maghemite Composition and Core-Shell Nanostructure from Magnetization Curve for Iron Oxide Nanoparticles. *J. Phys. Chem. C* **2018**, No. 122, 28292–28301.
(27) Jeong, U.; Teng, X.; Wang, Y.; Yang, H.; Xia, Y. Superparamagnetic Colloids: Controlled Synthesis and Niche Applications. *Adv. Mater.* **2007**, *19* (1), 33–60. https://doi.org/10.1002/adma.200600674.
(28) Krishnan, K. M. Biomedical Nanomagnetics: A Spin Through Possibilities in Imaging, Diagnostics, and Therapy. *IEEE Trans. Magn.* **2010**, *46* (7), 2523–2558. https://doi.org/10.1109/TMAG.2010.2046907.
(29) Bedanta, S.; Kleemann, W. Supermagnetism. *J. Phys. Appl. Phys.* **2009**, *42* (1), 013001. https://doi.org/10.1088/0022-3727/42/1/013001.
(30) Frenkel, J.; Doefman, J. Spontaneous and Induced Magnetisation in Ferromagnetic Bodies. *Nature* **1930**, *126* (3173), 274–275. https://doi.org/10.1038/126274a0.
(31) Laurent, S.; Forge, D.; Port, M.; Roch, A.; Robic, C.; Vander Elst, L.; Muller, R. N. Magnetic Iron Oxide Nanoparticles: Synthesis, Stabilization, Vectorization, Physicochemical Characterizations, and Biological Applications. *Chem. Rev.* **2008**, *108* (6), 2064–2110. https://doi.org/10.1021/cr068445e.
(32) Lartigue, L. Synthesis and Characterization of Iron Based Nanoparticles, Université de Montpellier II, 2010.

(33) Kolhatkar, A.; Jamison, A.; Litvinov, D.; Willson, R.; Lee, T. Tuning the Magnetic Properties of Nanoparticles. *Int. J. Mol. Sci.* **2013**, *14* (8), 15977–16009. https://doi.org/10.3390/ijms140815977.

(34) Cullity, B. D.; Graham, C. D. *Introduction to Magnetic Materials*, 2nd ed.; IEEE/Wiley: Hoboken, N.J, 2009.

(35) Liu, Y.; Liu, X.; Dolci, M.; Leuvrey, C.; Pardieu, E.; Derory, A.; Begin, D.; Begin-Colin, S.; Pichon, B. P. Investigation of the Collective Properties in Monolayers of Exchange-Biased $Fe_{3-\delta}O_4$@CoO Core–Shell Nanoparticles. *J. Phys. Chem. C* **2018**, *122* (30), 17456–17464. https://doi.org/10.1021/acs.jpcc.8b04615.

(36) Toulemon, D.; Pichon, B. P.; Cattoën, X.; Man, M. W. C.; Begin-Colin, S. 2D Assembly of Non-Interacting Magnetic Iron Oxide Nanoparticles via"Click" Chemistry. *Chem. Commun.* **2011**, *47* (43), 11954. https://doi.org/10.1039/c1cc14661k.

(37) Panissod, P.; Drillon, M. Magnetic Ordering Due to Dipolar Interaction in Low Dimensional Materials. In *Magnetism: Molecules to Materials IV*; Miller, J. S., Drillon, M., Eds.; Wiley-VCH Verlag GmbH & Co. KGaA: Weinheim, FRG, 2001; pp 233–270. https://doi.org/10.1002/3527600698.ch7.

(38) Frankamp, B. L.; Boal, A. K.; Tuominen, M. T.; Rotello, V. M. Direct Control of the Magnetic Interaction between Iron Oxide Nanoparticles through Dendrimer-Mediated Self-Assembly. *J. Am. Chem. Soc.* **2005**, *127* (27), 9731–9735. https://doi.org/10.1021/ja051351m.

(39) Dolci, M.; Liu, Y.; Liu, X.; Leuvrey, C.; Derory, A.; Begin, D.; Begin-Colin, S.; Pichon, B. P. Exploring Exchange Bias Coupling in $Fe_{3-\delta}O_4$@CoO Core-Shell Nanoparticle 2D Assemblies. *Adv. Funct. Mater.* **2018**, *28* (26), 1706957. https://doi.org/10.1002/adfm.201706957.

(40) Kechrakos, D.; Trohidou, K. N. Dipolar Interaction Effects in the Magnetic and Magnetotransport Properties of Ordered Nanoparticle Arrays. *J. Nanosci. Nanotechnol.* **2008**, *8* (6), 2929–2943. https://www.ingentaconnect.com/content/asp/jnn/2008/00000008/00000006/art00019.

(41) Meiklejohn, W. H.; Bean, C. P. New Magnetic Anisotropy. *Phys. Rev.* **1956**, *102* (5), 1413–1414. https://doi.org/10.1103/PhysRev.102.1413.

(42) Nogués, J.; Sort, J.; Langlais, V.; Skumryev, V.; Suriñach, S.; Muñoz, J. S.; Baró, M. D. Exchange Bias in Nanostructures. *Phys. Rep.* **2005**, *422* (3), 65–117. https://doi.org/10.1016/j.physrep.2005.08.004.

(43) Kamil Akmaldinov. Ferromagnetic/Antiferromagnetic Exchange Bias Nanostructures for Ultimate Spintronic Devices, Grenoble, Grenoble, 2006.

(44) Gangopadhyay, S.; Hadjipanayis, G. C.; Sorensen, C. M.; Klabunde, K. J. Exchange Anisotropy in Oxide Passivated Co Fine Particles. *J. Appl. Phys.* **1993**, *73* (10), 6964–6966. https://doi.org/10.1063/1.352398.

(45) Nogués, J.; Lederman, D.; Moran, T. J.; Schuller, I. K. Positive Exchange Bias in Fe F 2 -Fe Bilayers. *Phys. Rev. Lett.* **1996**, *76* (24), 4624–4627. https://doi.org/10.1103/PhysRevLett.76.4624.

(46) Estrader, M.; López-Ortega, A.; Estradé, S.; Golosovsky, I. V.; Salazar-Alvarez, G.; Vasilakaki, M.; Trohidou, K. N.; Varela, M.; Stanley, D. C.; Sinko, M.; et al. Robust Antiferromagnetic Coupling in Hard-Soft Bi-Magnetic Core/Shell Nanoparticles. *Nat. Commun.* **2013**, *4*. https://doi.org/10.1038/ncomms3960.

(47) Baaziz, W.; Pichon, B. P.; Lefevre, C.; Ulhaq-Bouillet, C.; Greneche, J.-M.; Toumi, M.; Mhiri, T.; Bégin-Colin, S. High Exchange Bias in $Fe_{3-\delta}O_4$@CoO Core Shell Nanoparticles Synthesized by a One-Pot Seed-Mediated Growth Method. *J. Phys. Chem. C* **2013**, *117* (21), 11436–11443. https://doi.org/10.1021/jp402823h.

(48) Wen, G. H.; Zheng, R. K.; Fung, K. K.; Zhang, X. X. Microstructural and Magnetic Properties of Passivated Co Nanoparticle Films. *J. Magn. Magn. Mater.* **2004**, *270* (3), 407–412. https://doi.org/10.1016/j.jmmm.2003.09.008.

(49) Nogués, J.; Ivan K Schuller. Exchange Bias. *J. Magn. Magn. Mater.* **1999**, *192*, 203–232.

(50) Oscar Iglesias; Amilcar Labarta; Xavier Battle. Exchange Bias Phenomenology and Models of Core/Shell Nanoparticles. *Cond Mat* **2008**.

(51) Lund, M. S.; Macedo, W. A. A.; Liu, K.; Nogués, J.; Schuller, I. K.; Leighton, C. Effect of Anisotropy on the Critical Antiferromagnet Thickness in Exchange-Biased Bilayers. *Phys. Rev. B* **2002**, *66* (5). https://doi.org/10.1103/PhysRevB.66.054422.

(52) Liu, X.; Pichon, B. P.; Ulhaq, C.; Lefèvre, C.; Grenèche, J.-M.; Bégin, D.; Bégin-Colin, S. Systematic Study of Exchange Coupling in Core–Shell $Fe_{3-\delta}O_4$@CoO Nanoparticles. *Chem. Mater.* **2015**, *27* (11), 4073–4081. https://doi.org/10.1021/acs.chemmater.5b01103.

(53) Prados, C.; Pina, E.; Hernando, A.; Montone, A. Reversal of Exchange Bias in Nanocrystalline Antiferromagnetic Ferromagnetic Bilayers. *J. Phys. Condens. Matter* **2002**, *14* (43), 10063–10074. https://doi.org/10.1088/0953-8984/14/43/305.

(54) Ali, M.; Marrows, C. H.; Hickey, B. J. Onset of Exchange Bias in Ultrathin Antiferromagnetic Layers. *Phys. Rev. B* **2003**, *67* (17), 172405. https://doi.org/10.1103/PhysRevB.67.172405.

(55) Binek, C.; He, X.; Polisetty, S. Temperature Dependence of the Training Effect in a Co ⁄ Co O Exchange-Bias Layer. *Phys. Rev. B* **2005**, *72* (5), 054408. https://doi.org/10.1103/PhysRevB.72.054408.

(56) Zheng, R. K.; Wen, G. H.; Fung, K. K.; Zhang, X. X. Training Effect of Exchange Bias in γ − Fe 2 O 3 Coated Fe Nanoparticles. *Phys. Rev. B* **2004**, *69* (21), 214431. https://doi.org/10.1103/PhysRevB.69.214431.

(57) Vasilakaki, M.; Eftaxias, E.; Trohidou, K. N. Monte Carlo Study of the Exchange Bias and the Training Effect in Nanoparticles with Core/Shell Morphology. *Phys. Status Solidi A* **2008**, *205* (8), 1865–1871. https://doi.org/10.1002/pssa.200723671.

(58) Mumtaz, A.; Maaz, K.; Janjua, B.; Hasanain, S. K.; Bertino, M. F. Exchange Bias and Vertical Shift in CoFe2O4 Nanoparticles. *J. Magn. Magn. Mater.* **2007**, *313* (2), 266–272. https://doi.org/10.1016/j.jmmm.2007.01.007.

(59) Ijiri, Y.; Borchers, J. A.; Erwin, R. W.; Lee, S.-H.; van der Zaag, P. J.; Wolf, R. M. Perpendicular Coupling in Exchange-Biased Fe 3 O 4 / CoO Superlattices. *Phys. Rev. Lett.* **1998**, *80* (3), 608–611. https://doi.org/10.1103/PhysRevLett.80.608.

(60) Moran, T. J.; Nogués, J.; Lederman, D.; Schuller, I. K. Perpendicular Coupling at Fe–FeF2 Interfaces. *Appl. Phys. Lett.* **1998**, *72* (5), 617–619. https://doi.org/10.1063/1.120823.

(61) Koon, N. C. Calculations of Exchange Bias in Thin Films with Ferromagnetic/Antiferromagnetic Interfaces. *Phys. Rev. Lett.* **1997**, *78* (25), 4865–4868. https://doi.org/10.1103/PhysRevLett.78.4865.

(62) Arenholz, E.; Liu, K.; Li, Z.; Schuller, I. K. Magnetization Reversal of Uncompensated Fe Moments in Exchange Biased Ni⁄FeF2 Bilayers. *Appl. Phys. Lett.* **2006**, *88* (7), 072503. https://doi.org/10.1063/1.2173716.

(63) Malozemoff, A. P. Random-Field Model of Exchange Anisotropy at Rough Ferromagnetic-Antiferromagnetic Interfaces. *Phys. Rev. B* **1987**, *35* (7), 3679–3682. https://doi.org/10.1103/PhysRevB.35.3679.

(64) Han, D.-H.; Zhu, J.-G.; Judy, J. H. NiFe/NiO Bilayers with High Exchange Coupling and Low Coercive Fields. *J. Appl. Phys.* **1997**, *81* (8), 4996–4998. https://doi.org/10.1063/1.364964.

(65) Leighton, C.; Nogués, J.; Jönsson-Åkerman, B. J.; Schuller, I. K. Coercivity Enhancement in Exchange Biased Systems Driven by Interfacial Magnetic Frustration. *Phys. Rev. Lett.* **2000**, *84* (15), 3466–3469. https://doi.org/10.1103/PhysRevLett.84.3466.

(66) López-Ortega, A.; Estrader, M.; Salazar-Alvarez, G.; Estradé, S.; Golosovsky, I. V.; Dumas, R. K.; Keavney, D. J.; Vasilakaki, M.; Trohidou, K. N.; Sort, J.; et al. Strongly Exchange Coupled Inverse Ferrimagnetic Soft/Hard, MnxFe3−xO4/FexMn3−xO4, Core/Shell Heterostructured Nanoparticles. *Nanoscale* **2012**, *4* (16), 5138. https://doi.org/10.1039/c2nr30986f.

(67) Skoropata, E.; Desautels, R. D.; Chi, C.-C.; Ouyang, H.; Freeland, J. W.; van Lierop, J. Magnetism of Iron Oxide Based Core-Shell Nanoparticles from Interface Mixing with Enhanced Spin-Orbit Coupling. *Phys. Rev. B* **2014**, *89* (2). https://doi.org/10.1103/PhysRevB.89.024410.

(68) Sartori, K.; Cotin, G.; Bouillet, C.; Halté, V.; Bégin-Colin, S.; Choueikani, F.; Pichon, B. P. Strong Interfacial Coupling through Exchange Interactions in Soft/Hard Core–Shell Nanoparticles as a Function of Cationic Distribution. *Nanoscale* **2019**, *11* (27), 12946–12958. https://doi.org/10.1039/C9NR02323B.

(69) Kools, J. C. S. Exchange-Biased Spin-Valves for Magnetic Storage. *IEEE Trans. Magn.* **1996**, *32* (4), 3165–3184. https://doi.org/10.1109/20.508381.

(70) Tang, D. D.; Wang, P. K.; Speriosu, V. S.; Le, S.; Kung, K. K. Spin-Valve RAM Cell. *IEEE Trans. Magn.* **1995**, *31* (6), 3206–3208. https://doi.org/10.1109/20.490329.

(71) McDonald, I. J.; Jamer, M. E.; Krycka, K. L.; Anber, E.; Foley, D.; Lang, A. C.; Ratcliff, W. D.; Heiman, D.; Taheri, M. L.; Borchers, J. A.; et al. Exchange Bias in Bulk α-Fe/γ-Fe $_{70}$ Mn $_{30}$ Nanocomposites for Permanent Magnet Applications. *ACS Appl. Nano Mater.* **2019**, *2* (4), 1940–1950. https://doi.org/10.1021/acsanm.8b02319.

(72) Li, K.; Wu, Y.; Guo, Z.; Zheng, Y.; Han, G.; Qiu, J.; Luo, P.; An, L.; Zhou, T. Exchange Coupling and Its Applications in Magnetic Data Storage. *ChemInform* **2007**, *38* (35). https://doi.org/10.1002/chin.200735223.

(73) López-Ortega, A.; Estrader, M.; Salazar-Alvarez, G.; Roca, A. G.; Nogués, J. Applications of Exchange Coupled Bi-Magnetic Hard/Soft and Soft/Hard Magnetic Core/Shell Nanoparticles. *Phys. Rep.* **2015**, *553*, 1–32. https://doi.org/10.1016/j.physrep.2014.09.007.

(74) Skumryev, V.; Stoyanov; Zhang; Hadjipanayis; Givord; Nogués. Beating the Superparamagnetic Limit with Exchange Bias. *Nature* **2003**, *423* (6942), 847–850. https://doi.org/10.1038/nature01750.

(75) Dutta, P.; Pal, S.; Seehra, M. S.; Shah, N.; Huffman, G. P. Size Dependence of Magnetic Parameters and Surface Disorder in Magnetite Nanoparticles. *J. Appl. Phys.* **2009**, *105* (7), 07B501. https://doi.org/10.1063/1.3055272.

(76) Shendruk, T. N.; Desautels, R. D.; Southern, B. W.; van Lierop, J. The Effect of Surface Spin Disorder on the Magnetism of γ-Fe $_2$ O $_3$ Nanoparticle Dispersions. *Nanotechnology* **2007**, *18* (45), 455704. https://doi.org/10.1088/0957-4484/18/45/455704.

(77) Martınez, B.; Obradors, X.; Balcells, L.; Rouanet, A.; Monty, C. Low Temperature Surface Spin-Glass Transition in g-Fe2O3 Nanoparticles. *Phys. Rev. Lett.* **1998**, *80* (1), 4.

(78) Wang, H.; Zhu, T.; Zhao, K.; Wang, W. N.; Wang, C. S.; Wang, Y. J.; Zhan, W. S. Surface Spin Glass and Exchange Bias in Fe 3 O 4 Nanoparticles Compacted under High Pressure. *Phys. Rev. B* **2004**, *70* (9), 092409. https://doi.org/10.1103/PhysRevB.70.092409.

(79) Kavich, D. W.; Dickerson, J. H.; Mahajan, S. V.; Hasan, S. A.; Park, J.-H. Exchange Bias of Singly Inverted FeO / Fe 3 O 4 Core-Shell Nanocrystals. *Phys. Rev. B* **2008**, *78* (17), 174414. https://doi.org/10.1103/PhysRevB.78.174414.

(80) Pichon, B. P.; Gerber, O.; Lefevre, C.; Florea, I.; Fleutot, S.; Baaziz, W.; Pauly, M.; Ohlmann, M.; Ulhaq, C.; Ersen, O.; et al. Microstructural and Magnetic Investigations of Wüstite-Spinel Core-Shell Cubic-Shaped Nanoparticles. *Chem. Mater.* **2011**, *23* (11), 2886–2900. https://doi.org/10.1021/cm2003319.

(81) Song, Q.; Zhang, Z. J. Shape Control and Associated Magnetic Properties of Spinel Cobalt Ferrite Nanocrystals. *J. Am. Chem. Soc.* **2004**, *126* (19), 6164–6168. https://doi.org/10.1021/ja049931r.

(82) Wetterskog, E.; Tai, C.-W.; Grins, J.; Bergström, L.; Salazar-Alvarez, G. Anomalous Magnetic Properties of Nanoparticles Arising from Defect Structures: Topotaxial Oxidation of Fe $_{1-x}$ O|Fe $_{3-\delta}$ O $_4$ Core|Shell Nanocubes to Single-Phase Particles. *ACS Nano* **2013**, *7* (8), 7132–7144. https://doi.org/10.1021/nn402487q.

(83) Ong, Q. K.; Lin, X.-M.; Wei, A. Role of Frozen Spins in the Exchange Anisotropy of Core−Shell Fe@Fe $_3$ O $_4$ Nanoparticles. *J. Phys. Chem. C* **2011**, *115* (6), 2665–2672. https://doi.org/10.1021/jp110716g.

(84) Hwang, Y.; Angappane, S.; Park, J.; An, K.; Hyeon, T.; Park, J.-G. Exchange Bias Behavior of Monodisperse Fe3O4/γ-Fe2O3 Core/Shell Nanoparticles. *Curr. Appl. Phys.* **2012**, *12* (3), 808–811. https://doi.org/10.1016/j.cap.2011.11.011.

(85) Cabreira-Gomes, R.; G. Silva, F.; Aquino, R.; Bonville, P.; Tourinho, F. A.; Perzynski, R.; Depeyrot, J. Exchange Bias of MnFe2O4@γFe2O3 and CoFe2O4@γFe2O3 Core/Shell Nanoparticles. *J. Magn. Magn. Mater.* **2014**, *368*, 409–414. https://doi.org/10.1016/j.jmmm.2014.03.003.

(86) LaMer, V. K.; Dinegar, R. H. Theory, Production and Mechanism of Formation of Monodispersed Hydrosols. *J. Am. Chem. Soc.* **1950**, *72* (11), 4847–4854.

(87) Lassenberger, A.; Grünewald, T. A.; van Oostrum, P. D. J.; Rennhofer, H.; Amenitsch, H.; Zirbs, R.; Lichtenegger, H. C.; Reimhult, E. Monodisperse Iron Oxide Nanoparticles by Thermal Decomposition: Elucidating Particle Formation by Second-Resolved in Situ Small-Angle X-Ray Scattering. *Chem. Mater.* **2017**, *29* (10), 4511–4522. https://doi.org/10.1021/acs.chemmater.7b01207.

(88) Schladt, T. D.; Schneider, K.; Schild, H.; Tremel, W. Synthesis and Bio-Functionalization of Magnetic Nanoparticles for Medical Diagnosis and Treatment. *Dalton Trans.* **2011**, *40* (24), 6315. https://doi.org/10.1039/c0dt00689k.

(89) van Embden, J.; Chesman, A. S. R.; Jasieniak, J. J. The Heat-Up Synthesis of Colloidal Nanocrystals. *Chem. Mater.* **2015**, *27* (7), 2246–2285. https://doi.org/10.1021/cm5028964.

(90) Huang, J.-H.; Parab, H. J.; Liu, R.-S.; Lai, T.-C.; Hsiao, M.; Chen, C.-H.; Sheu, H.-S.; Chen, J.-M.; Tsai, D.-P.; Hwu, Y.-K. Investigation of the Growth Mechanism of Iron Oxide Nanoparticles via a Seed-Mediated Method and Its Cytotoxicity Studies. *J. Phys. Chem. C* **2008**, *112* (40), 15684–15690. https://doi.org/10.1021/jp803452j.

(91) Kwon, S. G.; Hyeon, T. Formation Mechanisms of Uniform Nanocrystals via Hot-Injection and Heat-up Methods. *Small* **2011**, *7* (19), 2685–2702.

(92) Morales, M. A.; Skomski, R.; Fritz, S.; Shelburne, G.; Shield, J. E.; Yin, M.; O'Brien, S.; Leslie-Pelecky, D. L. Surface Anisotropy and Magnetic Freezing of MnO Nanoparticles. *Phys. Rev. B* **2007**, *75* (13), 134423. https://doi.org/10.1103/PhysRevB.75.134423.

(93) Tadic, M.; Nikolic, D.; Panjan, M.; Blake, G. R. Magnetic Properties of NiO (Nickel Oxide) Nanoparticles: Blocking Temperature and Neel Temperature. *J. Alloys Compd.* **2015**, *647*, 1061–1068. https://doi.org/10.1016/j.jallcom.2015.06.027.

(94) Goya, G. F.; Berquó, T. S.; Fonseca, F. C.; Morales, M. P. Static and Dynamic Magnetic Properties of Spherical Magnetite Nanoparticles. *J. Appl. Phys.* **2003**, *94* (5), 3520–3528. https://doi.org/10.1063/1.1599959.

(95) Caizer, C.; Savii, C.; Popovici, M. Magnetic Behaviour of Iron Oxide Nanoparticles Dispersed in a Silica Matrix. *Mater. Sci. Eng. B* **2003**, *97* (2), 129–134. https://doi.org/10.1016/S0921-5107(02)00403-8.

(96) Walter, A. Elaboration de nano-objets magnétiques dendronisés à vocation théranostic, Université de Strasbourg, 2014.

(97) Skoropata, E.; Su, T. T.; Ouyang, H.; Freeland, J. W.; van Lierop, J. Intermixing Enables Strong Exchange Coupling in Nanocomposites: Magnetism through the Interfacial Ferrite in γ − Fe 2 O 3 / NiO. *Phys. Rev. B* **2017**, *96* (2). https://doi.org/10.1103/PhysRevB.96.024447.

(98) He, X.-M.; Zhang, C.-W.; Guo, F.-F.; Yan, S.-M.; Li, Y.-T.; Liu, L.-Q.; Zhang, H.-G.; Du, Y.-W.; Zhong, W. Exchange-Biased Hybrid γ-Fe $_2$ O $_3$ /NiO Core–Shell Nanostructures: Three-Step Synthesis, Microstructure, and Magnetic Properties. *Phys. Chem. Chem. Phys.* **2019**, *21* (22), 11967–11976. https://doi.org/10.1039/C9CP01265F.

(99) Panagiotopoulos, I.; Basina, G.; Alexandrakis, V.; Devlin, E.; Hadjipanayis, G.; Colak, L.; Niarchos, D.; Tzitzios, V. Synthesis and Exchange Bias in γ-Fe $_2$ O $_3$ /CoO and Reverse CoO/γ-Fe $_2$ O $_3$ Binary Nanoparticles. *J. Phys. Chem. C* **2009**, *113* (33), 14609–14614. https://doi.org/10.1021/jp8085446.

(100) Lima, E.; Winkler, E. L.; Tobia, D.; Troiani, H. E.; Zysler, R. D.; Agostinelli, E.; Fiorani, D. Bimagnetic CoO Core/CoFe $_2$ O $_4$ Shell Nanoparticles: Synthesis and Magnetic Properties. *Chem. Mater.* **2012**, *24* (3), 512–516. https://doi.org/10.1021/cm2028959.

(101) Lavorato, G. C.; Lima Jr, E.; Tobia, D.; Fiorani, D.; Troiani, H. E.; Zysler, R. D.; Winkler, E. L. Size Effects in Bimagnetic CoO/$CoFe_2O_4$ Core/Shell Nanoparticles. *Nanotechnology* **2014**, *25* (35), 355704. https://doi.org/10.1088/0957-4484/25/35/355704.

(102) Lavorato, G. C.; Lima, E.; Troiani, H. E.; Zysler, R. D.; Winkler, E. L. Tuning the Coercivity and Exchange Bias by Controlling the Interface Coupling in Bimagnetic Core/Shell Nanoparticles. *Nanoscale* **2017**, *9* (29), 10240–10247. https://doi.org/10.1039/C7NR03740F.

(103) Lavorato, G. C.; Peddis, D.; Lima, E.; Troiani, H. E.; Agostinelli, E.; Fiorani, D.; Zysler, R. D.; Winkler, E. L. Magnetic Interactions and Energy Barrier Enhancement in Core/Shell Bimagnetic Nanoparticles. *J. Phys. Chem. C* **2015**, *119* (27), 15755–15762. https://doi.org/10.1021/acs.jpcc.5b04448.

(104) Gaudisson, T.; Sayed-Hassan, R.; Yaacoub, N.; Franceschin, G.; Nowak, S.; Grenèche, J.-M.; Menguy, N.; Sainctavit, Ph.; Ammar, S. On the Exact Crystal Structure of Exchange-Biased Fe_3O_4–CoO Nanoaggregates Produced by Seed-Mediated Growth in Polyol. *CrystEngComm* **2016**, *18* (21), 3799–3807. https://doi.org/10.1039/C6CE00700G.

(105) Desautels, R. D.; Skoropata, E.; Chen, Y.-Y.; Ouyang, H.; Freeland, J. W.; van Lierop, J. Increased Surface Spin Stability in γ-Fe_2O_3 Nanoparticles with a Cu Shell. *J. Phys. Condens. Matter* **2012**, *24* (14), 146001. https://doi.org/10.1088/0953-8984/24/14/146001.

(106) Masala, O.; Seshadri, R. Spinel Ferrite/MnO Core/Shell Nanoparticles: Chemical Synthesis of All-Oxide Exchange Biased Architectures. *J. Am. Chem. Soc.* **2005**, *127* (26), 9354–9355. https://doi.org/10.1021/ja051244s.

(107) Sun, X.; Frey Huls, N.; Sigdel, A.; Sun, S. Tuning Exchange Bias in Core/Shell FeO/Fe_3O_4 Nanoparticles. *Nano Lett.* **2012**, *12* (1), 246–251. https://doi.org/10.1021/nl2034514.

(108) Lak, A.; Kraken, M.; Ludwig, F.; Kornowski, A.; Eberbeck, D.; Sievers, S.; Litterst, F. J.; Weller, H.; Schilling, M. Size Dependent Structural and Magnetic Properties of FeO–Fe3O4 Nanoparticles. *Nanoscale* **2013**, *5* (24), 12286. https://doi.org/10.1039/c3nr04562e.

(109) Khurshid, H.; Li, W.; Chandra, S.; Phan, M.-H.; Hadjipanayis, G. C.; Mukherjee, P.; Srikanth, H. Mechanism and Controlled Growth of Shape and Size Variant Core/Shell FeO/Fe3O4 Nanoparticles. *Nanoscale* **2013**, *5* (17), 7942. https://doi.org/10.1039/c3nr02596a.

(110) Sytnyk, M.; Kirchschlager, R.; Bodnarchuk, M. I.; Primetzhofer, D.; Kriegner, D.; Enser, H.; Stangl, J.; Bauer, P.; Voith, M.; Hassel, A. W.; et al. Tuning the Magnetic Properties of Metal Oxide Nanocrystal Heterostructures by Cation Exchange. *Nano Lett.* **2013**, *13* (2), 586–593. https://doi.org/10.1021/nl304115r.

(111) Fullerton, E. E.; Jiang, J. S.; Bader, S. D. Hard/Soft Magnetic Heterostructures: Model Exchange-Spring Magnets. *J. Magn. Magn. Mater.* **1999**, *200* (1–3), 392–404. https://doi.org/10.1016/S0304-8853(99)00376-5.

(112) Nakhjavan, B.; Tahir, M. N.; Panthöfer, M.; Gao, H.; Gasi, T.; Ksenofontov, V.; Branscheid, R.; Weber, S.; Kolb, U.; Schreiber, L. M.; et al. Controlling Phase Formation in Solids: Rational Synthesis of Phase Separated Co@Fe2O3 Heteroparticles and CoFe2O4 Nanoparticles. *Chem. Commun.* **2011**, *47* (31), 8898. https://doi.org/10.1039/c1cc13204k.

(113) Nandwana, V.; Chaubey, G. S.; Yano, K.; Rong, C.; Liu, J. P. Bimagnetic Nanoparticles with Enhanced Exchange Coupling and Energy Products. *J. Appl. Phys.* **2009**, *105* (1), 014303. https://doi.org/10.1063/1.3054441.

(114) Lee, J.-H.; Jang, J.; Choi, J.; Moon, S. H.; Noh, S.; Kim, J.; Kim, J.-G.; Kim, I.-S.; Park, K. I.; Cheon, J. Exchange-Coupled Magnetic Nanoparticles for Efficient Heat Induction. *Nat. Nanotechnol.* **2011**, *6* (7), 418–422. https://doi.org/10.1038/nnano.2011.95.

(115) Kim, C. W.; Kim, Y. H.; Cha, H. G.; Kim, J. C.; Kang, Y. S. A Study on the Exchange-Coupling Effect of $Nd_2Fe_{14}B$/CoFe Forming Core/Shell Shape. *Mol. Cryst. Liq. Cryst.* **2007**, *472* (1), 155/[545]-160/[550]. https://doi.org/10.1080/15421400701545460.

(116) Lamichanne, M.; Rai, B. K.; Mishra, S. R.; Nguyen, V. V.; Liu, J. P. Magnetic Properties Hard-Soft SmCo₅-FeNi and SmCo₅-FeCo Composites Prepared by Electroless Coating Technique. *Open J. Compos. Mater.* **2012**, *02* (04), 119–124. https://doi.org/10.4236/ojcm.2012.24014.

(117) Song, Q.; Zhang, Z. J. Controlled Synthesis and Magnetic Properties of Bimagnetic Spinel Ferrite $CoFe_2O_4$ and $MnFe_2O_4$ Nanocrystals with Core–Shell Architecture. *J. Am. Chem. Soc.* **2012**, *134* (24), 10182–10190. https://doi.org/10.1021/ja302856z.

(118) Juhin, A.; López-Ortega, A.; Sikora, M.; Carvallo, C.; Estrader, M.; Estradé, S.; Peiró, F.; Baró, M. D.; Sainctavit, P.; Glatzel, P.; et al. Direct Evidence for an Interdiffused Intermediate Layer in Bi-Magnetic Core–Shell Nanoparticles. *Nanoscale* **2014**, *6* (20), 11911–11920. https://doi.org/10.1039/C4NR02886D.

(119) Sudakar, C.; Kutty, T. R. N. Structural and Magnetic Characteristics of Cobalt Ferrite-Coated Nano-Fibrous γ-Fe2O3. *J. Magn. Magn. Mater.* **2004**, *279* (2–3), 363–374. https://doi.org/10.1016/j.jmmm.2004.02.005.

(120) Zan, F.; Ma, Y.; Ma, Q.; Xu, Y.; Dai, Z.; Zheng, G.; Wu, M.; Li, G. Magnetic and Impedance Properties of Nanocomposite $CoFe_2O_4$ /$Co_{0.7}Fe_{0.3}$ and Single-Phase $CoFe_2O_4$ Prepared Via a One-Step Hydrothermal Synthesis. *J. Am. Ceram. Soc.* **2013**, n/a-n/a. https://doi.org/10.1111/jace.12437.

(121) Zeng, H.; Sun, S.; Li, J.; Wang, Z. L.; Liu, J. P. Tailoring Magnetic Properties of Core⁄shell Nanoparticles. *Appl. Phys. Lett.* **2004**, *85* (5), 792–794. https://doi.org/10.1063/1.1776632.

(122) Salazar-Alvarez, G.; Lidbaum, H.; López-Ortega, A.; Estrader, M.; Leifer, K.; Sort, J.; Surinach, S.; Baró, M. D.; Nogués, J. Two-, Three-, and Four-Component Magnetic Multilayer Onion Nanoparticles Based on Iron Oxides and Manganese Oxides. *J. Am. Chem. Soc.* **2011**, *133* (42), 16738–16741.

(123) O'Handley, R. C. *Modern Magnetic Materials: Principles and Applications*; Wiley: New York, 2000.

(124) Salazar-Alvarez, G.; Sort, J.; Suriñach, S.; Baró, M. D.; Nogués, J. Synthesis and Size-Dependent Exchange Bias in Inverted Core−Shell MnO|Mn_3O_4 Nanoparticles. *J. Am. Chem. Soc.* **2007**, *129* (29), 9102–9108. https://doi.org/10.1021/ja0714282.

(125) Dwight, K.; Menyuk, N. Magnetic Properties of Mn 3 O 4 and the Canted Spin Problem. *Phys. Rev.* **1960**, *119* (5), 1470–1479. https://doi.org/10.1103/PhysRev.119.1470.

(126) Krycka, K. L.; Borchers, J. A.; Laver, M.; Salazar-Alvarez, G.; L?pez-Ortega, A.; Estrader, M.; Suri?ach, S.; Bar?, M. D.; Sort, J.; Nogu?s, J. Correlating Material-Specific Layers and Magnetic Distributions within Onion-like Fe3O4/MnO/?-Mn2O3 Core/Shell Nanoparticles. *J. Appl. Phys.* **2013**, *113* (17), 17B531. https://doi.org/10.1063/1.4801423.

(127) Gavrilov-Isaac, V.; Neveu, S.; Dupuis, V.; Taverna, D.; Gloter, A.; Cabuil, V. Synthesis of Trimagnetic Multishell $MnFe_2O_4$ @$CoFe_2O_4$ @$NiFe_2O_4$ Nanoparticles. *Small* **2015**, *11* (22), 2614–2618. https://doi.org/10.1002/smll.201402845.

(128) De Toro, J. A.; Marques, D. P.; Muñiz, P.; Skumryev, V.; Sort, J.; Givord, D.; Nogués, J. High Temperature Magnetic Stabilization of Cobalt Nanoparticles by an Antiferromagnetic Proximity Effect. *Phys. Rev. Lett.* **2015**, *115* (5). https://doi.org/10.1103/PhysRevLett.115.057201.

(129) Brice-Profeta, S.; Arrio, M.-A.; Tronc, E.; Menguy, N.; Letard, I.; Cartier dit Moulin, C.; Noguès, M.; Chanéac, C.; Jolivet, J.-P.; Sainctavit, Ph. Magnetic Order in - Nanoparticles: A XMCD Study. *J. Magn. Magn. Mater.* **2005**, *288*, 354–365. https://doi.org/10.1016/j.jmmm.2004.09.120.

(130) Byrne, J. M.; Coker, V. S.; Moise, S.; Wincott, P. L.; Vaughan, D. J.; Tuna, F.; Arenholz, E.; van der Laan, G.; Pattrick, R. A. D.; Lloyd, J. R.; et al. Controlled Cobalt Doping in Biogenic Magnetite Nanoparticles. *J. R. Soc. Interface* **2013**, *10* (83), 20130134–20130134. https://doi.org/10.1098/rsif.2013.0134.

(131) Guinier, A.; Fournet, G. *Small-Angle Scattering of X-Rays*; John Wiley & Sons, Inc, 1955.

(132) Cousin, F. Small Angle Neutron Scattering. *EPJ Web Conf.* **2015**, *104*, 01004. https://doi.org/10.1051/epjconf/201510401004.

(133) Disch, S.; Wetterskog, E.; Hermann, R. P.; Wiedenmann, A.; Vainio, U.; Salazar-Alvarez, G.; Bergström, L.; Brückel, T. Quantitative Spatial Magnetization Distribution in Iron Oxide Nanocubes and Nanospheres by Polarized Small-Angle Neutron Scattering. *New J. Phys.* **2012**, *14* (1), 013025. https://doi.org/10.1088/1367-2630/14/1/013025.

(134) Krycka, K. L.; Booth, R. A.; Hogg, C. R.; Ijiri, Y.; Borchers, J. A.; Chen, W. C.; Watson, S. M.; Laver, M.; Gentile, T. R.; Dedon, L. R.; et al. Core-Shell Magnetic Morphology of Structurally Uniform Magnetite Nanoparticles. *Phys. Rev. Lett.* **2010**, *104* (20). https://doi.org/10.1103/PhysRevLett.104.207203.

(135) Krycka, K. L.; Borchers, J. A.; Booth, R. A.; Hogg, C. R.; Ijiri, Y.; Chen, W. C.; Watson, S. M.; Laver, M.; Gentile, T. R.; Harris, S.; et al. Internal Magnetic Structure of Magnetite Nanoparticles at Low Temperature. *J. Appl. Phys.* **2010**, *107* (9), 09B525. https://doi.org/10.1063/1.3358049.

(136) Oberdick, S. D.; Abdelgawad, A.; Moya, C.; Mesbahi-Vasey, S.; Kepaptsoglou, D.; Lazarov, V. K.; Evans, R. F. L.; Meilak, D.; Skoropata, E.; van Lierop, J.; et al. Spin Canting across Core/Shell Fe3O4/MnxFe3−xO4 Nanoparticles. *Sci. Rep.* **2018**, *8* (1). https://doi.org/10.1038/s41598-018-21626-0.

CHAPTER I

Increasing the size of $Fe_{3-d}O_4$ nanoparticles by performing a multistep seed-mediated growth approach

$Fe_{3-d}O_4(@Fe_{3-d}O_4)n$

Submitted to Crystal Growth & Design on October 1st, 2019

Introduction

Magnetic nanoparticles are very attractive for a wide range of applications because of their unique size-dependent properties.[1–3] Therefore, a very active research field aims at tuning accurately their magnetic properties. To achieve this goal, new synthesis strategies have to be developed to modulate the size, the chemical composition or the crystallinity of the nanoparticles. Nanoparticles can be synthesized through various techniques among which the thermal decomposition of metal precursors in solution presents the great advantage to produce nanoparticles with well controlled structural characteristics.[4,5] Indeed, at the nanoscale, narrow size distribution, well defined shape and crystalline quality are critical parameters to tune precisely the magnetic properties.[6] Although the thermal decomposition process is a very powerful technique to achieve that goal, it is very complex to master because of the variety of experimental parameters that influence the reaction kinetics. According to the LaMer theory,[7] the mechanism pathway consists in a short burst of nucleation from a supersaturated solution of monomers which results from the decomposition of a metal precursor, followed by the slow growth of nanoparticles.

Among a variety of chemical compositions, iron oxide nanoparticles have been widely explored during the last decades for biomedical applications because they combine superparamagnetic properties, low toxicity and cheapness thanks to the abundance of their constituents.[8–10] In this purpose, the fine control of the size distribution with the highest possible accuracy in the range below 20 nm has been extensively investigated. Therefore, the stability of the metal precursor against temperature is critical and depends on the coordination state of metal with ligands[11–16] as well as on the stabilizing agent and the boiling temperature of the solvent.[17–19] Furthermore, the temperature has to be controlled very precisely in order to separate the nucleation step from the growth step. The experimental conditions significantly influence the crystalline quality of the nanoparticles which is also critical to enhance their magnetic properties.

An alternative to synthesize nanoparticles with accurate structural and enhanced magnetic properties consists in performing a seed-mediated growth approach. The size of iron oxide nanoparticles was reported to increase from 8 to 16 nm by adapting the iron oxide seed concentration while performing the decomposition of $Fe(acac)_3$ precursor.[20,21] Nanoparticles were also synthesized by increasing the precursor concentration while the seed concentration remained constant.[22,23] The potential of the approach was clearly demonstrated by Hyeon *et al.* who reported on the incremental 1 nm size-controlled synthesis of iron oxide nanoparticles with sizes from 6 to 13 nm.[24] The seed mediated growth approach was also performed by controlling the slow addition of precursor upon the synthesis of nanoparticles in order to produce nanoparticle with sizes from 6 to 18 nm.[25,26] However, this growth process resulted in magnetic defects in the seed and antiphase boundaries in the grown layer which altered the magnetic properties. The seed-mediated growth approach is very powerful in controlling the nanoparticle size.

Herein, we report on an original multistep seed-mediated growth approach based on the thermal decomposition of iron stearate in order to incrementally increase the size of iron oxide nanoparticles. To the best of our knowledge, it is the first time that iron oxide nanoparticles have been synthesized by performing successively up to five times the thermal decomposition of iron stearate. The crystal structure and the chemical composition of nanoparticles have been investigated systematically in order to study precisely the effect of multi-step seed-mediated growth on their magnetic properties.

Experimental Section

Synthesis of Fe (II) stearate precursor

Iron (II) stearate was synthesized following an already published protocol[13,27] by precipitation of sodium stearate (98.8 %, TCI) and ferrous chloride (99 % Acros Organic) salt in distilled water. Typically, 9.8 g (32 mmol) of sodium stearate were dissolved in 320 mL of distilled water. The aqueous solution was stirred at reflux for 30 min until complete dissolution of the stearate. Then, 3.16 g of iron (II) chloride tetra hydrate (16 mmol) were dissolved in 160 mL of distilled water and were added to the previous mixture under vigorous stir. A light orange precipitate immediately appears and the solution was kept at reflux and under stir for 15 min. The mixture was then cooled down to room temperature and the orange precipitate was separated by centrifugation (14 000 rpm, 10 min) followed by a filtration with a Buchner funnel. The product was washed 3 times with distilled water. Finally, it was dried for 14 h in an oven at 65 °C.

Synthesis of 10 nm iron oxide cores

Core magnetite nanoparticles were synthesized through a thermal decomposition technique following a previously reported method.[19] Briefly, 1.38 g (2.22 mmol) of the above mentioned home-made iron (II) stearate precursor were transferred in a two-necked round-bottom flask where 1.254 g (4.44 mmol) of oleic acid (99 %, Alfa aesar) and 20 mL of ether dioctyl (99 %, Sigma) were added. The mixture was then stirred at 100 °C for 30 min in order to remove water and solvent residues. After this, the set-up was connected to a condenser and the mixture was heated up at reflux (290 °C) for 2 hours with a heating ramp of 5 °C/min. The resulting black solution was then cooled down to 100 °C and the iron oxide nanoparticles were precipitated by adding an excess of acetone to be recovered with a centrifugation method (14 000 rpm, 5 min). Finally, the nanoparticles were washed several times by a mixture of chloroform: acetone (1 : 5) and stored in chloroform.

Addition of an iron oxide layer

The addition of an iron oxide layer on the nanoparticles was performed through a seed-mediated growth approach adapted from an already published protocol.[28] To add this layer on the nanoparticle, half of the volume of the iron oxide nanoparticles that were previously synthesized and stored in chloroform was transferred in a two-necked round bottom flask. The solvent was evaporated under vacuum before adding iron (II) stearate, oleic acid, 10 mL of ether dioctyl and 20mL of 1-octadecene. Iron (II) stearate and oleic acid were added according to the molar ratio $R = FeSt_{2\ shell} / FeSt_{2\ core} = 2$ (Table 5). The mixture was then stirred at 100 °C for 30 min before connecting the flask to the condenser. Here, the solution was heated-up at reflux (approximately 310 °C) for 2 hours with a heating ramp of 5 °C/min. The resulting black solution was then cooled down to 100 °C and the nanoparticles were precipitated by adding an excess of acetone in order to be recovered after centrifugation (14 000 rpm, 5 min). Finally, the nanoparticles were washed several times with a mixture of chloroform: acetone (1 : 5) and stored in chloroform. This protocol was repeated four times in order to synthesize iron oxide nanoparticles with up to four iron oxide layers.

Table 5.Iron (II) stearate and oleic acid quantities added for the different numbers of layers.

Layer number	m iron (II) stearate (g)	n iron (II) stearate (mmol)	m oleic acid (g)	n oleic acid (mmol)
1	1.384	2.22	1.273	4.51
2	0.690	1.11	0.646	2.29
3	0.345	0.55	0.335	1.19
4	0.174	0.28	0.160	0.57

Characterization techniques

Fourier transform infrared

Fourier transform infrared (FTIR) spectroscopy was performed using a Perkin Elmer Spectrum spectrometer in the energy range 4000−400 cm^{-1} on samples diluted in KBr pellets.

Granulometry

Granulometry measurements were performed by using a Malvern Zetasizer nanoseries. 5 mL of a dilute colloidal suspension of the nanoparticles in chloroform were deposited in a 5 mL quartz cuvette. The equilibration time was fixed to 120 s with a temperature of 25 °C. Finally, a single measurement consisting of 7 runs of 30 s was performed.

Transmission electron microscopy

Transmission electron microscopy (TEM) and high resolution TEM (HR-TEM) were performed by using JEOL 2100 LaB6 with a 0.2 nm point to point resolution. The nanoparticle sizes were calculated by measuring at least 300 nanoparticles from TEM micrographs by using the Image-J software. The layer thickness corresponds to half of the difference between nanoparticle sizes which were measured before and after adding the next layer. The size distribution was calculated by fitting these data with a log normal function.

X-ray diffraction

X-ray diffraction (XRD) patterns were recorded using a Bruker D8 Advance equipped with a monochromatic copper radiation (K_α = 0.154056 nm) and a Sol-X detector in the 20− 80° 2θ range with a scan step of 0.02°. High purity silicon powder (a = 0.543082 nm) was systematically used as an internal standard. Profile matching refinements were performed through the Fullprof software[29] using the modified Thompson-Cox-Hasting (TCH) pseudo-Voigt profile function.[30]

^{57}Fe Mössbauer spectroscopy

^{57}Fe Mössbauer spectra were performed at 77 K using a conventional constant acceleration transmission spectrometer with a ^{57}Co(Rh) source and a bath cryostat. Then, an in-field Mössbauer spectrum was collected at 11 K using a cryomagnetic device that generates an external magnetic field parallel to the γ-beam. The samples consist of 5 mg Fe/cm^2 powder concentrated in a small surface due to the rather low quantities. The spectra were fitted by means of the MOSFIT program[31] involving asymmetrical lines and lines with Lorentzian profiles, and an α-Fe foil was used as the calibration sample. The values of isomer shift are quoted relative to that of α-Fe at 300 K.

SQUID magnetometry

Magnetic measurements were performed on samples by using a Superconducting Quantum Interference Device (SQUID) magnetometer (Quantum Design MPMS-XL 5). Temperature dependent zero-field cooled (ZFC) and field cooled (FC) magnetization (M(T)) curves were recorded as follows: the powder sample was introduced in the SQUID at room temperature and cooled down to 5 K with no applied field after applying a careful degaussing procedure. A magnetic field of 7.5 mT was applied, and the ZFC magnetization curve was recorded upon heating from 5 to 300 K. The sample was then cooled down to 5 K under the same applied field, and the FC magnetization curve was recorded upon heating from 5 to 300 K. Magnetization curves as a function of a magnetic field (M(H)) were measured at 5 and 300 K. The magnetization was then measured at constant temperature by sweeping the magnetic field from +7 T to −7 T, and then from −7 T to +7 T. Magnetization saturation (M_S) was measured from M(H) curves recorded at 5 K.

Results and discussion

Synthesis strategy

Iron oxide nanoparticles were synthesized through a successive seed-mediated growth process (Figure 13) by adapting our previous work.[28] Pristine iron oxide nanoparticles (IOC) of 6.2 nm were synthesized through the thermal decomposition of a home-made iron (II) stearate precursor in dioctyl ether (T_b = 290 °C) in the presence of oleic acid.[19] These nanoparticles were then used as seeds in order to grow successively iron oxide layers by performing again the thermal decomposition of iron (II) stearate up to four times. Nanoparticles were washed after each synthesis step in order to remove residues and side products which may alter the growth steps. Then, half of the previously synthesized nanoparticles were used as seeds to grow the next layer. The quantity of iron stearate added in the reaction medium was defined as the molar ratio R = n $FeSt_{2\ layer\ n}$ / n $FeSt_{2\ core}$ = 2. The $Fe_{3-d}O_4(@Fe_{3-d}O_4)_n$ (with $1 \leq n \leq 4$) nanoparticles were named according to pristine nanoparticles used as iron oxide core (IOC) onto which n layers of iron oxide were successively grown (IOCSn).

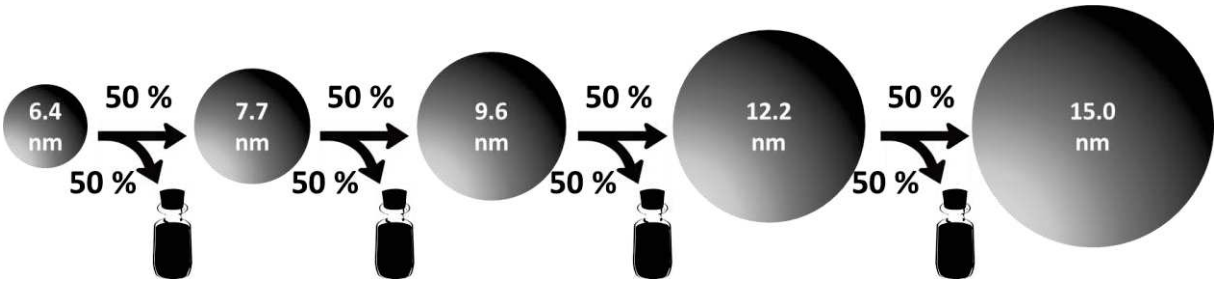

Figure 13. Schematic illustration showing the successive seed-mediated growth approach used to synthesize iron oxide nanoparticles (IOCSn).

Small iron oxide nanoparticles of 6.2 nm of size were grown up to a size of 15.0 nm thanks to a succession of five thermal decompositions according to a multi-seed-mediated growth approach.

Transmission electron microscopy

TEM micrographs show that the size of nanoparticles increased gradually from 6.4 ± 0.8 nm to 15.0 ± 3.4 nm after each thermal decomposition step according to the same ratio R = 2 (Figure 14, Table 6, Figure S1). The size distribution became slightly broader and the morphology deviated from spheres to faceted shapes. This behavior was ascribed to the different surface energies of facets which induced different plane growth and growth kinetics.[32–34] Indeed, each facet corresponds to a different crystal plane with different densities of Fe and O atoms.

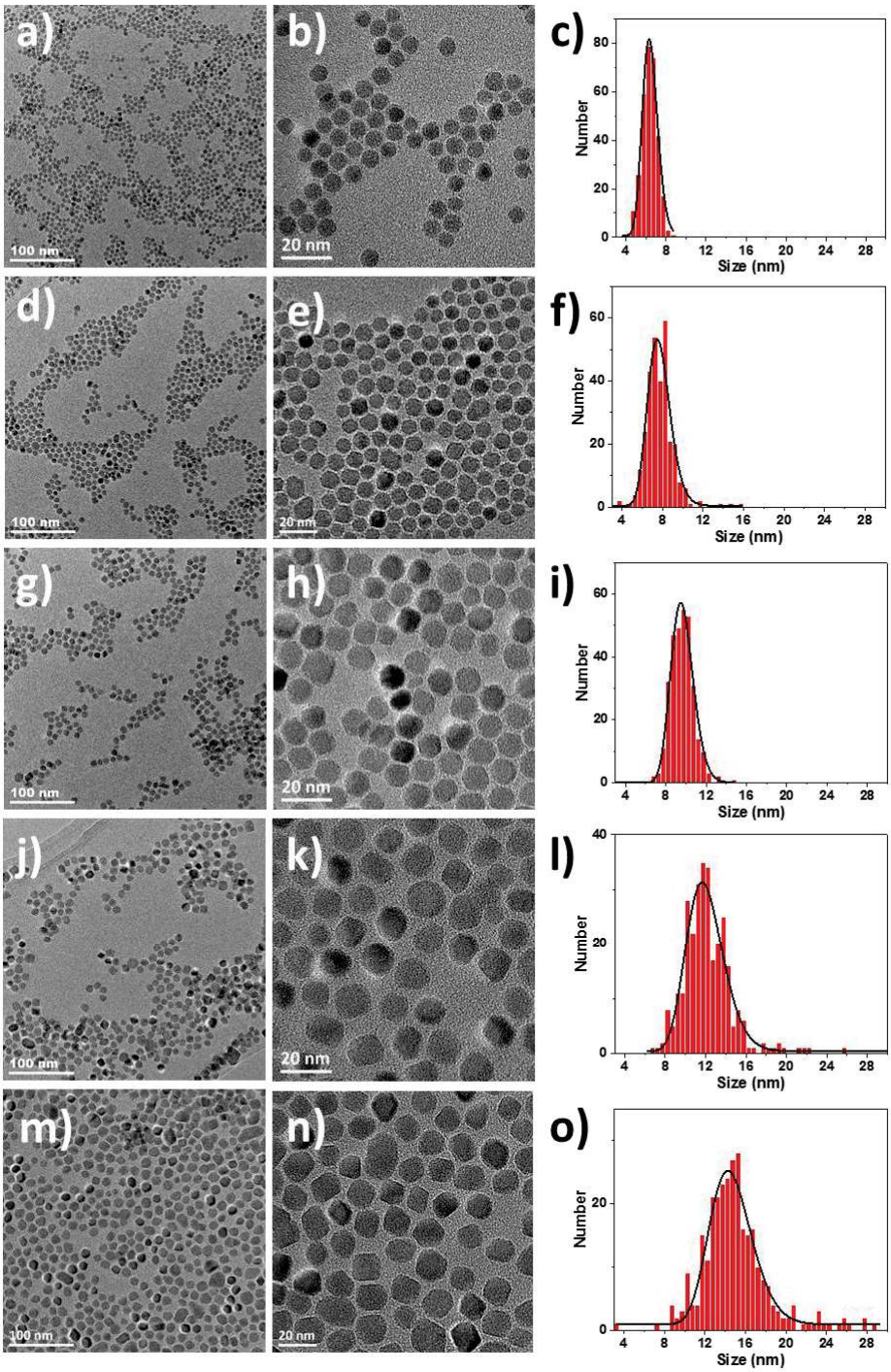

Figure 14. TEM micrographs of IOC (a, b), IOCS1 (d, e), IOCS2 (g, h), IOCS3 (j, k), IOCS4 (m, n) with c, f, I, l, o) their related size distributions with lognormal fitting (black line).

Table 6. Structural characteristics of IOCSn nanoparticles.

	IOC	IOCS1	IOCS2	IOCS3	IOCS4
TEM size (nm)	6.4 ± 0.8	7.7 ± 1.4	9.6 ± 1.2	12.2 ± 2.7	15 ± 3.4
Size increase (nm)	-	0.7	1.0	1.3	1.4
Layer volume (nm^3)	-	101	224	488	816
Cell parameter (Å)	8.378 ± 0.020	8.349 ± 0.010	8.364 ± 0.010	8.352 ± 0.010	8.348 ± 0.010
Crystal size (nm)	6.4 ± 0.2	8.0 ± 0.2	9.3 ± 0.3	10.9 ± 0.4	12.3 ± 0.5

TEM micrographs evidenced the growth of the size of the nanoparticles from 6.4 to 15.0 nm among the succession of the thermal decomposition. The close to sphere shape of the native iron oxide nanoparticles slightly deviate with the growth of the successive layers. However, considering a succession of five thermal decompositions, the shape and size distribution of the final nanoparticles remain reasonable.

Fourier-transform infra-red and granulometry

The chemical composition of the nanoparticles was studied by FT-IR spectroscopy (Figure 15a, b). Bands corresponding to the C-H bonds of alkyl chains of oleic acid molecules were observed at 2 923 ($\nu_{as}CH_2$) and 2 853 cm^{-1} (ν_sCH_2). Bands at 1 521 cm^{-1} ($\nu_{as}COO^-$) and 1 446 cm^{-1} (ν_sCOO^-) correspond to the C-O bonds of the carboxylic acid group which interact with the nanoparticle surface.[35] The difference between frequencies of both bands, $\Delta = \nu_{as}(COO^-) - \nu_s(COO^-)$, depends on the coordination mode of the oleic acid with the nanoparticle surface: chelating bidendate (Δ < 110 cm^{-1}), bridging bidendate (140 < Δ < 190 cm^{-1}) or chelating monodendate (Δ = 200-320 cm^{-1}). Here, Δ is 78 cm^{-1} which corresponds to a chelating bidentate interaction in accordance with Bronstein and al.[11] The absence of any contribution at 1 710 cm^{-1} ($\nu_{C=O}$) agree with the removal of free oleic acid after washing.
A broad band between 750 and 500 cm^{-1} corresponding to the Fe-O vibration mode was also observed. Several oscillations with the most intense contributions at 570 and 638 cm^{-1} agreed with the presence of maghemite.[19] In contrast, the presence of magnetite which displays a broad band centered at 570 cm^{-1} with a small shoulder at 700 cm^{-1} could not be observed directly.[36] Furthermore, the amount of oleic acid can be evaluated with respect to iron oxide nanoparticles thanks to the intensity ratio of ν_{as}(C-H)/ν(Fe-O) (Figure 15a) which is equal to 1.1, 1.1, 0.81, 0.79 and 0.82 for IOC, IOCS1, IOCS2, IOCS3 and IOCS4, respectively. Considering the size increase from IOC to IOCS1 and that this ratio is the same, we expect the amount of OA to be lower with respect to the number of IOCS1 than IOC nanoparticles. The peak centered to 721 cm^{-1} for IOCS3 and IOCS4 (Figure 15b), was attributed to the scissoring of H-C-H bond of free stearate that remains in the sample. Further washes could not be performed because granulometry measurements (intensity count) showed a second contribution corresponding to a much larger hydrodynamic diameter than the size measured from TEM, thus resulting in aggregated nanoparticles (Figure 15d). Nevertheless, granulometry measurements performed in volume count (Figure 15c) displayed monomodal distributions of hydrodynamic diameters centered to 8.2, 11.1, 13.1, 17.7 and 19.9 nm for IOC, IOCS1, IOCS2, IOCS3 and IOCS4, respectively. The gradual increase of the hydrodynamic diameter is clearly correlated to the increase of the nanoparticle sizes. These values are slightly larger than the TEM sizes because of the presence of oleic acid at the surface of the nanoparticles. Therefore, FT-IR spectroscopy and granulometry measurements agree with partially oxidized iron oxide nanoparticles coated with oleic acid molecules grafted at their surface.

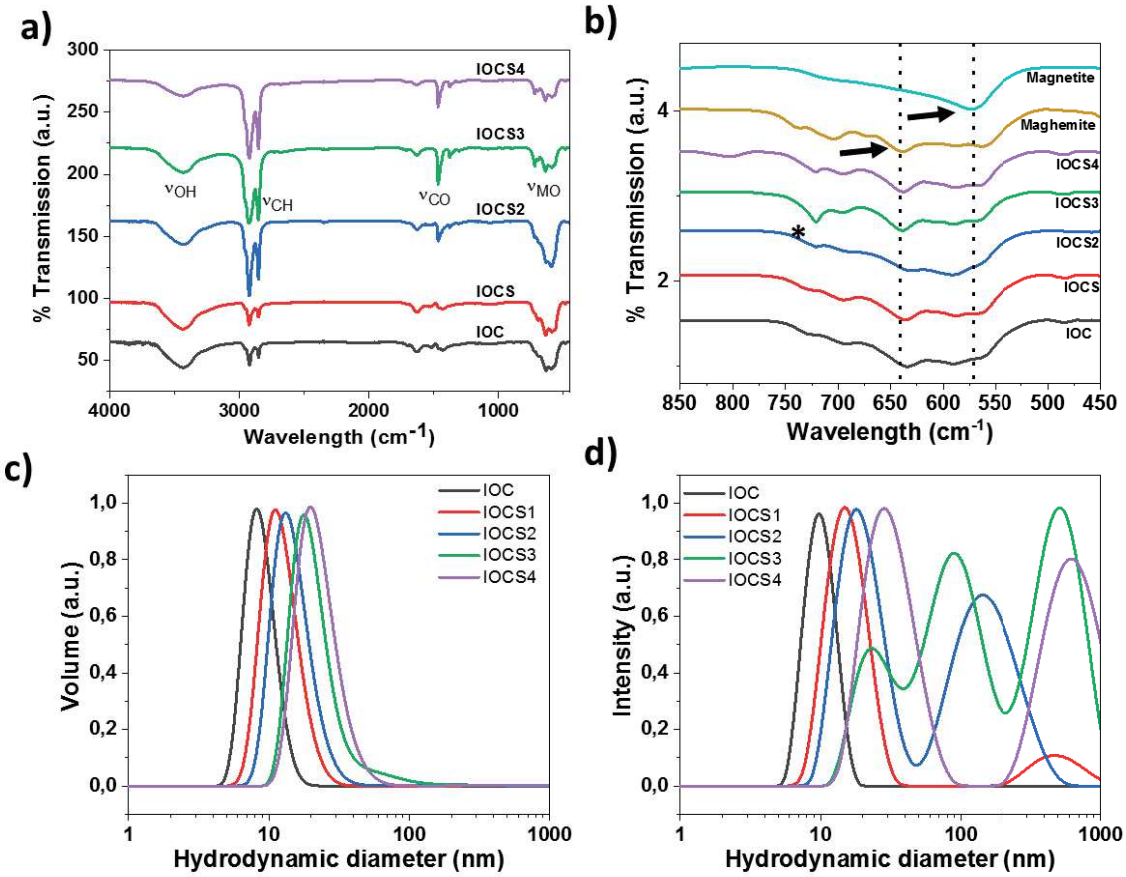

Figure 15. IOCSn nanoparticles. a, b) FT-IR spectra with b) an enlargement in the range 850 – 450 cm^{-1}. Black arrows indicate the major contributions of magnetite and maghemite. Dotted lines are guides to the eyes. The star indicates the contribution of free iron stearate. Granulometry measurements performed on nanoparticle suspensions in chloroform plotted as c) volume count and, as d) intensity count.

FT-IR spectroscopy has evidenced that oleic acid molecules are grafted at the surface of each nanoparticles. The presence of this ligand ensures the nanoparticles form stable suspensions in most organic solvent, as shown by granulometry measurements. The shape and displacement of the M-O vibration band in FT-IR spectroscopy allowed to conclude on the presence of oxidation within the different nanoparticles due to their exposition to air during the intermediate washes.

High-resolution transmission electron microscopy

High resolution TEM (HR-TEM) (Figure 16) was performed in order to get a deeper insight in the crystal structure of nanoparticles. HR-TEM micrographs show continuous lattice fringes all across each nanoparticle which agree with single crystal structure. The calculations of Fast Fourier transforms (FFT) with a Bragg filter from HR-TEM micrographs showed several spots which correspond to *hkl* reflections that are in accordance with the iron oxide spinel (either magnetite or maghemite) structure (Table S1). The calculation of reverse FFT avoided the incoherent background and displayed continuous and straight lattice fringes all across each IOCSn nanoparticle. Therefore, no dislocation or crystal defect was observed in the nanoparticles.[37] It shows the successive epitaxial growth of each iron oxide layers from the IOCSn nanoparticles.

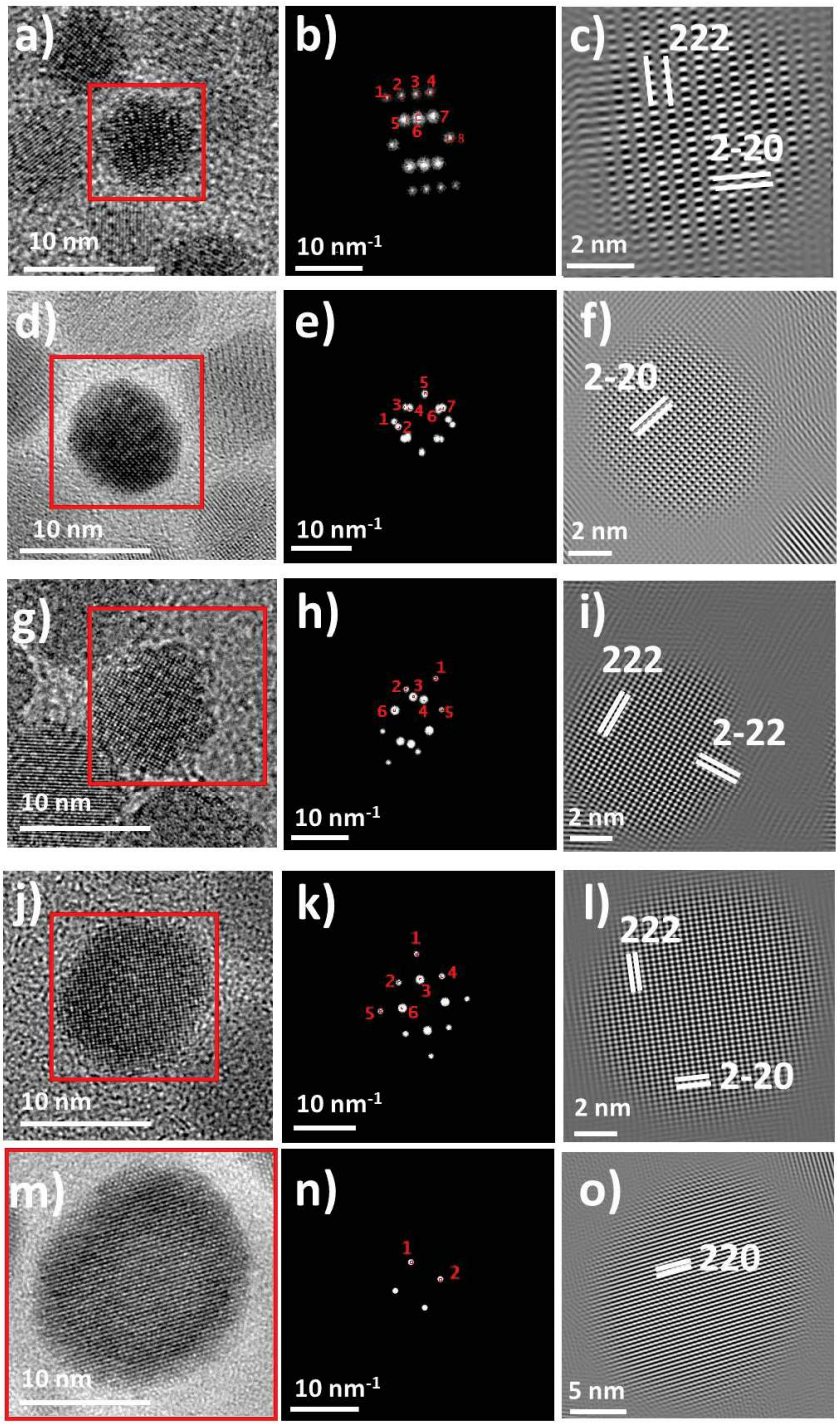

Figure 16. a, d, g, j, m) HR-TEM micrographs of IOCSn. b, e, h, k, n) FFT corresponding to the zone of interest in TEM micrograph (red square) and calculated with a Bragg filter. c, f, I, l, o) Inverse FFT of the filtered FFT according to the indexed diffraction spots in FFT corresponding to specific hkl reflections (Table S2).

HR-TEM has demonstrated that the different iron oxide layers are epitaxially grown at the surface of the nanoparticles, as expected from seed-mediated growth synthesis. It results that the core(@shell)n nanoparticles display single crystal like structures.

X-ray diffraction

XRD patterns recorded for each IOCSn nanoparticle are all typical of the AB_2O_4 spinel structure (Fd-3m space group) of iron oxide (Figure 17a). The diffraction peaks become narrower after each decomposition step. It agrees with the epitaxial growth of each iron oxide layer resulting in larger crystal domains. Rietveld refinement showed that the crystal size increased from 6.4 nm (IOC) to 12.3 nm (IOCS4). All these values are consistent with TEM sizes according to the experimental error. Cell parameters are intermediate to magnetite (a = 8.396 Å, JCPDS card n° 19-062) and maghemite (a = 8.338 Å, JCPDS card n° 39-1346) (Table 6). It agrees with the partial oxidation of nanoparticles at their surface, thus corresponding to the chemical composition $Fe_{3-d}O_4$. This result is in accordance with FT-IR spectroscopy analysis and is typical of small iron oxide nanoparticles synthesized by the thermal decomposition method.[19,36,38] It is worth noting that the evolution of the chemical compositions differs from our previous works on the "one pot" synthesis of nanoparticles which showed that the cell parameter was closer to magnetite when the nanoparticle size increased.[18,19,38] It is well established that despite the high reducing reaction medium, the surface of nanoparticles spontaneously oxidized when they are exposed to air upon washing. Therefore, the structure of IOC nanoparticles is expected to consist of a magnetite core with a gradient of Fe^{2+} that decreases from the center to the surface of the nanoparticle.[19] In this study, each iron oxide layer grown onto the IOCSn nanoparticle is oxidized upon washing and mainly consists of maghemite. Indeed, we showed that the thickness of the oxidized layer is about 2 nm[19] which is larger than the average thickness of each layer (< 1.4 nm) (Table 1). Therefore, the values of cell parameters agree with the increase of the maghemite content with the size of IOCSn nanoparticles (Figure 17b). IOCS1 shows a lower cell parameter than expected, possibly due to longer exposition times to air upon washing.

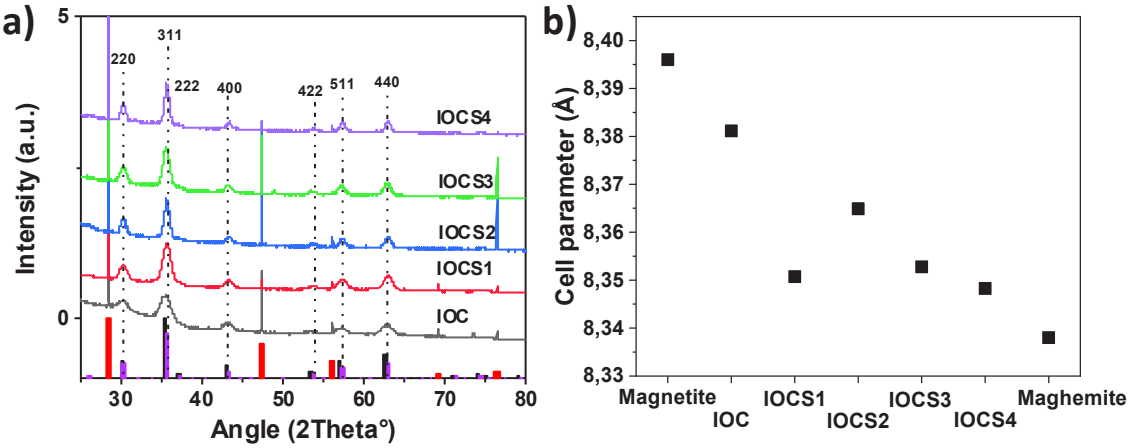

Figure 17. a) XRD patterns recorded for IOCSn nanoparticles. Diagrams correspond to references (black bars: Fe_3O_4 (JPCDS card n°19-062) and magenta bars: γ-Fe_2O_3 (JCPDS card n° 00-039-1346). b) Cell parameters calculated for each IOCSn sample. Blue and orange lines correspond to magnetite (8.396 Å) and maghemite (8.338 Å) references respectively.

The indexation of X-ray diffraction patterns point out the solely presence of the spinel structure for each IOCSn nanoparticles, in agreement with a $Fe_{3-d}O_4$ structure. The narrowing of the peaks from IOC to IOCS4 shows the crystal size increase among the growth of the different iron oxide layers, in agreement with TEM size measurements. And the calculation of the mean cell parameters reveal a tendency on the gradual increase of the oxidation state in the whole nanoparticles as long as the layers are grown, in accordance with the oxidation of the different layers that might be favored by the intermediate washes.

Mössbauer spectroscopy

^{57}Fe transmission Mössbauer spectroscopy was performed in order to get more precise information on the oxidation degree of Fe atoms and their site occupancy in the spinel structure. Spectra recorded at 77 K without any applied field (Figure 18) show a sextet for each size of nanoparticle which is in agreement with a magnetic blocked state i.e. ferrimagnetism at low temperature. Nevertheless, the broad lines of the magnetic sextets for IOC and IOCS1 evidenced the presence of a superparamagnetic relaxation phenomena. In contrast, the lines of sextets became narrower after each decomposition step which is consistent with the increase of the nanoparticle size, i.e. slower superparamagnetic relaxation, and higher magnetic anisotropy energy (see the section on magnetic properties below).
Mössbauer spectra were fitted in order to extract hyperfine parameters such as the isomer shift and the hyperfine field which are very helpful to estimate the chemical composition of nanoparticles (Table 7). In magnetite, Fe^{3+}_{Td} and Fe^{3+}_{Oh} display at 77K (below the Verwey transition) rather close values of isomer shifts (0.40 mm/s and 54 mm/s, respectively) which clearly differ from that of Fe^{2+}_{Oh} (1.15 mm/s).[39] While the low resolution of sextets for IOC and IOCS1 only allows to extract average values of the isomer shift (0.46 and 0.44 mm/s), well resolved sextets recorded for IOCS2, IOCS3 and IOCS4 could be fitted with several components corresponding to specific site occupancies and the oxidation states of Fe cations.
The mean values of the isomer shifts calculated for IOC (0.46 mm/s) and IOCS1 (0.44 mm/s) are consistent with the presence of Fe^{3+} species, i.e. a composition of nanoparticles which is very close to that of maghemite. Nevertheless, the presence of Fe^{2+} species cannot be strictly ruled out according to the cell parameters calculated for IOC. For IOCS2, three isomer shifts values of 0.47, 0.42 and 0.42 mm/s were attributed to Fe^{3+} in Oh and Td sites. A fourth contribution (1.02 mm/s) was unambiguously ascribed to Fe^{2+} in Oh sites. Nevertheless, Fe^{2+} species represent a very low contribution of about 4 % which leads to a general formula of $(Fe^{3+})[Fe_{0.12}{}^{2+}Fe_{1.88}{}^{3+}]O_4$. In addition, the spectra of IOCS3 and IOCS4 were fitted by two contributions (0.41 and 0.45 mm/s) corresponding to Fe^{3+} species. A third contribution (1.07 and 1.09 mm/s) corresponding to Fe^{2+} was also used. The decrease of this contribution while the nanoparticles size increases is consistent with the very low Fe^{2+}content as observed from XRD and FT-IR.
The values calculated for hyperfine fields are intermediate to the ones of Fe^{2+}_{Td} (34.5 T) and Fe^{3+}_{Td} (50.7 T) / Fe^{3+}_{Oh} (52.8 T)[40] for IOC and IOCS1. For IOCS2-4, they are much closer to the ones of Fe^{3+} and increased with the nanoparticles size from 49.5 T to 51 T. It is consistent with a lower content of Fe^{2+} when the size of IOCSn nanoparticles increases although no contribution was calculated for Fe^{2+} species. According to these results, we expect that each layer n grown successively onto each IOCSn-1 nanoparticle was fully oxidized upon washing under air.

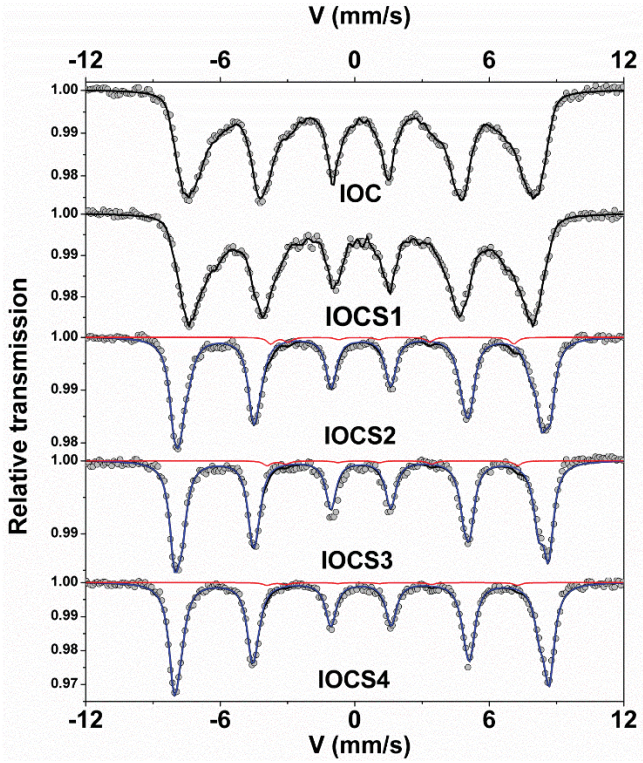

Figure 18. 57Fe Mössbauer spectra recorded at 77 K and under zero magnetic field. Blue curves correspond to the final fits and red curves to the residues.

Table 7. Refined values of hyperfine parameters calculated from the fit of 57Fe Mössbauer spectra recorded at 77 K and under zero magnetic field. IS, Γ, QS, 2ε, Bhf correspond to the isomer shift (value relative to that of a-Fe at 300 K, width at half height, quadrupole splitting or quadrupole shift and hyperfine field.

Sample	IS (mm/s)	Γ (mm/s)	QS or 2ε (mm/s)	B_{hf} (T)	Relative subspectral area (%)
	± 0.01	**± 0.02**	**± 0.01**	**± 0.5**	**± 2**
IOC	**0.46**	-	**-0.01**	**41**	**Mean**
IOCS1	**0.44**	-	**-0.01**	**41.8**	**Mean**
IOCS2	0.47	0.51	0.02	51.9	34
	0.42	0.57	0.02	49.9	44
	0.42	0.68	-0.09	47.1	18
	1.02	0.4	1.11	34.3	4
	0.46	-	**0.05**	**49.5**	**Mean**
IOCS3	0.45	0.52	0.02	51.5	57
	0.41	0.55	-0.01	49.2	40
	1.07	0.40	1.65	34.4	4
	0.435	-	**0.01**	**50.5**	**Mean**
IOCS4	0.45	0.55	0.02	51.7	69
	0.41	0.59	-0.03	49.5	29
	1.09	0.40	1.50	34.4	2
	0.441	-	**0.01**	**51**	**Mean**

^{57}Fe Mössbauer spectroscopy has demonstrated that the layer grown at the surface of the nanoparticles were oxidized, hence the proportion of Fe^{2+}/Fe^{3+} has decreased. The Fe^{2+} contribution observed is attributed to the core of the nanoparticles. Such results agrees with the behavior observed in XRD and FT-IR.

SQUID magnetometry measurements

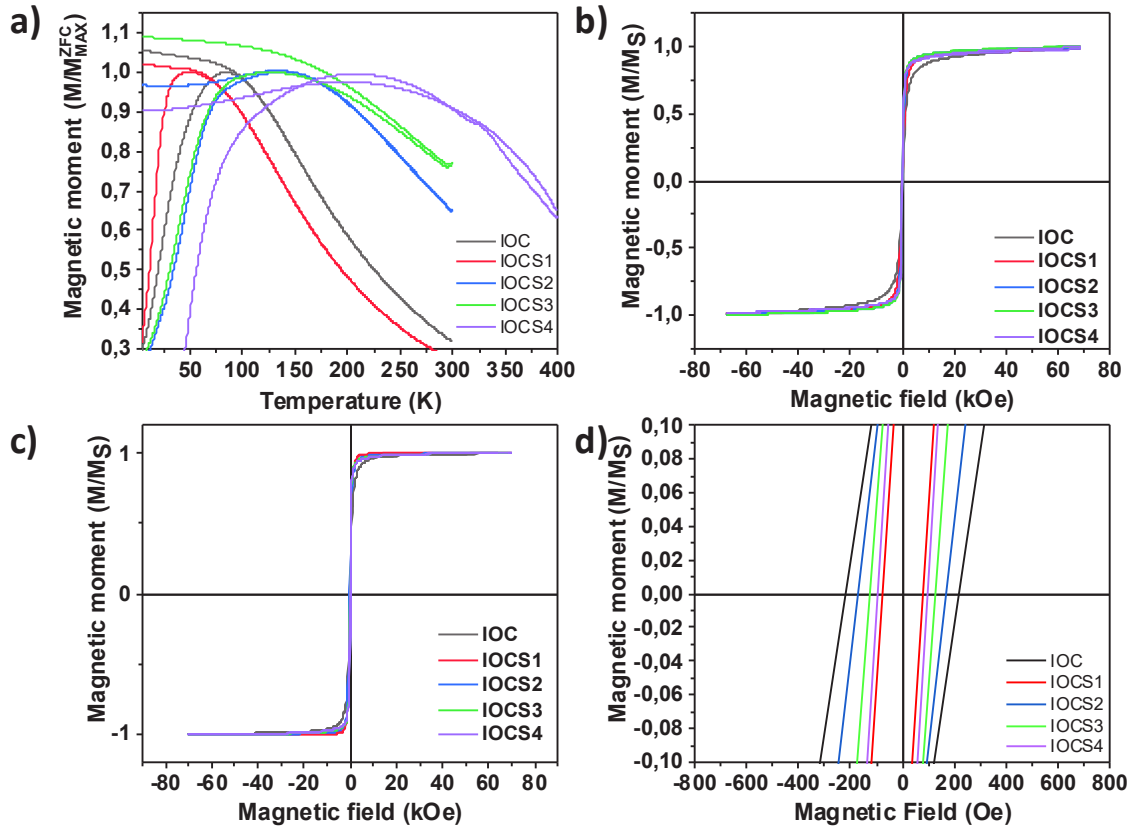

Figure 19. a) Temperature dependent magnetization curves. Magnetic field dependent magnetization curves recorded at b) 300K, c) 5 K with d) an enlargement of M(H) curve recorded at 5 K.

Table 8. Magnetic properties of IOCSn nanoparticles. T_{max} corresponds to the maximum of the magnetization versus the temperature. T_B, H_C, M_S and M_R are respectively the Blocking temperature, the coercive field, the magnetization at saturation and the remanent magnetization.

Echantillon	T_{max} (K)	T_B (K)	Hc 5K (Oe)	Ms 5K (emu/g)	M_R/M_S
IOC	84	22	219	85 ± 5	0.21
IOCS1	50	15	80	74 ± 5	0.20
IOCS2	130	45	171	50 ± 5	0.54
IOCS3	124	42	127	53 ± 5	0.27
IOCS4	203	33	96	78 ± 5	0.31

The magnetic properties of IOCSn nanoparticles were studied by SQUID magnetometry (Figure 19). Temperature dependent magnetization curves (Figure 19a) were recorded under a static magnetic field of 75 Oe after zero field cooling (ZFC) and field cooling (FC) under 75 Oe**.** The maximum of magnetization (T_{max}) in the ZFC curves is generally ascribed to the blocking temperature T_B which refers to the transition between a blocked magnetic domain and the superparamagnetic behavior. According to the Stoner-Wohlfarth (SW) model,[41] T_B is expected to increase with the nanoparticle size where the magnetocrystalline energy (E_a) is defined as:

$$E_a = KV = 25\ k_B T_B \qquad \text{(equation 1)}$$

with K the anisotropy constant, V the nanoparticle volume and k_B the Boltzmann constant.

Although T_{max} increases with the nanoparticle size, it is worth noting that below a critical nanoparticle size, the surface anisotropy significantly contributes to the magnetic anisotropy energy. Therefore, K includes both volume and surface contributions and becomes the effective anisotropy constant K_{eff}. As a consequence, the highest contribution of surface anisotropy in IOC may explain the higher T_{max} than IOCS1. Furthermore, the SW model was reported for isolated nanoparticles. In this study, all nanoparticles were studied in the powder form, which means that they are submitted to dipolar interactions.[35,42–44] T_{max} being well known to increase with dipolar interactions, it cannot be assimilated to T_B. The dipolar energy (E_{dip}) is described as :[45]

$$E_{dip} = \frac{\mu_0 \mu^2}{4\pi d^3} \qquad \text{(Equation 2)}$$

where $\mu = M_S V$ with M_S the saturation magnetization and d, the interparticle distance.

In this study, nanoparticles being studied as powders, the distance between them depends essentially on the quantity of oleic acid grafted at their surface. As shown by FT-IR spectra, the ratio between iron oxide and oleic acid is the same for IOC and IOCS1. Therefore, the volume of IOCS1 being larger than IOC, we expect the average interparticle distance to be larger between IOCS1 than IOC nanoparticles. According to equation 2, although the magnetic moment is larger in IOCS1 than IOC, the dipolar energy is expected to be the weakest in IOCS1, thus consistent with a lower T_{max} for IOCS1 than IOC.

IOCS2 and IOCS3 also display very close T_{max} which can be explained by a similar phenomenon. ZFC curves are much broader than the ones of smaller nanoparticles which cannot solely be explained by the size distribution. Indeed, nanoparticles being studied as powders, it means that the structure of their assemblies is 3D random with a very broad distribution of interparticle distances, i.e. the strength of dipolar energy. Therefore, broad ZFC curves correspond to the distribution of energy barriers between the superparamagnetic state and a blocked magnetic state which depends on the size (E_a) and on the spatial arrangement (E_{dip}) of the nanoparticles. This behavior is confirmed by the largest nanoparticle IOCS4 which display the broadest ZFC curve.

According to the work of Bruvera and al.**,**[46] the blocking temperatures (T_B) at which happens the transition between the blocked state and superparamagnetism is described more accurately as a distribution of the anisotropy energy barriers according to :

$$f(T_B) \approx d(M_{ZFC}\text{-}M_{FC})/dT \qquad \text{(Equation 3)}$$

In this case, T_B is considered to be independent of the size distribution of nanoparticles. Although these values may be affected by dipolar interactions,[47] they are rather close to expected values, except for IOCS4 which should be the highest (Table 8, Figure S2).

M(H) curves were also recorded at 300 K (Figure 19b) and 5 K (Figure 19c, d) under a magnetic field of +/- 7 T. At 300 K, both branches perfectly overlap for IOC, IOCS1, IOCS2 and IOCS3 and agree with the superparamagnetic behavior. In contrast, IOCS4 displays a small opened hysteresis cycle corresponding to a coercive field (H_C) of 43 Oe which agrees with the M(T) ZFC curve. At 5 K, the hysteresis loop of each sample was opened. H_C decreases from 219 Oe (IOC) to 96 Oe (IOCS4) according to the increase of the nanoparticle size. These results agree with stronger dipolar interactions.[19,48,49] In addition, the H_C of IOCS1 (80 Oe) was expected to be higher and may be ascribed to shorter interparticle distances as mentioned above.

The M_R/M_S ratio (Table 8), also called the alignment ratio, is used to describe the mean orientation of the magnetic moments of the nanoparticles. It increased from 0.21 (IOC) to 0.31 (IOCS4) with the size of the nanoparticles in accordance with super spin glass resulting from stronger dipolar interactions.[47] IOCS2 displays a different value of 0.5 which corresponds to the random orientation of isolated nanoparticles.[50]

The variation of the magnetization saturation (M_S) is also incoherent with the nanoparticle size increase (Table 8, Figure S3). Considering the size of IOC (6.4 nm) and IOCS1 (7.7 nm) their M_S values (85 emu/g and 74 emu/g, respectively) are very high according to the literature. For instance, iron oxide nanoparticles with sizes of 5-8 nm displayed M_S of 50-60 emu/g whatever "one pot"[51] or seed mediated growth[25] synthesis based on thermal decomposition. As mentioned above, surface effects predominate on the volume contribution in the case of nanoparticle below a critical size. In the case of nanoparticles with a high crystalline quality, M_S can be close to the ones of bulk magnetite (92 emu/g) and maghemite (76 emu/g). A M_S value of 79 emu/g was reported for small iron oxide nanoparticles of 5 nm due their high crystalline quality.[52] The M_S values of IOCS2 (50 emu/g) and IOCS3 (53 emu/g) agree with previous reports and may be ascribed to the lower contribution of surface anisotropy and crystalline quality.[19] In contrast, the significant increase of M_S for IOCS4 (74 emu/g) is ascribed to the highest volume contribution than surface effect although the magnetite content does not increase**.** It is worth noting that Espinosa et *al.*[25] reported on the decrease of M_S when the nanoparticle size was increased from 6 to 18 nm by seed-mediated growth. This behavior was ascribed to the presence of interfacial magnetic frustration due to structural defects in the seeds and also to the development of additional anisotropy source for larger size of nanoparticles.

SQUID magnetometry measurements agrees on the global increase of T_{max} and T_B coherently with the growth of the nanoparticles. Some disparities were nevertheless attributed to the presence of dipolar interactions. The growth of layers on the seeds resulted in the decrease of H_C measured at 5 K from IOC to IOCS4, due to the increase of dipolar interactions. At 300 K all nanoparticles display a superparamagnetic behavior except IOCS4 which shows a small H_C of 43 Oe in agreement with M(T) results. The alignment ratio evidenced a tendency to increase from IOC to IOCS4, in agreement with a super spin glass behavior arising from stronger dipolar interactions. The variation of M_S was however incoherent with no tendency and high M_S values for IOC, IOCS1 and IOCS4 compared to the literature. These observations were attributed to surface effects but also from interfacial magnetic frustration resulting from structural defects.

General discussion

The size of iron oxide nanoparticles increased linearly after each decomposition step. This behavior was ascribed to the constant precursor/seed molar ratio used to grow successively iron oxide layers. The shape of nanoparticles is close to faceted spheres although it deviates slightly after the growth of each layer. Such a behavior can be explained by the different surface energy of facets which induce different growth kinetics. According to LaMer theory,[7] the synthesis of nanoparticles depends on the concentration of monomers which result from the thermal decomposition of iron stearate. Above a critical concentration, seeds are formed in the solution. Therefore, the monomer concentration decreases below a second critical concentration thus resulting in the growth of crystals from seeds. In our study, the seed mediated growth is significantly dependent on the precursor/seeds ratio and on the reaction time which are critical parameters for hetero nucleation growth.[23] It happens according to two different stages. Firstly, the production of monomers resulting from the decomposition of iron stearate generates homo-nucleation in the solution that may avoid the seeds from a rapid growth. Then, a second burst of nucleation happens and leads to the formation of new germs at the surface of the seeds. Then, the remaining monomers and the small germs from the first burst of nucleation act as a monomer tank that participates to a monomer equilibrium in the solution through the dissolution of the first germs and the crystal growth onto the nanoparticles. The dissolution of germs is favored by the Gibbs-Thomson equation which describes the dependence of the solubility of the germs as a function of 1/(exp(diameter)).[53] Below a critical radius, the nanoparticles dissolve according to the Ostwald ripening process thus generating new monomer equilibria which contribute to the growth of nanoparticles and lead to narrow size distribution at the equilibrium.

Besides the size increase of nanoparticle through a multi-step seed-mediated growth process, the chemical composition of nanoparticles is strongly affected by the synthesis method. It is well known that the pristine nanoparticles consist of a magnetite core with a surface layer oxidized in maghemite with a gradient composition from their surface. In this study, the size increase of iron oxide nanoparticles through a seed-mediated growth process resulted in the gradual increase of maghemite with respect to magnetite. In contrast, the “one pot” synthesis of nanoparticles resulted in the increase of magnetite content with the nanoparticle size.[19] Therefore, it means that in our case, magnetite is directly oxidized after the growth of each layer n at the surface of IOCSn-1 nanoparticles. Therefore, we expect the pristine magnetite core to be preserved while the thickness and volume of the maghemite layer increased gradually. Although it is usually admitted that the oxidation of magnetite in maghemite generates structural defects in the crystal structure, HR-TEM revealed the high crystallinity of our nanoparticles, whatever the number of seed mediated growth steps. Each nanoparticle displays a single crystal structure and no structural defects could be observed from reverse FFT. These results were partially confirmed by XRD patterns which showed the increase of the crystal size, thus agreeing with the epitaxial growth of the iron oxide layer at the surface of nanoparticles.

The increase of nanoparticle size resulted in the global enhancement of the effective magnetic anisotropy energy as well as the dipolar energy. However, the former is directly affected by the amount of oleic acid which is grafted at the surface of nanoparticles. Some inconsistencies in the evolution to T_{max} and H_C with the increase of nanoparticle size can be explained by irregular average interparticle distances in random assemblies. Therefore, some incoherent variations of dipolar interactions alter the evolution of magnetic parameters thus avoiding, in some case, their rational variation as function of the nanoparticle size. The surface anisotropy energy also enhanced significantly M_S in the case of the smallest nanoparticles feature by high crystallinity.

Conclusion

The successive seed-mediated growth process allowed us to increase the size of iron oxide nanoparticles from 6 to 15 nm. Although the morphology deviated slightly from spheres, the seed-mediated growth was performed up to four times. Each iron oxide layer n was grown successively by epitaxy from the surface of iron oxide IOCSn-1 nanoparticles without any structural defects. Such a strategy preserved the core with high magnetite content while the maghemite surface layer increased gradually. The increase of the nanoparticle size resulted in the enhancement of the effective magnetic anisotropy energy. The successive seed-mediated growth approach that we report here opens new perspective toward the design of nanoparticles with tunable magnetic properties which are highly desired for the development of applications related to mass storage media or biomedicine.

References

(1) Gutfleisch, O.; Willard, M. A.; Brück, E.; Chen, C. H.; Sankar, S. G.; Liu, J. P. Magnetic Materials and Devices for the 21st Century: Stronger, Lighter, and More Energy Efficient. *Advanced Materials* **2011**, *23* (7), 821–842.

(2) Singamaneni, S.; Bliznyuk, V. N.; Binek, C.; Tsymbal, E. Y. Magnetic Nanoparticles: Recent Advances in Synthesis, Self-Assembly and Applications. *Journal of Materials Chemistry* **2011**, *21* (42), 16819–16845.

(3) Thomson, B. D. T. a. T. Nanofabricated and Self-Assembled Magnetic Structures as Data Storage Media. *Journal of Physics D: Applied Physics* **2005**, *38* (12), R199.

(4) Lu, A.-H.; Salabas, E. L.; Schüth, F. Magnetic Nanoparticles: Synthesis, Protection, Functionalization, and Application. *Angewandte Chemie International Edition* **2007**, *46* (8), 1222.

(5) Hyeon, T.; Lee, S. S.; Park, J.; Chung, Y.; Na, H. B. Synthesis of Highly Crystalline and Monodisperse Maghemite Nanocrystallites without a Size-Selection Process. *J. Am. Chem. Soc.* **2001**, *123* (51), 12798–12801.

(6) Bedanta, S.; Kleemann, W. Supermagnetism. *J. Phys. D: Appl. Phys.* **2008**, *42* (1), 013001.

(7) La Mer, V. K.; Dinegar, R. H. Theory, Production and Mechanism of Formation of Monodispersed Hydrosols. *Journal of the American Chemical Society* **1950**, *72* (11), 4847–4854.

(8) Laurent, S.; Forge, D.; Port, M.; Roch, A.; Robic, C.; Vander Elst, L.; Muller, R. N. Magnetic Iron Oxide Nanoparticles: Synthesis, Stabilization, Vectorization, Physicochemical Characterizations, and Biological Applications. *Chemical Reviews* **2008**, *108* (6), 2064.

(9) Tartaj, P.; Morales, M. P.; Gonzalez-Carreño, T.; Veintemillas-Verdaguer, S.; Serna, C. J. The Iron Oxides Strike Back: From Biomedical Applications to Energy Storage Devices and Photoelectrochemical Water Splitting. *Advanced Materials* **2011**, *23* (44), 5243–5249.

(10) Nemati, Z.; Alonso, J.; Rodrigo, I.; Das, R.; Garaio, E.; García, J. Á.; Orue, I.; Phan, M.-H.; Srikanth, H. Improving the Heating Efficiency of Iron Oxide Nanoparticles by Tuning Their Shape and Size. *J. Phys. Chem. C* **2018**, *122* (4), 2367–2381.

(11) Bronstein, L. M.; Huang, X.; Retrum, J.; Schmucker, A.; Pink, M.; Stein, B. D.; Dragnea, B. Influence of Iron Oleate Complex Structure on Iron Oxide Nanoparticle Formation. *Chem. Mater.* **2007**, *19* (15), 3624–3632.

(12) Cotin, G.; Kiefer, C.; Perton, F.; Ihiawakrim, D.; Blanco-Andujar, C.; Moldovan, S.; Lefevre, C.; Ersen, O.; Pichon, B.; Mertz, D.; et al. Unravelling the Thermal Decomposition Parameters for The Synthesis of Anisotropic Iron Oxide Nanoparticles. *Nanomaterials* **2018**, *8* (11), 881.

(13) Cotin, G.; Kiefer, C.; Perton, F.; Boero, M.; Özdamar, B.; Bouzid, A.; Ori, G.; Massobrio, C.; Begin, D.; Pichon, B.; et al. Evaluating the Critical Roles of Precursor Nature and Water Content When Tailoring Magnetic Nanoparticles for Specific Applications. *ACS Applied Nano Materials* **2018**, *1* (8), 4306–4316.

(14) Hufschmid, R.; Arami, H.; Ferguson, R. M.; Gonzales, M.; Teeman, E.; Brush, L. N.; Browning, N. D.; Krishnan, K. M. Synthesis of Phase-Pure and Monodisperse Iron Oxide Nanoparticles by Thermal Decomposition. *Nanoscale* **2015**, *7* (25), 11142–11154.

(15) Kovalenko, M. V.; Bodnarchuk, M. I.; Lechner, R. T.; Hesser, G.; Schäffler, F.; Heiss, W. Fatty Acid Salts as Stabilizers in Size- and Shape-Controlled Nanocrystal Synthesis: The Case of Inverse Spinel Iron Oxide. *J. Am. Chem. Soc.* **2007**, *129* (20), 6352–6353.

(16) Pichon, B. P.; Gerber, O.; Lefevre, C.; Florea, I.; Fleutot, S.; Baaziz, W.; Pauly, M.; Ohlmann, M.; Ulhaq, C.; Ersen, O.; et al. Microstructural and Magnetic Investigations of Wüstite-Spinel Core-Shell Cubic-Shaped Nanoparticles. *Chem. Mater.* **2011**, *23*, 2886–2900.

(17) Guardia, P.; Di Corato, R.; Lartigue, L.; Wilhelm, C.; Espinosa, A.; Garcia-Hernandez, M.; Gazeau, F.; Manna, L.; Pellegrino, T. Water-Soluble Iron Oxide Nanocubes with High Values of Specific Absorption Rate for Cancer Cell Hyperthermia Treatment. *ACS Nano* **2012**, *6* (4), 3080–3091.

(18) Demortiere, A.; Panissod, P.; Pichon, B. P.; Pourroy, G.; Guillon, D.; Donnio, B.; Begin-Colin, S. Size-Dependent Properties of Magnetic Iron Oxide Nanocrystals. *Nanoscale* **2011**, *3* (1), 225.

(19) Baaziz, W.; Pichon, B. P.; Fleutot, S.; Liu, Y.; Lefevre, C.; Greneche, J.-M.; Toumi, M.; Mhiri, T.; Begin-Colin, S. Magnetic Iron Oxide Nanoparticles: Reproducible Tuning of the Size and Nanosized-Dependent Composition, Defects, and Spin Canting. *J. Phys. Chem. C* **2014**, *118* (7), 3795–3810.

(20) Sun, S.; Zeng, H. Size-Controlled Synthesis of Magnetite Nanoparticles. *J. Am. Chem. Soc.* **2002**, *124* (28), 8204–8205.
(21) Sun, S.; Zeng, H.; Robinson, D. B.; Raoux, S.; Rice, P. M.; Wang, S. X.; Li, G. Monodisperse MFe_2O_4 (M = Fe, Co, Mn) Nanoparticles. *J. Am. Chem. Soc.* **2004**, *126* (1), 273–279.
(22) Song, Q.; Zhang, Z. J. Shape Control and Associated Magnetic Properties of Spinel Cobalt Ferrite Nanocrystals. *J. Am. Chem. Soc.* **2004**, *126* (19), 6164–6168.
(23) Huang, J.-H.; Parab, H. J.; Liu, R.-S.; Lai, T.-C.; Hsiao, M.; Chen, C.-H.; Sheu, H.-S.; Chen, J.-M.; Tsai, D.-P.; Hwu, Y.-K. Investigation of the Growth Mechanism of Iron Oxide Nanoparticles via a Seed-Mediated Method and Its Cytotoxicity Studies. *J. Phys. Chem. C* **2008**, *112* (40), 15684–15690.
(24) Park, J.; Lee, E.; Hwang, N.-M.; Kang, M.; Kim, S. C.; Hwang, Y.; Park, J.-G.; Noh, H.-J.; Kim, J.-Y.; Park, J.-H.; et al. One-Nanometer-Scale Size-Controlled Synthesis of Monodisperse Magnetic Iron Oxide Nanoparticles. *Angewandte Chemie International Edition* **2005**, *44* (19), 2872–2877.
(25) Espinosa, A.; Muñoz-Noval, A.; García-Hernández, M.; Serrano, A.; Morena, J. J. de la; Figuerola, A.; Quarta, A.; Pellegrino, T.; Wilhelm, C.; García, M. A. Magnetic Properties of Iron Oxide Nanoparticles Prepared by Seeded-Growth Route. *J Nanopart Res* **2013**, *15* (4), 1514.
(26) Levy, M.; Quarta, A.; Espinosa, A.; Figuerola, A.; Wilhelm, C.; García-Hernández, M.; Genovese, A.; Falqui, A.; Alloyeau, D.; Buonsanti, R.; et al. Correlating Magneto-Structural Properties to Hyperthermia Performance of Highly Monodisperse Iron Oxide Nanoparticles Prepared by a Seeded-Growth Route. *Chem. Mater.* **2011**, *23* (18), 4170–4180.
(27) Xu, Z.; Shen, C.; Tian, Y.; Shi, X.; Gao, H.-J. Organic Phase Synthesis of Monodisperse Iron Oxide Nanocrystals Using Iron Chloride as Precursor. *Nanoscale* **2010**, *2* (6), 1027–1032.
(28) Baaziz, W.; Pichon, B. P.; Lefevre, C.; Ulhaq-Bouillet, C.; Greneche, J.-M.; Toumi, M.; Mhiri, T.; Begin-Colin, S. High Exchange Bias in Fe3O4@CoO Core Shell Nanoparticles Synthesized by a One-Pot Seed-Mediated Growth Method. *The Journal of Physical Chemistry C* **2013**, *117* (21), 11436.
(29) Rodriguez-Carvajal, J. Recent Advances in Magnetic Structure Determination by Neutron Powder Diffraction. *Physica B: Condensed Matter* **1993**, *192*, 55–69.
(30) Thompson, P.; Cox, D. E.; Hastings, J. B. Rietveld Refinement of Debye–Scherrer Synchrotron X-Ray Data from Al2O3. *J Appl Cryst* **1987**, *20* (2), 79–83.
(31) Teillet, J.; Varret, F. *MOSFIT Software*; Université du Maine, Le Mans, France.
(32) Feld, A.; Weimer, A.; Kornowski, A.; Winckelmans, N.; Merkl, J.-P.; Kloust, H.; Zierold, R.; Schmidtke, C.; Schotten, T.; Riedner, M.; et al. Chemistry of Shape-Controlled Iron Oxide Nanocrystal Formation. *ACS Nano* **2019**, *13* (1), 152–162.
(33) Liu, X.; Pichon, B. P.; Ulhaq, C.; Lefèvre, C.; Grenèche, J.-M.; Bégin, D.; Bégin-Colin, S. Systematic Study of Exchange Coupling in Core–Shell Fe3−δO4@CoO Nanoparticles. *Chem. Mater.* **2015**, *27* (11), 4073–4081.
(34) Sartori, K.; Choueikani, F.; Gloter, A.; Begin-Colin, S.; Taverna, D.; Pichon, B. P. Room Temperature Blocked Magnetic Nanoparticles Based on Ferrite Promoted by a Three-Step Thermal Decomposition Process. *J. Am. Chem. Soc.* **2019**, *141* (25), 9783–9787.
(35) Toulemon, D.; Pichon, B. P.; Cattoen, X.; Man, M. W. C.; Begin-Colin, S. 2D Assembly of Non-Interacting Magnetic Iron Oxide Nanoparticles via “Click” Chemistry. *Chemical Communications* **2011**, *47* (43), 11954–11956.
(36) Daou, T. J.; Pourroy, G.; Begin-Colin, S.; Greneche, J. M.; Ulhaq-Bouillet, C.; Legare, P.; Bernhardt, P.; Leuvrey, C.; Rogez, G. Hydrothermal Synthesis of Monodisperse Magnetite Nanoparticles. *Chemistry of Materials* **2006**, *18* (18), 4399–4404.
(37) López-Ortega, A.; Lottini, E.; Bertoni, G.; de Julián Fernández, C.; Sangregorio, C. Topotaxial Phase Transformation in Cobalt Doped Iron Oxide Core/Shell Hard Magnetic Nanoparticles. *Chem. Mater.* **2017**, *29* (3), 1279–1289.
(38) Santoyo Salazar, J.; Perez, L.; de Abril, O.; Truong Phuoc, L.; Ihiawakrim, D.; Vazquez, M.; Greneche, J.-M.; Begin-Colin, S.; Pourroy, G. Magnetic Iron Oxide Nanoparticles in 10-40 Nm Range: Composition in Terms of Magnetite/Maghemite Ratio and Effect on the Magnetic Properties. *Chemistry of Materials* **2011**, *23* (6), 1379–1386.
(39) Doriguetto, A. C.; Fernandes, N. G.; Persiano, A. I. C.; Filho, E. N.; Grenèche, J. M.; Fabris, J. D. Characterization of a Natural Magnetite. *Phys Chem Minerals* **2003**, *30* (5), 249–255.
(40) Daou, T. J.; Begin-Colin, S.; Greneche, J. M.; Thomas, F.; Derory, A.; Bernhardt, P.; Legare, P.; Pourroy, G. Phosphate Adsorption Properties of Magnetite-Based Nanoparticles. *Chemistry of*

Materials **2007**, *19* (18), 4494.
(41) Stoner, E. C.; Wohlfarth, E. P. Mechanism of Magnetic Hysteresis in Heterogeneous Alloys. *Philosophical Transactions of the Royal Society A* **1948**, *240* (826), 599–642.
(42) Bae, C. J.; Angappane, S.; Park, J. G.; Lee, Y.; Lee, J.; An, K.; Hyeon, T. Experimental Studies of Strong Dipolar Interparticle Interaction in Monodisperse Fe3O4 Nanoparticles. *Applied Physics Letters* **2007**, *91* (10), 102502.
(43) Frankamp, B. L.; Boal, A. K.; Tuominen, M. T.; Rotello, V. M. Direct Control of the Magnetic Interaction between Iron Oxide Nanoparticles through Dendrimer-Mediated Self-Assembly. *J. Am. Chem. Soc.* **2005**, *127* (27), 9731–9735.
(44) Fleutot, S.; Nealon, G. L.; Pauly, M.; Pichon, B. P.; Leuvrey, C.; Drillon, M.; Gallani, J.-L.; Guillon, D.; Donnio, B.; Begin-Colin, S. Spacing-Dependent Dipolar Interactions in Dendronized Magnetic Iron Oxide Nanoparticle 2D Arrays and Powders. *Nanoscale* **2013**, *5* (4), 1507.
(45) Mørup, S.; Hansen, M. F.; Frandsen, C. Magnetic Interactions between Nanoparticles. *Beilstein Journal of Nanotechnology* **2010**, *1*, 182–190.
(46) Bruvera, I. J.; Mendoza Zélis, P.; Pilar Calatayud, M.; Goya, G. F.; Sánchez, F. H. Determination of the Blocking Temperature of Magnetic Nanoparticles: The Good, the Bad, and the Ugly. *Journal of Applied Physics* **2015**, *118* (18), 184304.
(47) Muscas, G.; Concas, G.; Laureti, S.; Testa, A. M.; Mathieu, R.; De Toro, J. A.; Cannas, C.; Musinu, A.; Novak, M. A.; Sangregorio, C.; et al. The Interplay between Single Particle Anisotropy and Interparticle Interactions in Ensembles of Magnetic Nanoparticles. *Phys. Chem. Chem. Phys.* **2018**, *20* (45), 28634–28643.
(48) Pichon, B. P.; Pauly, M.; Marie, P.; Leuvrey, C.; Begin-Colin, S. Tunable Magnetic Properties of Nanoparticles 2D Assemblies Addressed by Mixed SAMs. *Langmuir* **2011**, *27*, 6235–6243.
(49) Dolci, Mathias; Lei, Yuting; Lacroix, Lise Marie; Kiefer, Céline; Leuvrey, Cédric; Begin-Colin, Sylvei; Pichon, Benoit P. Effect of Dipolar Interactions on the Assembly Process of Iron Oxide Nanoparticles Promoted by the CuAAC « Click » Chemistry Reaction. *submitted*.
(50) Kechrakos, D.; Trohidou, K. N. Magnetic Properties of Dipolar Interacting Single-Domain Particles. *Physical Review B* **1998**, *58* (18), 12169.
(51) Baaziz, W.; Pichon, B. P.; Liu, Y.; Grenèche, J.-M.; Ulhaq-Bouillet, C.; Terrier, E.; Bergeard, N.; Halté, V.; Boeglin, C.; Choueikani, F.; et al. Tuning of Synthesis Conditions by Thermal Decomposition toward Core–Shell CoxFe1–XO@CoyFe3–YO4 and CoFe2O4 Nanoparticles with Spherical and Cubic Shapes. *Chem. Mater.* **2014**, *26* (17), 5063–5073.
(52) Batlle, X.; Pérez, N.; Guardia, P.; Iglesias, O.; Labarta, A.; Bartolomé, F.; García, L. M.; Bartolomé, J.; Roca, A. G.; Morales, M. P.; et al. Magnetic Nanoparticles with Bulklike Properties (Invited). *Journal of Applied Physics* **2011**, *109* (7), 07B524.
(53) Kwon, S. G.; Hyeon, T. Formation Mechanisms of Uniform Nanocrystals via Hot-Injection and Heat-Up Methods. *Small* **2011**, *7* (19), 2685–2702.

Chapter II

Strong interfacial coupling through exchange interactions in soft/hard core-shell nanoparticles as function of cationic distribution

$Fe_{3-d}O_4$ – Co doped, $Fe_{3-d}O_4$@$CoFe_2O_4$, $Fe_{3-d}O_4$@CoO

Published by Sartori et al. in Nanoscale, 2019, 11, 27, 12946

Introduction

The combination of two different components at the nanoscale is a very attractive strategy to design new materials with enhanced and tunable magnetic properties.[1] Beyond multifunctionality resulting from the physical properties of each entity, the design of a well-defined interface is expected to favor synergistic properties which means the enhancement of the properties of each entity by the other and vice versa. In that purpose, core-shell nanoparticles combining hard and soft magnetic phases with high quality of the interface have been widely investigated during the last decade. Indeed, the soft-hard interface usually generates exchange coupling of interfacial spins which enhances the magnetic anisotropy of nanoparticles. The most popular bimagnetic nanoparticles are certainly those combining a ferro(i)magnetic (F(i)M) and an antiferromagnetic (AFM) phases, acting respectively as soft and hard phases, in core-shell structures which result in exchange bias coupling.[2,3,4] Hard and soft F(i)M phases can be also associated in order to generate spring exchange magnets.[5] Such core-shell nanoparticles combine the high coercive field (H_C) of the hard phase and the high magnetization saturation (M_S) of the soft phase. Therefore, by adapting the magnetic materials constituting the core-shell structure of nanoparticles, one can tune efficiently these magnetic parameters and the effective magnetic anisotropy energy (E_{eff}), thus creating efficient magnetic nanomaterials for specific applications.[6] For instance, high M_s and low E_{eff} are required for efficient shielding properties.[7] In contrast, magnetic resonance imaging (MRI) and hyperthermia needs high M_S and low E_{eff}.[8] Magnetic recording requires intermediate M_S with high E_{eff} in order to satisfy magnetic stability over years.[9]

Due to the high modularity of their magnetic properties, Ferrites (MFe_2O_4 with M=Fe, Ni, Zn, Co) have been widely investigated.[10] Indeed, Ferrites consist in the spinel structure AB_2O_4 were cations are distributed in octahedral (O_h) sites and tetrahedral (T_d) sites. In direct spinel, cations A(II) occupy T_d sites and cations B(III) occupy O_h sites. Depending on the nature of cations and experimental conditions, the inverse spinel structure may be preferred, i.e. cations A(II) occupy half of O_h sites which means that cations B(III) are distributed half in the Oh sites and half in the T_d sites. Therefore, ferrites can be used advantageously as hard or soft magnetic phases because of the flexibility of their chemical composition and of the distribution of cations.

During the last decade, a variety of core-shell nanoparticles using Ferrite as core or shell were reported in order to modulate their magnetic properties.[11–14,15,16,17,18] This strategy represents an interesting alternative to rare earth contents in permanent magnets. For instance, $Fe_{3-d}O_4$ which is cheap and non-toxic was covered with hard magnetic shells in order to enhance their magnetic anisotropy energy and to shift the superparamagnetic limit above room temperature. CoO which combines high anisotropy constant (2 orders of magnitude higher than $Fe_{3-d}O_4$) and good epitaxial relationship with Ferrite was often used as hard magnetic phase.[19–22,23,24] The high quality of crystal interface resulted in giant exchange bias coupling with high coercive field (H_C) and exchange field (H_E) up to 20 kOe and 5.1 kOe, respectively,[19] and enhanced effective magnetic anisotropy energy.

Ferrites were also considered as hard magnetic shell which led to the production of F(i)M@F(i)M core-shell nanoparticles.[8,25–28,29,11,30] In contrast to AFM CoO which magnetic order vanishes above T_N, hard Ferrites display higher Curie temperature (T_C) than room temperature (790 K for $CoFe_2O_4$).[10] Furthermore, according to their common crystal structure and negligible lattice mismatch, they allow the excellent quality of the crystal interface in core-shell nanoparticles. According to Song et al.,[25] the increase of the hard shell thickness grown onto a soft-core resulted in the significant enhancement of H_C and E_{eff}. In contrast, in inverse hard@soft core-shell nanoparticles, a thicker soft shell results in the decrease of H_C and softer enhancement of E_{eff}. Therefore, soft@hard core-shell nanoparticles are better candidate to enhance the energy product of permanent magnet and the magnetic anisotropy energy of superparamagnets.

The large variety of core-shell nanoparticles investigated during the last decade certainly accounts from the recent advances in synthesis methods such as the thermal decomposition of metal precursors.[31,32] This approach encountered a huge success because of its ability to produce nanoparticles with narrow size distributions as well as highly stable suspensions. The development of new characterization techniques (STEM, HAADF, EELS…) based on Transmission Electronic Microscopy (TEM) also opened wide perspectives toward the understanding of the core-shell structure. For instance, cation inversion at the interface in core-shell nanoparticles was investigated recently by performing EELS with atomic resolution.[33] In addition, local probe analysis techniques such as ^{56}Fe Mossbauer as well as specific element XAS and XMCD contributed efficiently to determine precisely the chemical composition and distribution of atoms in the crystal structure. Nevertheless, understanding the structure and magnetic properties correlation in bimagnetic core-shell nanoparticles is still challenging. Indeed, the high similarity of the crystal structure of both magnetic phases combined to high temperature (> 200 °C) during the synthesis process usually favor intermixing at the core-shell interface which influences significantly exchange coupling, i.e. the overall magnetic properties of nanoparticles.[12,23,32,20] In a previous work,[19,21] we reported the effect of the amount of Co precursor on the core-shell structure of $Fe_{3-d}O_4$@CoO nanoparticles. A discontinuous CoO shell was grown for high amounts of Co precursor which disfavored the exchange-biased properties. In contrast, low amounts of Co precursor led to the dramatic enhancement of H_C, high T_B and low H_E. We attributed indirectly this behavior to the diffusion of Co^{2+} cations which was favored by vacancies in O_h sites at the surface of $Fe_{3-d}O_4$ spinel nanoparticles. Recently, we improved our understanding of the thermal decomposition process.[35] Therefore, we expect to demonstrate a better control of the shell structure by using accurate characterization techniques such as EELS, XAS and XMCD.

Herein, we report on core-shell nanoparticles which combine a soft core ($Fe_{3-d}O_4$) and a hard shell ($CoFe_2O_4$ or CoO). Core-shell nanoparticles were synthesized by the seed mediated growth based on the thermal decomposition method.[19] We took advantage of the thermal stability of the Co precursor which clearly affects the kinetics of the shell formation and resulted in different reaction mechanism pathways. Although each nanoparticle displays enhanced magnetic properties, the efficiency of the interfacial exchange coupling is significantly dependent of the site distribution of Co^{2+} cations in the shell and in the interface.

Experimental section

Nanoparticles synthesis

Commercial cobalt stearate, $CoSt_2$_S from STREM (Co 9-10%) and $CoSt_2$_T from TCI (>95%) were used as received.

Precursor synthesis

Iron stearate (II) was prepared according to an already published protocol[35] by precipitation of sodium stearate (98.8%, TCI), and ferrous chloride (99%, Accros Organic) salt in an aqueous solution. Briefly, sodium stearate (9.8 g, 32 mmol) was transferred into a 2 necked to a round-bottomed flask and solubilized in distilled H_2O (d-H_2O, 80 ml). The solution was heated to reflux and stirred for 30 min until complete dissolution of the stearate. Separately, $FeCl_2.4H_2O$ (3.16 g, 16 mmol) was dissolved in d-H_2O (40 ml) and added onto the sodium stearate solution under vigorous stirring. A light orange precipitate was formed immediately. The solution was kept for 15 min under stirring at this temperature. Thereafter, the solution was allowed cooling down to room temperature. The obtained precipitate was washed once by centrifugation (hot d-H_2O, 14000 rpm, 10 min). The product was filtrated with a Buchner funnel, then dried in an oven at 65 °C for 24 h.

Core shell nanoparticles synthesis

CS_CoF1 was synthesized according to a previous synthesis parameters, see ref [54]. Typically, iron oxide nanoparticles were synthesized first by the thermal decomposition of 1.38 g of an iron (II) stearate homemade precursor with 1.24 g of oleic acid in 20mL of dioctyl ether. The mixture was heat and stirred at 100°C for 30 min in order to remove water. Then the temperature was increased to 290°C (boiling point of ether dioctyl) with a heating rate of 5°C/min and kept at reflux for 2h. Then, the mixture was cooled down to 100°C, 10mL of the black solution was extracted and washed by centrifugation in order to get the raw iron oxide nanoparticles as reference. Then, 0.134 g of a cobalt (II) stearate was added as well as 20mL of octadecene. No OA was added. The mixture was stirred under argon at 100°C for 40min to remove water residues. Then, it was heat under argon to 318°C (boiling point) with a heating rate of 1°C/min and kept at reflux for 3h. Finally, the mixture was cooled down and washed 12 times by centrifugation at 14 000 rpm for 5min by adding chloroform and hot acetone or chloroform and ethanol.

The synthesis of CS_CoF2 and CS_CoO nanoparticles was adapted from our previous work.[19,54] First, iron oxide nanoparticles were synthesized by performing the thermal decomposition of as synthesized iron stearate (II) in presence of oleic acid (OA, 99%, Alfa Aesar) in dioctylether (DOE, 99%, Sigma). The iron stearate (1.38 g for $FeSt_2$, 2.2 mmol) was mixed with OA (1.24 g, 4.4 mmol) in 20 ml of DOE in a two-necked round-bottom flask. The mixture was stirred and heated at 120 °C for 1 h without reflux condenser in order to remove volatile molecule residues during the solubilization process. The reflux condenser was then connected to the flask and the solution was heated under air to reflux for 2h (T_b ≈ 290 °C) with a heating rate of 5 °C/min. After cooling the resulting black solution down to 80 °C, 10 mL of the solution were removed from the flask. In a second step, $CoSt_2$ and OA (1.24 g, 4.4 mmol) were dissolved in 20 mL of octadecene and subsequently added to the remaining solution kept at 80°C. The amount of $CoSt_2$ was calculated to correspond to molar ratios R = $CoSt_2/FeSt_2$. The reaction medium was heated again to reflux for 1 h with a heating rate of 1°C/min. Finally, the black product was washed four times by centrifugation at 14 000 rpm for 5 min by adding ethanol and chloroform. Final suspensions of nanoparticles were stored in THF.

Different molar ratios R were used by varying the mass of $CoSt_2$: 0.134 g (R=0.2) and 1.37 g (R=2). The obtained nanoparticles were denoted as CS_CoF1, CS_CoF2 and CS_CoO (Table 9).

Table 9. Experimental conditions for core-shell nanoparticle synthesis.

	CS_CoF1	***CS_CoF2***	***CS_CoO***
CoSt2	*STREM*	*TCI*	*STREM*
R= CoSt2/FeSt2	*0.2*	*0.2*	*2*
OA added with CoSt2 (g)	*0*	*1.24*	*1.24*

Characterization techniques

Transmission electron microscopy

Transmission electron microscopy (TEM) were performed on a JEOL 2100 LaB6 with a 0,2nm point to point resolution. EDX were performed with a JEOL Si(Li) detector. The nanoparticle sizes were calculated by measuring at least 300 nanoparticles from TEM micrographs by using the Image J software. The shell thickness corresponds to half of the difference between nanoparticle sizes which were measured before and after Co decomposition. The size distribution was calculated by fitting with a Gaussian function that fits well with our data.

High resolution TEM (HRTEM), HAADF-STEM, EFTEM and EELS measurements and electron diffraction (ED) were performed with a CS-corrected JEOL 2100F electron microscope at probe level and a 0,12nm resolution in STEM mode microscope operating at 200 kV accelerating voltage equipped with a GATAN GIF 200 electron imaging filter. STEM images were taken in high-angle annular dark field (HAADF) mode with a 0.12 nm probe. Electron energy loss spectroscopy (EELS) was performed in the diffraction mode. Energy filtering TEM (EFTEM) images were recorded on the Fe and Co edges with a 20 eV window, which gives a 1.5 nm resolution imaging.

Fourier transform infrared

Fourier transform infrared (FTIR) spectroscopy was performed using a Perkin Elmer Spectrum spectrometer in the energy range 4000−400 cm^{-1} on samples diluted in KBr pellets.

Thermogravimetry

Thermogravimetry (TG) analysis was performed using a SDTQ600 from TA instrument. Measurements were performed on dried powders under air in the temperature range of 20 to 600 °C at a heating rate of 5 ° C/min.

X-ray diffraction

X-ray diffraction (XRD) using a Bruker D8 Advance equipped with a monochromatic copper radiation (Kα = 0.154056 nm) and a Sol-X detector in the 20− 70° 2θ range with a scan step of 0.02°. High purity silicon powder (a = 0.543082 nm) was systematically used as an internal standard.

X-Ray absorption

XAS and XMCD signals for both Fe L2,3 edges (700 – 735 eV) and Co L2,3 edges (770 – 805 eV) were recorded on the DEIMOS beamline at synchrotron SOLEIL.[62] The measurement protocol was detailed earlier in ref [41]. The colloidal suspensions were drop-casted on silicon substrates and dried at room temperature. In contrast to other samples, CS_CoF1 was diluted in a KBr powder to improve its stability during the measurement. The silicon substrates were screwed on a sample holder which was

introduced into the cryomagnet.[62] All spectra were measured in Total Electron Yield (TEY) at 4.2 K, in UHV conditions (10-10 mbar) and under applied magnetic field H (H^+ = +6.5 Tesla and H^- = -6.5 Tesla). The beam size is 800*800 μm^2 and the resolution is 100 meV. XAS and XMCD spectra were plotted by considering the absorption cross-section measured with left (σ_L) and right (σ_R) circularly polarized X-rays. Isotropic XAS were plotted as as $\sigma_{XAS}= (\sigma_+ +\sigma_-)/2$ and XMCD spectra were plotted as $\sigma_{XMCD}= (\sigma_+-\sigma_-)$ where $\sigma_+ = [\sigma_L(H^+) + \sigma_R(H^-)]/2$ and $\sigma_- = [\sigma_L(H^-) + \sigma_R(H^+)]/2$. The circularly polarized X-rays are provided by an Apple-II HU-52 helical undulator for both XAS and XMCD measurements while EMPHU65 undulator with a polarization switching rate of 1Hz was used to record hysteresis at a fixed energy.[62]

SQUID magnetometry

Magnetic measurements were performed on samples by using a Superconducting Quantum Interference Device (SQUID) magnetometer (Quantum Design MPMS-XL 5). Temperature dependent zero-field cooled (ZFC) and field cooled (FC) magnetization curves were recorded as follows: the sample was introduced in the SQUID at room temperature and cooled down to 5 K with no applied field after applying a careful degaussing procedure. A magnetic field of 7.5 mT was applied, and the ZFC magnetization curve was recorded upon heating from 5 to 400 K. The sample was then cooled down to 5 K under the same applied field, and the FC magnetization curve was recorded upon heating from 5 to 400 K. Magnetization curves as a function of a magnetic field (M(H) curves) applied in the plane of the substrate were measured at 5 and 400 K. The sample was also introduced in the SQUID at high temperature and cooled down to 5 K with no applied field (ZFC curve) after applying a subsequent degaussing procedure. The magnetization was then measured at constant temperature by sweeping the magnetic field from +7 T to −7 T, and then from −7 T to +7 T. To evidence exchange bias effect, FC M(H) curves have been further recorded after heating up at 400 K and cooling down to 5 K under a magnetic field of 7 T. The FC hysteresis loop was then measured by applying the same field sweep as for the ZFC curve. The coercive field (H_C) and the M_R/M_S ratio were measured from ZFC M(H) curves. The exchange bias field (H_E) was measured from FC M(H) curves. Magnetization saturation (M_S) was measured from hysteresis recorded at 5 K.

Results and discussion

Synthesis strategy

Nanoparticles which consist in a core of $Fe_{3-d}O_4$ and a shell of Co-Ferrite or CoO were synthesized by a two-step seed mediated growth process based on the thermal decomposition method. First, $Fe_{3-d}O_4$ nanoparticles were synthesized by performing the thermal decomposition of iron stearate (FeSt2) precursor in dioctylether (T_b = 288 °C). Second, cobalt stearate (CoSt2) precursor was decomposed in octadecene (T_b = 318 °C). Two parameters were explored: (i) the stability of Co complex against temperature prior to decomposition and, (ii) the amount of CoSt2 defined as the CoSt2/FeSt2 molar ratio R (Table 10). Two different CoSt2 precursors were used, CoSt2-S and CoSt2-T, in order to control the growth kinetic of the Co-content shell. Core-shell nanoparticles named CS_CoF1 and CS-CoF2 were obtained with CoSt2-S and CoSt2-T (R=0.2), respectively. CS_CoO was obtained with CoSt2-S (R=2). Both steps were performed in the presence of oleic acid (except step 2 for CS_CoF1) which was used as a stabilizing agent in order to regulate the growth kinetic.[35] Oleic acid was also used as a surfactant to produce highly stable colloidal suspensions of nanoparticles which is a prerequisite for potential applications.

Table 10. Experimental conditions and structural characteristics of nanoparticles. Core and shell values were calculated from nanoparticle size variations measured from TEM micrographs. Cell parameters and crystal sizes were calculated from XRD patterns.

	CS_CoF1	CS_CoF2	CS_CoO
Co precursor	CoSt2-S	CoSt2-T	CoSt2-S
R= CoSt2/FeSt2	0.2	0.2	2
OA added with CoSt2 (g)	0	1.24	1.24
Core diameter (nm)	7.2±0.8	10.3±1.1	8.8±0.7
Core-shell diameter (nm)	7.2±0.8	12.3±1.4	10.2±1.1
Shell thickness (nm)	_	1.0±0.6	0.7±0.4
Fe:Co at. ratio by EDX	80 : 20	85 : 15	49 : 51
Cell parameter (Å)	8.401 ± 0.010	8.398 ± 0.010	8.372 ± 0.010
Crystallite size (nm)	5.4 ± 0.1	9.7 ± 0.1	8.4 ± 0.1

$Fe_{3-d}O_4$ Co-doped, $Fe_{3-d}O_4$@$CoFe_2O_4$ and $Fe_{3-d}O_4$@CoO nanoparticles were synthesized through a succession of two thermal decompositions. The composition of the nanoparticles were modified by adapting the nature of the precursor and its' quantity.

Transmission electron microscopy

TEM micrographs show that intermediate nanoparticles collected before the decomposition step of CoSt2 all exhibit well-defined narrow size distribution and spherical shape (Figure 20a-c). Further, nanoparticles obtained after the two-step decomposition process exhibit narrow size distribution with size dispersion below 10 % (Figure 20d-f). All samples show well-defined spherical shape (with some facets for CS_CoF2). The comparison of nanoparticles shows that mean sizes increased after performing the decomposition of CoSt2; except for CS_CoF1 which size remain unchanged (Table 10). Nevertheless, EDX analysis showed the presence of Co element in all nanoparticles after the decomposition of Co precursors (Table 10).

Elemental mapping was performed by using electron filtered (EF) TEM or electron energy loss spectroscopy spectrum imaging (EELS-SI) at Fe L-edge (red) and Co L-edge (green) (Figure 21g-i). Images show that Fe and Co are distributed homogeneously on an area exactly corresponding the projection of CS_CoF1 and CS_CoF2 nanoparticles (Figure 21). In the case of CS_CoO, Fe is localized in area slightly smaller than the 2D projection of nanoparticles while Co is distributed homogeneously on a slightly larger area. These results were confirmed by EELS core−loss profiles (Figure 21j-l). Therefore, all nanoparticles consist in a core-shell structure.

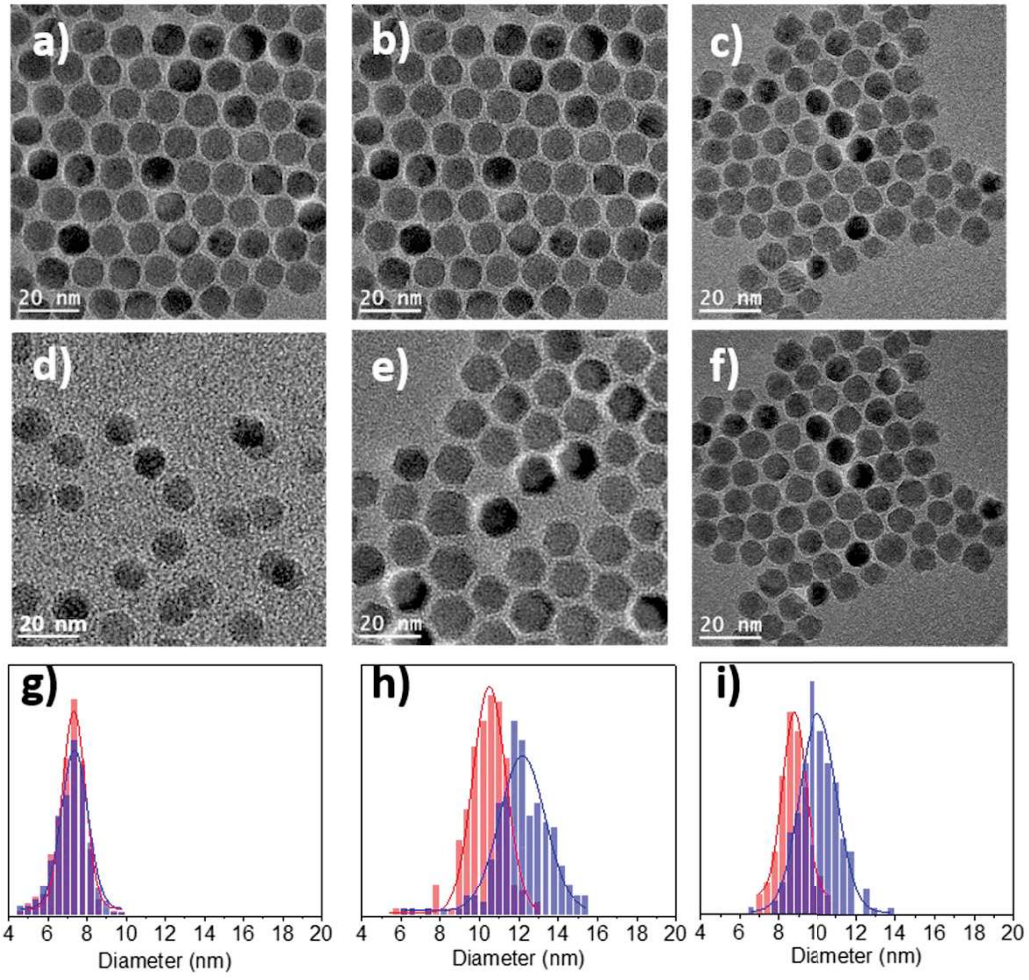

Figure 20. TEM micrographs of nanoparticles synthesized before (a,b,c) and after (d,e,f) performing the thermal decomposition of CoSt2 and the corresponding size distributions for a,d,g) CS_CoF1. b,e,h) CS_CoF2. c,f,i) CS_CoO.

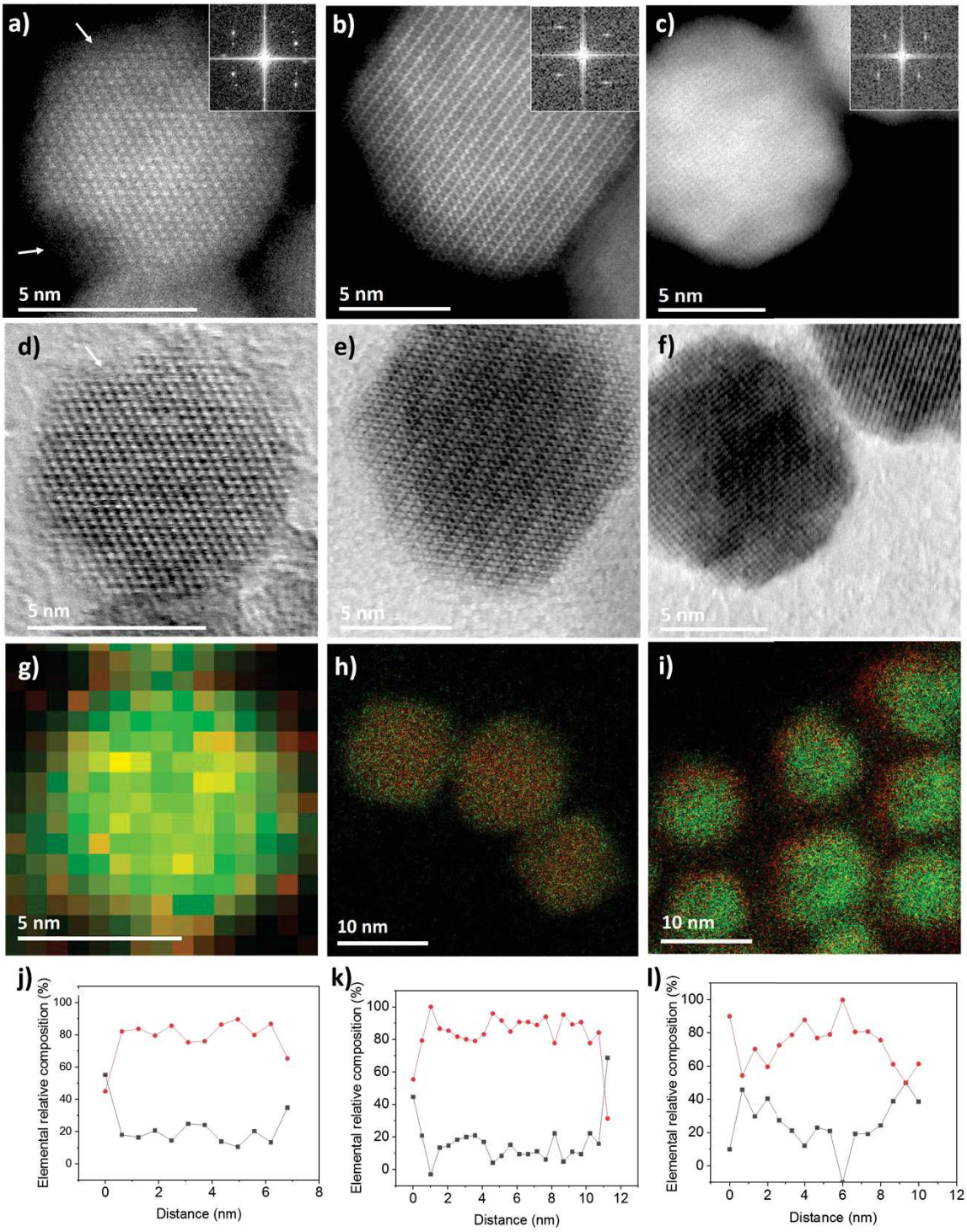

Figure 21. a,d,g,j) CS_CoF1, b,e,h,k) CS_CoF2, c,f,i,l) CS_CoO. STEM images of nanoparticles showing spinel structure in magnetite cores in a,b,c) high-angle annular dark field and d,e,f) bright field modes. Inset are Fast Fourier Transform calculated from dark field images. g,h,i) Composite integrated maps of the Fe (green) and Co (red) element EELS signal. j,k,l) EELS core–loss profiles performed across a single nanoparticle showing the relative composition of Fe (red circle) and Co (black square).

High-angle annular dark field (HAADF) micrographs show homogenous crystal structures for all samples. Continuous lattice fringes with distances corresponding to the Ferrite spinel structure were confirmed by Fast Fourier Transform (Figure 21a-f). It is worth noting that CS_CoF1 displays a less structured shell as shown by arrows.

While the shape of the core nanoparticles appears to be very close to spheres with a narrow size distribution, TEM micrographs show that the shape of the core@shell nanoparticles is slightly altered for $Fe_{3-d}O_4$@$CoFe_2O_4$ and $Fe_{3-d}O_4$@CoO nanoparticles contrary to $Fe_{3-d}O_4$ Co-doped nanoparticles which display a morphology similar to the core. Size measurements from TEM micrographs evidenced the size increasing of the core@shell nanoparticles, in agreement with the growth of the $CoFe_2O_4$ and CoO shells. At the opposite, no change of size was measured for Co-doped $Fe_{3-d}O_4$ nanoparticles. While EDX agrees on the presence of Fe and Co atoms in each system.
The single crystal like structure for each nanoparticle was proved with HAADF micrographs. This result shows good epitaxial relationship between the core and shell. EELS-SI and EELS profile investigated the atomic spatial distribution of Fe and Co and proved the Co-doped $Fe_{3-d}O_4$, $Fe_{3-d}O_4$@$CoFe_2O_4$ and $Fe_{3-d}O_4$@CoO structures.

X-ray diffraction

The indexation of XRD patterns of CS_CoF1 and CS_CoF2 show that all peaks can be indexed to the Fd-3m spinel structure of iron oxide (Figure 22). Cell parameters of 8.40 ± 0.01 Å were calculated for both samples (Table 10). The cell parameters of Fe_3O_4 and $CoFe_2O_4$ being very close (magnetite, Fe_3O_4, a = 8.396 Å, JCPDS card n° 19-062 and Co-Ferrite, $CoFe_2O_4$, a = 8.3919 Å, JCPDS card n° 22-1086), it is not possible to distinguish both chemical compositions using XRD. Nevertheless, this value being close to the one of Fe_3O_4, it shows that Fe^{2+} cations were not oxidized despite what is usually reported.[36] In contrast, the cell parameter (8.372 Å) of CS_CoO is intermediate to the one of magnetite and maghemite (γ-Fe_2O_3, a = 8.338 Å, JCPDS card n° 39-1346), which agree with the partial oxidation of Fe^{2+}cations, certainly at the core-shell interface. Additional peaks correspond to the Fm-3m wüstite structure of CoO (JCPDS card n° 70-2856). Calculated crystal diameters of the spinel phase are smaller than the size of pristine iron oxide nanoparticles that were measured from TEM micrographs (Table 10). The thermal decomposition of CoSt2 precursors induce some defects in the crystal structure as observed by HAADF-STEM for CS_CoF1 which may result from the diffusion of Co atoms in the iron oxide core.
The Co/Fe ratio measured by EDX allowed us to calculate the thickness of the Co-content shells. In the case of CS_CoF1, a thickness of 0.9 nm corresponding to a Co-Ferrite layer was calculated although no size variation was observed. We expect a thicker non stoichiometric Co-ferrite layer with gradient composition.[37,38,34] The core size would agree with the crystallite size determined from XRD pattern (5.4 nm). The thickness calculated for CS_CoF2 (1 nm) well agree with the size variation corresponding to the growth of a Co-Ferrite shell. For CS_CoO, the estimated thickness (1.1 nm) is larger than the value calculated from TEM micrographs (0.7 nm). Therefore, we expect the diffusion of Co^{2+} within the $Fe_{3-d}O_4$ core;[12,23] thus resulting in a Co-doped Ferrite layer at the $Fe_{3-d}O_4$/CoO interface.

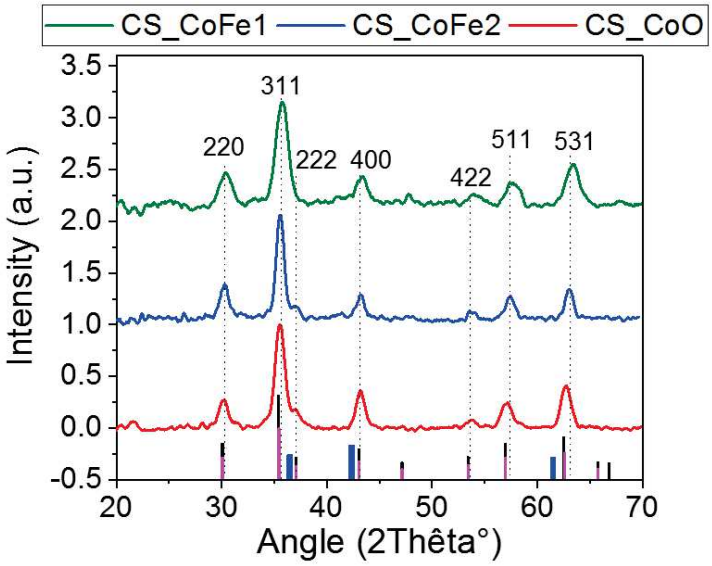

Figure 22. XRD patterns of core-shell nanoparticles. The blue, magenta and black bars correspond to the Fe_3O_4, $CoFe_2O_4$ and CoO phases, respectively.

The XRD patterns of $Fe_{3-d}O_4$@$CoFe_2O_4$ and Co-doped $Fe_{3-d}O_4$ can be indexed with an inverse spinel structure as Fe_3O_4 or $CoFe_2O_4$. Due to close cell parameters, it is not possible to distinguish them. An additional contribution of CoO wüstite phase allows to fully index the XRD pattern of $Fe_{3-d}O_4$@CoO nanoparticles. The calculation of the cell parameters evidenced the presence of a higher quantity in CS_CoF1 and CS_CoF2 than in CS_CoO which was attributed to a different synthesis process.
A comparison between the crystal size of the core@shell nanoparticles determined from XRD patterns with the calculations of the shell thickness according to EDX measurements allow to conclude on the presence of interfacial diffusion of Co cations.

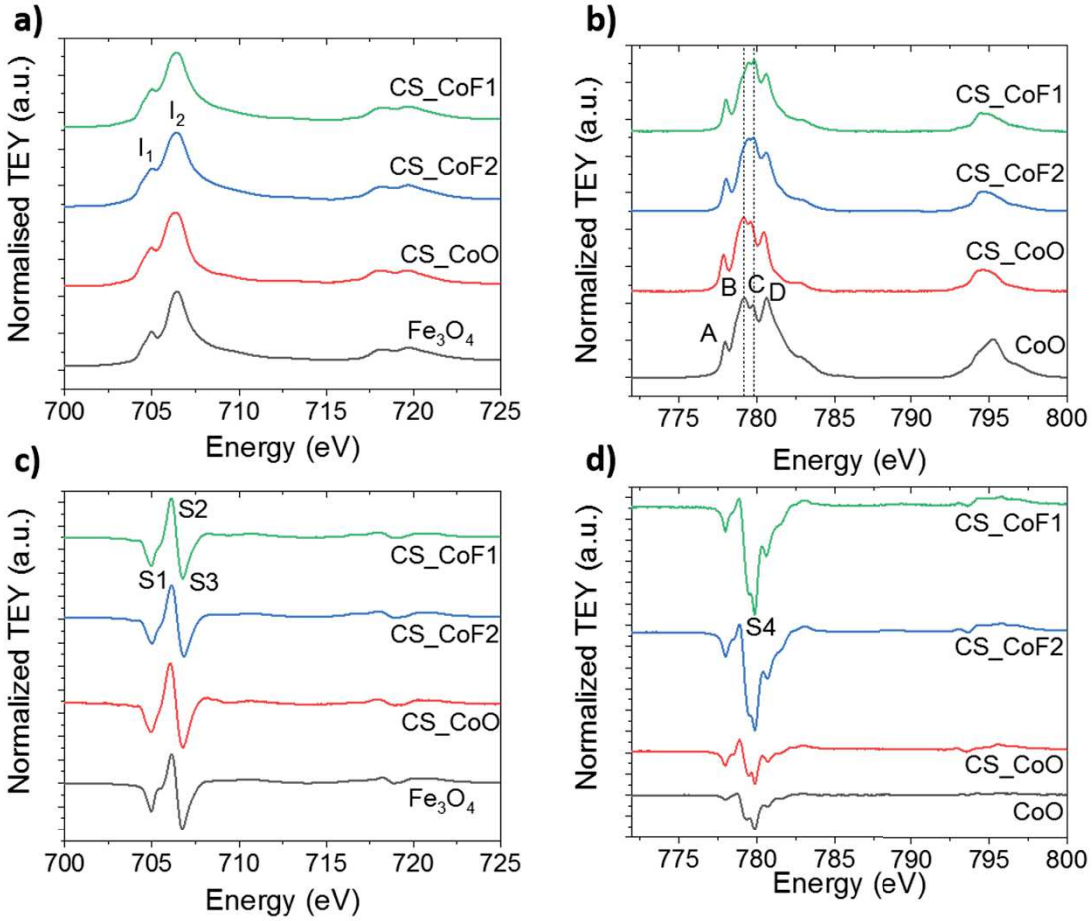

Figure 23. Experimental isotrope XAS (a,b) and XMCD (c,d) spectra recorded at Fe (a,c) and Co (b,d) $L_{2,3}$-edges, at 4.2K and under 6.5T.

To get a better understanding on the core-shell structure and their interface, we performed X-ray absorption spectroscopy (XAS) and X-ray magnetic circular dichroism (XMCD) measurements. These techniques allow to discriminate Fe and Co atoms in order to know their site occupancies and valences in the crystal structures (Figure 23). XAS and XMCD spectra recorded at the Fe $L_{2,3}$ edges are all typical of the inverse spinel structure of iron oxide (Figure 23a,c).[39] In XAS spectra, the I_1 peak can be ascribed to a major contribution of Fe^{2+} and to a minor contribution of Fe^{3+} in O_h sites while the I_2 peak can be ascribed to Fe^{3+} in O_h and T_d sites (Table 11).[40] Identical I_1/I_2 ratios (0.51) were calculated for all three core-shell nanoparticles as already reported for MFe_2O_4 nanoparticles (where M is a 3d transition element).[40,41] These ratios show that the occupancy of O_h and T_d sites by Fe cations is intermediate to magnetite (0.71) and maghemite (0.35) as calculated from Pellegrin *et al*.[39] In addition, the ratio calculated for pristine $Fe_{3-d}O_4$ nanoparticles (0.45) also reflects the intermediate composition resulting from the surface oxidation of Fe_3O_4 in γ-Fe_2O_3.[42] The lowest amount of Fe^{2+} is confirmed by the shoulder at 707 eV (Figure S7) which shows the lowest intensity for $Fe_{3-d}O_4$ nanoparticles. Therefore, core-shell nanoparticles present a higher amount of Fe^{2+} with respect to Fe^{3+} than pristine nanoparticles. It is explained by the in situ growth of the shell which prevented the oxidation of the iron oxide surface when nanoparticles were exposed to air. Nevertheless, I_1/I_2 ratios of CS_CoF1 and CS_CoF2 differs from Fe_3O_4 because of the Co-Ferrite shell (see below on XAS and XMCD spectra recorded at Co edges).

In XMCD spectra, S_x peaks refer to Fe^{2+} and Fe^{3+} in O_h sites (S_1), Fe^{3+} in T_d sites (S_2) and Fe^{3+} in O_h sites (S_3). The positive and negative values of these peaks agree with the orientation of the corresponding spins with respect to the applied magnetic field. It confirms the antiparallel coupling of Fe^{3+} cations in

O_h and T_d sites in the spinel structure. The intensity ratio of these peaks calculated as $S=(S_1+S_2)/(S_2+S_3)$[42] (Table 11) are also intermediate to pristine $Fe_{3-d}O_4$ nanoparticles (0.76) and pure Fe_3O_4 (1.27).[43] The values for CS_CoF1 and CS_CoF2 are ascribed to the presence of Co-Ferrite which also exhibit an intermediate S ratio (S = 0.66 calculated from ref.[41]). Considering the Fe_3O_4 core in both samples, the slightly lower S value of CS_CoF2 than CS_CoF1 is indicative of a higher content of Co-Ferrite. The S ratio of CS_CoO is correlated to the partial oxidation of Fe^{2+} although a Co-doped layer at the $Fe_{3-d}O_4$/CoO interface certainly exists (see below).

Table 11. Intensity ratios of peaks calculated from XAS and XMCD spectra of CS_CoF1, CS_CoF2, CS_CoO and pristine $Fe_{3-d}O_4$ nanoparticles. Ratios were calculated for Fe_3O_4 and γ-Fe_2O_3 from experimental data in the mentioned references.

	CS_CoF1	CS_CoF2	CS_CoO	$Fe_{3-d}O_4$	Fe_3O_4	γ-Fe_2O_3
Description	Fe_3O_4 @$CoFe_2O_4$	Fe_3O_4 @$CoFe_2O_4$	Fe_3O_4 @CoO	$Fe_{3-d}O_4$	Fe_3O_4	γ-Fe_2O_3
I1/I2	0.51	0.51	0.51	0.45	0.71[39]	0.35[39]
S=(S1+S2)/(S2+S3)	0.85	0.82	0.82	0.76	1.27[43]	0.61[43]

The site occupancy of Co was also investigated by recording isotropic XAS spectra at the Co $L_{2,3}$ edge (Figure 23b). The spectrum of CS_CoO is very similar to the one of CoO nanoparticles and is typical of CoO.[18,44] In contrast, the spectra of CS_CoF2 and CS_CoF1 are similar and typical of $CoFe_2O_4$ nanoparticles.[41] It is worth noting that the intensity ratios between B and C peaks of CS_CoF1 (0.96) and CS_CoF2 (0.98) are very close to the value observed for $CoFe_2O_4$ nanoparticles (0.96).[41] In contrast, CS_CoO (1.06) is the closest to CoO (1.08).[44]

XMCD spectra all show an intense negative peak for each sample (Figure 23d). It means that Co cations display similar electronic state (Co^{2+}, d^7 high spin state) and environment (O_h symmetry). It is well known that Co XMCD spectra are rather difficult to investigate. Nevertheless, spectra of CS_CoF1 and CS_CoF2 show negative peaks which are 4 times more intense than CS_CoO. It is ascribed to Co^{2+} ions which occupy O_h sites in the spinel phase ($CoFe_2O_4$) where spins are all aligned in the opposite direction of the applied magnetic field.[41] In contrast, the site occupancy of Co^{2+} ions in the CoO phase results in the antiparallel coupling of spins. XMCD being sensitive to the magnetic contribution of elements, no magnetic signal is expected. Therefore, the observed signal may account from uncompensated Co^{2+} spins at the CoO shell surface (break of symmetry) as observed for CoO nanoparticles.[45] It may also account from the diffusion of Co^{2+} at the core-shell interface which resulted in the formation of a Co-doped Ferrite layer as suggested by EDX and XRD results. The wide panel of techniques that we used in this study unambiguously demonstrated the formation of a Co-ferrite shell for CS_CoF1 (despite no size variation) and CS_CoF2, as well as a Co-Ferrite interfacial layer in addition to the CoO shell in CS_CoO.

XAS and XMCD experiments performed at the Fe edge, showed that the simple iron oxide nanoparticles are oxidized due to their exposition upon air. The presence of a higher amount of Fe^{2+} in the core@shell nanoparticles compared to the iron oxide core was demonstrated by XAS, XMCD measurements. Such consideration was attributed to the in-situ growth of the nanoparticles where the shell prevent the iron oxide core from a further oxidation by exposure to air. The investigation of the I_1/I_2 and (S1+S2)/(S2+S3) ratios allowed to investigate on the growth of the cobalt ferrite shell in $Fe_{3-d}O_4$@$CoFe_2O_4$ and Co-doped $Fe_{3-d}O_4$ nanoparticles. This was further confirm with XAS and XMCD spectra recorded at the Co edge that also evidenced a small quantity of interfacial cobalt ferrite in $Fe_{3-d}O_4$@CoO nanoparticles resulting from the atomic diffusion of Co atoms in the iron oxide core.

SQUID magnetometry

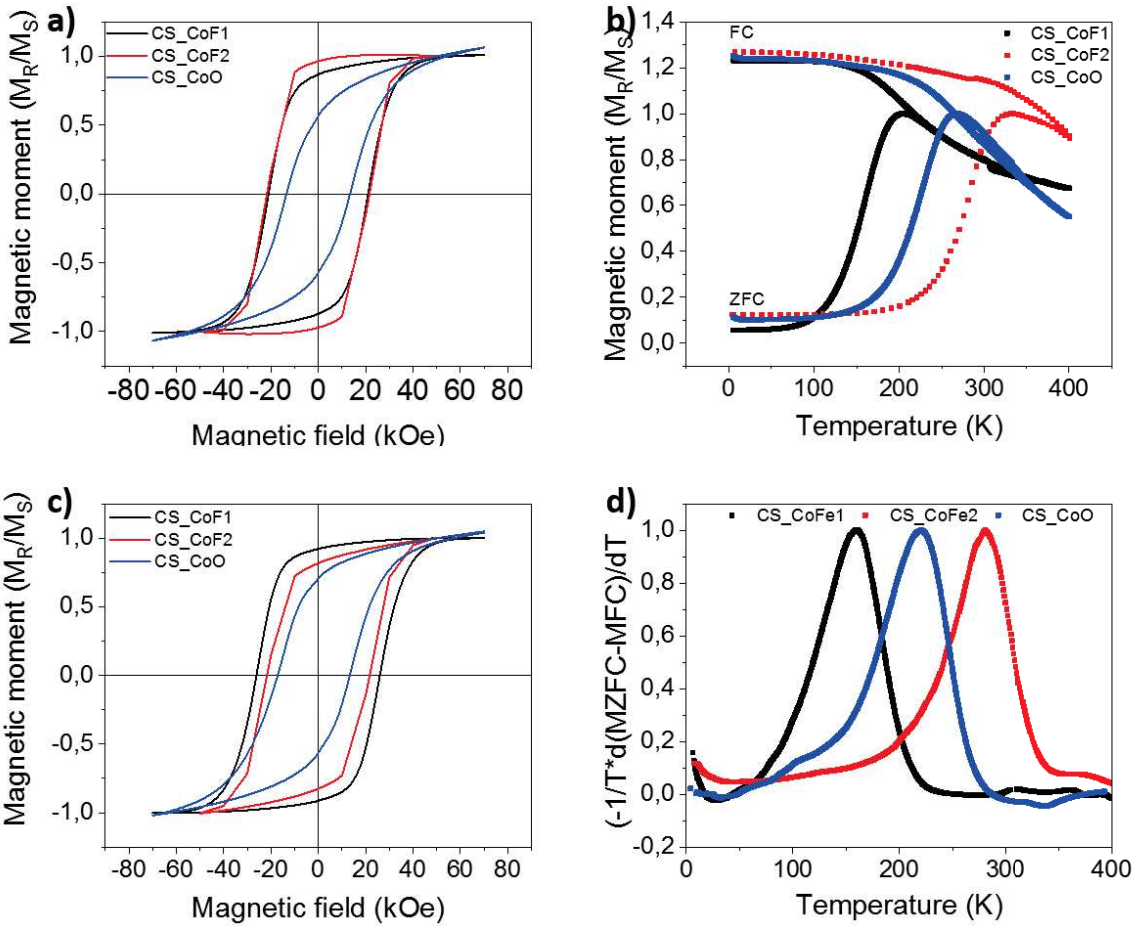

Figure 24. Magnetic properties of core-shell nanoparticles. Magnetization curves recorded against a magnetic field a) 5K under zero field cooling (ZFC) and c) 5K after field cooling (FC) under 7 T. b) Temperature dependent magnetization curves. d) Distribution of blocking temperatures calculated from b).

Table 12. Magnetic properties of core-shell nanoparticles.

	CS_CoF1	CS_CoF2	CS_CoO
H_C (Oe) (5K ZFC)	21 000	21 700	13 400
H_C (Oe) (10K FC)	26 100	21 700	15 300
H_E (Oe)	90	50	2 000
T_{MAX} (K)	203	330	269
Max f(T_B) (K)	159	284	**220**
K_{eff} ($J.m^{-3}$)	$2.8\ 10^5$	$1.0\ 10^5$	$1.4\ 10^5$

The magnetic properties of the core-shell nanoparticles were investigated by SQUID magnetometry (Figure 24). Temperature dependent magnetization curves were recorded after zero field cooling (ZFC) and field cooling (FC) in order to study the effective magnetic anisotropy energy (E_{eff}) of the nanoparticles. The maximum of the ZFC curves at T_{max} is usually interpreted as the cross-over between blocked and superparamagnetic behaviors which significantly depends on the core-shell structure

(Figure 24b). Nevertheless, the blocking temperature (T_B), at which such a change of magnetic behavior happens, is more accurately considered as an energy barrier distribution $f(T_B) \approx -(1/T)(d(M_{ZFC}-M_{FC})/dT)$ (Figure 24d).[14,46]
CS_CoF2 displays the highest T_B (284 K) while CS_CoF1 displays the lowest value (159 K) which is directly related to the core size.[12] These values are much larger than the ones of the corresponding $Fe_{3-d}O_4$ core sizes of 7 nm (62 K) and 11 nm (142 K) as we reported earlier.[36] Such an enhancement of T_B is directly correlated to the Co-Ferrite shell which results in exchange coupling between the soft core and the hard shell.[6] Considering each core and shell volumes with $K(CoFe_2O_4) \approx 1\text{-}6. 10^5$ J.m^{-3} [8,47] and $K(Fe_3O_4) \approx 1\text{-}5. 10^4$ J.m^{-3},[5,17] $K_{shell}V_{shell}$ is larger than $K_{core}V_{core}$ and results in the pinning of interfacial $Fe_{3-d}O_4$ soft spins by Co-Ferrite hard spins. Therefore, the effective magnetic anisotropy energy (E_{eff}) of exchange coupled core-shell nanoparticles can be assimilated to the effective anisotropy of the shell:[48]

$$E_{eff} = K_{eff}V \approx K_{shell}V_{Shell} = 25\ K_BT_B \quad (1)$$

with K_{eff} the effective anisotropy constant, V the total volume of the nanoparticle and k_B the Boltzman constant. It is worth to note that K_{eff} is higher for CS_CoF1 ($2.81.10^5$ J.m^{-3}) than CS_CoF2 ($1.01.10^5$ J.m^{-3}) although its core and shell volumes are much smaller (137 and 58 nm^3) than the former (572 and 402 nm^3). CS_CoO displays an intermediate T_B (220 K) to the ones of CS_CoF1 and CS_CoF2 (Figure 24d, Table 12). It is also much higher than the corresponding $Fe_{3-d}O_4$ core and agree with exchange bias coupling between the FiM core and the AFM shell as we already reported on similar $Fe_{3-d}O_4$@CoO NPs.[48] Indeed, the magnetic anisotropy energy of the AFM CoO shell ($K_{shell}V_{shell} = 1.99.10^{-19}$ J) is larger than the one of the core $K_{core}V_{core}$ ($1.78.10^{-20}$ J).

M(H) curves recorded at 300 K for each sample perfectly overlap which agrees with superparamagnetic behavior (see annexes). In contrast, wide-opened hysteresis observed at 5 K correspond to blocked magnetic moments. The hard shells grown onto the soft cores result in M(H) curves with larger hysteresis at 5 K than the corresponding $Fe_{3-d}O_4$ cores (few hundreds of Oe).[36] H_C is significantly enhanced to 26 100 Oe (CS_CoF1) and 21 700 Oe (CS_CoF2) , reaching values which are much higher than the ones reported for similar systems.[8,25,27] Furthermore, M(H) curves recorded at 5 K displays smooth increase of magnetization; i.e. no kinks that could be correlated to two separated magnetic phases could be observed. Therefore, M(H) curves show that both $Fe_{3-d}O_4$ and Co-Ferrite phases are intimately oriented and respond coherently to temperature and magnetic field as required for exchange coupled soft-hard magnetic systems.[25]
It is worth to note that the smallest nanoparticle CS_CoF1 exhibits the largest H_C. Considering the Stoner-Wohlfarth expression ($H_C = 2K/M_S$), the highest K_{eff} and the lowest M_S (which is correlated to the smaller $Fe_{3-d}O_4$ core) result in the highest H_C. It shows that the core-shell structure of CS_CoF1 results in the most efficient soft/hard interfacial exchange coupling.
Nevertheless, this expression usually refers to the energy required to overcome the magnetocrystalline energy (E_a). In exchange coupled nanoparticles, it corresponds to the energy required to inverse the spins pinned at the hard-soft interface. The highest H_C value of CS_CoF1 shows that the pinning of interfacial spins represents the highest contribution and is inversely proportional to the size of the soft core as reported for inverted hard-soft core-shell nanoparticles.[12] Furthermore, such a high H_C may be explained by strains or defects in the crystal structure[50] resulting from the diffusion of Co. It may enhance spins anisotropy in comparison to a $CoFe_2O_4$ shell grown under thermodynamic control as in the case of CS_CoF2.

FC M(H) curves recorded after cooling down under a field of 7 T exhibit very small shifts of the hysteresis curve to negative fields with respect to ZFC M(H) curves (90 Oe for CS_CoF1and 50 Oe for CS_CoF2). It can be explained by the coupling energy between both phases which is larger than the magnetic anisotropy energy of the Co-Ferrite phase.[10] The hard $CoFe_2O_4$ phase rotates with the soft $Fe_{3-d}O_4$ phase along the applied magnetic field. Nevertheless, weak exchange fields (H_E) are relatively common for soft/hard nanoparticles[12,4,51,52] and may originate from interparticle exchange between

core and surface spin canted.[53,26] In contrast, CS_CoO exhibits the largest H_E (2 000 Oe) because J_{int} ($2.23.10^{-20}$ J) < $K_{shell}V_{shell}$ ($1.99.10^{-19}$ J) results in exchange bias coupling.[2] Nevertheless, considering our previous work,[59] the value of H_C (15 300 Oe) is very high and may be ascribed to the interfacial layer of Co doped Ferrite.[54,55]

Finally, magnetization saturation (M_S) which was measured at 5 K is also directly influenced by the core-shell structure (Table 12). The M_S value of CS_CoF1 (67 emu/g) is larger than the one measured for $Fe_{3-d}O_4$ nanoparticles with similar size of 7 nm (55 emu/g)[36] which agree with the presence of a Co doped-Ferrite shell. The incorporation of Co^{2+} (+3μ_B) results in the enhancement of magnetization saturation.[56] The $Fe_{3-d}O_4$@$CoFe_2O_4$ core-shell structure of CS_CoF2 is confirmed by the M_S value (63 emu/g) which is intermediate to 10 nm sized $Fe_{3-d}O_4$ (61 emu/g) and 12 nm sized $CoFe_2O_4$ (66 emu/g) nanoparticles. As expected, M_S is the smallest for CS CoO (46 emu/g) because of the AFM CoO shell.[19] It increases to 65 emu/g when only considering the $Fe_{3-d}O_4$ core of 8.8 nm which is larger than the value measured for nanoparticles of similar size (59 emu/g).[36] It may be explained by the presence of a Co-doped layer at the core-shell interface resulting from diffusion.

The growth of a cobalt ferrite shell on an iron oxide core allowed to increase drastically H_C and T_B of the native iron oxide nanoparticles through a soft-hard exchange coupling. The same strong magnetic exchange coupling occurs in Co-doped iron oxide nanoparticles that also showed a drastic enhancement of H_C but a less drastic increase of T_B compared to CS_Fe2. Such observation can be attributed to a lower concentration of cobalt ferrite within CS_Fe1 than in CS_Fe2. Nevertheless, in both cases, the magnetic anisotropy energy of the native iron oxide nanoparticles has been increased.
M(H) curves of $Fe_{3-d}O_4$@CoO nanoparticles recorded after field cooling display a shift of the hysteresis on the applied magnetic field axis. It arises from the presence of an exchange bias coupling between the FiM core and the AFM shell. Such magnetic coupling allows to increase T_B, H_C and K_{eff} in the core@shell nanoparticles compared to the simple iron oxide core nanoparticles. Furthermore, the presence of an interfacial cobalt ferrite shell within the $Fe_{3-d}O_4$@CoO nanoparticles participates to the enhancement of H_C in favoring a strong magnetic exchange-bias coupling within the core@shell nanoparticles.
M_S values were increased by the growth of a cobalt ferrite shell and by the doping of the iron oxide core with Co cations. However in $Fe_{3-d}O_4$@CoO nanoparticles, M_S has decreased because of the AFM contribution of the CoO shell.

Element specific hysteresis

Element specific XMCD M(H) curves recorded at Fe and Co edges at 4 K bring complementary information on the exchange interaction between Fe and Co atoms as function of site occupancy in the core-shell structure (Figure 25). M(H) curves all exhibit a smooth shape and slow approach to magnetization which is consistent with magnetometry measurements. M(H) curves recorded at the Fe1 edge is at the opposite to the ones recorded at Fe2, Fe3 and Co edges. It corresponds to the ferromagnetic coupling between Fe^{2+}, Fe^{3+} and Co^{2+} in O_h sites and antiferromagnetic coupling between the formers and Fe^{3+} in T_d sites. For each sample, similar H_C values calculated at Fe and Co edges (in the experimental error) agree with strong exchange coupling of Co and Fe atoms, whatever the core-shell structure Table 13).[52] H_C measured at the Co edge are slightly larger than the ones measured at Fe edges which may be attributed to the harder shell.[12] It is also worth to note that CS_CoF1 displays a smaller H_C than CS_CoF2. Such a difference from SQUID magnetometry can be explained by the dilution of CS_CoF1 in KBr (required for sample preparation in the case of XMCD measurements) which increases interparticle distance and hampers exchange coupling at the core shell interface.[45,46] Furthermore, the opened hysteresis in M(H) curve at Co edge recorded for CS_CoO unambiguously shows the presence of ferromagnetically coupled spins of Co^{2+} cations which occupy O_h sites in the spinel structure, i.e. the presence of a Co-doped ferrite interfacial layer. In addition, the

non-saturation at high magnetic fields corresponds to the linear contribution of antiferromagnetically coupled Co^{2+} spins which occupy O_h sites in the CoO wüstite structure and to the uncompensated spins at the CoO surface (Figure S 8).

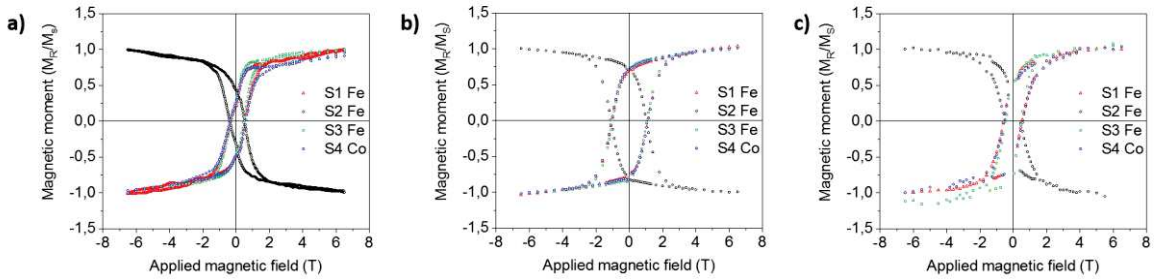

Figure 25. Element specific XMCD M(H) curves recorded at Fe and Co edges at 4 K. a) CS_CoF1. b) CS_CoF2. c) CS_CoO.

Table 13. Coercive field measured from XMCD specific elemental M(H) curves.

H_C (kOe)	CS_CoF1	CS_CoF2	CS_CoO
S1 Fe	4.4 ± 0.2	10.8 ± 0.2	5.5± 0.4
S2 Fe	4.7 ± 0.2	10.6 ± 0.2	4.4 ± 0.4
S3 Fe	4.1 ± 0.2	10.4 ± 0.2	5.0± 0.4
S4 Co	5.2 ± 0.2	10.9 ± 0.2	5.8± 0.4

Each sample show similar coercive field opening at the Fe and Co edges, agreeing with a strong magnetic exchange coupling for $Fe_{3-d}O_4$@$CoFe_2O_4$ and Co-doped $Fe_{3-d}O_4$ nanoparticles. The same behavior was observed for $Fe_{3-d}O_4$@CoO which also testify the presence of a strong exchange-bias coupling in the $Fe_{3-d}O_4$@CoO nanoparticles. The large opening of the hysteresis at the Co edge is attributed to the interfacial cobalt ferrite. Indeed, as the CoO shell is an antiferromagnet, its contribution to the opening of the hysteresis is null although it participates to the smooth and slow approach to saturation in the hysteresis.

General discussion

A Co content shell was grown at the surface of $Fe_{3-d}O_4$ nanoparticles in three different mechanism pathways which depend on the experimental conditions such as the CoSt2 precursor and the stabilizing agent OA. The comparison of CS_CoF1 and CS_CoF2 core-shell nanoparticles shows that different Co precursors in the same amount with respect to Fe precursor (R= 0.2) result in two different core-shell structures. Although both Co precursors resulted in the formation of a Co Ferrite shell, CoSt2-T resulted in the size increase (CS_CoF2) while CoSt2-S did not (CS_CoF1). According to La Mer theory,[59] the thermal decomposition of metal precursors resulted in the formation of monomers which above a critical concentration initiate the nucleation step followed by the growth step after the concentration decreased. The kinetic of the monomer formation is highly dependent on the stability of the CoSt2 precursor. Thermogravimetric (TG) curves show that CoSt2-T is more stable against decomposition than CoSt2-S (Figure S 9a). As we reported earlier,[35] differential thermogravimetry (DTG) curves confirmed that the monomer formation leading to nucleation happens at a lower temperature range for CoSt2-S (154-210 °C) than CoSt2-T (172-247 °C) (Figure S 9b). Although the different thermal stability is usually explained by the coordination of Co with stearate molecules, both FTIR spectra (Figure S 10) show a difference of 144cm^{-1} between v_s COO^- and v_{as} COO^- bands which corresponds to a bidentate coordination mode.[60] Therefore, the lowest stability of CoSt2-S is certainly due to the higher content of impurities. The stability of the precursor also depends on the presence of the stabilizing agent in the reaction medium. Indeed, the absence of OA in the case of CS_CoF1, significantly favored the decomposition of CoSt2-S at lower temperatures in comparison to CoSt2-T in presence of OA during the synthesis of CS_CoF2. Therefore, we expect that the decomposition at lower temperature combined to low amounts of CoSt2-S favored the diffusion of Co monomers in the surface layer of iron oxide nanoparticles which result in less structured surface layer as shown by arrows in HAADF micrographs (Figure 21a).[11,37] The diffusion of Co in vacancies is favoured by the high temperature (about 300 °C) of the reaction medium.[38,61,23] This observation is supported by the absence of the CoO phase from the XRD pattern. XAS and XMCD spectra confirmed the presence of Co^{2+} cations in O_h sites of a spinel structure. Therefore, we expect CS_CoF1 to consist in a $Fe_{3-d}O_4$ core and a Co-Ferrite shell with a gradient concentration of cobalt with the highest concentration at the surface of nanoparticles.

In contrast, the higher thermal stability of CoSt2-T in presence of oleic acid resulted in the growth of a $CoFe_2O_4$ shell which predominated over the Co diffusion. It is worth to note that, all samples, no FeSt2 was added with CoSt2-T. Therefore, we expect Co monomers to react with residual Fe monomers from the decomposition of FeSt2. In order to light on this finding, we performed the second decomposition process by heating the reaction medium up to 310 °C after going down to 100 °C without adding CoSt2-T precursor. TEM micrographs showed the increase of the size of iron oxide nanoparticles from 9.6 ± 1.2 nm to 11.0 ± 1.1 nm (Figure S 11). It may also result from Ostwald ripening of small nanoparticles as shown by size distribution. An alternative may come from residual iron monomers from the solution.[20] Both pathways would favour the formation of Co-Ferrite shell at the surface of $Fe_{3-d}O_4$ nanoparticles when performing a thermal decomposition with CoSt2-T.

In the case of CS_CoO, the increase of CoSt2-S amount by 10 (R=2) in presence of oleic acid resulted in the formation of a homogeneous CoO layer. It shows that the increase of concentration of CoSt2-S results in a different growth mechanism of the shell. It is worth to note that the presence of oleic acid favors a continuous and homogeneous shell. Indeed we reported previously on similar experimental conditions without further addition of oleic acid upon adding CoSt2 which resulted in a discontinuous and polycristalline shell.[21] Here, oleic acid increased the thermal stability of CoSt2-S which slowed down the monomer formation, and thus the growth process. Furthermore, the same amount of CoSt2_T (R=2), also in presence of oleic acid, led to CS_CoF3 (Figure S 12) which consists of a Co-ferrite

shell. It confirms that the formation of $CoFe_2O_4$ and CoO shells are directly dependent on the thermal stability of the precursor.

Although the Co-Ferrite phase could not be discriminated from Fe_3O_4 by XRD, EFTEM confirmed the presence of Co element. XAS and XMCD measurements showed that Co^{2+} cations occupy O_h sites in a spinel structure corresponding to the formation of a Co-Ferrite phase in CS_CoF1 and CS_CoF2 nanoparticles. In the case of CS_CoO, the growth of the continuous CoO shell was certainly preceded by the diffusion of Co^{2+} from the solution to vacancies at the $Fe_{3-d}O_4$ surface followed by restructuration as reported recently for similar Fe_3O_4@CoO core-shell nanoparticles prepared by the polyol method.[22] It was confirmed by Co/Fe atomic ratio calculated from EDX and element specific XMCD magnetization curves which showed that Co^{2+} were magnetically coupled to Fe^{3+} cations in a spinel structure.

The magnetic properties are directly dependent on the core-shell structure. All core-shell nanoparticles display enhanced magnetic anisotropies in comparison to the corresponding $Fe_{3-\delta}O_4$ cores which result from exchange coupling at the soft-hard interface. Indeed, both $CoFe_2O_4$ and CoO shell display a larger magnetic anisotropy energy than $Fe_{3-d}O_4$ cores which allow the pinning of interfacial Fe spins by Co spins. Given the huge increase of H_C and T_B values, such a phenomenon is particularly efficient thanks to the high epitaxial relationship between Fe ferrite and Co ferrite or CoO. When the FiM Co-Ferrite shell is coupled with the FiM $Fe_{3-d}O_4$ core, the larger interfacial coupling energy than the magnetic anisotropy energy of the hard shell results in the simultaneous rotation of both phases. In contrast, when the AFM CoO shell is coupled with the FiM $Fe_{3-d}O_4$ core through exchange bias, the higher magnetic anisotropy energy of the CoO phase than the interfacial coupling energy resulted first in the rotation of the FiM soft phase followed by the rotation of the AFM phase which was correlated to the H_E (shift of hysteresis curves to negative magnetic field valuesafter field cooling). It is worth to note that, although the CoO shell displays the largest magnetic anisotropy energy, it does not result in the best enhancement of the effective magnetic anisotropy energy of the $Fe_{3-d}O_4$ core. Indeed, the Co-Ferrite shell with the largest $Fe_{3-d}O_4$ core (CS_CoF2) resulted in the highest T_B. In contrast, CS_CoF1 displays the largest H_C after field cooling which is directly correlated to the highest K_{eff}. Although this value is very surprising when considering the nanoparticle size and core (below 7 nm), it may be ascribed to the diffusion of Co atoms in the γ–Fe_2O_3 structure. Finally, the magnetic properties show that, for the studied particular systems, exchange coupling between soft and hard FiM phases is more efficient than between FiM and AFM phases.

Conclusion

We have reported on the synthesis of core-shell magnetic nanoparticles by performing a seed mediated growth through thermal decomposition of Fe and Co precursors. Such a synthesis strategy led us to control precisely narrow size distribution and well-defined shape of core-shell nanoparticles. Each nanoparticle consists of a $Fe_{3-d}O_4$ core and a Co-Ferrite or CoO shell with chemical compositions that were modulated as a function of the experimental conditions. Indeed, the thermal stability and concentration of the Co stearate resulted in three different mechanism pathways: (i) the diffusion of Co in the γ–Fe_2O_3 surface layer of pristine $Fe_{3-d}O_4$ nanoparticles, (ii) the growth of a $CoFe_2O_4$ shell at the surface of pristine $Fe_{3-d}O_4$ nanoparticles resulting from the simultaneous reaction of Co and Fe monomers and, (iii) the growth of a CoO shell accompanied with the diffusion of Co in the $Fe_{3-d}O_4$ surface layer inducing a Co-doped ferrite layer at the $Fe_{3-d}O_4$ /CoO interface. Co cations were quantified (EDX, AAS), spatially resolved as homogeneous shells at the surface of the $Fe_{3-d}O_4$ core (EFTEM/EELS), and calculated as Co-Ferrite and CoO crystal structures (XRD). XAS and XMCD allowed us characterizing the distribution of Fe and Co cations in O_h and T_d sites of spinel and wüstite phases. Beyond confirming the formation of Co-Ferrite and CoO shells, it allowed us highlighting the presence of an intermediate Co-doped Ferrite layer at the $Fe_{3-d}O_4$ /CoO interface. The composition and the structure of the shell has a strong influence on the magnetic properties. The FiM hard phase results in more efficient exchange coupling. Furthermore, the formation of Co-Ferrite through diffusion results in the most efficient enhancement of magnetic anisotropy. In addition, the growth of a CoO AFM shell also includes the formation of an interfacial layer of Co-Ferrite by diffusion of Co^{2+} which contributes to the enhancement of the magnetic properties. Finally, this work brings new information on the way exchange coupled core-shell nanoparticles can be designed to adapt their magnetic properties as a function of foreseen applications.

References

1 C.-W. Nan and Q. Jia, *MRS Bull.*, 2015, **40**, 719–724.
2 J. Nogues, J. Sort, V. Langlais, V. Skumryev, S. Surinach, J. S. Munoz and M. D. Baro, *Phys. Rep.*, 2005, **422**, 65–117.
3 M.-H. Phan, J. Alonso, H. Khurshid, P. Lampen-Kelley, S. Chandra, K. Stojak Repa, Z. Nemati, R. Das, Ó. Iglesias and H. Srikanth, *Nanomaterials*, 2016, **6**, 221.
4 Iglesias, scar, A. Labarta, lcar and X. Batlle, *J. Nanosci. Nanotechnol.*, 2008, **8**, 2761.
5 E. E. Fullerton, J. S. Jiang and S. D. Bader, *J. Magn. Magn. Mater.*, 1999, **200**, 392–404.
6 A. López-Ortega, M. Estrader, G. Salazar-Alvarez, A. G. Roca and J. Nogués, *Phys. Rep.*, 2015, **553**, 1–32.
7 L. Xi, Z. Wang, Y. Zuo and X. Shi, *Nanotechnology*, 2011, **22**, 045707.
8 J.-H. Lee, J. -t. Jang, J. -s. Choi, S. H. Moon, S. -h. Noh, J. -w. Kim, J.-G. Kim, I.-S. Kim, K. I. Park and J. Cheon, *Nat Nano*, **6**, 418.
9 V. Skumryev, S. Stoyanov, Y. Zhang, G. Hadjipanayis, D. Givord and J. Nogués, *Nature*, 2003, **423**, 850–853.
10 A. Broese van Groenou, P. F. Bongers and A. L. Stuyts, *Mater. Sci. Eng.*, 1969, **3**, 317–392.
11 J. Cheon, J.-I. Park, J. Choi, Y. Jun, S. Kim, M. G. Kim, Y.-M. Kim and Y. J. Kim, *Proc. Natl. Acad. Sci.*, 2006, **103**, 3023–3027.
12 A. Lopez-Ortega, M. Estrader, G. Salazar-Alvarez, S. Estrade, I. V. Golosovsky, R. K. Dumas, D. J. Keavney, M. Vasilakaki, K. N. Trohidou, J. Sort, F. Peiro, S. Surinach, M. D. Baro and J. Nogues, *Nanoscale*, 2012, **4**, 5138.
13 J. E. Lima, E. L. Winkler, D. Tobia, H. E. Troiani, R. D. Zysler, E. Agostinelli and D. Fiorani, *Chem. Mater.*
14 G. C. Lavorato, E. Lima, H. E. Troiani, R. D. Zysler and E. L. Winkler, *Nanoscale*, 2017, **9**, 10240–10247.
15 E. Lottini, A. López-Ortega, G. Bertoni, S. Turner, M. Meledina, G. Van Tendeloo, C. de Julián Fernández and C. Sangregorio, *Chem. Mater.*, 2016, **28**, 4214–4222.
16 H. Zeng, J. Li, Z. L. Wang, J. P. Liu and S. Sun, *Nano Lett.*, 2004, **4**, 187–190.
17 P. K. Manna, S. M. Yusuf, M. Basu and T. Pal, *J. Phys. Condens. Matter*, 2011, **23**, 506004.
18 W. Baaziz, B. P. Pichon, Y. Liu, J.-M. Grenèche, C. Ulhaq-Bouillet, E. Terrier, N. Bergeard, V. Halté, C. Boeglin, F. Choueikani, M. Toumi, T. Mhiri and S. Begin-Colin, *Chem. Mater.*, 2014, **26**, 5063–5073.
19 W. Baaziz, B. P. Pichon, C. Lefevre, C. Ulhaq-Bouillet, J.-M. Greneche, M. Toumi, T. Mhiri and S. Begin-Colin, *J. Phys. Chem. C*, 2013, **117**, 11436.
20 T. Gaudisson, R. Sayed-Hassan, N. Yaacoub, G. Franceschin, S. Nowak, J.-M. Grenèche, N. Menguy, P. Sainctavit and S. Ammar, *CrystEngComm*, 2016, **18**, 3799–3807.
21 X. Liu, B. P. Pichon, C. Ulhaq, C. Lefèvre, J.-M. Grenèche, D. Bégin and S. Bégin-Colin, *Chem. Mater.*, 2015, **27**, 4073–4081.
22 G. Franceschin, T. Gaudisson, N. Menguy, B. C. Dodrill, N. Yaacoub, J.-M. Grenèche, R. Valenzuela and S. Ammar, *Part. Part. Syst. Charact.*, 2018, **35**, 1800104.
23 E. Skoropata, R. D. Desautels, C. C. Chi, H. Ouyang, J. W. Freeland and J. van Lierop, *Phys. Rev. B*, 2014, **89**, 024410.
24 I. Panagiotopoulos, G. Basina, V. Alexandrakis, E. Devlin, G. Hadjipanayis, L. Colak, D. Niarchos and V. Tzitzios, *J. Phys. Chem. C*, 2009, **113**, 14609.
25 Q. Song and Z. J. Zhang, *J. Am. Chem. Soc.*, 2012, **134**, 10182.
26 R. Cabreira-Gomes, F. Gomes da Silva, R. Aquino, P. Bonville, F. A. Tourinho, R. Perzynski and J. Depeyrot, *Exchange bias of MnFe2O4@gamma Fe2O3 and CoFe2O4@gamma Fe2O3 core/shell nanoparticles*, 2014.
27 Q. Zhang, I. Castellanos-Rubio, R. Munshi, I. Orue, B. Pelaz, K. I. Gries, W. J. Parak, P. del Pino and A. Pralle, *Chem. Mater.*, 2015, **27**, 7380–7387.
28 M. Angelakeris, Z.-A. Li, M. Hilgendorff, K. Simeonidis, D. Sakellari, M. Filippousi, H. Tian, G. Van Tendeloo, M. Spasova, M. Acet and M. Farle, *J. Magn. Magn. Mater.*, 2015, **381**, 179–187.
29 N. Daffé, M. Sikora, M. Rovezzi, N. Bouldi, V. Gavrilov, S. Neveu, F. Choueikani, P. Ohresser, V. Dupuis, D. Taverna, A. Gloter, M.-A. Arrio, P. Sainctavit and A. Juhin, *Adv. Mater. Interfaces*, 2017,

4, 1700599.
30 S. D. Oberdick, A. Abdelgawad, C. Moya, S. Mesbahi-Vasey, D. Kepaptsoglou, V. K. Lazarov, R. F. L. Evans, D. Meilak, E. Skoropata, J. van Lierop, I. Hunt-Isaak, H. Pan, Y. Ijiri, K. L. Krycka, J. A. Borchers and S. A. Majetich, *Sci. Rep.*, , DOI:10.1038/s41598-018-21626-0.
31 A.-H. Lu, E. L. Salabas and F. Schüth, *Angew. Chem. Int. Ed.*, 2007, **46**, 1222.
32 S. Singamaneni, V. N. Bliznyuk, C. Binek and E. Y. Tsymbal, *J. Mater. Chem.*, 2011, **21**, 16819–16845.
33 P. Torruella, A. Ruiz-Caridad, M. Walls, A. G. Roca, A. López-Ortega, J. Blanco-Portals, L. López-Conesa, J. Nogués, F. Peiró and S. Estradé, *Nano Lett.*, 2018, **18**, 5854–5861.
34 A. Juhin, A. López-Ortega, M. Sikora, C. Carvallo, M. Estrader, S. Estradé, F. Peiró, M. Dolors Baró, P. Sainctavit, P. Glatzel and J. Nogués, *Nanoscale*, 2014, **6**, 11911–11920.
35 G. Cotin, C. Kiefer, F. Perton, M. Boero, B. Özdamar, A. Bouzid, G. Ori, C. Massobrio, D. Begin, B. Pichon, D. Mertz and S. Begin-Colin, *ACS Appl. Nano Mater.*, , DOI:10.1021/acsanm.8b01123.
36 W. Baaziz, B. P. Pichon, S. Fleutot, Y. Liu, C. Lefevre, J.-M. Greneche, M. Toumi, T. Mhiri and S. Begin-Colin, *J. Phys. Chem. C*, 2014, **118**, 3795–3810.
37 G. Salazar-Alvarez, J. Sort, A. Uheida, M. Muhammed, S. Surinach, M. D. Baro and J. Nogues, *J. Mater. Chem.*, 2007, **17**, 322.
38 E. Tronc, J.-P. Jolivet, J. Lefebvre and R. Massart, *J. Chem. Soc. Faraday Trans. 1 Phys. Chem. Condens. Phases*, 1984, **80**, 2619–2629.
39 E. Pellegrin, M. Hagelstein, S. Doyle, H. O. Moser, J. Fuchs, D. Vollath, S. Schuppler, M. A. James, S. S. Saxena, L. Niesen, O. Rogojanu, G. A. Sawatzky, C. Ferrero, M. Borowski, O. Tjernberg and N. B. Brookes, *Phys. Status Solidi B*, 1999, **215**, 797–801.
40 H. J. Lee, G. Kim, D. H. Kim, J.-S. Kang, C. L. Zhang, S.-W. Cheong, J. H. Shim, S. Lee, H. Lee, J.-Y. Kim, B. H. Kim and B. I. Min, *J. Phys. Condens. Matter*, 2008, **20**, 295203.
41 N. Daffé, F. Choueikani, S. Neveu, M.-A. Arrio, A. Juhin, P. Ohresser, V. Dupuis and P. Sainctavit, *J. Magn. Magn. Mater.*, 2018, **460**, 243–252.
42 S. Brice-Profeta, M.-A. Arrio, E. Tronc, N. Menguy, I. Letard, C. Cartier dit Moulin, M. Noguès, C. Chanéac, J.-P. Jolivet and P. Sainctavit, *J. Magn. Magn. Mater.*, 2005, **288**, 354–365.
43 J. Li, N. Menguy, M.-A. Arrio, P. Sainctavit, A. Juhin, Y. Wang, H. Chen, O. Bunau, E. Otero, P. Ohresser and Y. Pan, *J. R. Soc. Interface*, 2016, **13**, 20160355.
44 S. Y. Istomin, O. A. Tyablikov, S. M. Kazakov, E. V. Antipov, A. I. Kurbakov, A. A. Tsirlin, N. Hollmann, Y. Y. Chin, H.-J. Lin, C. T. Chen, A. Tanaka, L. H. Tjeng and Z. Hu, *Dalton Trans.*, 2015, **44**, 10708–10713.
45 A. G. Roca, I. V. Golosovsky, E. Winkler, A. López-Ortega, M. Estrader, R. D. Zysler, M. D. Baró and J. Nogués, *Small*, 2018, **14**, 1703963.
46 I. J. Bruvera, P. Mendoza Zélis, M. Pilar Calatayud, G. F. Goya and F. H. Sánchez, *J. Appl. Phys.*, 2015, **118**, 184304.
47 A. López-Ortega, E. Lottini, C. de J. Fernández and C. Sangregorio, *Chem. Mater.*, 2015, **27**, 4048–4056.
48 J. A. De Toro, D. P. Marques, P. Muñiz, V. Skumryev, J. Sort, D. Givord and J. Nogués, *Phys. Rev. Lett.*, 2015, **115**, 057201.
49 Y. Liu, X. Liu, M. Dolci, C. Leuvrey, E. Pardieu, A. Derory, D. Begin, S. Begin-Colin and B. P. Pichon, *J. Phys. Chem. C*, , DOI:10.1021/acs.jpcc.8b04615.
50 B. P. Pichon, O. Gerber, C. Lefevre, I. Florea, S. Fleutot, W. Baaziz, M. Pauly, M. Ohlmann, C. Ulhaq, O. Ersen, V. Pierron-Bohnes, P. Panissod, M. Drillon and S. Begin-Colin, *Chem Mater*, 2011, **23**, 2886–2900.
51 J. Nogues and I. K. Schuller, *J. Magn. Magn. Mater.*, 1999, **192**, 203.
52 M. Estrader, A. López-Ortega, S. Estradé, I. V. Golosovsky, G. Salazar-Alvarez, M. Vasilakaki, K. N. Trohidou, M. Varela, D. C. Stanley, M. Sinko, M. J. Pechan, D. J. Keavney, F. Peiró, S. Suriñach, M. D. Baró and J. Nogués, *Nat. Commun.*, 2013, **4**, 2960.
53 A. Mumtaz, K. Maaz, B. Janjua, S. K. Hasanain and M. F. Bertino, *J. Magn. Magn. Mater.*, 2007, **313**, 266.
54 X. Liu, B. P. Pichon, C. Ulhaq, C. Lefevre, J.-M. Greneche, D. Begin and S. Begin-Colin, *Chem. Mater.*, 2015, **27**, 4073.

55 N. Flores-Martinez, G. Franceschin, T. Gaudisson, P. Beaunier, N. Yaacoub, J.-M. Grenèche, R. Valenzuela and S. Ammar, *Part. Part. Syst. Charact.*, **0**, 1800290.
56 R. Kumar, H. Kumar, M. Kumar, R. R. Singh and P. B. Barman, *J. Supercond. Nov. Magn.*, 2015, **28**, 3557–3564.
57 J. Nogues, V. Skumryev, J. Sort, S. Stoyanov and D. Givord, *Phys. Rev. Lett.*, 2006, **97**, 157203.
58 M. Dolci, Y. Liu, X. Liu, C. Leuvrey, A. Derory, D. Begin, S. Begin-Colin and B. P. Pichon, *Adv. Funct. Mater.*, 2018, **28**, 1706957.
59 V. K. La Mer and R. H. Dinegar, *J. Am. Chem. Soc.*, 1950, **72**, 4847–4854.
60 L. M. Bronstein, X. Huang, J. Retrum, A. Schmucker, M. Pink, B. D. Stein and B. Dragnea, *Chem Mater*, 2007, **19**, 3624.
61 A. Uheida, G. Salazar-Alvarez, E. Björkman, Z. Yu and M. Muhammed, *J. Colloid Interface Sci.*, 2006, **298**, 501–507.
62 P. Ohresser, E. Otero, F. Choueikani, K. Chen, S. Stanescu, F. Deschamps, T. Moreno, F. Polack, B. Lagarde, J.-P. Daguerre, F. Marteau, F. Scheurer, L. Joly, J.-P. Kappler, B. Muller, O. Bunau and P. Sainctavit, *Rev. Sci. Instrum.*, 2014, **85**, 013106.

CHAPTER III

Exchange-biased hybrid magnetic nanoparticles

$Fe_{3-d}O_4$@CoO@$Fe_{3-d}O_4$

Preliminary results of this chapter were published as a communication in the Journal of the American Chemical Society.

Sartori and al. J. Am. Chem. Soc., 2019, 11, 27, 12946

Introduction

Tuning the size, shape and chemical composition of magnetic nanoparticles allows to tune their magnetic properties.[1–3] However, size reduction down to the nanoscale results in a decrease of the anisotropy energy barrier that is usually lower than the thermal energy at room temperature. Hence, the magnetic moment of the nanoparticles fluctuates at such a temperature: they are in a superparamagnetic state.[4,5] This property is of high interest for magnetic hyperthermia[6] but is disadvantageous for other applications. Indeed, magnetic recording media require to have blocked magnetic moments with the macro-spin of the magnetic monodomain nanoparticles oriented up or down. Today, these small permanent magnets are essentially based on rare-earth materials that are produced in China.[7,8] However, due to the European dependency towards China and the high pollution generated by the extraction of the rare earth materials, it is important to find an alternative. Here we decided to use ferrimagnetic (FiM) iron oxide nanoparticles of 10 nm size which are made of an abundant and environmentally friendly material. To increase their magnetic stability against temperature, it is possible to coat them with an antiferromagnetic (AFM) shell composed of CoO.[9] The synthesis of $Fe_{3-d}O_4$@CoO allows then to increase the superparamagnetic limit which nevertheless stays under room temperature due to the Néel temperature of the CoO AFM phase (T_N CoO = 290 K).[10] In order to increase even more the magnetic stability towards temperature, we suggest here to double the FiM/AFM interface by synthesizing core@shell@shell $Fe_{3-d}O_4$@CoO@$Fe_{3-d}O_4$ nanoparticles through a seed-mediated growth process with a succession of 3 thermal decompositions. To study systematically the influence of the second shell thickness, we synthesized three different $Fe_{3-d}O_4$@CoO@$Fe_{3-d}O_4$ from the same $Fe_{3-d}O_4$@CoO nanoparticles by tuning the quantity of metallic precursor in the mixture during the last thermal decomposition. These new core@shell@shell nanoparticles show surprising magnetic properties which arise from their original structure that have been investigated down to the very last detail. Moreover, thanks to a concerted coupling between two different magnetic mechanisms, the magnetic properties of $Fe_{3-d}O_4$@CoO@$Fe_{3-d}O_4$ nanoparticles are overtaking the ones of other core@shell and core@multi-shelled magnetic properties.[11–15]

Experimental section

Iron stearate precursor synthesis

Iron stearate was synthesized according to an already published protocol[16] as follow:
A 1 L two-necked round bottom flask was charged with 9.8 g (32 mmol) of sodium stearate (98.8 %, TCI) and 320 mL of distilled water. The mixture was heated at reflux under magnetic stirring until all the stearate was dissolved. Afterwards, 3.80 g (16 mmol) of iron (II) chloride tetrahydrated dissolved in 160 mL of distilled water were poured in the round bottom flask. The mixture was kept another 15 min at reflux and under magnetic stirring. Then, the solution was allowed to cool down. The orange precipitate was collected by centrifugation (15 000 rpm, 5 min) and washed by filtration with a Buchner funnel. Finally, the powder was dried in an oven at 65 °C for one night.

Cobalt stearate precursor synthesis

Cobalt stearate was synthesized through the adaptation of the iron (II) stearate protocol:
A 1 L two-necked round bottom flask was charged with 9.8 g (32 mmol) of sodium stearate (98.8 %, TCI) and 320 mL of distilled water. The mixture was heated at reflux under magnetic stirring until all the stearate was dissolved. Afterwards, 3.16 g (16 mmol) of cobalt (II) chloride hexahydrated dissolved in 160 mL of distilled water were poured in the round bottom flask. The mixture was kept another 15 min at reflux and under magnetic stirring. Then, the solution was allowed to cool down. The orange precipitate was collected by centrifugation (15 000 rpm, 5 min) and washed by filtration with a Buchner funnel. Finally, the powder was dried in an oven at 65 °C for one night.

Iron oxide core synthesis

Small iron oxide nanoparticles were synthesized as previously described.[1] Typically, 1.38 g of iron (II) stearate (2.22 mmol) has been poured in a two-necked round bottom flask and dispersed in 20 mL of ether dioctyl (B_P = 290 °C). Then, 1.254 g of oleic acid (4.44 mmol) were added. The mixture was then heated to 120 °C for 30 min under magnetic stir to remove water traces and solvent residues. After this time, the stir was stopped and the mixture was heated at reflux for 120 min with a heating ramp of 5 °C/min under air. The resultant black solution was then cooled down to 100 °C and nanoparticles were precipitated through the addition of acetone. They were recover thanks to a centrifugation process (14 000 rpm, 5 min) and were redispersed in chloroform. The nanoparticles were washed 5 times in a mixture of chloroform : hot acetone (1 : 7) followed by centrifugation and were finally stored in chloroform.

$Fe_{3-d}O_4$@CoO core@shell nanoparticles synthesis

Core@shell $Fe_{3-d}O_4$@CoO nanoparticles were synthesized through a seed-mediated growth approach where 90 % of the cleaned iron oxide core nanoparticles were poured in a two-necked round bottom flask. After the chloroform was evaporated under vacuum, 10 mL of ether dioctyl were deposit in the flask which has been sonicated for 5 min. Then, 1.246 g of cobalt (II) stearate (2 mmol) precursor were poured and 20 mL of 1-octadecene (B_P = 320 °C) were added and 1.130 g of oleic acid (4 mmol) were finally poured. The solution was then sonicated for another 5 min and heated at 120 °C for 30 min under magnetic stir to remove water and solvent residues. After this time, the stir was stopped and the flask was connected to the condenser to heat the mixture at reflux for 120 min with a heating ramp of 1 °C/min under air. At the end, the remaining black solution was allowed to cool down to 100 °C and the nanoparticles were recovered through the addition of acetone followed by a centrifugation (14 000 rpm, 5 min). The nanoparticles were then redispersed in chloroform and washed 11 times by

centrifugation in a mixture of chloroform : hot acetone (1 : 7). The washed nanoparticles were finally stored in chloroform.

$Fe_{3-d}O_4$@CoO@$Fe_{3-d}O_4$ core@shell@shell nanoparticles synthesis

Core@shell@shell $Fe_{3-d}O_4$@CoO@$Fe_{3-d}O_4$ were synthesized through a second seed-mediated growth approach were 25 % of the washed $Fe_{3-d}O_4$@CoO nanoparticles were poured in a two-necked round bottom flask. The solvent was evaporated under vaccum and the nanoparticles were redispersed by sonication in 20 mL of ether dioctyl. The flask were filled with iron (II) stearate according to a R ratio equal to 0.5 (denoted CSSA), 1 (denoted CSSB) and 1.5 (denoted CSSC) where R is defined as $R = \left[n_{shell\ precursor}/n_{core\ precursor}\right]$. Finally, oleic acid was poured in the mixture with $n_{oleic\ acid} = 2n_{shell\ precursor}$. The exact quantities of iron (II) stearate and oleic acid are depicted in Table 14. The mixture was then heated at 120 °C under magnetic stir for 30 min to remove water and solvent traces. After this time, the stir was stopped and the flask was connected to a condenser to heat the mixture at reflux for 120 min with a heating ramp of 1 °C. At the end of the synthesis, the remaining black solution was allowed to cool down to 100 °C before adding acetone to precipitate the nanoparticles. The nanoparticles were finally recovered by centrifugation (14 000 rpm, 5min) before being redispersed in chloroform. They were finally washed one more time with a mixture of chloroform : acetone (1 : 7) and recovered by centrifugation. The washed nanoparticles are stored in chloroform.

Table 14. Quantities of shell precursor according to R ratio

Sample	R ratio	m (iron (II) stearate)	n (iron (II) stearate)	m (oleic acid)	n (oleic acid)
		g	mmol	g	mmol
CSSA	0,5	0,156	0,25	0,141	0,50
CSSB	1	0,311	0,50	0,282	1,00
CSSC	1,5	0,468	0,75	0,423	1,50

Characterization techniques

Transmission electron microscopy

Transmission electron microscopy (TEM) were performed on a JEOL 2100 LaB6 with a 0.2nm point to point resolution. EDX were performed with a JEOL Si(Li) detector. The nanoparticle sizes were calculated by measuring at least 300 nanoparticles from TEM micrographs by using the Image J software. The shell thickness corresponds to half of the difference between nanoparticle sizes which were measured before and after Co decomposition. The size distribution was calculated by fitting with a Gaussian function.

High resolution scanning transmission electron microscopy (STEM) and electron energy-loss spectroscopy (EELS) analysis were performed using a Cs aberration-corrected STEM, the NION UltraSTEM200 coupled with a high-sensitivity EEL spectrometer. Convergence and collection semiangles in EELS experiments were respectively 35 mrad and 50 mrad. CS, CSSA and CSSB were analysed with the STEM microscope operated at 100 kV acceleration voltage, while CSSC experiment was performed at 60 kV.

X-ray diffraction

X-ray diffraction (XRD) using a Bruker D8 Advance equipped with a monochromatic copper radiation (Kα = 0.154056 nm) and a Sol-X detector in the 20− 70° 2θ range with a scan step of 0.02°. High purity silicon powder (a = 0.543082 nm) was systematically used as an internal standard.

Fourier transform infrared

Fourier transform infrared (FTIR) spectroscopy was performed using a Perkin Elmer Spectrum spectrometer in the energy range 4000−400 cm^{-1} on samples diluted in KBr pellets.

Granulometry

Granulometry measurements were performed using a nano-sizer Malvern (nano ZS) zetasizer at a scattering angle of 173° with 1 measure of 7 runs of 30 seconds.

X-ray absorption

XAS and XMCD spectra were recorded at the $L_{2,3}$ edges of Fe and Co, on the DEIMOS beamline at SOLEIL synchrotron.[17] All spectra were recorded at 4.2 K under UHV conditions (10^{-10} mbar) and using total electron yield (TEY). The measurement protocol has previously been detailed by Daffé and al.[18] An external parallel magnetic field H^+ (respectively antiparallel H^-) was applied on the sample while a σ_+ polarized (σ_- polarized respectively) perpendicular beam was directed on the sample. Isotropic XAS signals were obtained by taking the mean of the σ_++σ_- sum where $\sigma_+ = [\sigma_L(H^+) + \sigma_R(H^-)]/2$ and $\sigma_- = [\sigma_L(H^-) + \sigma_R(H^+)]/2$ with σ_L and σ_R the absorption cross section measured respectively with left and right circularly polarized X-rays. XMCD spectra were obtained by taking the σ_+-σ_- dichroic signal with a ± 6.5 T applied magnetic field. The circularly polarized X-rays are provided by an Apple-II HU-52 undulator for both XAS and XMCD measurements while EMPHU65 with a polarization switching rate of 10 Hz was used to record hysteresis cycle at fixed energy.[17]

The samples consist of a silicon substrate where the colloidal suspension of the nanoparticles (ferrofluids) were drop cast to evaporate the solvent at room temperature. The substrates were then fixed on a copper sample holder. Measurements were performed between 700 and 740 eV at the iron edge and between 770 and 800 eV at the cobalt edge with a resolution of 100 meV and a beam size of 800*800 µm. Both XMCD and isotropic XAS signals presented here are normalized by dividing the raw signal by the edge jump of the isotropic XAS.

Mössbauer

^{57}Fe Mössbauer spectra were performed at 77 K using a conventional constant acceleration transmission spectrometer with a ^{57}Co(Rh) source and a bath cryostat. Then, an in-field Mössbauer spectrum was collected at 11 K using a cryomagnetic device that generates an external magnetic field parallel to the γ-beam. The samples consist of 5 mg Fe/cm^2 powder concentrated in a small surface due to the rather low quantities. The spectra were fitted by means of the MOSFIT program[19] involving asymmetrical lines and lines with Lorentzian profiles, and an α-Fe foil was used as the calibration sample. The values of isomer shift are quoted relative to that of α-Fe at 300 K.

SQUID magnetometry

Magnetic measurements were performed on samples by using a Superconducting Quantum Interference Device (SQUID) magnetometer (Quantum Design MPMS-XL 5). Temperature dependent zero-field cooled (ZFC) and field cooled (FC) magnetization curves were recorded as follows: the sample was introduced in the SQUID at room temperature and cooled down to 5 K with no applied field after applying a careful degaussing procedure. A magnetic field of 7.5 mT was applied, and the ZFC magnetization curve was recorded upon heating from 5 to 400 K. The sample was then cooled down to 5 K under the same applied field, and the FC magnetization curve was recorded upon heating from 5 to 400 K. Magnetization curves as a function of a magnetic field (M(H) curves) applied in the plane of the substrate were measured at 5 and 400 K. The sample was also introduced in the SQUID at

high temperature and cooled down to 5 K with no applied field (ZFC curve) after applying a subsequent degaussing procedure. The magnetization was then measured at constant temperature by sweeping the magnetic field from +7 T to −7 T, and then from −7 T to +7 T. To evidence exchange bias effect, FC M(H) curves have been further recorded after heating up at 400 K and cooling down to 5 K under a magnetic field of 7 T. The FC hysteresis loop was then measured by applying the same field sweep as for the ZFC curve. The coercive field (H_C) and the M_R/M_S ratio were measured from ZFC M(H) curves. The exchange bias field (H_E) was measured from FC M(H) curves. Magnetization saturation (M_S) was measured from hysteresis recorded at 5 K.

Thermogravimetry

Thermogravimetry (TG) analysis was performed using a SDTQ600 from TA instrument. Measurements were performed on dried powders under air in the temperature range of 20 to 600 °C at a heating rate of 5 ° C/min.

Polarized-small angle neutron scattering

Polarized-Small Angle Neutron Scattering (p-SANS) experiments were performed on the PA20 SANS instrument[20] at LLB and reactor Orphée with a fixed neutron wavelength λ of 4.5 Å. The sample to detector distance was set to 2 m getting a total accessible range from 0.017 to 0.237 $Å^{-1}$. The detector is a ^{3}He 2D detector of 64x64cm^2 with a 5x5 mm pixel size (128x128 pixels in total). The direct beam is absorbed by a central Cd beam stopper to avoid damaging the detector. The incoming neutron beam is polarized (or not), collimated and directed to the sample placed in a 10 tesla cryomagnet. Nanoparticles stored in chloroform were drop casted on a sapphire glass to evaporate the sample until a nice black crust was obtained. The dry powder was then press between two sapphire windows of 10 mm diameter and placed in a copper sample holder with a Cd ring to minimize background scattering. The sample holder was then placed in the cryomagnet, perpendicular to the incoming beam. The magnetic field is oriented horizontally and perpendicular to the neutron beam direction. The empty cell and the direct beam were measured to correct the data for transmission and background scattering.

Results and discussion

Synthesis strategy

Core-shell-shell nanoparticles composed of $Fe_{3-d}O_4$@CoO@$Fe_{3-d}O_4$ were expected to be synthesized by a seed-mediated growth approach through a succession of three thermal decompositions (Figure 26). The first step consists in the synthesis of iron oxide nanoparticles (denoted C) by the decomposition of a home-made iron (II) stearate ($FeSt_2$) precursor in ether dioctyl (B_P = 288 °C) in presence of oleic acid as stabilizing agent. Secondly, a home-made cobalt (II) stearate ($CoSt_2$) was added to the iron oxide nanoparticles used as seeds with a R_1 ratio equal to 2 [where R_1 = n($CoSt_2$)/n($FeSt_2$)] and was decomposed in a mixture of octadecene (B_P = 318 °C) and ether dioctyl (2 : 1) with oleic acid. Finally, the core@shell nanoparticles (denoted CS) were used as seeds in presence of iron (II) stearate with a R_2 ratio equal to 0.5, 1 or 1.5 [where R_2 = n($FeSt_{2\ shell}$)/n($FeSt_{2\ core}$)] which was decomposed in the same conditions as for the core in order to form a second shell. The final core@shell@shell nanoparticles (denoted CSSA, CSSB, CSSC for R_2 = 0.5, 1, 1.5) were stored in chloroform as a stable colloidal suspension.

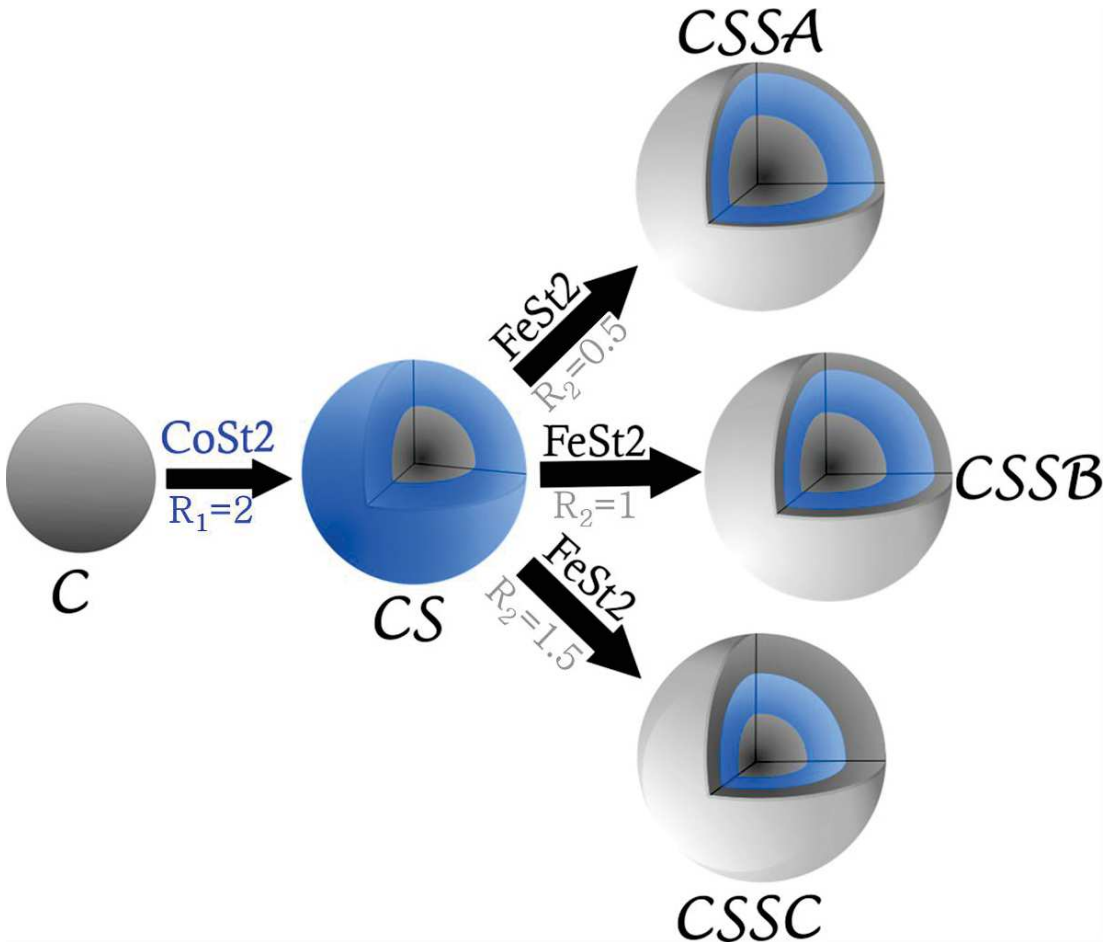

Figure 26. Schematic illustration showing the successive three steps seed-mediated growth approach used to synthesize $Fe_{3-d}O_4$@CoO@$Fe_{3-d}O_4$ nanoparticles.

Table 15. Experimental conditions and structural characteristics of nanoparticles. Core and shell values were obtained from TEM micrographs. Cell parameters and crystallite sizes were calculated from XRD patterns.

	C	CS	CSSA	CSSB	CSSC
R_x = n(shell)/n(core)	-	2	0,5	1	1,5
Diameter (nm)	10.1 ± 1.1	14.0 ± 1.5	14.5 ± 1.5	15.1 ± 1.7	15.6 ± 2.3
Shell thickness (nm)	-	2.0	0,3	0,6	0,8
Fe : Co at. Ratio by EDX	-	45 : 55	57 : 43	68 : 32	73 : 27
Hydrodynamic diameter (nm)	12	16	18	21	21
Cell parameter (Å)	8.379 ± 0.01	8.409 ± 0.01	8.391 ± 0.01	8.401 ± 0.01	8.412 ± 0.01
Crystal size (nm)	8.0 ± 0.1	9.1 ± 0.1	11.4 ± 0.1	12.2 ± 0.1	12.7 ± 0.1

Core@shell@shell nanoparticles of expected composition of $Fe_{3-d}O_4$@CoO@$Fe_{3-d}O_4$ were synthesized though a succession of three thermal decompositions using seed-mediated growth approaches.

Transmission Electron Microscopy

TEM micrographs (Figure 27a, b, c) show that core nanoparticles are very close to a spherical morphology with a well-controlled size dispersion centered at 10.1 nm. The decomposition of $CoSt_2$ on the iron oxide seeds produce nanoparticles that are larger than core nanoparticles, with a mean size of 14.0 ± 1.5 nm corresponding to a mean shell thickness of 2.0 nm (Figure 27d, e, f). A further thermal decomposition of $FeSt_2$ on the core@shell seeds allows to get nanoparticles that have a larger size than CS of 14.5 ± 1.5(CSSA), 15.1 ± 1.7 (CSSB) and 15.6 ± 2.3 (CSSC) nm corresponding to a mean shell thickness of 0.3, 0.6 and 0.8 nm respectively (Figure 27g-o). In the course of the different thermal decompositions, the nanoparticles are less spherical and the size distribution is broadened. This is due to a non-homogeneous deposition of the different shells that grow with a preferential orientation on the seeds.[21] Nevertheless, considering a 3 steps seed-mediated growth by thermal decomposition synthesis, the morphology and size dispersion of the nanoparticles are satisfactory.

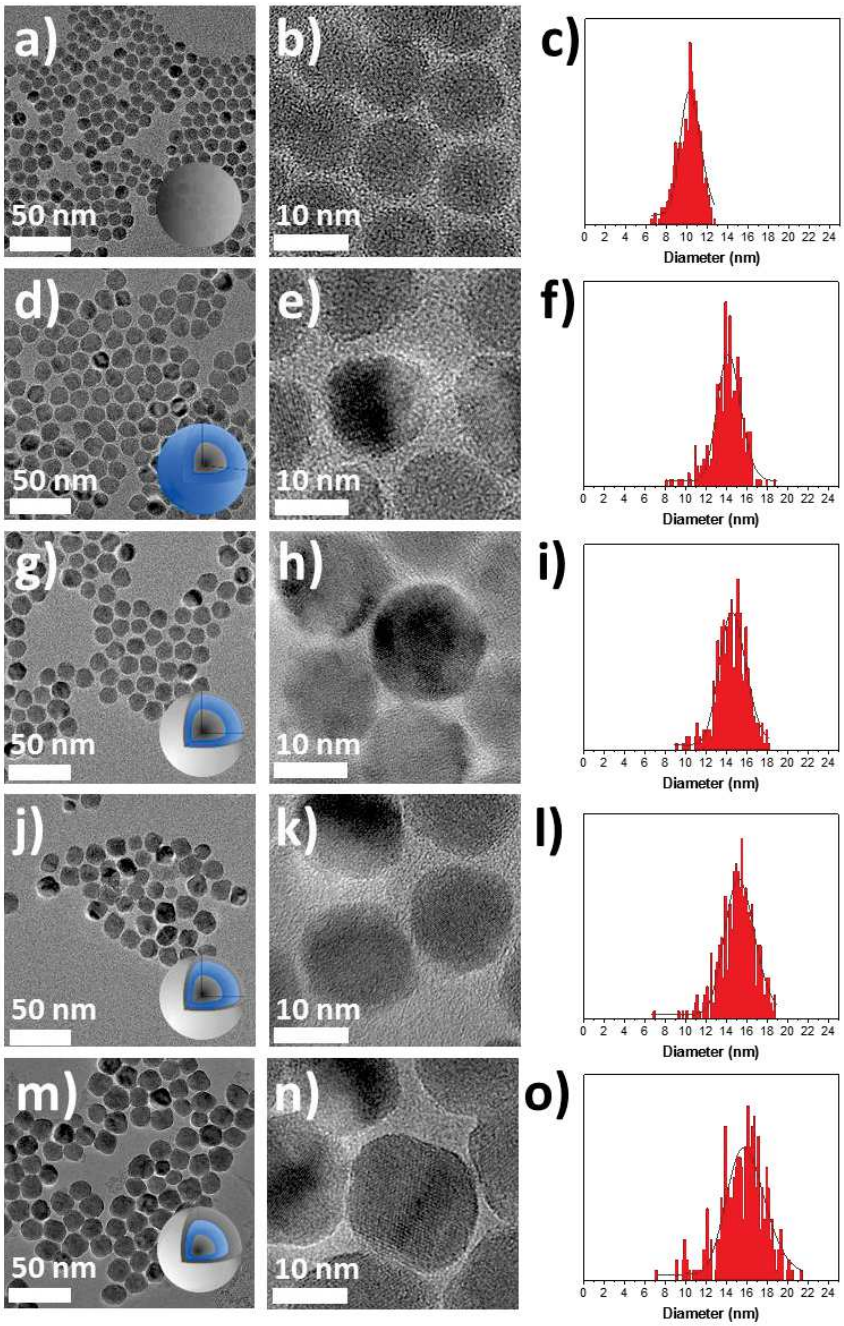

Figure 27. TEM micrographs with their schematic representations in inset of core (a, b), CS (d, e), CSSA (g,h), CSSB (j,k), CSSC (m, n) nanoparticles and their corresponding size distribution (c, f, i, l, o).

High resolution dark field STEM micrographs were recorded to investigate the crystal structure of the nanoparticles. It evidenced continuous and straight lattice fringes with no defects all across each nanoparticle, whatever their composition (CS, CSSA, CSSC). In some areas, the lattice fringes' periodicity is doubled. An FFT calculated on areas corresponding to simple and double periodicity of the lattice fringes for each nanoparticle showed spots that were attributed to two different crystal phases. The FFT for the simple periodicity of the lattice fringes showed spots that are attributed to the 400 (CS), 111 (CSSA), 220 (CSSB) and 222 (CS and CSSC) reflections of the Fe_3O_4 spinel phase. While the FFT of the double periodicity area of the lattice fringes show spots that are attributed to the 200 (CS), 111 (CSSB) and 111 (CS and CSSC) reflection of the CoO wüstite phase. The double periodicity of the lattice fringes arises from the interpenetration of the Fe_3O_4 and CoO phases, which is favored by the

epitaxial growth of the CoO shell from the iron oxide seed, due to a crystallization in the similar space group and to a very low lattice mismatch of both phases.
Figure 28b shows the lattice expansion against the distance across the nanoparticles (dashed lines) for CS. Hence, Geometrical Phase Analysis (GPA) is a useful analysis to evidence the presence of strains within an object. The simple periodicity is taken as a reference and as long as the double periodicity lattice fringes are probed, the lattice expansion presents strains in the order of 2 % that agrees with the lattice mismatch of the wüstite and the spinel phase. Indeed, the iron oxide spinel phase has a cell parameter of 8.396 Å (JCPDS card n° 19-062) and the CoO wüstite phase has a cell parameter of 4.26 Å (JCPDS card n°00-048-1719) which multiplied by 2 gives a cell parameter of 8.52 Å for CoO, corresponding to a difference of 1.5 % between both phases. A similar strain was observed in the case of CSSC. Hence it is expected that strains on the order of 2 % should also be present in CSSA and CSSB.

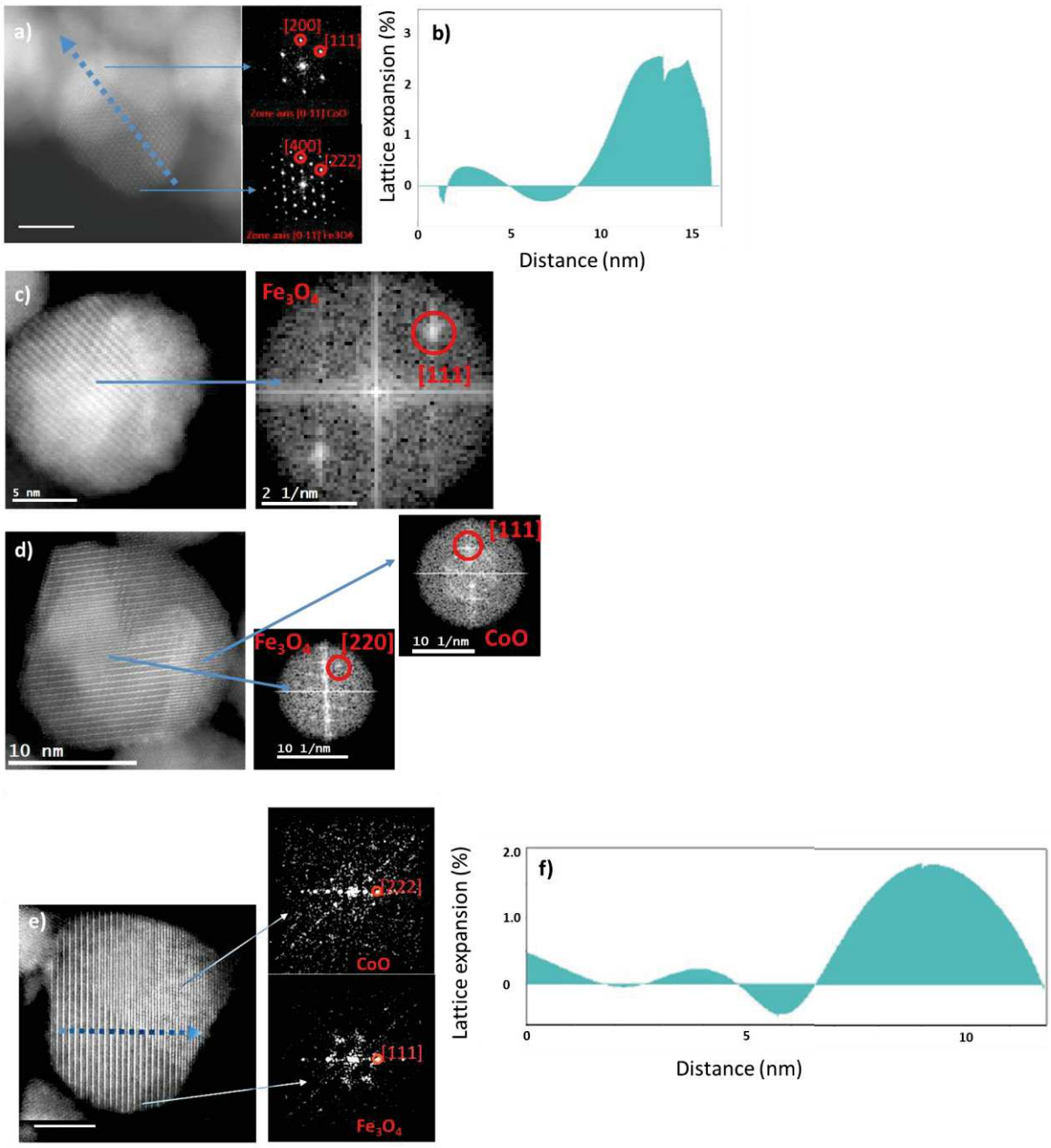

Figure 28. a, c, d, e) High resolution dark field STEM micrographs with specific FFT on zone axis and b, f) Geometrical Phase Analysis (GPA) analysis showing variation of lattice mismatch of a,b) CS c) CSSA d) CSSB and e,f) CSSC

Energy dispersive X-ray spectrometry (EDX) performed on the CS nanoparticles Table 15 displays the presence of a large amount of Co (55 %) compared to Fe (45 %) which should correspond to a 0.5 nm thick CoO shell if assuming perfect Fe_3O_4@CoO core@shell structure with a core size of 10.1 nm (Figure 27). However, TEM measurement has evidenced a thicker shell of 2.0 nm. Such a difference can be explained by the presence of interfacial diffusion as we have suggested in such systems[22] and also by the formation of a cobalt ferrite shell due to a partial solubilisation of the iron oxide seed and its recrystallization into cobalt ferrite during the synthesis of the shell, as evidenced by Lentijo-Mozo and al.[23] Indeed, for similar volumes of CoO and $CoFe_2O_4$, there are 32 Co atoms in CoO and 8 Co atoms in $CoFe_2O_4$. Thus, the larger shell thickness measured in TEM micrographs compared to the calculated one from EDX spectroscopy is due to the presence of cobalt ferrite.

All CSS display a higher Fe:Co atomic ratio than CS which agree with the formation of a second shell at the CS surface. Furthermore, CSSA, CSSB and CSSC are featured by 57:43, 68:32 and 73:27 % of Fe:Co atomic ratios respectively which evidences the increase of Fe quantity and agrees with a thicker second shell as long as more $FeSt_2$ were decomposed on CS. Considering the EDX ratios, a measured iron oxide core of 10.1 nm and a calculated CoO thickness of 0.5 nm, CSSA, CSSB and CSSC would display a second shell thickness of 0.9, 1.9 and 2.4 nm which is much higher than the measured thicknesses of 0.3, 0.6 and 0.8 nm respectively. However, if instead of considering a calculated CoO thickness of 0.5 nm, a measured CoO shell thickness of 2.0 nm is considered, CSSA, CSSB and CSSC would display a second shell thickness of 0, 0.4 and 0.9 nm respectively, which is close to the measured thicknesses. As this calculation is based on the cell's volume, it evidences that the thickness of the first shell is closer to 2.0 nm than 0.5 nm to calculate the thickness of the second shell. Hence, this result also supports the presence of interfacial diffusion within the $Fe_{3-d}O_4$/CoO interface. However, due to the low thickness of the second shell, it does not allow to clearly evidence the presence of interfacial diffusion at the CoO/$Fe_{3-d}O_4$ interface.

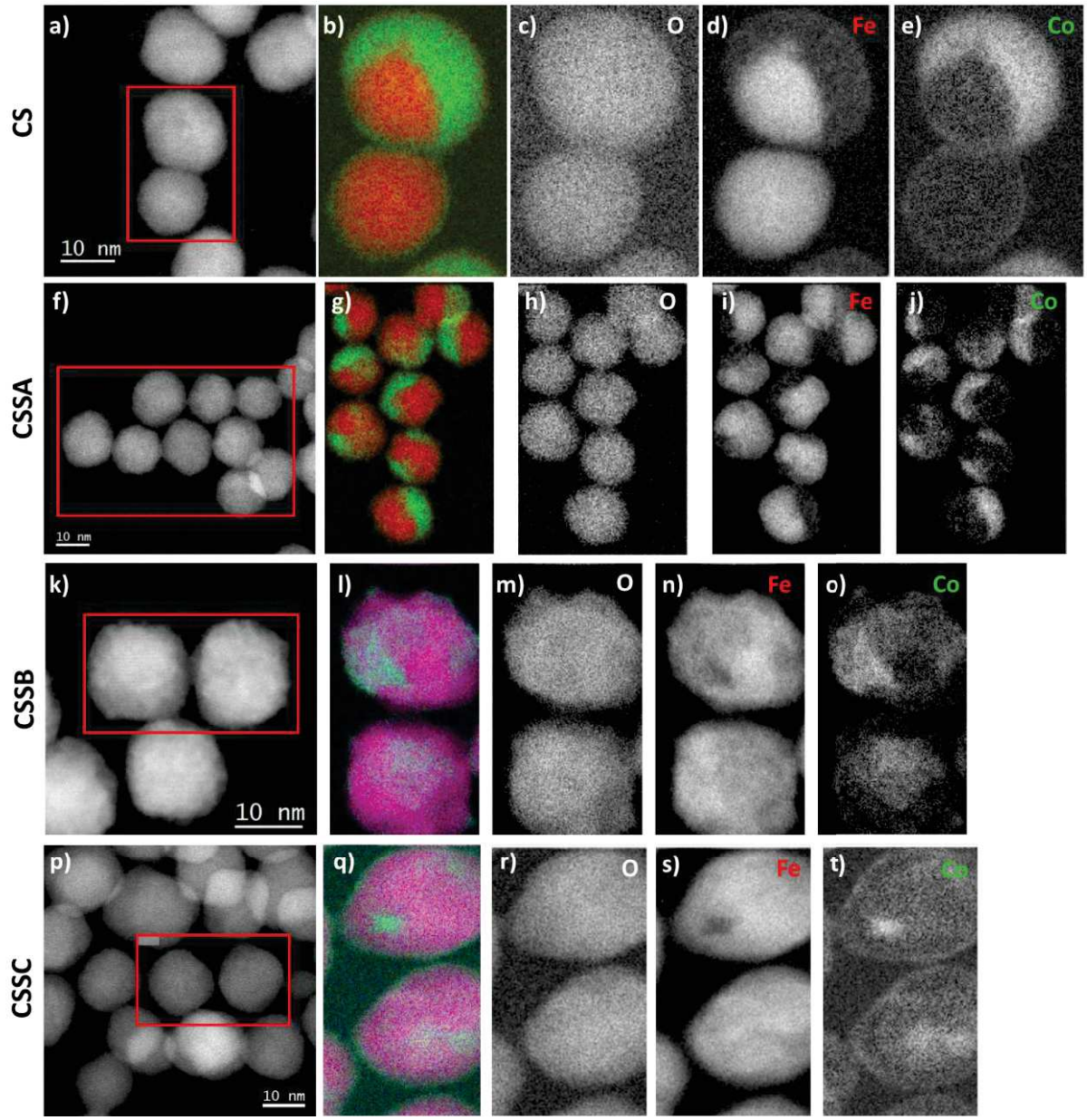

Figure 29. a, f, k, p) High resolution dark field micrographs with corresponding b, g, l, q) EELS-SI composite mapping and EELS mapping at the c, h, m, r) O K-edge, d, I, n, s) Fe and e, j, o, t) Co L-edges for a-e) CS, f-j) CSSA, k-o) CSSB and p-t) CSSC nanoparticles.

The Co and Fe atoms distributions across the core@shell and core@shell@shell nanoparticles was further investigated by elemental mapping with electron loss spectroscopy spectrum imaging (EELS-SI) at the Fe L-edge (red), Co L-edge (green) and oxygen K-edge (blue).
EELS-SI micrograph in Figure 29a-e of CS nanoparticle evidence the presence of Fe atoms in the center of the nanoparticle with Co atoms surrounding the Fe-rich core according to a non-homogeneous spatial distribution. This is in agreement with previous results obtained by Liu and al. on 3 dimensions $Fe_{3-d}O_4$@CoO core@shell nanoparticles.[13]

Composite EELS-SI mapping of CSSA (Figure 29f-j) shows a discontinuous layer of Fe surrounding the CS nanoparticles agreeing with a core@shell@shell structure. Some Co and Fe atoms seem to overlap according to a cobalt ferrite structure due to a possible solubilisation-recrystallisation of the CS seed during the synthesis of the second shell. Furthermore, separately EELS-SI mapping recorded at the Fe and Co L-edges show the presence of Fe and Co rich regions evidencing the inhomogeneous growth of

the $Fe_{3-d}O_4$ shell on the nanoparticles. In order to determine if the last iron oxide shell grows on the CoO shell or on the uncoated iron oxide core, further analysis must be performed.

In CSSB, composite EELS-SI mapping (Figure 29k-o) reveals an inhomogeneous growth of the second iron oxide shell on CS. It also shows a larger area of the second iron oxide shell on the CS nanoparticles than for CSSA, agreeing with a higher Fe:Co ratio for CSSB than for CSSA, as shown by EDX.

Increasing the R ratio in CSSC (Figure 29p-t) also leads to the presence of Co and Fe rich region as shown by EELS-SI mapping. The atomic spatial distribution also evidence a larger iron oxide surrounding layer compared to CSSA and CSSB nanoparticles, in accordance with EDX.

Hence, EELS-SI mapping has shown the inhomogenous growth of the shells on the seeds nanoparticles. It also evidenced the qualitative expansion of the iron oxide second shell on the seed nanoparticles as long as the R ratio is increased (CSSA → CSSC).

Size measurements from TEM micrographs show the size increase of the nanoparticles in agreement with the deposition and growth of the shells. While the iron oxide core nanoparticles display a close to sphere shape, the morphology of the nanoparticles slightly changes in the course of the different seed-mediated growth synthesis.
EDX Fe:Co atomic ratios evidenced the presence of Fe and Co atoms in the core@shell and increased in the core@shell@shell nanoparticles in agreement with the growth of the iron oxide shell. Compared to theoretical perfect core@shell and core@shell@shell structures, it was demonstrated that some interfacial cobalt ferrite is present within the nanoparticles.
The epitaxial growth of the shells on the seed nanoparticles were demonstrated by HAADF micrographs and the presence of CoO was shown by the indexation of FFT picture taken at different positions on the nanoparticles.
HAADF and EELS-SI agrees on the hetero atomic distribution of Fe and Co atoms with Co- and Fe-rich area. Such observation was attributed to the preferential growth of the shells on the faceted seeds. Nevertheless, these experiments show that in CS, the iron oxide core is surrounded by a CoO shell and that in the CSS, Fe atoms gradually covers the surface of the seeds according to the increase of the iron precursor poured in solution for the seed-mediated growth synthesis.
GPA showed the presence of crystal strains within the different phases of the nanoparticles that was attributed to the low lattice mismatch.

Fast Fourier infra-red spectroscopy

Fast Fourier infra-red spectroscopy (FT-IR), in Figure 30a, shows several bands in the range 4 000 to 400 cm^{-1} for CS, CSSA, CSSB and CSSC. The bands at 2 923 and 2 846 cm^{-1} arise from symmetric and antisymmetric stretching vibration of alkyl chains (νC-H) from the fatty chain of the oleic acid molecules. The bands at 1 632 and 1 457 cm^{-1} arise from the antisymmetric and symmetric stretching vibration of the carboxylic acid function (νCOO^-) of the oleic acid surfactant grafted at the surface of the nanoparticles.[1,24] Moreover, the absence of the band at 1 710 cm^{-1}, attributed to the C=O stretches from free carboxylic acid groups evidences the removal of the free oleic acid after washing. According to ref.[25,26], the wavenumber separation Δ, between $\nu_{as}(COO^-)$ and $\nu_s(COO^-)$ gives information on the coordination mode of the oleic acid with the nanoparticles. For a large Δ (200-320 cm^{-1}), the coordination mode is monodentate, for Δ lower than 110 cm^{-1}, it is chelating bidentate and for 140 < Δ < 190 cm^{-1}, it is bridging bidentate. However, the presence of several bands in the region of $\nu_{as}COO^-$ and ν_sCOO^-, forbid us to give a clear conclusion on the value of Δ and evidences the presence of a distribution of coordination mode at the surface of the nanoparticles.
The enlargement of FT-IR spectra in the range 450 – 800 cm^{-1} Figure 30b point up large bands with periodic oscillations that arise from experimental acquisition errors of the apparatus. The large band

centered around 590 cm^{-1} is attributed to the Fe-O band which shapes and displacement gives further information on the oxidation state of the iron oxide phase.[27] Indeed, a perfect Fe_3O_4 nanoparticle would display a large band centered at 574 cm^{-1} with a shoulder at 700 cm^{-1} while its oxidized phase, y-Fe_2O_3, displays several oscillations in the range 450 to 800 cm^{-1} with a maximum centered at 639 cm^{-1}.[27] Here, this maximum is the highest for the core nanoparticles (601 cm^{-1}) in agreement with a partially oxidized object. Then this maximum decreases from 599 cm^{-1} (CS) to 582 cm^{-1} (CSSC) when the shells are grown, which agrees with higher amount of Fe_3O_4 (574 cm^{-1}).
In the FT-IR spectrum of CS nanoparticles, an additional band centered at 510 cm^{-1} is present which is attributed to a Co-O vibration band that agrees with the presence of CoO.[28] And, the absence of this Co-O band from CoO in CSSA, CSSB and CSSC agrees with the reduction of the CoO content and the rise of iron oxide and cobalt ferrite. But, according to the work of Jacintho and al.[29], FT-IR analysis does not allow to dissociate Fe-O and Co-O bands in the $CoFe_2O_4$ structure as $CoFe_2O_4$ displays a single band centered at 591 cm^{-1} which is overlapped with the one of iron oxide.

Finally, the band at 720 cm^{-1} which is only present in the CS nanoparticles (see star) arises from scissoring of H-C-H bond of remaining free stearate molecules that are still present despite 10 washes. Actually, the presence of free stearate could have been avoided with further washes but this operation lead to the aggregation of the nanoparticles in the case of the $Fe_{3-d}O_4$@CoO nanoparticles.

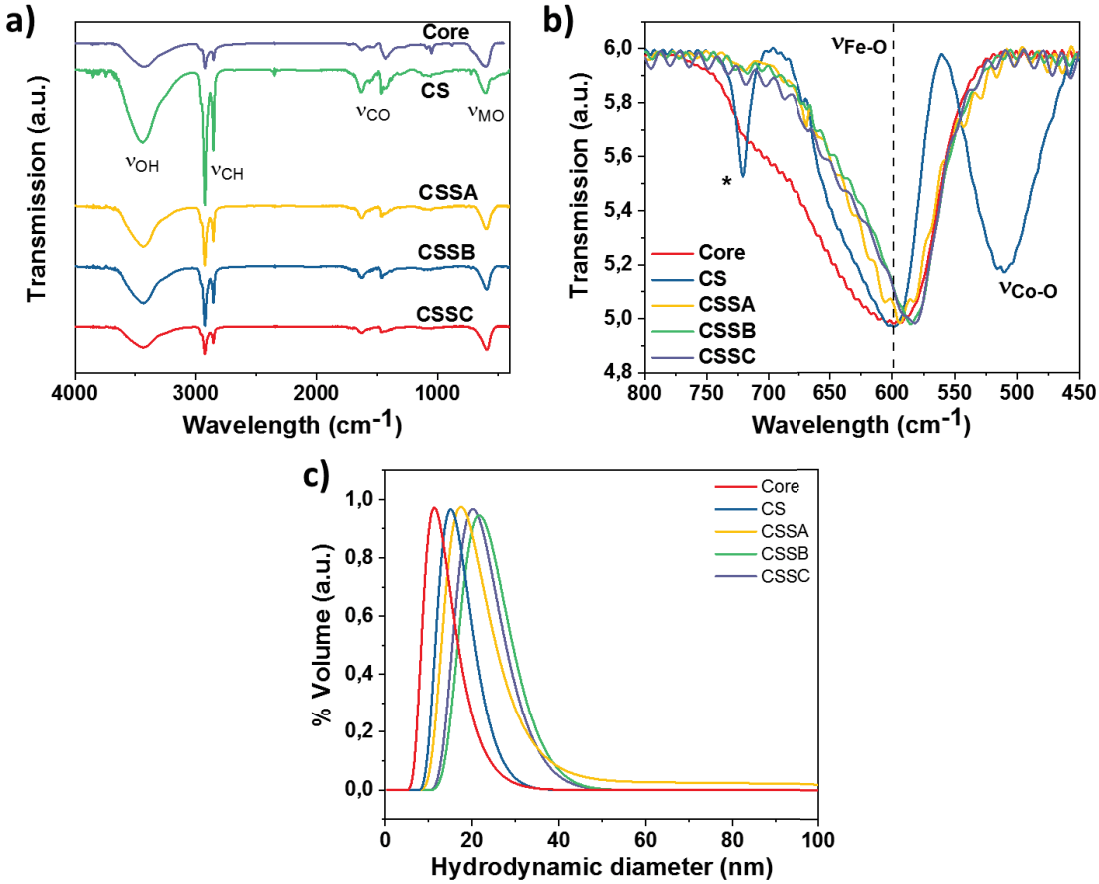

Figure 30. a) FT-IR spectra of C, CS, CSSA, CSSB and CSSC nanoparticles, b) enlargement of FT-IR spectra from 450 to 790 cm^{-1}. c) Granulometry (DLS) measurements in volume performed on nanoparticles in suspension in chloroform.

The presence of oleic acid ligands grafted at the surface of the different nanoparticles was evidenced by FT-IR spectroscopy. Furthermore, a deeper look at the M-O band allowed to point out the good synthesis of the CoO shell in the CS nanoparticles and the reduction of the CoO phase in the CSS nanoparticles coherently with a partial solubilisation-recrystallisation in cobalt ferrite. The displacement of the M-O band around 600 cm^{-1} allowed to conclude that the iron oxide core was partially oxidized, that the synthesis of the CoO shell through a thermal decomposition allowed to chemically reduce the core and then to protect it against oxidation. Last, the synthesis and growth of the second shell surprisingly appears to gradually bring more Fe^{2+}in the CSS nanoparticles while owing to the small thickness of this shell it was expected to be fully oxidized.

Granulometry

Thanks to the presence of oleic acid molecules grafted at their surface, the nanoparticles suspensions are stable in a variety of organic solvents such as chloroform, THF, toluene, hexane. Figure 30c presents granulometry measurements (DLS) corresponding to volume counts plotted as a function of the distribution of hydrodynamic diameter performed on nanoparticles in suspension in chloroform. The monomodal distributions of sizes evidences that no aggregation is present in the nanoparticles suspension with hydrodynamic diameters that are centered to 11, 15, 17, 22 and 20 nm for C, CS, CSSA, CSSB and CSSC, respectively which follows the TEM size evolution. However, the hydrodynamic diameters are slightly larger than the measured TEM sizes (Table 15) due to the presence of the oleic acid at the surface of the nanoparticles that contributes to the light scattering. The hydrodynamic diameters increase as the size of the nanoparticles increases gradually. The hydrodynamic diameter of CSSC is slightly lower than CSSB which may be explained by a lower amount of oleic acid grafted at the surface of the nanoparticles in suspension in chloroform.

The presence of the oleic acid ligands grafted at the surface of the nanoparticles allows them to be stable in suspension in most organic solvents.

X-ray diffraction

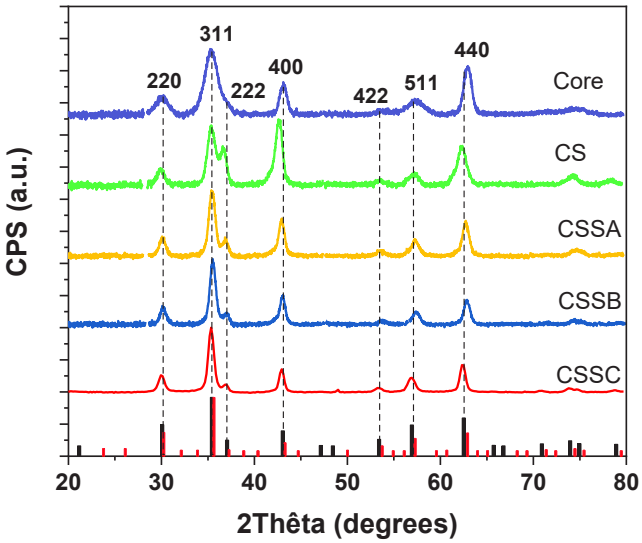

Figure 31. X-ray diffraction patterns of C, CS, CSSA, CSSB and CSSC nanoparticles. The black and red bars correspond to the Fe_3O_4 (JCPDS card n° 19-062) and CoO (JCPDS card n°00-048-1719) phases respectively. As $CoFe_2O_4$ displays the same diffractogram as Fe_3O_4 due to similar structures, the theoretical diffractogram of $CoFe_2O_4$ is not presented here for the sake of legibility.

XRD patterns recorded for each nanoparticle show peaks which were indexed to the inverse spinel structure of iron oxide (Figure 31). Additional peaks corresponding to a wüstite phase were also observed in the patterns of CS and CSS nanoparticles. These peaks and especially the peak related to the [222] hkl plan progressively vanish as the second shell grows, which agrees with a reduction of the CoO phase and/or an increase of the spinel ferrite phase. Moreover, peaks become narrower as the shell are grown. Hence, the average crystals sizes determined by the Debye-Scherrer's equation correspond to 8.0, 9.1, 11.4, 12.2 and 12.7 nm for C, CS, CSSA, CSSB and CSSC respectively. The increase of these crystals sizes agrees with TEM results i.e. the increase of the nanoparticle's size and the epitaxial growth of the shells. However, the calculated crystallite sizes from the Debye-Scherrer equation are smaller than sizes measured from TEM micrographs. Such a difference may be explained by the 2D projection of the faceted nanoparticles on TEM micrographs which tend to overestimate the nanoparticle's size.
The calculated cell parameter of the iron oxide core (C) is between the one of magnetite (a = 8.396 Å, JCPDS card n° 19-062) and maghemite (a = 8.338 Å, JCPDS card n° 39-1346) which is usually ascribed to the oxidation of magnetite into maghemite at the surface of the nanoparticles.[1] CS displays a cell parameter which is slightly larger than the cell parameter of magnetite which can be attributed to the presence of the CoO shell (a = 4.26 Å) where, to get a perfect epitaxy of the iron oxide phase, two lattices of CoO are required with, in theory, 2a = 8.52 Å[10] and thus induce strains at the $Fe_{3-d}O_4$/CoO interface.
Furthermore, the addition of the second shell on the $Fe_{3-d}O_4$@CoO nanoparticles leads to similar cell parameters considering the experimental errors. However, it was expected that the formation of a second $Fe_{3-d}O_4$ shell would decrease the cell parameter, according to surface oxidation. Nevertheless, our values can be ascribed to the presence of $CoFe_2O_4$ (a = 8.3919, JCPDS card n°00-022-1086) which may results from cationic diffusion at the CoO/$Fe_{3-d}O_4$ and $Fe_{3-d}O_4$/CoO interfaces[22] or to the partial resolubilisation of the CoO shell which recrystallized in cobalt ferrite during the synthesis of the second shell.[30] And as the cobalt ferrite is grown on the CoO shell, it also induces some strains that allows to get such high cell parameters values.

XRD patterns were indexed with a Fe_3O_4 spinel structure for each nanoparticles. An additional wüstite CoO component were required to complete the indexation of the CS, CSSA, CSSB and CSSC XRD patterns. The contribution of the CoO wüstite phase decreases in proportion among the growth of the second iron oxide shell. This result is attributed to the growth of the iron oxide shell in proportion to the wüstite phase but also to the decrease of the CoO content to form interfacial cobalt ferrite. The narrowing of the peaks evidenced the increase of the crystal size from C to CSSC, in agreement with good epitaxial relationship between the core and shells. Calculated cell parameters increase from C to CS in agreement with a higher amount of Fe^{2+} and with the presence of crystal strains as shown by GPA. They remain equivalent in the CSS nanoparticles due to the persistence of the crystal strains and also show that the iron oxide shell at the surface of the nanoparticles is not subjected to oxidation upon exposure to air.

Small-angle X-ray scattering

Small-Angle X-ray Scattering (SAXS) is a powerful analysis technique which is highly complementary to TEM, XRD and granulometry measurements. Indeed, SAX allows to probe a large amount of nanoparticles in suspension in solution in order to determine the size, the polydispersity and the form factor of the nanoparticles (Figure 32**)**.[31]

Here, the measured intensity is expressed as a function of the scattering wave vector $Q = (2\pi/\lambda)\sin(\theta)$ where λ is the photon wavelength and θ is the scattering angle. Moreover, Q is proportional to the volume of the particles and to their nuclear contrast which depends on their chemical composition. The nuclear contrast is defined as the difference of the scattering length density (SLD) between the

nanoparticles and the solvent. The SLD depends on the chemical composition and density of the nanoparticles. Here our nanoparticles coated with oleic acid were dispersed in toluene. The volume densities of Fe_3O_4 [32], $CoFe_2O_4$, CoO,[32] oleic acid[33] and toluene[33] were used to calculate the different SLDs (Table 16). According to equation 1, the calculated SLD values are in agreement with the experimental values in the literature. As the contrast between inorganic and organic materials is low (5 %), the contribution of oleic acid and toluene towards SLDs were negligible.[34]

$$SLD = \sum_i \frac{c_i b_i}{V_i}$$

Equation 1. Determination of the SLD where c_i, b_i and V_i are respectively the atomic concentration, the scattering length and the atomic volume of the i^{th} constituent.

Table 16. SLD (Δη) calculated from volume densities for each components. Note that the constrast are very close between Fe_3O_4 and $CoFe_2O_4$ due to the neighbouring Z values of Fe and Co.

Material	Density (g/cm^3)	Δη (10^{-6} Å^{-2})
Fe_3O_4[35]	5.18	40.5
$CoFe_2O_4$[34]	5.3	40.8
CoO[32]	6.44	47.6
Oleic acid[34]	0.89	8.1
Toluene[33]	0.87	8

SAXS was performed on CS, CSSA, CSSB and CSSC. All SAXS curves, present several oscillations, consistent with the narrow size distributions of the nanoparticles.[36] These oscillations are shifted to lower Q values from CS to CSSC which is expected from an increase of the nanoparticle size[36] as calculated from TEM and XRD data.

In order to study precisely the size and the chemical composition of each nanoparticle, experimental curves were fitted.
A simple sphere model (Figure 32a) allowed us to fit the experimental curves in order to calculate the mean radius and the mean SLD of each nanoparticle (Table 17). The mean radius of nanoparticles increased gradually as a function of the amount of Fe stearate used in the third decomposition step. Values of 6.7 ± 0.1 nm for CS to 7.4 ± 0.1 (CSSA), 7.9 ± 0.1 (CSSB) and 8.3 ± 0.1 nm (CSSC) are in agreement with the TEM measurements (7.1 ± 0.8, 7.4 ± 0.8, 7.7 ± 0.9 and 7.9 ± 1.2 nm of "radius" (half-size) for CS, CSSA, CSSB and CSSC respectively). The corresponding polydispersity is similar for each nanoparticle (10-13 %) and agrees with values measured from TEM micrographs (Table 15). SLDs decrease concomitantly from 46.0 10^{-6} Å^{-2} (CS) to 45.5 (CSSA), 44.6 (CSSB) and 43.9 (CSSC) 10^{-6} Å^{-2}. The mean SLD of each nanoparticle being a volume weighted value of the SLDs of the different phases present in the nanoparticle,[31] they agree with the reduction of the CoO phase and with the increase of the Ferrite phase upon the growth of the second shell.

The significant difference between the SLD of Ferrite (Fe_3O_4, y-Fe_2O_3, $CoFe_2O_4$) and wüstite (CoO) phases allows to fit the data with a core@shell model to get a deeper insight in the structure and the chemical composition of the nanoparticles.[35] Indeed, due to the small size variation from CS to CSS nanoparticles (Table 15), it was not possible to use a core@shell@shell model to describe the CSS nanoparticles. Thus the shell in the model actually corresponds to the two shells: -CoO@$Fe_{3-d}O_4$. Furthermore, we considered a similar mean radius of 4.8 ± 0.1 nm for the $Fe_{3-d}O_4$ core for each CS and CSS nanoparticles although we expected the cationic diffusion at the $Fe_{3-d}O_4$/CoO interface. This value was estimated according to TEM micrographs and was supported by the good matching of our fits with the experimental curves. The shell thickness increases coherently with previous observations: 1.9, 2.5, 3.0 and 3.3 ± 0.1 nm for CS, CSSA, CSSB and CSSC respectively and is in agreement with the TEM

observations (considering the size variation including both shells in the case of CSS nanoparticles). Also, the addition of the core radius and the shell thickness leads to mean overall radius of 6.6, 7.3, 7.9 and 8.1 ± 0.2 nm respectively. These values agree with the values of the simple sphere models and confirm the validity of our core-shell model that is in accordance with TEM size measurements considering the standard deviations

This fit also leads to reasonable polydispersity (CS 12 %, CSSA 11 %, CSSB 10 %, CSSC 12 %), that are consistent with TEM results.

SLDs determined for each core are very similar with a mean value of 43.5 10^{-6} $Å^{-2}$ that is higher than the theoretical SLD values of Fe_3O_4, y-Fe_2O_3 or $CoFe_2O_4$ and lower than the one of CoO. Hence it evidences a contribution of CoO in the core which accounts for 42 % with a contribution of spinel ferrite of 58 %. Indeed, the SLD of Fe_3O_4, y-Fe_2O_3 and $CoFe_2O_4$ being very close, it is not possible to distinguish them. Hence, according to the mean fitted SLD value, the core is composed of two phases with in the center, the spinel ferrite phase with a diameter of 8.0 nm surrounded by a CoO phase of 0.8 nm thick. Such a high contribution of CoO in the core was not expected and disagrees with TEM and XRD analysis. Nevertheless, as we used a spherical model and as the nanoparticles are not real spheres, it can evidence the inhomogenous spatial distribution of the CoO shell on the iron oxide core.

Furthermore, SLDs of shells are larger than the one of cores (47.1, 46.1, 46.2, 45.8 $Å^{-2}$ for CS, CSSA, CSSB and CSSC, respectively) and are between the SLDs of spinel ferrites and CoO. Moreover, they agree with a greater contribution of CoO in the shell than in the core. In CS, the SLD is slightly lower than the theoretical value of CoO, which may be indicative of the presence of a small amount of Co-Ferrite resulting from cationic diffusion at the $Fe_{3-d}O_4$/CoO interface although such a variation is within the experimental error. Plus, the SLD of the shell decreases when the size of CSS increases which is consistent with the increase of ferrite content in the shell.

Considering the core and shell volume for each nanoparticle, mean SLD values were calculated from the ones of cores and shells (45.8, 45.4, 45.6 and 45.3 10^{-6} $Å^{-2}$ for CS, CSSA, CSSB and CSSC respectively). These values are close to the ones determined with the simple sphere model, hence confirming the validity of the core@shell model.

Finally, SLDs of Ferrites and CoO, were used to determine the composition of the shells with 93, 78, 79 and 74 % of CoO and 7, 22, 21 and 26 % of ferrites, respectively for CS, CSS A, B, C. Hence, the shell of CS was calculated to be composed of a 0.2 nm thick $CoFe_2O_4$ surrounded by a 1.7 nm thick CoO. According to these results, we can calculate the composition of the shell of the different CSS nanoparticles:

- The shell of CSSA is composed of 0.2 nm thick $CoFe_2O_4$ surrounded by 2.0 nm thick CoO that is also surrounded by 0.3 nm thick spinel ferrite.
- The shell of CSSB is composed of 0.2 nm thick $CoFe_2O_4$ surrounded by 2.4 nm thick CoO that is also surrounded by 0.4 nm thick spinel ferrite.
- The shell of CSSC is composed of 0.2 nm thick $CoFe_2O_4$ surrounded by 2.5 nm thick CoO that is also surrounded by 0.6 nm thick spinel ferrite.

Even though the increase of the spinel ferrite in CS, CSSA, CSSB and CSSC is coherent, the thickness of the CoO phase as well as the mean SLD values in the nanoparticles are too high compared to what was expected according to the previous analysis (TEM, EDX, XRD). It evidences thus the limitation of the core@shell model used here where it does not allow to extract the structure of the nanoparticles. Nevertheless, the evolution of the SLD allows to roughly compare the nanoparticles. Hence, it shows that CS has a high amount of CoO which decreases in favor of the increase of the spinel ferrite content from CSSA to CSSB and that the overall diameter of the nanoparticles increase from CS to CSSC.

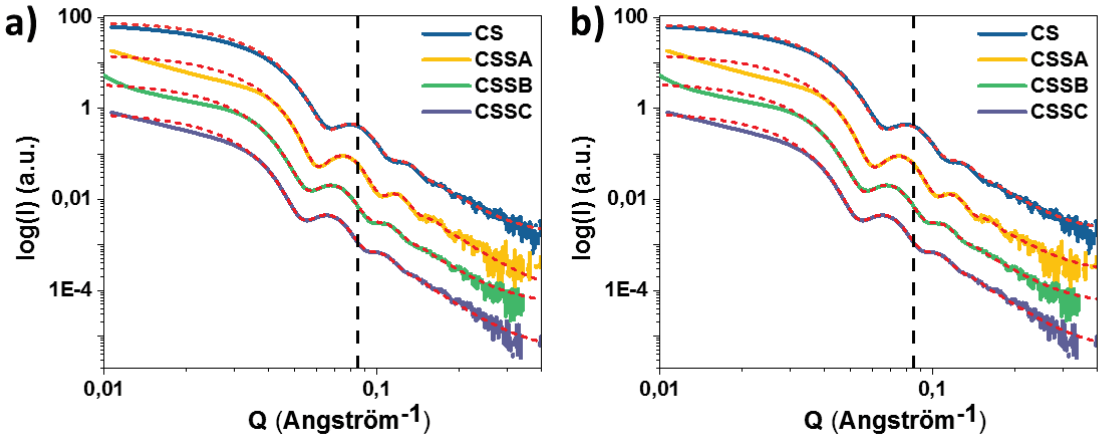

Figure 32. Small-angle X-ray scattering of CS, CSSA, CSSB and CSSC nanoparticles fitted with a) a simple sphere model, b) a core@shell model. The red dotted curves are the corresponding fit and the dashed vertical line highlights the peak shift.

Table 17. Experimental values deduced from the fit on SAXS data.

$\Delta\eta$, $\Delta\eta_1$ and η_2 are the SLD of the whole sphere, of the core and shell's from the core@shell model respectively; σ corresponds to the polydispersity.

	Simple sphere model			Core@shell model				
Sample	Radius (nm)	σ (%)	$\Delta\eta_1$ (10^{-6} Å^{-2})	Core radius (nm)	Shell thickness (nm)	σ (%)	$\Delta\eta_1$ (10^{-6} Å^{-2})	$\Delta\eta_2$ (10^{-6} Å^{-2})
CS	6.7	13	46.0	4.7 ± 0.1	1.9 ± 0.1	12 ± 1	44.2 ± 0.1	47.1 ± 0.1
CSSA	7.4	10	45.5	4.8 ± 0.1	2.5 ± 0.1	11 ± 1	43.5 ± 0.1	46.1 ± 0.1
CSSB	7.9	12	44.6	4.9 ± 0.1	3.0 ± 0.1	10 ± 1	43.5 ± 0.1	46.2 ± 0.1
CSSC	8.2	11	43.9	4.8 ± 0.1	3.3 ± 0.1	12 ± 1	42.9 ± 0.1	45.8 ± 0.1

A fit of the SAXS curves according to a simple sphere model and with a core@shell sphere model allowed to analyze the chemical composition of the nanoparticles. However, it appears that the calculated proportion of CoO was unreasonable compared to the other analysis (TEM, EDS, XRD). Hence this technique only allows to conclude on the global size increasing from CS to CSSC nanoparticles and on the presence of a large quantity of CoO in CS nanoparticles which decreases after the growth of the second ferrite shell.

X-ray absorption (XAS, XMCD)

Thanks to the chemical selectivity and the valence sensitivity, soft X-ray Absorption Spectroscopy (XAS) and X-ray Magnetic Circular Dichroism (XMCD) experiments are particularly powerful to probe separately the cationic environment of Fe and Co atoms. Indeed, it is possible with XAS-XMCD to discriminate different structures that crystallized in similar space groups. As an example, it is possible to discriminate the wüstite phase from the inverse spinel phase, and also to discriminate two different inverse spinel structures such as magnetite, maghemite and cobalt-ferrite. Hence, these techniques are particularly adapted to study the oxidation state of Fe_3O_4 in y-Fe_2O_3 and the interfacial diffusion of Co and Fe cations in our CSS nanoparticles. Combined to simulation based on Multiplet Ligand Field (MLF) theory, XMCD allows to determine the amount of each cation in each environment (Td vs Oh). Then, the contribution of each element on the magnetic properties can be quantitatively determined.

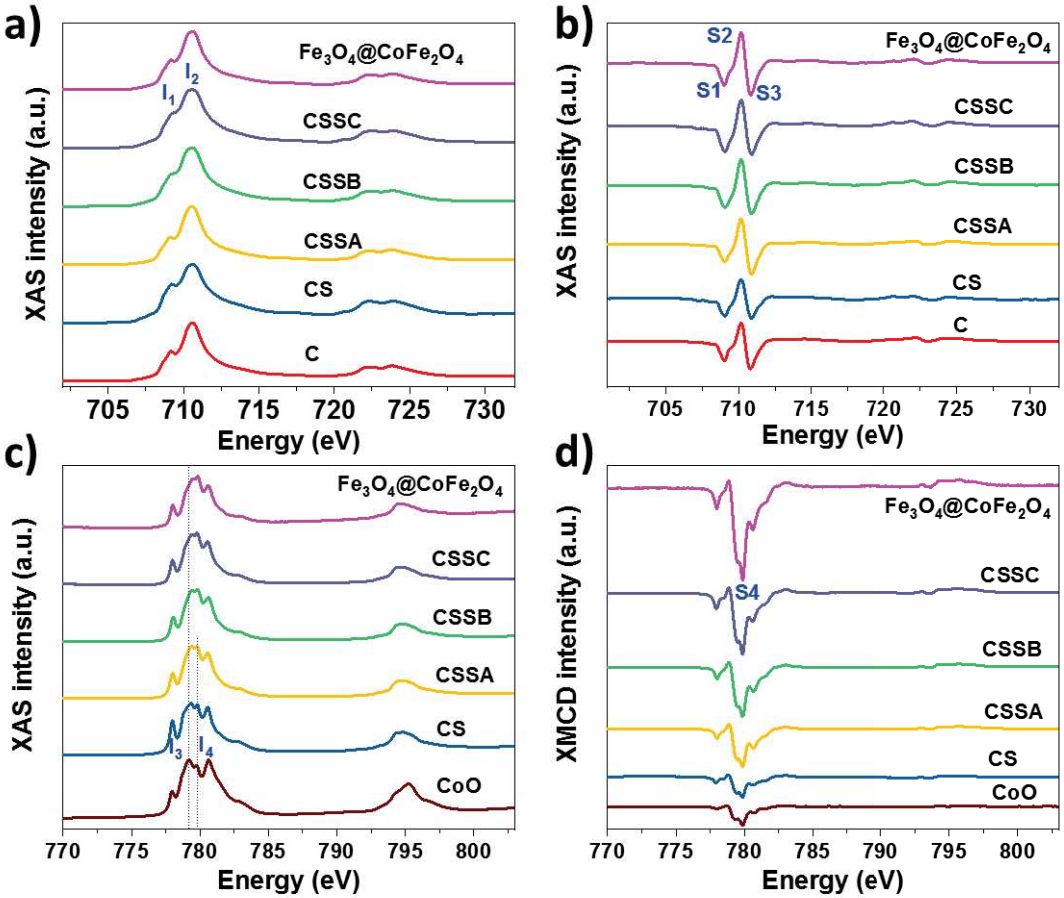

Figure 33. a, c) XAS and b, d) XMCD spectra recorded for C, CS, CSSA, CSSB and CSSC nanoparticles at the a, b) Fe edges and c, d) Co edges.

The isotropic XAS and XMCD spectra recorded at the Fe $L_{2,3}$ edges on Figure 33a and b all look similar and are typical of ferrite structures.[37–39] In XAS spectra recorded at the Fe edge (Figure 33a), the intensity of I_1 peak arises mainly from the contribution of Fe^{2+} in octahedral sites (Oh), while the intensity of I_2 peak is mostly due to Fe^{3+} in Oh sites. Thus the intensity ratio I_1/I_2 gives information on the quantity of Fe^{2+} cations: an increase of I_1/I_2 indicates an increase of Fe^{2+}. The isotropic XAS spectra Figure 33a displays a higher I_1/I_2 ratio for CS (0.82) than its core (0.56) which evidences an increase of Fe^{2+} content in CS. We attribute this behavior to the chemical reduction of the $Fe_{3-d}O_4$ core during the formation of the CoO shell and to the protection of the core by the CoO shell that avoids surface oxidation upon storage.[22] The addition of a thin iron oxide layer (CSSA) on CS led to a decrease of this ratio to 0.52 which increased when the shell thickness grew (CSSA : 0.52 → CSSB: 0.61 → CSSC: 0.65).

XMCD spectra recorded at the Fe $L_{2,3}$ edges (Figure 33b), present three main peaks in the L_3 region. Peak S1 corresponds to Fe^{2+} and Fe^{3+} in Oh sites, S2 corresponds to Fe^{3+} in tetrahedral sites (Td) and S3 is attributed to Fe^{3+} in Oh sites. Peaks S1 and S3 are coupled antiparallel to peak S2 due to the ferrimagnetic behavior of the inverse spinel structure where Fe^{2+} and Fe^{3+} cations in Oh sites are coupled antiparallel to Fe^{3+} in Td sites. In the XMCD spectrum of C, the peak S1 is very low in intensity with an oscillation between S1 and S2 which corresponds to an iron oxide spinel structure with a deficiency in Fe^{2+} atoms.[37,39] Moreover, according to the work of Brice-Profeta and al.[37] the intensity of the S1 peak is very low in Fe_3O_4 compared to γ-Fe_2O_3. The S=(S1+S2)/(S2+S3) ratio allows to determine qualitatively the Fe^{2+} content when compared to reference samples : Fe_3O_4 is correlated to the highest S value of 1.27 while γ-Fe_2O_3 is associated to the lowest S value of 0.61.[40]
The S ratio first increases from C (0.83) to CS (0.95) showing the core preservation from oxidation in the CS structure, and then decreases from CS to CSSA before increasing again up to CSSC (0.95) which is similar to CS (0.95). As the S ratio does not show a linear evolution from magnetite to maghemite, it is possible to determine a δ index that allows to determine directly the deficiency of Fe^{2+} content in $Fe_{3-d}O_4$ in terms of maghemite (δ = 0.33; no Fe^{2+}) / magnetite structure (δ = 0; 8 Fe^{2+} cations in a cell). Indeed, Pellegrin and al.[41] present XMCD spectra of iron oxide with different oxidation degrees from the maghemite to the magnetite structure that allows to determine the δ index from the S ratio. Moreover, according to a similar structure and the absence of Fe^{2+} in maghemite and in cobalt-ferrite, it is not possible to distinguish both phases in XMCD spectra at the Fe edge. And as the presence of interfacial atomic diffusion leads to the creation of cobalt ferrite phase, the δ index actually describes the composition of the nanoparticles in terms of magnetite / Fe^{2+} deficient phase.
Hence, C sample which is only composed of iron oxide, has an intermediate δ index (0.26) that agrees with a partially oxidized composition corresponding to 79 % of maghemite and 21 % of magnetite. Then δ decreases to 0.19 for CS which is in agreement with a higher content of Fe^{2+} as expected from previous results. This δ of 0.19 in CS corresponds to a composition of 43 % of magnetite and 57 % of Fe^{2+} deficient phase. In CSSA, δ reaches 0.29 and decreases to 0.23 for CSSB and to 0.19 for CSSC evidencing a lower Fe^{2+} content in CSSA compared to CS, and the increase of Fe^{2+}content as the second shell is grown. Hence, CSSA is composed of 88 % of Fe^{2+} deficient phase and 12 % of magnetite while CSSB displays 70 % of Fe^{2+} deficient phase and 30 % of magnetite, finally, CSSC has the same magnetite (43 %) and Fe^{2+} deficient phase content (57 %) than CS.
Moreover, the comparison of our δ values with δ of a pure $CoFe_2O_4$ nanoparticle (δ $CoFe_2O_4$ = 0.33) and with a Fe_3O_4@$CoFe_2O_4$ nanoparticles (δ=0.26)[22] allows us to conclude on the presence of interfacial atomic diffusion as shown by the high increase of δ from CS to CSSA, and that not all the iron oxide present in the nanoparticles were converted into cobalt ferrite as evidenced by the decrease of δ from CSSA to CSSC.[42] These results are in agreement with XAS analysis and we attributed the increase of Fe^{2+} content while the $Fe_{3-d}O_4$ shell is grown, to arise from the construction of the Fe_3O_4 shell at the surface of CS where surprisingly the second shell seems to be less subjected to surface oxidation than the iron oxide core.

The calculation, using Ligand Field Multiplet theory, of the contribution of Fe^{2+}(Oh), Fe^{3+}(Oh) and Fe^{3+}(Td) is very difficult to proceed. Indeed, the different environments of Fe cations like magnetite, maghemite and cobalt ferrite affects the spin-orbit coupling, the local symmetry and the crystal field. However, a first approach is considered that consists in using parameters of magnetite nanoparticles from the literature to calculate the contribution of Fe^{2+} and Fe^{3+}. Linear combinations performed to fit the XAS and XMCD spectra are also illustrated in Figure 34. The variations of the Fe^{2+}/Fe^{3+} ratio extracted from LFM is fully in agreement with results obtained with the (S1+S2)/(S2+S3) ratio and with δ from $Fe_{3-\delta}O_4$. Hence it confirms our observations with the chemical reduction of the core and its' protection by the CoO shell in CS nanoparticles and the further growth and increase of iron oxide shell in CSSA, CSSB and CSSC nanoparticles.

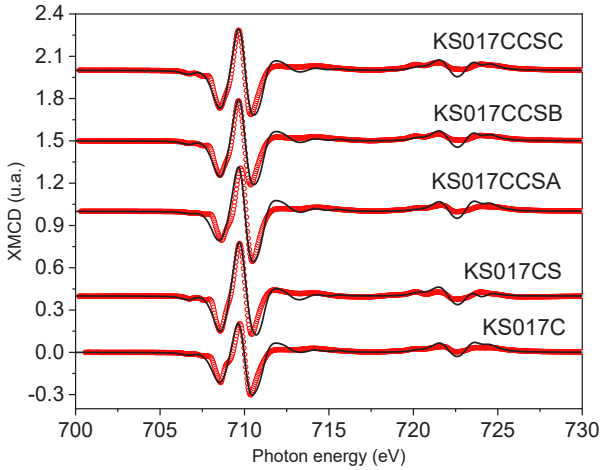

Figure 34. Experimental (red) and calculated (black) curves of C, CS, CSSA, CSSB and CSSC nanoparticles. Calculated curves were produced by linear combinations of theoretical XMCD curves of magnetite and maghemite produced by the CTM4XAS software.

Complementary information were obtained by performing similar experiment at the Co $L_{2,3}$ edges. Isotropic XAS (Figure 33c) agrees with the presence of Co^{2+} in Oh sites of a ferrite structure[43] and show several peaks where the two most intense ones (I_3 and I_4) are of interest. Indeed, in the case of perfect CoO nanoparticles, I_4 is low[44] while in cobalt ferrite, I_4 increases to almost reach the intensity of I_3.[45] Here, the intensity of peak I_4 increases during the growth of the nanoparticle evidencing the creation and the increase of cobalt ferrite within the nanoparticle.

XMCD spectra recorded at the Co $L_{2,3}$ edges also agrees with the sole presence of Co^{2+} in Oh sites.[40,44] As CoO is an antiferromagnet, no contribution of Co^{2+} in Oh sites should be visible in the XMCD spectra. XMCD being a magnetic dichroic analysis, the spins of a pure antiferromagnet which compensates each other's do not contribute to the XMCD signal. However, the XMCD spectra of the CoO nanoparticles used as reference, show a small XMCD signal (Figure 33d) that is attributed to Co^{2+} spins canted at the surface of the nanoparticle due to the breaking of symmetry.[46]

The XMCD spectra were normalized to the edge of the jump of the XAS spectra, i.e. they are normalized to the amount of cations. In this frame, the maximum intensity of peak S4 corresponds to the quantity of non-compensated magnetic spins of Co^{2+} with respect to the amount of Co^{2+} cations in the nanoparticles. The intensity of peak S4 reaches 20 % of the XAS intensity for CoO nanoparticles and 23 % for CS which are very close. However, in the CoO reference, it corresponds to a higher amount of surface spins given the flower shape and the large nanoparticle's size (40 nm) (Figure S 15), given the size and spherical shape of CS it results mostly from interfacial diffusion. Peak S4 increases to 42, 54 and 68 % in CSSA, CSSB and CSSC respectively which is related to a change of Co environment from AFM to FiM and evidences thus the increase of cobalt ferrite content in the nanoparticle.

Given the long time and high temperature used for the thermal decomposition, we investigated the potential ability of a further diffusion of Co atoms from the CoO shell in the $Fe_{3-d}O_4$ core during the synthesis of the second $Fe_{3-d}O_4$ shell. A new series of samples (C2, CS2) composed of a $Fe_{3-d}O_4$@CoO reheated (CS2 reheated) nanoparticles were analyzed. The structural analysis for this new series of samples are detailed in the annexes. Briefly, the $Fe_{3-d}O_4$ core (C2) has a size of 8.3 nm, the $Fe_{3-d}O_4$@CoO core@shell (CS2) has a size of 10.8 nm corresponding to a CoO shell thickness of 1.3 nm. The $Fe_{3-d}O_4$@CoO core@shell reheated (CS2r) has a size of 9.7 nm which corresponds to a reduction of 0.6 nm compared to CS2. Such phenomenon is attributed to a partial resolubilisation of the outer part of CS2 during the synthesis of CS2r.[23] Moreover, XRD patterns showed the presence of the iron oxide spinel structure for each nanoparticles and the presence of the CoO wüstite phase in CS2 and CS2r. And as the peaks from the 222 and 400 reflection decrease in CS2r compared to CS2, it agrees with a decrease

of the CoO phase which can result from the resolubilisation of a part of the CoO shell. Nevertheless, such analysis does not allow to probe the atomic diffusion, thus XAS and XMCD experiments were performed.

XAS spectra recorded at the Fe edge of C2, CS2 and CS2r are presented in Figure 35a,b. Sample C2 has a low I_1/I_2 ratio equal to 0.57, evidencing a great surface oxidation. This ratio increases to 0.78 for CS2 and stays almost identical for CS2 reheated with a value of 0.81. The XMCD spectrum of C2 recorded at the Fe edge also agrees with a partially oxidized iron oxide structure[41] as evidenced by the S ratio (0.75). This ratio increases slightly to 0.77 in CS and increased further to 0.83 in CS2 reheated, corresponding to δ values of 0.30, 0.29 and 0.26 for C2, CS2 and CS2 reheated respectively. Hence, it shows a low reduction of the iron oxide core in CS2 which was expected to be more efficient. Nevertheless, in CS2r, δ is lower than in CS2 which can be attributed to a size reduction of the CoO shell. Indeed, the total electron yield record mode is mostly sensitive to the 2 to 5 first nanometers.[47] Thus, a size reduction of the CoO shell leads to a larger contribution of the iron oxide core that can evidence a false apparent increase of the Fe^{2+} content.
Moreover, as the I_1/I_2 ratio increases between CS2 and CS2r, being higher than the one of magnetite nanoparticles and close to the one of $Fe_{3-d}O_4$@$CoFe_2O_4$ nanoparticles, and as the S ratio and δ are close to the values of $Fe_{3-d}O_4$@$CoFe_2O_4$ nanoparticles, it evidences the possibility of a further interfacial atomic diffusion during the reheating of CS nanoparticles.

XAS spectra recorded at the Co $L_{2,3}$ edges brings further information where the intensity of pic I_3 stays identical in CS2 and in CS2r as shown by the difference CS2-CS2r (Figure 35a), and suggests the absence of Co diffusion. Moreover, XMCD intensities at the Co $L_{2,3}$ edges are very close with 26 and 29 % for CS2 and for CS2r and the difference of XMCD evidences very similar curves of CS2 and CS2r.

Thus, XAS and XMCD results at the Fe and Co $L_{2,3}$ edges evidenced that the atomic diffusion in CS is very limited when the nanoparticles are reheated. These results are in agreement with the work of Lentijo-Mozo and al.[23] who evidenced the stops of atomic diffusion in core@shell nanoparticles as long as a stoichiometric layer of $CoFe_2O_4$ is formed.

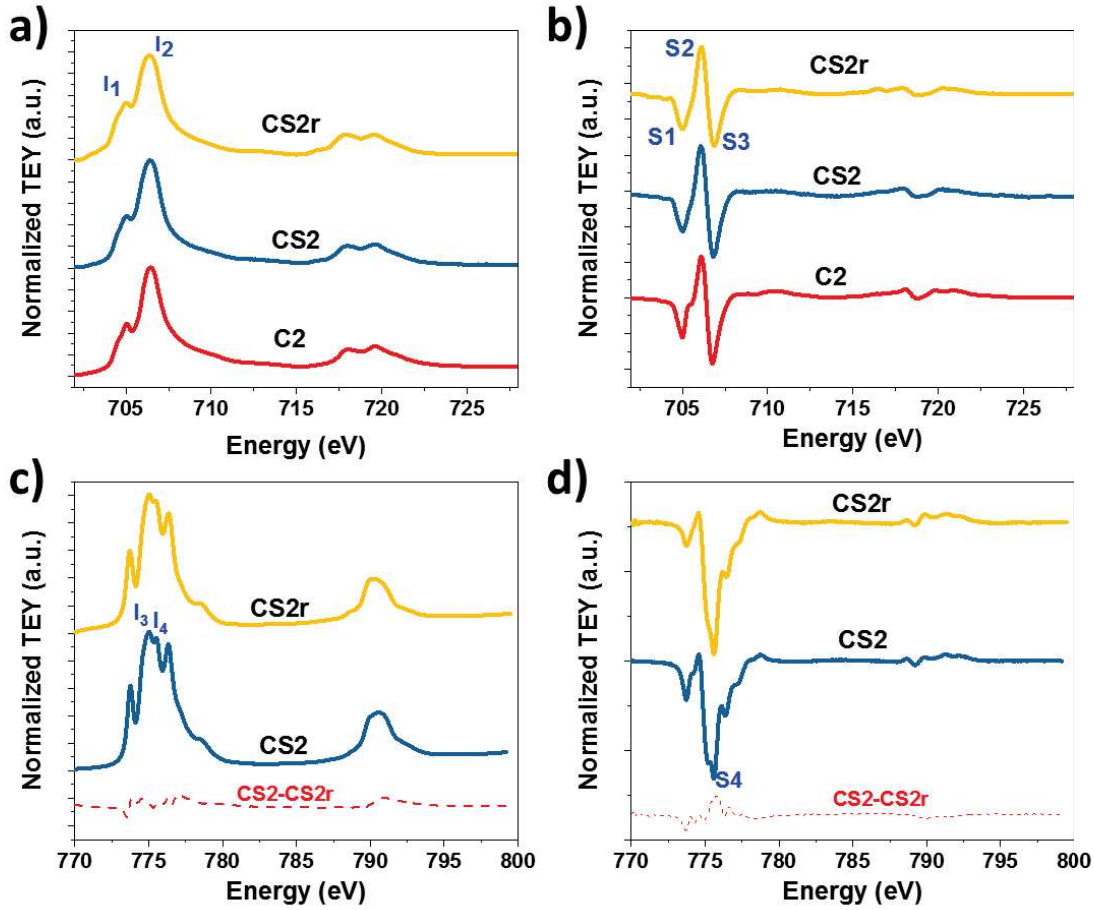

Figure 35. a, c) XAS and b, d) XMCD spectra at the a, b) iron and c, d) cobalt edge of a $Fe_{3-\delta}O_4$@CoO nanoparticle (CS2) that has been subjected to a reheating (CS2r).

Table 18. XAS and XMCD ratio of the different samples and of references

Sample	Diameter (nm)	I1/I2	(S1+S2)/(S2+S3)	δ	S4 (%)	Fe^{2+}/Fe^{3+} (CTM4XAS)
C	10.1	0.56	0.83	0.26	-	14 %
CS	14	0.82	0.95	0.19	23	22 %
CSSA	14.5	0.52	0.77	0.29	42	7 %
CSSB	15.1	0.61	0.89	0.23	54	18 %
CSSC	15.6	0.65	0.95	0.19	68	19 %
C2	8.3	0.57	0.75	0.30	-	-
CS2	10.8	0.78	0.77	0.29	26	-
CS2r	9.7	0.81	0.83	0.26	29	-
Fe_3O_4@$CoFe_2O_4$ From ref[22]	7.2	0.82	0.85	0.25	102	-
Magnetite reference	-	0.71	1.14	0	-	-
Maghemite reference[41]	-	0.35	0.69	0.33	-	-

XAS and XMCD spectra were recorded at the Co and Fe $L_{2,3}$ edges for C, CS, CSSA, CSSB and CSSC nanoparticles. At the Fe edge, XAS and XCMD agree on a higher Fe^{2+} content in the CS nanoparticles compared to C. Such a behavior is in agreement with previous analysis and is attributed to the chemical reduction of the iron oxide core and its protection against oxidation by the CoO shell. The Fe^{2+} content then decreases from CS to CSSA according to the synthesis of interfacial cobalt ferrite. From CSSA to CSSC, the proportion of Fe^{2+} increases gradually, in agreement with the growth of the iron oxide shell. XAS and XMCD recorded at the Co $L_{2,3}$ edge evidence the presence of interfacial cobalt ferrite within the CS nanoparticles. These experiments also show the further increase of the cobalt ferrite amount from CS to CSSC.

In the meantime, a second series of samples consisting of a reheated $Fe_{3-d}O_4$@CoO core@shell nanoparticles and its non-reheated version were analyzed. It results that the submission of a $Fe_{3-d}O_4$@CoO core@shell nanoparticle to a reheating led to the further but very slight further diffusion of the Co atoms in the iron oxide core, increasing slightly the amount of interfacial cobalt ferrite.
Hence owing to this and to the use of the surface sensitive total electron yield recording mode, the variation of the Fe^{2+} in the CS and CSS nanoparticles arises mostly from the surface, showing that the second iron oxide shell surprisingly displays a high content of Fe^{2+}.

These conclusions are supported by LFM analysis performed at the Fe $L_{2,3}$ edge.

Element specific hysteresis

In order to get information on the magnetic coupling between the different phases of the nanoparticles, element specific magnetization curves were recorded at 4 K between -6.5 and +6.5 T, at fixed energy corresponding to Fe S1, S2, S3 and to Co S4 edges. In each samples, the coercive field (H_C) is equivalent at S1, S2, S3 and S4 edges with 10.9, 10.8, 10.9 and 9.6 kOe for CS, CSSA, CSSB and CSSC respectively, and evidences thus the strong coupling between each phases in the nanoparticles (detailed H_C values are presented in annexes). Moreover, our values are higher than the reported values measured at similar temperatures for $Fe_{3-d}O_4$@CoO nanoaggregates of 9.9 nm (H_C = 3 kOe)[48], and of magnetite doped cobalt ferrite of size 40.3 nm (H_C = 2.1 and 3.9 kOe at Fe and Co edges)[40] which we attribute to the presence of stronger exchange coupling effects in our nanoparticles than for the previously reported nanoparticles.

Table 19. Selective hysteresis magnetic characteristics.

	H_C (kOe)	M_R/M_S S1 (%)	M_R/M_S S2 (%)	M_R/M_S S3 (%)	Mean of M_R/M_S at Fe edges (%)	M_R/M_S S4 (%)
CS	10,9	69	66	65	67 ± 2.0	55
CSSA	10,8	60	63	64	62 ± 2.0	59
CSSB	10,9	58	61	60	60 ± 1.5	62
CSSC	9,6	60	64	62	62 ± 2.0	62

The M_R/M_S ratio, also called the squareness ratio, gives further information on the squareness of the hysteresis. For CS, the mean M_R/M_S ratio at the iron edge of 67 % is higher than the 55 % measured at the cobalt edge which in both case appears to be lower than for randomly spherical ferrite nanoparticles[49] (83-87 %) and for cobalt ferrites nanoparticles (M_R/M_S = 82 % and 89 % at the Fe and Co edges respectively).[40] However, these ratios are higher than the reported values for $MnFe_2O_4$@$CoFe_2O_4$ nanoparticles of 7 nm diameters (20 % at the Co edge),[18] $Co_{0.73y}Zn_{0.73(1-y)}Fe_{2.18}\square_{0.09}O_4$ (40 % for y = 0.40 and 29 % for y = 0 both at the Fe edge)[45] and chains of iron oxide nanoparticles (33 % at the Fe edge).[40] Thus, our M_R/M_S ratios are intermediate between iron oxide and cobalt ferrite values and while the hysteresis of cobalt ferrites depicts a nice parallelogram shape, the hysteresis of

iron oxide nanoparticles has a non-square shape[40] which is typical of a soft material.[50] The shape of CS hysteresis at the Fe and Co edges are thus in between the shape of iron oxide and cobalt ferrite and evidence the interdiffusion process leading to the creation of a hard interfacial cobalt ferrite phase in agreement with XAS-XMCD experiments.

For CSSA, CSSB and CSSC, their M_R/M_S ratios are similar at the Fe (62, 60, 62 respectively) and Co (59, 62, 62) edges, considering experimental errors. At the Fe edge, this ratio decreases compared to the one of CS (67 %), evidencing a less square shape and so a greater contribution of the iron oxide soft phase that arises from the addition of iron oxide as a second shell. Moreover, it shows here that not all the iron oxide of the second shell has been transformed into cobalt ferrite through interdiffusion and recrystallization process. However, this ratio increases at the Co edge getting closer to the value of cobalt ferrite reported in the work of Li and al.[40] which is in agreement with the increase of hard phase content and thus to the increase of cobalt ferrite content in the nanoparticles at the expense of the CoO phase, as evidence in XAS-XMCD experiments.

According to the work of Daffé and al.[18], as our hysteresis are slightly slanted and not as square as for their $MnFe_2O_4@CoFe_2O_4$ nanoparticles at the Mn edge, it would show the presence of a small spin canting effect at the Fe and Co edges. However, we attributed this shape to the soft phase influence and from the magnetic influence of the AFM CoO phase due to the strong coupling effect.

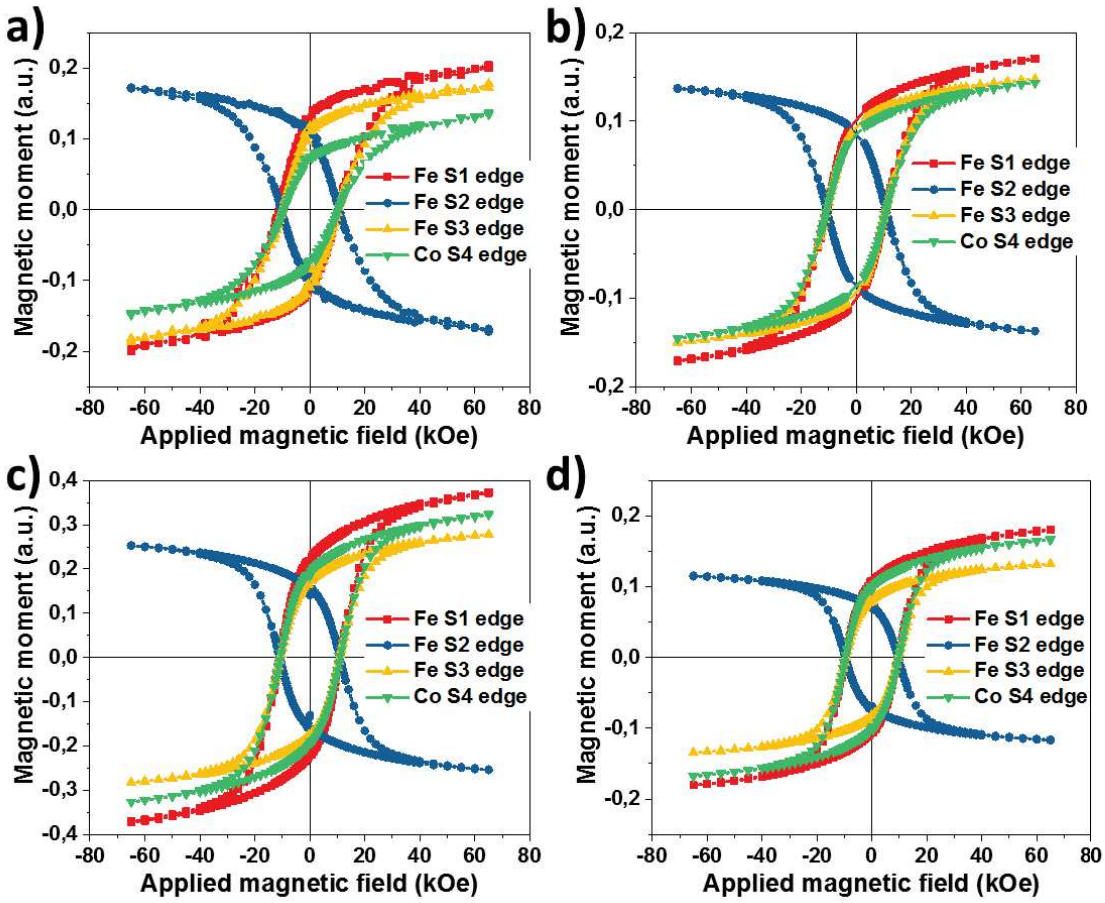

Figure 36. Element-specific magnetization curves recorded at 4 K by XMCD at the Fe and Co $L_{2,3}$ edges in a) CS, b) CSSA, c) CSSB, d) CSSC.

Selective hysteresis recorded for each nanoparticles at the Fe S1, S2, S3 and Co S4 edges show similar coercive fields for each sample, agreeing thus with a strong magnetic coupling of the phases within the CS and CSS nanoparticles. The shape of the hysteresis evolves coherently with the increase of the hard and soft phases within the nanoparticles. The slow and smooth approach to saturation in CS and CSS nanoparticles can be attributed to the contribution of the AFM CoO phase.

Mössbauer spectroscopy

In order to get complementary information on the Fe environments and valence state in our samples, ^{57}Fe Mössbauer experiments were performed. Mössbauer is a very powerful spectroscopic technique as it measures directly the contribution of different phases that are characterized by a change of their isomer shift (IS). Moreover, the hyperfine field (B_{hf}) describes the magnetic environment of the ^{57}Fe atoms, and the quadrupole shift gives precious information on their local electronic structure.

Each Mössbauer spectra recorded at 77 K without applying a magnetic field, displays a resolved sextet which is in agreement with a magnetic blocked state at this temperature. However, the presence of a small doublet at the center of C and CS spectra denotes a contribution of a superparamagnetic behavior due to the fastest spin relaxation of the nanoparticles than the time of measurement of the Mössbauer technique. Such an observation is in contradiction with the literature where for small iron oxide nanoparticles of 11 nm[51] and for Fe_3O_4@CoO nanoparticles of 13 nm, no superparamagnetic contributions were observed at 77 K.[13] The synthesis of CSS nanoparticles and all the other characterizations techniques have consumed a lot of C and CS nanoparticles hence, only a small amount of C and CS nanoparticles were analyzed in Mössbauer contrary to what is generally needed. As the concentration of the nanoparticles was low in the powder, we attributed the superparamagnetic contributions to arise from isolated nanoparticles that have a lower T_B than packed nanoparticles.[52]
Nevertheless, Mössbauer spectra of each sample were fitted with at least 4 components (Figure 37) where the refined values are presented in Table 20.

In C, the isomer shift (IS) value of 1.16 mm/s corresponds to Fe^{2+} in octahedral (Oh) sites that displays a subspectral area of 4 % while lower IS of 0.61 mm/s corresponds to Fe^{3+} in Oh sites that account for 38 %. The lowest values of IS of 0.49 and 0.35 mm/s are attributed to Fe^{3+} in tetrahedral (Td) sites which accounts for 58 %.[53,54] The isomer shift of 0.65 arises from a superparamagnetic contribution that displays no hyperfine field and a subspectral area of 3 % as evidenced in the spectra in Figure 37. Despite the presence of a superparamagnetic contribution, the values are consistent with the ones generally reported for iron oxide nanoparticles.[55,56] However, the Fe^{2+} content is lower than the expected value of 10 % and the ratio $Fe_{Td}^{3+}/Fe_{Oh}^{2+,3+}$ is equal to 1.38 for C, which is higher than the expected value of 0.50 for pure magnetite.[54,57,58] This ratio is highly influenced by the stoichiometry of the iron oxide phase hence, by its Fe^{2+} content i.e. the proportion of magnetite/maghemite.[55,57,59] Intensities ratio that are higher than 0.50 are attributed to the oxidation of Fe^{2+} in Fe^{3+} in Oh sites that are accompanied by vacancies formation.[56] Thus, the high intensity ratio and the low Fe^{2+} content are attributed to the presence of maghemite in the structure which arises from a spontaneous oxidation to air of the surface of the nanoparticles (see chapter I). These observation is also supported by the mean IS (0.504 mm/s[56]) value pondered by the different subspectral areas that is lower than <IS> = 0.61 mm/s for $Fe_{2.95}O_4$ nanoparticles.

Mössbauer spectra of the CS nanoparticles displays a resolved sextet where the two internal peaks arise from the superparamagnetic contribution that accounts for 6 % with a mean isomer shift value of 0.345 mm/s. Also, the pronounced shoulders on the two external peaks are attributed to a higher content of Fe^{2+} than in C. This is reflected by a lower $Fe_{Td}^{3+}/Fe_{Oh}^{2+,3+}$, than for the C nanoparticles, that is equal to 0.59, approaching the 0.50 of a pure magnetite. Moreover, the Fe^{2+} integration is increased to 6 % which is consistent with a higher content of magnetite phase in CS than in C. This result is in agreement with XRD and XMCD results, demonstrating again that the core can be reduced during a further thermal decomposition and will be then protected by the CoO shell. Moreover, in CS, the hyperfine field B_{hf} of Fe^{3+} Oh has increased from 49.0 T (in C) to 53.1 T (in CS) such as B_{hf} of Fe^{3+} in Td sites that have increased from 49.2 T (in C) to 50.6 T (in CS). This is attributed to longer Fe-O distances due to the presence of Co in the nearest neighbors of Fe^{3+} [58,60] which evidences the interfacial atomic

diffusion.[61] Plus, if we consider the iron oxide core to correspond to a magnetite structure with <IS> = 0.61 mm/s (for $Fe_{2.95}O_4$ [56]) and <IS> = 0.451 mm/s for $(Co_{0.05}Fe_{0.95})[Co_{0.95}Fe_{1.05}]O_4$,[62] we can determine a proportion of interfacial $CoFe_2O_4$ that corresponds to 51 % of the Fe-containing phase, hence a thickness of 1.07 nm of cobalt ferrite. However, this result is an approximation as we used a linear model of magnetite – cobalt ferrite composition whereas the diffusion of cobalt has probably generated a gradient of Co at the interfaces, as evidenced by the work of Skoropata and al.[61]

In CSSA, the superparamagnetic contributions vanished, such as the shoulders on the two external sextets that are way less pronounced, evidencing a lower Fe^{2+} content than in CS. This is consistent with the refined values where CSSA displays a lower <IS> of 0.489 mm/s than CS (0.528 mm/s). Moreover, the contribution of Fe^{2+} (IS = 1.16 mm/s) decreased to 2 % while the contributions of Fe^{3+} has increased. Thus, the $Fe_{Td}^{3+}/Fe_{Oh}^{2+,3+}$ ratio has increased to 0.73 being more distant from the 0.50 of the magnetite phase. Also, the B_{hf} of Fe^{3+} in Oh and Td sites are high: 53.7 and 51.1 respectively, hence evidencing the interfacial atomic diffusion at the CoO/2nd shell. According to the low thickness determined by TEM measurements, the presence of interfacial diffusion evidenced in TEM and XMCD, the intensity ratio of 1.14 for a $(Co_{0.05}Fe_{0.95})[Co_{0.95}Fe_{1.05}]O_4$ nanoparticles determined by Mössbauer experiments, it has been calculated that CSSA is composed of 76 % of cobalt ferrite for 24 % of Fe_3O_4 in the whole volume. Considering that the second shell is only composed of cobalt ferrite for calculus simplification, this would correspond to a total shell thickness of 0.6 nm of $CoFe_2O_4$. This is larger than the mean thickness of 0.3 nm measured from TEM micrographs. Such discrepancy can be explained by different factors: the further diffusion of the Co cations in the iron oxide core as evidenced in XMCD, the possible gradient composition in the whole nanoparticles,[61] the non-homogeneity of the nanoparticles or due to size distribution.

Mössbauer spectra of CSSB do not show any superparamagnetic contribution at 77 K such as CSSA nanoparticles. The Fe^{2+} contribution (IS = 1.16 mm/s) increase from 2 to 3 % between CSSA to CSSB. Such consideration participates to the increase of the mean <IS> of CSSB to 0.51 mm/s. This observation is coherent with the increase of Fe^{2+} content observed in XMCD, XRD and FT-IR analysis. The $Fe_{Td}^{3+}/Fe_{Oh}^{2+,3+}$ ratio increases to 0.82 which is higher than CSSA. As the Fe^{2+} content has increased compared to CSSA, such high ratio cannot be attributed to a deficiency in Fe^{2+} but is attributed to Fe cation vacancies which actually agree with the increase of the cobalt ferrite content within the nanoparticles. This is supported by the high hyperfine fields of 53.5 and 51 T determined for Fe^{3+} in Oh and Td sites respectively.
The <IS> of CSSB allowed to determine a proportion of 63 % of $CoFe_2O_4$ which shows a decrease compared to CSSA. Considering that the second shell would only be composed of cobalt ferrite for the sake of simplicity (which is not exactly true as we know that there are some iron oxide), it is possible to determine a 0.5 nm thick second shell. This value is close to the 0.6 nm thick measured from TEM micrographs. The slight difference can be attributed to the presence of iron oxide, size distribution and also the diffusion of Co cations.

The refined values of the Mössbauer spectrum of CSSC show a similar content of Fe^{2+} of 3 % than for CSSB (IS = 1.16 mm/s). However the mean isomer shift value of CSSC decrease to 0.485 mm/s compared to the 0.51 mm/s determined for CSSB. This decrease cannot be attributed to the decrease of Fe^{2+} content as shown previously. The ratio $Fe_{Td}^{3+}/Fe_{Oh}^{2+,3+}$ is calculated to be equivalent to 0.92 that is higher than for CSSB and shows the further increase of cobalt ferrite. Hence, considering the higher volume of CSSC compared to CSSB, we can conclude on the increase of both Fe^{2+} and cobalt ferrite compared to CSSB, agreeing thus with FT-IR, XRD and XMCD analysis. This consideration also explains the higher cobalt ferrite concentration of 79 % calculated from the mean isomer shift of CSSC. The concentration of cobalt ferrite allow to determine a 0.6 nm thick cobalt ferrite shell in CSSC. This is close to the 0.8 nm thick determined from TEM size measurements. However this value may not be exactly true due to calculus simplifications and to the above cited limitations (see CSSA and CSSB).

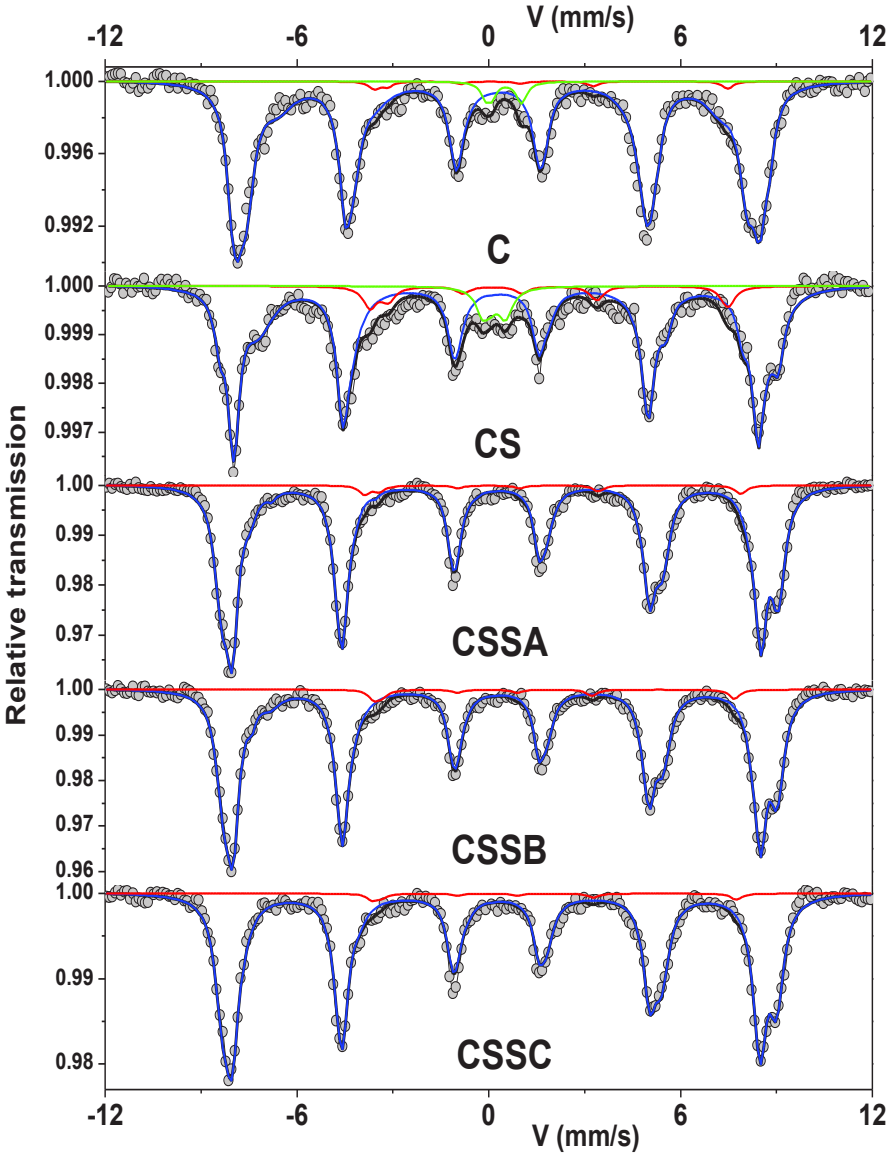

Figure 37. Mössbauer spectra of C, CS, CSSA, CSSB and CSSC nanoparticles.

Table 20. Refined values of hyperfine parameters obtained from Mössbauer experiments. Mean values are presented in bold.

Sample	isomer shift relative to α-Fe (mm/s)	Width at half height (mm/s)	quadrupole shift (mm/s)	Hyperfine field (T)	Relative subspectral area (%)
C	0,49	0,36	0,01	51,3	15
	0,35	0,63	-0,11	49,2	43
	0,61	0,82	0,18	49	35
	1,16	0,4	1,9	34	4
	0,65	0,4	1,04	-	3
	0,504	-	**0,13**	**47,5**	-
CS	0,55	0,73	-0,01	53,1	34
	0,49	0,37	0,02	50,6	31
	0,55	0,81	0,15	47,2	23
	1,16	0,44	1,88	34	6
	0,345	0,46	0,58	-	6
	0,528	-	**0,19**	**46,7**	-
CSSA	0,53	0,54	-0,03	53,7	43
	0,4	0,41	0,02	51,1	42
	0,49	0,48	0,03	48,8	8
	0,64	0,57	0,49	45,1	5
	1,16	0,4	2	34,7	2
	0,489	-	**0,06**	**51,4**	-
CSSB	0,55	0,54	-0,05	53,5	42
	0,41	0,43	0,03	51	45
	0,525	0,39	0,12	48,4	5
	0,72	0,52	0,28	46,5	5
	1,16	0,4	2,1	34,7	3
	0,51	-	**0,08**	**51,2**	-
CSSC	0,52	0,53	-0,05	53,6	39
	0,49	0,47	0,01	51,1	48
	0,63	0,67	-0,29	49,3	10
	1,16	0,4	1,8	33,2	3
	0,485	-	**0,01**	**51,4**	-

Mössbauer spectroscopy has demonstrated the increase of Fe^{2+} from C to CS, in agreement with previous results. It has also shown the presence of interfacial cobalt ferrite within CS. This increase of cobalt ferrite in CSSA is due to a double interface, resulting in the decrease of the overall Fe^{2+} content due to the low amount of Fe precursor added during the synthesis of the second shell. However, the contribution of Fe^{2+} increases then in CSSB and CSSC while the quantity of cobalt ferrite also increases from CSSA to CSSC.

Mössbauer spectroscopy allows to determine a 1.07 nm thick interfacial cobalt at the $Fe_{3-d}O_4$/CoO interface for CS nanoparticles which is considered to not change in CSS nanoparticles. Furthermore, according to the same method, a 0.6, 0.5 and 0.6 nm thick second shell for CSSA, CSSB and CSSC nanoparticles were calculated. These values are close to the TEM thickness but may differ from the reality as they results from mathematical approximations.

SQUID magnetometry

The magnetic properties were investigated by SQUID magnetometry. Magnetic moment recorded against temperature after field-cooling and zero-field-cooling (FC-ZFC) are presented in Figure 38a,b. The maximum of the ZFC curve, called T_{max}, describes the maximum magnetic moment as a function of the temperature i.e. a thermodynamic equilibrium where the magnetic anisotropic energy is similar to the thermal energy (KV ≈ kT). However, the true blocking temperature (T_B), that is a distribution of the energy barrier, is a more accurate consideration. T_B is considered to be the inflection point of the ZFC curve and can be precisely extracted by applying the following equation: $f(T_B) = [dM_{ZFC} - M_{FC}]/[dT]$.[63] The temperature dependent magnetization curve of the core display a T_{max} of 150 K and a T_B of 93 K which are in agreement with reported value for iron oxide nanoparticles of 10 nm.[1] The deposition of a CoO shell on the $Fe_{3-d}O_4$ core leads to an increase of T_{max} to 290 K which is coherent with previous works,[13,61] hence an increase of T_B to 266 K. However, such a system is not expected to show a T_{max} higher than 290 K because at this temperature, the AFM CoO phase loses its magnetic order (T_N CoO = 290 K) and its ability to pin the ferrimagnetic iron oxide phase. When a $Fe_{3-d}O_4$ shell is grown and increased on CS, T_{max} and T_B increase. For CSSC T_{max} reaches a value higher than 400 K and T_B reaches a maximum value of 335 K (62 °C). Even if our calculations of $d(M_{ZFC}-M_{FC})/dT$ gives coherent values, these values may be affected by interparticles interactions as discussed in chapter I and also by incomplete FC-ZFC curves for the CSS nanoparticles. However, our T_{max} values of the CSS nanoparticles are higher compared to other core@shell@shell nanoparticles such as $MnFe_2O_4$@$CoFe_2O_4$@$NiFe_2O_4$[12] and FeO@Fe_3O_4@Mn_3O_4[11] nanoparticles who reported T_{max} values of only 220 K and 190 K respectively. Moreover, the absence of kinks in the FC-ZFC curves evidence a strong coupling between the different parts of the nanoparticles.[11]

The equation $K_{eff}V = 25k_BT_B$ shows the evolution of the effective magnetic anisotropy (K_{eff}) as a function of T_B (from the $d(M_{ZFC}-M_{FC})/dT$) and of the volume (V) of the nanoparticles. In this equation, K_{eff} depends on the magnetic anisotropy of the nanoparticles but also on their environment i.e. on interparticles interactions and was calculated to correspond to 6.0, 6.4, 6.7, 6.3 and 5.8 10^4 J/m^3 for C, CS, CSSA, CSSB and CSSC respectively. K_{eff} of C is higher than the reported value of K = 2 10^4 J/m^3 for bulk magnetite at 4 K[64,65] which is attributed to the presence of dipolar interactions in the nanoparticles. Then, K_{eff} increases to 6.4 10^4 J/m^3 in CS which can be attributed to dipolar interactions between the FiM cores[66] but also to the pinning effect of the soft-FiM iron oxide core (K_{core} = 2 10^4 J/m^3[64,65]) by the hard-AFM CoO shell (K_{shell} = 5 10^5 J/m^3[67]) as expected from the exchange-bias process.[68,69] Then, K_{eff} increases to 6.7 10^4 J/m^3 for CSSA which can arise from a further pinning of the second $Fe_{3-d}O_4$ shell by the CoO shell. Finally, K_{eff} decreases as the second iron oxide shell grows which is concomitant with the content increase of the weakly anisotropic iron oxide soft shell.[70] The further decrease of K_{eff} in CSSB and CSSC can also be related to a decrease of the CoO content through diffusions process where K_{eff} of the CoO shell will decrease. Also, as $K_{CoFe2O4}$ bulk (2-3 10^5 J/m^3)[71,72] is similar to K_{CoO}, it is possible that the interfacial anisotropy ($K_{eff}V$) becomes of the same order and even higher than $K_{CoO}V_{CoO}$ which is known to reduce the exchange-bias coupling.[9]

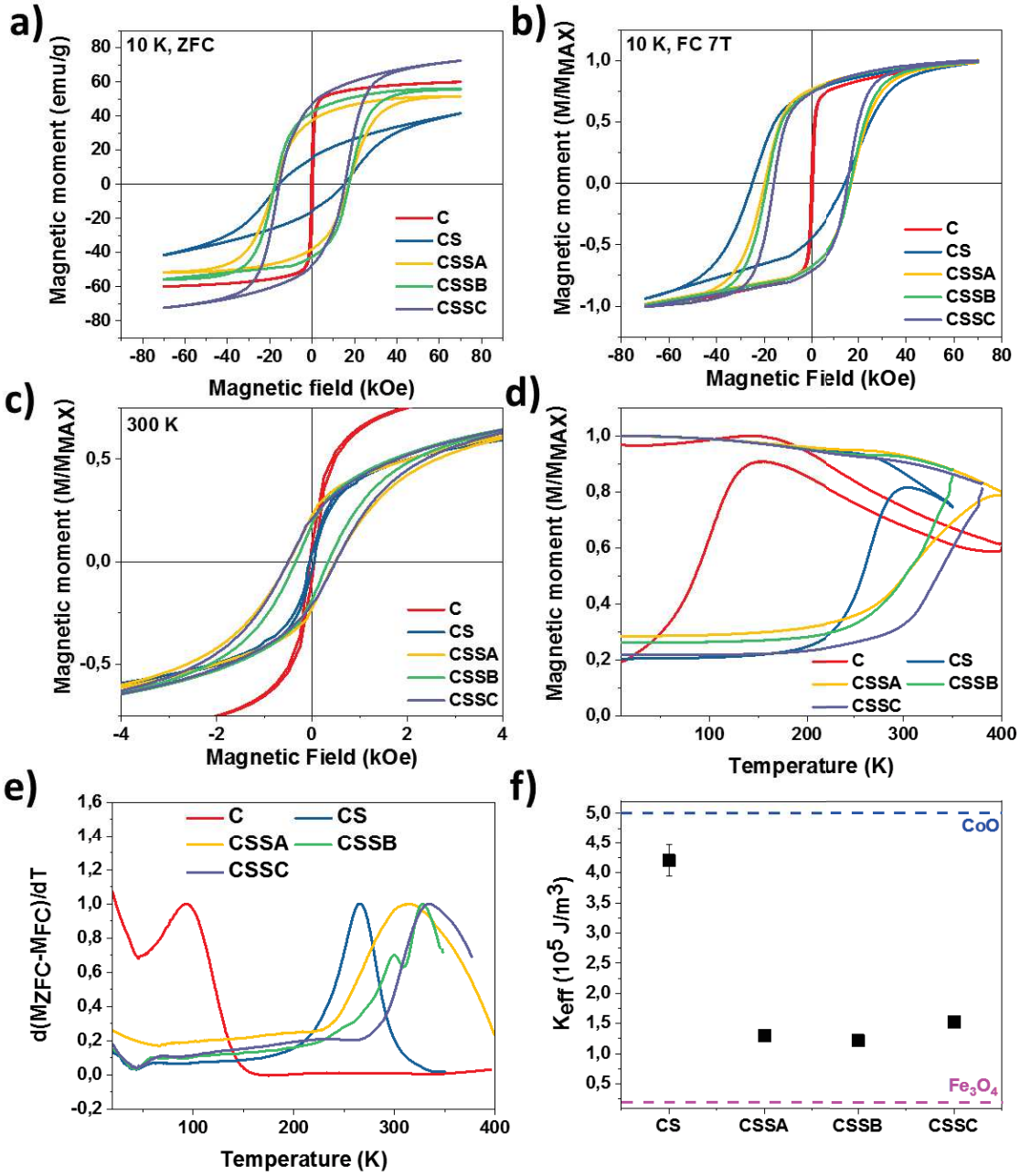

Figure 38. Magnetic properties of core@shell@shell nanoparticles. Magnetization curves recorded against a magnetic field a) at 10 K under zero field cooling (ZFC) b) at 10 K after field cooling under 7T c) at 300 K. d) Temperature dependent magnetization curves. e) Distribution of blocking temperatures according to $d(M_{ZFC}-M_{FC})/dT$. f) Effective magnetic anisotropy (K_{eff}) in function of the different nanoparticles determined from the fit of $H_C = f(T)$ according to the Stoner-Wohlfarth model.

Table 21. Magnetic characteristics

	C	CS	CSSA	CSSB	CSSC
Diameter (nm)	10.1 ± 1.1	14.0 ± 1.5	14.5 ± 1.5	15.1 ± 1.7	15.6 ± 2.3
Thickness (nm)	-	2.0	0,3	0,6	0,8
H_C 300 K (ZFC) (kOe)	0	0	0.5	0.3	0.5
H_C 10 K (ZFC) (kOe)	0.4	16.4	17.5	17.2	15.0
H_C 10 K (FC) kOe	0.4	19.8	18.5	17.9	15.8
H_E (kOe)	0	5.3	2.8	0.9	0.5
T_{max} (K)	150	290	400	>400	>400
T_B (K)	93	266	310	298, 328	335
M_S at 5 K (ZFC) (emu/g)	60	41	51	55	72
M_R/M_S at 5 K (ZFC) (%)	24	38	59	68	66
K_{eff} (10^4 J.m^{-3}) (from T_B)	6.0	6.4	6.7	6.3	5.8
K_{eff} (10^4 J.m^{-3}) (from Stoner-Wohlfarth)	-	42.1	13.0	12.2	15.3

The magnetization curves recorded against a magnetic field at 300 K show closed hysteresis for C and CS which agrees with a superparamagnetic behavior in agreement with their blocking temperature and with the literature.[1,13,61]
Also, accordingly to FC-ZFC curves in Figure 38d, a coercive field is present at 300 K only for the CSS nanoparticles (Figure 38c) that shows a blocked magnetic behavior at room temperature contrary to other type of multi-shelled nanoparticles reported in the literature.[11,12,73] Surprisingly, CSSA, CSSB and CSSC show similar H_C at 300 K despite a different relative composition. It evidences a similar coupling in the three samples despite a different structure. Hence, at high temperature, the magnetic properties are no longer driven by a simple FiM/AFM exchange-bias coupling, where T_N CoO = 290 K, but by a hard-soft and a FiM/AFM coupling ensured by the presence of iron oxide, cobalt monoxide and cobalt ferrite.

Magnetization curves recorded against a magnetic field at 10 K show the opening of the hysteresis for C and CS. C nanoparticles have a H_C of 0.4 kOe which is in agreement with the literature. CS nanoparticles have a H_C of 16.4 kOe which is higher than the reported value of 3.0 kOe for a γ-Fe_2O_3 core with a size of 7.2 nm and a CoO shell of 0.7 nm thick.[61] Our H_C is also higher than the 8.4 kOe measured at 5 K for $Fe_{3-d}O_4$@CoO nanoparticles with a core size of 9.6 nm and a CoO shell thickness of 1.5 nm.[13] Earlier, we also have reported smaller H_C measured at 10 K for $Fe_{3-d}O_4$@CoO nanoparticles with a core diameter of 8.8 nm and a shell thickness of 0.7 nm than for our CS nanoparticles.[22] Such a high H_C for CS can be attributed to a different proportion of iron oxide and CoO[69] but also to a high crystal quality of our nanoparticles and to a more effective exchange-bias coupling that is increased for more important interface's roughness.[74] Also, as shown by Figure 38b, for the CS nanoparticles, a vertical shift of the hysteresis after FC is observed. This shift is characteristic of interfacial uncompensated magnetic moments in the AFM phase of the exchange bias coupling, and is proportional to the number of uncompensated spins.[69] This vertical shift then vanished with the addition of a thin iron oxide shell on the CS nanoparticles. Moreover, this addition also leads to a further increase of H_C to 17.5 kOe for CSSA which then decreases to 17.2 (CSSB) and 15.0 (CSSC) kOe when growing the shell. This behavior agrees with the evolution of K_{eff} determined previously from $K_{eff}V = 25k_BT_B$ and evidences the increase of the soft-part contribution to the magnetic properties.[50] Furthermore, the slow and smooth approach to saturation at high fields of the M(H) curves in CS, CSSA, CSSB and CSSC with a decrease of H_C also evidences the strong coupling between the core and shells within the nanoparticles.[75]

Temperature dependent H_C measurements of CS, CSSA, CSSB and CSSC are presented in Figure 39 which shows the decrease of H_C as the temperature increases. The dependence of H_C against the temperature has been fitted according to the Stoner-Wohlfarth model[76] in order to determine a more precise value the effective magnetic anisotropy constant ($K_{eff, ST}$) :

$$H_C = 0.48 H_K \left[1 - \left(\frac{T}{T_B}\right)^{0.5}\right] \quad \textit{Equation 2}$$

With the anisotropic field $H_K = \frac{2K_{eff,ST}}{M_S}$

The fitting procedure is detailed in supplementary information. Note that this formula is only true for oriented nanoparticles without size distribution. However, this model was used as an approximation.

The fit presented in the red curve of Figure 39 could be perfected with the addition of a temperature term that takes into account the dipolar interactions. However, this simple model shows that $K_{eff, ST}$ are one order of magnitude higher than K_{eff} calculated with $H_C = 0.48 H_K \left[1 - \left(\frac{T}{T_B}\right)^{0.5}\right]$ Equation 2 and are in between the magnetic anisotropies of bulk Fe_3O_4 and CoO as evidenced by Figure 38f. Thus this model is more accurate to describe the effective anisotropic constant. Moreover, $K_{eff, ST}$ of CS (42.1 10^4 J/m^3) is in agreement with the literature[22,61] showing the validity of this model despite the presence of dipolar interactions. Also, CS has a $K_{eff, ST}$ close to K_{CoO} which decreases with the decomposition of $FeSt_2$ on CS to 13.0 and 12.2 10^4 J/m^3 for CSSA and CSSB respectively. As previously, we attributed this to the creation of interfacial cobalt ferrite that increases the interfacial magnetic anisotropy constant hence decreasing the exchange-bias coupling.[9] Then, $K_{eff, ST}$ increases to 15.3 10^4 J/m^3 in CSSC which is probably related to the high quantity of cobalt-ferrite that drives the overall magnetic anisotropy in concert with the exchange-bias coupling.

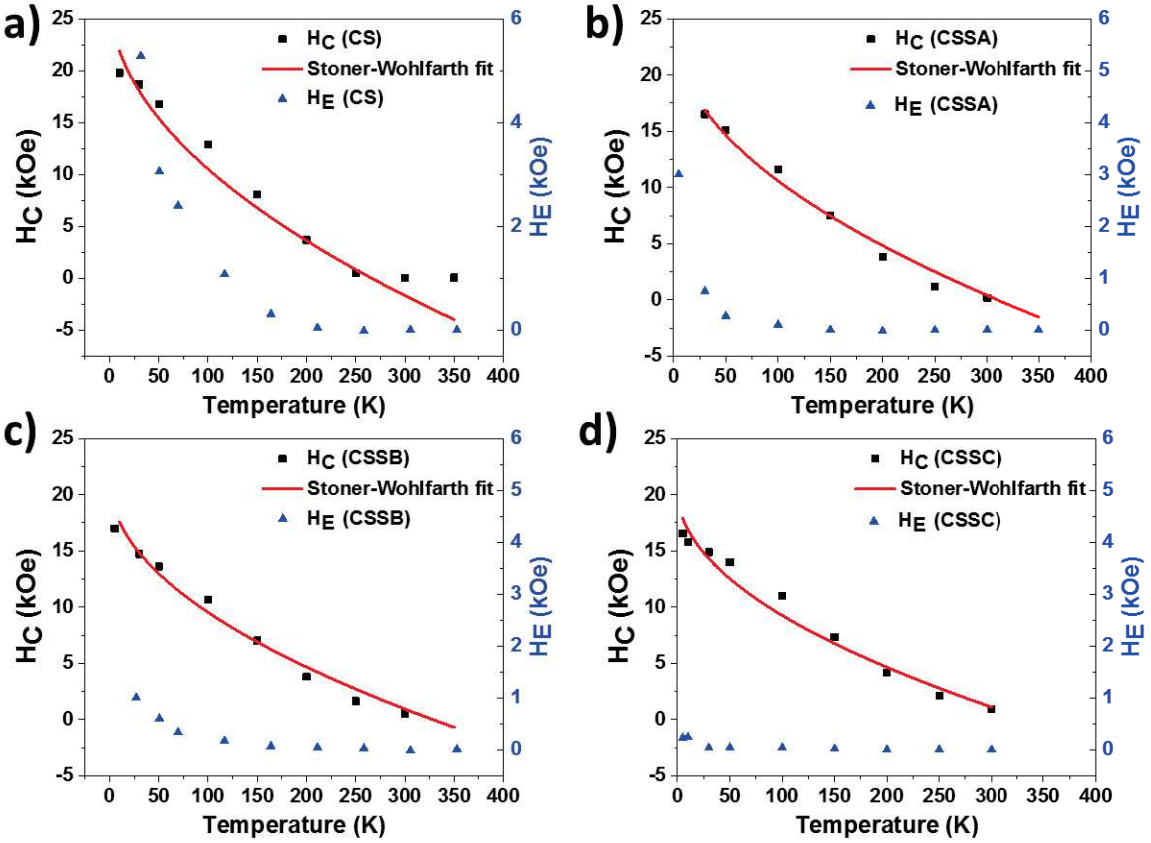

Figure 39. Temperature dependence of coercive fields (black squares) and exchange field (blue triangles) of a) CS, b) CSSA, c) CSSB and d) CSSC. Temperature dependence of coercive fields were fitted for each sample according to the Stoner Wohlfarth equation (red curves). Details of the fit are available in annexes.

Magnetization curves recorded against a magnetic field at 10 K after cooling under an applied magnetic field of 7 T are presented in Figure 38b. H_C show an increase of their values compared to H_C in ZFC mode, as expected from the presence of the field cooled procedure that aligns surface spins.[69] Moreover, the exchange bias property is evidenced by a shift of the hysteresis curve on the applied magnetic field axis, induced by the spin polarization of the FiM phase by the AFM phase. This shift is characterized by an exchange-field (H_E) where $H_E = (H^+ - H^-)/2$. As for H_C, H_E decreases as the temperature is decreased coherently with other studies.[21,61,77]

At low temperatures, the H_C of the core nanoparticles has been increased from 0.4 to 16 kOe thanks to the addition of the CoO shell and to the exchange-bias effect which is characterized by a high H_E of 5.3 kOe.[69] This H_E is higher than the reported value of 0.2 kOe for γ-Fe_2O_3@CoO nanoparticles[61] and of the 2.0[22] and 4.3 kOe[10,13] for $Fe_{3-d}O_4$@CoO nanoparticles synthesized in similar conditions. Hence, the quality of the $Fe_{3-d}O_4$/CoO interface in our CS nanoparticles is better than in the other reported systems which agrees with the presence of a high H_C at 10 K.[10] The addition of a thin $Fe_{3-d}O_4$ shell on the CS nanoparticle (CSSA) leads to a further increase of H_C (18.5 kOe) but to a decrease of H_E to 2.8 kOe. And the growth of the $Fe_{3-d}O_4$ shell denotes a decrease of H_C from 18.5 (CSSA) to 17.2 (CSSB) and 15.0 (CSSC) kOe which can be attributed to the increase of the soft phase content (i.e. the iron oxide phase)[50,78] as shown by XMCD measurements. Nevertheless, the lowest H_C value of our CSS (15.0 kOe for CSSC) is higher than the reported values for the other core@multi-shell magnetic nanoparticles: 1.2 kOe for FeO@Fe_3O_4@MnO@Mn_3O_4[11], 7.7 kOe for $MnFe_2O_4$@$CoFe_2O_4$@$NiFe_2O_4$.[12] Hence, our core@shell@shell nanoparticles display a more stable magnetization than the other core@shell@shell nanoparticles.

Furthermore, H_E evidences a continuous decrease from CSSA (2.8 kOe) which almost vanishes in CSSC (0.5 kOe). Agreeing thus with the decrease of the exchange-bias coupling effect that can arise from a higher interfacial energy of $CoFe_2O_4$ ($K_{CoFe2O4}V_{CoFe2O4}$) than CoO ($K_{CoO}V_{CoO}$).[21,79] However, the remaining small H_E in CSSC is similar to the reported H_E value of Salazar-Alvarez and al.[11] who reported a small increase of H_E from 380 Oe ($FeO@Fe_3O_4$) to 510 Oe ($FeO@Fe_3O_4@MnO@Mn_3O_4$). It evidences thus, that our CSS nanoparticles still display an exchange-bias coupling at low temperature.

Moreover, temperature dependent H_E (Figure 39) shows that H_E vanishes at 200, 120, 150 and 20 K for CS, CSSA, CSSB and CSSC which evidences a trend to decrease the vanishing temperature of H_E in parallel with a reduction of the CoO content in the nanoparticles. However, there is a small incoherence on the vanishing temperature of CSSB which is a bit higher than for CSSA and is probably related to their different structure. Nevertheless, the lack of H_E at high temperature evidences that the opening of the hysteresis curve at 300 K is not driven by the exchange-bias coupling.[61]
Thus, the decrease of H_C and H_E as the second iron oxide shell grows is in agreement with the decrease of the exchange-bias coupling where the CoO content decreases in favor of a cobalt ferrite structure, leading to a similar or lower magnetic anisotropy energy of the AFM CoO phase than the interfacial exchange energy.[9] Indeed, as the volume of the CoO phase decreases, its magnetic anisotropy energy decreases: $E_{CoO} = K_{CoO}V_{CoO}$. Also, as cobalt ferrite which is featured by a similar K to CoO, is formed at the interface, the interfacial energy coupling $J_{int}=K_{CoFe2O4}V_{CoFe2O4}$ becomes of the same order or higher than $K_{CoO}V_{CoO}$.[9]

Saturation magnetization were determined after removing the mass of organic ligands in the nanoparticles thanks to TGA experiments. Table 21 shows that the core nanoparticle has a typical M_S value for partially oxidized iron oxide nanoparticles. M_S decreases to 41 emu/g when adding a CoO shell on the core, coherently with previous studies where a M_S of 34.8 emu/g was found for CS nanoparticles with similar chemical compositions.[13] This reduction is due to the contribution of the AFM CoO phase. Then, in CSSA, CSSB and CSSC, M_S increases from 51 to 72 emu/g which agrees with the decrease of the CoO content in favor of cobalt ferrite. Moreover, M_S of CSSC is equal to pure iron oxide nanoparticles of 15 nm diameter (M_S = 71 emu/g)[1] and, M_S values of CSSA, CSSB and CSSC are higher than the reported values of 49 and 9 emu/g for tri-magnetic nanoparticles such as $FeO@Fe_3O_4@MnO$ and $FeO@Fe_3O_4@MnO@Mn_3O_4$ nanoparticles respectively,[11] or to the 65 emu/g of $MnFe_2O_4@CoFe_2O_4@NiFe_2O_4$.[12]

The M_R/M_S ratio of hysteresis curves recorded at 5 K in ZFC gives precious information on the squareness of the hysteresis hence to the magnetic hardness of the studied material. For the iron oxide C sample, this ratio is equal to 24 % which is lower than the 50 % expected for non-interacting randomly oriented nanoparticles with uniaxial anisotropy.[80,81] Hence, this small value can be attributed to the presence of dipolar interactions between the nanoparticles.[82,83] Nevertheless, this small value is higher than the reported values of 2 % for spherical iron oxide nanoparticles of 13 nm or than the 16 % for 10 nm large iron oxide nanoparticles.[83] The M_R/M_S ratio increases then to 38 % in CS and increases further to 59 in CSSA and to 62 % in CSSB and CSSC. Thus, the hysteresis curves displays a shape closer to the square configuration as the shells are deposited and grown onto the core which denotes a greater contribution of a hard phase that we attribute to the increase of cobalt-ferrite content within the nanoparticles.[50] Hence, as H_C are very large and as the ratio M_R/M_S in our systems increases, it allows to get a large energy product $(BH)_{max}$ at 5 K which is displayed by the surface area of the largest rectangle in the second quadrant of the hysteresis curve. However, the energy product decreases at 300 K with a H_C of 500 Oe and a M_R/M_S ratio of 24, 20 and 21 % for CSSA, CSSB and CSSC respectively. This is lower than for rare-earth based nanoparticles but higher than ferrite based nanoparticles. Thus, the CSS nanoparticles are very promising for permanent magnet but still need some improvement.[8,50]

The addition of a hard magnetic CoO shell on the iron oxide core allowed to increase T_B up to 266 K i.e. very close to the T_N of CoO. This is concomitant with the increase of the effective magnetic anisotropy in agreement with a strong exchange-bias coupling within CS.
M(T) curves evidenced the gradual increase of T_B above room temperature for CSSA, CSSB and CSSC. This observation is supported by the presence of a small coercive field at room temperature. The three CSS nanoparticles display a similar H_C at 300 K which shows a similar magnetic coupling within the nanoparticles.
Effective magnetic anisotropy were calculated from the fit of the $H_C=f(T)$ according to the Stoner-Wohlfarth model and also from the $K_{eff}V=25k_BT_B$ equation. It has been demonstrated that K_{eff} determined from the Stoner-Wohlfarth model gives more reasonable values than with the other equation. Hence $K_{eff,ST}$ has been drastically increased from C to CS with the addition of the AFM CoO shell. It then decreases in CSSA with the addition of the soft counterpart that was attributed to the growth of the cobalt ferrite phase which decreased the strength of the exchange bias coupling. Then $K_{eff,\ ST}$ increased slightly in CSSC probably due to the presence of the high quantity of cobalt ferrite that drives the magnetic coupling. Indeed, it was observed in M(H) curves recorded at 10 K after field cooling that CS displayed a high H_E, in agreement with an efficient exchange-bias coupling. Then H_E decreases in CSSA and almost vanishes in CSSC. This result shows the reduction of the exchange-bias strength that was attributed to the increase of J_{int} that gets closer to the $K_{AFM}V_{AFM}$.
At low temperature without field cooling, CS displays a high increase of H_C compared to C due to the presence of a strong exchange-bias coupling. H_C further increase in CSSA, this was attributed to the further pinning of the second shell be the CoO phase. Then the decrease of H_C in CSSB and CSSC was related to the increase of the soft iron oxide counterpart and to the decrease of the exchange-bias coupling through the increase of the cobalt ferrite phase.
Saturation magnetization evidenced coherent values of C and CS. M_S then increase from CS to CSSC, in agreement with the increase of the cobalt ferrite content. Such as for the M_R/M_S ratio which increases from CSSA to CSSC showing the increase of the hard counterpart.

Polarized- small angle neutron scattering

Small Angle Neutron Scattering (SANS) is a very powerful technique, complementary of SAXS experiments, as it allows to probe the nucleus on a wide volume of nanoparticles in order to extract the nuclear form factor, nanoparticle size, polydispersity and chemical composition.[84,85] Hence, it is possible with SANS to determine the chemical composition of the probed materials.

Polarized SANS (p-SANS) takes benefit of the neutron spin interaction with the magnetic induction inside materials and makes it possible to probe the magnetization distribution inside nanoparticles through the direct access to the magnetic form factor $F_M(Q)$,[86] but also to probe the magnetic inter-particle interactions. It is thus a complementary technique to XMCD experiments. In the present case, p-SANS under an external magnetic field has been used to determine the magnetic radius of core and shell with their respective magnetic contrast.[14]
Polarized SANS measurements were performed using dry powders on the PA20 SANS instrument at the Laboratoire Léon Brillouin (CEA Saclay).

In p-SANS, we measure the cross-section $d\sigma(Q)/d\Omega$ using the two polarized states (+ and -) of the neutron beam (the spin of a neutron is ½):[87]

$$\frac{d\sigma^+}{d\Omega}(Q) = I^+(Q) = [F_N^2(Q) - 2PF_N(Q)F_M(Q)sin^2\alpha + F_M^2(Q)sin^2\alpha]S(Q) \quad \textit{Equation 3}$$

$$\frac{d\sigma^-}{d\Omega}(Q) = I^-(Q) = [F_N^2(Q) + 2P\varepsilon F_N(Q)F_M(Q)sin^2\alpha + F_M^2(Q)sin^2\alpha]S(Q) \quad \textit{Equation 4}$$

Where F_N and F_M are the nuclear and magnetic form factors, respectively, where the "nuclear" term refers to the interaction with the nucleus and hence the chemical structure while the "magnetic" term refers to the interaction of the neutron spin with the magnetic induction in the. P is the degree of polarization of the incident neutron beam (here P = 0.94), ε the spin flip efficiency (ε = 0.935), α the azimuthal angle between the scattering vector Q and the magnetization direction $\vec{\mu}$ and S(Q) is the structure factor that depends on inter-particles interactions.
For non-interacting nanoparticles, S(Q) = 1 and

$$F_N(Q) = V_p(\Delta\rho)F_{N,geo}(Q) \quad \textit{Equation 5}$$

$$F_M(Q) = V_m(\Delta\rho_m)F_{M,geo}(Q) \quad \textit{Equation 6}$$

With V_p the volume of the particle, V_m the magnetic volume, $\Delta\rho$ the neutron scattering length density (SLD) contrast, $\Delta\rho_m$ the magnetic neutron SLD contrast and $F_{N,geo}$ and $F_{M,geo}$ are the geometrical nuclear and magnetic form factor, respectively. The SLD contrast $\Delta\rho$ is defined as the difference between the particle's (or magnetic) SLD ρ_p (or ρ_m) and the matrix ρ_{medium}. Working on dry powders, we assume $\rho_{medium} = 0$. Thus,

$$\Delta\rho = \rho_p = \sum_i \frac{c_i b_i}{V_i} \quad \textit{Equation 7}$$

$$\Delta\rho_m = \rho_m = p\sum_i \frac{c_i \mu_i^{\perp}}{V_p} \quad \textit{Equation 8}$$

Where c_i, b_i, V_i and $\mu_i^{\perp}$ are the atomic concentration, the nuclear SLD, the atomic volume of constituent i in the sample and the projection of the magnetic moment of i[th] atom onto the plane perpendicular to the scattering vector $\vec{Q}$ (expressed in Bohr magnetons) respectively. And $p = (\gamma r_0) = (e^2\gamma)/(2mc^2) = 0.27 \times 10^{-12}$ cm, with r_0 the radius of the electron and γ the Landé factor for neutrons ($\gamma = 1.913$).
Theoretical ρ_p of Fe_3O_4, $CoFe_2O_4$ and CoO were calculated from *SLD calculator*[88] as it depends on the material's density and it's chemical formula leading to values of 6.9, 6.1, 4.3 (x10^{-6}) Å^{-2} respectively, that are in accordance with the literature for Fe_3O_4[89] and $CoFe_2O_4$[84] while no reference for ρ_{CoO} has been found.

For measurements performed at 250 K with no applied magnetic field, the sum $[I^+(Q)+I^-(Q)]/2$ leads to a non-polarized signal :

$$\frac{I^+(Q)+I^-(Q)}{2} = \frac{I_N(Q)}{2} = 2[F_N^2(Q) + (1-\varepsilon)PF_N(Q)F_M(Q)sin^2\alpha + F_M^2(Q)sin^2\alpha] \quad \textit{Equation 9}$$

Where $sin^2\alpha = 0$ hence, $I_N(Q) = F_N^2(Q)$. On the other hand, the difference of $I^-(Q)$ and $I^+(Q)$ for measurements performed at 150 K with an applied magnetic field of 3 T allows to extract the magnetic part knowing $F_N(Q)$ from the previous operation:

$$I^-(Q) - I^+(Q) = 2P(1+\varepsilon)F_N(Q)F_M(Q)sin^2\alpha \quad \textit{Equation 10}$$

Nuclear observations

2D maps of the *unpolarized* scattered intensity are presented in Figure 40a-d. CS sample in Figure 40a displays a symmetric ring corresponding to a broad major peak at 0.0498 $Å^{-1}$ in the 1D curves that is attributed to a structure factor due to position correlations between the nanoparticles. This structure factor evidences thus a mean distance between the nanoparticles on the order of of $< d >= (2\pi)/Q = 12.6$ nm which is close to the center to center distance between nanoparticles (2r = 14 nm from TEM measurement sizes). Aggregation is thus observed in the CS sample but not in the other ones. For higher Q values, the peak at 0.0891 $Å^{-1}$ is known to arise from the (111) Bragg reflection of the face-centered cubic symmetry.[89] The presence of a second oscillation in the 1D curve shows a good monodispersity of the nanoparticle. This curve has been fitted using *Grasp* software **[REF]** with a core@shell model according to the following expression:

$$I(Q) = bck + \frac{scale}{(4/3)\pi(radius+shell)^3 * 10^{-8}} * \left((\rho_{core} - \rho_{shell}) * F_1 + (\rho_{shell} - \rho_{matrix}) * F_2\right)^2$$

Equation 11

$$\text{With } F_1 \text{ , } F_2 \propto Q * \left(\frac{4}{3}\right)\pi * (radius + shell)^3$$

The fitted values for CS are depicted in Table 22. Core radius (4.5 nm) and shell thickness (2.2 nm) are in good agreement with TEM size measurements considering the error bars (half-size of 5.1 ± 0.6 nm for the TEM core size with a 2.0 ± 0.8 nm thick shell). However, the core SLD is low, 6.0 vs 6.9 and 6.7 (10^{-6}) $Å^{-2}$ for Fe_3O_4 and y-Fe_2O_3 being close to the SLD of $CoFe_2O_4$ (6.1 10^{-6} $Å^{-2}$). As the core cannot be only composed of cobalt ferrite as shown by previous analysis, it evidences the contribution of CoO in the core's SLD. Moreover, the shell's SLD is a bit higher than what is expected 4.6 vs 4.3 (10^{-6}) $Å^{-2}$ for CoO. Both core's and shell's SLD suggest thus a small intermixing between core and shells or a non-homogeneous growth of CoO on the iron oxide core as evidenced by the TEM micrographs.

The 2D SANS maps of core@shell@shell nanoparticles (Figure 40b, c and d) are symmetrical along the azimuthal angle and their 1D corresponding curves I(Q) (Figure 40e) present different regimes:

- At low Q values, between 0.03 and 0.05 $Å^{-1}$, a plateau with a slope is present in the experimental curves that corresponds to a Guinier regime for single nanoparticles which evidences the absence of aggregation in CSSA, CSSB and CSSC.[90–92]
- For higher Q values, we can observe two distinct oscillations that is a good indication of the high level of monodispersity of the nanoparticles.

To fit the data of the CSS nanoparticles, the same core@shell model on Grasp software (developed by Charles Dewhurst, ILL) was used as for CS. In this model, the fitted core has been taken to correspond to the $Fe_{3-d}O_4$ core while the fitted shell corresponds to the sum of the two expected shell of -CoO@$Fe_{3-d}O_4$: one thick shell and the other one so thin that it is not possible to clearly discriminate them. The results of the fit matches well with the experimental curves. Each core radius were fixed to 4.3 nm in accordance with TEM size measurement (half-size of 5.1 ± 0.6 nm for C) and resulted in calculated shell thicknesses of 2.3, 2.8 and 3.0 nm for CSSA, CSSB and CSSC respectively, which all agree with TEM size measurements (2.3, 2.6 and 2.8 nm for CSSA, CSSB and CSSC respectively). The calculated polydispersity (40 – 50 %) is however overestimated compared to the other analysis, evidencing the complexity of the system.

In CSSA, the SLD of the core slightly increased to 6.1 10^{-6} $Å^{-2}$ being therefore closer to $CoFe_2O_4$ (6.1 10^{-6} $Å^{-2}$) and to Fe_3O_4 (6.9 10^{-6} $Å^{-2}$) as such as for its shell which has increased to 5.7 10^{-6} $Å^{-2}$. It evidences the very slight increase of ferrite content in the core due to a possible crystal restructuration favored by the high temperature. In the shell, the ferrite content has also increased thanks to interfacial atomic diffusion process at the CoO/$Fe_{3-d}O_4$ interface and/or thanks to partial solubilisation recrystallization of the CoO shell into cobalt-ferrite followed by the eventual growth of iron oxide, in accordance with XMCD experiments. When the thickness of the second $Fe_{3-d}O_4$ shell is increased in CSSB and CSSC, both SLDs of the core (6.3 and 6.6 10^{-6} $Å^{-2}$ respectively) and shell (6.0 and 7.0 10^{-6} $Å^{-2}$ respectively) also increased. These results show an increase of the iron oxide content in the core and in the shell which can be attributed to a decrease of the overall CoO content in the nanoparticle in favor of cobalt-ferrite but also to the growth of iron oxide in the second shell.

According to the SLDs values inferred from the fits and to $\Delta\rho = \rho_p = \sum_i \frac{c_i b_i}{V_i}$ Equation 7, it is possible to roughly determine the composition of the nanoparticles considering only CoO and Fe_3O_4 components for sake of simplicity. It shows that a high amount of CoO is present in the CS (62 %) nanoparticles as expected according to previous measurements. This amount decreases to 38, 29 and 6 % for CSSA, CSSB and CSSC respectively, in accordance with TEM, XRD and XMCD analysis.

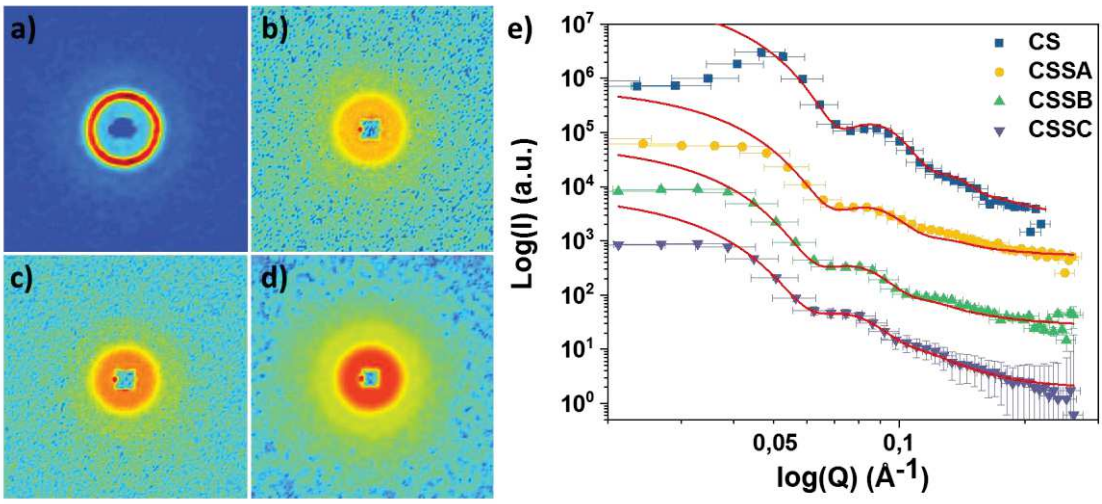

Figure 40. SANS 2D maps of a) CS, b) CSSA, c) CSSB and d) CSSC. e) Corresponding radially averaged SANS intensity in function of scattering vector Q with refinement in red.

Table 22. Nuclear and magnetic fitted parameters and calculated Fe_3O_4 and CoO content in the nanoparticles according to nuclear SLD fitted values.

	CS	CSSA	CSSB	CSSC
Nuclear core radius (nm)	4.5	4.3	4.3	4.3
Nuclear shell thickness (nm)	2.2	2.3	2.8	3.0
Nuclear core SLD (10^{-6} Å^{-2})	6.0	6.1	6.3	6.6
Core Fe_3O_4 content (%)	65	69	77	88
Core CoO content (%)	35	31	23	12
Nuclear shell SLD (10^{-6} Å^{-2})	4.6	5.7	6.0	7.0
Shell Fe_3O_4 content (%)	12	54	65	100
Shell CoO content (%)	88	46	35	0
Averaged Fe_3O_4 content (%)	**39**	**62**	**71**	**94**
Averaged CoO content (%)	**61**	**38**	**29**	**6**
Magnetic core radius (nm)	-	4.6	4.9	3.7
Magnetic shell thickness (nm)	-	2.0	2.5	3.4
Magnetic core SLD (10^{-6} Å^{-2})	-	1.1	1.3	1.1
Magnetic shell SLD (10^{-6} Å^{-2})	-	0.8	1.0	0.9
Averaged nanoparticle SLD (10^{-6} Å^{-2})	-	**0.9**	**1.1**	**0.9**
Magnetic moment (%)	8.8	9.0	12.7	12.9

The study of the nuclear contributions in SANS shows that the CS nanoparticles are slightly aggregated which may results from their dry. The fit of the SANS curve allows to determine a core size of 9 nm and a 2.2 nm thick CoO shell for CS which is coherent with other analysis (TEM, EDX, XRD and Mössbauer spectroscopy). The investigation of the SLDs values point out the presence of interfacial cobalt ferrite in CS.

Similar studies performed on the CSS nanoparticles show the increase of the shell thickness among the growth of the nanoparticles. The SLDs values evidenced the increase of the cobalt ferrite content in CSSA compared to CS, in accordance with other analysis. Then in CSSB and in CSSC, the SLDs values show the decrease of the CoO content in favor of the iron oxide phase. Furthermore, SANS allowed to determine that CS is composed of 62 % of CoO and this content drops to 38, 29 and 6 % for CSSA, CSSB and CSSC respectively.

Magnetic observations

To observe the magnetic behavior of the nanoparticles, p-SANS experiments were performed at 150 K and under an applied magnetic field of 3 T allowing to get blocked and saturated magnetic nanoparticles. The insets of Figure 41 evidence the 2D map of $I^+(Q)$-$I^-(Q)$ signal where an asymmetrical shape is observed: no signal is present for a 50° integration parallel to the applied magnetic field (horizontal cut) (see annexes), while for an integration of 50° perpendicular to the applied magnetic field (vertical cut), a magnetic signal is observed which can be related to the magnetic for factor $F_M(Q)$ of the nanoparticles.[93] Hence, it is an indication of a $\sin^2\alpha$ dependence for the magnetic contrast[87,94] as evidenced in $I^-(Q) - I^+(Q) = 2P(1+\varepsilon)F_N(Q)F_M(Q)sin^2\alpha$ Equation 10. The peaks in $F_M(Q)$ appears at similar Q values as for $F_N(Q)$ which shows that magnetic volumes are close to nuclear volumes determined in the $[I^+(Q)+I^-(Q)]/2$ experiments. This is evidenced by the results of the fits of the magnetic core radius and shell thickness (Table 22) which shows the absence of spin canting effects[92] that is attributed to the presence of CoO which still participates to the pinning of the FiM spins even in CSSC.

However, a fit to the magnetic contribution of the CS sample was not possible due to the presence of a substantial structure factor that distorted our observations. In bulk Fe_3O_4, $\rho_{mag} = 1.46\ 10^{-6}$ Å^{-2} [95] whereas an antiferromagnet, bulk CoO has $\rho_{mag} = 0$ Å^{-2}. The fitted values show an increase of the shell thickness although the magnetic contrasts do not show a clear variation between the samples. However, the magnetic SLD is close but lower than Fe_3O_4 with a shell SLD that is always lower than the core SLD, agreeing thus with a probable intermixing of the iron oxide phase with the CoO antiferromagnetic phase.

The ratio $\left(I_{mag,max}(Q)\right)^2/\left(I_{n,max}(Q)\right)^2$ allows to roughly determine the net magnetic moment of each nanoparticles where for bulk magnetite nanoparticles, it is equal to 4.4 %.[89] Here, the net magnetic moment are higher than for bulk magnetite nanoparticles and increases from 8.8 % (CS) to 9.0 (CSSA), 12.7 (CSSB) and 12.9 % (CSSC) (Table 22). It evidences thus the increase of the effective magnetic anisotropy of the nanoparticles.

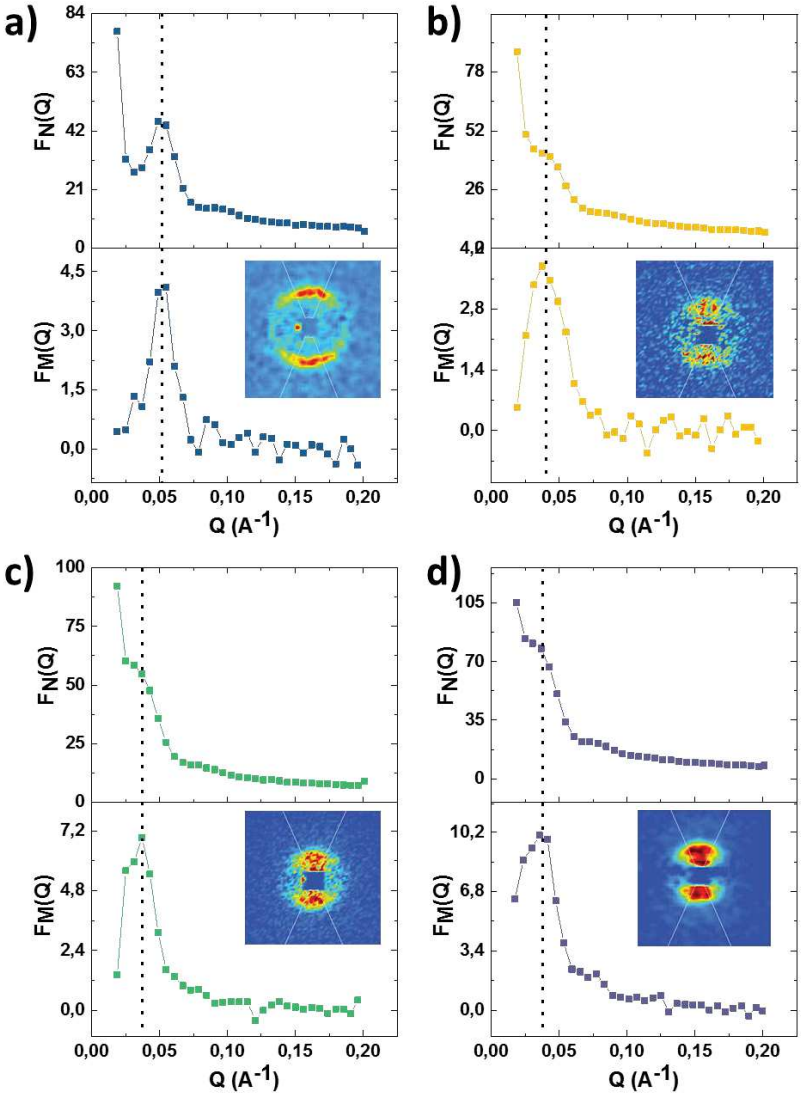

Figure 41. 1D curves $[I^+(Q)+I^-(Q)]/2$ nuclear factor (top) and $I^+(Q)-I^-(Q)$ perpendicular magnetic factor with in insets their corresponding 2D magnetic patterns, where the angular sectors (white lines) evidence the integration area to plot the 1D curves (bottom) of a) CS, b) CSSA, c) CSSB d) CSSC. Colored lines are guide to the eyes and black dotted line evidence the correspondence between maximum of magnetic and nuclear factors.

The magnetic structure of the nanoparticles were investigated with p-SANS experiments. They showed a $\sin^2\alpha$ dependence of the signal that arises from the presence of an anisotropic magnetic scattering

triggered by an external magnetic field and magnetization of the sample. The close correspondence and similarities of the $F_M(Q)$ and $F_N(Q)$ factors indicates that the magnetic volumes are similar to the nuclear volumes. It shows the absence of spin canting effect or non-magnetic layer that would induce a distinctly different magnetic pattern as compared to nuclear pattern. This was attributed to the presence of the CoO phase that pins the magnetic moment of the FiM spins. The fine study of the magnetic SLDs points out the presence of intermixing between the iron oxide and CoO part of the nanoparticles.

Finally, the net magnetic moment of the nanoparticles increases with the growth of the nanoparticles, in accordance with the increase of K_{eff}.

General discussion

In the literature, we found only a few references on core@shell@shell magnetic nanoparticles composed of more than one magnetic type.[11,12,14,15]

- Catala and al.[15] have synthesized surfactant free core@shell@shell magnetic nanoparticles analogous of Prussian blue through a succession of co-precipitation method.
- Salazar-Alvarez and al.[11] has mixed a succession of 2 thermal decomposition methods with intermediate oxidation processes to synthesize $FeO@Fe_3O_4@MnO@Mn_3O_4$ nanoparticles.
- Krycka and al.[14] have synthesized $Fe_3O_4@MnO@y\text{-}Mn_2O_3$ nanoparticles through a seed growth approach with the thermal decomposition followed by a passivation in air of the MnO shell.
- Gavrilov and al.[12] has synthesized $MnFe_2O_4@CoFe_2O_4@NiFe_2O_4$ nanoparticles through a seed-mediated growth process of 3 thermal decomposition.

Here, we decided to also use a seed-mediated growth approach with the succession of three thermal decompositions to synthesize $Fe_{3-d}O_4@CoO@Fe_{3-d}O_4$ nanoparticles. According to a previous work on simple CS nanoparticles,[13] a systematic study consisting in synthesizing three different CSS from the same CS by the decomposition of different quantity of metallic precursors allows us to finely compare the structural and magnetic properties of each CSS.

TEM micrographs show that the nanoparticle's shape deviates from a perfect sphere by the addition and growth of shells. Hence, as evidenced by EELS-SI and EELS spectrum imaging, the nanoparticles are not completely homogeneously covered: the CoO shell does not fully cover the iron oxide core in CS and the CSS nanoparticles evidence some CoO rich area surrounded by iron oxide. This is due to a preferential growth orientation of the shells on the faceted seeds nanoparticles[13,21,96,97] where in seed-mediated growth synthesis, the newly formed monomers deposit on the facets of the highest energy according to $V_{deposition}$ and lately migrates on the facets of the lowest energy according to $V_{migration}$ with V the kinetic speed.[98] Thus the kinetic difference between $V_{deposition}$ and $V_{migration}$ greatly affects the shape of the resulting nanoparticles. But, even if the CS and CSS nanoparticles have lost their spherical shape compared to the core, they still display a shape close to sphere especially after a succession of thermal decompositions.
Furthermore, the partial solubilisation of the seed nanoparticles followed by a recrystallization during the decomposition of the newly added precursor allows to synthesize mixed iron oxide – cobalt ferrite interfaces.[23] Hence the growth of a CoO or iron oxide shell is facilitated by the presence of this interfacial cobalt ferrite.[22,61] This, plus a crystallization of iron oxide, cobalt-ferrite and CoO in similar space groups and with a good matching of their cell parameters allow a nice epitaxial growth of each layer. The good epitaxial relationships are lately revealed by the narrowing of the X-ray diffractogram's peaks compared to the seed nanoparticles and by continuous and periodic lattice fringes without any defect in STEM micrographs.

Moreover, the iron oxide core nanoparticles are partially oxidized at the surface as shown by XRD, FT-IR, XAS-XMCD and Mössbauer spectroscopy. This oxidation is favored by the exposition of the nanoparticles to air upon washing after their synthesis and allows to transform a portion of magnetite into maghemite at the surface of the nanoparticles, hence to create vacancies in octahedral sites (see chapter I).[1] These vacancies help to incorporate Co^{2+} cations through a diffusion process[61] and by a partial solubilisation – recrystallization of the seeds[23] during the synthesis of the CoO shell in CS nanoparticles.

A further thermal decomposition of $FeSt_2$ precursor on CS led to the synthesis of CSS nanoparticles. These nanoparticles display several crystal phases with epitaxial matches as evidenced by HR-TEM and HAADF. The good epitaxy of each phases (the core and the two shells) is also displayed by the XRD diffractograms where the crystal size increases as a function of the addition and growth of each shell. Furthermore, this epitaxial relationship is ensured by the good matching of the lattice parameters

between iron oxide spinel structure and CoO wüstite phases. It is also favored by the presence of interfacial cobalt ferrite as discussed previously. It is worth to note that despite the presence of interfacial cobalt ferrite, strains of 2 % induced by lattice mismatch exist. Nevertheless, the presence of strains does not break the crystal symmetry of the nanoparticles.

The creation of interfacial cobalt ferrite has been demonstrated through the use of different techniques:

- SAXS curves evidence the low polydispersity of each nanoparticles and their fit with a core@shell model allows to extract core radius and shell thickness that agree with TEM size measurements. Moreover, the extracted SLD values are in between the one of magnetite and CoO as such as cobalt ferrite, evidencing thus the presence of interfacial cobalt ferrite. Nevertheless, the SLD has also shown the high contribution of CoO close to the core in each nanoparticle and close to the shells in the CSS nanoparticles. According to XRD, EDS and EELS-SI analysis, such a high content is overestimated and show the limitation of the fitting model.
- SANS is complementary from SAX as it probes the nucleus. As SAX, SANS allowed to determine core radius and shell thicknesses that are in accordance with SAX and TEM size measurements. From SANS SLD, it was possible to determine mean compositions of the nanoparticles that agrees with XRD, EDS and EELS-SI analysis.
- XAS XMCD analysis are a tool of choice to discriminate the chemical environment of different cations. Hence, the shape of the XAS and XMCD spectra at the Fe $L_{2,3}$ edges get closer to a $Fe_{3-d}O_4$@$CoFe_2O_4$ nanoparticles and at the Co $L_{2,3}$ edges, the XMCD intensity evidences the creation of a FiM phase. Moreover, selective hysteresis has shown that the nanoparticles display a strong coupling effect that is evidenced by similar H_C at the different edges.
- Contrary to XAS XMCD, Mössbauer only probes the ^{57}Fe chemical environment. However, thanks to a precise fit of the Mössbauer spectra, it is possible to get direct complementary information to XMCD concerning the oxidation state of the material and the atomic environment of the Fe^{2+} and Fe^{3+} atoms. Indeed, the hyperfine field of Fe cations in Oh and Td sites in Mössbauer spectroscopy, are influenced by the presence of Co cations as first neighbors while in the same time, the isomer shift values show the Fe^{2+} variation in the structure.

Moreover, it was possible to determine the composition of the nanoparticles. In SAXS, CS was determined to display an iron oxide core of 9.1 nm diameter with a CoO shell thickness of 2.0 nm that corresponds to an overall composition of 33 % of magnetite and 67 % of CoO. Hence, the core size is in between TEM (10.1 nm) and XRD (8.0 nm) size while the CoO shell thickness is perfectly in accordance with TEM size measurements (2.0 nm). These results were confirmed by SANS because the iron oxide core was determined to have a size of 9.0 nm with a shell of 2.2 nm thick. This corresponds to an overall composition of 38 % of magnetite and 62 % of CoO.

As Mössbauer spectroscopy only probes the Fe environment, it is not possible to determine a CoO shell thickness in CS. However, this analysis has shown the presence of Co-ferrite which is expected as a 1.1 nm thick interfacial layer (49 %) corresponding to the same amount to the $Fe_{3-d}O_4$ core (51 %). Hence, by considering each analysis, the CS nanoparticles should be composed of a 7.8 to 9.0 nm diameter of iron oxide with a 1.1 nm thick cobalt ferrite shell and a 1.5 to 2.0 nm thick CoO shell.
However, this calculus does not take into account the possible gradient composition of interfacial cobalt ferrite[23,61] nor the further limited diffusion of Co atoms in the core during the third thermal decomposition as shown by CS2r sample in the XMCD experiments. But it allows to get a rough estimation of the chemical composition of CS.

Mössbauer and XMCD analysis has evidenced the interfacial atomic diffusion of Co^{2+} in the $Fe_{3-d}O_4$ core in CS or the partial solubilisation of the CoO shell and its recrystallization in cobalt ferrite. But they have also evidenced a greater contribution of Fe^{2+} in CS that is attributed to the chemical reduction of the iron oxide core by the reacting medium and with its protection by the CoO shell. This surprising result is in accordance with previous results where it has been further investigated.[22]
Magnetometry measurements on CS has shown that they display typical magnetic properties of $Fe_{3-d}O_4$@CoO nanoparticles with the presence of exchange-bias coupling that increases T_{max} up to the T_N of CoO (i.e. 290 K) with a wide opening of the hysteresis at low temperature and the shift of the hysteresis at low temperature after a field cooling procedure.

The further decomposition of $FeSt_2$ precursor resulted in the size increase of the CS nanoparticles. For low amount of $FeSt_2$, the Fe^{2+} content decreased significantly as shown by XMCD and Mössbauer. It agrees with the formation of a 0.2 nm thick shell of Co-Ferrite at the CS surface, certainly by solubilisation/recrystallization process. For higher amount of $FeSt_2$, the Fe^{2+} content increased gradually with the size increase of CSS and concomitantly to Co-Ferrite as shown by XMCD. As the nanoparticles are not totally homogeneously covered, it is possible that higher amounts of Fe monomers create new nucleation points on CS which then increase the amount of cobalt ferrite. It is also possible that the diffusion occurs further on the specific nucleation sites without creating new ones, and that as the Fe monomers are sufficient, magnetite starts to form on the cobalt ferrite. It is well known that for such small volumes, magnetite is spontaneously oxidized into maghemite.[1] Nevertheless, XMCD and Mössbauer showed that the Fe^{2+}content increased with the nanoparticle size. The morphology of CSS nanoparticles being close to the shape of CS, we expect that magnetite grew at the CS surface of the nanoparticles. Hence, the stability of Fe^{2+} against oxidation in air remains unclear.

Besides SAXS and SANS confirmed the size increase of CS nanoparticles, SLD variations also evidenced the higher $Fe_{3-d}O_4$ content and the presence of interfacial cobalt ferrite. Moreover, SANS showed that the core radius was reduced of 0.2 nm for CSSA, CSSB and CSSC in comparison with CS which is ascribed to the further diffusion of Co cations within the $Fe_{3-d}O_4$ surface layer. These results were confirmed by XMCD performed on CS2r which showed that reheating at 300 °C increased slightly the diffusion of Co across the $Fe_{3-d}O_4$/CoO interface. However, the core SANS SLDs increase in CSS and is higher than $CoFe_2O_4$ SLD, being close to magnetite SLD in CSSC as such as the shell's SLD. This behavior is concomitant with the increase of Fe^{2+} content observed in other analysis but the core is not expected to have more Fe^{2+} as it is protected by the CoO shell, even with the existence of a solubilisation – recrystallization of the nanoparticle with the third thermal decomposition. It is thus attributed to a restructuration of the core favored by the further thermal decomposition proceeded at high temperature.

p-SANS also showed that the magnetic diameters are similar to the nuclear diameters for each nanoparticles and agrees with a size increase. The magnetic intensity ratio $\left(I_{mag,max}(Q)\right)^2/\left(I_{n,max}(Q)\right)^2$ increases from CS to CSSC which evidences an increase of $F_M(Q)$, hence of the magnetic volume according to equation 10. Moreover, this ratio is higher than bulk magnetite which evidences the increase of the magnetic anisotropy of the nanoparticles.
It is also evidenced by magnetometry measurements which show large opening of the hysteresis curve at low temperature for CS, CSSA, CSSB and CSSC while C only displays a small H_C. This opening is concomitant with the presence of a magnetic coupling within the nanoparticles. This coupling also allows to increase T_B at 290 K for CS and above room temperature for the CSS. Thus, the CSS nanoparticles display a H_C at 300 K. Plus, as their H_C are similar at 300 K, it evidences the perfect magnetic compensation of each phase.

The nature of this magnetic coupling is difficult to determine precisely. Indeed, as H_E vanishes between 0 and 150 K for the CSS, their magnetic properties are not dominated by an exchange-bias coupling at room temperature.[61] But, as long as they display a H_E at low temperature, it shows that an exchange-bias coupling exists in each CSS. Plus, this exchange-bias coupling decreases when the CoO phase is replaced by the Co-ferrite phase.
Interfacial atomic diffusion generate cobalt ferrite layers at both interfaces which display a J_{int} that becomes higher than $K_{CoO}V_{CoO}$ of the AFM CoO phase. Hence, it leads to a decrease of the exchange-bias coupling.[21,69] On the another hand, as the exchange-bias coupling does not dominate the magnetic properties at room temperature, another magnetic mechanism occurs. As cobalt ferrite has a higher KV than magnetite it can lead to the apparition of a hard-soft exchange-coupling in the nanoparticles.[12,73] Indeed, in Fe_3O_4@$CoFe_2O_4$ nanoparticles, this hard-soft exchange coupling allows to increase T_{max} to 240 K[99] although the nanoparticles are still superparamagnetic at room temperature.[73] Furthermore the addition of an iron oxide shell on a $Fe_{3-d}O_4$@$CoFe_2O_4$ core@shell nanoparticle ($Fe_{3-d}O_4$@$CoFe_2O_4$@$Fe_{3-d}O_4$) does not allow to get blocked nanoparticles at room temperature (see following chapter). Moreover, as shown by selective hysteresis, all Fe and Co atoms are coupled together: hence, all phases within the nanoparticles are coupled together. We attribute thus, the high T_B and the opening of the hysteresis of the CSS nanoparticles at 300 K to arise from a nice balance between a hard-soft exchange coupling and an exchange-bias coupling that are dominated by the fine intermixed layers according to Skoropata and al.[61]

Moreover, M_R/M_S ratios in XMCD are equivalent to M_R/M_S ratios for SQUID measurements at 5K in the CSS nanoparticles. A 300 K, the H_C is around 500 Oe for each CSS with a M_R/M_S ratio of 24, 20 and 21 % for CSSA, CSSB and CSSC respectively. Hence, we have drastically increased the magnetic stability of ferrite based nanoparticles with a size below 16 nm. The magnetic properties at 300 K are very promising for such nanoparticles. Nevertheless, they still need a further development to increase the energy product in order to use them for permanent nano-magnet.[8]

Conclusion

The successive thermal decomposition of $FeSt_2$, $CoSt_2$ and $FeSt_2$ accompanied with a seed-mediated growth method allows to synthesize core@multishelled nanoparticles. Due to the presence of interfacial diffusion, their structure is more complex than the expected Fe_3O_4@CoO@Fe_3O_4 structure and contains some cobalt ferrite at the $Fe_{3-d}O_4$/CoO and CoO/$Fe_{3-d}O_4$ interfaces. This new structure allows to tune the magnetic properties of the nanoparticles which display a blocked magnetic moment at room temperature for a size smaller than 16 nm. Their interesting magnetic properties are driven by the interfacial cobalt-ferrite and are produced by a nice balance between two different magnetic couplings: the exchange-bias coupling and the hard-soft coupling. Moreover, thanks to the presence of a coercive field at room temperature, these ferrites-based nanoparticles offers a high potential for a further development in the aim for permanent nano-magnets applications.

References

(1) Baaziz, W.; Pichon, B. P.; Fleutot, S.; Liu, Y.; Lefevre, C.; Greneche, J.-M.; Toumi, M.; Mhiri, T.; Begin-Colin, S. Magnetic Iron Oxide Nanoparticles: Reproducible Tuning of the Size and Nanosized-Dependent Composition, Defects, and Spin Canting. *J. Phys. Chem. C* **2014**, *118* (7), 3795–3810. https://doi.org/10.1021/jp411481p.

(2) Guardia, P.; Labarta, A.; Batlle, X. Tuning the Size, the Shape, and the Magnetic Properties of Iron Oxide Nanoparticles. *J. Phys. Chem. C* **2011**, *115* (2), 390–396. https://doi.org/10.1021/jp1084982.

(3) Nemati, Z.; Alonso, J.; Rodrigo, I.; Das, R.; Garaio, E.; García, J. Á.; Orue, I.; Phan, M.-H.; Srikanth, H. Improving the Heating Efficiency of Iron Oxide Nanoparticles by Tuning Their Shape and Size. *J. Phys. Chem. C* **2018**, *122* (4), 2367–2381. https://doi.org/10.1021/acs.jpcc.7b10528.

(4) Frenkel, J.; Doefman, J. Spontaneous and Induced Magnetisation in Ferromagnetic Bodies. *Nature* **1930**, *126* (3173), 274–275. https://doi.org/10.1038/126274a0.

(5) Bedanta, S.; Kleemann, W. Supermagnetism. *J. Phys. Appl. Phys.* **2009**, *42* (1), 013001. https://doi.org/10.1088/0022-3727/42/1/013001.

(6) Jang, J.; Nah, H.; Lee, J.-H.; Moon, S. H.; Kim, M. G.; Cheon, J. Critical Enhancements of MRI Contrast and Hyperthermic Effects by Dopant-Controlled Magnetic Nanoparticles. *Angew. Chem.* **2009**, *121* (7), 1260–1264. https://doi.org/10.1002/ange.200805149.

(7) Coey, J. M. D. Permanent Magnet Applications. *J. Magn. Magn. Mater.* **2002**, 16.

(8) Poudyal, N.; Ping Liu, J. Advances in Nanostructured Permanent Magnets Research. *J. Phys. Appl. Phys.* **2013**, *46* (4), 043001. https://doi.org/10.1088/0022-3727/46/4/043001.

(9) Nogués, J.; Sort, J.; Langlais, V.; Skumryev, V.; Suriñach, S.; Muñoz, J. S.; Baró, M. D. Exchange Bias in Nanostructures. *Phys. Rep.* **2005**, *422* (3), 65–117. https://doi.org/10.1016/j.physrep.2005.08.004.

(10) Baaziz, W.; Pichon, B. P.; Lefevre, C.; Ulhaq-Bouillet, C.; Greneche, J.-M.; Toumi, M.; Mhiri, T.; Bégin-Colin, S. High Exchange Bias in $Fe_{3-\delta}O_4$@CoO Core Shell Nanoparticles Synthesized by a One-Pot Seed-Mediated Growth Method. *J. Phys. Chem. C* **2013**, *117* (21), 11436–11443. https://doi.org/10.1021/jp402823h.

(11) Salazar-Alvarez, G.; Lidbaum, H.; López-Ortega, A.; Estrader, M.; Leifer, K.; Sort, J.; Surinach, S.; Baró, M. D.; Nogués, J. Two-, Three-, and Four-Component Magnetic Multilayer Onion Nanoparticles Based on Iron Oxides and Manganese Oxides. *J. Am. Chem. Soc.* **2011**, *133* (42), 16738–16741.

(12) Gavrilov-Isaac, V.; Neveu, S.; Dupuis, V.; Taverna, D.; Gloter, A.; Cabuil, V. Synthesis of Trimagnetic Multishell $MnFe_2O_4$@$CoFe_2O_4$@$NiFe_2O_4$ Nanoparticles. *Small* **2015**, *11* (22), 2614–2618. https://doi.org/10.1002/smll.201402845.

(13) Liu, X.; Pichon, B. P.; Ulhaq, C.; Lefèvre, C.; Grenèche, J.-M.; Bégin, D.; Bégin-Colin, S. Systematic Study of Exchange Coupling in Core–Shell $Fe_{3-\delta}O_4$@CoO Nanoparticles. *Chem. Mater.* **2015**, *27* (11), 4073–4081. https://doi.org/10.1021/acs.chemmater.5b01103.

(14) Krycka, K. L.; Borchers, J. A.; Laver, M.; Salazar-Alvarez, G.; L?pez-Ortega, A.; Estrader, M.; Suri?ach, S.; Bar?, M. D.; Sort, J.; Nogu?s, J. Correlating Material-Specific Layers and Magnetic Distributions within Onion-like Fe3O4/MnO/?-Mn2O3 Core/Shell Nanoparticles. *J. Appl. Phys.* **2013**, *113* (17), 17B531. https://doi.org/10.1063/1.4801423.

(15) Catala, L.; Brinzei, D.; Prado, Y.; Gloter, A.; Stéphan, O.; Rogez, G.; Mallah, T. Core-Multishell Magnetic Coordination Nanoparticles: Toward Multifunctionality on the Nanoscale. *Angew. Chem. Int. Ed.* **2009**, *48* (1), 183–187. https://doi.org/10.1002/anie.200804238.

(16) Cotin, G.; Kiefer, C.; Perton, F.; Boero, M.; Özdamar, B.; Bouzid, A.; Ori, G.; Massobrio, C.; Begin, D.; Pichon, B.; et al. Evaluating the Critical Roles of Precursor Nature and Water Content When Tailoring Magnetic Nanoparticles for Specific Applications. *ACS Appl. Nano Mater.* **2018**, *1* (8), 4306–4316. https://doi.org/10.1021/acsanm.8b01123.

(17) Ohresser, P.; Otero, E.; Choueikani, F.; Chen, K.; Stanescu, S.; Deschamps, F.; Moreno, T.; Polack, F.; Lagarde, B.; Daguerre, J.-P.; et al. DEIMOS: A Beamline Dedicated to Dichroism Measurements in the 350–2500 EV Energy Range. *Rev. Sci. Instrum.* **2014**, *85* (1), 013106.
(18) Daffé, N.; Sikora, M.; Rovezzi, M.; Bouldi, N.; Gavrilov, V.; Neveu, S.; Choueikani, F.; Ohresser, P.; Dupuis, V.; Taverna, D.; et al. Nanoscale Distribution of Magnetic Anisotropies in Bimagnetic Soft Core-Hard Shell $MnFe_2O_4$@$CoFe_2O_4$ Nanoparticles. *Adv. Mater. Interfaces* **2017**, *4* (22), 1700599. https://doi.org/10.1002/admi.201700599.
(19) Teillet, J.; Varret, F. *MOSFIT Software*; Université du Maine, Le Mans, France.
(20) Chaboussant, G.; Désert, S.; Lavie, P.; Brûlet, A. PA20 : A New SANS and GISANS Project for Soft Matter, Materials and Magnetism. *J. Phys. Conf. Ser.* **2012**, *340*, 012002. https://doi.org/10.1088/1742-6596/340/1/012002.
(21) Lima, E.; Winkler, E. L.; Tobia, D.; Troiani, H. E.; Zysler, R. D.; Agostinelli, E.; Fiorani, D. Bimagnetic CoO Core/$CoFe_2O_4$ Shell Nanoparticles: Synthesis and Magnetic Properties. *Chem. Mater.* **2012**, *24* (3), 512–516. https://doi.org/10.1021/cm2028959.
(22) Sartori, K.; Cotin, G.; Bouillet, C.; Halté, V.; Bégin-Colin, S.; Choueikani, F.; Pichon, B. P. Strong Interfacial Coupling through Exchange Interactions in Soft/Hard Core–Shell Nanoparticles as a Function of Cationic Distribution. *Nanoscale* **2019**, *11* (27), 12946–12958. https://doi.org/10.1039/C9NR02323B.
(23) Lentijo-Mozo, S.; Deiana, D.; Sogne, E.; Casu, A.; Falqui, A. Unexpected Insights about Cation-Exchange on Metal Oxide Nanoparticles and Its Effect on Their Magnetic Behavior. *Chem. Mater.* **2018**, *30* (21), 8099–8112. https://doi.org/10.1021/acs.chemmater.8b04331.
(24) Zhang, L.; He, R.; Gu, H.-C. Oleic Acid Coating on the Monodisperse Magnetite Nanoparticles. *Appl. Surf. Sci.* **2006**, *253* (5), 2611–2617. https://doi.org/10.1016/j.apsusc.2006.05.023.
(25) Nakamoto, K. *Infrared and Raman Spectra of Inorganic and Coordination Compounds*, 6th ed.; Wiley: Hoboken, N.J, 2009.
(26) Ren, Y.; Iimura, K.; Kato, T. Structure of Barium Stearate Films at the Air/Water Interface Investigated by Polarization Modulation Infrared Spectroscopy and Π− *A* Isotherms. *Langmuir* **2001**, *17* (9), 2688–2693. https://doi.org/10.1021/la000872e.
(27) Daou, T. J.; Grenèche, J. M.; Pourroy, G.; Buathong, S.; Derory, A.; Ulhaq-Bouillet, C.; Donnio, B.; Guillon, D.; Begin-Colin, S. Coupling Agent Effect on Magnetic Properties of Functionalized Magnetite-Based Nanoparticles. *Chem. Mater.* **2008**, *20* (18), 5869–5875. https://doi.org/10.1021/cm801405n.
(28) Tang, C.-W.; Wang, C.-B.; Chien, S.-H. Characterization of Cobalt Oxides Studied by FT-IR, Raman, TPR and TG-MS. *Thermochim. Acta* **2008**, *473* (1–2), 68–73. https://doi.org/10.1016/j.tca.2008.04.015.
(29) Jacintho, G. V. M.; Brolo, A. G.; Corio, P.; Suarez, P. A. Z.; Rubim, J. C. Structural Investigation of MFe_2O_4 (M = Fe, Co) Magnetic Fluids. *J. Phys. Chem. C* **2009**, *113* (18), 7684–7691. https://doi.org/10.1021/jp9013477.
(30) Sytnyk, M.; Kirchschlager, R.; Bodnarchuk, M. I.; Primetzhofer, D.; Kriegner, D.; Enser, H.; Stangl, J.; Bauer, P.; Voith, M.; Hassel, A. W.; et al. Tuning the Magnetic Properties of Metal Oxide Nanocrystal Heterostructures by Cation Exchange. *Nano Lett.* **2013**, *13* (2), 586–593. https://doi.org/10.1021/nl304115r.
(31) Li, T.; Senesi, A. J.; Lee, B. Small Angle X-Ray Scattering for Nanoparticle Research. *Chem. Rev.* **2016**, *116* (18), 11128–11180. https://doi.org/10.1021/acs.chemrev.5b00690.
(32) Patnaik, P. *Handbook of Inorganic Chemicals*; McGraw-Hill handbooks; McGraw-Hill: New York, 2003.
(33) Lide, D. R. *Handbook of Chemistry and Physics*, 84th ed.; CRC Press, 2003.
(34) Fernández van Raap, M. B.; Mendoza Zélis, P.; Coral, D. F.; Torres, T. E.; Marquina, C.; Goya, G. F.; Sánchez, F. H. Self Organization in Oleic Acid-Coated CoFe2O4 Colloids: A SAXS Study. *J. Nanoparticle Res.* **2012**, *14* (9), 1072. https://doi.org/10.1007/s11051-012-1072-5.
(35) Krycka, K. L.; Borchers, J. A.; Salazar-Alvarez, G.; López-Ortega, A.; Estrader, M.; Estradé, S.; Winkler, E.; Zysler, R. D.; Sort, J.; Peiró, F.; et al. Resolving Material-Specific Structures within

Fe $_3$ O $_4$ |γ-Mn $_2$ O $_3$ Core|Shell Nanoparticles Using Anomalous Small-Angle X-Ray Scattering. *ACS Nano* **2013**, *7* (2), 921–931. https://doi.org/10.1021/nn303600e.

(36) Szczerba, W.; Costo, R.; Veintemillas-Verdaguer, S.; Morales, M. del P.; Thünemann, A. F. SAXS Analysis of Single- and Multi-Core Iron Oxide Magnetic Nanoparticles. *J. Appl. Crystallogr.* **2017**, *50* (2), 481–488. https://doi.org/10.1107/S1600576717002370.

(37) Brice-Profeta, S.; Arrio, M.-A.; Tronc, E.; Menguy, N.; Letard, I.; Cartier dit Moulin, C.; Noguès, M.; Chanéac, C.; Jolivet, J.-P.; Sainctavit, Ph. Magnetic Order in - Nanoparticles: A XMCD Study. *J. Magn. Magn. Mater.* **2005**, *288*, 354–365. https://doi.org/10.1016/j.jmmm.2004.09.120.

(38) Torres, T. E.; Roca, A. G.; Morales, M. P.; Ibarra, A.; Marquina, C.; Ibarra, M. R.; Goya, G. F. Magnetic Properties and Energy Absorption of CoFe $_2$ O $_4$ Nanoparticles for Magnetic Hyperthermia. *J. Phys. Conf. Ser.* **2010**, *200* (7), 072101. https://doi.org/10.1088/1742-6596/200/7/072101.

(39) Zhu, X.; Kalirai, S. S.; Hitchcock, A. P.; Bazylinski, D. A. What Is the Correct Fe L23 X-Ray Absorption Spectrum of Magnetite? *J. Electron Spectrosc. Relat. Phenom.* **2015**, *199*, 19–26. https://doi.org/10.1016/j.elspec.2014.12.005.

(40) Li, J.; Menguy, N.; Arrio, M.-A.; Sainctavit, P.; Juhin, A.; Wang, Y.; Chen, H.; Bunau, O.; Otero, E.; Ohresser, P.; et al. Controlled Cobalt Doping in the Spinel Structure of Magnetosome Magnetite: New Evidences from Element- and Site-Specific X-Ray Magnetic Circular Dichroism Analyses. *J. R. Soc. Interface* **2016**, *13* (121), 20160355. https://doi.org/10.1098/rsif.2016.0355.

(41) E. Pellegrin et al. Characterization of Nanocrystalline Y-Fe2O3 with Synchrotron Radiation Techniques. *Phys Stat Sol* **1999**, *215*, 797.

(42) Daffé, N.; Choueikani, F.; Neveu, S.; Arrio, M.-A.; Juhin, A.; Ohresser, P.; Dupuis, V.; Sainctavit, P. Magnetic Anisotropies and Cationic Distribution in CoFe 2 O 4 Nanoparticles Prepared by Co-Precipitation Route: Influence of Particle Size and Stoichiometry. *J. Magn. Magn. Mater.* **2018**, *460*, 243–252. https://doi.org/10.1016/j.jmmm.2018.03.041.

(43) Moyer, J. A.; Vaz, C. A. F.; Negusse, E.; Arena, D. A.; Henrich, V. E. Controlling the Electronic Structure of Co 1 − x Fe 2 + x O 4 Thin Films through Iron Doping. *Phys. Rev. B* **2011**, *83* (3). https://doi.org/10.1103/PhysRevB.83.035121.

(44) Haverkort, M. W. Spin and Orbital Degrees of Freedom in Transition Metal Oxides and Oxide Thin Films Studied by Soft X-Ray Absorption Spectroscopy, 2005.

(45) Hochepied, J. F.; Sainctavit, P.; Pileni, M. P. X-Ray Absorption Spectra and X-Ray Magnetic Circular Dichroism Studies at Fe and Co L 2, 3 Edges of Mixed Cobalt–Zinc Ferrite Nanoparticles: Cationic Repartition, Magnetic Structure and Hysteresis Cycles. *J. Magn. Magn. Mater.* **2001**, *231* (2), 315–322.

(46) Roca, A. G.; Golosovsky, I. V.; Winkler, E.; López-Ortega, A.; Estrader, M.; Zysler, R. D.; Baró, M. D.; Nogués, J. Unravelling the Elusive Antiferromagnetic Order in Wurtzite and Zinc Blende CoO Polymorph Nanoparticles. *Small* **2018**, *14* (15), 1703963. https://doi.org/10.1002/smll.201703963.

(47) Manna, P. K.; Skoropata, E.; Ting, Y.-W.; Lin, K.-W.; Freeland, J. W.; van Lierop, J. Interface Mixing and Its Impact on Exchange Coupling in Exchange Biased Systems. *J. Phys. Condens. Matter* **2016**, *28* (48), 486004. https://doi.org/10.1088/0953-8984/28/48/486004.

(48) Gaudisson, T.; Sayed-Hassan, R.; Yaacoub, N.; Franceschin, G.; Nowak, S.; Grenèche, J.-M.; Menguy, N.; Sainctavit, Ph.; Ammar, S. On the Exact Crystal Structure of Exchange-Biased Fe $_3$ O $_4$ –CoO Nanoaggregates Produced by Seed-Mediated Growth in Polyol. *CrystEngComm* **2016**, *18* (21), 3799–3807. https://doi.org/10.1039/C6CE00700G.

(49) Wohlfarth, E. P. Remanent Magnetization of Fine Particles. *J. Phys. Radium* **1959**, *20* (2–3), 295–297. https://doi.org/10.1051/jphysrad:01959002002-3029500.

(50) López-Ortega, A.; Estrader, M.; Salazar-Alvarez, G.; Roca, A. G.; Nogués, J. Applications of Exchange Coupled Bi-Magnetic Hard/Soft and Soft/Hard Magnetic Core/Shell Nanoparticles. *Phys. Rep.* **2015**, *553*, 1–32. https://doi.org/10.1016/j.physrep.2014.09.007.

(51) Baaziz, W.; Pichon, B. P.; Grenèche, J.-M.; Begin-Colin, S. Effect of Reaction Environment and in Situ Formation of the Precursor on the Composition and Shape of Iron Oxide Nanoparticles Synthesized by the Thermal Decomposition Method. *CrystEngComm* **2018**, No. 20, 7206.
(52) Toulemon, D.; Liu, Y.; Cattoën, X.; Leuvrey, C.; Bégin-Colin, S.; Pichon, B. P. Enhanced Collective Magnetic Properties in 2D Monolayers of Iron Oxide Nanoparticles Favored by Local Order and Local 1D Shape Anisotropy. *Langmuir* **2016**, *32* (6), 1621–1628. https://doi.org/10.1021/acs.langmuir.5b04145.
(53) Berry, F. J.; Skinner, S.; Thomas, M. F. 57Fe Mo¨ssbauer Spectroscopic Examination of a Single Crystal of Fe3O4. 7.
(54) Doriguetto, A. C.; Fernandes, N. G.; Persiano, A. I. C.; Filho, E. N. Characterization of a Natural Magnetite. *Phys Chem Miner.* **2003**, *30*, 249–255.
(55) Salazar, J. S.; Perez, L.; de Abril, O.; Phuoc, L. T.; Ihiawakrim, D.; Vazquez, M.; Greneche, J.-M.; Begin-Colin, S.; Pourroy, G. Magnetic Iron Oxide Nanoparticles in 10-40 Nm Range: Composition in Terms of Magnetite/Maghemite Ratio and Effect on the Magnetic Properties. *Chem. Mater.* **2011**, 8.
(56) Daou, T. J.; Pourroy, G.; Bégin-Colin, S.; Grenèche, J. M.; Ulhaq-Bouillet, C.; Legaré, P.; Bernhardt, P.; Leuvrey, C.; Rogez, G. Hydrothermal Synthesis of Monodisperse Magnetite Nanoparticles. *Chem. Mater.* **2006**, *18* (18), 4399–4404. https://doi.org/10.1021/cm060805r.
(57) *Applications of Mössbauer Spectroscopy*; Cohen, R. L., Ed.; Academic Press: New York, 1976.
(58) Deepak, F. L.; Bañobre-López, M.; Carbó-Argibay, E.; Cerqueira, M. F.; Piñeiro-Redondo, Y.; Rivas, J.; Thompson, C. M.; Kamali, S.; Rodríguez-Abreu, C.; Kovnir, K.; et al. A Systematic Study of the Structural and Magnetic Properties of Mn-, Co-, and Ni-Doped Colloidal Magnetite Nanoparticles. *J. Phys. Chem. C* **2015**, *119* (21), 11947–11957. https://doi.org/10.1021/acs.jpcc.5b01575.
(59) Khollam, Y. B.; Dhage, S. R.; Potdar, H. S.; Deshpande, S. B.; Bakare, P. P.; Kulkarni, S. D.; Date, S. K. Microwave Hydrothermal Preparation of Submicron-Sized Spherical Magnetite (Fe3O4) Powders. *Mater. Lett.* **2002**, *56* (4), 571–577. https://doi.org/10.1016/S0167-577X(02)00554-2.
(60) Liu, M.; Lu, M.; Wang, L.; Xu, S.; Zhao, J.; Li, H. Mössbauer Study on the Magnetic Properties and Cation Distribution of CoFe2O4 Nanoparticles Synthesized by Hydrothermal Method. *J. Mater. Sci.* **2016**, *51* (11), 5487–5492. https://doi.org/10.1007/s10853-016-9853-3.
(61) Skoropata, E.; Desautels, R. D.; Chi, C.-C.; Ouyang, H.; Freeland, J. W.; van Lierop, J. Magnetism of Iron Oxide Based Core-Shell Nanoparticles from Interface Mixing with Enhanced Spin-Orbit Coupling. *Phys. Rev. B* **2014**, *89* (2). https://doi.org/10.1103/PhysRevB.89.024410.
(62) Grigorova, M.; Blythe, H. J.; Blaskov, V.; Rusanov, V.; Petkov, V.; Masheva, V.; Nihtianova, D.; Martinez, Ll. M.; Muñoz, J. S.; Mikhov, M. Magnetic Properties and Mössbauer Spectra of Nanosized CoFe2O4 Powders. *J. Magn. Magn. Mater.* **1998**, *183* (1–2), 163–172. https://doi.org/10.1016/S0304-8853(97)01031-7.
(63) Bruvera, I. J.; Mendoza Zélis, P.; Pilar Calatayud, M.; Goya, G. F.; Sánchez, F. H. Determination of the Blocking Temperature of Magnetic Nanoparticles: The Good, the Bad, and the Ugly. *J. Appl. Phys.* **2015**, *118* (18), 184304. https://doi.org/10.1063/1.4935484.
(64) Gilmore, K.; Idzerda, Y. U.; Klem, M. T.; Allen, M.; Douglas, T.; Young, M. Surface Contribution to the Anisotropy Energy of Spherical Magnetite Particles. *J. Appl. Phys.* **2005**, *97* (10), 10B301. https://doi.org/10.1063/1.1845973.
(65) Cao, C.; Tian, L.; Liu, Q.; Liu, W.; Chen, G.; Pan, Y. Magnetic Characterization of Noninteracting, Randomly Oriented, Nanometer-Scale Ferrimagnetic Particles. *J. Geophys. Res.* **2010**, *115* (B7), B07103. https://doi.org/10.1029/2009JB006855.
(66) Dolci, M.; Liu, Y.; Liu, X.; Leuvrey, C.; Derory, A.; Begin, D.; Begin-Colin, S.; Pichon, B. P. Exploring Exchange Bias Coupling in $Fe_{3-\delta}O_4$@CoO Core-Shell Nanoparticle 2D Assemblies. *Adv. Funct. Mater.* **2018**, *28* (26), 1706957. https://doi.org/10.1002/adfm.201706957.
(67) Meiklejohn, W. H.; Bean, C. P. New Magnetic Anisotropy. *Phys. Rev.* **1956**, *102* (5), 1413–1414. https://doi.org/10.1103/PhysRev.102.1413.

(68) Skumryev, V.; Stoyanov; Zhang; Hadjipanayis; Givord; Nogués. Beating the Superparamagnetic Limit with Exchange Bias. *Nature* **2003**, *423* (6942), 847–850. https://doi.org/10.1038/nature01750.
(69) Oscar Iglesias; Amilcar Labarta; Xavier Battle. Exchange Bias Phenomenology and Models of Core/Shell Nanoparticles. *Cond Mat* **2008**.
(70) Polishchuk, D.; Nedelko, N.; Solopan, S.; Ślawska-Waniewska, A.; Zamorskyi, V.; Tovstolytkin, A.; Belous, A. Profound Interfacial Effects in CoFe2O4/Fe3O4 and Fe3O4/CoFe2O4 Core/Shell Nanoparticles. *Nanoscale Res. Lett.* **2018**, *13* (1). https://doi.org/10.1186/s11671-018-2481-x.
(71) Chen, R.; Christiansen, M. G.; Anikeeva, P. Maximizing Hysteretic Losses in Magnetic Ferrite Nanoparticles *via* Model-Driven Synthesis and Materials Optimization. *ACS Nano* **2013**, *7* (10), 8990–9000. https://doi.org/10.1021/nn4035266.
(72) Suzuki, Y.; van Dover, R. B.; Gyorgy, E. M.; Phillips, J. M.; Felder, R. J. Exchange Coupling in Single-Crystalline Spinel-Structure (Mn,Zn) Fe 2 O 4 /Co Fe 2 O 4 Bilayers. *Phys. Rev. B* **1996**, *53* (21), 14016–14019. https://doi.org/10.1103/PhysRevB.53.14016.
(73) Lee, J.-H.; Jang, J.; Choi, J.; Moon, S. H.; Noh, S.; Kim, J.; Kim, J.-G.; Kim, I.-S.; Park, K. I.; Cheon, J. Exchange-Coupled Magnetic Nanoparticles for Efficient Heat Induction. *Nat. Nanotechnol.* **2011**, *6* (7), 418–422. https://doi.org/10.1038/nnano.2011.95.
(74) Eftaxias, E.; Trohidou, K. N. Numerical Study of the Exchange Bias Effects in Magnetic Nanoparticles with Core/Shell Morphology. *Phys. Rev. B* **2005**, *71* (13). https://doi.org/10.1103/PhysRevB.71.134406.
(75) López-Ortega, A.; Estrader, M.; Salazar-Alvarez, G.; Estradé, S.; Golosovsky, I. V.; Dumas, R. K.; Keavney, D. J.; Vasilakaki, M.; Trohidou, K. N.; Sort, J.; et al. Strongly Exchange Coupled Inverse Ferrimagnetic Soft/Hard, MnxFe3−xO4/FexMn3−xO4, Core/Shell Heterostructured Nanoparticles. *Nanoscale* **2012**, *4* (16), 5138. https://doi.org/10.1039/c2nr30986f.
(76) Nunes, W. C.; Folly, W. S. D.; Sinnecker, J. P.; Novak, M. A. Temperature Dependence of the Coercive Field in Single-Domain Particle Systems. *Phys. Rev. B* **2004**, *70* (1), 014419. https://doi.org/10.1103/PhysRevB.70.014419.
(77) Gonzalez, J.; Andres, J.; Lopez, A.; De Toro, J.; Normile, P.; Muniz, P.; Riveiro, J.; Nogués, J. Maximizing Exchange-Bias in Co/CoO Core/Shell Nanoparticles by Lattice Matching between the Shell and the Embedding Matrix. *Chem. Mater.* **2017**.
(78) Song, Q.; Zhang, Z. J. Controlled Synthesis and Magnetic Properties of Bimagnetic Spinel Ferrite $CoFe_2O_4$ and $MnFe_2O_4$ Nanocrystals with Core–Shell Architecture. *J. Am. Chem. Soc.* **2012**, *134* (24), 10182–10190. https://doi.org/10.1021/ja302856z.
(79) Skoropata, E.; Su, T. T.; Ouyang, H.; Freeland, J. W.; van Lierop, J. Intermixing Enables Strong Exchange Coupling in Nanocomposites: Magnetism through the Interfacial Ferrite in γ − Fe 2 O 3 / NiO. *Phys. Rev. B* **2017**, *96* (2). https://doi.org/10.1103/PhysRevB.96.024447.
(80) Kechrakos, D.; Trohidou, K. N. Effects of Dipolar Interactions on the Magnetic Properties of Granular Solids. *J. Magn. Magn. Mater.* **1998**, *177–181*, 943–944. https://doi.org/10.1016/S0304-8853(97)00762-2.
(81) Cullity, B. D.; Graham, C. D. *Introduction to Magnetic Materials*, 2nd ed.; IEEE/Wiley: Hoboken, N.J, 2009.
(82) Hadjipanayis, G.; Sellmyer, D. J.; Brandt, B. Rare-Earth-Rich Metallic Glasses. I. Magnetic Hysteresis. *Phys. Rev. B* **1981**, *23* (7), 3349–3354. https://doi.org/10.1103/PhysRevB.23.3349.
(83) Goya, G. F.; Berquó, T. S.; Fonseca, F. C.; Morales, M. P. Static and Dynamic Magnetic Properties of Spherical Magnetite Nanoparticles. *J. Appl. Phys.* **2003**, *94* (5), 3520–3528. https://doi.org/10.1063/1.1599959.
(84) Bonini, M.; Wiedenmann, A.; Baglioni, P. Study of Ferrite Ferrofluids by Small-Angle Scattering of Polarized Neutrons. *J. Appl. Crystallogr.* **2007**, *40* (s1), s254–s258.
(85) *Nanoscale Magnetic Materials and Applications*; Liu, J. P., Fullerton, E., Gutfleisch, O., Sellmyer, D. J., Eds.; Springer US: Boston, MA, 2009. https://doi.org/10.1007/978-0-387-85600-1.

(86) Mikolasek, M.; Ridier, K.; Bessas, D.; Cerantola, V.; Félix, G.; Chaboussant, G.; Piedrahita-Bello, M.; Angulo-Cervera, E.; Godard, L.; Nicolazzi, W.; et al. Phase Stability of Spin-Crossover Nanoparticles Investigated by Synchrotron Mössbauer Spectroscopy and Small-Angle Neutron Scattering. *J. Phys. Chem. Lett.* **2019**, *10* (7), 1511–1515. https://doi.org/10.1021/acs.jpclett.9b00335.

(87) Manna, P. K.; Yusuf, S. M.; Mukadam, M. D.; Kohlbrecher, J. Evidence of a Core–Shell Structure in the Antiferromagnetic La0.2Ce0.8CrO3 Nanoparticles by Neutron Scattering. *Appl. Phys. A* **2012**, *109* (2), 385–390. https://doi.org/10.1007/s00339-012-7262-2.

(88) SLD calculator https://sld-calculator.appspot.com/.

(89) Krycka, K. L.; Borchers, J. A.; Booth, R. A.; Hogg, C. R.; Ijiri, Y.; Chen, W. C.; Watson, S. M.; Laver, M.; Gentile, T. R.; Harris, S.; et al. Internal Magnetic Structure of Magnetite Nanoparticles at Low Temperature. *J. Appl. Phys.* **2010**, *107* (9), 09B525. https://doi.org/10.1063/1.3358049.

(90) Ridier, K.; Gillon, B.; André, G.; Chaboussant, G.; Catala, L.; Mazérat, S.; Mallah, T. Small-Angle Neutron Scattering Study of the Short-Range Organization of Dispersed $CsNi[Cr(CN)_6]$ Nanoparticles. *J. Appl. Phys.* **2015**, *118* (11), 114304. https://doi.org/10.1063/1.4930935.

(91) Cousin, F. Small Angle Neutron Scattering. *EPJ Web Conf.* **2015**, *104*, 01004. https://doi.org/10.1051/epjconf/201510401004.

(92) Disch, S.; Wetterskog, E.; Hermann, R. P.; Wiedenmann, A.; Vainio, U.; Salazar-Alvarez, G.; Bergström, L.; Brückel, T. Quantitative Spatial Magnetization Distribution in Iron Oxide Nanocubes and Nanospheres by Polarized Small-Angle Neutron Scattering. *New J. Phys.* **2012**, *14* (1), 013025. https://doi.org/10.1088/1367-2630/14/1/013025.

(93) Ijiri, Y.; Kelly, C. V.; Borchers, J. A.; Rhyne, J. J.; Farrell, D. F.; Majetich, S. A. Detection of Spin Coupling in Iron Nanoparticles with Small Angle Neutron Scattering. *Appl. Phys. Lett.* **2005**, *86* (24), 243102. https://doi.org/10.1063/1.1947906.

(94) *Modern Techniques for Characterizing Magnetic Materials*; Zhu, Y., Ed.; Kluwer Academic Publishers: Boston, 2005.

(95) Krycka, K. L.; Booth, R. A.; Hogg, C. R.; Ijiri, Y.; Borchers, J. A.; Chen, W. C.; Watson, S. M.; Laver, M.; Gentile, T. R.; Dedon, L. R.; et al. Core-Shell Magnetic Morphology of Structurally Uniform Magnetite Nanoparticles. *Phys. Rev. Lett.* **2010**, *104* (20). https://doi.org/10.1103/PhysRevLett.104.207203.

(96) Lee, K. S.; Anisur, R. M.; Kim, K. W.; Kim, W. S.; Park, T.-J.; Kang, E. J.; Lee, I. S. Seed Size-Dependent Formation of Fe_3O_4/MnO Hybrid Nanocrystals: Selective, Magnetically Recyclable Catalyst Systems. *Chem. Mater.* **2012**, *24* (4), 682–687. https://doi.org/10.1021/cm2027724.

(97) Macpherson, H. A.; Stoldt, C. R. Iron Pyrite Nanocubes: Size and Shape Considerations for Photovoltaic Application. *ACS Nano* **2012**, *6* (10), 8940–8949. https://doi.org/10.1021/nn3029502.

(98) Xia, Y.; Xia, X.; Peng, H.-C. Shape-Controlled Synthesis of Colloidal Metal Nanocrystals: Thermodynamic versus Kinetic Products. *J. Am. Chem. Soc.* **2015**, *137* (25), 7947–7966. https://doi.org/10.1021/jacs.5b04641.

(99) Salazar-Alvarez, G.; Sort, J.; Uheida, A.; Muhammed, M.; Suriñach, S.; Baró, M. D.; Nogués, J. Reversible Post-Synthesis Tuning of the Superparamagnetic Blocking Temperature of γ-Fe_2O_3 Nanoparticles by Adsorption and Desorption of Co(II) Ions. *J Mater Chem* **2007**, *17* (4), 322–328. https://doi.org/10.1039/B613026G.

CHAPTER IV

Exchange-coupled nanomagnet

$Fe_{3-d}O_4@CoFe_2O_4@Fe_{3-d}O_4$

Introduction

Although the interfacial coupling between a FiM soft phase and an AFM hard phase is very efficient to enhance the magnetic anisotropy of nanoparticles, it is still dependent on the selection of the AFM phase which is rather limited according to the crystal matching and thermal stability of the AFM order. Furthermore, we have demonstrated in the previous chapter that the structure of $Fe_{3-d}O_4@CoO@Fe_{3-d}O_4$ nanoparticles is much more complex than expected. The diffusion of cations at both interfaces resulted in interfacial layers of $CoFe_2O_4$. Its anisotropy constant being one order of magnitude higher than $Fe_{3-d}O_4$ and according to their quasi perfect crystal adequacy – both phases are spinel structures with negligible lattice mismatch (< 0.5 %) – $CoFe_2O_4$ has a strong influence on the magnetic properties of $Fe_{3-d}O_4@CoO@Fe_{3-d}O_4$ nanoparticles. Therefore, to rationalize our study, we designed a new and original chemical structure of nanoparticles which consists of $Fe_{3-d}O_4@CoFe_2O_4@Fe_{3-d}O_4$. In this case, the magnetic anisotropy energy does not depend on the Néel temperature of the AFM phase since all phases are FiM. Therefore, the interfacial coupling is expected to happen between the soft $Fe_{3-d}O_4$ phase and the hard $CoFe_2O_4$ phase as we have demonstrated in chapter II on core-shell nanoparticles. In this study, we have investigated the combination of two soft/hard and hard/soft interfaces on the magnetic properties of nanoparticles.

Experimental section

Iron stearate precursor synthesis

Iron stearate was synthesized according to an already published protocol[1] as follow:
A 1 L two-necked round bottom flask was charged with 9.8 g (32 mmol) of sodium stearate (98.8 %, TCI) and 320 mL of distilled water. The mixture was heated at reflux under magnetic stirring until all the stearate was dissolved. Afterwards, 3.80 g (16 mmol) of iron (II) chloride tetrahydrated dissolved in 160 mL of distilled water were poured in the round bottom flask. The mixture was kept another 15 min at reflux and under magnetic stirring. Then, the solution was allowed to cool down. The orange precipitate was collected by centrifugation (15 000 rpm, 5 min) and washed by filtration with a Buchner funnel. Finally, the powder was dried in an oven at 65 °C for 15 hours.

Cobalt stearate precursor synthesis

Cobalt stearate was synthesized through the adaptation of the iron (II) stearate protocol:
A 1 L two-necked round bottom flask was charged with 9.8 g (32 mmol) of sodium stearate (98.8 %, TCI) and 320 mL of distilled water. The mixture was heated at reflux under magnetic stirring until all the stearate was dissolved. Afterwards, 3.16 g (16 mmol) of cobalt (II) chloride hexahydrated dissolved in 160 mL of distilled water were poured in the round bottom flask. The mixture was kept another 15 min at reflux and under magnetic stirring. Then, the solution was allowed to cool down. The orange precipitate was collected by centrifugation (15 000 rpm, 5 min) and washed by filtration with a Buchner funnel. Finally, the powder was dried in an oven at 65 °C for 15 hours.

C, CS and CSS nanoparticle synthesis

Iron oxide core nanoparticles, labeled C, were synthesized by the thermal decomposition of a home-made iron (II) stearate following an already published protocol.[2]
A two-necked round bottom flask was charged with 1.38 g (2.22 mmol) of a home-made iron (II) stearate, 1.254 g (4.44 mmol) of oleic acid (99% Alfa aesar) and 20 mL of ether dioctyl (B_P = 290 °C, 97 % Fluka). The brownish mixture was heated at 100 °C under a magnetic stir for 30 min in order to remove water residues and to homogenize the solution. The magnetic stir was then removed and the flask was connected to a reflux condenser before heating the solution at reflux for 2 h with a heating ramp of 5°C/min. At the end, the mixture was allowed to cool down to 100 °C and 4 mL of the solution was removed and washed to serve as a reference (C sample) while in the rest of the solution, 0.29 g (0.46 mmol) of cobalt (II) stearate, 0.791 g (2.8 mmol) of oleic acid and 32 mL of 1-octadecene was added. The mixture was heated at 100 °C for 30 min under a magnetic stir to remove water residues and to homogenize the solution. Afterwards, the magnetic stir was stopped and 0.585 g (0.94 mmol) of iron (II) stearate was poured in the mixture. The flask was then connected to a reflux condenser in order to heat the solution at reflux for another 2 h with a heating ramp of 1 °C/min. At the end, the mixture was allowed to cool down and the nanoparticles were precipitated by the addition of an excess of acetone. They were then collected by centrifugation and washed by centrifugation with a mixture of chloroform : acetone (1 : 5). The final nanoparticles, labeled CS, were stored in chloroform.
Later, 50 % of CS nanoparticles suspended in chloroform were transferred in a two-necked round bottom flask where 0.548 g (0.88 mmol) of iron (II) stearate, 0.497 g (1.76 mmol) of oleic acid and 20 mL of ether dioctyl were added. The mixture was then heated at 100 °C under a magnetic stir in order to homogenize the solution and to remove water residues. After 30 min, the magnetic stir was stopped and the flask was connected to a reflux condenser. The mixture was then heated at reflux for 2 h with a heating ramp of 1 °C/min. At the end, the solution was allowed to cool down and the nanoparticles were precipitated by the addition of an excess of acetone. They were then collected by centrifugation

and washed by centrifugation with a mixture of chloroform : acetone (1 : 5). The final nanoparticles, labeled CSS, were stored in chloroform.

Characterization techniques

Transmission electron microscopy

Transmission electron microscopy (TEM) were performed on a JEOL 2100 LaB6 with a 0,2nm point to point resolution. EDX were performed with a JEOL Si(Li) detector. The nanoparticle sizes were calculated by measuring at least 300 nanoparticles from TEM micrographs by using the Image J software. The shell thickness corresponds to half of the difference between nanoparticle sizes which were measured before and after Co decomposition. The size distribution was calculated by fitting with a Gaussian function that fits well our data.

Scanning transmission electron microscopy (STEM) experiments were carried out using a probe aberration corrected Titan (Thermo Fisher Scientific) equipped with a high-brightness field emission gun. While the electron gun was operated at 300 keV for acquisition of high-angle annular dark field (HAADF) STEM images to obtain maximum spatial resolution, the high energy was lowered to 80 keV for electron energy-loss spectroscopy (EELS) to minimize beam damage, to increase the EELS signal and to improve energy resolution (~1 eV). The Gatan Imaging filter (GIF, Gatan Inc) was operated at 0.2 eV /px in order that the O-K, the Fe-L and the Co-L edges can be analyzed simultaneously. Sample preparation was done by drop casting 2 µL of the NP dispersion on Holey-C grids followed by 14s of plasma cleaning.

X-ray diffraction

X-ray diffraction (XRD) using a Bruker D8 Advance equipped with a monochromatic copper radiation (Kα = 0.154056 nm) and a Sol-X detector in the 20− 70° 2θ range with a scan step of 0.02°. High purity silicon powder (a = 0.543082 nm) was systematically used as an internal standard.

Fourier transform infra-red

Fourier transform infrared (FT-IR) spectroscopy was performed using a Perkin Elmer Spectrum spectrometer in the energy range 4000−400 cm^{-1} on samples diluted in KBr pellets.

Granulometry

Granulometry measurements were performed using a nano-sizer Malvern (nano ZS) zetasizer at a scattering angle of 173° with 1 measure of 7 runs of 30 seconds.

X-ray absorption

XAS and XMCD spectra were recorded at the $L_{2,3}$ edges of Fe and Co, on the DEIMOS beamline at SOLEIL synchrotron.[3] **[Ref Deimos]** All spectra were recorded at 4.2 K under UHV conditions (10^{-10} mbar) and using total electron yield (TEY). The measurement protocol has previously been detailed by Daffé and *al.*[4] An external parallel magnetic field H^+ (respectively antiparallel H^-) was applied on the sample while a σ_+ polarized (σ_- polarized respectively) perpendicular beam was directed on the sample. Isotropic XAS signals were obtained by taking the mean of the $\sigma_+ + \sigma_-$ sum where $\sigma_+ = [\sigma_L(H^+) + \sigma_R(H^-)]/2$ and $\sigma_- = [\sigma_L(H^-) + \sigma_R(H^+)]/2$ with σ_L and σ_R the absorption cross section measured respectively with left and right circularly polarized X-rays. And XMCD spectra were obtained by taking the $\sigma_+ - \sigma_-$ dichroic signal with a ± 6.5 T applied magnetic field. The circularly polarized X-rays are provided by an Apple-II HU-52 undulator for both XAS and XMCD measurements while EMPHU65 with a polarization switching rate of 10 Hz was used to record hysteresis cycle at fixed energy.[3]
The samples consist of a silicon substrate where the colloidal suspension of the nanoparticles (ferrofluids) was previously drop casted to evaporate the solvent at room temperature. The substrates

were then fixed on a cupper sample holder. Measurements were performed between 700 and 740 eV at the iron edge and between 770 and 800 eV at the cobalt edge with a resolution of 100 meV and a beam size of 800*800 µm. Both XMCD and isotropic XAS signals presented here are normalized by dividing the raw signal by the edge jump of the isotropic XAS.

Mössbauer spectroscopy

^{57}Fe Mössbauer spectra were performed at 77 K using a conventional constant acceleration transmission spectrometer with a ^{57}Co(Rh) source and a bath cryostat. The samples consist of 5 mg Fe/cm^2 powder concentrated in a small surface due to the rather low quantities. The spectra were fitted by means of the MOSFIT program[5] involving asymmetrical lines and lines with Lorentzian profiles, and an α-Fe foil was used as the calibration sample. The values of isomer shift are quoted relative to that of α-Fe at 300 K.

SQUID magnetometry

SQUID magnetic measurements were performed on samples by using a Superconducting Quantum Interference Device (SQUID) magnetometer (Quantum Design MPMS-XL 5). Temperature dependent zero-field cooled (ZFC) and field cooled (FC) magnetization curves were recorded as follows: the sample was introduced in the SQUID at room temperature and cooled down to 5 K with no applied field after applying a careful degaussing procedure. A magnetic field of 7.5 mT was applied, and the ZFC magnetization curve was recorded upon heating from 5 to 400 K. The sample was then cooled down to 5 K under the same applied field, and the FC magnetization curve was recorded upon heating from 5 to 400 K. Magnetization curves as a function of a magnetic field (M(H) curves) applied in the plane of the substrate were measured at 5 and 400 K. The sample was also introduced in the SQUID at high temperature and cooled down to 5 K with no applied field (ZFC curve) after applying a subsequent degaussing procedure. The magnetization was then measured at constant temperature by sweeping the magnetic field from +7 T to −7 T, and then from −7 T to +7 T. To evidence exchange bias effect, FC M(H) curves have been further recorded after heating up at 400 K and cooling down to 5 K under a magnetic field of 7 T. The FC hysteresis loop was then measured by applying the same field sweep as for the ZFC curve. The coercive field (H_C) and the M_R/M_S ratio were measured from ZFC M(H) curves. The exchange bias field (H_E) was measured from FC M(H) curves. Magnetization saturation (M_S) was measured from hysteresis recorded at 5 K.

Themogravimetry

Thermogravimetry (TG) analysis was performed using a SDTQ600 from TA instrument. Measurements were performed on dried powders under air in the temperature range of 20 to 600 °C at a heating rate of 5 ° C/min.

Results and discussion

Synthesis strategy

Core@shell@shell nanoparticles were synthesized through a succession of three thermal decompositions of metal complexes. Firstly, pristine $Fe_{3-d}O_4$ nanoparticles (C) were synthesized through the thermal decomposition of iron (II) stearate ($FeSt_2$) in dioctyl ether (B_P = 290 °C) in presence of oleic acid used as surfactant. Then, a mixture of cobalt (II) stearate ($CoSt_2$) : $FeSt_2$ (1:2) in octadecene (B_P = 320 °C), according to $R_1 = (n_{shell1\ precursor})/(n_{core\ precursor})$=0.8, and oleic acid was added to a suspension of $Fe_{3-d}O_4$ nanoparticles. Hence, a cobalt-ferrite ($CoFe_2O_4$) shell was grown at the surface of pristine $Fe_{3-d}O_4$ nanoparticles in order to synthesize core@shell nanoparticles (CS). Finally, $FeSt_2$ ($R_2 = (n_{shell2\ precursor})/(n_{core\ precursor})$=1) was again decomposed thermally in ether dioctyl in presence of CS nanoparticles with the aim to grow a second $Fe_{3-d}O_4$ shell and to synthesize $Fe_{3-d}O_4$@$CoFe_2O_4$@$Fe_{3-d}O_4$ (CSS) nanoparticles.

Electron microscopy

TEM micrographs show that C nanoparticles display a homogeneous shape close to sphere and a narrow size distribution centered to 8.0 ± 0.9 nm. CS nanoparticles are larger than C (10.0 ± 1.5 nm), which corresponds to an average shell thickness of 1.0 nm. CSS nanoparticles are the largest (13.1 ± 2.2 nm) and include a second shell with a thickness of 1.6 nm.
It is worth to note that in the course of the different thermal decomposition, the shape of CS and CSS deviates from the spherical shape observed for C. This is due to the preferential growth of shells on the faceted seed nanoparticles which results in the broadening of size distribution.[6,7] Despite this fact, CS and CSS nanoparticles still display a good homogeneity of size distribution and shape.

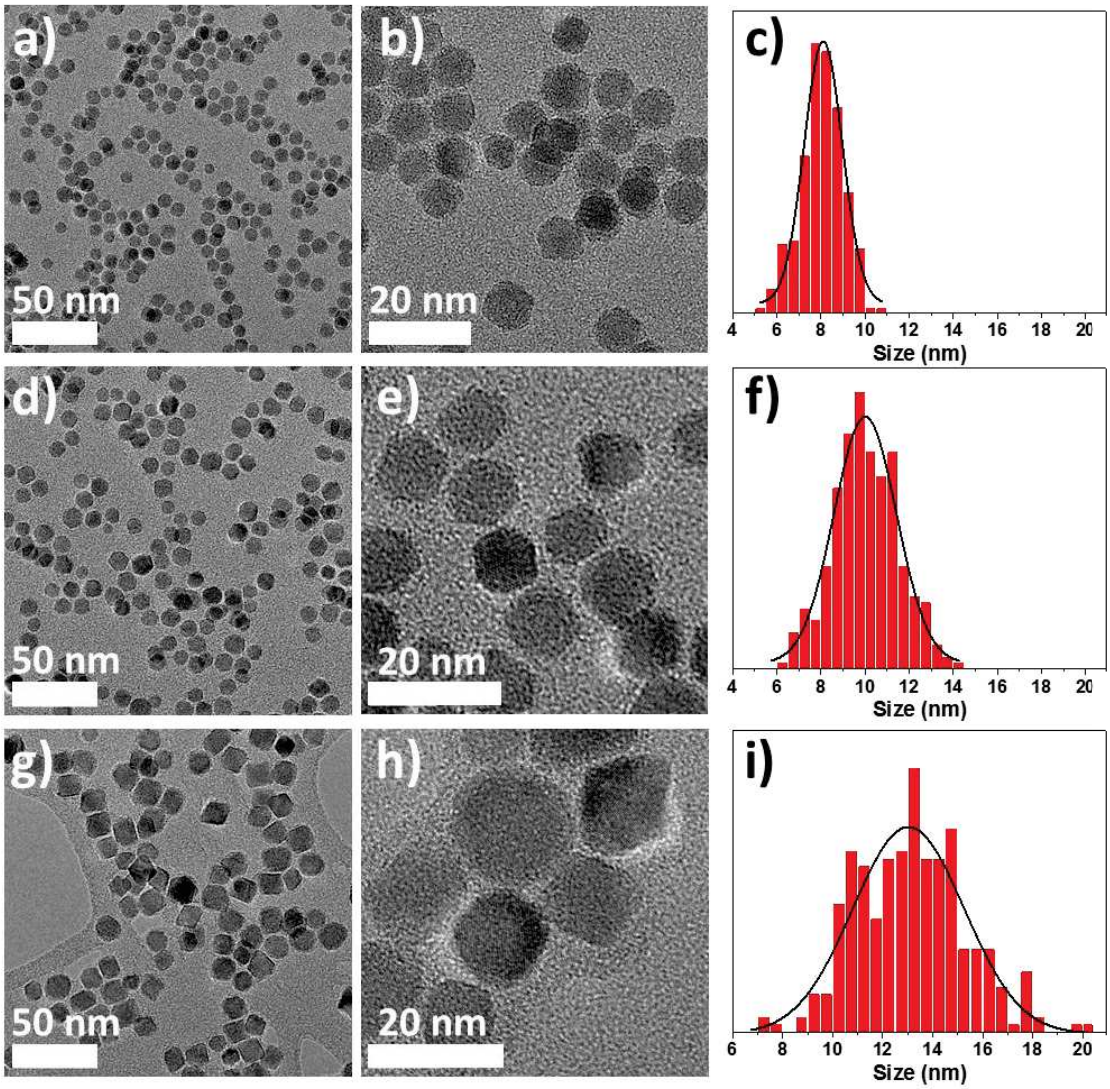

Figure 42. TEM micrographs of a, b) C nanoparticles, d, e) CS nanoparticles and g, h) CSS nanoparticles with (c, f, i) their corresponding size distributions.

Table 23. Structural characteristics of nanoparticles. Mean core sizes and shell thicknesses were calculated from TEM micrographs. Cell parameters and crystal sizes were calculated by refining XRD patterns.

	C	CS	CSS
Size (nm)	8.0 ± 0.9	10.0 ± 1.5	13.1 ± 2.2
Shell thickness (nm)	-	1.0	1.6
Fe : Co at. Ratio by EDX	-	86 : 14	94 : 6
Hydrodynamic diameter (nm)	8.7	13.5	18.2
Cell parameter (A)	8.370 ± 0.01	8.412 ± 0.01	8.410 ± 0.01
Crystal size (nm)	7.4 ± 0.5	10.1 ± 0.5	12.0 ± 0.5

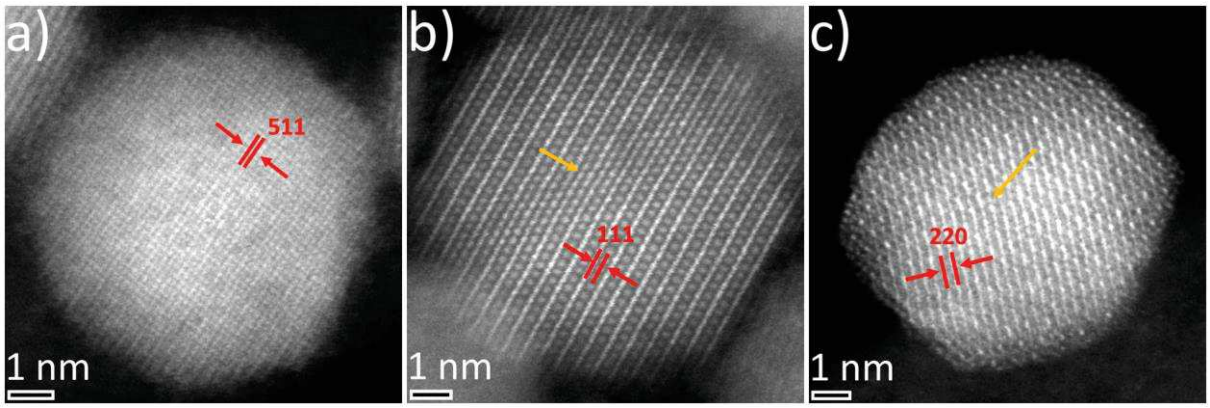

Figure 43. STEM-HAADF micrographs of a) C, b) CS and c) CSS nanoparticles showing the microstructures with zone axis 422, 112 and 110 respectively. Red indications show the indexation of hkl plans. Yellow arrows show stacking defects.

STEM-HAADF micrographs of C, CS and CSS nanoparticles display straight and continuous lattice fringes evidencing the single crystal-like structure of nanoparticles resulting from the successive epitaxial growth of the different shells. Crystal defects were observed in a few nanoparticles that are shown in the Figure 43. As the lines are still continuous, the defects are attributed to stacking defects. The inter-reticular distances between two fringes can all be attributed to a spinel ferrite phase such as magnetite or cobalt ferrite, confirming the chemical structure expected in the nanoparticles. These observations are supported by FFT micrographs of STEM HAADF micrographs (Figure 44). Moreover, FFT micrographs of the core and of the shell (Figure 44) show similar pattern for CS and CSS nanoparticles, agreeing with good epitaxial relationship between the core and shells.

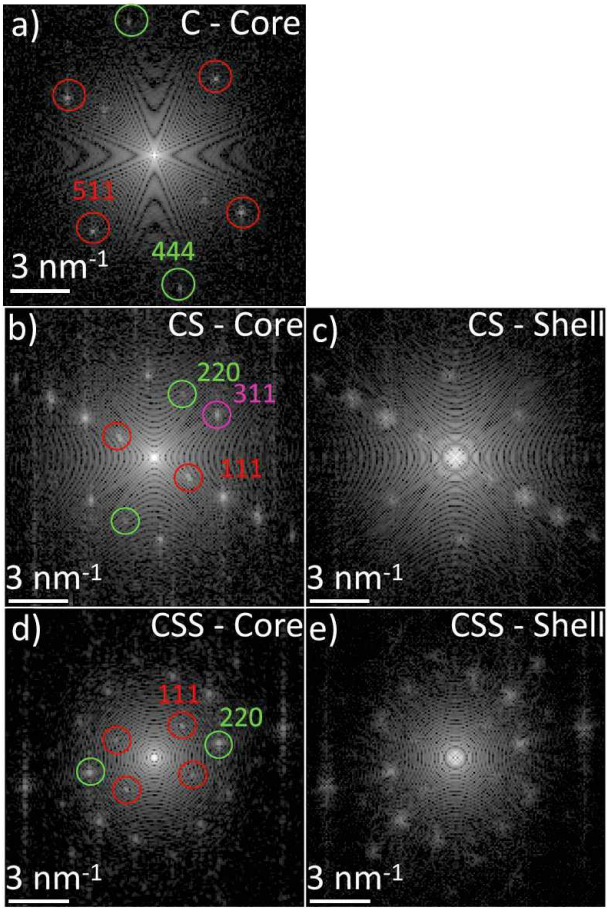

Figure 44. FFT performed on a) the core of C, b) the core and c) the shell of CS and d) the core and e) two shells of CSS from STEM HAADF micrographs. Colored circles evidence the related hkl reflection plan attributed from the jcpds file of magnetite and cobalt ferrite (n° 19-062 and 00-022-1086 respectively).

Energy dispersive X-ray spectrometry (EDX) performed on CS nanoparticles evidenced the presence of Fe (86 at. %) and Co (14 at. %). These values agree with the atomic ratios of Fe (84 %) and Co (16 %) calculated for a Fe_3O_4 core of 8.0 nm and a $CoFe_2O_4$ shell thickness of 1.0 nm thick as measured from TEM micrographs. In contrast to the $Fe_{3-d}O_4$@CoO nanoparticles,[8,9] this result evidence the lack of interfacial diffusion as expected by the synthesis of $CoFe_2O_4$ at the surface of the iron oxide seeds. EDX atomic ratios measured for CSS showed the increase of Fe (94 at. %) vs. Co (6 at. %). These values also agree with ratios calculated for a perfect Fe_3O_4@$CoFe_2O_4$@Fe_3O_4 core@shell@shell structure as measured from TEM micrographs (Fe : 93 at. % and Co : 7 at. %). This result also show the absence of interfacial diffusion which can be related to the presence of interfacial stoichiometric cobalt-ferrite.[10]

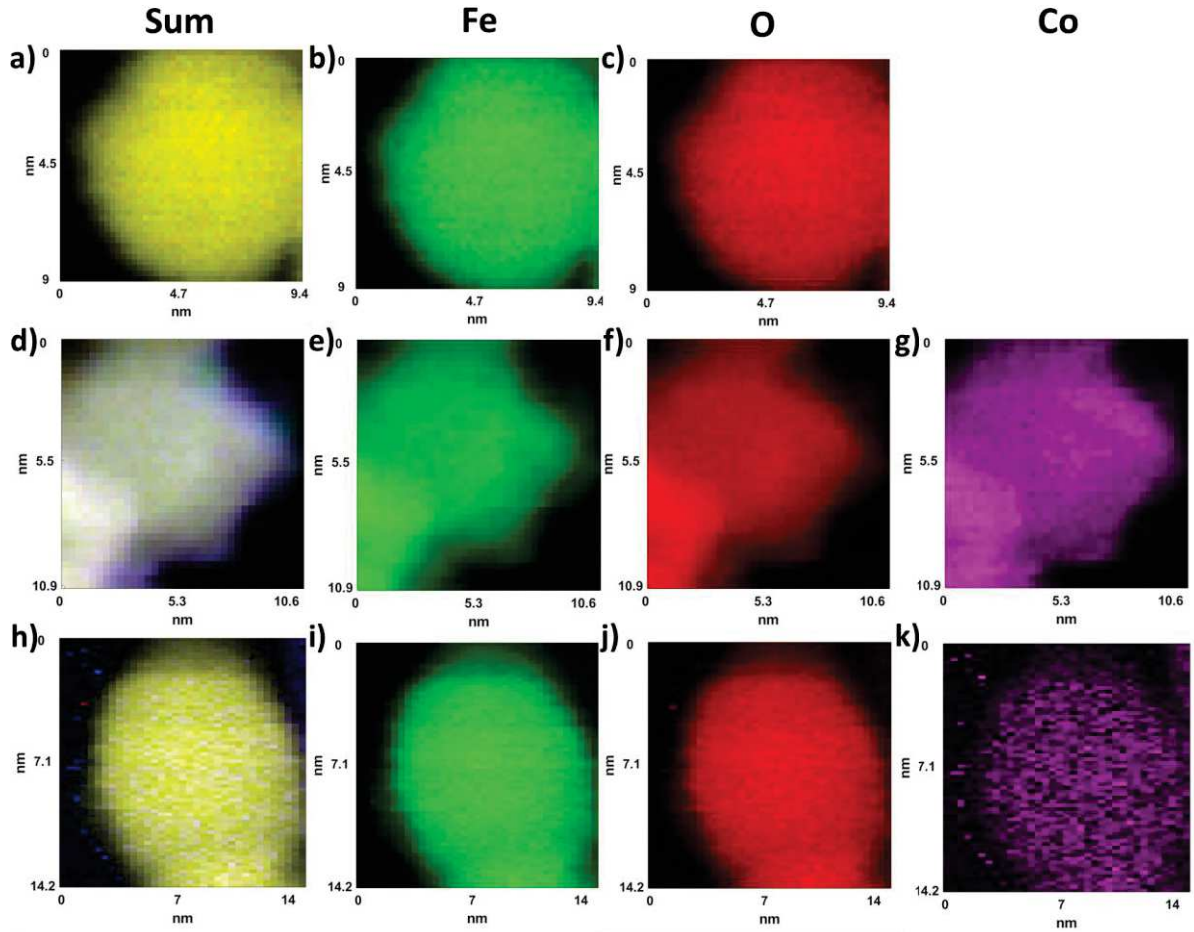

Figure 45. Elemental mapping performed by "EELS-SI" on isolated nanoparticles a-c) C, d-g) CS, h-k) CSS with a, d, h) the sum of the composite b, e, i) Fe-edge, c, f, j) O-edge and g, k) Co-edge.

The spatial distribution of Fe, O and Co atoms was investigated by performing elemental mapping with electron energy loss spectroscopy spectrum imaging (EELS-SI) at the Fe L-edge (green), Co L-edge (magenta) and O K-edge (red). EELS-SI micrographs and EELS-SI spectra of C nanoparticles evidence a homogeneous atomic distribution of Fe and O atoms all across the nanoparticle which agrees with an iron oxide structure. In the case of CS nanoparticles, Fe, O and Co spatial distributions also overlapped, which agree with the expected $Fe_{3-d}O_4$@$CoFe_2O_4$ core@shell structure. Finally, CSS nanoparticles also display a homogeneous spatial distribution of Fe, Co and O atoms all across the nanoparticle while the Fe/Co atomic ratio tends to increase in comparison with CS nanoparticles. It agrees with the expected $Fe_{3-d}O_4$@$CoFe_2O_4$@$Fe_{3-d}O_4$ core@shell@shell structure.

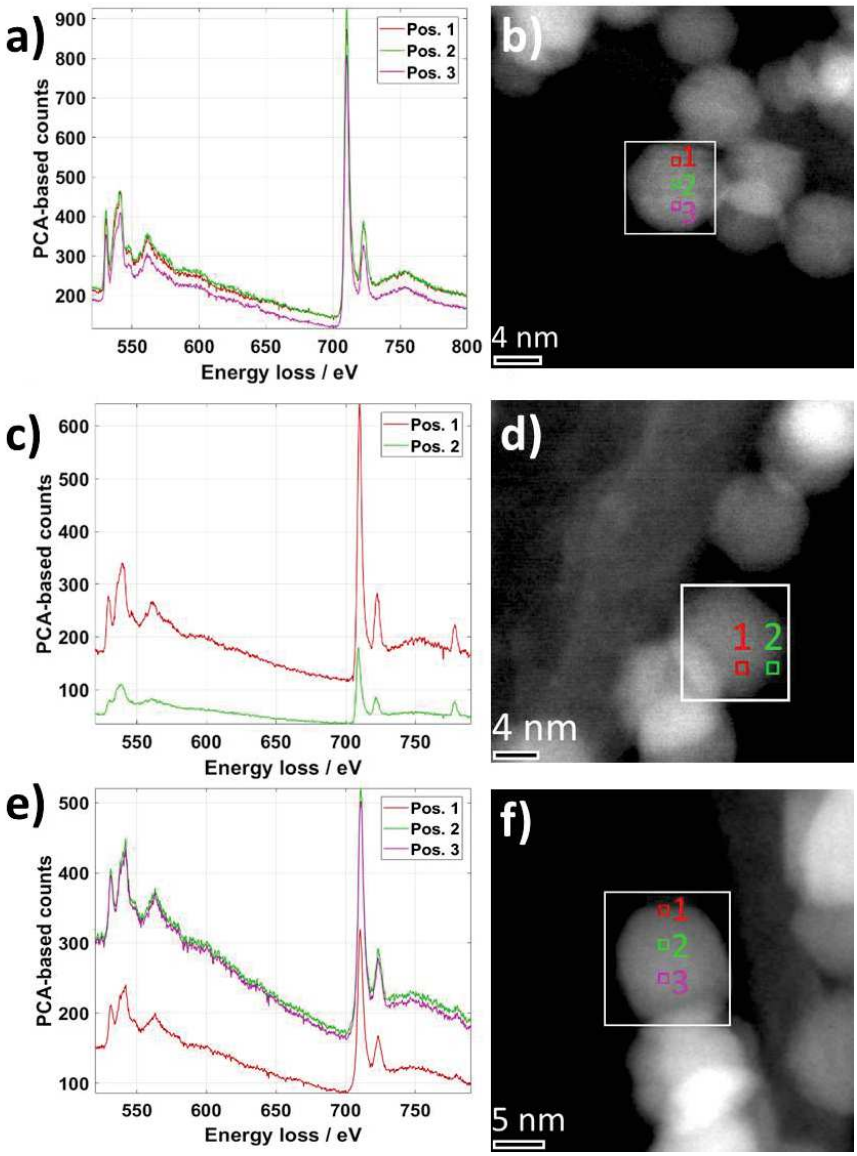

Figure 46. a, c, e) EELS spectra corresponding to specific positions displayed in b, d, f) the corresponding high resolution dark field micrographs of a, b) C, c, d) CS, e, f) CSS nanoparticles.

To further investigate the atomic spatial distribution in C, CS and CSS nanoparticles, EELS spectra were recorded with a resolution of 5 Å at different positions (Figure 46a). EELS spectra recorded from the edge to the center of a C nanoparticle are very similar, which corresponds to a homogeneous chemical composition.

EELS-SI spectra of CS evidence a lower intensity spectra on the edge than in the center of the nanoparticles, in accordance with a spherical morphology (Figure 46b). EELS-SI spectra show a high concentration of Fe atoms and the presence of Co atoms in the center of the nanoparticle. On the edge, the intensity of Fe atoms decreases while the intensity of Co atoms increases. Moreover, the shape of the EELS-SI spectra at the Oxygen *K*-edge is different on the edge of the nanoparticle compared to the center of CS or to the C nanoparticles. These observations agree with the expected $Fe_{3-d}O_4$@$CoFe_2O_4$ core@shell structure in agreement with EELS-SI micrographs. They are supported by the EELS section performed on CS nanoparticles (Figure 47) which shows the presence of iron and cobalt in the center of the nanoparticles while the Co content increases on the edge, concomitantly with a slight decrease of the Fe content.

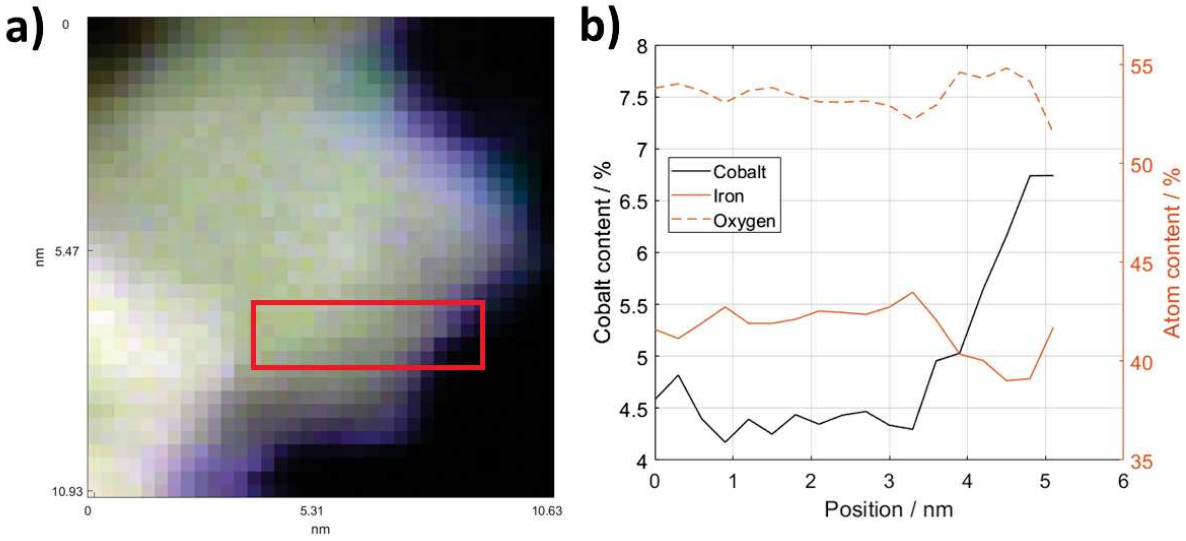

Figure 47. a) EELS-SI mapping of CS nanoparticles, the red rectangle show the working area to perform the b) EELS section

EELS spectra recorded from the edge to the center of a CSS nanoparticle also show that the intensity of all peaks are lower on the edges than in the center of the nanoparticles, agreeing with a shape close to sphere (Figure 46c). They also show signals corresponding to the O-K, Fe-L and Co-L edges whatever on the edge or on the center of the nanoparticle. However, no signal of Co was expected at the edge of the CSS nanoparticle as the second shell of 1.6 nm thick was expected to be solely composed of iron oxide. Therefore, the presence of such a low amount of Co on the edge may arise from the partial solubilisation and recrystallization of the cobalt ferrite shell of CS during the seed-mediated growth synthesis of the second shell in CSS.[10]

Geometrical phase analysis (GPA) performed on CS and CSS nanoparticles are presented in Figure 48. The reference region corresponds to the red line, and strain maps in Figure 48 show the presence of a few strains rich areas with crystal strains higher than 10 % and other large areas without strains. Unfortunately, due to the small size of the nanoparticles, it was not possible to calculate a mean strain in the nanoparticles. Nevertheless, qualitatively, the mean strains are much lower than 10 % in the whole nanoparticles. Indeed, the nanoparticles are too small to record a perfect GPA signal. The use of a small area as reference produce high experimental errors. Nevertheless, it shows the presence of strains that may arise from the lattice mismatch of the core@shell(@shell) nanoparticles.

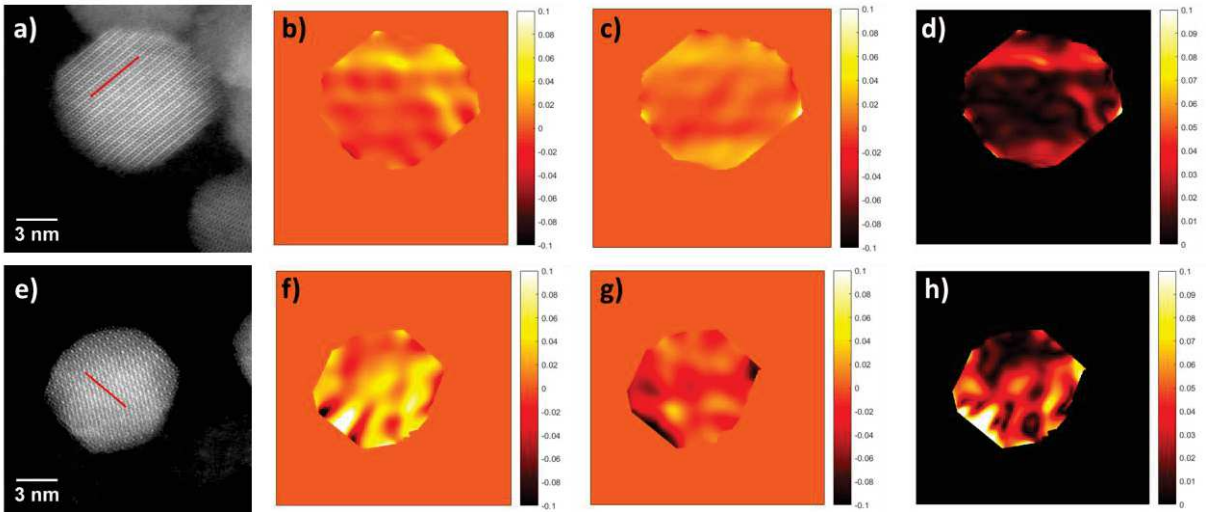

Figure 48. Geometrical Phase Analysis (GPA) of a, b, c, d) CS and e, f, g, h) CSS nanoparticles with a, e) the STEM micrographs corresponding to the strain maps b, f) parallel and c, g) perpendicular to the marked line in red. d, h) are the total amplitude.

TEM micrographs showed the size increase of the nanoparticles from C to CSS agreeing with the good deposition of the shells. HAADF micrographs and FFT performed on the edge and in the center of the nanoparticles evidenced good epitaxial relationship of the shells with the core. HAADF also showed the presence of slight stacking faults which may arise from the complexe structure of the CS and CSS nanoparticles. EELS-SI allowed drawing the chemical distribution of Co and Fe atoms which is in agreement with the expected structure of C and CS while the expected second iron oxide shell in CSS is almost not perceptible. However, EELS section performed at different positions revealed the spherical structure of each nanoparticle and the good synthesis of the $Fe_{3-d}O_4$, $Fe_{3-d}O_4@CoFe_2O_4$ and $Fe_{3-d}O_4@CoFe_2O_4@Fe_{3-d}O_4$ nanoparticles. Such analysis is in agreement with EDX measurements that showed the presence of both Co and Fe atoms in CS nanoparticles while the Fe:Co ratio increased for the CSS nanoparticles. Finally, GPA analysis evidenced the presence of strains within the nanoparticles.

Fourier transform infra-red

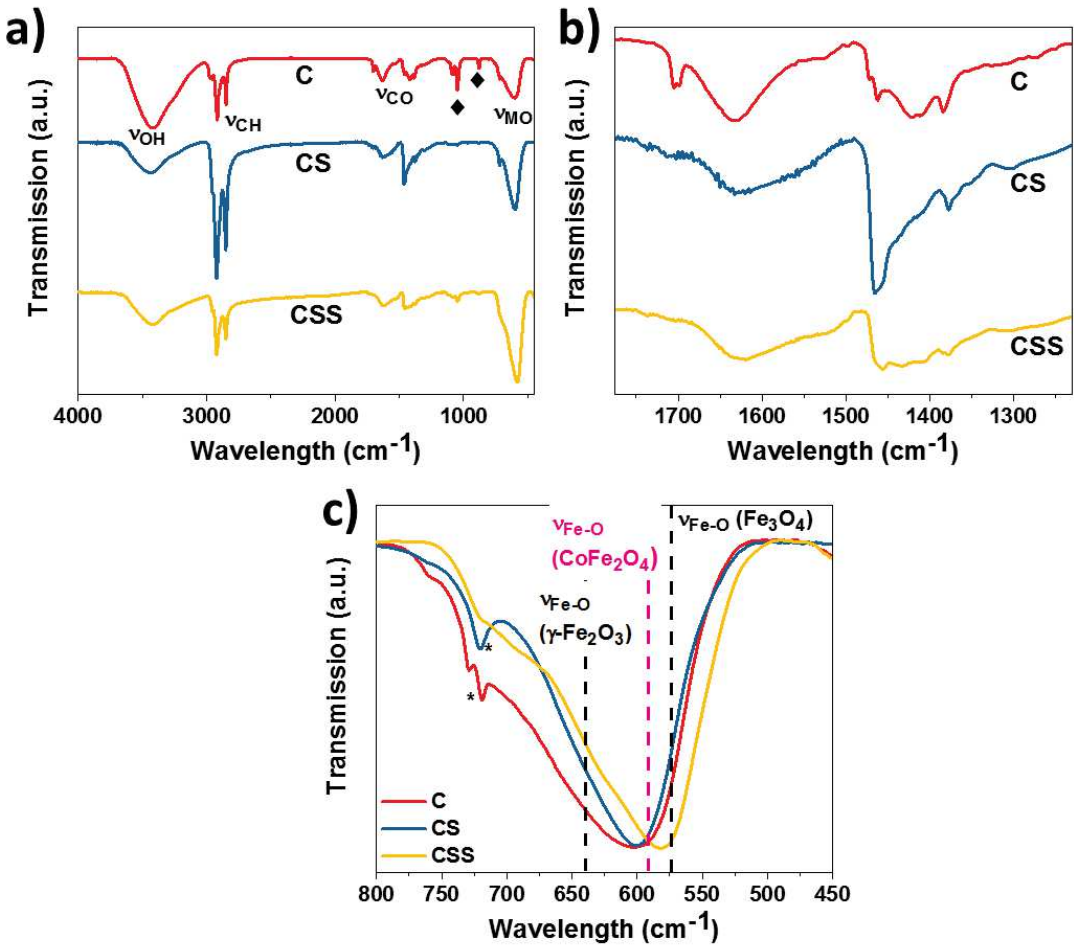

Figure 49. a) FT-IR spectra of C, CS and CSS with an enlargement of the FT-IR spectra in the range b) 1 230 to 1 775 cm^{-1} and c) 450 to 800 cm^{-1}. The bands at 879 and 1 044 cm^{1} (♦) in C and CSS do not belong to oleic acid or remaining stearates and are attributed to the presence of impurities.

Fourier transform infrared (FT-IR) spectra display several bands in the range from 4 000 to 450 cm^{-1} for C, CS and CSS. The bands at 2 918 and 2 849 cm^{-1} are respectively attributed to the symmetric and antisymmetric stretching vibration mode of alkyl chains (νC-H) from the oleic acid molecule. The bands centered at 1 635 and 1 414 cm^{-1} are attributed to the symmetric and antisymmetric stretching vibration mode of the carboxylic acid function (νCOO^-) of the oleic acid molecule grafted at the surface of the nanoparticles.[2,11] The non-observation of a band at 1 710 cm^{-1} attributed to the C=O stretches of free carboxylic acid groups evidence the absence of remaining free oleic acid molecules, except for

C. The distance Δ between the two $\nu_{as}(COO^-)$ and $\nu_s(COO^-)$ bands allows to determine the coordination mode of the organic surfactant grafted at the surface of the nanoparticles according to ref.[12–14] Indeed, for a large Δ distance of 320 to 200 cm^{-1}, the coordination mode is monodentate. For Δ lower than 110 cm^{-1}, it is chelating bidentate and for intermediate values of Δ between 190 and 140 cm^{-1}, it is bridging bidentate. In our study, the presence of several bands in the region of $\nu_{as}(COO^-)$ and $\nu_s(COO^-)$ bands corresponds to the existence of several coordination modes as we observed previously for nanoparticles with similar structures (see chapter III).

An enlargement of these FT-IR spectra in the region from 800 to 450 cm^{-1} evidenced large bands centered around 600 cm^{-1} which gives further indications on the chemical composition of the nanoparticles.[15] Fe_3O_4 magnetite (high Fe^{2+} content) displays a single band at 574 cm^{-1} with a shoulder at 700 cm^{-1} while γ-Fe_2O_3 maghemite (no Fe^{2+}) shows several oscillations from 800 to 600 cm^{-1} with a maximum centered at 639 cm^{-1}.[15] C nanoparticles display a broad band centered to 602 cm^{-1} which agrees with a composition between Fe_3O_4 and γ-Fe_2O_3 according to the general formula $Fe_{3-d}O_4$.[2] The position of this band for CS shifts down to 600 cm^{-1} and becomes narrower which agrees with a higher content in Fe_3O_4. We attributed it to results from the protection against oxidation of the iron oxide core thanks to the presence of the $CoFe_2O_4$ shell during the synthesis of CS. Indeed, in the case of $Fe_{3-d}O_4$(@$CoFe_2O_4$)$_x$@CoO nanoparticles, it was proved that the growth of a CoO shell limits the surface oxidation of the $Fe_{3-d}O_4$ core (see chapter III). Furthermore, the shift of this band can also be related to the formation of the cobalt ferrite shell where in this range, the M-O vibration mode displays a maximum centered at 590 cm^{-1}.[16] In the case of CSS, the band shifts down to 581 cm^{-1} which is lower than the $CoFe_2O_4$ band (590 cm^{-1}) and becomes closer to magnetite (574 cm^{-1}). Hence, the second shell would mainly consists of magnetite although we expected it to be fully oxidized. Baaziz and al.[2]

Finally, the bands at 721 cm^1 in C and CS (*) are attributed to the scissoring mode of the H-C-H bond of iron stearate and cobalt stearate. Although it could have been removed by further washes, we decided to not wash further the nanoparticles in order to avoid the aggregation of the nanoparticles.

FT-IR spectroscopy agrees with the presence of oleic acid molecules grafted at the surface of each nanoparticles which avoid them from an eventual aggregation. The displacement of the M-O vibration band has given further details on the evolution of the oxidation state in the nanoparticles and on the synthesis and possible growth of the $CoFe_2O_4$ shell. Surprisingly, according to FT-IR, the second iron shell does not seem to be subjected to oxidation and the CSS nanoparticles contain a high proportion of Fe^{2+} atoms.

Granulometry

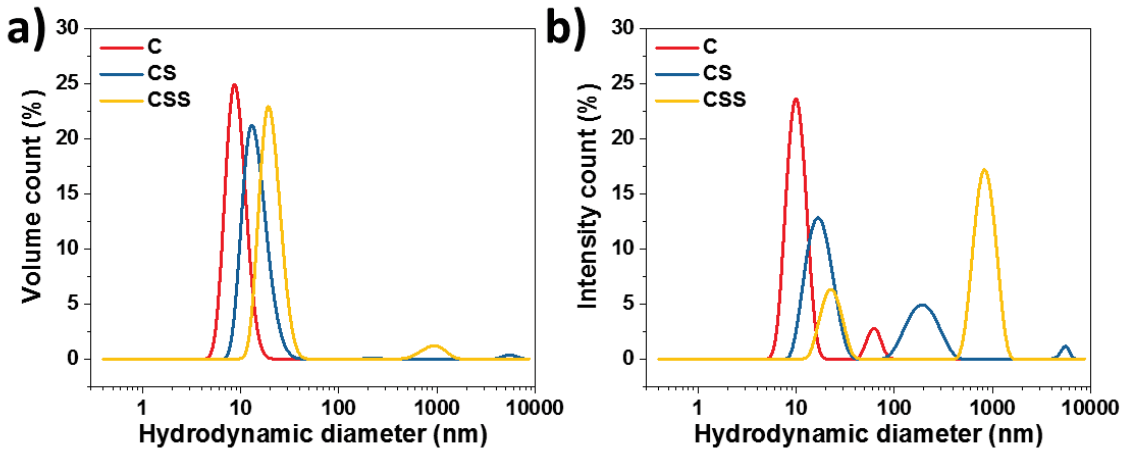

Figure 50. Granulometry measurements. The hydrodynamic diameter is plotted as a) volume count and b) intensity counts for C, CS and CSS.

Thanks to the presence of oleic acid grafted at the surface of the nanoparticles, their suspension is stable in most of organic solvents such as chloroform, toluene, THF, hexane. This stability was probed by granulometry measurements performed on C, CS and CSS nanoparticles in suspension in chloroform. Granulometry evidenced a monomodal distribution of hydrodynamic diameters plotted as volume counts for C, CS and CSS **(**Figure 50a). Some very small contributions corresponding to aggregates were observed for CS and CSS. They were highlighted by the distribution of hydrodynamic diameters plotted as intensity counts which showed supplementary contributions of aggregates for C nanoparticles. Nevertheless, according to the major peaks in volume count, C, CS and CSS display hydrodynamic diameters of 8.7, 13.1 and 23.1 nm respectively. These values are larger than sizes measured from TEM micrographs because granulometry measurements are sensitive to inorganic nanoparticles coated with surfactant organic molecules.

Granulometry experiments evidenced that the nanoparticles are stable in suspension in most organic solvent thanks to the presence of oleic acid as surfactant.

X-ray diffraction

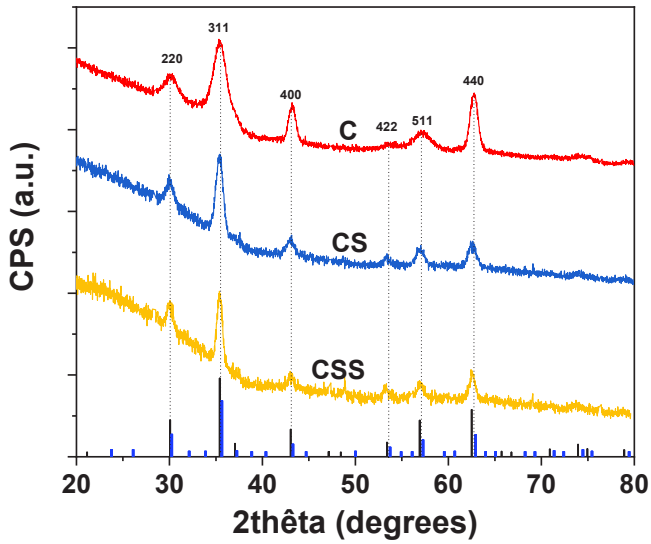

Figure 51. XRD patterns of C, CS and CSS nanoparticles. Black and blue bars correspond to the Fe_3O_4 (JCPDS card n° 19-062) and $CoFe_2O_4$ (JCPDS card n°00-022-1086) phases respectively.

XRD patterns recorded for each nanoparticle show peaks that were attributed to the reverse spinel structure (Figure 51). Due to a crystallization in the same Fd-3m space group and similar cell parameters for Fe_3O_4 and $CoFe_2O_4$ [a(Fe_3O_4) = 8.396 Å, JCPDS card n°19-062 and a($CoFe_2O_4$) = 8.392 Å, JCPDS card n°00-022-1086], both phases could not be discriminated by XRD. Nevertheless, the reduction of the peaks width with the addition of shells agrees with the increase of the crystal size. It confirms the good epitaxial relationship between the phases as observed by HR-TEM micrographs. Crystal sizes of 7.4, 10.1 and 12.0 nm for C, CS and CSS were calculated by the Debye-Scherrer equation (Table 23). The slightly smaller crystal sizes than the size measured from TEM micrographs can be explained by the 2D projection of the faceted nanoparticles by the electron beam that tends to overestimate the nanoparticles size.

The cell parameter of C nanoparticles (8.370 Å) is intermediate to the ones of magnetite (a = 8.396 Å, JCPDS card n° 19-062) and maghemite (a = 8.338 Å, JCPDS card n° 39-1346) which confirms the partial oxidation of C at their surface as shown by FT-IR analysis.[2] For CS nanoparticles, the cell parameter (8.412 Å) becomes larger than magnetite and cobalt ferrite. Such a high cell parameter was not expected due to crystallization in similar space groups with very close cell parameters. In articles on Fe_3O_4@$CoFe_2O_4$ nanoparticles, no data about cell parameters were found in order to explain this behavior.[17–22] However, Lopez-Ortega and al.[23] reported on the synthesis of $Co_{0.6\text{-}0.7}Fe_{2.4\text{-}2.3}O_4$ nanoparticles of different sizes with a cell parameters of 8.40-8.42 Å. They attributed the high cell parameters to arise from the stabilization of a pure cobalt-doped magnetite phase with Fe^{2+} that were not oxidized and to the presence of strains for such small size. Thus we can also attribute our high value to the presence of crystal strains that were observed with GPA. Hence, the structure of CS nanoparticles may consists in a non-oxidized magnetite core and a cobalt-ferrite shell.
The calculated cell parameter for CSS (8.410 Å) is similar to the cell parameter of CS. Hence, despite the growth of the $Fe_{3\text{-}d}O_4$ shell, it shows that the crystal structure of the CS nanoparticle has not been affected. We attributed the second shell to generate similar crystal strains at the second interface as in CS. Furthermore, the similar value of the lattice parameter agree with FT-IR analysis, i.e. a non-oxidized shell of magnetite which is very surprising when considering the exposition of nanoparticle to air prior to analysis.

The increase of the crystal size from C to CSS measured from X-ray diffraction patterns evidence the good epitaxial growth of the shells on the seed. While the cell parameter of the iron oxide core is coherent with the literature, the one of the CS and CSS nanoparticles appear to be higher than expected. Such high cell parameters can be inferred to arise from a high Fe^{2+} content, from the growth of the cobalt ferrite shell but also from the presence of crystal strains as evidenced by GPA. The similar cell parameters calculated for CS and CSS traduce a similar chemical composition of the second shell of the CSS compared to the whole chemical structure of the CS nanoparticles.

Mössbauer spectroscopy

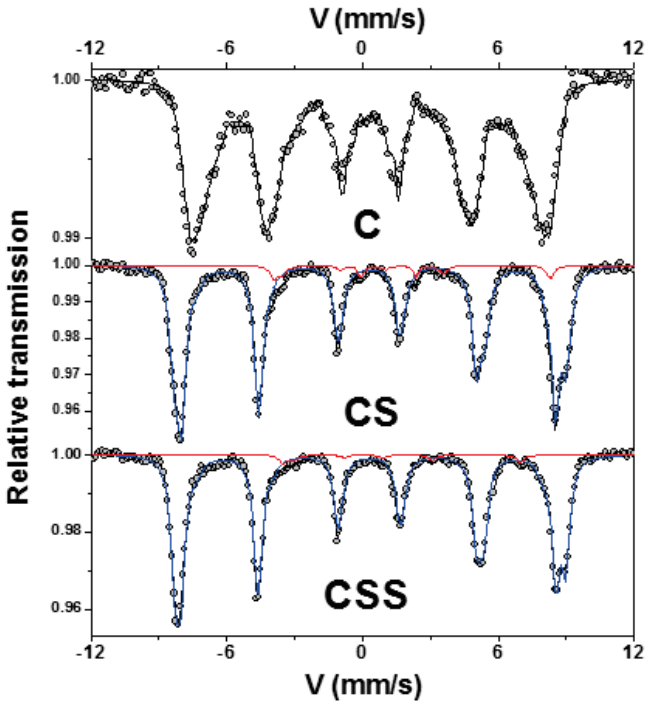

Figure 52. Mössbauer spectra of C, CS and CSS recorded at 77 K without applying a magnetic field.

^{57}Fe Mössbauer spectroscopy allows to get information on the valence state of each Fe atoms, the local electronic structure and the magnetic environment which are described by the isomer shift δ, the quadrupolar shift ε and the hyperfine field B_{hf}, respectively. It is a complementary technique to XAS-XMCD to determine the chemical composition of spinel structures.

^{57}Fe Mössbauer spectra were recorded for each nanoparticle at 77 K without applying any magnetic field. They all display a resolved sextet, consistent with magnetic blocked state. C nanoparticles display a broadening of the sextet lines which is ascribed to the faster relaxation time of a fraction of spins than the measurement time of the experiment ($\tau_m = 10^{-10} - 10^{-7}$ s)[24]. Such a superparamagnetic contribution can be attributed to a fraction of nanoparticle with small size (about 6.0 nm) as shown by size distribution (Figure 1c). This superparamagnetic contribution is also observed for CS (< 2 %) while it disappeared for CSS. These results are consistent with the literature. Iron oxide nanoparticles of 11 nm measured at 77 K display no superparamagnetic contributions in Mössbauer experiments,[25] while smaller iron oxide nanoparticles of 4.6 nm measured at 70 K display important superparamagnetic contributions.[26]

Because of the broad contribution of the sextet recorded for C nanoparticles, it was not possible to fit its spectra. Nevertheless, the mean isomer shift (0.44 mm/s) which is independent on the fitting procedure, lies between bulk magnetite (δ = 0.61 mm/s) and maghemite (δ = 0.40 mm/s).[27,28] A linear extrapolation allows to calculate that C is composed of 19 % of magnetite and 81 % of maghemite which is higher than the magnetite content (5%) reported for iron oxide nanoparticles with similar size.[2] We attributed such discrepancy to the use of a different precursor.[9]

In CS sample, the mean isomer shift value increases to 0.51 mm/s which is correlated to a larger amount of Fe^{2+} than C, in accordance with previous analysis (see chapter III). More precisely, the fitting values evidence a contribution of the isomer shift centered to 1.27 mm/s which is ascribed to 6 % of Fe^{2+} where one third of these Fe^{2+} does not display any hyperfine field and are in a superparamagnetic state at 77 K. However, this amount of superparamagnetic Fe^{2+} represents only 2 % of the total ^{57}Fe atoms (Fe^{2+} and Fe^{3+}) in CS nanoparticles, showing that the proportion of superparamagnetic ferrite is very low. Thus we attributed this small proportion to arise from the smallest nanoparticles of cobalt ferrite as discussed previously.
Two main contributions centered to lower isomer shifts of 0.53 and 0.54 mm/s were attributed to Fe^{3+} in Oh sites that account for 38 and 6 %, respectively. A third contributions centered to 0.41 mm/s was attributed to Fe^{3+} in Td sites and accounts for 50 %. Hence, it is possible to calculate a $Fe_{Td}^{3+}/Fe_{Oh}^{2+,3+}$ ratio which is equal to 0.5 in the case of a pure magnetite. The higher ratio of 1 calculated for CS usually corresponds to a lack of Fe^{2+} although it may also be attributed to a superstoichiometry in oxygen or to the presence of vacancies.[29] Furthermore, in $CoFe_2O_4$, Co^{2+} cations replace the Fe^{2+} in Oh sites, which participates to increase the $Fe_{Td}^{3+}/Fe_{Oh}^{2+,3+}$ ratio compared to a pure magnetite.
The high hyperfine field of 53.4 and 51.0 T for Fe^{3+} in Oh and Td sites respectively are attributed to long Fe-O distances due to the presence of Co cations in the nearest neighbors,[30,31] which correspond to the presence of cobalt ferrite. At the opposite, the hyperfine fields of 47.6 and 37.6 T measured for Fe^{3+} and Fe^{2+} in Oh sites (6 % and 4 %, respectively) evidence that a small portion of iron oxide corresponding to the core is not in contact with Co^{2+} cations.

Previous studies showed that $Fe_{2.95}O_4$ and $(Co_{0.05}Fe_{0.95})[Co_{0.95}Fe_{1.05}]O_4$ nanoparticles display mean isomer shifts of 0.61 mm/s[32]) and 0.45 mm/s,[33] respectively. Therefore, the mean isomer shift of CS (0.51 mm/s), would correspond to a composition of 63 % of $CoFe_2O_4$ and 37 % of magnetite, i.e. a core size of 6.8 nm and a shell thickness of 1.6 nm. As the $CoFe_2O_4$ calculated thickness is slightly larger than the measured thickness from TEM micrographs, we expect the formation of the $CoFe_2O_4$ shell to proceed first following a partial solubilisation of the iron oxide core which recrystallize in cobalt ferrite.[10] Such a mechanism is in accordance with our previous study on $Fe_{3-d}O_4$@CoO reheated nanoparticles (see sample CS2r, chapter III).

In CSS, the mean isomer shift decreases to 0.49 mm/s which evidence a lower content of Fe^{2+}. More precisely, it corresponds to a contribution of 3 % centered to 1.04 mm/s. Other contributions centered to lower isomer shifts (0.53 and 0.50 mm/s) were attributed to Fe^{3+} in Oh sites (6 % and 46 %, respectively). A third contribution centered to 0.33 mm/s was attributed to Fe^{3+} in Td sites (45 %). The lower ratio $Fe_{Td}^{3+}/Fe_{Oh}^{2+,3+}$ (0.82) than CS (1) is ascribed to an increase of iron oxide compared to the cobalt ferrite content, in accordance with XAS, XMCD measurements. The high hyperfine fields of 52.5 and 51.8 T for Fe^{3+} in Oh and Td sites that accounts for 46 % and 45 %, respectively, are attributed to long Fe-O distances due to Co atoms as near neighbors. Their subspectral area slightly increased in comparison to the CS nanoparticles (about 3 points). The increase of the $CoFe_2O_4$ fraction is more clearly observed from the mean isomer shift which corresponds to 75 % of $CoFe_2O_4$ and 25 % of Fe_3O_4. It is confirmed by the low contributions of Fe^{3+} and Fe^{2+} in Oh sites (6 % and 3 %) which do not interact with Co atoms (47.1 and 32.4 T) and which correspond to a lower relative proportion of the core within

the nanoparticle. Therefore, the size increase from CS to CSS is mainly ascribed to the formation of $CoFe_2O_4$.

The decrease of Fe^{2+} from CS to CSS in Mössbauer is at the opposite of XMCD experiment while both experiments agrees on the increase of cobalt ferrite within the nanoparticles. However, it has been calculated from Mössbauer experiments that the volume of iron oxide has increased from CS to CSS. Thus the very slight decrease in Fe^{2+} can be attributed to volume effects where the increase of cobalt ferrite content is more consequent than the increase of the iron oxide content.
Indeed, considering that the Fe : Co atomic ratio from EDX measurements increases from CS to CSS, Mössbauer and XMCD measurements evidence that the iron oxide in the second shell displays a similar chemical structure than the core in CS.

The decrease of Fe^{2+} from CS to CSS in Mössbauer is at the opposite of XMCD while both experiments agree on the increase of cobalt ferrite within the nanoparticles. From Mössbauer, it is possible to calculate the composition of the CSS nanoparticles which consist of a core of 6.8 nm surrounded by a 2.9 nm thick $CoFe_2O_4$ shell and a 0.3 nm thick Fe_3O_4 shell. These results show that an additional $CoFe_2O_4$ layer of 1.3 nm was grown on CS nanoparticles during the synthesis of CSS, thus consistent with the slight decrease of Fe^{2+} with respect to Fe^{3+}. In this case, the chemical structure of the second $CoFe_2O_4$@$Fe_{3-d}O_4$ shell is similar to the composition of the CS nanoparticles which is supported by a similar cell parameters of CS and CSS. Moreover, the additional iron oxide shell was observed with FT-IR and EDX spectroscopy. It was also observed by XAS and XMCD which tend to over-estimate the Fe^{2+} contribution because of the surface sensitivity of the TEY recording mode.

Table 24. Refined values of hyperfine parameters calculated from the fit of ^{57}Fe Mössbauer spectra recorded at 77 K and under zero magnetic field.

Sample	isomer shift relative to α-Fe (mm/s)	Width at half height (mm/s)	quadrupole shift (mm/s)	Hyperfine field (T)	Relative subspectral area (%)
C	**0.44**	-	**0.04**	-	**42.8**
CS	0.53	0.49	-0.04	53.4	38
	0.41	0.43	0.02	51	50
	0.54	0.5	0.02	47.6	6
	1.27	0.4	2.18	37.6	4
	1.27	0.23	2.37	-	2
	0.51	-	**0.12**	**50.5**	-
CSS	0.5	0.47	0.08	52.5	46
	0.33	0.4	-0.07	51.8	45
	0.53	0.5	-0.09	47.1	6
	1.04	0.4	1.74	32.4	3
	0.49	-	**0.05**	**51.2**	-

The refinement of the Mössbauer spectra recorded for C, CS and CSS nanoparticles shows that C nanoparticles is partially oxidized. CS nanoparticles display a higher content of Fe^{2+} compared to the core, in accordance with the preservation of the core against oxidation thanks to the cobalt ferrite shell.

The high hyperfine fields of the Fe atoms show that they are close to Co atoms, agreeing with a cobalt ferrite structure. Mössbauer spectroscopy allowed to calculate that CS is actually composed of a core of 6.8 nm in size, surrounded by a 1.6 nm thick $CoFe_2O_4$ shell. It was calculated that in the CSS nanoparticles, the thickness of the cobalt ferrite shell increase to 2.9 nm and that a 0.3 nm thick of $Fe_{3-\delta}O_4$ shell surrounds all of this. The growth of the cobalt ferrite shell was favored by the presence of remains of Co precursors during the synthesis of the second shell but also due to a possible partial solubilisation-recrystallisation process occurring in seed-mediated growth approach.

X-ray absorption

X-ray absorption spectra (XAS) and X-ray magnetic circular dichroism (XMCD) experiments were performed at the DEIMOS beamline at synchrotron SOLEIL. XAS and XMCD are particularly suited to study the chemical composition and the structure of nanoparticles as they allow to probe separately the site occupancy in the spinel structure of Fe and Co cations. Moreover, thanks to their orbital selectivity, it is possible to discriminate the valence state of a cation. Hence, this technique is complementary to XRD and EELS-mapping as it allows to determine precisely the chemical composition of each core and shells and especially to differentiate maghemite, magnetite and cobalt-ferrite phases.

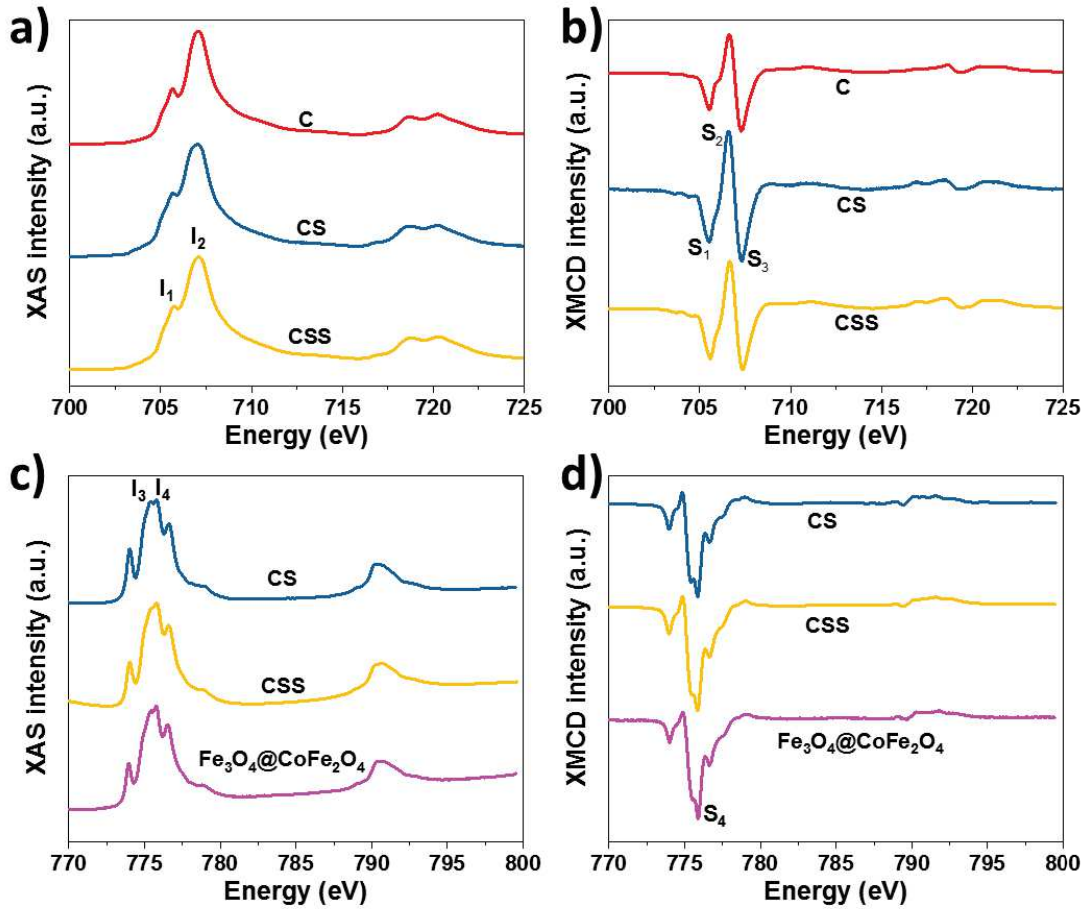

Figure 53. a, c) Isotropic XAS and b, d) XMCD spectra at the a, b) Fe $L_{2,3}$ edges and at the c, d) Co $L_{2,3}$ edges of C, CS and CSS nanoparticles.

The isotropic XAS and XMCD spectra recorded at the Fe $L_{2,3}$ edges (Figure 53) are all typical of a spinel ferrite structure.[34–36] XAS spectra evidenced two main contributions in the L_3 region where the intensity of peak I_1 arises mainly from the contribution of Fe^{2+} in octahedral sites (Oh) while the intensity of peak I_2 arises mainly from the contribution of Fe^{3+} in octahedral and tetrahedral (Td) sites. Hence, the intensity ratio I_1/I_2 brings further information on the Fe^{2+} content within the nanoparticles. Indeed, the

Fe^{2+} rich content phase of Fe_3O_4 magnetite and the γ-Fe_2O_3 maghemite phase (no Fe^{2+}) correspond to a ratio of 0.71[37] and 0.35,[37] respectively. C nanoparticles display a I_1/I_2 ratio of 0.53 that is between the one of magnetite and maghemite and agrees with previous analysis on a partially oxidized $Fe_{3-d}O_4$ nanoparticles. It increases to 0.64 for CS nanoparticles, which agrees with a greater contribution of Fe^{2+} as observed for $Fe_{3-d}O_4$@CoO nanoparticles (see chapter III). Indeed, it was attributed to the preservation of Fe^{2+} in the core against oxidation thanks to the presence of the cobalt ferrite shell (see chapter III).[9]
In CSS, the I_1/I_2 ratio is of 0.62 being similar to CS. As the TEY recording mode is mostly sensitive to the surface,[38,39] the Fe cations from the second shell represent the largest contribution to this value. Therefore, the second shell seems to display a similar ratio between Fe^{2+} and Fe^{3+} to the one in the CS nanoparticles. It shows thus that the two $CoFe_2O_4$@$Fe_{3-d}O_4$ shells have a similar chemical composition to the CS nanoparticles. However, considering the slight decrease, it may show some slight oxidation of Fe^{2+} at the surface of the second shell.

XMCD spectra recorded at the Fe $L_{2,3}$ edges display three main peaks in the L_3 region where the S1 peak is attributed to Fe^{2+} and Fe^{3+} in Oh sites while the S3 peak arises from the contribution of Fe^{3+} in Oh sites. The S2 peak corresponds to Fe^{3+} in Td sites and displays an opposite contribution to peaks S1 and S3 due to the antiparallel magnetic coupling of Fe cations in Td sites compared to Oh sites. It is typical of the ferrimagnetic coupling of Fe spins in the inverse spinel structure of iron oxide and cobalt ferrite. Moreover, the intensity ratio between peaks S1-S2 and S2-S3 allows to quantify the oxidation state of the Fe^{2+}. Hence, pure magnetite displays a (S1+S2)/(S2+S3) ratio of 1.14 while maghemite displays a ratio of 0.69.[37] For C, this ratio (0.77) is intermediate to magnetite and maghemite as expected for partially oxidized iron oxide nanoparticles (see chapter II and III). It then increases to 0.85 for CS, thus getting closer to magnetite, which agrees with the chemical protection of the core, against oxidation, by the shell as observed in the case of $Fe_{3-d}O_4$@CoO nanoparticles (see chapter III). As the total electron yield recording mode (TEY) is mostly sensitive to the surface, this high ratio also mean that the core has a high quantity of Fe^{2+}. In CSS, this ratio increases to 0.90, getting closer to the one of magnetite in agreement with FTIR and XRD measurements. This variation agrees with the growth of an iron oxide shell, in agreement with XAS measurements at the Fe $L_{2,3}$ edges. It also evidences a great Fe^{2+} content despite the low thickness of the second shell.

Isotropic XAS spectra recorded at the Co $L_{2,3}$ edges confirmed the presence of Co^{2+} in Oh sites of a spinel ferrite structure.[36,39] The CS spectra also showed that the I_4 peak displays a slightly higher intensity than I_3 which is even more clearly observed for CSS. This result qualitatively shows the increase of the cobalt ferrite content[9,40] from CS to the CSS nanoparticles.

The XMCD spectra at the Co $L_{2,3}$ edges also show the occupancy of Oh sites by Co^{2+} cations,[39,41] in agreement with previous studies on similar nanoparticles.[9] All spectra were normalized to the edge of the energy jump. Therefore, the intensity of the S4 peak reflects the quantity of uncompensated Co spins normalized by the quantity of Co atoms within the nanoparticles.[42]
According to the work of Daffé and *al.*[43], a pure $CoFe_2O_4$ nanoparticle can reach 86 % of intensity for the S4 peak. CS and CSS nanoparticles both display a high intensity of 95 % and 108 %, which confirms the presence of cobalt ferrite within the nanoparticles, in agreement with XAS results. Moreover, their intensity is higher than the one of the previously cited nanoparticles. This can be attributed to a higher spin canting effect in the small $CoFe_2O_4$ nanoparticles of 6.7 nm of diameter but also to a different synthesis protocol compared to the CS and CSS nanoparticles.
The Fe_3O_4@$CoFe_2O_4$ reference sample displays an important XMCD signal where the intensity of peak S4 reaches 102 %, supporting the presence of $CoFe_2O_4$ in CS and CSS nanoparticles. We attributed the increase of the intensity of peak S4 from CS to CSS, to the presence of remaining of cobalt stearate in CS (see FT-IR) that reacted during the growth of the $Fe_{3-d}O_4$ shell to increase the cobalt ferrite content.

Table 25. XAS and XMCD ratio of the different samples and of references.

Sample	Size (nm)	I1/I2	(S1+S2)/(S2+S3)	S4 (%)
C	8.0	0.53	0.77	-
CS	10.0	0.64	0.85	95
CSS	13.1	0.62	0.90	108
Fe_3O_4@$CoFe_2O_4$ From ref	7.2	0.82	0.85	102
Magnetite reference	-	0.71	1.14	-
Maghemite reference	-	0.35	0.69	-

XAS, XMCD curves recorded at the Fe edges showed that the iron oxide core displays a slight oxidized structure which is due to its small size, as discussed in the literature. The Fe^{2+} content then increases in CS by means of the core protection by the cobalt ferrite shell. In CSS, the Fe^{2+} content increases even more, in accordance with FT-IR and XRD analysis. Thus the iron oxide second shell appears to be only slightly oxidized while due to its small thickness, it was expected to be fully oxidized. In parallel, XAS and XMCD spectra recorded at the Co edge evidenced the increase of the cobalt ferrite content from CS to CSS nanoparticles. Thus the second shell of CSS displays a similar chemical structure than the one of the whole CS nanoparticles, explaining thus the similar cell parameters calculated for CS and CSS from the XRD patterns.

Element specific hysteresis

Element-specific magnetization curves were recorded at 4 K between + 6.5 and – 6.5 T at the Fe S2, S3 and Co S4 peak energies for CS and at the Fe S2 and Co S4 peak energies for CSS.

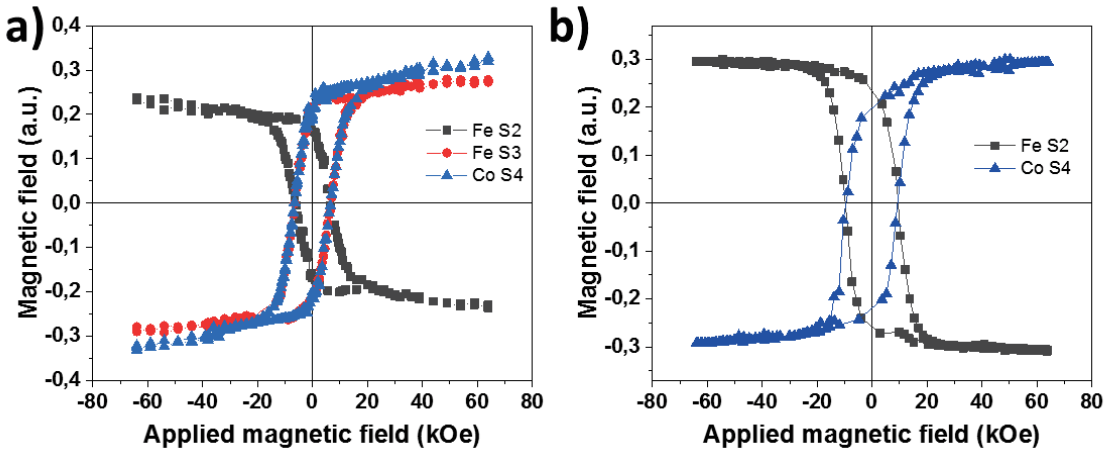

Figure 54. Element-specific magnetization curves recorded at 4 K by XMCD at the Fe and Co $L_{2,3}$ edges in a) CS, b) CSS.

The selective hysteresis curves recorded for CS at different energies showed similar coercive fields (H_C) with a mean value of 6.5 kOe. It shows that Fe spins in Td and Oh sites and Co spins in Oh sites are magnetically coupled together in both core and shell (see chapter III).[9,44]
The H_C of CS are much larger than the reported values of 2.1 (Fe edge) and 3.9 (Co edge) kOe measured at 3 K for Co-doped magnetosomes.[39] Such high H_C for our nanoparticles can be explained by the good

quality of our interface as well as by a larger volume of cobalt ferrite. However, the high $<H_C>$ of CS, featured by a size of 10.0 nm, is lower than the reported value of 10.7 kOe for $Fe_3O_4@CoFe_2O_4$ of 12.3 nm synthesized in similar conditions and measured at 4 K.[9] We attributed such discrepancy to volume effects.[45,46]

The selective hysteresis curve of CSS recorded at different energies also evidenced similar H_C with $<H_C>$ = 9.5 kOe. The increase of H_C from CS to CSS can be attributed to an increase of the volume of the nanoparticles,[45,46] an increase of cobalt ferrite within the nanoparticles as TEY is mostly sensitive to the surface, or with the increase of hard-soft coupling due to the double iron oxide/cobalt ferrite interface.
The $<H_C>$ of CSS is still lower than the H_C of 10.7 kOe recorded for $Fe_3O_4@CoFe_2O_4$ of 12.3 nm[9] which is attributed to a lower content of cobalt ferrite in CSS than for the reported nanoparticles. Moreover, the $<H_C>$ of CSS is also lower than the reported value of 10.9 kOe for $Fe_{3-d}O_4@(CoFe_2O_4)_x(CoO)_y(CoFe_2O_4)_z@Fe_{3-d}O_4$ nanoparticles measured at 4 K (sample CSSB from chapter III). The $Fe_{3-d}O_4@(CoFe_2O_4)_x(CoO)_y(CoFe_2O_4)_z@Fe_{3-d}O_4$ nanoparticles display a core size of 10.1 nm with a $(CoFe_2O_4)_x(CoO)_y$ first shell of 2.0 nm thick and a second shell of 0.6 nm thick. Hence the higher $<H_C>$ for the $Fe_{3-d}O_4@(CoFe_2O_4)_x(CoO)_y(CoFe_2O_4)_z@Fe_{3-d}O_4$ can be attributed to volume effects and/or to a more efficient interfacial coupling effects due to the presence of the CoO phase that induces FiM-AFM exchange-biased coupling.

The M_R/M_S ratio, also called the alignment ratio, describes the orientation of spins. For CS and CSS nanoparticles, the average M_R/M_S ratios are similar (73 and 74 % respectively) showing a similar magnetic hardness in both systems. A deeper look evidences that the alignment ratio at the Co edge is slightly lower than at the Fe edge. This effect has already been observed for Co doped magnetite[39] where the authors do not discuss this trend. However, we attributed this to the harder magnetic behavior of the CoO phase than the $Fe_{3-d}O_4$ one, where magnetic moments in the CoO structure are strongly directed along the easy magnetization axis. Hence the the magnetization in the CoO structure has more difficulties to align with the external applied magnetic field than in the $Fe_{3-d}O_4$ one, giving rise to a higher M_S and a lower alignment ratio.
Moreover, the M_R/M_S ratio of CS and CSS are lower than the 83-87 % expected for randomly spherical ferrite nanoparticles[47] but is close to the 82 and 89 % (Fe and Co edges respectively) of magnetite doped cobalt nanoparticles.[39] It is also higher than the previous reported values of 60 and 62 % (Fe and Co edges respectively) for $Fe_{3-d}O_4@(CoFe_2O_4)_x(CoO)_y@Fe_{3-d}O_4$ nanoparticles (chapter III) agreeing thus with a harder magnet in CSS.

Table 26. Magnetic characteristics of element specific magnetization curves.

Sample	H_C Fe S2 (kOe)	H_C Fe S3 (kOe)	H_C Co S4 (kOe)	$<H_C>$ (kOe)	M_R/M_S Fe S2 (%)	M_R/M_S Fe S2 (%)	M_R/M_S Co S4 (%)	$<M_R/M_S>$ (%)
CS	6,3	6,7	6,6	**6,5**	74	79	69	**74**
CSS	9,7	-	9,4	**9,5**	79	-	67	**73**

The H_C measured at the different Fe and Co edges for CS and CSS nanoparticles are identical in a nanoparticle, evidencing strong magnetic coupling within the nanoparticles. The increase of the mean H_C from CS to CSS can be attributed to the increase of the hard cobalt ferrite content in agreement with previous analysis. CS and CSS evidenced similar alignement ratio which demonstrate a similar hard-soft behavior related to a similar chemical structure in accordance with the determination of the cell parameters from XRD patterns.

SQUID magnetometry

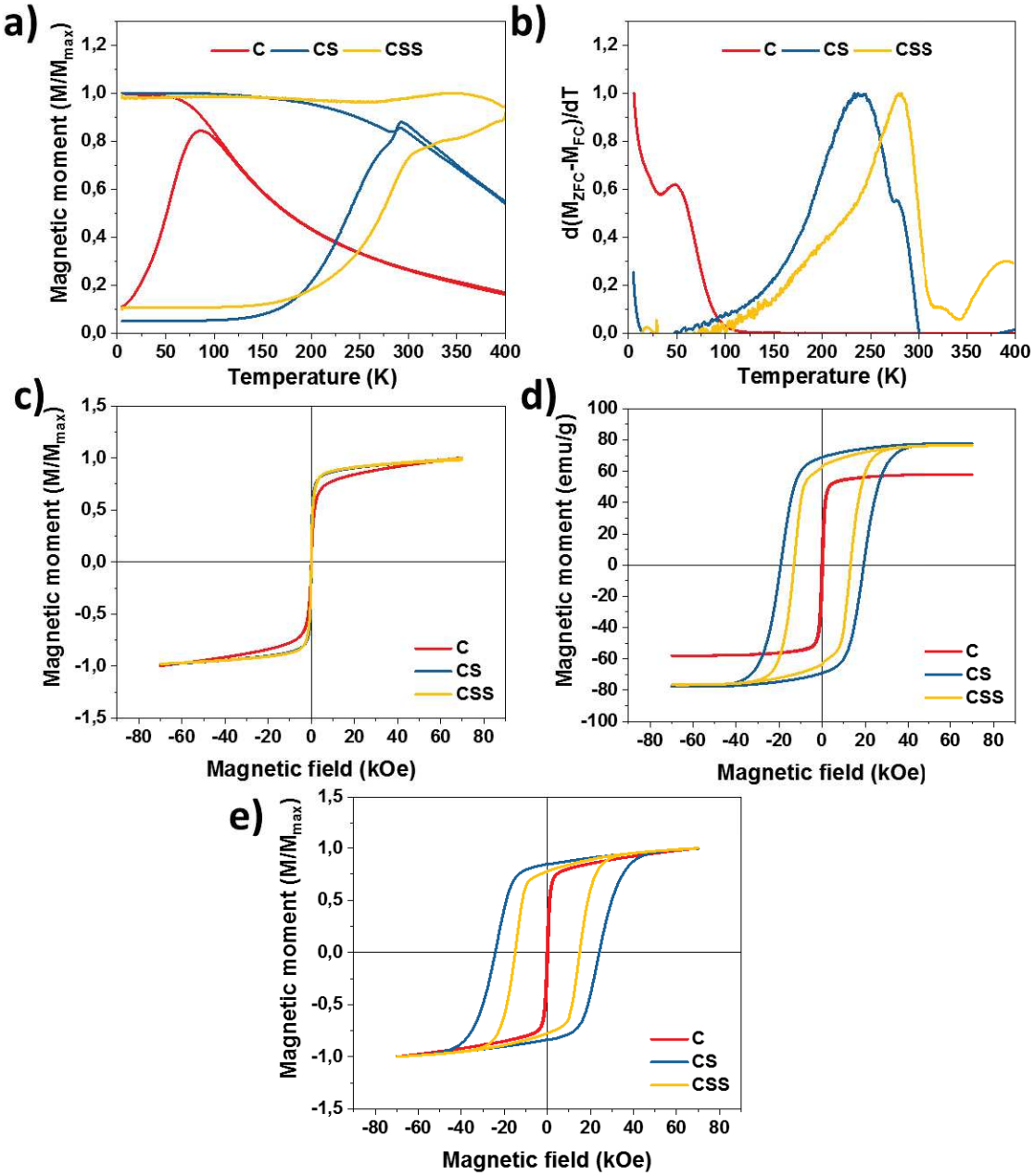

Figure 55. Magnetic characterizations of C, CS and CSS. a) Magnetization curves recorded against temperature after zero field cool (ZFC) and field cool (FC). b) $d(M_{ZFC}-M_{FC})/dT$ curves against temperature. Magnetization measurements recorded against a magnetic field at c) 300 K, d) 5 K after ZFC, and e) 10 K after FC of 7 T.

The magnetic properties of C, CS and CSS were investigated by SQUID magnetometry. Magnetization curves recorded against temperature after zero field cooling (ZFC) and field cooling (FC) are presented in Figure 55a. The maximum of the ZFC curve (T_{max}) is usually ascribed to the transition temperature between blocked magnetic moments and the superparamagnetic behavior where $E_{thermal}=E_{anisotropy}$ ($25k_BT=KV$).

A T_{max} of 86 K was measured for C which agree with values reported for similar iron oxide nanoparticles.[2] T_{max} increased to 290 K for CS nanoparticles that consists of a 6.8 nm iron oxide core and a cobalt Ferrite shell thickness of 1.6 nm. Such T_{max} is higher than the 260 K measured for cobalt-doped γ-Fe_2O_3 nanoparticles of 10.2 nm diameter.[20] However it is lower than the 330 K reported for

an iron oxide core of 6.3 nm and a cobalt ferrite shell of 1.0 nm thick.[22] $Fe_{3-d}O_4$@$CoFe_2O_4$ nanoparticles with different shell thickness showed that T_{max} was markedly enhanced by the addition of a very thin cobalt ferrite layer on the iron oxide core. In contrast, thicker shells had no significant further effect on T_{max}. In consequence, the increase of T_{max} is mainly governed by interfacial effects. In our study, the lower T_{max} of CS than for $Fe_{3-d}O_4$@$CoFe_2O_4$[22] can be attributed to a lower quality of the interface happening due to the different synthesis conditions.
Furthermore, the T_{max} of $CoFe_2O_4$ nanoparticles is high: 300 K for 11.0 nm of diameter,[23] 315 K for 12.7 nm diameter,[36] and 340 K for 12.0 nm diameter.[48] Considering that T_{max} has been significantly increased from C to CS, and that the cobalt ferrite content is much lower than for pure cobalt ferrite, it confirms that in our study, the increase of T_{max} results from exchange-coupling between $Fe_{3-d}O_4$ and $CoFe_2O_4$ layers.[49]

The ZFC M(T) curve of CSS shows a continuous increase of the magnetization above 250 K. A kink in the FC curve around 350 K is attributed to a superferromagnetic behavior which results from strong dipolar interactions between nanoparticles. In superferromagnetism, nanoparticles strongly interact together, leading to the creation of super magnetic domains that displays far higher T_{max} than isolated nanoparticles.[50,51]
Nevertheless, we attributed the T_{max} of the CSS nanoparticles to the first kink in the ZFC M(T) curve at around 301 K. Thus, T_{max} has increased of 10 K from CS to CSS nanoparticles. The T_{max} of CSS nanoparticles, which are featured by an iron oxide core of 6.8 nm, a $CoFe_2O_4$ and a $Fe_{3-d}O_4$ shells of 2.9 and 0.3 nm thick respectively, is higher than an estimated T_{max} of 260 K for Co-doped γ-Fe_2O_3 nanoparticles (10.2 nm diameter).[20] It is also higher than the 280 K estimated from FC-ZFC curves of Fe_3O_4@$CoFe_2O_4$ nanoparticles with a 6.3 nm core diameter and a 0.05 nm thick shell.[22] And it is close to the T_{max} of pure $CoFe_2O_4$ nanoparticles of 11.0 nm (300 K)[23] and 12.7 nm sized (315 K) although CSS is featured by a lower content of $CoFe_2O_4$ than pure cobalt ferrite nanoparticles.[36]
Furthermore, the T_{max} of CSS remains lower than the T_{max} of 330 K measured for two different structures reported for $Fe_{3-d}O_4$@$CoFe_2O_4$ nanoparticles: a core size of 6.3 nm and a shell thickness of 1.0 nm[22] or by a core size of 10.3 nm and a 1.0 nm thick shell.[9] Such discrepancy may be attributed to the different operating conditions in the case of the latter,[22] however, the former was synthesized in a similar way. Moreover, size increasing allows to increase T_{max} thanks to a higher magnetic anisotropy energy (KV). CSS is larger than the two formers cited nanoparticles. Thus we attributed the lower T_{max} of CSS compared to the two last cited nanoparticles to arise from a higher Fe/Co ratio as shown by EDX. Indeed, while ref[9] evidenced a 85:15 Fe/Co atomic ratio, CSS only displays a 94:6 ratio.

Compared to T_{max}, the blocking temperature, T_B, is more accurately described by the distribution of energy barriers between blocked and flipped magnetic moments. T_B can be easily extracted from the ZFC-FC M(T) curves using the following equation:[52]

$$f(T_B) = [dM_{ZFC} - M_{FC}]/[dT]$$

T_B was calculated as 48, 239 and 280 K for C, CS and CSS, respectively. These values are slightly lower than T_{max}. CSS also displays a second contribution to 390 K corresponding to a smaller fraction than the one at 280 K. This second T_B is attributed to the supermagnetic domains generated by strong dipolar interactions (superferromagnetism).

In the ZFC M(T) and the $d(M_{ZFC}-M_{FC})/dT$ curves, the width of the curves evidence the distribution of energy barriers which is related to the size distribution of the nanoparticles (and superferromagnetic domains in the case of CSS) that remains reasonable.

Moreover, T_B has also been determined from the values of the coercive fields (H_C) of CS and CSS measured at different temperatures which were fitted according to the Stoner-Wohlfarth model (Figure 56):[53]

$$H_C = 0.48H_K\left[1-\left(\frac{T}{T_B}\right)^{0.5}\right]$$

With the anisotropic field $H_K = \frac{2K_{eff}}{M_S}$

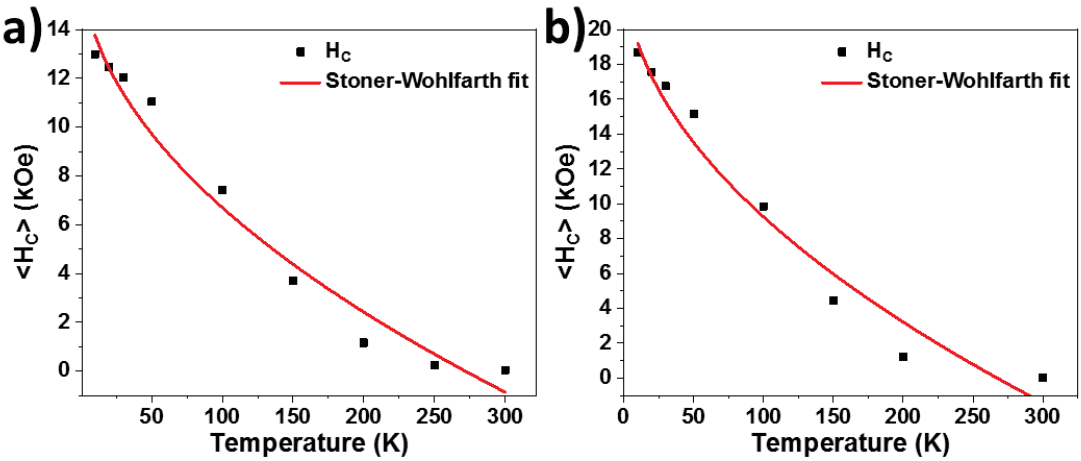

Figure 56. Fitting of the temperature dependence of H_C recorded with SQUID magnetometry according to the Stoner-Wohlfarth model of a) CS and b) CSS.

Thus CS and CSS display T_B(S-W) of 272 and 267 K which are different from T_B determined from d(M_{ZFC}-M_{FC})/dT measurements. Also, from the fit, a lower T_B(S-W) of CSS than CS has been determined which is in contradiction with T_B and T_{max} measurements. Moreover, due to the size increase of CSS compared to CS, and the presence of strong magnetic coupling of the phases within the nanoparticles, T_B(S-W) is expected to increase which shows that the results obtained with the Stoner-Wohlfarth fit are false. Indeed, as the nanoparticles are in the powder form, they are subjected to dipolar interactions which have an effect on the magnetic behavior of the nanoparticles.[24,54] Thus the nanoparticles should be diluted in a matrix in order to separate them from a sufficient distance to avoid the dipolar interactions to measure the T_B of the solely nanoparticles.

Nevertheless, T_{max} and T_B measured from d(M_{ZFC}-M_{FC})/dT increase from CS to CSS coherently with the size increase of the nanoparticles, even if their value can be altered by the presence of dipolar interactions. We will thus use T_B from d(M_{ZFC}-M_{FC})/dT for further investigations.

According to the T_B from d(M_{ZFC}-M_{FC})/dT values, it is possible to determine the effective magnetic anisotropy constant K_{eff} of the nanoparticles from the following equation $K_{eff}V = 25k_BT_B$. Hence C displays a K_{eff} of 6.2 10^4 J/m^3 which is in accordance with K_{eff} of iron oxide nanoparticles of similar size (see chapter III). This is however higher than the magnetic anisotropy constant of bulk magnetite (2.0 10^4 J/m^3)[55] due to the presence of surface anisotropy which represents an important contribution in the case of nanoparticles because of the high surface/volume ratio.[56,57] Then K_{eff} increases to 15.7 10^4 J/m^3 for CS which is between $K_{magnetite}$ and $K_{CoFe2O4}$ ($K_{CoFe2O4}$ = 20-30 10^4 J/m^3 [58,59]) in bulk, confirming the mixed composition of magnetite and cobalt ferrite of CS. Moreover, K_{eff} of CS is higher than the 1.8 10^4 J/m^3 reported for Fe_3O_4@$CoFe_2O_4$ nanoparticles.[21] and is lower than the 58.0 10^4 J/m^3 for Fe_3O_4@$CoFe_2O_4$ nanoparticles[22] Such differences can be attributed to a different quality of the interface as discussed for the blocking temperature, but it can also be attributed to different measurement protocols were Lee and al. measured the effective anisotropy field to determine K_{eff}

while Polishchuk and al. determined it from $(M_{ZFC})/(M_S)$ measurements. Furthermore, as T_B is influenced by the presence of dipolar interactions, it can also affect K_{eff}.
Then in CSS, K_{eff} decreases to 8.2 10^4 J/m^3 despite the increase of the cobalt ferrite shell and the growth of the iron oxide shell. The added cobalt ferrite has a volume four times larger than the volume of the added iron oxide shell. Thus the decrease of K_{eff} in CSS compared to CS is attributed to the presence of magnetic defects within the volume of CSS. But also, to the addition of the soft iron oxide magnetic phase also that participates slightly to decrease this K_{eff} in CSS.

In order to estimate the strength of the hard-soft coupling at the $CoFe_2O_4/Fe_{3-d}O_4$ interface, magnetic anisotropy energy (KV) of each part of the nanoparticles were calculated. Table 27 shows that the contribution of the soft $Fe_{3-d}O_4$ is three orders of magnitude lower than the contribution of the hard $CoFe_2O_4$. Consequently, the hard phase is responsible of the total magnetic anisotropy energy of the nanoparticles. In CS, $K_{CS}V_{CS}$ = 1.46 10^{-19} J/m^3 corresponding to a theoretical $T_{B,\,KV}$ of 423 K according to $KV=25k_BT_B$. For CSS, $K_{CSS}V_{CSS}$ = 2.27 10^{-19} J/m^3 corresponding to a $T_{B,\,KV}$ of 658 K. Although, these values are clearly over estimated, we can notice that $\Delta T_{B,\,KV}$ = 658-423 = 235 K. However, from $d(M_{ZFC}-M_{FC})/dT$ ΔT_B of 280 – 239 = 19K is derived. The large difference between $\Delta T_{B,\,KV}$ and ΔT_B evidenced the lack or very weak hard-soft exchange coupling at the second $CoFe_2O_4/Fe_{3-d}O_4$ interface.
In consequence, the increase of T_{max} from CS to CSS is attributed to volume effect with the increase of the cobalt ferrite shell and the deposition of iron oxide at the surface.

Table 27. Magnetic anisotropy energy of C, CS and CSS nanoparticles, calculated from theoretical magnetic anisotropy of K_{Fe3O4} = 2.0 10^4 J/m^3 [55] and $K_{CoFe2O4}$ = 2.5 10^5 J/m^3.[58,59] The volumes of the nanoparticles were determined according to Mössbauer experiments which are more realistic than from TEM size measurements.

	C	**CS**		**CSS**	
		Cœur	**Shell**	**Shell1**	**Shell2**
Volume (m^3)	2,68 10^{-25}	1,65 10^{-25}	5,71 10^{-25}	8,83 10^{-25}	3,22 10^{-25}
KV (J/m^3)	5,36 10^{-21}	3,29 10^{-21}	1,43 10^{-19}	2,21 10^{-19}	6,43 10^{-21}

Magnetization curves recorded against an applied magnetic field, M(T), at 300 K show closed hysteresis for C, CS and CSS which agree with superparamagnetic behavior. This is in accordance with the T_B of 280 K determined from $d(M_{ZFC}-M_{FC})/dT$ and show that the magnetic moment of the superferromagnetic domain is null (i.e. they are also in a superparamagnetic state) or very small at room temperature.

In contrast, M(H) curves recorded at 5 K for all samples show opened hysteresis corresponding to blocked magnetic moments. C nanoparticles display a H_C of 300 Oe which agrees with similar nanoparticles.[2] It is dramatically larger (19.2 kOe) for CS because of the strong magnetic exchange-coupling between the hard $CoFe_2O_4$ shell and the soft $Fe_{3-d}O_4$ core.[49] It is much larger than the reported values of 6.8 kOe[22] and 10 kOe[21] for Fe_3O_4@$CoFe_2O_4$ nanoparticles with a core of 6.3 and 9 nm of diameter and a shell thickness of 1.0 and 2.0 nm respectively measured at the same temperature. Such behavior can be attributed to stronger exchange-coupling within CS.
The decrease of H_C to 13.1 kOe for CSS can arise from the presence of magnetic defects within the nanoparticles, coherently with the evolution of K_{eff}. It can also be attributed to the increase of the soft iron oxide content as shown by the following equations:[60–62]

$$H_C = 2\frac{K_H f_H + K_S f_S}{M_H f_H + M_S f_S}$$

Where K and f correspond to the anisotropy constant and volume fraction respectively whilst, H and S subscripts refer to the hard and soft phase respectively. Assuming that K_H = 14 K_S ; $M_H \approx M_S$ and that $(2K_H)/M = H_H$,[60] it results that

$$H_C = H_H\left(1 - \frac{1}{14} f_S\right)$$

M(H) curves recorded for CS and CSS after cooling down to 10 K upon exposure to a magnetic field of 7 T showed larger H_C than ZFC M(H) curves. It is ascribed to the magnetic coupling of soft spins with the applied magnetic field during the field cooling procedure. Moreover, the hysteresis curves were not shifted to low magnetic fields which results from exchange bias coupling between soft FiM and hard AFM phases.[8,63,64] Therefore, this analysis confirms the absence of any AFM phase such as CoO. The hard magnetic phase only consists of FiM $CoFe_2O_4$ grown at the surface of the iron oxide core.

Saturation magnetization (M_S) value measured at 5 K for C (58 emu/g) agree with our previous work on similar nanoparticles.[2] M_S increased to 78 emu/g in CS, which is consistent with the growth of a $CoFe_2O_4$ shell (3 μ_B for $CoFe_2O_4$ vs 4 µB for Fe_3O_4). It is slightly higher than values measured (71 – 76 emu/g) for similar systems[20,22] and very close to pure $CoFe_2O_4$ nanoparticles of about 13 nm (79 emu/g)[36,48]
Furthermore, the M_S of CS is higher than for iron oxide nanoparticles of 11.0 and 15.0 nm (61 and 71 emu/g),[2] or for 12.2 nm (53 emu/g) (see chapter I). Hence, the increase of M_S from C to CS is related to the presence of cobalt ferrite.

CSS nanoparticles display a similar M_S to CS nanoparticles of 77 emu/g. As CSS displays a larger volume than CS nanoparticles, it evidences that the second shell has a similar chemical composition than the CS nanoparticles. This observation is supported by Mössbauer experiments that allowed to determine that the second shell is indeed composed of a mixture of $CoFe_2O_4$ and Fe_3O_4.

The M_R/M_S ratio gives precious information on the hardness of the studied material. For non-interacting randomly oriented nanoparticles with uniaxial anisotropy, the M_R/M_S ratio is equal to 50 %.[65,66] Here, C sample displays a M_R/M_S ratio of 26 % which is in accordance with previous measurements (see chapter I and III) and, the low ratio is attributed to the presence of dipolar interactions between the nanoparticles.[67,68] This ratio increases to 88 % in CS which is higher than the 38 % obtained for Fe_3O_4@CoO nanoparticles (see chapter III) or than the 35 % for Co doped maghemite nanoparticles.[20] This high ratio for CS evidences a hard magnetic behavior that is attributed to a higher content of the hard cobalt ferrite than the previously cited Co doped maghemite nanoparticles. The reduced M_R/M_S ratio of CSS is similar to the one of CS which agrees with the fact that the hard layer determines the shape of the hysteresis.[61]

Table 28. Magnetometer characteristics of C, CS and CSS.

	C	CS	CSS
Size (nm)	8.0	10.0	13.1
Shell thickness (nm)	-	1.0	1.5
H_C 5 K (ZFC) kOe	0.3	19.2	13.1
H_C 10 K (FC) kOe	0.3	24.1	15
H_E 10 K (FC) Oe	0	0	0
T_{max} (K)	86	290	301-400
T_B (K)	48	239	280 / 327
T_B S-W (K)	-	272	267
K_{eff} (10^4 J.m^{-3})	6.2	15.8	8.2
M_S 5K (ZFC) emu/g	58	78	77
M_R/M_S (%)	26	89	82

SQUID magnetometry showed the drastic increase of H_C and T_B from C to CS, coherently with a strong hard-soft magnetic coupling. It is correlated to the enhancement of the effective magnetic anisotropy. T_B is further increased in the CSS nanoparticles although it is less important. It is accompanied by the decrease of H_C and K_{eff} while the alignment ratio and the saturation magnetization remain similar from CS to CSS, consistant with a similar chemical structure of the second shell compared to the whole CS nanoparticles. Such observations correlated to the decrease of H_C and the increase of T_B betray the lack of an efficient exchange coupling at the second hard/soft interface. Hence H_C decreases as the soft phase is added on the nanoparticles, and T_B increases due to volume effects that mostly arise from the increase of the cobalt ferrite shell volume.

General discussion

To synthesize Fe_3O_4@$CoFe_2O_4$ CS nanoparticles, we did not strictly stop the reaction of the iron oxide core and have just decreased the temperature to 100 °C in order to add $CoSt_2$. Then the reaction medium was homogenized for 30 min before adding $FeSt_2$ and heating at reflux. These steps was expected to destabilize the fresh $CoSt_2$ which decomposed at higher temperature than $FeSt_2$[9] but also to use the remains of $FeSt_2$ from the core synthesis to help synthesizing a cobalt ferrite shell. Then, in order to synthesize an iron oxide shell, the core@shell was washed to get rid of the maximum of remaining stearates and side products before decomposing the $FeSt_2$. Despite our efforts, it was not possible to remove all the remaining stearate from CS without leading to the aggregation of the nanoparticles as evidenced by FT-IR and granulometry measurements. Thus it is possible that some remaining $CoSt_2$ with CS has decomposed during the synthesis of CSS thus resulting in the increase of the cobalt ferrite content.

The shape of the nanoparticles was affected by the successive thermal decomposition steps which was attributed to a preferential growth on the facets of the seeds.[23] Moreover, it also affects the size distribution that became slightly larger. However, considering a succession of three thermal decomposition steps, the shape and the size distribution of the nanoparticles remains reasonable. TEM size measurements has shown the size increasing of the nanoparticles from C to CSS, in accordance with the seed-mediated growth synthesis. EDX atomic ratio evidenced the presence of Fe and Co atoms in the CS structure and the increase of the Fe:Co ratio in the CSS structure, in accordance with the expected $Fe_{3-d}O_4$@$CoFe_2O_4$ and $Fe_{3-d}O_4$@$CoFe_2O_4$@$Fe_{3-d}O_4$ structure of CS and CSS respectively. HAADF micrographs revealed a single crystal-like structure for each nanoparticles, thanks to the negligible lattice mismatch between both spinel structures. So does XRD patterns that evidenced the increase of the crystal size and the increase of the mean cell parameter from C to CSS. The high cell parameters of CS and CSS determined from XRD patterns were attributed to the growth of the $CoFe_2O_4$ and $Fe_{3-d}O_4$ shell and with the presence of low crystal strains as evidenced by GPA analysis.

FT-IR, XAS and XMCD on CS nanoparticles have shown the good synthesis of the $CoFe_2O_4$ shell which was supported by EELS-SI experiments that have clearly revealed the good $Fe_{3-d}O_4$@$CoFe_2O_4$ structure. Thanks to Mössbauer experiments, it was possible to determine that CS nanoparticles are composed of an iron oxide core diameter of 6.8 nm and a cobalt ferrite shell of 1.6 nm thickness. Thus, the core diameter is smaller than the size of the pristine iron oxide measured from TEM micrographs. It results from a partial solubilisation of the core during the synthesis of the shell followed by the seed-mediated growth of $CoFe_2O_4$ (see sample CS2r in chapter III).[10]

In CSS nanoparticles, FT-IR and XAS XMCD spectroscopies agreed with the synthesis of an iron oxide shell that surprisingly contains a high content of Fe^{2+}. However, XAS, XMCD have also shown the increase of the $CoFe_2O_4$ content. This is in accordance with the fact that M_S (CS) and M_S (CSS) are identical, indicating thus that the second shell has a similar chemical composition than CS nanoparticles. It also agrees with the similar cell parameters calculated from XRD measurements for CS and CSS. In CSS, we considered that the iron oxide core was not modified by the further thermal decomposition as it is protected by the first shell. Thus Mössbauer experiments allowed to calculate that the cobalt ferrite shell thickness has increased from 1.6 (CS) to 2.9 (CSS) nm followed by the growth of a 0.3 nm thick iron oxide shell. The growth of the cobalt ferrite shell was certainly favored by the presence of $CoSt_2$ precursors which remained in the solution as shown by FT-IR spectroscopy. However, further washes would lead to the possible aggregation of the nanoparticles. The non-observation of Fe on the edge of CSS by EELS-SI experiments, although a resolution of (5 Å), confirms the very thin $Fe_{3-d}O_4$ shell.

Moreover, according to previous results on pure iron oxide nanoparticles of size smaller than 8 nm,[2] such a thin iron oxide shell of 0.3 nm was expected to be fully oxidized. Owing to the surface sensitivity of the TEY recording mode for XAS and XMCD measurements, these experiments surprisingly showed that this thin iron oxide shell actually contains some Fe^{2+}. Further investigations has to be performed in order to determine the origin of this occurrence that was also observed for other $Fe_{3-d}O_4$@CoO@$Fe_{3-d}O_4$ nanoparticles.

Selective hysteresis has demonstrated that coercive fields at the Fe and Co edges are similar, agreeing with direct and strong magnetic coupling in CS and CSS nanoparticles. The high values of H_C show the presence of $CoFe_2O_4$ in CS and CSS nanoparticles. Moreover, CS and CSS have similar M_R/M_S ratios due to a similar chemical composition of the second shell in CSS compared to the entire CS nanoparticles.

Thanks to a strong magnetic exchange-coupling in CS nanoparticles, T_B has been significantly increased from 48 K (C nanoparticles) to 239 K. We have demonstrated that the low increase of T_B in CSS (280 K) compared to CS is mostly due to volume effect where the cobalt ferrite shell was grown. Indeed, Polishchuk and al.[22] have shown that T_{max} (de facto T_B) of $Fe_{3-d}O_4$@$CoFe_2O_4$ nanoparticles is increased for thin cobalt ferrite shell while thicker shell does not allow to increase it significantly further. Unfortunately, the growth of the very thin second iron oxide shell does not allow to produce an efficient double interfacial exchange-coupling. In contrast, the third thermal decomposition resulted in the increase the thickness of the cobalt ferrite shell. Finally, although very thin, the iron oxide shell resulted in the decrease of K_{eff} and H_C measured at 5 K.

Conclusion

To conclude, the core@shell@shell Fe_3O_4@$CoFe_2O_4$@Fe_3O_4 nanoparticles were synthesized through a succession of three thermal decompositions according to seed-mediated growth approaches. All the analysis agrees on the Fe_3O_4@$CoFe_2O_4$ structure for CS nanoparticles which actually displays an iron oxide core of 6.8 nm surrounded by a 1.6 nm thick $CoFe_2O_4$ shell. We have shown that the third thermal decomposition on CS has increased the thickness of the $CoFe_2O_4$ shell to 2.9 nm, surrounded by a very thin iron oxide shell of 0.3 nm. The similar chemical composition of the second shell in CSS compared to the CS nanoparticles is supported by FT-IR, XRD, and M_S measurements. The presence of the $Fe_{3-d}O_4$ shell in CSS has a low impact on the magnetic properties of the nanoparticles and only decreased H_C and K_{eff} compared to CS. From C to CS nanoparticles, T_B measurements has showed a significant increase with the addition the cobalt ferrite shell. However, in CSS, T_B does not increase significantly and the higher T_B of CSS compared to CS is thus attributed to volume effects rather than to a double interfacial FiM/FiM exchange coupling. Nevertheless, the structure of CSS allowed to increase T_B to about 301 K although the amount of Co atoms is much lower than pure $CoFe_2O_4$ nanoparticles which are larger than 13.5 nm to display similar magnetic properties.

References

(1) Cotin, G.; Kiefer, C.; Perton, F.; Boero, M.; Özdamar, B.; Bouzid, A.; Ori, G.; Massobrio, C.; Begin, D.; Pichon, B.; et al. Evaluating the Critical Roles of Precursor Nature and Water Content When Tailoring Magnetic Nanoparticles for Specific Applications. *ACS Appl. Nano Mater.* **2018**, *1* (8), 4306–4316. https://doi.org/10.1021/acsanm.8b01123.

(2) Baaziz, W.; Pichon, B. P.; Fleutot, S.; Liu, Y.; Lefevre, C.; Greneche, J.-M.; Toumi, M.; Mhiri, T.; Begin-Colin, S. Magnetic Iron Oxide Nanoparticles: Reproducible Tuning of the Size and Nanosized-Dependent Composition, Defects, and Spin Canting. *J. Phys. Chem. C* **2014**, *118* (7), 3795–3810. https://doi.org/10.1021/jp411481p.

(3) Ohresser, P.; Otero, E.; Choueikani, F.; Chen, K.; Stanescu, S.; Deschamps, F.; Moreno, T.; Polack, F.; Lagarde, B.; Daguerre, J.-P.; et al. DEIMOS: A Beamline Dedicated to Dichroism Measurements in the 350–2500 EV Energy Range. *Rev. Sci. Instrum.* **2014**, *85* (1), 013106.

(4) Daffé, N.; Choueikani, F.; Neveu, S.; Arrio, M.-A.; Juhin, A.; Ohresser, P.; Dupuis, V.; Sainctavit, P. Magnetic Anisotropies and Cationic Distribution in CoFe 2 O 4 Nanoparticles Prepared by Co-Precipitation Route: Influence of Particle Size and Stoichiometry. *J. Magn. Magn. Mater.* **2018**, *460*, 243–252. https://doi.org/10.1016/j.jmmm.2018.03.041.

(5) Teillet, J.; Varret, F. MOSFIT Software; Université Du Maine, Le Mans, France.

(6) Lima, E.; Winkler, E. L.; Tobia, D.; Troiani, H. E.; Zysler, R. D.; Agostinelli, E.; Fiorani, D. Bimagnetic CoO Core/CoFe $_2$ O $_4$ Shell Nanoparticles: Synthesis and Magnetic Properties. *Chem. Mater.* **2012**, *24* (3), 512–516. https://doi.org/10.1021/cm2028959.

(7) Macpherson, H. A.; Stoldt, C. R. Iron Pyrite Nanocubes: Size and Shape Considerations for Photovoltaic Application. *ACS Nano* **2012**, *6* (10), 8940–8949. https://doi.org/10.1021/nn3029502.

(8) Sartori, K.; Choueikani, F.; Gloter, A.; Begin-Colin, S.; Taverna, D.; Pichon, B. P. Room Temperature Blocked Magnetic Nanoparticles Based on Ferrite Promoted by a Three-Step Thermal Decomposition Process. *J. Am. Chem. Soc.* **2019**, *141* (25), 9783–9787. https://doi.org/10.1021/jacs.9b03965.

(9) Sartori, K.; Cotin, G.; Bouillet, C.; Halté, V.; Bégin-Colin, S.; Choueikani, F.; Pichon, B. P. Strong Interfacial Coupling through Exchange Interactions in Soft/Hard Core–Shell Nanoparticles as a Function of Cationic Distribution. *Nanoscale* **2019**, *11* (27), 12946–12958. https://doi.org/10.1039/C9NR02323B.

(10) Lentijo-Mozo, S.; Deiana, D.; Sogne, E.; Casu, A.; Falqui, A. Unexpected Insights about Cation-Exchange on Metal Oxide Nanoparticles and Its Effect on Their Magnetic Behavior. *Chem. Mater.* **2018**, *30* (21), 8099–8112. https://doi.org/10.1021/acs.chemmater.8b04331.

(11) Zhang, L.; He, R.; Gu, H.-C. Oleic Acid Coating on the Monodisperse Magnetite Nanoparticles. *Appl. Surf. Sci.* **2006**, *253* (5), 2611–2617. https://doi.org/10.1016/j.apsusc.2006.05.023.

(12) Nakamoto, K. *Infrared and Raman Spectra of Inorganic and Coordination Compounds*, 6th ed.; Wiley: Hoboken, N.J, 2009.

(13) Ren, Y.; Iimura, K.; Kato, T. Structure of Barium Stearate Films at the Air/Water Interface Investigated by Polarization Modulation Infrared Spectroscopy and Π− *A* Isotherms. *Langmuir* **2001**, *17* (9), 2688–2693. https://doi.org/10.1021/la000872e.

(14) Bronstein, L. M.; Huang, X.; Retrum, J.; Schmucker, A.; Pink, M.; Stein, B. D.; Dragnea, B. Influence of Iron Oleate Complex Structure on Iron Oxide Nanoparticle Formation. *Chem. Mater.* **2007**, *19* (15), 3624–3632. https://doi.org/10.1021/cm062948j.

(15) Daou, T. J.; Grenèche, J. M.; Pourroy, G.; Buathong, S.; Derory, A.; Ulhaq-Bouillet, C.; Donnio, B.; Guillon, D.; Begin-Colin, S. Coupling Agent Effect on Magnetic Properties of Functionalized Magnetite-Based Nanoparticles. *Chem. Mater.* **2008**, *20* (18), 5869–5875. https://doi.org/10.1021/cm801405n.

(16) Jacintho, G. V. M.; Brolo, A. G.; Corio, P.; Suarez, P. A. Z.; Rubim, J. C. Structural Investigation of MFe $_2$ O $_4$ (M = Fe, Co) Magnetic Fluids. *J. Phys. Chem. C* **2009**, *113* (18), 7684–7691. https://doi.org/10.1021/jp9013477.

(17) Das, R.; Robles, J.; Glassell, M.; Kalappattil, V.; Phan, M. H.; Srikanth, H. Magnetic Anisotropy and Switching Behavior of Fe3O4/CoFe2O4 Core/Shell Nanoparticles. *J. Electron. Mater.* **2019**, *48* (3), 1461–1466. https://doi.org/10.1007/s11664-018-6778-4.

(18) Lavorato, G.; Winkler, E.; Rivas-Murias, B.; Rivadulla, F. Thickness Dependence of Exchange Coupling in Epitaxial Fe 3 O 4 / CoFe 2 O 4 Soft/Hard Magnetic Bilayers. *Phys. Rev. B* **2016**, *94* (5). https://doi.org/10.1103/PhysRevB.94.054405.

(19) Cheon, J.; Park, J.-I.; Choi, J.; Jun, Y.; Kim, S.; Kim, M. G.; Kim, Y.-M.; Kim, Y. J. Magnetic Superlattices and Their Nanoscale Phase Transition Effects. *Proc. Natl. Acad. Sci.* **2006**, *103* (9), 3023–3027.

(20) Salazar-Alvarez, G.; Sort, J.; Uheida, A.; Muhammed, M.; Suriñach, S.; Baró, M. D.; Nogués, J. Reversible Post-Synthesis Tuning of the Superparamagnetic Blocking Temperature of γ-Fe $_2$ O $_3$ Nanoparticles by Adsorption and Desorption of Co(II) Ions. *J Mater Chem* **2007**, *17* (4), 322–328. https://doi.org/10.1039/B613026G.

(21) Lee, J.-H.; Jang, J.; Choi, J.; Moon, S. H.; Noh, S.; Kim, J.; Kim, J.-G.; Kim, I.-S.; Park, K. I.; Cheon, J. Exchange-Coupled Magnetic Nanoparticles for Efficient Heat Induction. *Nat. Nanotechnol.* **2011**, *6* (7), 418–422. https://doi.org/10.1038/nnano.2011.95.

(22) Polishchuk, D.; Nedelko, N.; Solopan, S.; Ślawska-Waniewska, A.; Zamorskyi, V.; Tovstolytkin, A.; Belous, A. Profound Interfacial Effects in CoFe2O4/Fe3O4 and Fe3O4/CoFe2O4 Core/Shell Nanoparticles. *Nanoscale Res. Lett.* **2018**, *13* (1). https://doi.org/10.1186/s11671-018-2481-x.

(23) López-Ortega, A.; Lottini, E.; Fernández, C. de J.; Sangregorio, C. Exploring the Magnetic Properties of Cobalt-Ferrite Nanoparticles for the Development of a Rare-Earth-Free Permanent Magnet. *Chem. Mater.* **2015**, *27* (11), 4048–4056. https://doi.org/10.1021/acs.chemmater.5b01034.

(24) Matthias, P. Structuration de nanoparticules magnétiques d'oxyde de fer en films et étude de leurs propriétés magnétiques et de magnétotransport, 2010.

(25) Baaziz, W.; Pichon, B. P.; Grenèche, J.-M.; Begin-Colin, S. Effect of Reaction Environment and in Situ Formation of the Precursor on the Composition and Shape of Iron Oxide Nanoparticles Synthesized by the Thermal Decomposition Method. *CrystEngComm* **2018**, No. 20, 7206.

(26) Tuček, J.; Zboril, R.; Petridis, D. Maghemite Nanoparticles by View of Mössbauer Spectroscopy. *J. Nanosci. Nanotechnol.* **2006**, *6* (4), 926–947. https://doi.org/10.1166/jnn.2006.183.

(27) Yaacoub, N.; Mortada, H.; Nehme, Z.; Greneche, J.-M. Chemical Inhomogeneity in Iron Oxide@CoO Core–Shell Nanoparticles: A Local Probe Study Using Zero-Field and In-Field ^{57} Fe Mössbauer Spectrometry. *J. Nanosci. Nanotechnol.* **2019**, *19* (8), 5014–5019. https://doi.org/10.1166/jnn.2019.16794.

(28) de Bakker, P. M. A.; De Grave, E.; Vandenberghe, R. E.; Bowen, L. H. Mössbauer Study of Small-Particle Maghemite. *Hyperfine Interact.* **1990**, *54* (1–4), 493–498. https://doi.org/10.1007/BF02396078.

(29) Daou, T. J.; Begin-Colin, S.; Grenèche, J. M.; Thomas, F.; Derory, A.; Bernhardt, P.; Legaré, P.; Pourroy, G. Phosphate Adsorption Properties of Magnetite-Based Nanoparticles. *Chem. Mater.* **2007**, *19* (18), 4494–4505. https://doi.org/10.1021/cm071046v.

(30) Deepak, F. L.; Bañobre-López, M.; Carbó-Argibay, E.; Cerqueira, M. F.; Piñeiro-Redondo, Y.; Rivas, J.; Thompson, C. M.; Kamali, S.; Rodríguez-Abreu, C.; Kovnir, K.; et al. A Systematic Study of the Structural and Magnetic Properties of Mn-, Co-, and Ni-Doped Colloidal Magnetite Nanoparticles. *J. Phys. Chem. C* **2015**, *119* (21), 11947–11957. https://doi.org/10.1021/acs.jpcc.5b01575.

(31) Liu, M.; Lu, M.; Wang, L.; Xu, S.; Zhao, J.; Li, H. Mössbauer Study on the Magnetic Properties and Cation Distribution of CoFe2O4 Nanoparticles Synthesized by Hydrothermal Method. *J. Mater. Sci.* **2016**, *51* (11), 5487–5492. https://doi.org/10.1007/s10853-016-9853-3.

(32) Daou, T. J.; Pourroy, G.; Bégin-Colin, S.; Grenèche, J. M.; Ulhaq-Bouillet, C.; Legaré, P.; Bernhardt, P.; Leuvrey, C.; Rogez, G. Hydrothermal Synthesis of Monodisperse Magnetite Nanoparticles. *Chem. Mater.* **2006**, *18* (18), 4399–4404. https://doi.org/10.1021/cm060805r.

(33) Grigorova, M.; Blythe, H. J.; Blaskov, V.; Rusanov, V.; Petkov, V.; Masheva, V.; Nihtianova, D.; Martinez, Ll. M.; Muñoz, J. S.; Mikhov, M. Magnetic Properties and Mössbauer Spectra of Nanosized CoFe2O4 Powders. *J. Magn. Magn. Mater.* **1998**, *183* (1–2), 163–172. https://doi.org/10.1016/S0304-8853(97)01031-7.

(34) Zhu, X.; Kalirai, S. S.; Hitchcock, A. P.; Bazylinski, D. A. What Is the Correct Fe L23 X-Ray Absorption Spectrum of Magnetite? *J. Electron Spectrosc. Relat. Phenom.* **2015**, *199*, 19–26. https://doi.org/10.1016/j.elspec.2014.12.005.

(35) Brice-Profeta, S.; Arrio, M.-A.; Tronc, E.; Menguy, N.; Letard, I.; Cartier dit Moulin, C.; Noguès, M.; Chanéac, C.; Jolivet, J.-P.; Sainctavit, Ph. Magnetic Order in - Nanoparticles: A XMCD Study. *J. Magn. Magn. Mater.* **2005**, *288*, 354–365. https://doi.org/10.1016/j.jmmm.2004.09.120.

(36) Torres, T. E.; Roca, A. G.; Morales, M. P.; Ibarra, A.; Marquina, C.; Ibarra, M. R.; Goya, G. F. Magnetic Properties and Energy Absorption of $CoFe_2O_4$ Nanoparticles for Magnetic Hyperthermia. *J. Phys. Conf. Ser.* **2010**, *200* (7), 072101. https://doi.org/10.1088/1742-6596/200/7/072101.

(37) E. Pellegrin et al. Characterization of Nanocrystalline Y-Fe2O3 with Synchrotron Radiation Techniques. *Phys Stat Sol* **1999**, *215*, 797.

(38) Manna, P. K.; Skoropata, E.; Ting, Y.-W.; Lin, K.-W.; Freeland, J. W.; van Lierop, J. Interface Mixing and Its Impact on Exchange Coupling in Exchange Biased Systems. *J. Phys. Condens. Matter* **2016**, *28* (48), 486004. https://doi.org/10.1088/0953-8984/28/48/486004.

(39) Li, J.; Menguy, N.; Arrio, M.-A.; Sainctavit, P.; Juhin, A.; Wang, Y.; Chen, H.; Bunau, O.; Otero, E.; Ohresser, P.; et al. Controlled Cobalt Doping in the Spinel Structure of Magnetosome Magnetite: New Evidences from Element- and Site-Specific X-Ray Magnetic Circular Dichroism Analyses. *J. R. Soc. Interface* **2016**, *13* (121), 20160355. https://doi.org/10.1098/rsif.2016.0355.

(40) Hochepied, J. F.; Sainctavit, P.; Pileni, M. P. X-Ray Absorption Spectra and X-Ray Magnetic Circular Dichroism Studies at Fe and Co L 2, 3 Edges of Mixed Cobalt–Zinc Ferrite Nanoparticles: Cationic Repartition, Magnetic Structure and Hysteresis Cycles. *J. Magn. Magn. Mater.* **2001**, *231* (2), 315–322.

(41) Haverkort, M. W. Spin and Orbital Degrees of Freedom in Transition Metal Oxides and Oxide Thin Films Studied by Soft X-Ray Absorption Spectroscopy, 2005.

(42) Byrne, J. M.; Coker, V. S.; Moise, S.; Wincott, P. L.; Vaughan, D. J.; Tuna, F.; Arenholz, E.; van der Laan, G.; Pattrick, R. A. D.; Lloyd, J. R.; et al. Controlled Cobalt Doping in Biogenic Magnetite Nanoparticles. *J. R. Soc. Interface* **2013**, *10* (83), 20130134–20130134. https://doi.org/10.1098/rsif.2013.0134.

(43) Daffé, N.; Gavrilov, V.; Neveu, S.; Choueikani, F.; Arrio, M.-A.; Juhin, A.; Ohresser, P.; Dupuis, V.; Sainctavit, P. Small CoFe2O4 Magnetic Nanoparticles in Ferrofluids, Influence of the Synthesis on the Magnetic Anisotropies. *J. Magn. Magn. Mater.* **2019**, *477*, 226–231. https://doi.org/10.1016/j.jmmm.2019.01.048.

(44) Skoropata, E.; Su, T. T.; Ouyang, H.; Freeland, J. W.; van Lierop, J. Intermixing Enables Strong Exchange Coupling in Nanocomposites: Magnetism through the Interfacial Ferrite in $\gamma - Fe_2O_3$ / NiO. *Phys. Rev. B* **2017**, *96* (2). https://doi.org/10.1103/PhysRevB.96.024447.

(45) Sharifi Dehsari, H.; Asadi, K. Impact of Stoichiometry and Size on the Magnetic Properties of Cobalt Ferrite Nanoparticles. *J. Phys. Chem. C* **2018**, *122* (51), 29106–29121. https://doi.org/10.1021/acs.jpcc.8b09276.

(46) Nemati, Z.; Alonso, J.; Rodrigo, I.; Das, R.; Garaio, E.; García, J. Á.; Orue, I.; Phan, M.-H.; Srikanth, H. Improving the Heating Efficiency of Iron Oxide Nanoparticles by Tuning Their Shape and Size. *J. Phys. Chem. C* **2018**, *122* (4), 2367–2381. https://doi.org/10.1021/acs.jpcc.7b10528.

(47) Wohlfarth, E. P. Remanent Magnetization of Fine Particles. *J. Phys. Radium* **1959**, *20* (2–3), 295–297. https://doi.org/10.1051/jphysrad:01959002002-3029500.
(48) Song, Q.; Zhang, Z. J. Shape Control and Associated Magnetic Properties of Spinel Cobalt Ferrite Nanocrystals. *J. Am. Chem. Soc.* **2004**, *126* (19), 6164–6168. https://doi.org/10.1021/ja049931r.
(49) López-Ortega, A.; Estrader, M.; Salazar-Alvarez, G.; Roca, A. G.; Nogués, J. Applications of Exchange Coupled Bi-Magnetic Hard/Soft and Soft/Hard Magnetic Core/Shell Nanoparticles. *Phys. Rep.* **2015**, *553*, 1–32. https://doi.org/10.1016/j.physrep.2014.09.007.
(50) Bedanta, S.; Kleemann, W. Supermagnetism. *J. Phys. Appl. Phys.* **2009**, *42* (1), 013001. https://doi.org/10.1088/0022-3727/42/1/013001.
(51) Petracic, O.; Chen, X.; Bedanta, S.; Kleemann, W.; Sahoo, S.; Cardoso, S.; Freitas, P. P. Collective States of Interacting Ferromagnetic Nanoparticles. *J. Magn. Magn. Mater.* **2006**, *300* (1), 192–197. https://doi.org/10.1016/j.jmmm.2005.10.061.
(52) Bruvera, I. J.; Mendoza Zélis, P.; Pilar Calatayud, M.; Goya, G. F.; Sánchez, F. H. Determination of the Blocking Temperature of Magnetic Nanoparticles: The Good, the Bad, and the Ugly. *J. Appl. Phys.* **2015**, *118* (18), 184304. https://doi.org/10.1063/1.4935484.
(53) Nunes, W. C.; Folly, W. S. D.; Sinnecker, J. P.; Novak, M. A. Temperature Dependence of the Coercive Field in Single-Domain Particle Systems. *Phys. Rev. B* **2004**, *70* (1), 014419. https://doi.org/10.1103/PhysRevB.70.014419.
(54) Frankamp, B. L.; Boal, A. K.; Tuominen, M. T.; Rotello, V. M. Direct Control of the Magnetic Interaction between Iron Oxide Nanoparticles through Dendrimer-Mediated Self-Assembly. *J. Am. Chem. Soc.* **2005**, *127* (27), 9731–9735. https://doi.org/10.1021/ja051351m.
(55) O'Handley, R. C. *Modern Magnetic Materials: Principles and Applications*; Wiley: New York, 2000.
(56) Gilmore, K.; Idzerda, Y. U.; Klem, M. T.; Allen, M.; Douglas, T.; Young, M. Surface Contribution to the Anisotropy Energy of Spherical Magnetite Particles. *J. Appl. Phys.* **2005**, *97* (10), 10B301. https://doi.org/10.1063/1.1845973.
(57) Cao, C.; Tian, L.; Liu, Q.; Liu, W.; Chen, G.; Pan, Y. Magnetic Characterization of Noninteracting, Randomly Oriented, Nanometer-Scale Ferrimagnetic Particles. *J. Geophys. Res.* **2010**, *115* (B7), B07103. https://doi.org/10.1029/2009JB006855.
(58) Chen, R.; Christiansen, M. G.; Anikeeva, P. Maximizing Hysteretic Losses in Magnetic Ferrite Nanoparticles *via* Model-Driven Synthesis and Materials Optimization. *ACS Nano* **2013**, *7* (10), 8990–9000. https://doi.org/10.1021/nn4035266.
(59) Suzuki, Y.; van Dover, R. B.; Gyorgy, E. M.; Phillips, J. M.; Felder, R. J. Exchange Coupling in Single-Crystalline Spinel-Structure (Mn,Zn) Fe 2 O 4 /Co Fe 2 O 4 Bilayers. *Phys. Rev. B* **1996**, *53* (21), 14016–14019. https://doi.org/10.1103/PhysRevB.53.14016.
(60) Song, Q.; Zhang, Z. J. Controlled Synthesis and Magnetic Properties of Bimagnetic Spinel Ferrite $CoFe_2O_4$ and $MnFe_2O_4$ Nanocrystals with Core–Shell Architecture. *J. Am. Chem. Soc.* **2012**, *134* (24), 10182–10190. https://doi.org/10.1021/ja302856z.
(61) Masala, O.; Hoffman, D.; Sundaram, N.; Page, K.; Proffen, T.; Lawes, G.; Seshadri, R. Preparation of Magnetic Spinel Ferrite Core/Shell Nanoparticles: Soft Ferrites on Hard Ferrites and Vice Versa. *Solid State Sci.* **2006**, *8* (9), 1015–1022. https://doi.org/10.1016/j.solidstatesciences.2006.04.014.
(62) Zeng, H.; Sun, S.; Li, J.; Wang, Z. L.; Liu, J. P. Tailoring Magnetic Properties of Core⁄shell Nanoparticles. *Appl. Phys. Lett.* **2004**, *85* (5), 792–794. https://doi.org/10.1063/1.1776632.
(63) Oscar Iglesias; Amilcar Labarta; Xavier Battle. Exchange Bias Phenomenology and Models of Core/Shell Nanoparticles. *Cond Mat* **2008**.
(64) Meiklejohn, W. H.; Bean, C. P. New Magnetic Anisotropy. *Phys. Rev.* **1956**, *102* (5), 1413–1414. https://doi.org/10.1103/PhysRev.102.1413.
(65) Kechrakos, D.; Trohidou, K. N. Effects of Dipolar Interactions on the Magnetic Properties of Granular Solids. *J. Magn. Magn. Mater.* **1998**, *177–181*, 943–944. https://doi.org/10.1016/S0304-8853(97)00762-2.

(66) Cullity, B. D.; Graham, C. D. *Introduction to Magnetic Materials*, 2nd ed.; IEEE/Wiley: Hoboken, N.J, 2009.
(67) Hadjipanayis, G.; Sellmyer, D. J.; Brandt, B. Rare-Earth-Rich Metallic Glasses. I. Magnetic Hysteresis. *Phys. Rev. B* **1981**, *23* (7), 3349–3354. https://doi.org/10.1103/PhysRevB.23.3349.
(68) Goya, G. F.; Berquó, T. S.; Fonseca, F. C.; Morales, M. P. Static and Dynamic Magnetic Properties of Spherical Magnetite Nanoparticles. *J. Appl. Phys.* **2003**, *94* (5), 3520–3528. https://doi.org/10.1063/1.1599959.

Chapter V

AFM proximity effect of NiO on $Fe_{3-d}O_4$@CoO nanoparticles

$Fe_{3-d}O_4$@CoO@NiO

Introduction

The synthesis of $Fe_{3-d}O_4(@CoFe_2O_4)_x@CoO_y(@CoFe_2O_4)_z@Fe_{3-d}O_4$ nanoparticles (Chapter III) allowed to increase the blocking temperature of iron oxide based nanoparticles over room temperature with a low content of Co atoms and without rare earth elements. We have proved that the presence of a synergistic magnetic coupling between the iron oxide, cobalt ferrite and CoO phases were at the origin of their interesting magnetic properties. However, in order to use such nanoparticles for data storage applications, it is interesting to increase even further their magnetic stability against temperature and coercive field at room temperature. In this chapter, we attempt to investigate $Fe_{3-d}O_4$@CoO@NiO nanoparticles in order to combine the increase of the magnetic anisotropy constant resulting from CoO and the high Néel temperature (T_N) of NiO (525 K). Indeed, De Toro and *al.*[1] reported on Co@CoO nanoparticles dispersed in a NiO matrix which increased T_{max} from 70 to 360 K thanks to an antiferromagnetic proximity effect.

In the literature, no work reports on the synthesis of NiO nanoparticles resulting from the thermal decomposition and only a few reports on core@shell nanoparticles with NiO as shell. Thus, we report here on a first study on the synthesis of NiO nanoparticles, core@shell and core@shell@shell nanoparticles with NiO as last shell. Our strategy required to first choose an adapted Ni based organo-metallic precursor for thermal decomposition synthesis. The investigations and developments on the decomposition of Ni based organo-metallic precursors are presented in annexes. Such preliminary studies on the synthesis of core@shell and core@shell@shell nanoparticles with NiO as last shell. Once the synthesis conditions were satisfied, $Fe_{3-d}O_4$@NiO and $Fe_{3-d}O_4$@CoO@NiO nanoparticles were synthesized.

Synthesis strategy

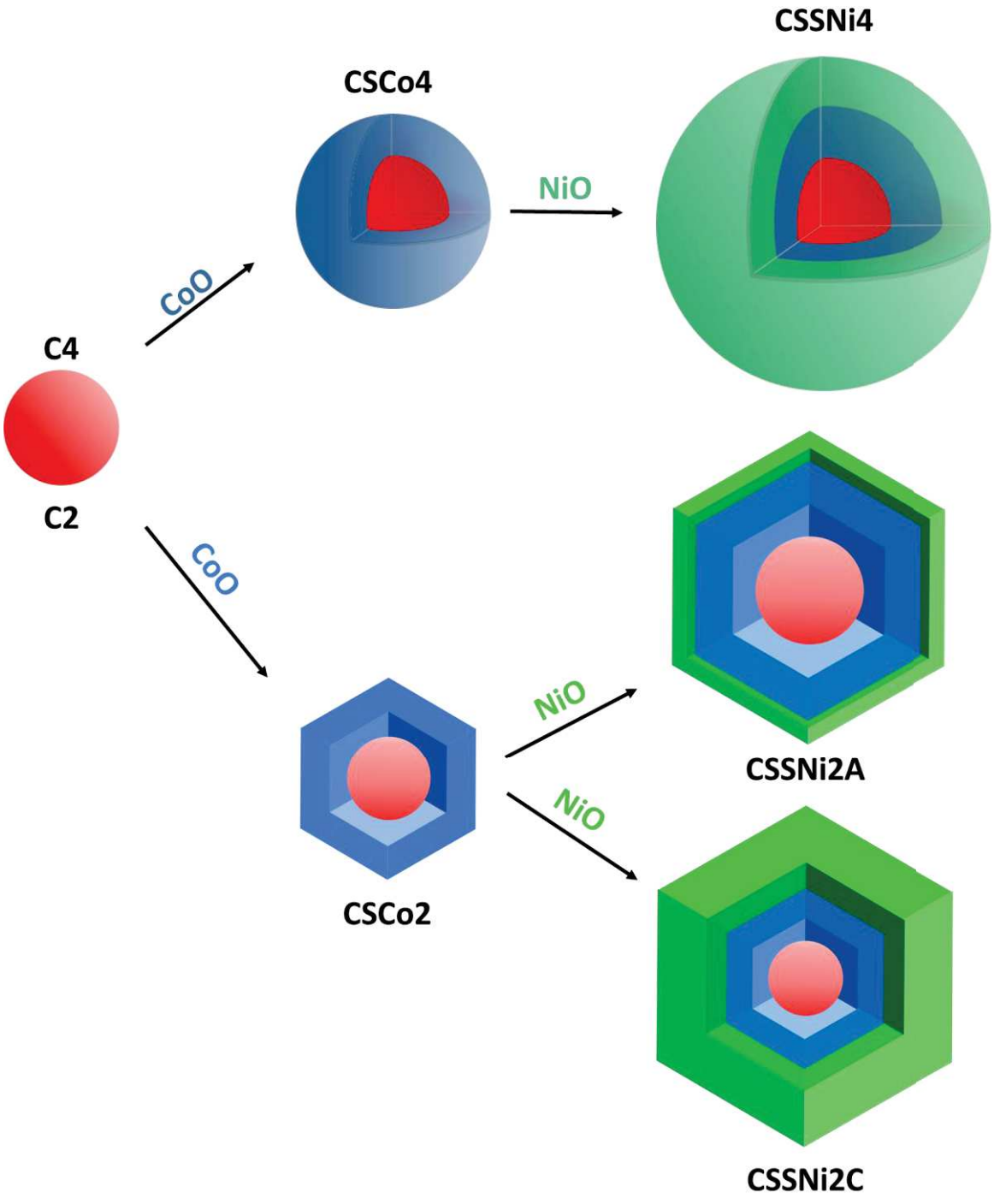

Figure 57. Schematic representation of the synthesis strategy followed to synthesize spherical and cubic $Fe_{3-d}O_4$@CoO@NiO nanoparticles.

In order to investigate the influence of the NiO thickness on the structural and magnetic properties of $Fe_{3-d}O_4$@CoO nanoparticles, different $Fe_{3-d}O_4$@CoO@NiO nanoparticles were synthesized through the adaptation of the core@shell@shell protocol described in chapter III. The iron oxide core was synthesized by the thermal decomposition of iron stearate in presence of oleic acid as surfactant in dioctyl ether. After washes, a fraction of the iron oxide core was used as seeds and poured with cobalt (II) stearate in presence of oleic acid in 1-octadecene to synthesize $Fe_{3-d}O_4$@CoO core@shell nanoparticles. Then the $Fe_{3-d}O_4$@CoO nanoparticles were used as seeds to grow an expected shell of NiO by the thermal decomposition of NiOct in presence of an equimolar mixture of oleic acid and hexadecylamine as surfactants in dioctyl ether.
Two series of $Fe_{3-d}O_4$@CoO@NiO nanoparticles were synthesized: a spherical (series 4) one and a cubic one (series 2).

Note: in this chapter, the samples were indexed according to additional samples presented in the annexes and that refer to preliminary studies on the thermal stability of Ni precursors and growth of NiO nanoparticles

Transmission electron microscopy

$Fe_{3-d}O_4$ core nanoparticles (C2 and C4) were synthesized by the thermal decomposition of a homemade iron stearate in dioctyl ether in presence of oleic acid as surfactant.[2] TEM micrographs show that C4 (Figure 58) and C2 (Figure 59) both display a close to sphere shape with a narrow size distribution centered to 9.2 ± 1.2 and 5.8 ± 0.7 nm. These iron oxide nanoparticles were used as seeds to grow a CoO shell thanks to the decomposition of a cobalt stearate in 1-octadecene with oleic acid.[3–6] The resulting $Fe_{3-d}O_4$@CoO nanoparticles display a close to sphere shape for CSCo4 (Figure 58) and a roundish cubic shape for CSCo2 (Figure 59) with edge-to-edge sizes of 10.7 ± 1.2 and 8.4 ± 0.9 which correspond to shell thicknesses of 0.8 and 1.3 nm respectively. CSCo4 displays a usual shape for such nanoparticles.[3–6] However, the roundish cubic shape of CSCo2 was at first surprising but can be attributed to a possible low hydration rate of the CoSt precursors which favors cubic shapes. Indeed, a dehydrated precursor decompose much easier than its hydrated version.[7] As the decomposition kinetic is faster, it favors the deposition rate toward the migration rate, leading to a cubic kinetic product.[8] EDX measurement performed on CSCo4 and CSCo2 gives Fe : Co atomic ratios of 54 : 46 for CSCo4 and 36 : 64 for CSCo2. Hence a higher Co content for CSCo2 than for CSCo4.

A third thermal decomposition was performed. Both types of $Fe_{3-d}O_4$@CoO nanoparticles were used as seeds in order to grow a NiO shell. NiOct was decomposed in dioctyl ether with an equimolar mixture of hexadecylamine and oleic acid. Different quantities of NiOct were decomposed according to a R ratio defined as $R = [(n_{NiOct\ shell})/(n_{FeSt2\ core})]$.
A R ratio of 0.8 was used for CSSNi4 (Figure 58) leading to the increase of the mean size to 11.2 ± 1.3 nm, corresponding to a new shell thickness of 0.3 nm. The shape of CSSNi4 nanoparticles was not altered by this third thermal decomposition being similar to the shape of the core@shell CSCo4 nanoparticles. Moreover, the EDX atomic ratio displays a low quantity of Ni in agreement with the size increase (60, 34 and 6 % of Fe, Co and Ni).

R ratios of 0.5 and 1.5 were used to synthesize CSSNi2A and CSSNi2C (Figure 59). While CSSNi2A nanoparticles do not show any modification of the shape or of the size that is centered to 8.4 ± 1.0, compared to the CSCo2 seeds, CSSNi2C evidenced a more cubic shape and a decrease of the size to 7.8 ± 1.0 compared to the CSCo2 seeds. Moreover, EDX analysis has evidenced that CSSNi2A is composed of 38 % of Fe, 52 % of Co and 10 % of Ni and CSSNi2C is composed of 36 % of Fe, 46 % of Co and 18 % of Ni. Hence, Ni is present in CSSNi2A and CSSNi2C and its proportion increased with the quantity of NiOct. Thus, the size decrease measured from the TEM micrographs of CSSNi2C compared to CSCo2 is probably due to a crystal restructuration of the nanoparticles that is further investigated in this chapter.

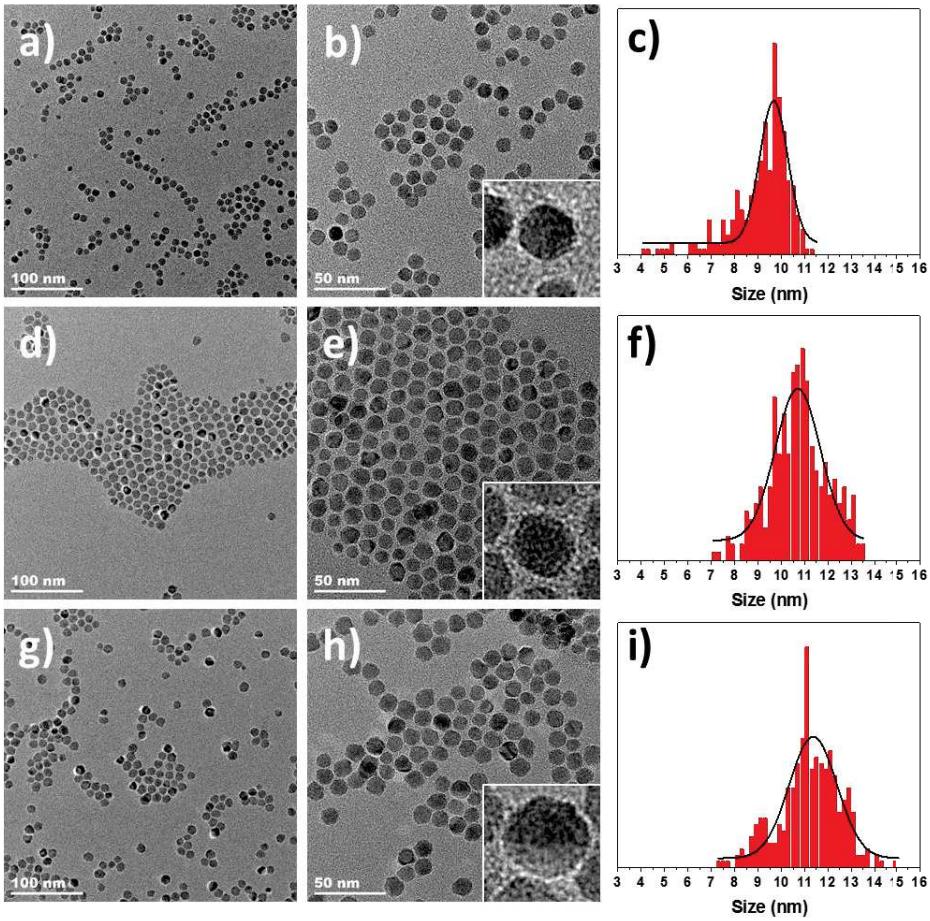

Figure 58. TEM micrographs of a, b) $Fe_{3-d}O_4$ iron oxide core C4, d, e) $Fe_{3-d}O_4$@CoO CSCo4 and g, h) $Fe_{3-d}O_4$@CoO@NiO CSSNi4 nanoparticles with c, f, i) their corresponding size distributions.

Table 29. Structural characteristics of C4, CSCo4 and CSSNi4 nanoparticles.

	C4	CSCo4	CSSNi4
Size (nm)	9.2 ± 1.2	10.7 ± 1.2	11.2 ± 1.3
Shell thickness (nm)	-	0.8	0.3
Volume (nm^3)	407	234	94
Crystal size (nm)	-	9.3 ± 0.1	9.8 ± 0.1
Cell parameter (Å)	-	8.399 ± 0.001	8.414 ± 0.001
Fe : Co : Ni at. Ratio (%)	-	54 : 46 : 0	60 : 34 : 6

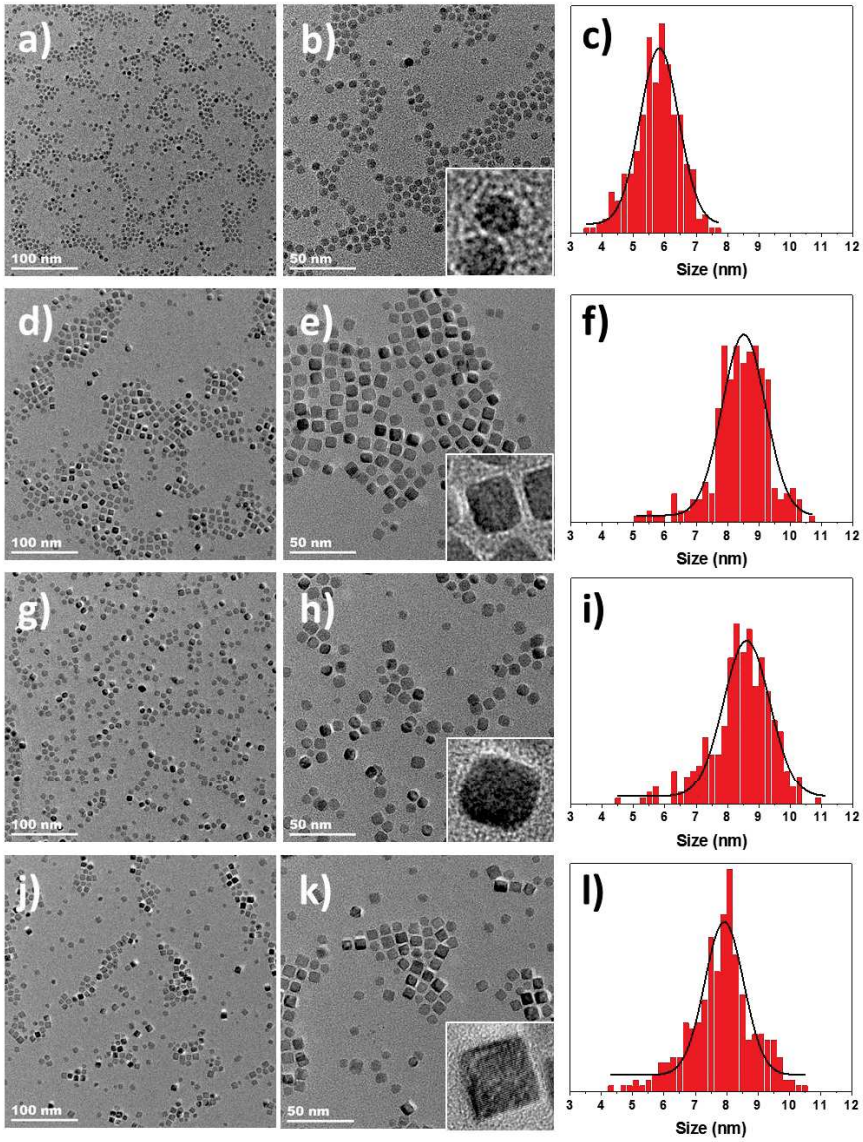

Figure 59. TEM micrographs of $Fe_{3-d}O_4$ (C2), $Fe_{3-d}O_4$@CoO (CSCo2), $Fe_{3-d}O_4$@CoO@NiO R=0.5 (CSSNi2A) and $Fe_{3-d}O_4$@CoO@NiO R= 1.5 (CSSNi2C).

Table 30. Structural characteristics of C2, CSCo2, CSSNi2A and CSSNi2C.

	C2	CSCo2	CSSNi2A	CSSNi2C
Size (nm)	5.8 ± 0.7	8.4 ± 0.9	8.4 ± 1.0	7.8 ± 1.0
Shell thickness (nm)	-	1.3	0	-0.3
Volume (nm^3)	102	310	0	-62
Crystal size (nm)	-	7.3 ± 0.1	7.0 ± 0.1	8.3 ± 0.1
Cell parameter (Å)	-	8.354 ± 0.001	8.273 ± 0.001	8.320 ± 0.001
Fe : Co : Ni at. Ratio (%)	-	36 : 64 : 0	38 : 52 : 10	36 : 46 : 18

Two different series of $Fe_{3-d}O_4$@CoO@NiO nanoparticles were synthesized according to almost identical protocols. Indeed, they were both synthesized following a three steps seed-mediated growth process. However, the precursors were more hydrated for the series 4 (C4, CSCo4 and CSSNi4) leading to spherical nanoparticles while a less hydrated precursor in series 2 (C2, CSCo2, CSSNi2A and CSSNi2C) allowed to synthesize cubic nanoparticles.

FT-IR spectroscopy

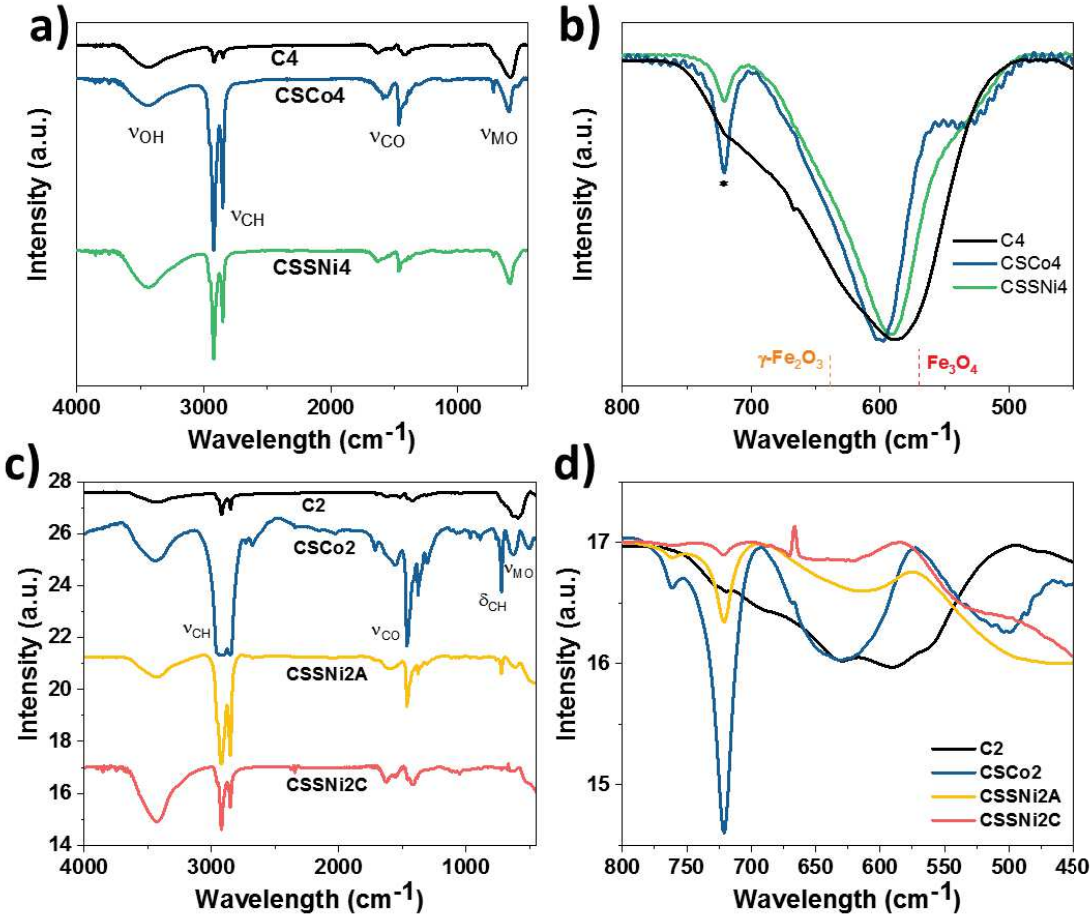

Figure 60. FT-IR analysis of a,b) C4, CSCo4, CSSNi4 and c, d) CSCo2, CSSNi2 nanoparticles in a, c) the range 4 000 – 450 cm^{-1} with b, d) an enlargement in the range 800 -450 cm^{-1}.

The FT-IR spectra of C4, CSCo4, CSSNi4, C2, CSCo2, CSSNi2A and CSSNi2C display similar bands in the range 4 000 to 450 cm^{-1} where the large band centered around 3 441 cm^{-1} corresponds to the vibration of ν(O-H) bonds of adsorbed water molecules. The bands centered at 2 919 and 2 850 cm^{-1} are attributed to the symmetric and antisymmetric stretches of C-H bonds of the alkyl chains respectively. The intense peak at 1 713 cm^{-1} in CSCo2 arises from the C=O stretches of free carboxylic acid groups. A peak at 720 cm^{-1} in CSCo4, CSSNi4, CSCo2 and CSSNi2A corresponds to the scissoring of H-C-H bonds of free stearate. Therefore, some reactants are still present in the sample that could not be removed in order to avoid the aggregation of nanoparticles upon further washings. Moreover, the FT-IR spectra of CSCo2 evidence a saturation of the signal around 3 000 cm^{-1} and large bands around 1 500 cm^{-1} which denotes a high remaining quantity of reactants despite 11 washes.

The bands at 1 577 and 1 467 cm^{-1} arise from the antisymmetric and symmetric stretches of C-O bonds of the carboxylic acid function of the oleic acid. The distance Δ between the two peaks can give further information on the coordination mode of ligands on the nanoparticles. However, the different spectra

evidence large bands, showing that the ligands are not grafted according to a single coordination mode.[9–11]

CSSNi4, CSSNi2A and CSSNi2C, were synthesized in presence of hexadecylamine. This ligand is also composed of an alkyl chain and displays thus the same ν(C-H) bands as oleic acid. Moreover, in the FT-IR spectra of CSSNi4, CSSNi2A and CSSNi2C, the amine termination of HDA should display a band at 1 620 cm^{-1} from the NH_2 scissoring and the N-H bending which is actually mixed with the band of the C-O stretches from oleic acid. Also, no band around 2 240 cm^{-1} from the stretching of C-N bond appears in CSSNi4, CSSNi2A or CSSNi2C spectra which can be attributed to the low content of hexadecylamine and to the natural very weak absorption of this band.[12] Thus, FT-IR analysis do not allow us to clearly discriminate oleic acid from hexadecylamine. However, as amine functions display weaker interactions with metals than carboxylic acid functions, we expect to have removed all the hexadecylamine from the solution.

Furthermore, the displacement of the M-O band brings precious information on the oxidation state of the iron oxide phase: a pure magnetite displays a broad band centered at 570 cm^{-1} with a shoulder at 700 cm^{-1} while maghemite displays a broad band with several oscillations where the most intense one is centered at 638 cm^{-1}.[2,13,14] For the iron oxide cores C4 and C2, the maximum of this band is centered at 587 and 590 cm^{-1} respectively which is between magnetite and maghemite maximums and agrees with a partially oxidized iron oxide nanoparticle. Hence C4 displays a higher Fe^{2+} content than C2 which agrees with its larger size. In CSCo4 and CSCo2, this maximum increases to 599 and 631 cm^{-1} getting closer to a maghemite composition which is in contradiction with previous studies on $Fe_{3-d}O_4$@CoO nanoparticles which evidenced the chemical reduction of the iron oxide core during the synthesis of the CoO shell, leading to a decrease in wavelength of the peaks' maximum. Further analysis will complete these observations. Both $Fe_{3-d}O_4$@CoO samples CSCo4 and CSCo2 a second peak centered at 527 and 502 cm^{-1} are attributed to the stretching vibration of the Co-O bond.[15]

Then, the synthesis of a second shell decreases the Fe-O peaks maximum to 591 and 611 cm^{-1} for CSSNi4 and CSSNi2A which cannot be attributed to a Ni-O stretching vibration that, according to the literature, displays a broad band with two peaks in the range 430 to 490 cm^{-1} [16,17] nor to the Co-O stretching vibration. Nevertheless, it may correspond to a further reduction of the iron oxide core or to the increase of cobalt ferrite phase at the iron oxide/CoO interface as a pure $CoFe_2O_4$ displays a M-O bond centered at 590 cm^{-1}. However, FT-IR spectroscopy solely does not allow to discriminate between these two process.[18] The FT-IR spectrum of CSSNi2C shows a flat band around 630 cm^{-1} and does not allow to determine the maximum's wavelength for the Fe-O band. Further analysis should be performed in order to investigate on the possible reduction of the iron oxide cores.

Hence, FT-IR spectroscopy showed that ligands are grafted at the surface of each nanoparticles.

Granulometry measurements

The presence of ligands grafted at the surface of the nanoparticles allow them to be suspended in organic solvents such as chloroform, THF or hexane. Granulometry measurements in intensity count evidenced several contributions of hydrodynamic diameters where the one of interests are centered to 14.0, 16.0 and 12.0 nm for C4, CSCo4 and CSSNi4 (Figure 61a) and 14.0, 11.0, 12.0 and 13.0 nm for C2, CSCo2, CSSNi2A and CSSNi2C (Figure 61c). Hydrodynamic diameters are higher than the size measured from TEM micrographs due to the presence of ligands grafted at the surface of the nanoparticles. The hydrodynamic diameter evolution does not follow the same evolution as the TEM measured size. Indeed, as the samples in a series do not display the same morphology neither the same chemical composition, it can influence the beam scattering and the results. Also, as shown by FT-

IR spectroscopy, CSCo4 displays more oleic acid in solution than CSSNi4 which may explain its larger hydrodynamic diameter. Moreover, the pattern in intensity count evidenced the presence of larger objects in C4, CSCo4, C2, CSCo2 and CSSNi2A suspended the solution which corresponds to eventual aggregates formed during the washes. However, their number is limited as granulometry measurements in volume count showed only a single and slight contribution of these aggregates in CSCo4. The variation of hydrodynamic diameters of C4, CSCo4 and CSSNi4 nanoparticles measured in volume count is in accordance with the hydrodynamic diameters measured in intensity count with a diameter centered at 11.0, 14.0 and 12.0 nm for C4, CSCo4 and CSSNi4 respectively (Figure 61b). However, the evolution of the hydrodynamic diameters in volume count showed a different evolution than the one observed in intensity count. Hence, the hydrodynamic diameters of C2, CSCo2, CSSNi2A and CSSNi2C are equivalent to 9, 10, 12 and 7 nm (Figure 61d). Such differences can be attributed to the different chemical composition of the nanoparticles but also to their different cubic shape that both affect the scattering of the incoming laser beam.

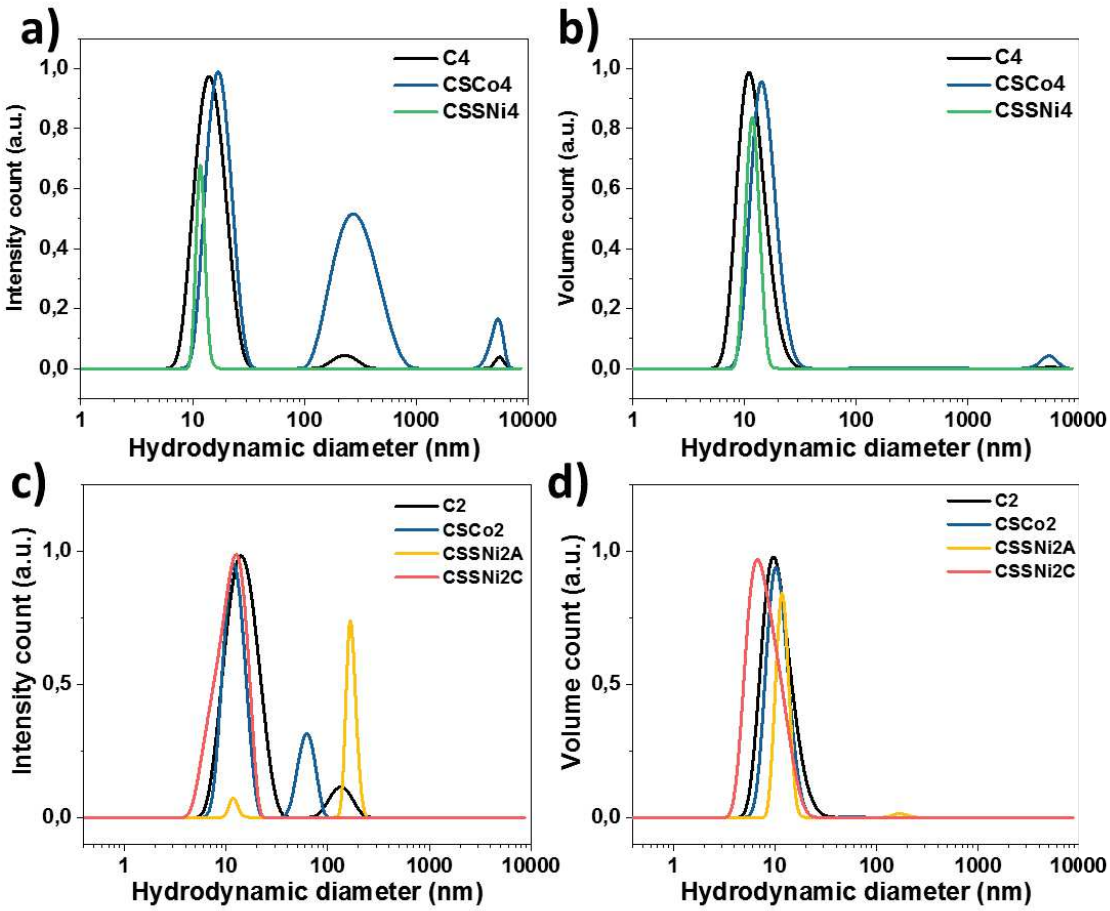

Figure 61. Granulometry measurements of a, b) C4, CSCo4, CSSNi4, c, d) C2, CSCo2, CSSNi2A and CSSNi2C nanoparticles in a, c) intensity count, b, d) volume count.

Granulometry measurements showed that the nanoparticles are stable in suspension in common organic solvents such as chloroform thanks to the presence of organic ligands grafted at their surface.

X-ray diffraction

XRD patterns for CSCo4, CSSNi4, CSCo2, CSSNi2A and CSSNi2C nanoparticles were recorded. However, due to the low amount of C4 and C2 nanoparticles that remained because of their consumption for the different seed-mediated growth synthesis steps, it was unfortunately not possible to record their proper XRD pattern. Hence XRD patterns of iron oxide nanoparticles (C4b and C2b) with similar sizes measured from TEM micrographs were presented.

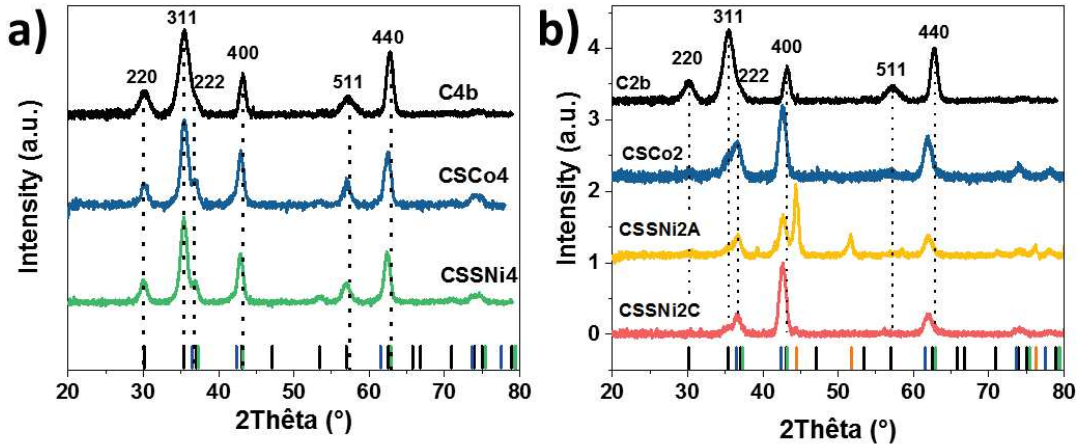

Figure 62. XRD patterns of a) C4b, CSCo4 and CSSNi4 and b) CSCo2, CSSNi2A and CSSNi2C nanoparticles. Black, blue, green and orange bars corresponds to Fe_3O_4 (JCPDS card n° 19-062), CoO (JCPDS card n° 70-2856), NiO (JCPDS card n° 47-1049) and Ni^0 (JCPDS card n° 04-010-6148) references.

XRD patterns of C4b, CSCo4, CSSNi4, C2b, CSCo2, CSSNi2A and CSSNi2C nanoparticles all evidence peaks that can be attributed to an inverse spinel structure. Additional contributions corresponding to a wüstite structure are also present that arise from the CoO shell grown at the surface of C4 (see 222 reflection) and C2 in the case of CSCo4 and CSCo2 and to CoO and NiO phases in the case of CSSNi4, CSSNi2A and CSSNi2C. Due to a crystallization in the same Fm-3m space group for CoO (JCPDS card n° 70-2856) and NiO (JCPDS card n° 47-1049), close cell parameters of 4.2612 and 4.1771 Å respectively, and the overlapping with the magnetite phase, it is not possible to discriminate CoO from NiO in CSSNi4, CSSNi2A and CSSNi2C. The contributions of the wüstite phase compared to the invert spinel structure in the XRD patterns of CSCo2, CSSNi2A and CSSNi2C are more important than in other $Fe_{3-d}O_4$@CoO nanoparticles (see sample CS in chapter III), suggesting that the wüstite quantity is higher than what was expected according to size measurements from TEM micrographs. As for the same edge-to-edge distance, a cubic shape displays a higher volume than a sphere shape, it may be related to CoO that grew according to a cubic shape on the sphere-like iron oxide core.

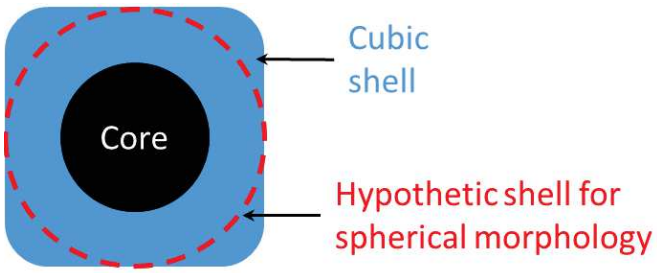

Figure 63. Schematic illustration of the growth of a cubic with round corner shape on a spherical core.

Moreover, in the XRD pattern of CSSNi2A two other contributions correspond to the presence of Ni^0 which was formed during the decomposition of NiOct due to high reducing synthesizing conditions. Hence, the CSSNi2A sample will not be analyzed further.

Peaks become narrower as long as shells are grown on the nanoparticles showing the single-like crystallinity of the nanoparticles due to low lattice mismatch between spinel and wüstite phases. Thanks to the Debye-Scherrer method, mean crystal sizes of 9.3 and 9.8 nm were determined for CSCo4 and CSSNi4 and 7.3, 7.0 and 8.3 nm for CSCo2, CSSNi2A and CSSNi2C. Crystal sizes appears to be smaller than the size measured from TEM micrographs due to the 2D projections of the faceted nanoparticles and also to the size distribution of the nanoparticles where the smallest nanoparticles participate to the enlargement of the XRD peaks and so to a faked reduction of the crystal size.

It is expected that the iron oxide cores C4b and C2b display mean cell parameters between the one of magnetite (8.396 Å, JCPDS card n° 19-062) and maghemite (8.338 Å, JCPDS card n° 39-1346) due to the expected presence of surface oxidation. Calculated cell parameters for CSCo4 and CSCo2 nanoparticles are equivalent to 8.399 ± 0.001 Å and 8.354 ± 0.001 Å. CSCo4 evidence a high cell parameter, close to the one of magnetite, demonstrating the presence of a high content of Fe^{2+} due to the chemical reduction of the iron oxide core and to the eventual presence of crystal strains resulting from lattice mismatch. Such results are in accordance with previous results obtained on similar nanoparticles (see chapters II, III and IV). However, the cell parameter of CSCo2 appears to be very low compared to the 8.40 (see chapter II) or 8.41 Å obtained previously for similar chemical compositions (see chapter III). This can be correlated to the high contribution of the wüstite phase present in the XRD pattern of CSCo2 which generate some mathematical errors on the determination of the full width at half maximum.
The cell parameter increases to 8.414 ± 0.001 Å in CSSNi4 evidencing an increase of strains which can be attributed to a further growth of the CoO phase but also to the growth of the NiO phase. This result is in agreement with the one obtained on $Fe_{3-d}O_4$@CoO@$Fe_{3-d}O_4$ (see chapter III) and $Fe_{3-d}O_4$@$CoFe_2O_4$@$Fe_{3-d}O_4$ (see chapter IV) nanoparticles. Geometrical Phase Analysis (GPA) will be performed latter to probe the strains intensities (see chapter III and IV). In order to discriminate the site occupancy of Fe, Co and Ni atoms, absorption spectra (XAS) and X-ray magnetic circular dichroism (XMCD) spectra were recorded on the DEIMOS beamline at synchrotron SOLEIL (see later).
However, in the other series, the calculated cell parameter decreases from CSCo2 to CSSNi2A (8.273 ± 0.001 Å) and CSSNi2C (8.320 ± 0.001 Å). They are lower than the cell parameter of maghemite (8.338 Å) which is the lowest cell parameter expected in such system. This decrease cannot be attributed to crystal strains but can be explained by the high contribution of wüstite CoO a = 4.2612 Å (JCPDS card n° 48-1719) and NiO phases as a_{NiO} = 4.117 Å (JCPDS card n° 47-1049) which crush the contribution of the spinel phase.

X-ray diffractions showed the presence of a spinel structure for each nanoparticles. The $Fe_{3-d}O_4$@CoO and $Fe_{3-d}O_4$@CoO@NiO nanoparticles evidenced the presence of a wüstite phase in their XRD patterns. The signature of the wüstite phase is even more pronounced for the cubic series (CSCo2, CSSNi2A and CSSNi2C). Due to the presence of Ni^0 in CSSNi2A, this sample is not analyzed further. XRD showed the increase of the crystal sizes. The high cell parameters calculated for CSCo4 and CSSNi4 agrees with a high contribution of Fe^{2+} and with the presence of crystal strains, in accordance with other core@shell@shell nanoparticles. ***[Chapter III and chapter IV]*** *However, the cell parameters calculated for CSCo2 and CSSNi2C appears to be very low contrary to our expectation and disagree with previous results. Their low cell parameters were attributed to high wüstite content.*

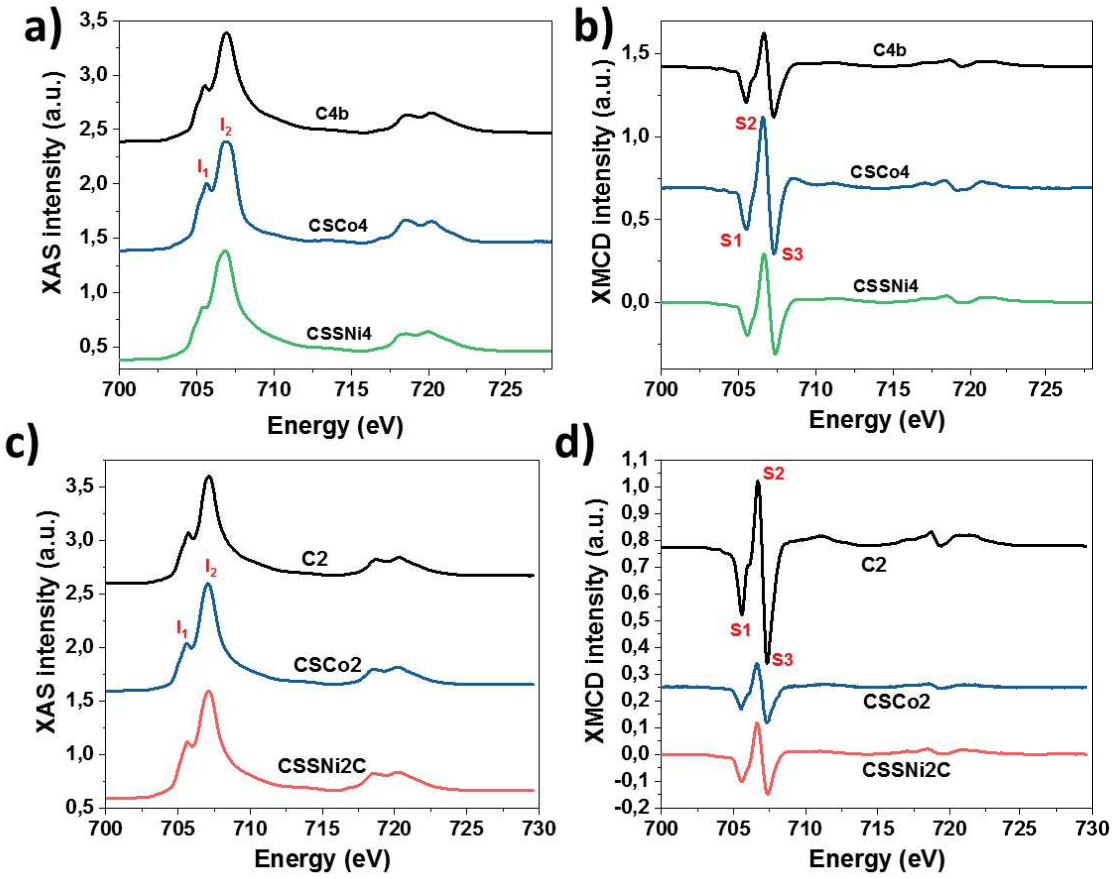

Figure 64. a, c) XAS and b, d) XMCD spectra recorded at the Fe $L_{2,3}$ edges of a, b) C4b, CSCo4, CSSNi4 and c, d) C2, CSCo2 and CSSNi2C nanoparticles recorded at the Fe $L_{2,3}$ edges. XAS and XMCD spectra are all normalized at the edge to the jump of the XAS signal.

Isotropic XAS spectra recorded at the Fe $L_{2,3}$ edges are all typical of an iron oxide invert spinel structure.[19–21] In isotropic XAS spectra recorded at the Fe $L_{2,3}$ edges, the intensity of peak I_1 arises mostly from the contribution of Fe^{2+} in octahedral (Oh) sites while the intensity of peak I_2 arises mostly from the contribution of Fe^{3+} in Oh sites. Hence, the ratio I_1/I_2 brings further information on the Fe^{2+} content in the sample where for example, a pure magnetite displays a calculated I_1/I_2 ratio of 0.71 while a pure maghemite displays 0.35 for the same ratio according to ref.[22]

Due to the low content remain of C4, we estimated a ratio of 0.56 for C4 according to XAS-XMCD experiment performed on a similar sample (C4b) (see chapter III). A ratio of 0.52 was calculated for C2. This ratio increases to 0.87 and 0.57 for CSCo4 and CSCo2 respectively, demonstrating a higher Fe^{2+} content in CSCo4 than in C4, which is at the opposite to FT-IR analysis but that is concordant with XRD measurements and previous works (see chapters II and III). Indeed, it has been proved previously that during the synthesis of the CoO shell, the iron oxide core undergoes a chemical reduction and is then protected by the CoO shell from a further oxidation by exposition of the nanoparticles to air.
In CSSNi4, the I_1/I_2 ratio decreased to 0.63, evidencing a lower Fe^{2+} content than for CSCo4. This result may be attributed to the fact that the beam has to scatter a thicker thickness because of the growth of the second shell and that XAS were recorded in the total electron yield (TEY) mode that is mostly sensitive to the first nanometers.[23,24] However, according to the small thickness of the CoO/NiO shell (1.1 nm from TEM size measurements), we actually expect that TEY to also probe the iron oxide core. Thus, this Fe^{2+} deficiency is better attributed to the presence of interfacial diffusion.

At the opposite, the I_1/I_2 ratio increases further to 0.70 in CSSNi2C evidencing a further increase of Fe^{2+} in the overall nanoparticles. Such behavior was not expected as considering a perfect core@shell@shell model and the absence of remaining iron precursor (see FT-IR analysis). Indeed, this ratio was expected to be similar or to decrease due the increase of shells and to the use of the TEY recording mode.

Table 31. XAS and XMCD structural characteristics of iron oxide, CSCo4 and CSSNi4.

Sample	Diameter (nm)	I1/I2	(S1+S2)/(S2+S3)	δ	S4 (%)	S5 (%)
Iron oxide	10.1	0.56	0.83	0.26	-	-
CSCo4	10.7	0.87	0.82	0.27	22	-
CSSNi4	11.2	0.63	0.82	0.27	43	22
Magnetite ref	-	0.71	1.14	0	-	-
Maghemite ref	-	0.35	0.69	0.33	-	-

Figure 65. XAS and XMCD structural characteristics of iron oxide, C2, CSCo2 and CSSNi2C.

Sample	Diameter (nm)	I1/I2	(S1+S2)/(S2+S3)	δ	S4 (%)	S5 (%)
C2	5.8	0.52	0.73	0.31	-	-
CSCo2	8.4	0.57	0.77	0.29	14	-
CSSNi2C	7.8	0.70	0.83	0.26	10	0.1
Magnetite ref	-	0.71	1.14	0	-	-
Maghemite ref	-	0.35	0.69	0.33	-	-

XMCD spectra recorded at the Fe $L_{2,3}$ edges brings further information on the Fe^{2+} content in the nanoparticles. In each spectrum, the small shoulder at 706 eV is characteristics of a Fe^{2+} deficiency which is reflected by the comparison between the intensity difference between IS1-S2I and IS2-S3I. Hence, the intensity ratio (S1+S2)/(S2+S3) brings further information on the Fe^{2+} deficiency of the iron oxide phase. It was calculated from ref[22] that a pure magnetite displays a value of 1.14 for this ratio while a pure maghemite displays a ratio of 0.69. Moreover, from this ratio, a delta value (δ) of 0 and 0.33 for magnetite and maghemite respectively can be determined which allows to express a general chemical formula of the iron oxide phase to be $Fe_{1-\delta}O_{4/3}$.

Thus the iron oxide nanoparticles displays a (S1+S2)/(S2+S3) ratio of 0.83 (δ = 0.26) and C2 displays a 0.73 ratio (δ = 0.31). Then this ratio slightly decreases to 0.82 in CSCo4 (δ = 0.27) and increases to 0.77 (δ = 0.29) for CSCo2. Owing to the chemical reduction of the iron oxide core and its' protection by the CoO shell in CSCo4 and CSCo2, we expect the (S1+S2)/(S2+S3) ratio to be closer to magnetite i.e. to increase as observed for other systems (see chapter II and III) and for CSCo2. Thus the slight decrease observed for CSCo4 is attributed to the use of another iron oxide reference C4b. Indeed, in XRD, the high cell parameter of CSCo4 supports this conclusion.
CSSNi4 displays strictly identical values to CSCo4 for the (S1+S2)/(S2+S3) ratio (0.82) and for δ (0.27). In CSSNi2C, the (S1+S2)/(S2+S3) ratio increases further to 0.83 (δ = 0.26). As TEY is surface sensitive, these analyses would show the increase of the Fe^{2+} content within both series. However, we proved in chapter III with the sample CS2r that the iron oxide core embedded in a CoO shell is stable during a reheating. Hence Mössbauer experiments will be performed latter in order to probe the electronic environment of Fe atoms and understand the origin of the Fe^{2+} content increase from $Fe_{3-d}O_4$@CoO to $Fe_{3-d}O_4$@CoO@NiO. EELS and EELS-SI experiments will also be performed to investigate the spatial distribution of Fe, Co and Ni atoms.

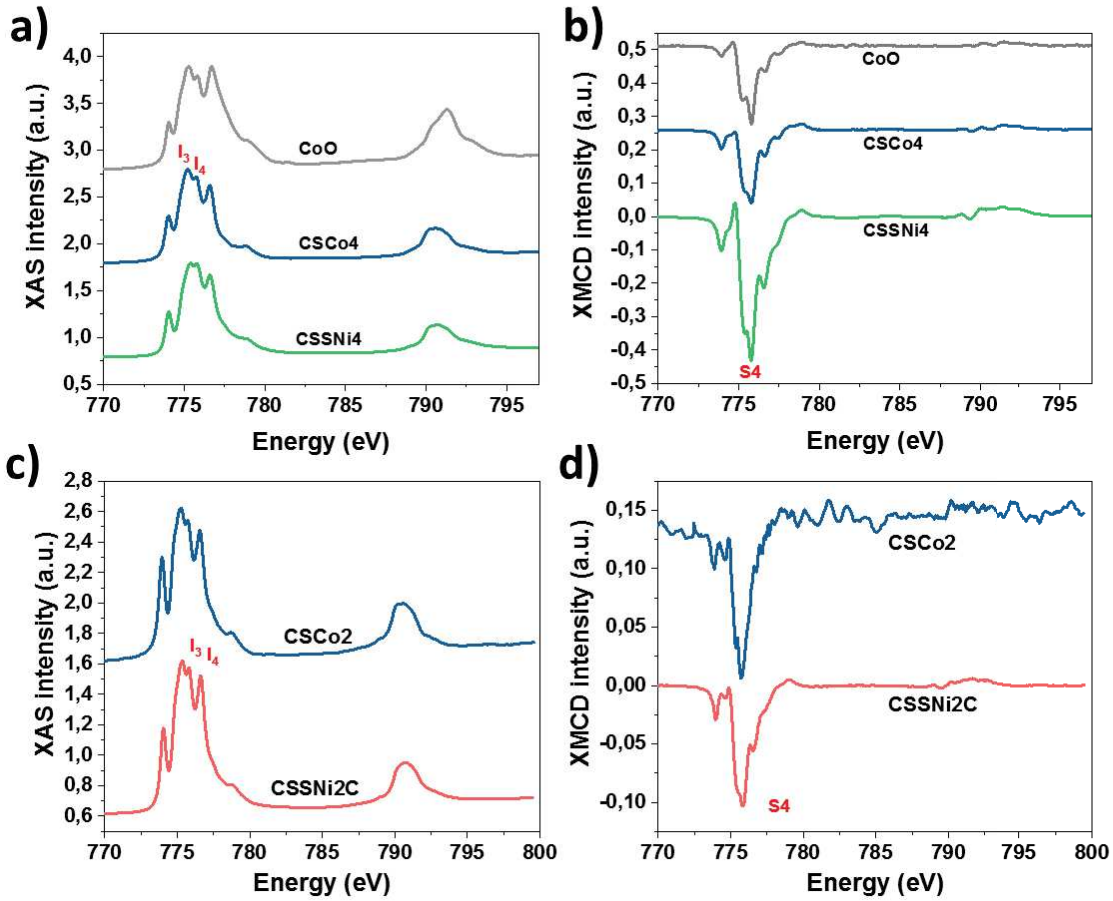

Figure 66. a, c) XAS and b, d) XMCD spectra recorded at the Co $L_{2,3}$ edges of a, b) CSCo4, CSSNi4 and c, d) CSCo2 and CSSNi2C nanoparticles recorded at the Co $L_{2,3}$ edges. All XAS and XMCD spectra are normalized at the edge to the jump of the XAS spectra.

Isotropic XAS and XMCD spectra recorded at the Co $L_{2,3}$ edges for CSCo4, CSSNi4, CSCo2 and CSSNi2C are typical of Co^{2+} in Oh sites of a spinel structure.[25] More specifically, in XAS spectra, intensity of peaks I_3 and I_4 is particularly interesting as in a perfect CoO structure, the intensity of peak I_4 is lower than the intensity of peak I_3.

In CSCo4 and CSCo2, the intensity of peak I_4 increases a bit compared to I_3 which agrees with the presence of CoO and of interfacial cobalt ferrite as demonstrated previously (see chapters II and III). The intensity of peak I_4 increases further in CSSNi4 and CSSNi2C and reaches the intensity of peak I_3 in the case of CSSNi4.

Peak S4 in the XCMD spectra of CSCo4 and CSCo2 reaches 22 and 14 % of intensity. This low intensity agrees with the presence of interfacial cobalt ferrite and of CoO according to a $Fe_{3-d}O_4$@CoO structure (see chapters II and III).

The intensity of peak S4 increases to 43 % in CSSNi4 while it decreases to 10 % for CSSNi2C. The increase of peak S4 observed for CSSNi4 is surprising. It evidences the increase of uncompensated spins of Co^{2+} compared to CSCo4. Such an observation was not expected as it has been proved previously (see sample CS2r in chapter III) that a further heating of a solely $Fe_{3-d}O_4$@CoO sample led to a very limited further Co^{2+} interfacial diffusion in the nanoparticles. Thus, the increase of uncompensated spins of Co^{2+} may arise from an increase of the cobalt ferrite content within the nanoparticles which is in agreement with XAS spectra of CSCo4 and CSSNi4 recorded at the Fe $L_{2,3}$ edges. It may also arise from a second interfacial layer of $Co_{1-x}Ni_xO$ where, due to a different magnetic moment between Ni^{2+} (2 μ_B) and Co^{2+} (1 μ_B for low spin configuration, 3 μ_B for high spin configuration), the spins do not compensates. The decrease of peak S4 in CSSNi2C compared to CSCo2 could be coherent with the expected $Fe_{3-d}O_4$@CoO@NiO structure as the TEY recording mode is sensitive to the surface. However,

the size of the $Fe_{3-d}O_4$@CoO@NiO nanoparticles is lower than the size of the corresponding $Fe_{3-d}O_4$@CoO nanoparticles. Moreover, XAS spectra recorded at the Co edge evidence slightly higher cobalt ferrite content within CSSNi2 compared to CSCo2. Thus, the decrease of peak S4 reflects the increase of the CoO phase which may be correlated to the further decomposition of cobalt stearate remains during the synthesis of the NiO shell.

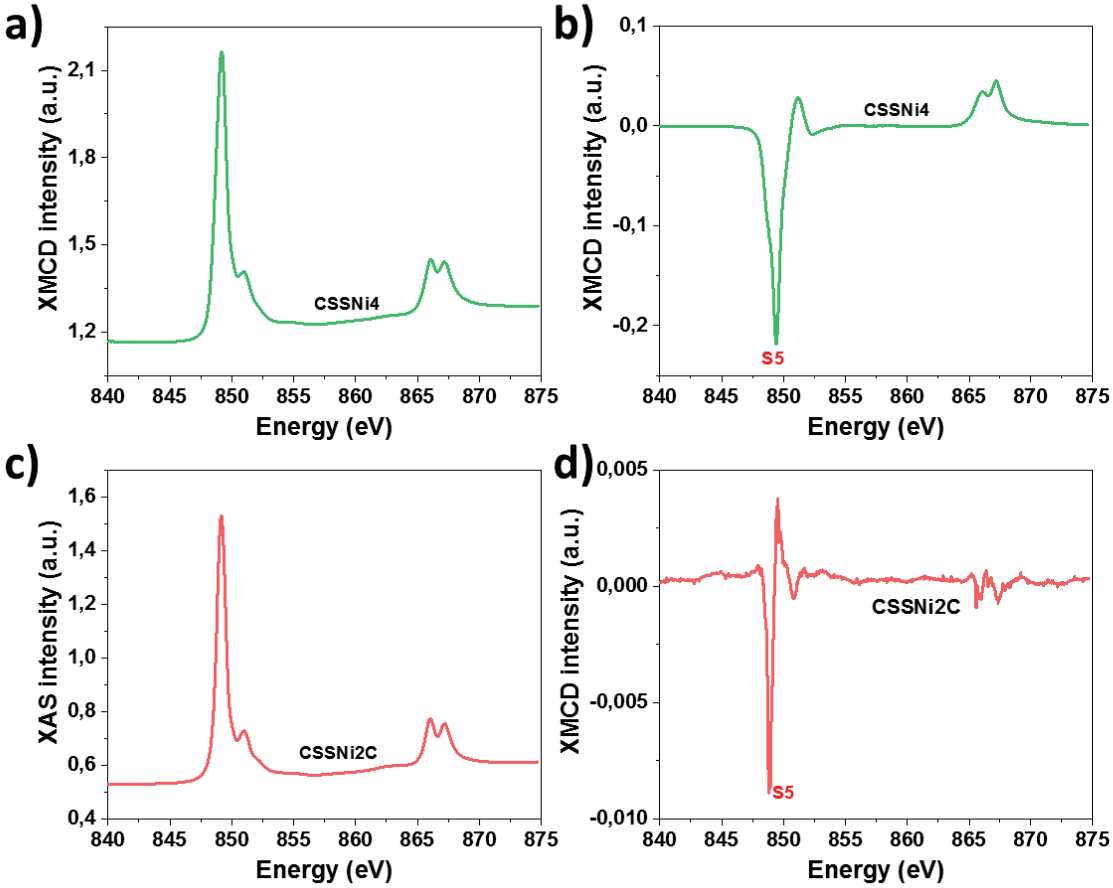

Figure 67. a, c) XAS and b, d) XMCD spectra recorded at the Ni $L_{2,3}$ edges of a, b) CSSNi4 and c, d) CSSNi2C recorded at the Ni $L_{2,3}$ edges. XAS and XMCD spectra are normalized at the edge to the jump of XAS spectra.

XAS and XMCD spectra recorded at the Ni $L_{2,3}$ edges for CSSNi4 bring further information on the Ni environment. They all agree with Ni^{2+} in Oh sites[23,26] where no clear differences were observed between the XAS and XMCD spectra of Ni^{2+} in a nickel ferrite or in a NiO structure.

The XMCD signal reaches an intensity of 22 % CSSNi4 which is very high for the solely NiO phase in analogy to the intensity of 23 % reached at the Co S4 edge for $Fe_{3-d}O_4$@CoO nanoparticles where this high intensity was attributed to the presence of interfacial cobalt ferrite. Owing to the small size thickness of Ni, the presence of this high contribution cannot solely be attributed to spin canting effects. Hence, this high intensity of the XMCD signal at the Ni S5 edge can be attributed to uncompensated spin moment of Ni^{2+} due to interfacial Co-O-Ni interactions that can be enhanced by the formation of an expected interfacial layer of $Co_{1-x}Ni_xO$. Furthermore, considering the small thickness of the CoO shell, it is possible that it has been solubilized during the growth of the NiO shell, resulting in a recrystallization in mixed spinel of Co and Ni according to $Co_{1-x}Ni_{1-y}Fe_{2+x+y}O_4$, in agreement with XAS and XMCD results obtained at the Fe and Co edges. The use of Mössbauer, EELS-SI and EELS techniques are mandatory here to determine the real structure of CSSNi4 nanoparticles.

At the opposite, S5 peak reaches a maximum of 1 % for CSSNi2C that agrees with the solely presence of an antiferromagnetic behavior of the NiO shell. It shows thus that the kinetic reaction in CSSNi2C is far different from the one of CSSNi4 and reinforce the faster deposition rate of Ni monomers toward

the diffusion rate that favors the cubic shape of CSSNi2C. Thus Ni atoms are located on the corners of the cube according to a high NiO concentration compared to the Ni cations that are in interaction with Co-O or involved in a $Co_{1-x}Ni_xO$ interfacial structure.

XAS XMCD recorded at the Fe $L_{2,3}$ edges show the increase of the Fe^{2+} content from the core to the core@shell, coherently with other reported analysis in Chapter II and Chapter III. They also surprisingly show the increase of Fe^{2+} content within the cubic $Fe_{3-d}O_4$@CoO@NiO nanoparticles (CSSNi2C) where further analysis such as Mössbauer analysis will be performed latter. XAS and XMCD recorded at the Co $L_{2,3}$ edges showed the presence of cobalt ferrite within CSCo4 and CSCo2, in accordance with other reported experiments on similar systems (Chapter II and Chapter III). The increase of the S4 peak for CSSNi4 is related to the increase of uncompensated Co^{2+} spins wich may be attributed to Co-O-Ni interactions that can be present in a $Co_{1-x}Ni_xO$ structure or the increase of the cobalt ferrite content. At the opposite, the decrease of S4 peak in CSSNi2C was attributed to the TEY recording which is surface sensitive and evidenced thus the furhter growth of CoO and the growth of the NiO shell at the surface of the CoO shell. XAS and XMCD spectra recorded at the Ni $L_{2,3}$ agree with Ni^{2+} cations in Oh sites. They show a high intensity of S5 peak for CSSNi4 which can be attributed to Ni^{2+} moment embedded in a $Co_{1-x}Ni_xO$ structure or in a mixed $Co_{1-x}Ni_{1-y}Fe_{2+x+y}O_4$ ferrite. On the contrary, a very weak signal was observed for CSSNi2C that shows the AFM configuration of the NiO phase.

Selective hysteresis

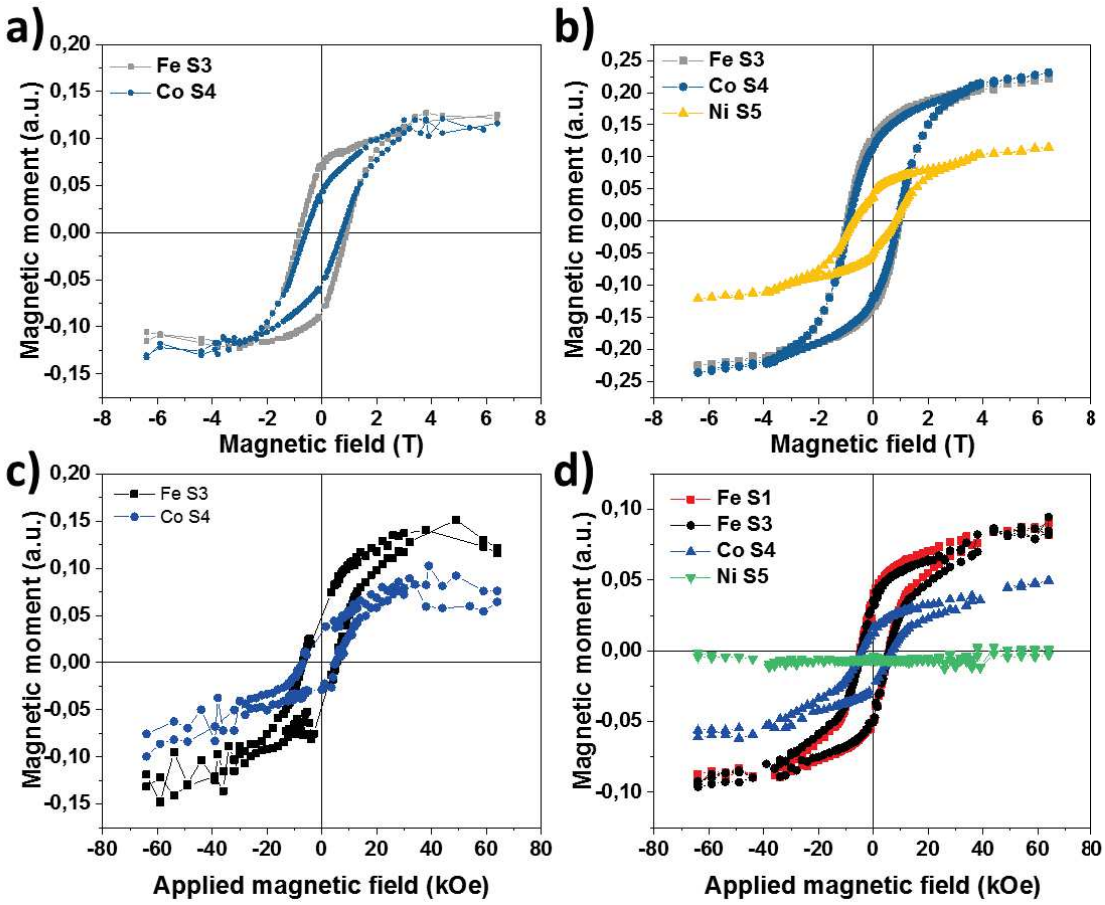

Figure 68. Element specific XMCD M(H) curves recorded at Fe S3, Co S4 and Ni S5 edges at 4 K for a) CSCo4, b) CSSNi4, c) CSCo2 and d) CSSNi2C nanoparticles. Curves are normalized as follow: $(H^+ + H^-)/(2*(H^+ - H^-))$.

Table 32. Magnetic characteristics of element specific XMCD of CSCo4, CSSNi4, CSCo2 and CSSNi2C samples recorded at the Fe S3, Co S4 and Ni S5 edges.

Sample	CSCo4		CSSNi4			CSCo2		CSSNi2C			
Edge	Fe S3	Co S4	Fe S3	Co S4	Ni S5	Fe S3	Co S4	Fe S1	Fe S3	Co S4	Ni S5
H_C (kOe)	8.6	6.6	9.5	9.0	7.6	6.3	6.0	5.3	5.0	5.5	0
M_R/M_S (%)	57	38	58	50	37	35	33	48	41	34	-

Selective hystereses were recorded at the Fe S3 and Co S4 edges for CSCo4 and CSCo2. They evidenced coercive fields of 8.6 and 6.6 kOe for CSCo4 and 6.3 and 6.0 for CSCo2 respectively. As the measured coercive fields are similar for CSCo2, it agrees with a strong magnetic exchange coupling between the iron oxide core and the uncompensated Co^{2+} cations (see chapters II and III and ref.[27]) that are mostly present in the interfacial cobalt ferrite layer. At the opposite, the difference of coercive field measured for CSCo4 demonstrates a low exchange coupling and the opening of the hysteresis at the Co S4 edge is attributed to the solely presence of interfacial cobalt ferrite.
The H_C measured for CSCo4 at the Fe S3 and Co S4 edges are lower than the H_C measured for other $Fe_{3-d}O_4$@CoO nanoparticles (10.9 kOe) featured by a core size of 10.1 nm and a shell thickness of 2.0 nm (see chapter III). Such consideration can be inferred to a less efficient exchange-bias coupling in CSCo4 and to volume effects where CSCo4 displays smaller core size and shell thickness than the above cited example. However, the H_C of CSCo4 is higher than the H_C of other $Fe_{3-d}O_4$@CoO nanoparticles (5.5 kOe) recorded for a core size of 8.8 nm and a CoO shell thickness of 0.7 nm. This can be attributed to a better crystallinity of CSCo4, leading to a more efficient exchange bias than for the reported nanoparticles.[28,29]
The measured H_C of CSCo2 are lower than for sphere-like $Fe_{3-d}O_4$@CoO nanoparticles featured by a core size of 10.1 nm and a shell thickness of 2.0 nm (10.9 kOe at the Fe and Co edges) (see chapter III) or than the CS nanoparticles featured by a core size of 9.2 nm and a shell thickness of 0.8 nm (8.6 kOe at the Fe S3 edge and 6.6 kOe at the Co S4 edge). Here CSCo2 displays an iron oxide core size of 5.8 nm and a shell thickness of 1.3 nm leading to the smallest H_C. In single component nanoparticles of γFe_2O_3 or $CoFe_2O_4$, it has been observed that for size smaller than 20 nm, the effective anisotropic constant and the surface anisotropy constant of cubic nanoparticles is lower than the one of spherical nanoparticles, leading to higher H_C [30,31] for the cubic morphology than for the spherical one. As the inverse was observed, we attributed such behavior to a lower content of interfacial cobalt in CSCo2 than for the other reported nanoparticles, as shown by the intensity of XMCD signal recorded at the Co edge (14 % for CSCo2, 23 % for chapter III and 30 % for Chapter II).

Selective hysteresis recorded at the Fe S3, Co S4 and Ni S5 edges in CSSNi4 evidence close coercive fields of 9.5, 9.0 and 7.6 kOe respectively. It evidences a strong magnetic coupling between the iron oxide core and the cobalt ferrite shell. However, the smaller H_C measured at the Ni S5 edge compared to the ones measured at the Fe S3 and Co S4 edges, shows a weaker magnetic coupling between the uncompensated Ni^{2+} and the iron oxide and cobalt ferrite shell. As we estimated the uncompensated Ni^{2+} to be involved in a $Co_{1-x}Ni_xO$ structure and that they are at the surface of the CoO shell, the weak coupling effect can be attributed to distance effect between the uncompensated Ni^{2+} moment and the iron oxide and cobalt ferrite phases that are surrounded by the CoO shell. Moreover, the coupling of the Ni-content phase can be allowed through the presence of Co-O-Ni interactions as evidenced in XMCD recorded at the Ni S5 edge.
Furthermore, the increase of H_C measured at the Fe S3 and Co S4 edges of CSSNi4 compared to CSCo4 can be attributed to the decrease of spin disorders favored by the high temperature conditions of the third thermal decomposition.

Element selective hysteresis of CSSNi2C evidence similar H_C of 5.3, 5.0 and 5.5 kOe at the Fe S1, Fe S2 and Co S4 edges which agrees with strong coupling effect where an additional hysteresis at the Fe S1 edge was recorded for CSSNi2C in order to prove that hysteresis cycles at different Fe edges display

the same behavior. However, the signal recorded at the Ni S5 edge does not show any opening of the hysteresis and evidence an antiferromagnetic behavior. This result is in accordance with XMCD experiments recorded at the Ni $L_{2,3}$ edges where no XMCD signal was observed. Hence it proves that Ni cations contained in CSSNi2C are not magnetically coupled to the rest of the nanoparticles which is probably due to the limitation of the Co-O-Ni interactions, and that they display a solely antiferromagnetic behavior. Moreover, the H_C measured at the Fe and Co edges are lower than in CSCo2 which can be attributed to a decrease of the shell thickness that were observed on size measurements from TEM micrographs, leading to a decrease of the volume of the cobalt ferrite shell.

The M_R/M_S ratio calculated at the Fe S3 edge for CSCo4 and CSCo2 is of 57 and 35 % respectively. The lower M_R/M_S ratio for CSCo2 than CSCo4 can be attributed to a higher M_S for CSCo2 due to its cubic shape that displays a higher surface anisotropy than the close to sphere shape of CSCo4. Both M_R/M_S ratio of CSCo4 and CSCo2 are lower than the value of 65 % measured for a $Fe_{3-d}O_4$@CoO nanoparticles with a 2.0 nm thick CoO shell according to TEM size measurements (see chapter III). At the Co edge, the M_R/M_S ratio is equivalent to 38 and 33 % for CSCo4 and CSCo2 respectively. They are close one from the other and are lower than the 55 % measured for a similar system (see chapter III). Regarding the slanted shape of the both hysteresis, their low values arise from the antiferromagnetic contribution of the CoO phase which increases M_S and to strong magnetic exchange coupling resulting in difficulties to saturate the hystereses at high fields.

The coating of the $Fe_{3-d}O_4$@CoO nanoparticles by a NiO shell allows to tune the M_R/M_S ratio calculated at the Fe S3 and Co S4 edges. Hence CSSNi4 displays M_R/M_S values of 58 (Fe S3) and 50 % (Co S4) and CSSNi2 evidences values of 48 and 41 %. For CSSNi4, the M_R/M_S ratio calculated at the Fe S3 edge is similar to the one of its corresponding core@shell (CSCo4), showing a similar hardness from the core. The alignement ratio increases at the Co S4 edge for CSSNi4 and at the Fe S3 and CoS4 edges for CSSNi2, this can be attributed to the presence of the AFM NiO phase which decreases the spin canting effect due to proximity effect.
Furthermore, these values remain low and evidence in each samples a slanted shape of the hysteresis with a slow and smooth approach to saturation, that is typical of highly anisotropic system due to the presence of magnetic exchange coupling within the nanoparticles.[27]

Selective hystereses recorded at the Fe S3, Co S4 and Ni S5 edges show the presence of a strong magnetic coupling within CSCo2, CSSNi4 and CSSNi2C. However, CSCo4 evidenced a weaker exchange coupling than the other probed nanoparticles. The slanted shape of the hysteresis arises from AFM contributions and their slow and smooth approaches to saturation are typical of highly anisotropic systems due to strong magnetic exchange coupling.[27] The growth of a NiO shell at the surface of the $Fe_{3-d}O_4$@CoO nanoparticles allowed to decrease spin canting effects and to increase their alignment ratio. Furthermore, these hystereses evidence the presence of atomic diffusion at the Ni $L_{2,3}$ edges for CSSNi4 (spherical shape) while CSSNi2C (cubic shape) evidence a pure AFM signal of the NiO shell.

SQUID magnetometry

Table 33. SQUID magnetic characteristics of CSCo4, CSSNi4, C2, CSCo2 and CSSNi2C nanoparticles.

	CSCo4	CSSNi4	C2	CSCo2	CSSNi2C
Diameter (nm)	10.7 ± 1.2	11.2 ± 1.3	5.8	8.4 ± 0.9	7.8 ± 1.0
Shell thickness (nm)	0.8	0.3	-	1.3	-0.3
Shell volume (nm^3)	234	94	-	310	-62
$\mathbf{H_C}$ 5 K ZFC (kOe)	20.5	18.0	0.15	18.0	14.5
$\mathbf{H_C}$ 10 K FC (kOe)	22.6	18.9	0.2	22.3	14.8
$\mathbf{H_E}$ 10 K FC (kOe)	2.1	1.6	-	2.5	4.7
$\mathbf{H_V}$ 10 K FC (memu)	-	-	-	0.64	0.33
$\mathbf{H_C}$ 300K ZFC (kOe)	0	0	0	0	0
$\mathbf{T_{max}}$ FC-ZFC (K)	294	294	30	210	223
$\mathbf{T_B}$ d(MZFC-MFC)/dT (K)	252	259	15	157	144
$\mathbf{K_{eff}}$ (10^5 J/m3)	1.4	1.2	0.51	1.75	2.00

Magnetic properties of samples CSCo4, CSSNi4, C2, CSCo2 and CSSNi2C were recorded with SQUID magnetometry. Magnetization curves recorded against an applied magnetic field at 300 K evidence superparamagnetic behavior for every sample. It agrees with magnetization curves recorded against temperature. Indeed, T_{max} of 294 K were measured for both CSCo4 and CSSNi4 which corresponds to T_B (determined from $d(M_{ZFC}-M_{FC})/dT$)[32] of 252 and 259 K respectively. Such result was expected for CSCo4 as in such system, the limitation of T_{max} to around 290 K is provided by the Neel temperature of the antiferromagnetic CoO shell (290 K) above which it loses its ability to produce exchange-bias effect due to the paramagnetic behavior of the AFM shell. The growth of a NiO shell on the seed nanoparticles do not affect T_{max} due to the fact that $K_{NiO}V_{NiO}$ ($7.5\ 10^5$ J/m^3) is lower than $K_{CSco4}V_{CSCo4}$ ($1.3\ 10^8$ J/m^3). And also because T_{max} of the solely NiO phase in CSSNi4 is lower than T_{max} of CSCo4.[23,33]

T_{max} of 30, 210 and 223 K were measured for C2, CSCo2 and CSSNi2C which corresponds to T_B of 15, 157 and 144 K respectively. Hence in CSCo2, the maximum T_{max} of 290 K corresponding to the T_N of CoO has not been reached which can be attributed to a smaller size compared to similar $Fe_{3-d}O_4$@CoO systems (see chapters II and III) but also to shape anisotropy where T_B of cubic nanoparticles is lower than for spherical nanoparticles of similar volumes.[30] In CSSNi2C, it is to note that despite a higher T_{max}, its' T_B is lower than CSCo2 which agrees with the smaller size of CSSNi2C. T_B of CSSNi2C is lower than the T_B of CSNi4 which can be attributed to the smaller size of CSSNi2C and also to its cubic shape where cubic shaped nanoparticles evidence lower T_B than their spherical shape.[30]

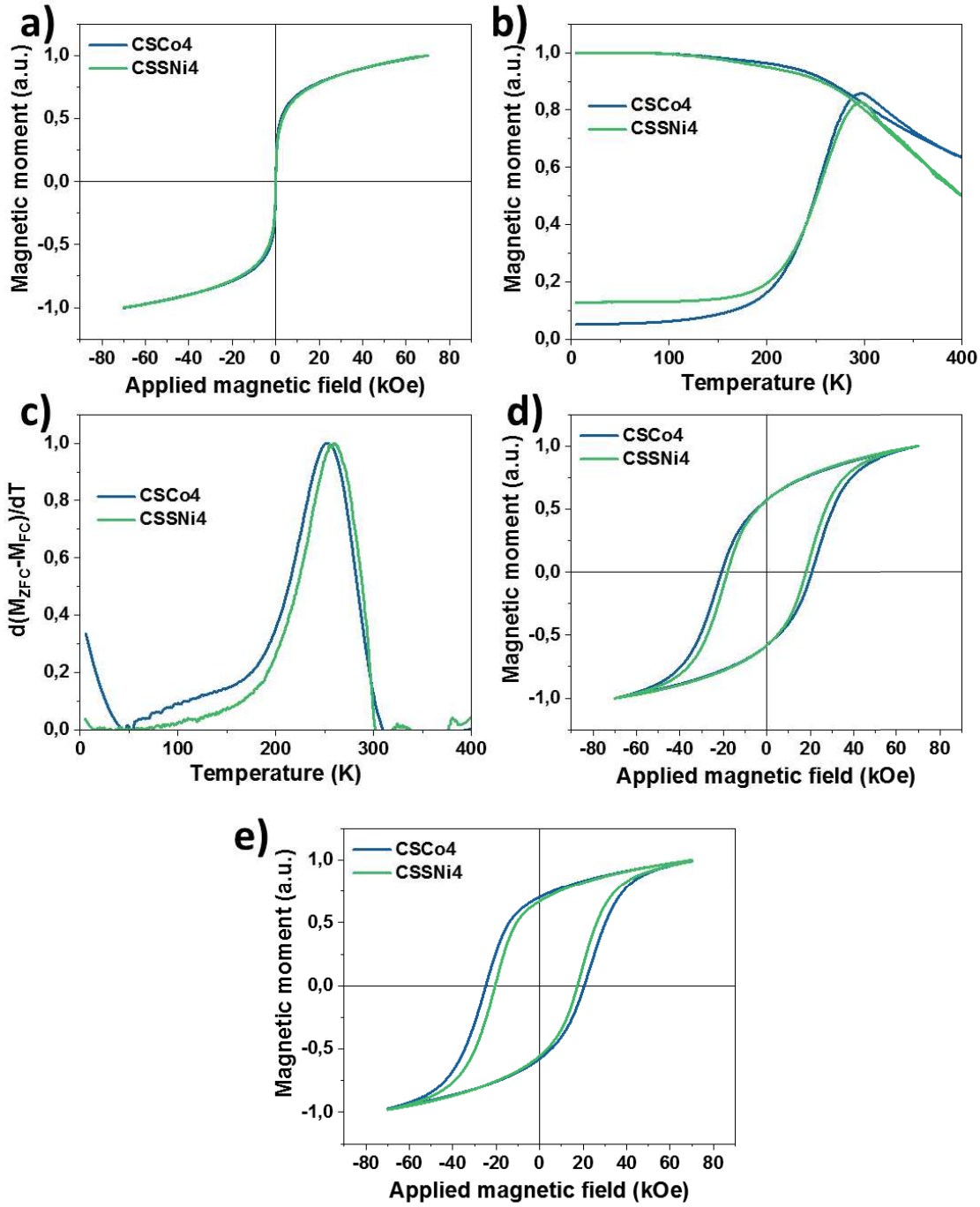

Figure 69. Magnetic properties of CSCo4 and CSSNi4: a) Magnetization recorded against an applied magnetic field at 300 K, b) Magnetization recorded against temperature recorded after FC and ZFC, c) $d(M_{ZFC}-M_{FC})/dT$ versus temperature, Magnetization recorded against an applied magnetic field d) at 5 K, e) at 10 K after field cooling under an applied magnetic field of 7 T

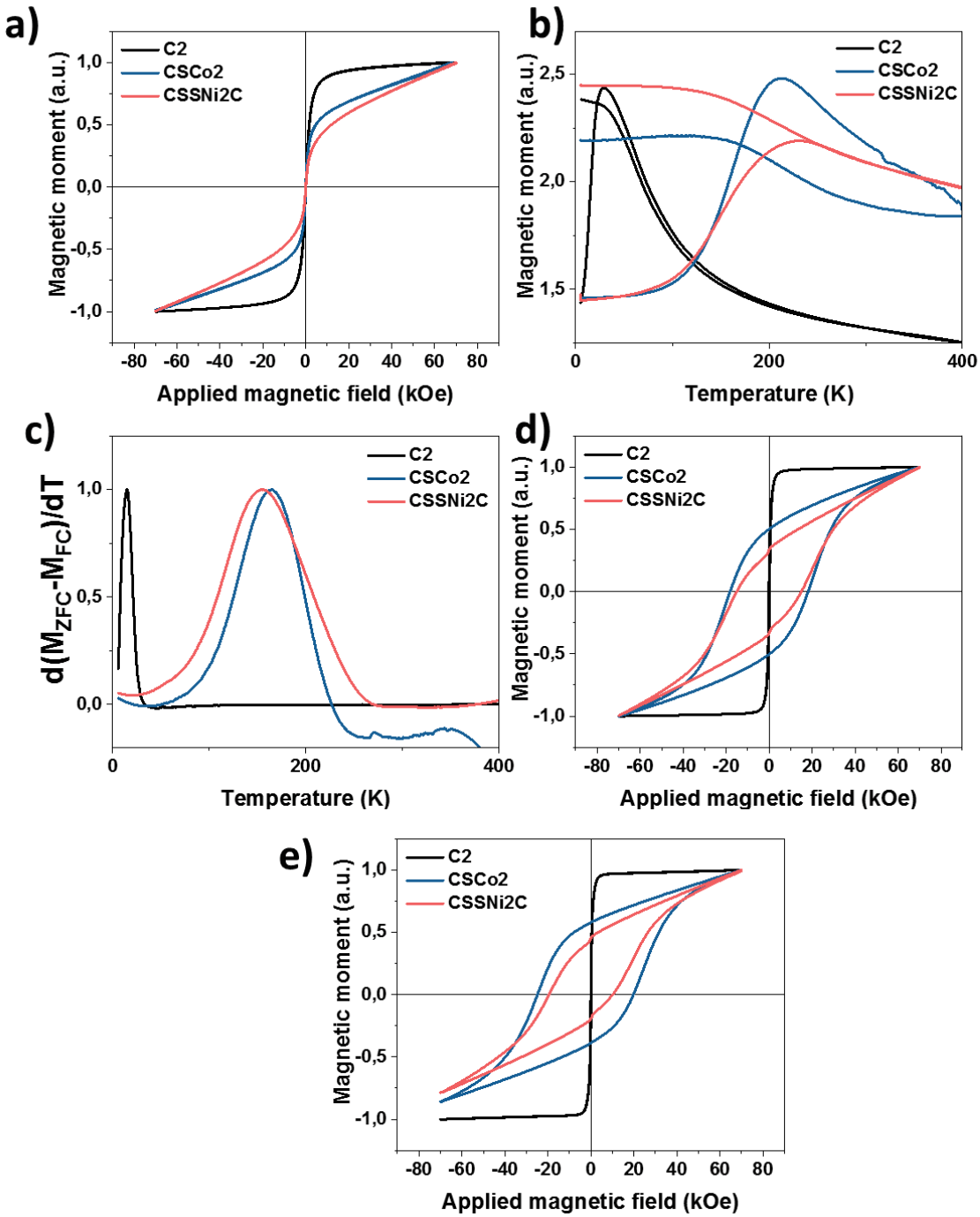

Figure 70. Magnetization recorded a) against a magnetic field at 300K, b) against temperature, against a magnetic field at c) 5 K, d) 10K after field cooling under an applied magnetic field of 7 T. e) $d(M_{ZFC}-M_{FC})/dT$.

Thanks to the Stoner-Wohlfarth equation ($K_{eff}V = 25k_BT_B$), K_{eff} of 5.1 10^4 J/m^3 was calculated for C2 nanoparticles. This is higher than the reported value of K = 2 10^4 J/m^3 for bulk magnetite at 4 K and can be attributed to size reduction which favor surface anisotropy.[34,35]

Then, K_{eff} of 1.4 and 1.75 10^5 J/m^3 were calculated for CSCo4 and CSCo2. This is higher than for C2 nanoparticles according to the CoO phase which is featured by an anisotropy constant of 5 10^5 J/m^3 [36] that increases the overall K_{eff} of the core@shell nanoparticles thanks to a strong magnetic coupling. K_{eff} of CSCo4 and CSCo2 are also higher than the 6.4 10^4 J/m^3 reported for $Fe_{3-d}O_4$@CoO nanoparticles of Chapter III and agree with the 1.4 10^5 J/m^3 reported for $Fe_{3-d}O_4$@CoO nanoparticles of Chapter II. The differences are attributed to volume effects.

A K_{eff} of 1.2 10^5 J/m^3 was calculated for CSSNi4 which is slightly lower than the one of its CSCo4 core@shell. The slight decrease of K_{eff} in CSSN compared to CS can be attributed to the decrease of the CoO shell (due to a partial solubilisation/recrystllisation process during the seed-mediated growth of the NiO shell) which displays a high anisotropy constant of 5 10^5 J/m^3 [36] and to the presence of NiO which is featured by a low anisotropy constant of 8 10^3 J/m^3.[37]
In CSSNi2C, K_{eff} increases to 2.00 10^5 J/m^3 while a decrease of K_{eff} was expected with the addition of the soft NiO phase. It can be attributed to the increase of the CoO content as shown by XAS and XMCD analysis but also to a size reduction of the nanoparticles that increases K_{eff} (see chapter II and ref[38]) as surface effects are more important than volume effects in small sized nanoparticles. It explains also the higher K_{eff} of CSSNi2C than CSSNi4.

Magnetization curves recorded against a magnetic field after zero field cooling (ZFC) at 5 K evidence H_C of 20.5 and 18.0 kOe for CSCo4 and CSSNi4 respectively. Hence, the growth of a soft magnetic NiO shell has decreased H_C. The same behavior is observed for the cubic series where H_C of 18.0 kOe was measured for CSCo2 and decreases to 14.5 for CSSNi2C.

Magnetization curves recorded against a magnetic field after field cooling (FC) under a magnetic field of 7 T evidence high H_C of 22.6 and 22.3 kOe for CSC4 and CSCo2 respectively. They are higher than their H_C measured after ZFC due to the orientation of the spins with the applied magnetic field during the FC process. The slightly lower H_C of CSCo2 than CSCo4 can be attributed to shape anisotropy where cubic nanoparticles of CSCo2 display a lower H_C than the spherical ones of CS[30] and/or to a lower content of interfacial cobalt ferrite as shown by XMCD measurements. Furthermore, The H_C of CSCo4 and CSCo2 are higher than the reported H_C of 19.8 kOe for $Fe_{3-d}O_4$@CoO nanoparticles with a core size of 10.1 nm and a shell thickness of 2.0 nm (see chapter III) or than the 15.3 kOe for similar nanoparticles with a core size of 8.8 nm and a shell thickness of 0.7 nm (see chapter II). The increase of H_C in such core@shell exchange-biased system is generally attributed to the presence of smaller cores that enhance the exchange-bias effects.[39] However, the core size of CSCo4 is larger than for the last cited examples, we attributed such consideration to a higher cobalt ferrite content in CSCo4 than for the examples as will be discussed later.
Moreover, under such experimental conditions, one can observe that the hysteresis cycle is shifted to lower values of the applied magnetic field which is the result of the exchange-bias coupling appearing between the ferrimagnetic core and the antiferromagnetic shell. This effect is characterized by the so called exchange field H_E and is equivalent to 1.6 and 2.5 kOe for CSCo4 and CSCo2 respectively. The higher H_E of CSCo2 than CSCo4 arises from a larger CoO volume in CSCo2 (310 nm^3) than in CSCo4 (234 nm^3).
The H_E in CSCo4 is low (2.1 kOe) compared to the other one of 5.3 and 2.0 kOe of the examples cited above respectively. The ratio $K_{shell}V_{shell}/K_{core}V_{core}$ is equivalent to 14.3 for CSCo4 which is similar to the 13.9 obtained for the previously cited $Fe_{3-d}O_4$@CoO nanoparticles (chapter II) but lower than the 43.0 obtained for the firstly cited $Fe_{3-d}O_4$@CoO nanoparticles (chapter III). Thus the high H_C of CSCo4 cannot be attributed to a stronger exchange-bias coupling nor to dipolar effects as long as stronger dipolar effects would increase T_B and decrease H_C.[40] Thus we attributed this higher H_C compared to the above cited examples to arise from a greater interfacial quantity of cobalt ferrite produced by diffusion and/or partial solubilisation-recrystallisation process during the synthesis of the CoO shell as $Fe_{3-d}O_4$@$CoFe_2O_4$ nanoparticles display high H_C with no exchange-field (see chapter IV).
The H_E of CSCo2 is higher than the one of the CS_CoO nanoparticles described in ref[6] due to a higher $K_{shell}V_{shell}/K_{core}V_{core}$ ratio (50.9) than for the cited example (13.9) and the smaller core of CSCo2 which makes a more efficient exchange bias coupling. However, H_E of CSCo2 is lower than the one of $Fe_{3-d}O_4$@CoO nanoparticles described in ref[5] which displays a lower $K_{shell}V_{shell}/K_{core}V_{core}$ of 43.0 than CSCo2. Hence, the less efficient exchange bias coupling of CSCo2 compared to the last described sample can be attributed to a lower interface quality or to a the different geometry of the CoO shell on the iron oxide core (cubic versus spherical).

Moreover, the hysteresis cycle recorded at 10 K after FC evidence a vertical shift for CSCo2 and CSSNi2C samples. Such observation is attributed to arise from uncompensated pinned moments of the AFM phase[28] that are generally located in a spin disordered part of the nanoparticles.[41]
This behavior has not been observed in similar $Fe_{3-d}O_4$@CoO spherical nanoparticles[3–6,42,43] and was thus attributed to a shape effect and more precisely on a surface effect where the uncompensated pinned moment should preferably be in the corners of the AFM phase of the CSCo2 nanoparticles. Moreover, the vertical shift is proportional to the number of uncompensated spins moments and decreases from 0.64 in CSCo2 to 0.33 in CSSNi2C evidencing that some nickel cations are present in the corners and antiferromagnetically coupled to the Co^{2+} cations.
In CSSNi4, H_C recorded at 10 K after FC is of 18.9 kOe which is lower than the 22.6 measured for CSCo4. The same behavior is observed for CSSNi2 which displays a lower H_C of 14.8 compared to CSCo2 (22.3 kOe). This can be attributed to the growth of the soft NiO shell, indeed, according to ref[44–46]

$$H_C = 2\frac{K_H f_H + K_S f_S}{M_H f_H + M_S f_S}$$

Where K and f corresponds to the anisotropy constant and volume fraction respectively whilst, H and S subscripts refer to the hard and soft phase respectively. Assuming that $K_H = 63\ K_S$; $M_H \approx M_S$ and that $(2K_H)/M = H_H$,[44] it results that

$$H_C = H_H\left(1 - \frac{1}{63} f_S\right)$$

In CSSNi4, the decrease of H_C can also be attributed to the decrease of the exchange bias coupling as shown by the decrease of H_E to 1.6 kOe (H_E CSCo4 = 2.1 kOe). The decrease of H_E arises from the growth of the soft NiO phase and to the possible reduction of the hard CoO volume due to solubilisation-recrystallisation[47] process during the synthesis of the second shell.
At the opposite, H_E has increased to 4.7 in CSSNi2C (H_E CSCo2 = 2.5 kOe), evidencing a more efficient exchange-bias coupling for CSSNi2C than for CSCo2. However, owing to the size decrease observed from CSCo2 to CSSNi2C, we expected a decrease of the CoO content hence on the decrease of $K_{CoO}V_{CoO}$. The increase of H_E is concomitant with the decrease of uncompensated pinned moment within the AFM (see H_V). Hence the higher H_E of CSSNi2C than CSCo2 can be attributed to a structural modification of the CoO phase, favoring the exchange-bias coupling.

SQUID magnetometry measurements showed that the growth of a NiO shell on $Fe_{3-d}O_4$@CoO@NiO nanoparticles do not increase their stability above room temperature. Indeed, their volume is too low to improve such stability. However, despite the low volume of the NiO phases added, they affected the magnetic properties of the native $Fe_{3-d}O_4$@CoO nanoparticles. Indeed, they decreased the H_C measured at low temperature in ZFC due to their low magnetic anisotropy constant. Depending on the shape of the nanoparticles, they increased (CSSNi4) or decreased (CSSNi2C) H_E and de facto the strength of the exchange-bias coupling. The decrease is coherent with an increase of the soft volume in CSSNi4 while the increase in CSSNi2C was attributed to a structural modification. Furthermore, the cubic shaped nanoparticles evidenced the presence of uncompensated pinned moment in the AFM which were attributed to be located in the corners of the cubes. The number of these uncompensated pinned moments were reduced by the addition of a NiO shell in CSSNi2C. Finally, NiO allowed to slightly decreases K_{eff} in CSSNi4 due to its low magnetic anisotropic constant. However, owing to the size decrease of CSSNi2C compared to CSCo2 and to the further addition of CoO as shown by XAS, XMCD, K_{eff} of CSSNi2C has been increased compared to K_{eff} of CSCo2.

Summary and conclusion

The synthesis of NiO nanoparticles is scarcely reported in the literature where no satisfying references were found on the synthesis of NiO nanoparticles through the thermal decomposition method. Hence a first study on the synthesis of NiO nanoparticles was performed. $Fe_{3-d}O_4$@NiO nanoparticles were also synthesized in order to investigate the seed-mediated growth synthesis parameters for the decomposition of Ni based organo-metallic precursors. These studies presented in annexes are the basements of the synthesized $Fe_{3-d}O_4$@CoO@NiO nanoparticles presented in this chapter.
Here, two different series of nanoparticles were synthesized: a cubic one and a spherical one.
In the spherical $Fe_{3-d}O_4$@CoO@NiO nanoparticles, all shells were magnetically coupled together according to selective hysteresis measurements. XMCD measurements evidenced a high intensity of the signal recorded at the Ni $L_{2,3}$ edges that was attributed to an interfacial layer of $Co_{1-x}Ni_XO$ that participates to strengthen the exchange coupling within the nanoparticle. However, SQUID magnetometry has shown that the growth of a NiO shell on the $Fe_{3-d}O_4$@CoO seed did not managed to increase T_{max} or T_B and at the opposite decrease the strength of the exchange coupling. It has also led to the overall decrease of K_{eff} compared to the $Fe_{3-d}O_4$@CoO native nanoparticles. Such behavior was attributed to the low magnetic anisotropic value of NiO and from its low volume.

In the second series of $Fe_{3-d}O_4$@CoO@NiO nanoparticles that display a cubic shape, XRD showed the high contribution of the CoO and NiO wüstite phases in the core@shell and core@shell@shell nanoparticles compared to the iron oxide spinel contribution. XAS and XMCD experiments demonstrated the presence of an AFM behavior for the NiO phase which is in accordance with selective hysteresis measurements and with the high wüstite content. Selective hysteresis performed at the Fe S3, Co S4 edges has also demonstrated a strong magnetic exchange coupling within the cubic $Fe_{3-d}O_4$@CoO@NiO nanoparticles. These strong magnetic exchange coupling is observed in SQUID magnetometry measurements that points out the increase of H_E in CSSNi2C compared to CSCo2, testifying a more efficient exchange bias coupling for CSSNi2C. However, H_C decreases in CSSNi2C in compliance with the growth of the soft NiO phase. This is also concomitant with the reduction of H_V that shows the compensation of the pinned magnetic moment. Furthermore, the third thermal decomposition led to a decrease in size of CSSNi2C compared to CSCo2 which generates an increase of the overall K_{eff} despite the growth of the NiO shell. However, T_B did not increase from CSCo2 to CSSNi2C with the growth of the NiO shell.

Thus, at the opposite of De Toro and al.[1] who reported on the increase of T_{max} by agencing Co@CoO nanoparticles in a NiO matrix, we did not succeed to increase further the thermal stability of $Fe_{3-d}O_4$@CoO based nanoparticles through the addition of a NiO shell. Such consideration is attributed to the volume of the soft NiO phase that is not sufficient to act on the magnetic properties of the $Fe_{3-d}O_4$@CoO nanoparticles due to their high effective magnetic anisotropy constant compared to the low $K_{NiO}V_{NiO}$. Thus the next step would be to embed $Fe_{3-d}O_4$@CoO nanoparticles in a NiO matrix or to increase much more the volume of the soft NiO shell.

References

(1) De Toro, J. A.; Marques, D. P.; Muñiz, P.; Skumryev, V.; Sort, J.; Givord, D.; Nogués, J. High Temperature Magnetic Stabilization of Cobalt Nanoparticles by an Antiferromagnetic Proximity Effect. *Phys. Rev. Lett.* **2015**, *115* (5). https://doi.org/10.1103/PhysRevLett.115.057201.

(2) Baaziz, W.; Pichon, B. P.; Fleutot, S.; Liu, Y.; Lefevre, C.; Greneche, J.-M.; Toumi, M.; Mhiri, T.; Begin-Colin, S. Magnetic Iron Oxide Nanoparticles: Reproducible Tuning of the Size and Nanosized-Dependent Composition, Defects, and Spin Canting. *J. Phys. Chem. C* **2014**, *118* (7), 3795–3810. https://doi.org/10.1021/jp411481p.

(3) Baaziz, W.; Pichon, B. P.; Lefevre, C.; Ulhaq-Bouillet, C.; Greneche, J.-M.; Toumi, M.; Mhiri, T.; Bégin-Colin, S. High Exchange Bias in $Fe_{3-\delta}O_4$ @CoO Core Shell Nanoparticles Synthesized by a One-Pot Seed-Mediated Growth Method. *J. Phys. Chem. C* **2013**, *117* (21), 11436–11443. https://doi.org/10.1021/jp402823h.

(4) Liu, X.; Pichon, B. P.; Ulhaq, C.; Lefèvre, C.; Grenèche, J.-M.; Bégin, D.; Bégin-Colin, S. Systematic Study of Exchange Coupling in Core–Shell $Fe_{3-\delta}O_4$ @CoO Nanoparticles. *Chem. Mater.* **2015**, *27* (11), 4073–4081. https://doi.org/10.1021/acs.chemmater.5b01103.

(5) Sartori, K.; Choueikani, F.; Gloter, A.; Begin-Colin, S.; Taverna, D.; Pichon, B. P. Room Temperature Blocked Magnetic Nanoparticles Based on Ferrite Promoted by a Three-Step Thermal Decomposition Process. *J. Am. Chem. Soc.* **2019**, *141* (25), 9783–9787. https://doi.org/10.1021/jacs.9b03965.

(6) Sartori, K.; Cotin, G.; Bouillet, C.; Halté, V.; Bégin-Colin, S.; Choueikani, F.; Pichon, B. P. Strong Interfacial Coupling through Exchange Interactions in Soft/Hard Core–Shell Nanoparticles as a Function of Cationic Distribution. *Nanoscale* **2019**, *11* (27), 12946–12958. https://doi.org/10.1039/C9NR02323B.

(7) Cotin, G.; Kiefer, C.; Perton, F.; Boero, M.; Özdamar, B.; Bouzid, A.; Ori, G.; Massobrio, C.; Begin, D.; Pichon, B.; et al. Evaluating the Critical Roles of Precursor Nature and Water Content When Tailoring Magnetic Nanoparticles for Specific Applications. *ACS Appl. Nano Mater.* **2018**, *1* (8), 4306–4316. https://doi.org/10.1021/acsanm.8b01123.

(8) Xia, Y.; Xia, X.; Peng, H.-C. Shape-Controlled Synthesis of Colloidal Metal Nanocrystals: Thermodynamic versus Kinetic Products. *J. Am. Chem. Soc.* **2015**, *137* (25), 7947–7966. https://doi.org/10.1021/jacs.5b04641.

(9) Zhang, L.; He, R.; Gu, H.-C. Oleic Acid Coating on the Monodisperse Magnetite Nanoparticles. *Appl. Surf. Sci.* **2006**, *253* (5), 2611–2617. https://doi.org/10.1016/j.apsusc.2006.05.023.

(10) Nakamoto, K. *Infrared and Raman Spectra of Inorganic and Coordination Compounds*, 6th ed.; Wiley: Hoboken, N.J, 2009.

(11) Ren, Y.; Iimura, K.; Kato, T. Structure of Barium Stearate Films at the Air/Water Interface Investigated by Polarization Modulation Infrared Spectroscopy and Π− *A* Isotherms. *Langmuir* **2001**, *17* (9), 2688–2693. https://doi.org/10.1021/la000872e.

(12) Chen, M.; Feng, Y.-G.; Wang, X.; Li, T.-C.; Zhang, J.-Y.; Qian, D.-J. Silver Nanoparticles Capped by Oleylamine: Formation, Growth, and Self-Organization. *Langmuir* **2007**, *23* (10), 5296–5304. https://doi.org/10.1021/la700553d.

(13) Morales, M. P.; Andres-Verges, M.; Veintemillas-Verdaguer; Montero, M. I.; Serna, C. J. Structural Effects on the Magnetic Properties of Y-Fe2O3 Nanoparticles. *J. Magn. Magn. Mater.* **1999**, *203*, 146–148.

(14) Morales, M. P.; Pecharroman, C.; Gonzalez-Carreño; Serna, C. J. Structural Characteristics of Uniform Y-Fe2O3 Particles with Different Axial (Length/Width) Ratios. *J. Solid State Chem.* **1994**, *108*, 158–163.

(15) Tang, C.-W.; Wang, C.-B.; Chien, S.-H. Characterization of Cobalt Oxides Studied by FT-IR, Raman, TPR and TG-MS. *Thermochim. Acta* **2008**, *473* (1–2), 68–73. https://doi.org/10.1016/j.tca.2008.04.015.

(16) Davar, F.; Fereshteh, Z.; Salavati-Niasari, M. Nanoparticles Ni and NiO: Synthesis, Characterization and Magnetic Properties. *J. Alloys Compd.* **2009**, *476* (1–2), 797–801. https://doi.org/10.1016/j.jallcom.2008.09.121.

(17) Sheena, P. A.; Priyanka, K. P.; Sabu, N. A.; Sabu, B.; Varghese, T. EFFECT OF CALCINATION TEMPERATURE ON THE STRUCTURAL AND OPTICAL PROPERTIES OF NICKEL OXIDE NANOPARTICLES. 10.

(18) Jacintho, G. V. M.; Brolo, A. G.; Corio, P.; Suarez, P. A. Z.; Rubim, J. C. Structural Investigation of MFe_2O_4 (M = Fe, Co) Magnetic Fluids. *J. Phys. Chem. C* **2009**, *113* (18), 7684–7691. https://doi.org/10.1021/jp9013477.

(19) Brice-Profeta, S.; Arrio, M.-A.; Tronc, E.; Menguy, N.; Letard, I.; Cartier dit Moulin, C.; Noguès, M.; Chanéac, C.; Jolivet, J.-P.; Sainctavit, Ph. Magnetic Order in - Nanoparticles: A XMCD Study. *J. Magn. Magn. Mater.* **2005**, *288*, 354–365. https://doi.org/10.1016/j.jmmm.2004.09.120.

(20) Zhu, X.; Kalirai, S. S.; Hitchcock, A. P.; Bazylinski, D. A. What Is the Correct Fe L23 X-Ray Absorption Spectrum of Magnetite? *J. Electron Spectrosc. Relat. Phenom.* **2015**, *199*, 19–26. https://doi.org/10.1016/j.elspec.2014.12.005.

(21) Torres, T. E.; Roca, A. G.; Morales, M. P.; Ibarra, A.; Marquina, C.; Ibarra, M. R.; Goya, G. F. Magnetic Properties and Energy Absorption of $CoFe_2O_4$ Nanoparticles for Magnetic Hyperthermia. *J. Phys. Conf. Ser.* **2010**, *200* (7), 072101. https://doi.org/10.1088/1742-6596/200/7/072101.

(22) E. Pellegrin et al. Characterization of Nanocrystalline Y-Fe2O3 with Synchrotron Radiation Techniques. *Phys Stat Sol* **1999**, *215*, 797.

(23) Skoropata, E.; Su, T. T.; Ouyang, H.; Freeland, J. W.; van Lierop, J. Intermixing Enables Strong Exchange Coupling in Nanocomposites: Magnetism through the Interfacial Ferrite in γ − Fe 2 O 3 / NiO. *Phys. Rev. B* **2017**, *96* (2). https://doi.org/10.1103/PhysRevB.96.024447.

(24) Li, J.; Menguy, N.; Arrio, M.-A.; Sainctavit, P.; Juhin, A.; Wang, Y.; Chen, H.; Bunau, O.; Otero, E.; Ohresser, P.; et al. Controlled Cobalt Doping in the Spinel Structure of Magnetosome Magnetite: New Evidences from Element- and Site-Specific X-Ray Magnetic Circular Dichroism Analyses. *J. R. Soc. Interface* **2016**, *13* (121), 20160355. https://doi.org/10.1098/rsif.2016.0355.

(25) Moyer, J. A.; Vaz, C. A. F.; Negusse, E.; Arena, D. A.; Henrich, V. E. Controlling the Electronic Structure of Co 1 − x Fe 2 + x O 4 Thin Films through Iron Doping. *Phys. Rev. B* **2011**, *83* (3). https://doi.org/10.1103/PhysRevB.83.035121.

(26) Ikeno, H. First-Principles Analysis of X-Ray Magnetic Circular Dichroism for Transition Metal Complex Oxides. *J. Appl. Phys.* **2016**, *120* (14), 142104. https://doi.org/10.1063/1.4961713.

(27) Estrader, M.; López-Ortega, A.; Estradé, S.; Golosovsky, I. V.; Salazar-Alvarez, G.; Vasilakaki, M.; Trohidou, K. N.; Varela, M.; Stanley, D. C.; Sinko, M.; et al. Robust Antiferromagnetic Coupling in Hard-Soft Bi-Magnetic Core/Shell Nanoparticles. *Nat. Commun.* **2013**, *4*. https://doi.org/10.1038/ncomms3960.

(28) Oscar Iglesias; Amilcar Labarta; Xavier Battle. Exchange Bias Phenomenology and Models of Core/Shell Nanoparticles. *Cond Mat* **2008**.

(29) López-Ortega, A.; Estrader, M.; Salazar-Alvarez, G.; Estradé, S.; Golosovsky, I. V.; Dumas, R. K.; Keavney, D. J.; Vasilakaki, M.; Trohidou, K. N.; Sort, J.; et al. Strongly Exchange Coupled Inverse Ferrimagnetic Soft/Hard, MnxFe3−xO4/FexMn3−xO4, Core/Shell Heterostructured Nanoparticles. *Nanoscale* **2012**, *4* (16), 5138. https://doi.org/10.1039/c2nr30986f.

(30) Salazar-Alvarez, G.; Qin, J.; Sepelak, V.; Bergmann, I.; Vasilakaki, M.; Trohidou, K. N.; Ardisson, J. D.; Macedo, W. A. A.; Mikhaylova, M.; Muhammed, M. Cubic versus Spherical Magnetic Nanoparticles: The Role of Surface Anisotropy. *J. Am. Chem. Soc.* **2008**, *130* (40), 13234–13239.

(31) Nemati, Z.; Alonso, J.; Rodrigo, I.; Das, R.; Garaio, E.; García, J. Á.; Orue, I.; Phan, M.-H.; Srikanth, H. Improving the Heating Efficiency of Iron Oxide Nanoparticles by Tuning Their Shape and Size. *J. Phys. Chem. C* **2018**, *122* (4), 2367–2381. https://doi.org/10.1021/acs.jpcc.7b10528.

(32) Bruvera, I. J.; Mendoza Zélis, P.; Pilar Calatayud, M.; Goya, G. F.; Sánchez, F. H. Determination of the Blocking Temperature of Magnetic Nanoparticles: The Good, the Bad, and the Ugly. *J. Appl. Phys.* **2015**, *118* (18), 184304. https://doi.org/10.1063/1.4935484.

(33) Winkler, E.; Zysler, R. D.; Vasquez Mansilla, M.; Fiorani, D.; Rinaldi, D.; Vasilakaki, M.; Trohidou, K. N. Surface Spin-Glass Freezing in Interacting Core–Shell NiO Nanoparticles. *Nanotechnology* **2008**, *19* (18), 185702. https://doi.org/10.1088/0957-4484/19/18/185702.

(34) Gilmore, K.; Idzerda, Y. U.; Klem, M. T.; Allen, M.; Douglas, T.; Young, M. Surface Contribution to the Anisotropy Energy of Spherical Magnetite Particles. *J. Appl. Phys.* **2005**, *97* (10), 10B301. https://doi.org/10.1063/1.1845973.

(35) Cao, C.; Tian, L.; Liu, Q.; Liu, W.; Chen, G.; Pan, Y. Magnetic Characterization of Noninteracting, Randomly Oriented, Nanometer-Scale Ferrimagnetic Particles. *J. Geophys. Res.* **2010**, *115* (B7), B07103. https://doi.org/10.1029/2009JB006855.

(36) Meiklejohn, W. H.; Bean, C. P. New Magnetic Anisotropy. *Phys. Rev.* **1956**, *102* (5), 1413–1414. https://doi.org/10.1103/PhysRev.102.1413.

(37) Tadic, M.; Nikolic, D.; Panjan, M.; Blake, G. R. Magnetic Properties of NiO (Nickel Oxide) Nanoparticles: Blocking Temperature and Neel Temperature. *J. Alloys Compd.* **2015**, *647*, 1061–1068. https://doi.org/10.1016/j.jallcom.2015.06.027.

(38) Bødker, F.; Mørup, S. Size Dependence of the Properties of Hematite Nanoparticles. *Europhys. Lett. EPL* **2000**, *52* (2), 217–223. https://doi.org/10.1209/epl/i2000-00426-2.

(39) Liu, Y.; Liu, X.; Dolci, M.; Leuvrey, C.; Pardieu, E.; Derory, A.; Begin, D.; Begin-Colin, S.; Pichon, B. P. Investigation of the Collective Properties in Monolayers of Exchange-Biased $Fe_{3-\delta}O_4$@CoO Core–Shell Nanoparticles. *J. Phys. Chem. C* **2018**, *122* (30), 17456–17464. https://doi.org/10.1021/acs.jpcc.8b04615.

(40) Matthias, P. Structuration de nanoparticules magnétiques d'oxyde de fer en films et étude de leurs propriétés magnétiques et de magnétotransport, 2010.

(41) Mumtaz, A.; Maaz, K.; Janjua, B.; Hasanain, S. K.; Bertino, M. F. Exchange Bias and Vertical Shift in CoFe2O4 Nanoparticles. *J. Magn. Magn. Mater.* **2007**, *313* (2), 266–272. https://doi.org/10.1016/j.jmmm.2007.01.007.

(42) Franceschin, G.; Gaudisson, T.; Menguy, N.; Dodrill, B. C.; Yaacoub, N.; Grenèche, J.-M.; Valenzuela, R.; Ammar, S. Exchange-Biased Fe3−xO4-CoO Granular Composites of Different Morphologies Prepared by Seed-Mediated Growth in Polyol: From Core–Shell to Multicore Embedded Structures. *Part. Part. Systmes Charact.* **2018**, No. 35, 1800104.

(43) Skoropata, E.; Desautels, R. D.; Chi, C.-C.; Ouyang, H.; Freeland, J. W.; van Lierop, J. Magnetism of Iron Oxide Based Core-Shell Nanoparticles from Interface Mixing with Enhanced Spin-Orbit Coupling. *Phys. Rev. B* **2014**, *89* (2). https://doi.org/10.1103/PhysRevB.89.024410.

(44) Song, Q.; Zhang, Z. J. Controlled Synthesis and Magnetic Properties of Bimagnetic Spinel Ferrite $CoFe_2O_4$ and $MnFe_2O_4$ Nanocrystals with Core–Shell Architecture. *J. Am. Chem. Soc.* **2012**, *134* (24), 10182–10190. https://doi.org/10.1021/ja302856z.

(45) Masala, O.; Hoffman, D.; Sundaram, N.; Page, K.; Proffen, T.; Lawes, G.; Seshadri, R. Preparation of Magnetic Spinel Ferrite Core/Shell Nanoparticles: Soft Ferrites on Hard Ferrites and Vice Versa. *Solid State Sci.* **2006**, *8* (9), 1015–1022. https://doi.org/10.1016/j.solidstatesciences.2006.04.014.

(46) Zeng, H.; Sun, S.; Li, J.; Wang, Z. L.; Liu, J. P. Tailoring Magnetic Properties of Core⁄shell Nanoparticles. *Appl. Phys. Lett.* **2004**, *85* (5), 792–794. https://doi.org/10.1063/1.1776632.

(47) Lentijo-Mozo, S.; Deiana, D.; Sogne, E.; Casu, A.; Falqui, A. Unexpected Insights about Cation-Exchange on Metal Oxide Nanoparticles and Its Effect on Their Magnetic Behavior. *Chem. Mater.* **2018**, *30* (21), 8099–8112. https://doi.org/10.1021/acs.chemmater.8b04331.

General conclusion

In the last hundred years, human activity has exponentially developed resulting in the drastic increase of the overall pollution. If all of us do not rapidly decrease the impact of this activity, the effect on the climate will be devastator within fifty years. In this frame, it is mandatory to find ecological alternative to the industrial sectors that pollutes the most. One of them is the production of rare earths where their extraction and purification procedures uses a lot of chemicals and pollutes the subsoils and our most precious resource: water. At the nanoscale, rare earths made component allow to produce permanent nano-magnet which can be used for data storage facilities.
Iron oxide in the form of magnetite/maghemite is an abundant, costless material with low cytotoxicity effect, displaying interesting magnetic properties in its bulk form. However, at the nanoscale for sizes below 20 nm which are interesting for data storage applications, iron oxide nanoparticles display superparamagnetic properties. Hence at this stage, it is not possible to use them for such application. Nevertheless, it is possible to increase the magnetic stability toward temperature of small iron oxide based nanoparticles using the exchange-bias coupling property. Indeed, the magnetic coupling of a soft FiM layer with an AFM hard magnetic one allows to increase the blocking temperature of the overall material up to the Neel temperature of the AFM phase. This is due to the pinning of the FiM magnetic moments by the AFM magnetic moments resulting from a strong magnetic exchange-coupling. This strong magnetic coupling is induced by good epitaxial relationships between the FiM and AFM phases. Hence, such prerequisite gives rise to a very limited number of materials which can be used to increase the magnetic anisotropy of iron oxide based nanoparticles. CoO was firstly retained as it crystallizes in a similar space group as iron oxide and his cell parameter participates to good epitaxial relationships. Furthermore, this AFM material displays a high magnetic anisotropy constant compared to $Fe_{3-d}O_4$ with a Neel temperature of 290 K.

The synthesis technique is a crucial stage to design such nanoparticles. We decided here to use the thermal decomposition method which allows to produce magnetic nanoparticles with high yields that is important for future developments. The thermal decomposition synthesis is ruled by the monomer concentration in solution which depends on the decomposition kinetic of the precursor. Thus, the fine adaptation of the different paremeters (concentration of precursor and surfactant, nature of the precursor, nature of the surfactant, solvent boiling temperature, heating ramp, hydration rate) allows to finely control the shape and size of the desired nanoparticles. The variety of parameters in the thermal decomposition makes it powerful to tune the chemical composition of the nanoparticles. Hence, it is possible to synthesize core@shell nanoparticles through a seed-mediated growth process using the thermal decomposition.

Chapter 1 reports on a preliminary study on the growth of iron oxide nanoparticles performed through a multi-seed mediated growth process in thermal decomposition allowed to grow the size of the nanoparticles from 6.5 to 15 nm by the deposition of 4 layers on an iron oxide core. It was the first time that so many thermal decomposition steps were performed successively to gincrease the size of iron oxide nanoparticles. It shows that even after a succession of five thermal decomposition steps, the nanoparticles display a controlled size and shape. Besides the growth of the iron oxide nanoparticles, we have also investigated their chemical composition by XRD, FT-IR and Mössbauer spectroscopy. Indeed, magnetite spontaneously oxidized into maghemite upon exposure to air. Every analysis techniques agree on the synthesis of oxidized layer on the top of the seeds which is coherent with their small thicknesses.

Earlier, the synthesis of $Fe_{3-d}O_4$@CoO nanoparticles according to a seed-mediated growth process thanks to a succession of two thermal decompositions, reported on the successful increase of the overall magnetic anisotropy.[1] The amount of cobalt precursor inserted in order to grow the CoO shell affected drastically the magnetic properties.[2] Indeed, for high amount of Co, a discontinuous CoO shell

disfavored the exchange-bias coupling while for low amount of Co precursors led to the drastic increase of H_C and T_B with a low H_E. Such behavior was indirectly attributed to the presence of interfacial Co^{2+} diffusion.
In Chapter 2, we investigated more deeply the effect of Co^{2+} diffusion on the resulting magnetic properties of $Fe_{3-d}O_4$@CoO nanoparticles, three different core@shell nanoparticles were synthesized.

- Co-doped $Fe_{3-d}O_4$ nanoparticles were synthesized by the diffusion of Co^{2+} atoms in the iron oxide core.
- A cobalt ferrite shell was directly grown onto the surface of an iron oxide core to synthesize $Fe_{3-d}O_4$@$CoFe_2O_4$ nanoparticles.
- $Fe_{3-d}O_4$@CoO nanoparticles were synthesized according to a previously described protocol.[1]

All three structures were succesfully synthesized by a seed-mediated growth process thanks to a succession of two thermal decompositions.
The structure of each system was finely studied by a wide set of techniques (TEM, EELS, EELS-SI, XRD, XAS and Mössbauer spectroscopy). The magnetic properties were then studied by XMCD and SQUID magnetometry. The nature of the shell has a strong influence on the resulting magnetic properties. Indeed, a Co-doped layer showed the most efficient enhancement of the magnetic anisotropy energy. A cobalt ferrite shell resulted in the most efficient exchange coupling. Finally, the growth of the CoO shell, which is concomitant to the synthesis of an interfacial cobalt ferrite layer resulting from the diffusion of Co^{2+}, enhanced the overall magnetic properties of the iron oxide based nanoparticles. The presence of the hard ferrimagnetic interfacial cobalt ferrite layer in the $Fe_{3-d}O_4$@CoO nanoparticles participated to the enhancement of the overall magnetic anisotropy energy which was observed through the increase of the blocking temperature from 60 K up to 220 K.

However, in such $Fe_{3-d}O_4$@CoO nanoparticles, it is not possible to reach a blocking temperature higher than the Néel temperature of the AFM CoO phase. Chapter 3 reported on the way we doubled the FiM/AFM interface by synthesizing core@shell@shell nanoparticles with the expected $Fe_{3-d}O_4$@CoO@$Fe_{3-d}O_4$ structure. The second $Fe_{3-d}O_4$ shell was grown according to different thicknesses. The structure of the final nanoparticles has been deeply investigated. TEM micrographs evidenced the growth of the nanoparticles from 10.1 to 15.6 nm among the different growth of the shells. HAADF and XRD measurements, showed the good epitaxial growth of the different shells with the presence of CoO within the core@shell and core@shell@shell nanoparticles. However, the growth of the CoO shell on the iron oxide was not as homogeneous as expected, so does for the growth of the second iron oxide shell, as shown by EELS and EELS-SI micrographs. Nevertheless, it resulted in the enhancement of the overall magnetic anisotropy and allowed to increase T_B from 93 to 335 K, concomitantly with the decrease of H_E from the core@shell to the core@shell@shell nanoparticles. The exchange-bias coupling almost vanished for the thicker second shell of $Fe_{3-d}O_4$@CoO@$Fe_{3-d}O_4$ nanoparticles. XAS, XMCD and Mössbauer experiments were used to investigate the Fe and Co environments and evidenced that the decrease of the exchange-bias coupling efficiency was due to the increase of interfacial cobalt ferrite. Furthermore, XAS and XMCD showed the surprising electronic stabilization of Fe^{2+} at the surface of the core@shell@shell nanoparticles whilst we expected the second shell to be fully oxidized. The increase of the interfacial cobalt ferrite layer resulted in a high $K_{FiM}V_{FiM}$ compared to $K_{CoO}V_{CoO}$, explaining the reason of the decrease of the exchange-bias effect. The structure was finally probed by small-angle neutron scattering that confirmed our conclusion on the increase of the interfacial cobalt ferrite layer at the expense of the CoO shell. Furthermore, polarized SANS were used to investigate the magnetic structure within the $Fe_{3-d}O_4$@CoO@$Fe_{3-d}O_4$. It showed the presence of magnetic anisotropy within the nanoparticles and that the magnetic radii were similar to the nuclear radii, according to the absence of spin canting effects.
At this stage, we were not sure on the reasons of the high blocking temperature of the $Fe_{3-d}O_4$@$(CoFe_2O_4)_x(CoO)_y(CoFe_2O_4)_z$@$Fe_{3-d}O_4$ nanoparticles. Indeed, the results did not allowed us to determine if the high blocking temperature was due either to the presence of a remain exchange-bias coupling either to a volume effect of the increase of the cobalt ferrite content.

In Chapter 4, we synthesized core@shell@shell nanoparticles with a cobalt ferrite saturated intermediate shell ($Fe_{3-d}O_4$@$CoFe_2O_4$@$Fe_{3-d}O_4$). TEM and XRD analysis agreed on the epitaxial growth of the shells on the nanoparticles and with the solely presence of a spinel structure. EELS-SI and EELS profiles demonstrated the $Fe_{3-d}O_4$@$CoFe_2O_4$ structure. However, it was not possible to discriminate the second $Fe_{3-d}O_4$ shell owing to its very thin thickness. Nevertheless, XAS XMCD and Mössbauer spectroscopies showed its presence. XAS and XMCD spectroscopies also evidenced the surprising presence of Fe^{2+} at the surface of the nanoparticles as in the previous chapter. Mössbauer spectroscopy, allowed us to determine the schematic chemical composition of each nanoparticle which consists in a 6.8 nm sized core surrounded by 2.9 nm and 0.3 nm thick of cobalt ferrite and iron oxide shells, respectively. The resulting magnetic properties were investigated by SQUID magnetometry and showed a high magnetic exchange coupling within the $Fe_{3-d}O_4$@$CoFe_2O_4$ nanoparticles that resulted in the drastic increase of T_B from 48 to 239 K. The growth of the second iron oxide shell increased further T_B, but less drastically, to 280 K. This growth was also accompanied by the decrease of K_{eff} and H_C. Such considerations are due to the increase of the volume of the soft ferrimagnetic counterpart and to a less efficient magnetic exchange coupling. The increase of T_B from the $Fe_{3-d}O_4$@$CoFe_2O_4$ to the $Fe_{3-d}O_4$@$CoFe_2O_4$@$Fe_{3-d}O_4$ nanoparticles was finally attributed to volume effects mainly due to the further growth of the $CoFe_2O_4$ shell during the third thermal decomposition step that was occurred in the presence of a high remains of Co precursors.
Hence, this chapter evidenced that the presence of the CoO phase in the $Fe_{3-d}O_4$@CoO@$Fe_{3-d}O_4$ nanoparticles synthesized in the previous chapter participates to the enhancement of the overall magnetic anisotropy of the resulting nanoparticles through a synergistic magnetic coupling with the interfacial cobalt ferrites.

We have shown that the growth of a CoO shell on small iron oxide nanoparticles allows to increase the magnetic stability against temperature. NiO has a very similar structure to CoO (same space group, close lattice parameter) with a very high Néel temperature (525 K). According to the work of De Toro and *al.*[3] T_B of Co@CoO nanoparticles was increased significantly through an antiferromagnetic proximity effect between the CoO shell and a NiO matrix. Therefore, we reported in Chapter 5 the transposition of our core@shell@shell approach in order to synthesize $Fe_{3-d}O_4$@CoO@NiO nanoparticles. We expected that the growth of a NiO shell on $Fe_{3-d}O_4$@CoO nanoparticles would benefit of an antiferromagnetic proximity of NiO. The synthesis of NiO nanoparticles with well defin size and shape by the thermal decomposition method was not reported yet in the literature. Thus, a first work on the synthesis development of NiO nanoparticles was performed. Even if the size and shape of the resulting NiO nanoparticles were not highly controlled, it was possible to synthesize satisfying $Fe_{3-d}O_4$@NiO nanoparticles. These preliminary studies are presented in the annexe and were mandatory to synthesize $Fe_{3-d}O_4$@CoO@NiO nanoparticles. Two different series were synthesized: a cubic and a spherical one. Their shape difference was due to a preferential growth of the CoO and NiO shell on the faceted seeds. Indeed, each facet displays different surface energy and in seed-mediated growth, the monomers nucleates firstly on the facets with the highest energy and migrates later to the facets with the lowest energy. The control of the deposition and the migration kinetics allows to control the final shape of the nanoparticles.
The synthesis of the $Fe_{3-d}O_4$@CoO@NiO nanoparticles was evidenced by the increase of the size measured from TEM micrographs for spherical nanoparticles. However, in the case of cubic nanoparticles, the growth of the NiO shell resulted in a size decrease of 0.3 nm. X-ray diffraction evidenced the presence of both spinel and wüstite phases in the core@shell and core@shell@shell nanoparticles. The wüstite contribution was larger for the cubic nanoparticles than for the spherical nanoparticles. XRD finally agreed on the epitaxial growth of CoO and NiO shells for every nanoparticles. XAS and XMCD measurements shows typical behavior for the $Fe_{3-d}O_4$@CoO nanoparticles. However, the growth of a NiO shell was surprisingly accompanied by an increase of the Fe^{2+} content within the nanoparticles. In order to conclude on this behavior, EELS-SI, EELS and Mössbauer analysis must be performed latter. The growth of the NiO shell showed an increase of the Co^{2+} magnetic moment for

the spherical shaped nanoparticles which was attributed to the presence of interfacial $Co_{1-x}Ni_xO$. At the opposite, it resulted in the decrease of the Co^{2+} magnetic moment for the spherical shaped nanoparticles. This behavior is coherent with the specific element M(H) curves that shoeds open hysteresis for the spherical shaped nanoparticles and an AFM behavior for the cubic shaped nanoparticles. The decrease of the Co^{2+} magnetic moment in the cubic shaped nanoparticles was attributed to the further growth of the CoO shell.
The growth of a NiO shell on $Fe_{3-d}O_4$@CoO nanoparticles was characterized by a decrease of H_C and K_{eff} in both cases which is due to the low magnetic anisotropy of the soft NiO phase. However, whilst H_E decreases for the spherical shaped nanoparticles, coherently with a decrease of the exchange-bias coupling due to the increase of the soft counterparts, H_E increased for the cubic system. This was attributed to a structural restructuration in the $Fe_{3-d}O_4$@CoO@NiO nanoparticles and to the further growth of the CoO shell. Finally, in both cases, the growth of a NiO shell on the $Fe_{3-d}O_4$@CoO nanoparticles did not allow to increase further T_B. This is due to the low volume of NiO phase. In consequence, in order to increase further the magnetic anisotropy of $Fe_{3-d}O_4$@CoO nanoparticles with an antiferromagnetic proximity effect, it is mandatory to increase the NiO volume by incorporating them in a NiO matrix.

To conclude, we have successfully increased the overall magnetic anisotropy energy of iron oxide based nanoparticles. In preserving a size smaller than 16 nm, we succeeded to increase T_B over room temperature with a low amount of Co and without any rare earth. The concomitant use of a wide panel of structural and magnetic analysis techniques was required to fully understand the structure-magnetic properties relationship. The next steps in order to go further is to

- set the $Fe_{3-d}O_4$@CoO nanoparticles in a NiO matrix
- and to control the assembly of $Fe_{3-d}O_4@(CoFe_2O_4)_x(CoO)_y(CoFe_2O_4)_z@Fe_{3-d}O_4$ nanoparticles on a substrate in order to study their collective properties. Indeed, magnetic nanoparticles which were studied in the powder state are submitted to dipolar interactions which significantly influence the magnetic properties.

Preliminary results on the preparation of assemblies of nanoparticles were already obtained. SEM micrographs of $Fe_{3-d}O_4@CoO@Fe_{3-d}O_4$ assembled on functionalized gold thin film supported onto a silicon substrates is presented in Figure 71. According to previous work in our research group,[4] the fine tuning of the diping time of the substrate in a dilute solution of nanoparticles allowed to control the nanoparticles density i.e. the distance between the nanoparticles, and de facto the collective magnetic properties.

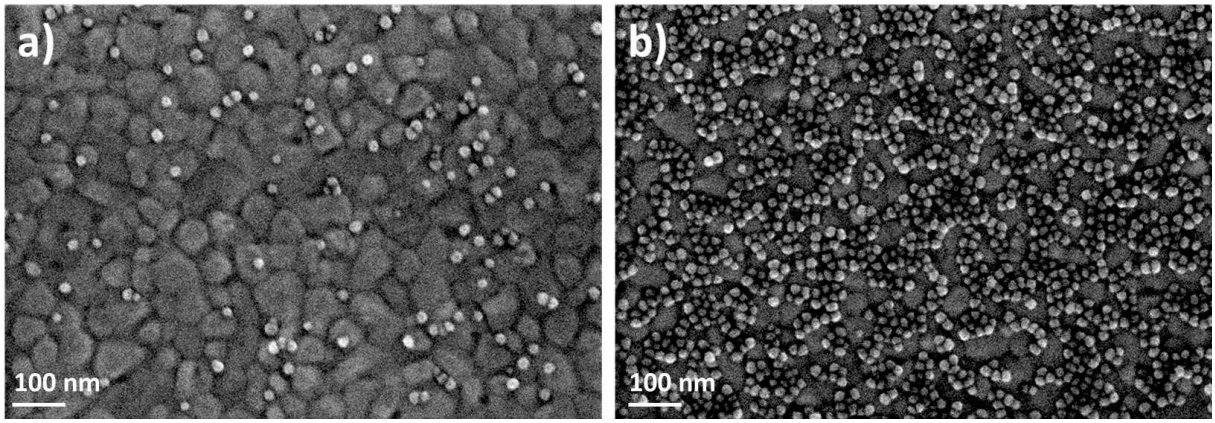

Figure 71. SEM micrographs of $Fe_{3-d}O_4@CoO@Fe_{3-d}O_4$ nanoparticles assembled onto a silicon substrate with a) low density, b) high density.

References

(1) Baaziz, W.; Pichon, B. P.; Lefevre, C.; Ulhaq-Bouillet, C.; Greneche, J.-M.; Toumi, M.; Mhiri, T.; Bégin-Colin, S. High Exchange Bias in $Fe_{3-\delta}O_4$@CoO Core Shell Nanoparticles Synthesized by a One-Pot Seed-Mediated Growth Method. *J. Phys. Chem. C* **2013**, *117* (21), 11436–11443. https://doi.org/10.1021/jp402823h.

(2) Liu, X.; Pichon, B. P.; Ulhaq, C.; Lefèvre, C.; Grenèche, J.-M.; Bégin, D.; Bégin-Colin, S. Systematic Study of Exchange Coupling in Core–Shell $Fe_{3-\delta}O_4$@CoO Nanoparticles. *Chem. Mater.* **2015**, *27* (11), 4073–4081. https://doi.org/10.1021/acs.chemmater.5b01103.

(3) De Toro, J. A.; Marques, D. P.; Muñiz, P.; Skumryev, V.; Sort, J.; Givord, D.; Nogués, J. High Temperature Magnetic Stabilization of Cobalt Nanoparticles by an Antiferromagnetic Proximity Effect. *Phys. Rev. Lett.* **2015**, *115* (5). https://doi.org/10.1103/PhysRevLett.115.057201.

(4) Pichon, B. P.; Demortière, A.; Pauly, M.; Mougin, K.; Derory, A.; Bégin-Colin, S. 2D Assembling of Magnetic Iron Oxide Nanoparticles Promoted by SAMs Used as Well-Addressed Surfaces. *J. Phys. Chem. C* **2010**, *114* (19), 9041–9048. https://doi.org/10.1021/jp101872u.

Annexes

Soft X-ray absorption (XAS, XMCD) principle

Principle

XAS and XMCD are elements specific techniques that are used to study the local structure, the spin configuration, the oxidation state, or the site-symmetry. In the case of spinel ferrite nanoparticles, XAS and XMCD have been valuable in determining the details of the electronic and magnetic structures in nanoparticles.

X-ray absorption and XMCD technic requires to have a stability of energy and resolution and a monochromatic beam with a high brilliance. A synchrotron allows to get a brilliance which is 10^{12} times higher than the brilliance of a common X-ray laboratory diffractometer. It allows also an energy tenability which offers to cover the absorption range of 3d transition elements.
To produce such a beam, a synchrotron source displays several parts (Figure 72): the first one is the source that produces the electrons. At SOLEIL, it consists in a tungsten filament which is heated by the application of an electric current. Afterwards, the electrons are accelerated in the linear accelerator (linac) to 100 MeV and send in a circular accelerator, the booster, which accelerates them up to 2.75 GeV. The electrons are then injected in a 113 m of diameter storage ring and gravitate several hours thanks to the ultra-high vacuum (UHV) conditions of 10^{-9} mbar.
Magnetic dipoles, undulators and wrigglers are present in the storage ring which serves to curve the trajectory of the electrons and to oscillate them. The electrons thus loose some energy and emit photons which are brought to the different beamlines. Thanks to the presence of radiofrequency sockets, the electrons can be reaccelerated in the storage ring for further photons emission.

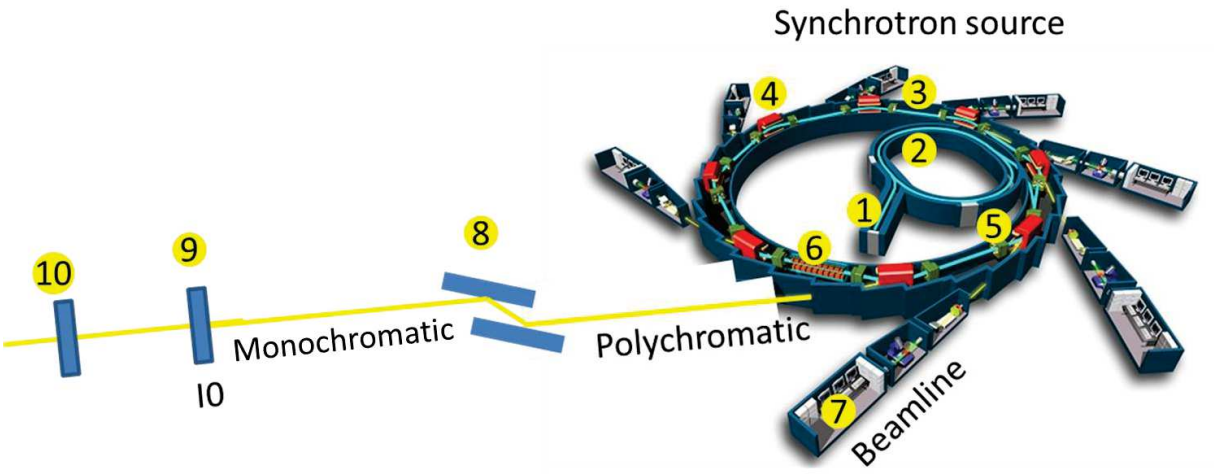

Figure 72. Schematic representation of the Synchrotron SOLEIL and XAS beamline principle. 1 : Electron gun and linac, 2 : Booster, 3 : storage ring, 4 : magnetic dipoles, undulators and wrigglers, 5 : radiofrequency cavities, 6 :undulator, 7 : beamline, 8: monochromator, 9: incidence flux monitor (measure of I0 current), 10: sample. Adapted from ref.[1]

Then, the produced x-rays passes through the monochromator and several optics systems in order to produce a monochromatic and focalized beam on the sample.

The use of an energy range of X-ray, allows to investigate different energetic transition. If the energy of the incident beam ($h\nu$) is equal to $\Delta E=Ef-Ei= h\nu$, an electron of the initial state (Ei) can be promoted to the final state (Ef). Thus XAS probes the empty states of an atom. Generally the chemical elements display different band gap (ΔE), hence the elements do not absorb X-rays at the same energy which

allow XAS experiments to be chemical selective (Table 34). In a XAS signal, several edge jumps are displayed, each one corresponding to a specific absorption of the core levels. More specifically, in soft XAS experiments on 3d transition metals, an electron of the core level is promoted from the 2p level to the 3d level (L edge) (

Figure 73).

Table 34. L_2 and L_3 edges of principal transition metals.

Element	L_2 edge (eV)	L_3 edge (eV)
Mn	650	639
Fe	720	707
Co	778	793
Ni	853	870
Cu	933	952

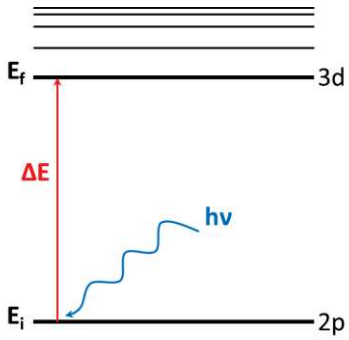

Figure 73. Schematic representation of a X photon absorption for 3d transition metals.

The probability to induce an electronic transition in an element in function of the time, is described by the Fermi golden-rule:

$$\Gamma_{if} = \frac{2\pi}{\hbar^2}\left|\langle f\left|\widehat{H_{int}}\right|i\rangle\right|^2 \delta(E_i - E_f - \hbar\omega)$$

<fl and li> corresponds to the multielectronic wavefunctions of the final and initial states respectively and $\hbar\omega$ is the incident photon energy. The δ distribution reports on the energy conservation where the energy transition occurs if E_f=E_i-hν. And $\widehat{H_{int}}$ is the interaction Hamiltonian that describes the interaction of X-rays with the electrons.

In soft XAS-XMCD, the quadripolar term can be neglected. Hence, in the case of the electronic dipole approximation, the matrix $\left|\langle f\left|\widehat{H_{int}}\right|i\rangle\right|$ becomes:

$$\Gamma_{if} = 4\pi^2\hbar\omega\alpha_0|\langle f|\vec{\varepsilon}.\vec{r}|i\rangle|^2\delta(E_i - E_f - \hbar\omega)$$

with $\alpha_0 = \frac{q^2}{4\pi\varepsilon_0\hbar c}$

α_0 is called the fine structure constant, $\vec{\varepsilon}$ is the photon polarization vector and $\vec{r}$ is the position vector.

The absorption cross section, is then obtained by considering every populated terms of the initial and final electronic configuration according to the degeneracy of the multielectronic wave function d_i.

$$\sigma_{if} = 4\pi^2\hbar\omega\alpha_0 \sum_{i,f} \frac{1}{d_i} |\langle f|\vec{\varepsilon}.\vec{r}|i\rangle|^2 \delta(E_i - E_f - \hbar\omega)$$

Which evidences the probability that an electronic transition from an initial state to a final state in function of the photon flux occurs.[2–4]
The electronic transition is allowed if the selection rules are respected. They depend on the initial electronic states associated to the quantum number n, l, m_l, m_s. In consequence, the system has to be able to:

- welcomes one of its' electron in a higher or lower orbital ($\Delta l = \pm 1$)
- conserves the spin of the electron ($\Delta m_s = 0$)
- conserves its' total kinetic moment ($\Delta j = 0, \pm 1$)

Moreover, in the case of a circularly polarized beam, an additional selection rule has to be considered where the excited electron is promoted to a different atomic orbital ($\Delta m = \pm 1$). Where $\Delta m = +1$ for a right helicity while $\Delta m = -1$ in case of a left helicity. For example, in Figure 74, in the case of a right polarized incident beam satisfying E=ΔE, an electron from the 1s orbital can be promoted to the I1,1> state. While for a left helicity, the electron of the 1s orbital would be promoted to the I1,-1> state which already contains electrons. According to this, it is obvious that the absorption cross section is affected by the light polarization, giving rise to a dichroic signal called X-ray magnetic circular dichroism (XMCD).

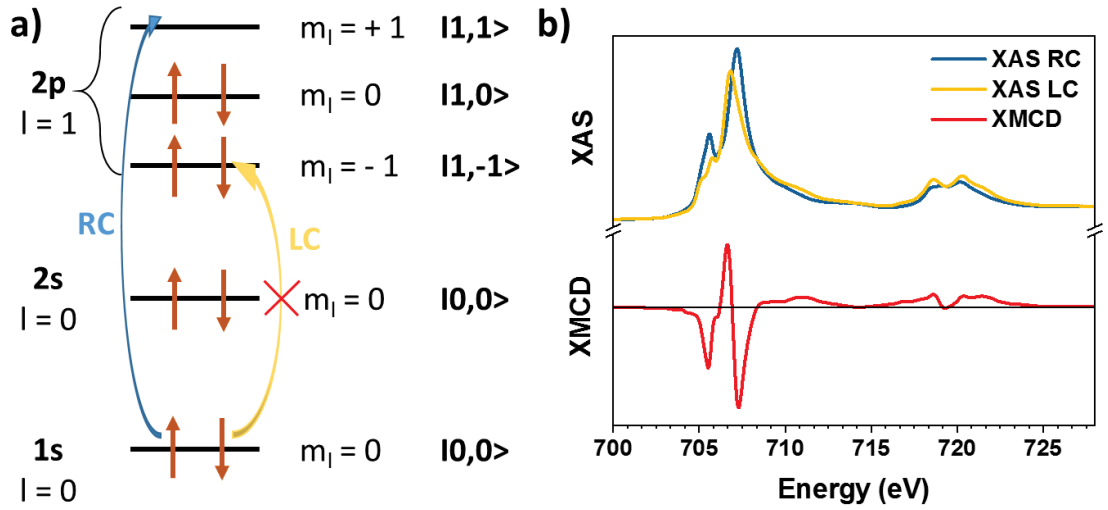

Figure 74. a) Schematic representation of the electronic configuration of an atom of 8 electrons subjected to a photon excitation. b) Polarized XAS and their corresponding XMCD recorded at the Fe $L_{2,3}$ edge.

Detection modes

For soft-XMCD measurements three different detection modes can be used:

The transmission mode: The transmission recorded mode is very powerful as it measures the difference between the incoming photon energy and the outgoing photon energy. Hence it directly probes the light absorption by the sample. This is a commonly used detection mode for hard X-rays spectroscopies as hard X-rays displays a high attenuation depth. At the opposite, soft X-rays display a low attenuation depth so that the use of this mode requires to get very thin samples without inhomogeneities at their surface. Thus the use of transmission mode for soft -XMCD on nanoparticles is a real challenge. It requires the preparation of very thin layers on SiN membrane.

The total fluorescence yield (FY): The removing of an electron in a material by the absorption of X-ray leave room to an electronic hole which is then filled by the transition of an electron from a higher energy level. This is accompanied by the emission of an Auger electron or of a X photon (X-ray fluorescence). The produced X photon has a mean free path equivalent to the incoming X-ray beam. The recording of the intensity of the fluorescent photons is called total fluorescent yield (TFY) and allows thus to be bulk sensitive. However, the possibility of self-absorption in the fluorescence mode alters the absorption spectra and reduce the use of this mode for drop-casted nanoparticles

The total electron yield (TEY): A commonly used detection mode for soft-XMCD is the total electron yield (TEY) mode, Figure 75 which consists in measuring the current directly on the sample. It actually probes the consumption of the electrons used to fill the hole left by secondary electrons that has been ejected from the probing atoms by the adsorption of X-rays. The measured current intensity is thus proportional to the absorption cross-section. As the electrons better interact with the sample than the X-rays, the recorded secondary electrons has a low kinetic energy, hence they mostly arise from the surface of the sample. It results that XAS is mostly sensitive to the surface and probes only the first five nanometers. Indeed, 80 % of the XAS signal is produced by the two first nanometers.

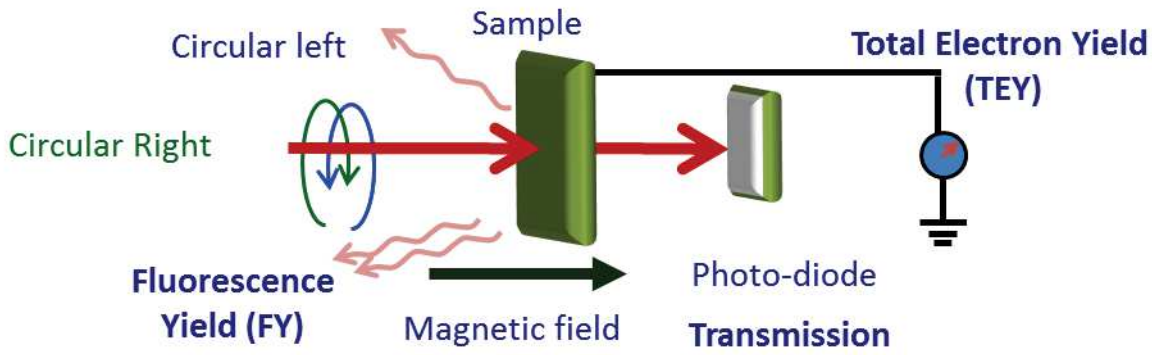

Figure 75. Schematic representation of the different recording modes.

CROMAG End-station of DEIMOS beamline

Soft-XAS and XMCD experiments were mainly performed on the DEIMOS (Dichroism Experimental Installation for Magneto-Optical Spectroscopy) beamline at SOLEIL synchrotron. They were recorded at the Fe, Co and Ni $L_{2,3}$ edges.
DEIMOS beamline is fully dedicated to the study of magnetic and electronic states of nanoscale structures with XAS and XMCD in the range of soft X-rays. Allowing to work on 2p to 3d transitions on 3d transition metals.
The beamline has been optimized for the requirements of the dichroism technique such as the optimization of the polarization, the stabilisation and reproducibility of the photon flux and photon energy.

The main end-station of DEIMOS beamline consists in a cryomagnet providing a magnetic induction of ± 7.0 T along the X-rays beam and ± 2T perpendicular to the beam for a temperature ranging from the mK to 350 K. the chamber is maintained in Ultra-High Vacuum (UHV) (10^{-10} mbar) continously as sample transfers do not require to break the vacuum. The beamline is equipped with two undulators that can be synchronized with the monochromator for XAS measurements or can deliver circularly polarized light for XMCD measurements. The Apple-II helical undulator with a period of 52.4 mm provides circularly polarized light over the full energy range (240-2500 eV) and horizontal and vertical linearly polarized light from 350 eV to 2500 eV. The second undulator is a hybrid electromagnet/permanent magnet helical undulator (EMPHU65) with a period of 65.0 mm optimized for a fast switching (5 Hz) of the circular polarized light.

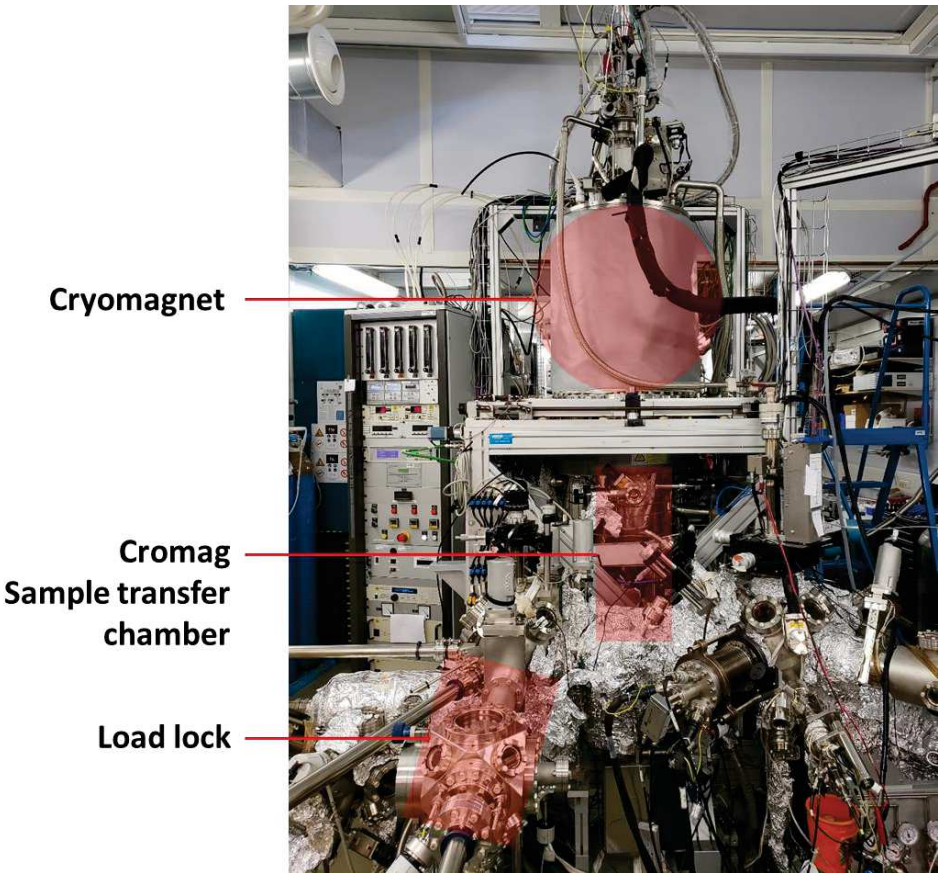

Figure 76. Picture of the DEIMOS beamline endstation.

Experiments

In this thesis, we worked at a maximum field of 6.5 T and temperatures of 4 K. The beam size was of 800x800 µm².

Several drops of concentrated ferrofluid were drop casted on a silicon wafer. When dried, a thin uniform layer of nanoparticles was formed. The Si wafer was then mounted on a cupper sample holder that can hold four different samples in the same time (seeFigure 77). The sample holder was transferred in the Cryo-Mag chamber. All the measurements were made using the total electron yield (TEY) detection mode at 4 K under ultra high vaccuum (10^{-10} mbar). We have recorded left and right circulary polarized X-ray absorption spectra in the TurboScan mode with the Apple-II HU52 helical undulator.

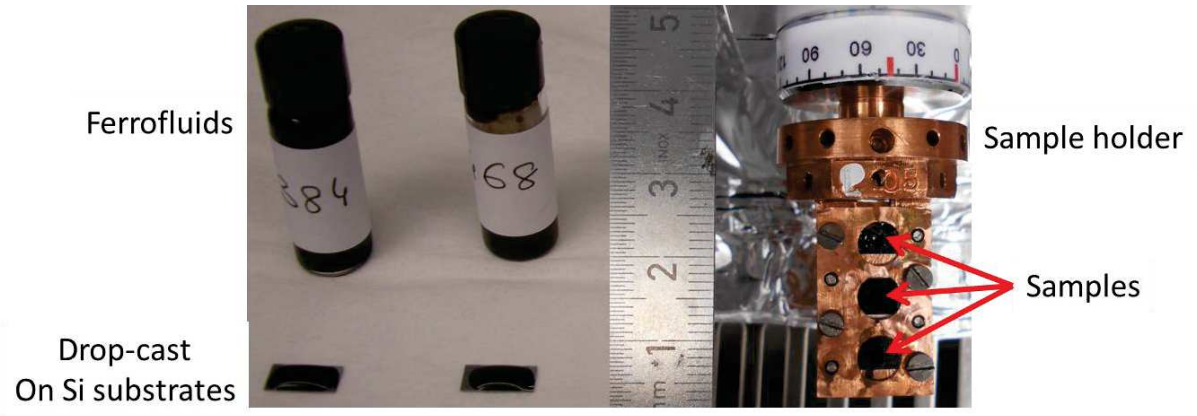

Figure 77. Ferrofluids drop casted on Si-waffer were dried at room conditions (left panel). Si wafers with nanopowders are mounted on the copper sample holder (right panel).

XAS spectra were recorded by both flipping the circular polarization (either left or right helicity) and the external magnetic field (either +H or -H) in order to improve the signal-to-noise ratio. For each element, we have recorded at least 16 XAS spectra with right polarization and 16 XAS spectra with left polarization. Isotropic XAS spectra were then obtained from the average of the right and left circularly polarized XAS while XMCD spectra were obtained from their difference. Isotropic signal were normalized to 1 and XMCD spectra were normalized to the maximum of the absorption edge determined from XAS spectra. XMCD detected magnetization curves were recorded by setting the monochromator at energies specific for the metal ions and specific for symmetry sites of the crystallographic structure and by sweeping the magnetic field from -H to +H. For the magnetization curves, we used EMPHU65 undulator. The X-ray circular helicity was switched at each point using the the EMPHU65 undulator.

Polarized small-angle neutron scattering: principles

This technic uses neutrons to probe the structure and dynamics of atoms present in the sample through nuclear scattering (interaction between the neutrons and the nuclei) and the magnetic structure through the magnetic scattering (arising from the interaction between the magnetic moment of the neutrons and that of the sample).

During this thesis, SANS experiments were performed at Laboratoire Léon Brillouin with the Orphée reactor where, a reaction of nuclear fission of U^{235} allows to produce 2.5 neutrons with an energy of 180 MeV per fission. Eight bars constituted of an alluminium-U^{235} alloy are placed in a small tank of 25x25 cm^2 which contains heavy water as coolant. The fission reaction is self-maintained and is controlled by the presence of hafnium control rods. This core is placed in a bigger tank containing heavy water as coolant and moderator. The second tank is surrounded by demineralized water to ensure a biological barrier against nuclear radiation. The total reactor has a 7.5 m of diameter. In the core the produced neutrons are too energetic to be used thus, the presence of a moderator surrounding the core allows to thermalize them before going in the beam tube which is directly inserted in the moderator. (Figure 78) The neutron beam is then transported to the end-station thanks to the use of neutron guides. Basically, they act as mirrors with Nickel as reflecting material.

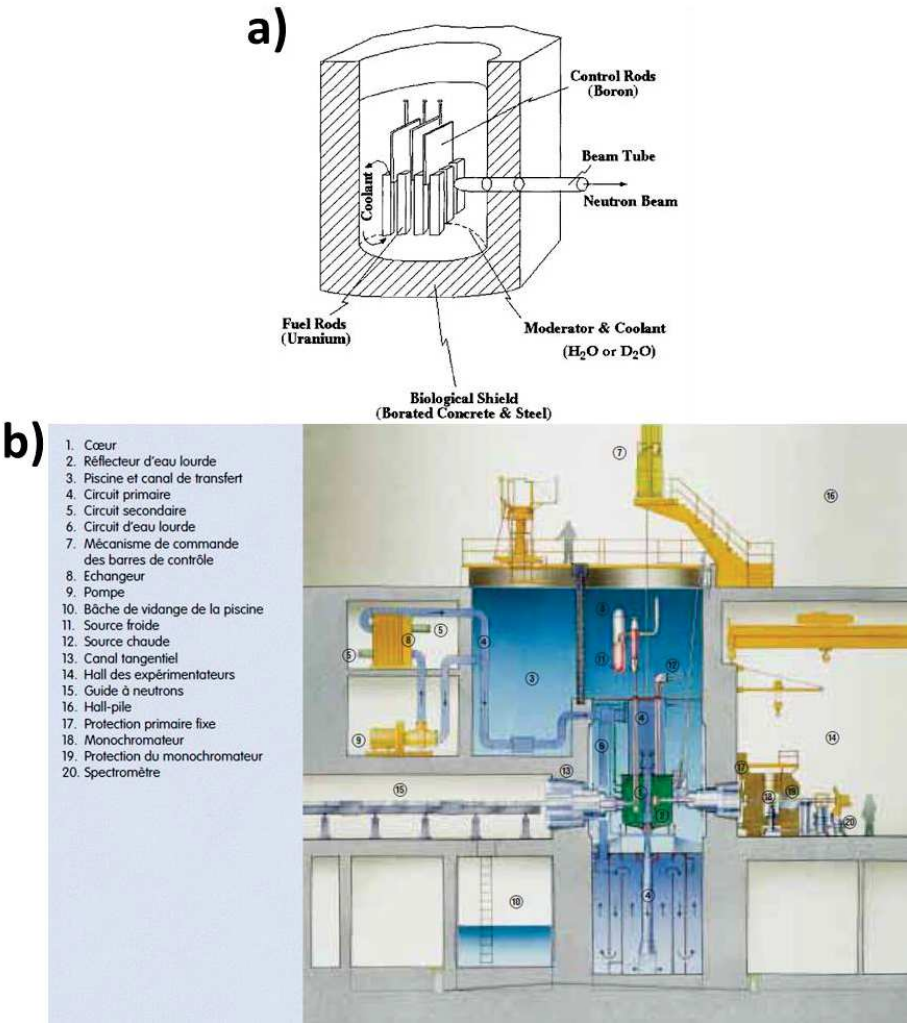

Figure 78. a) Schematic representation of the core of a neutron reactor.[5] b) Transversal cut of the Orphée reactor.[6]

A monochromator placed in the beamline select then the wavelength. On PA-20 spectrometer, the monochromator consists in a cylinder with helicoidal propellers which selects the wavelength according to its rotating speed. It is thus called velocity selector Figure 79. Afterwards the beam is collimated and then hits the samples.

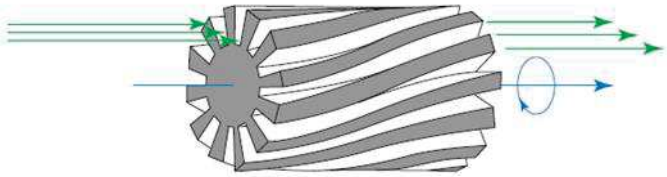

Figure 79. Monochromator : velocity selector.[6]

The incoming neutrons interact with the samples' nuclei resulting in a scattering pattern of neutrons which is measured by a large set of ^{3}He detectors (see Figure 80a for an example). The scattering processes can be either Bragg scattering in ordered systems (following Bragg law), diffuse scattering in disordered systems, inelastic scattering of phonons, and magnetic scattering in systems having net magnetization moments (Figure 80b). The sample consists in a drop casted solution of nanoparticles on a sapphire glass of 1 cm of diameter. A second sapphire glass is used to press the sample and the whole is placed on an aluminium sample holder which is suspended in a cryostat equipped with sapphire glass windows to allow the neutron beam in and out of the cryostat.

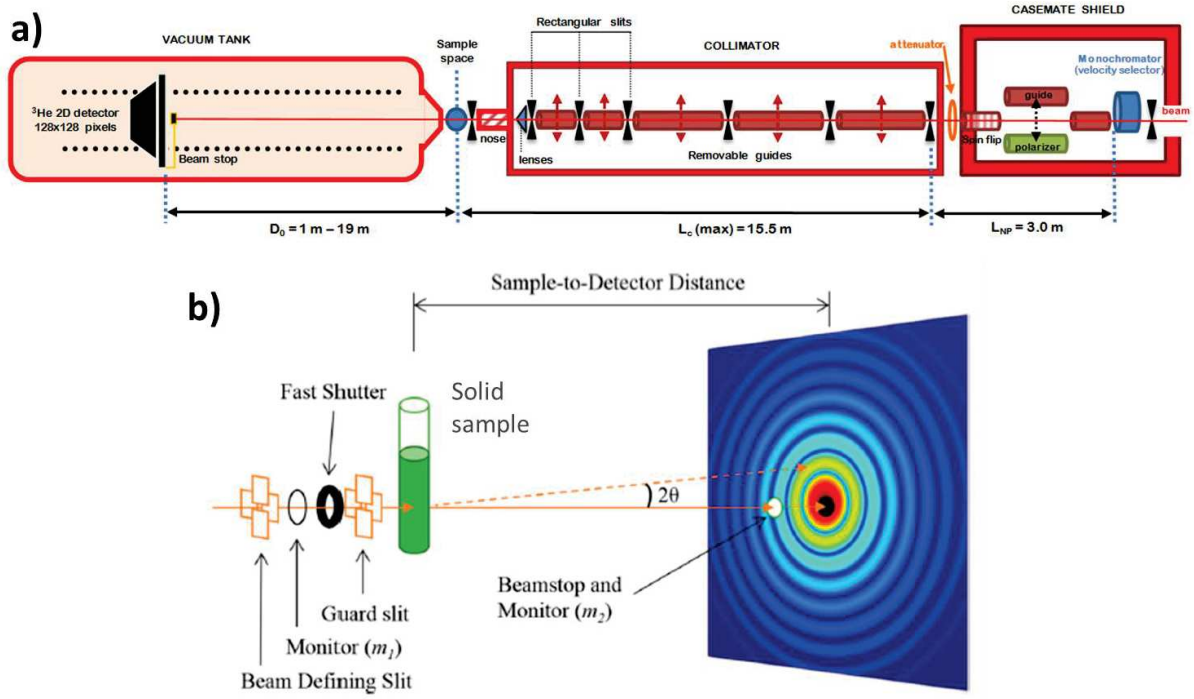

Figure 80. a) Schematic representation of the a) PA-20 G5-1 beamline available at Laboratoire Léon Brillouin, CEA Saclay[7] *b) scattered beam on an end-station.*[8]

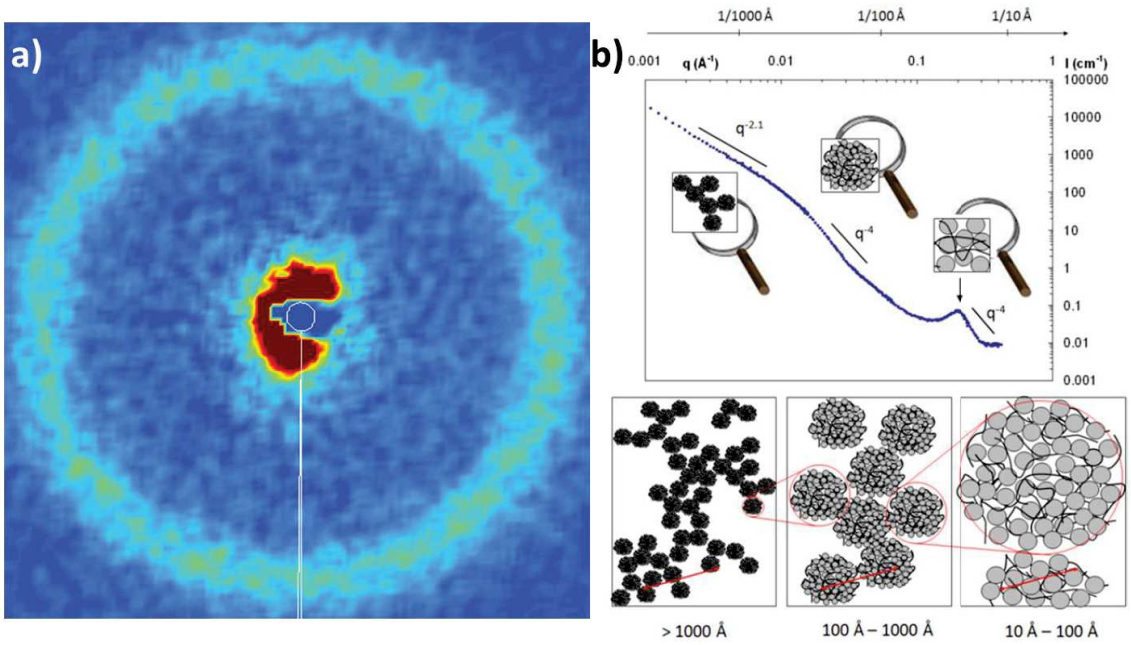

Figure 81. SANS a) 2D map and b) 1D curve with schematic representations for different wave vector Q range from [9]

The result is a 2D scattering map that can be circularly integrated to generate a 1D curve (Figure 81). The scattering angle 2θ is commonly transformed into the scattering vector Q. The resulting 1D curve I(Q) presents different regimes :

- The scattering at low Q values give information on the long-range spatial organization of the scattered objects
- Intermediate Q values show the size and the compactness of the objects
- And large Q values probe smaller details such as shape of the objects and their inner organization.

The I(Q) signal is expressed as:

$$I(Q) = F_N(Q)^2.S(Q) = \frac{d\sigma(Q)}{d\Omega}$$

Where F(Q), S(Q) and $\frac{d\sigma(Q)}{d\Omega}$ corresponds to the nuclear form factor, the structure factor and the differential cross-section respectively.

The form factor arises from the interferences between the scattering elements of an object and is thus inherent to one object. While the structure factor describes the correlations between the centers of mass of several scattered objects. In very dilute samples, where the interactions between objects can be considered very weak, the structure factor S(Q) is equal to 1. The differential cross section corresponds to the number of scattered neutrons in function of the time, solid angle and volume of the sample according to:

$$\frac{d\sigma(Q)}{d\Omega} \propto V^2\left(\rho_{obj} - \rho_{media}\right)$$

With V the volume of the object and (ρ) the scattering length density of the object and of the carrier liquid called media. Where the scattering length density depends on the atomic concentration c_i, the nuclear scattering length (ρ) and the volume of the constituent i (V_i) of the sample respectively.

$$\rho = \sum_i \frac{c_i b_i}{V_i}$$

At Q=0, the signal only depends on the volumic fraction (φ), the volume of the object and the difference of scattering length density:

$$I(Q) = \left(\rho_{obj} - \rho_{media}\right)^2 \varphi_{obj} V_{obj}^2$$

It is thus possible to determine the volume of the object whatever its shape and without any simulations.

For small Q values where Q^{-1} is larger than the size of the scattered objects, the 1D curve evidence a plateau from which it is possible to determine the gyration radius according to the Guinier regime.

$$I_{Guinier}(Q) = 1 - \frac{Q^2 R_g^2}{3}$$

Where R_g is the size of the moment of inertia of the object. For a sphere of R radius, $R_g^2 = \frac{3}{5}R^2$.

For intermediate regime, the curve show a decrease of I(Q) according to a $q^{-\alpha}$ slope where α depends on the shape of the object. α display values comprised between 1 and 4, 1 for single dimension objects and 4 for bulk objects. Moreover, this regime also allows to determine the size of the object and its' scattering length density by fitting the curve with a mathematical model. As an example, for a sphere or R radius,

$$I(Q) = \left[3\frac{\sin(QR) - qRcos(QR)}{(QR)^3}\right]^2$$

Finally, the largest Q values, corresponding to Q^{-1} smaller than the size of the object, probe the local environment. Here the signal is only sensitive to interfaces between two homogeneous materials of different scattering length densities (ρ_1 and ρ_2). In this so-called Porod regime, I(Q) shows a Q^{-4} dependency and is proportional to the surface area (S) per unit volume (V) of the sample according to:

$$I(Q) = \frac{2\pi S(\rho_2 - \rho_1)^2}{VQ^4}$$

Thus SANS is able to give a clear understanding of the shape and of the chemical composition of any object.

In this thesis, only the intermediate regime has been investigated in detail due to the presence of aggregates resulting from the liquid evaporation during the drop casting of the sample. This regime has been modeled thanks to the use of GRASP software developed by Charles Dewhurst (ILL Grenoble). According to this, it was possible to determine the core diameter, shell thickness, size distribution and chemical composition of both the core and the shells.

Moreover, the use of a neutron spin polarizer and a spin flipper allow to select the spin of the incoming neutrons (± 1/2) and thus to investigate the magnetic properties of the samples as the electronic spins of the atoms will interact with the neutron spin.
The magnetic SANS signal can be measured by taking two measurements, one with spin "up" and one with spin "down" configuration. The difference between the two measurements is proportional to the magnetic form factor $F_M(Q)$ as follows:

$$I(Q) = I^-(Q) - I^+(Q) = 2P(1+\epsilon)F_N F_M sin^2\alpha$$

Where $I^{\pm}(Q)$ is the SANS signal for up/down spin polarization, P is the polarization factor (P=0.94 on PA20), ϵ is the flipper efficiency (ϵ = 1), F_M is the magnetic form factor and α is the angle between the wave vector q and the applied magnetic field. The I(Q) signal will be analyzed in the same way than in the case of unpolarized neutron. The difference lies only in the fact that the results is composed of both nuclear and magnetic contributions. However, knowing first the nuclear contributions allow to determine the magnetic ones.

Thus the determination of $F_M(Q)$ allows to determine the magnetic properties of the nanoparticles in terms of magnetic size, magnetic size distribution and magnetic shape of the nanoparticles. Moreover, it is also possible to determine the chemical composition of the nanoparticles and especially to differentiate the magnetic core and magnetic shell in the same nanoparticle thanks to the density sensitivity of SANS. This technique also allows to determine the size of the magnetic core and the thickness of the magnetic shell.

The use of p-SANS concomitantly with an applied magnetic field gives information on the magnetic structure of the nanoparticles in order to extract the magnetic core and shell volumes as well as their density. It is possible to probe the magnetic frustration and the interfacial defects directly in the nanoparticles, such as spin canting effects for example.[10]

Polarized-Small Angle Neutron Scattering (p-SANS) experiments were performed on the PA20 SANS instrument[11] at LLB and reactor Orphée with a fixed neutron wavelength λ of 4.5 Å (Figure 80a). The sample to detector distance was set to 2 m getting a total accessible range from 0.017 to 0.237 $Å^{-1}$. The detector is a ^3He 2D detector of 64x64cm^2 with a 5x5 mm pixel size (128x128 pixels in total). The direct beam is adsorbed by a central Cd beam stopper to avoid damaging the detector. The incoming neutron beam is polarized (or not), collimated and directed to the sample placed in a 10 Tesla cryomagnet. Nanoparticles stored in chloroform were drop casted on a sapphire glass to evaporate the sample until a nice black crust was obtained. The dry powder was then press between two sapphire windows of 10 mm diameter and placed in a copper sample holder with a Cd ring to minimize background scattering. The sample holder was then placed in the cryomagnet, perpendicular to the incoming beam. The magnetic field is oriented horizontally and perpendicular to the neutron beam direction. The empty cell and the direct beam were measured to correct the data for transmission and background scattering.

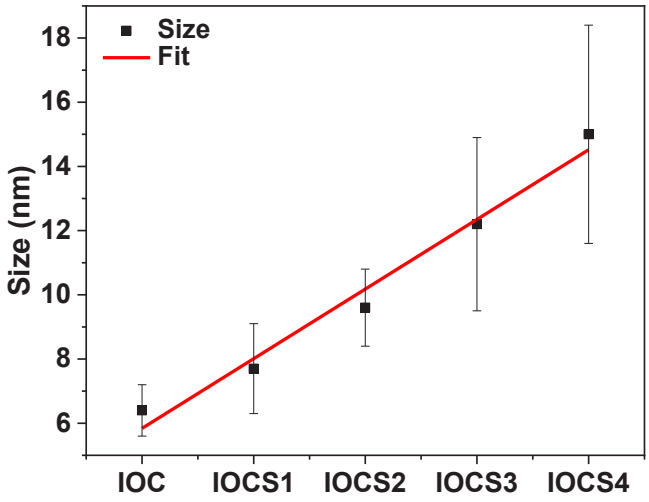

Figure S 1. Evolution of the nanoparticle diameter as a function of the number of layer. A linear fit gives the following equation: y = 2.17x+3.67.

Table S 1. Related hkl reflections from FFT of HR-TEM of figure 4.

Sample	Spot N°	hkl plan
IOC	1	444
	2	620
	3	531
	4	620
	5	311
	6	2-20
	7	222
	8	222
IOCS1	1	400
	2	222
	3	311
	4	2-20
	5	400
	6	220
	7	311
IOCS2	1	444
	2	422
	3	222
	4	2-22
	5	400
	6	311
IOCS3	1	444
	2	422
	3	222
	4	422
	5	631
	6	2-20
IOCS4	1	220
	2	2-20

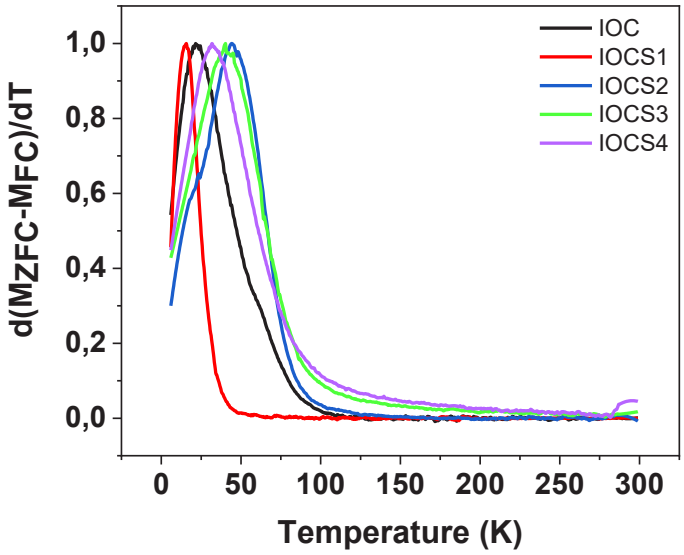

Figure S 2. d(MZFC-MFC)/dT curve calculated for IOCSn nanoparticles.

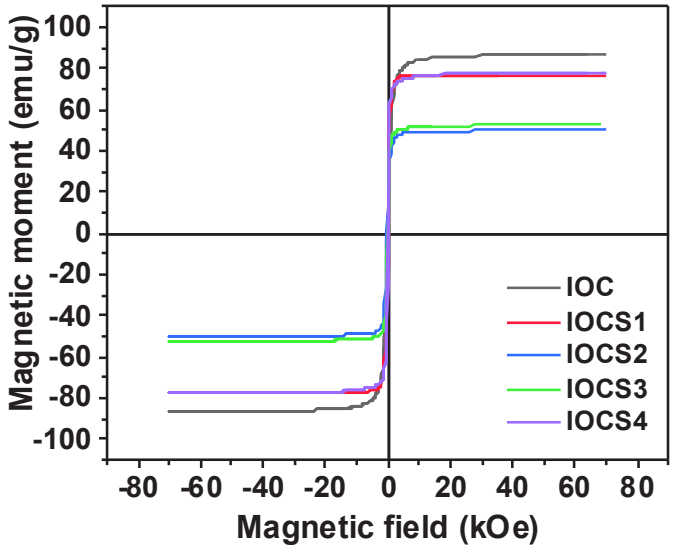

Figure S 3. M(H) curves recorded at 5 K and normalized to the mass of iron oxide nanoparticles determined from thermogravimetry analysis.

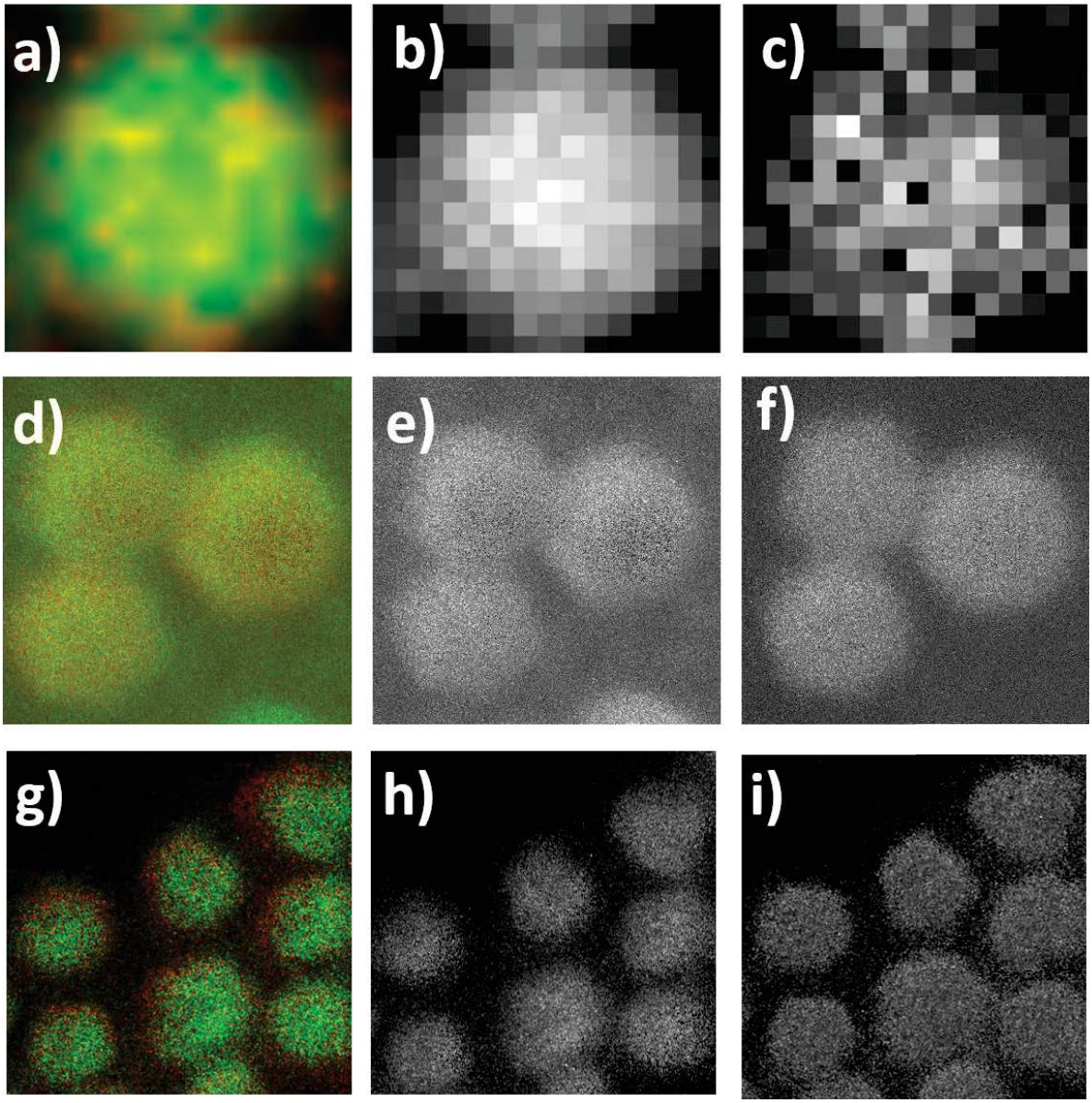

Figure S 4. Integrated maps of the element EELS signal of a-c) CS_CoF1, d-e) CS_CoF2, g-i) CS_CoO. a, d, g) Composite images showing Fe (green) and Co (red), b, e, h) Fe L2,3 signal and c, f, i) Co L2,3 signal showing the distribution of Fe and Co, respectively, in nanoparticles.

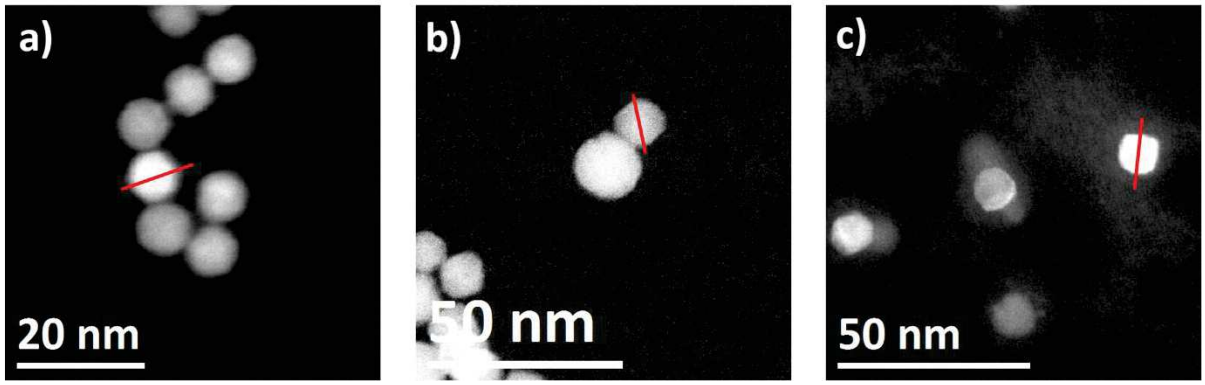

Figure S 5. Image spectra of a) CS_CoF1 b) CS_CoF2 c) CS_CoO with red lines corresponding to the EELS profile section shown in Figure 2.

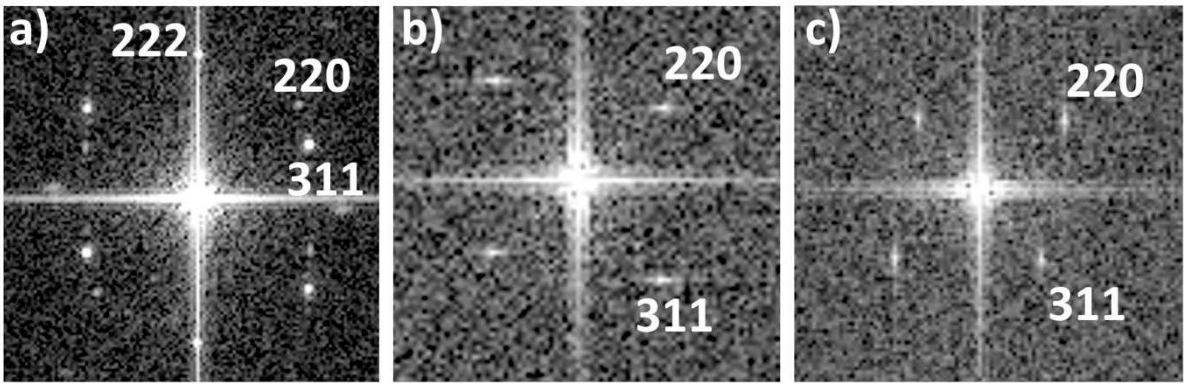

*Figure S 6. Fast Fourier Transform of HAADF micrographs for a) CS_CoF1, b) CS_CoF2 and c) CS_CoO showing the (*hkl*) orientations.*

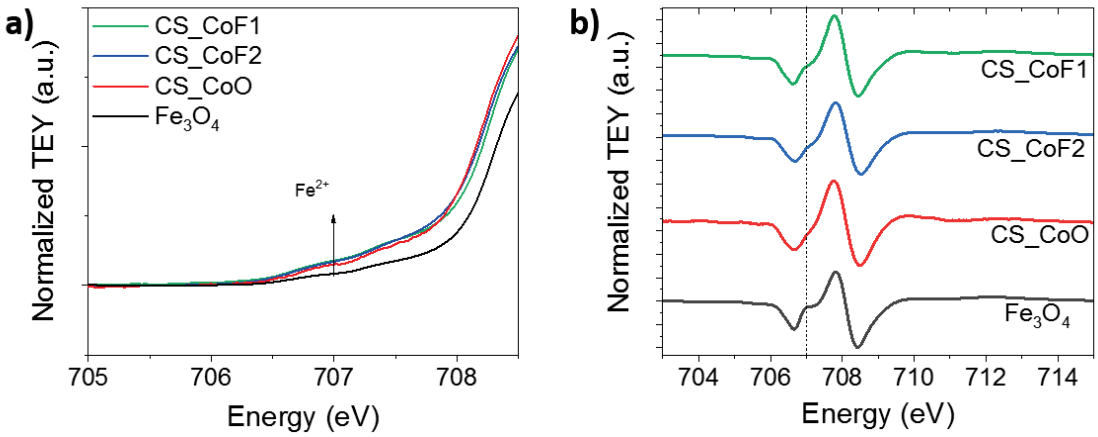

Figure S 7. Enlargement of a) XAS and b) XMCD spectra showing the shoulders at 707 eV.

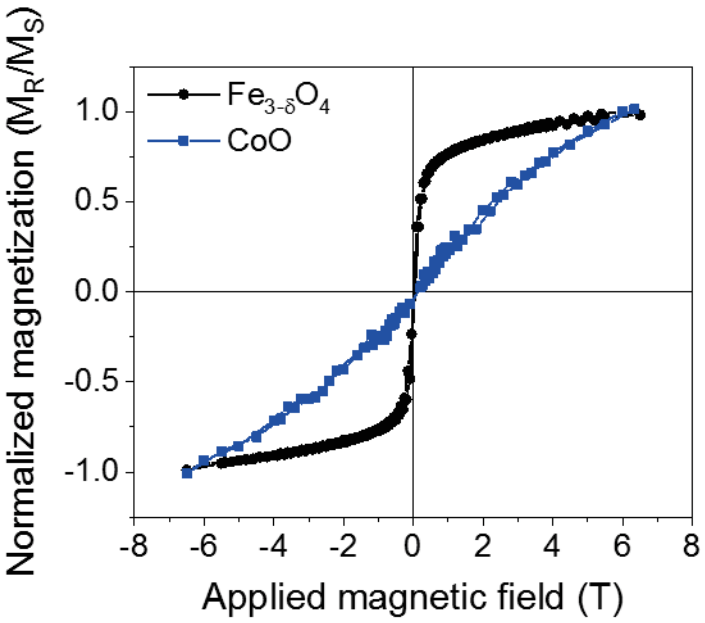

Figure S 8. Element specific XMCD M(H) curves recorded at Fe (S1) and Co edges at 4 K for $Fe_{3-\delta}O_4$ and CoO nanoparticles.

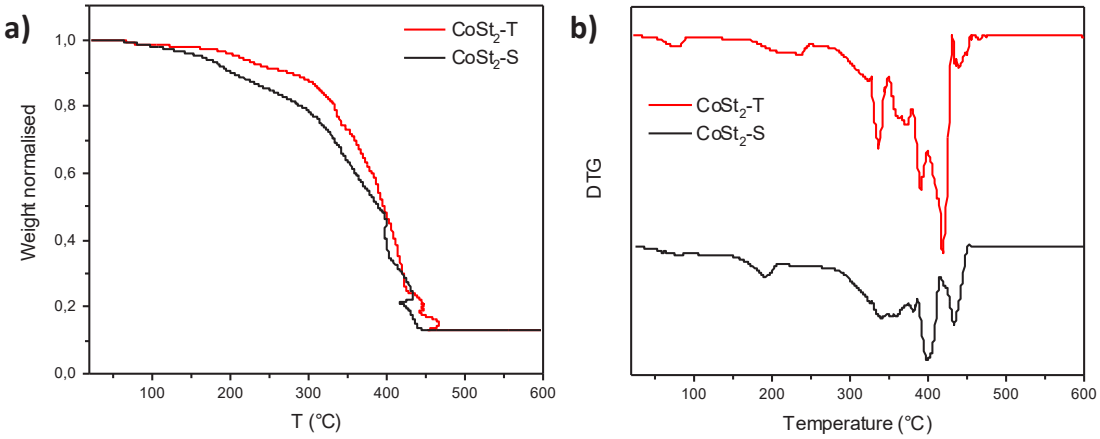

Figure S 9. a) Thermogravimetric curves and b) the corresponding thermodifferential curves of cobalt precursors used for the synthesis of core-shell nanoparticles.

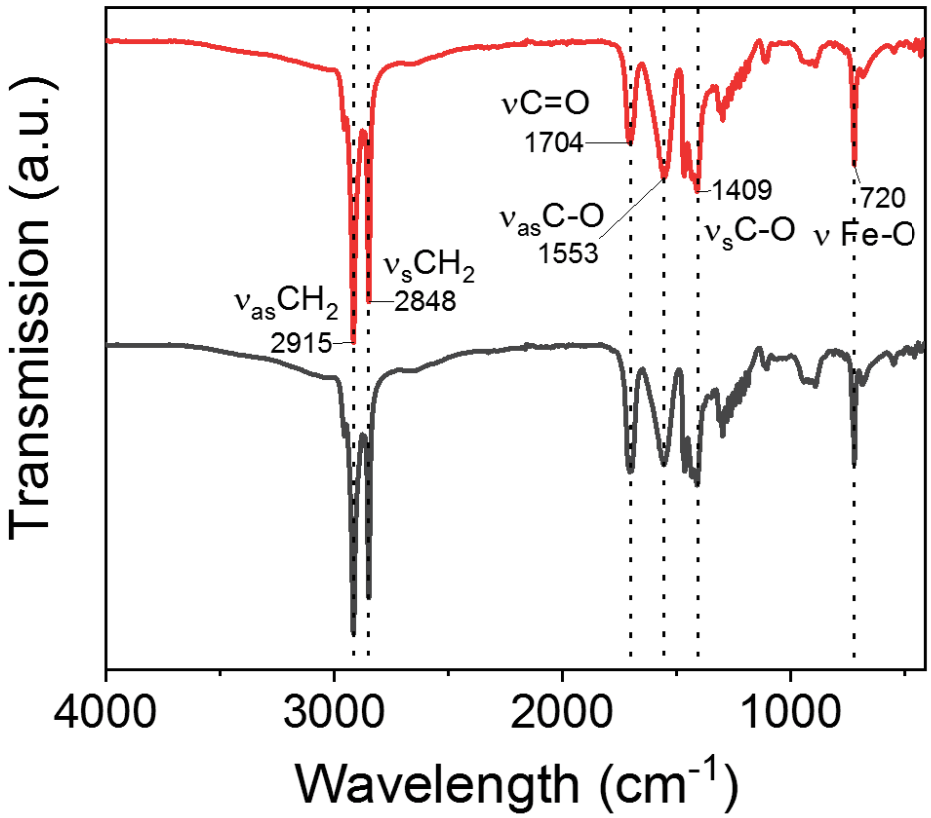

Figure S 10. FTIR spectra of Co precursors. CoSt2-T (up) and CoSt2-S (down).

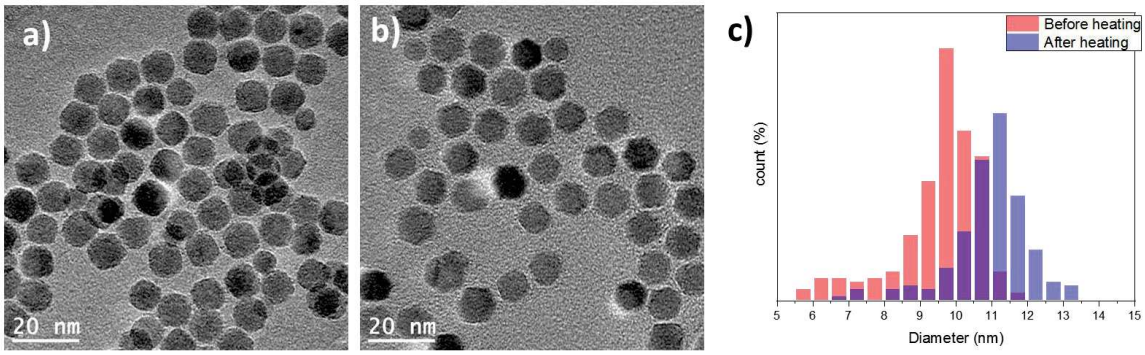

Figure S 11. TEM micrographs of iron oxide nanoparticles before (a) and after (b) performing the second heating without any addition of Co precursor in the reaction medium. c) Size distributions measured from TEM micrographs.

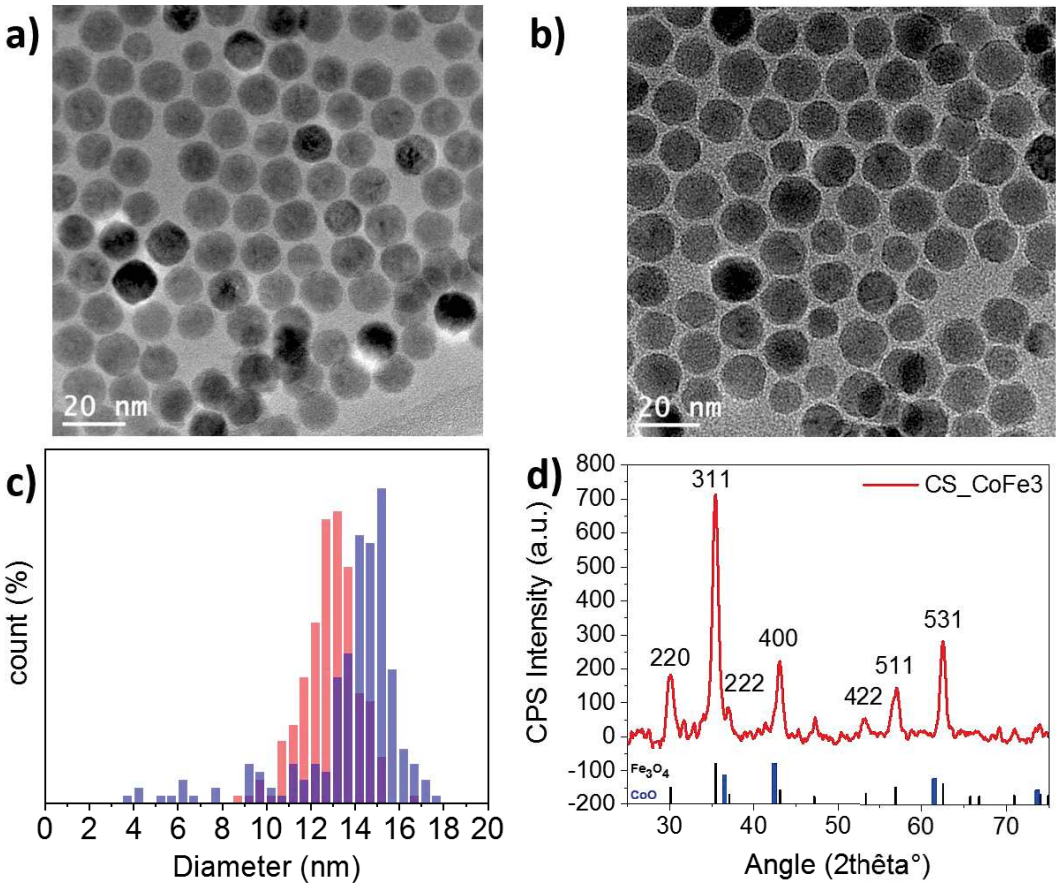

Figure S 12. TEM micrographs of (a) pristine iron oxide nanoparticles before and (b) core-shell nanoparticles CS_CoF3 after performing the thermal of CoSt2-T precursor (R =2). c) Size distributions measured from TEM micrographs. d) XRD pattern of core-shell nanoparticles showing the presence of the $Fe_{3-\delta}O_4$ spinel phase (black histogram) and wüstite CoO phase (blue histogram).

Nanoparticle	Fe	Co
8	73	27
9	68	32
10	71	29
11	68	32
12	66	34
13	63	37
14	59	41
15	60	40
16	66	34
17	65	35
Average	**66**	**34**

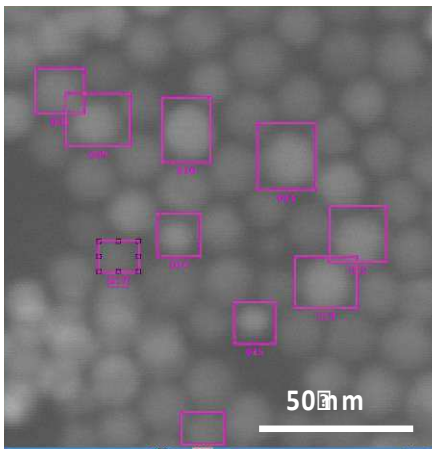

Figure S 13. EDX analysis performed on isolated nanoparticles of sample CS_CoF3.

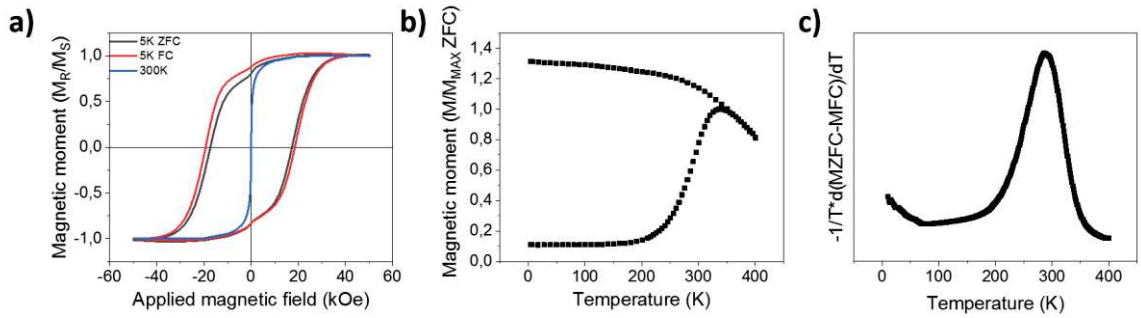

Figure S 14. Magnetic properties of core-shell nanoparticles for CS_CoF3. a) ZFC and FC M(H) curves recorded at 300 K and 5 K. b) ZFC and FC M(T) curves. c) The blocking temperature distribution corresponding to $f(T_B) \approx -(1/T)(d(M_{ZFC}-M_{FC})/dT)$.

Annexes of Chapter III

SAXS details

To fit the SAXS experimental curves, 2 different models were used. These models are found in the databank models of *Sasview* software.[12]
The simple sphere model is defined as

$$I(Q) = \frac{scale}{V}\left[3V(\Delta\eta)\frac{\sin(QR) - QRcos(QR)}{QR^3}\right]^2 + background$$

With V the volume of the particle, Δη the scattering length density and R the radius of the particle.

While the core@shell model general equation is written:

$$I(Q) = [F(Q, R + \Delta R, \Delta\eta_2) - F(Q, R, \Delta\eta_2 - \Delta\eta_1)]^2$$

Where R is the core radius, ΔR is the shell thickness, $\Delta\eta_1$ is the core scattering length density and $\Delta\eta_2$ is the shell scattering length density. F is the form factor defined as

$$F = \frac{4\pi R^3 \Delta\eta \times \sin(QR) - QRcos(QR)}{(QR)^3}$$

TEM of CoO nanoparticles

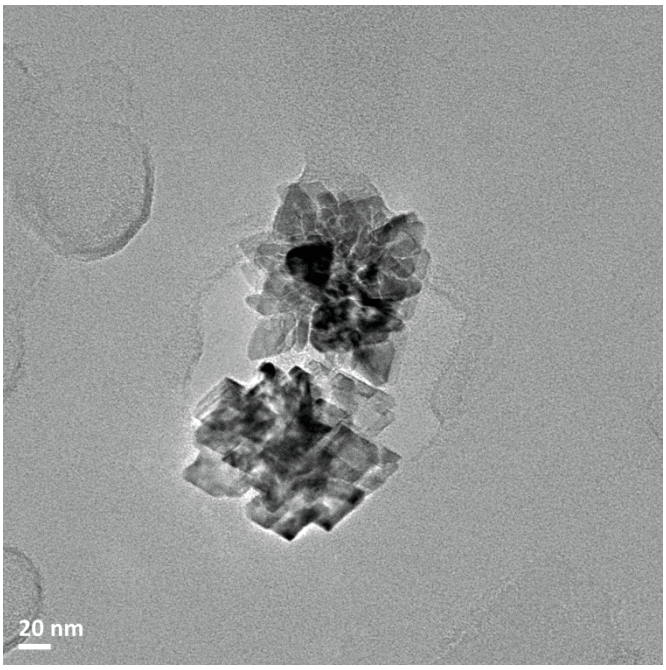

Figure S 15. TEM micrographs of a CoO nanoparticle used as a reference in the XAS-XMCD experiments.

Structural analysis of C2, CS2 and CS2 reheated

In order to study the influence of a second heating on a core@shell nanoparticle by the synthesis of a core@shell@shell nanoparticle, a second series of samples composed of a $Fe_{3-d}O_4$ core (C2), a $Fe_{3-d}O_4$@CoO core@shell (CS2) and a $Fe_{3-d}O_4$@CoO core@shell reheated (CS2r) nanoparticles were synthesized. There characterizations are presented bellow.

Synthesis strategy

The core and the core@shell nanoparticles were synthesized and washed in the exact same conditions as the synthesis of the core and the core@shell nanoparticles of the first series. The reheating of CS2 has then been proceeded as follow:
In a two-necked round bottom flask, 25 % of CS2 were deposited and the solvent was evaporated under vacuum. The nanoparticles were then redispersed in 20 mL of ether dioctyl (B_P = 290 °C) and 0.01398 g (5 10^{-5} mol) of oleic acid was added. The mixture was ultrasonicated for 2 minutes before being heated at 100 °C under a magnetic stir. After 30 min, the stir is removed and the flask was connected to a condenser. The mixture was then heated at reflux for 120 min with a heating rate of 5 °C/min. At the end, the resultat black solution is allowed to cool down to 100 °C and the nanoparticles were washed by the addition of an excess of acetone followed by centrifugation (14 000 rpm, 5 min). The nanoparticles were then recovered and washed two times more with a mixture of chloroform:acetone (1:5) followed by a centrifugation. Finally, the nanoparticles were stored in chloroform.

Transmission electron microscopy

TEM micrographs of C2 (Figure S16a, b) show spherical nanoparticles with a well-controlled shape and size distribution centered at 8.3 nm. The decomposition of a $CoSt_2$ on the iron oxide seeds gives CS2 nanoparticles that are larger than the core nanoparticles with a size of 10.8 nm corresponding to a shell thickness of 1.3 nm. CS2 nanoparticles have a less spherical shape than C2 and a slightly broadened size distribution in accordance with our results with the first series. A further thermal decomposition of the solely CS2 nanoparticles produce smaller nanoparticles with a size of 9.7 nm corresponding to a reduction of -0.6 nm. This result is in opposite with the work of Gavrilov Veronica,[13] who reheated $MnFe_2O_4$@$CoFe_2O_4$ and observed similar sizes of the nanoparticles with a decrease of the size distribution. However, the size reduction of our nanoparticles is in accordance with the work of Lentijo-Mozo and al.[14] who evidenced a partial resolubilisation of the seeds during the synthesis of the shell. Moreover, despite a size reduction, the CS2r nanoparticles displays a well-controlled morphology close to sphere and its size distribution has not evolved compared to the CS2 nanoparticles.

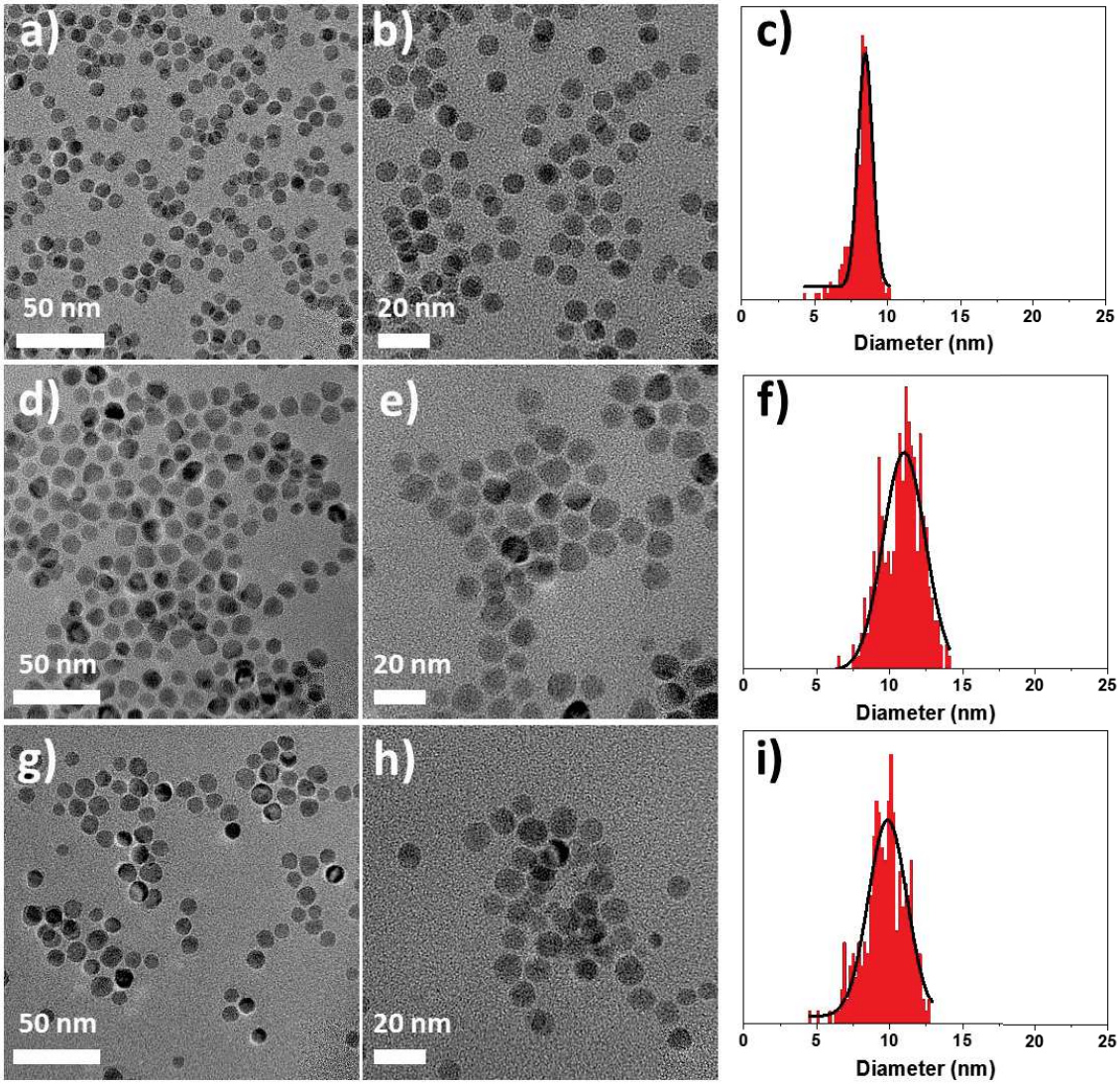

Figure S 16. TEM micrographs of a, b) C2, d,e) CS2, g,h) CS2 reheated and the size distribution of c) C2, f) CS2 and i) CS2 reheated.

Table S 2. Structural characterizations and magnetic properties of C2, CS2 and CS2 reheated.

	C2	CS2	CS2r
TEM Size (nm)	8.3 + 0.8	10.8 + 1.3	9.7+1.4
Shell thickness (nm)	-	1.3	-0.6
Fe:Co at. Ratio by EDX	-	43 : 57	58 : 42
Hydrodynamic diameter (nm)	9.9	13.7	18.1
Cell parameter (Å)	8.370 ± 0.01	8.425 ± 0.01	8.424 ± 0.01
Crystal size (nm)	7.4 ± 0.1	7.6 ± 0.1	7.8 ± 0.1
H_C 10 K ZFC (kOe)	0.3	17.3	16.6
H_C 10 K FC (kOe)	0.4	20.0	20.2
H_E 10 K FC (kOe)	-	2.6	1.8
T_{max} (K)	133	272	276
T_B (K)	78	237	237

Fourier transform infrared

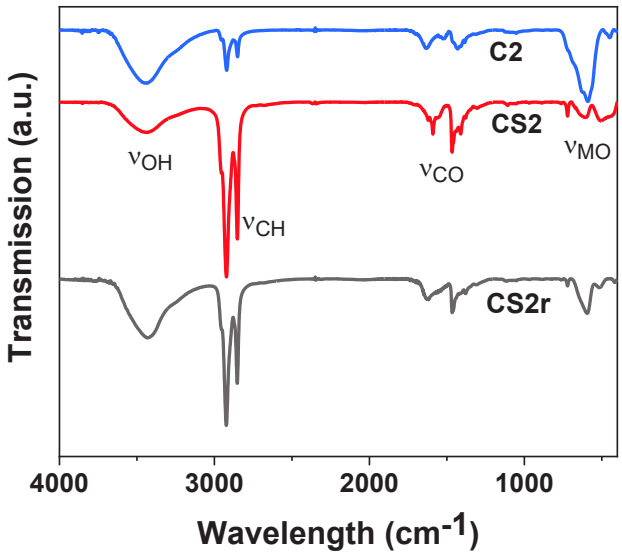

Figure S 17. FT-IR of C2, CS2 and CS2 reheated.

FT-IR spectra of C2, CS2 and CS2r nanoparticles are presented in Figure S17. The spectra are similar to the ones of the first series and agrees with oleic acid grafted on nanoparticles.

Granulometry

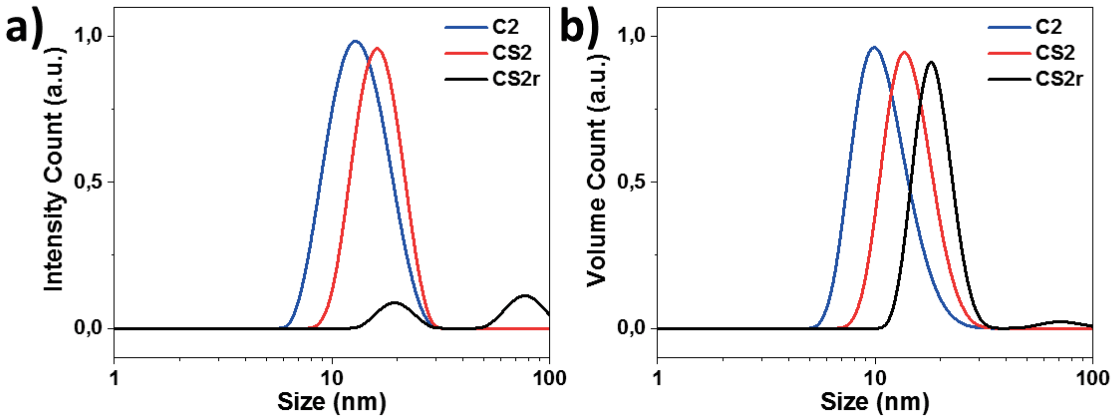

Figure S 18. Granulometry measurements for C2, CS2 and CS2 reheated.

Granulometry measurements in intensity count performed on C2, CS2 and CS2r evidences a monomodal distribution for C2 and CS2 while a beginning of aggregation for CS2r is perceptible. In volume count, C2 and CS2 also show a monomodal distribution centered at 9.9 and 13.7 nm respectively while CS2r evidences a first pic centered at 18.1 nm and a small and large band centered at 75 nm that corresponds to a small aggregation. Nevertheless, the hydrodynamic diameters increases through the different thermal decompositions. This result is in opposition with the TEM size which has evidenced a decrease of the size from CS2 to CS2r. Hence, the larger size of CS2r than CS2 in granulometry is attributed to arise from the contribution of the surfactant towards the light scattering.

SQUID magnetometry

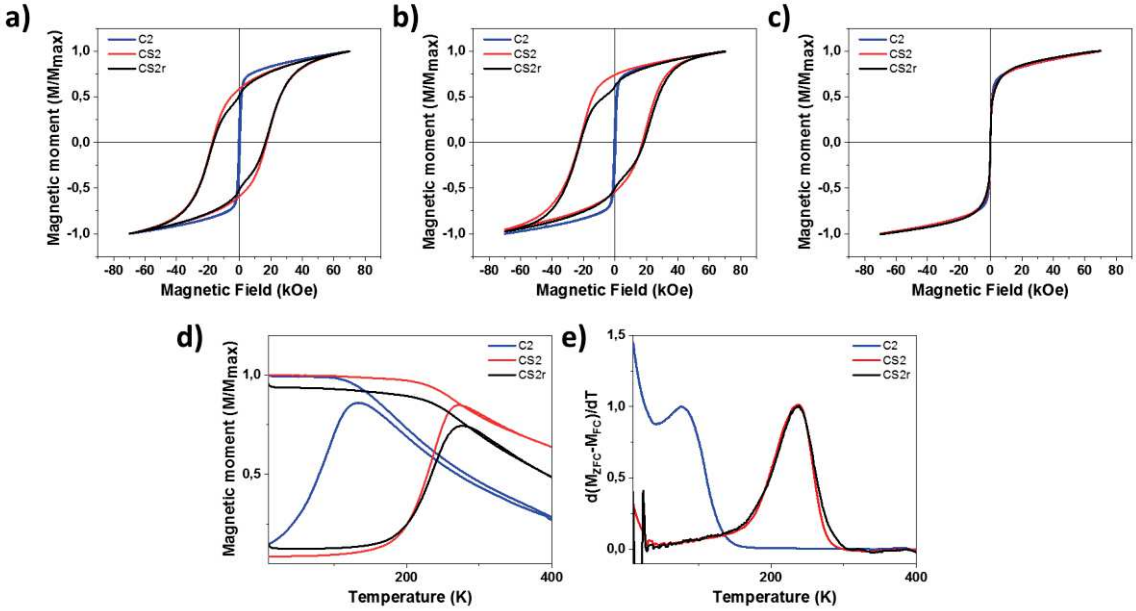

Figure S 19. Magnetic properties of C2, CS2 and CS2r nanoparticles. Magnetization curves recorded against a magnetic field a) at 10 K under zero field cooling (ZFC) b) at 10 K after field cooling under 7T c) at 300 K. d) Temperature dependent magnetization curves e) Distribution of blocking temperatures.

The magnetic properties of C2, CS2 and CS2r were investigated by SQUID measurements. The $Fe_{3-d}O_4$ core has typical magnetic properties of small iron oxide nanoparticles with a small H_C at 10 K of 0.3 kOe, a T_{max} of 133 K which corresponds to a T_B of 78 K and displays superparamagnetic properties at room temperature.[15] The CS2 nanoparticles also have typical magnetic properties of $Fe_{3-d}O_4$@CoO nanoparticles with a large hysteresis opening at 10 K ZFC with a H_C of 17.3 kOe that is even higher than for CS nanoparticles (16.4 kOe). This larger H_C probably arise from the smaller iron oxide core in the CS2 nanoparticles that enhanced the exchange-bias coupling.[16] M(H) curves recorded after FC evidences an increase of H_C to 20.0 kOe and a shift of the hysteresis characterized by a H_E of 2.6 kOe. Temperature dependent magnetization curves evidences a T_{max} of 272 K for CS2 which corresponds to a T_B of 237 K, coherently with other results.[16–18] The heating of CS2 at high temperature does not affect the T_B of CS2r that is similar to the T_B of CS2. Hence, as CS2, CS2r also display superparamagnetic properties at room temperature. However, for M(H) curves at 10 K ZFC H_C of CS2r is reduced to 16.6 kOe while at 10 K FC, it is similar to the H_C of CS2. Also, the H_E of CS2r has decreased to 1.8 kOe compared to CS2 and clearly evidences a decrease of the exchange-bias coupling. This may be attributed to a further diffusion of the Co^{2+} cations in the iron oxide core but also to a decrease of the CoO shell through a solubilisation process during the synthesis of CS2r as the size of CS2r has decreased.[14]

Details on Stoner Wohlfarth fit of H_C = f(T) of CS, CSSA, CSSB and CSSC

The Stoner-Wohflarth fit of H_C = f(T) was performed for CS, CSSA, CSSB and CSSC samples according to the following equation

$$H_C = 0.48 H_K \left[1 - \left(\frac{T}{T_B}\right)^{0.5}\right]$$

With the anisotropic field $H_K = \frac{2K_{eff,ST}}{M_S}$

Here M_S and T_B were fixed to the values determined from M(H) curves recorded at 5 K and from d(M_{ZFC}-M_{FC})/dT respectively. The H_C were recorded for different temperatures comprised between 5 and 350 K. The values of $K_{eff,ST}$ were firstly limited between the bulk magnetic anisotropy values of Fe_3O_4 (K = 2 10^4 J/m^3 at 4 K[19,20]) and CoO (K = 5 10^5 J/m^3 [21]) which are the two extremes. They were secondly released for a second fit to confirm the obtained values.

Table S 3. Summary of the fitting conditions used for the Stoner-Wohlfarth fit of H_C = f(T) for CS, CSSA, CSSB and CSSC nanoparticles.

	CS	CSSA	CSSB	CSSC
T_B (K)	266	310	298, 328	335
M_S at 5 K (ZFC) (emu/g)	41	51	55	72
$K_{eff,ST}$ (10^4 J.m^{-3}) (from Stoner-Wohlfarth)	42.1	13.0	12.2	15.3

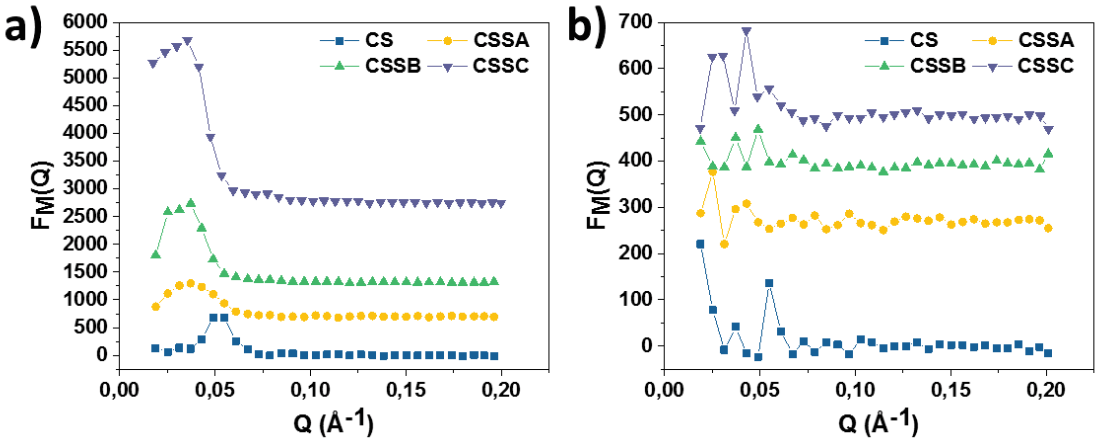

Figure S 20. Comparison of p-SANS magnetic factor a) in perpendicular, b) in parallel.

Table S 4. Coercive field of selective hysteresis measured at 4 K (in kOe).

	Fe S1	Fe S2	Fe S3	Co S4
C	0,3	0,8	0,3	-
CS	10,9	10,5	10,2	9,9
CSSA	10,8	10,7	10,7	10,8
CSSB	10,9	10,9	10,8	10,9
CSSC	9,6	9,6	9,6	9,7

Ligand field multiplet (LFM) calculation

The Contribution of Fe^{2+} and Fe^{3+} is also determined using CTM4XAS software.[22] For the calculation of $L_{2,3}$ edges spectra, this software takes into account the important interactions in the case of free ion in the spherical symmetry added with the local symmetry and crystal field contributions. Our approach consists to simulate the contribution of the Fe^{2+}(Oh), Fe^{3+}(Oh) and Fe^{3+}(Td) in the XAS and XMCD spectra using parameters of magnetite nanoparticles from the literature.

Table S 5. Parameters used to calculate the contribution Fe2+(Oh), Fe3+(Oh) and F3+(Td) via the software CTM4XAS.

	Fe^{2+} (Oh) $2p^63d^6 \rightarrow 2p^53d^7$	Fe^{3+} (Oh) $2p^63d^5 \rightarrow 2p^53d^6$	Fe^{3+} (Td) $2p^63d^5 \rightarrow 2p^53d^6$
Cristal field (10Dq)	1.4 eV	1.5 eV	-0.7 eV
Spin-orbit coupling (fundamental state)	0.1 eV	0.59 eV	0.59 eV
Spin-orbit coupling (excited state)	8.35 eV	8.35 eV	8.35 eV
Slater integrals factor	60 %	60 %	60 %
Exchange field	27.4 meV	27.4 meV	19.4 meV
Convolutions of transitions multiplets **Γ3 (L3 edge)** **Γ2 (L2 edge)** **σ**	0.3 eV 0.5 eV 0.25		

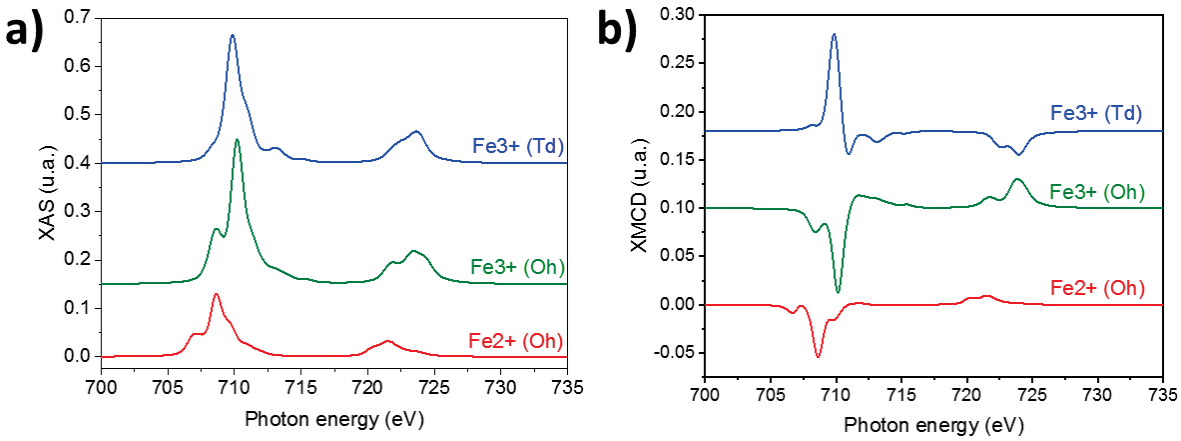

Figure S 21. a) XAS and b) XMCD spectra contribution of Fe^{2+}(Oh), Fe^{3+}(Oh) and Fe^{3+}(Td) for magnetite nanoparticles.

Annexes of Chapter V: Preliminary studies on the thermal decomposition of Ni based organo-metallic precursors

Synthesis of NiO nanoparticles in the literature

The first step was to perform the thermal decomposition of a Ni precursor in order to synthesize NiO nanoparticles which display a controlled shape and size distribution centered at less than 20 nm and that are stable in suspension in common organic solvents such as chloroform, toluene and cyclohexane. In the literature, only a few references were found on the thermal decomposition synthesis of NiO nanoparticles (Table 35). We have thus enlarged our researches on solid state reactions and heat treatment. The different synthesis conditions are reported in the following tab.

Table 35. Reported synthesis conditions of NiO nanoparticles.

1st author	Precursor	Solvent	Caping agent	Heating ramp	Size (nm)	Shape
Chen[23]	Nickel (II) oleate	1-octadecene	Oleic acid	3,3 °C/min to 320 °C for 30 min	20	Dot-like
Dharmaraj[24]	nickel acetate	DMF	Polyvinyl acetate	3h at 150 °C then the powder was heat treated at 450 °C	40-50	Cubic
Davar[25]	[bis(2-hydroxyacetophanto) nickel (II)]	Triphenylphosphine	Oleylamine	235 °C for 40 min	14-22	Nearly spherical
Park[26]	Ni-oleylamine complexe	Tributylphosphine	Tributylphosphine	200 °C for 30 min	5	Highly spherical
Li[27]	$Ni(acac)_2$	hexadecylamine	Trioctylphosphine oxide	220 °C	14	Triangle
Jana[28]	Nickel myristate	Not specified	Myristic acid	340 °C	Not specified	Triangle
Hosny[29]	Nickel anthranilic acid	-	-	50°C to 700 °C	8	Spherical
Farhadi[30]	$[Ni(NH_3)_6](NO_3)_2$	-	-	250 °C	12	Spherical
Wang[31]	Nickel acetate	-	-	400 °C for 2 h	10	Nearly spherical

Most of the results found in the literature were not satisfying as the shape and the size distribution of the nanoparticles were not highly controlled as it is for other type of nanoparticles such as for iron oxide nanoparticles.[15,32] However, Park and al.[26] managed to obtain highly spherical NiO nanoparticles stable in suspension through the thermal decomposition of a nickel-oleylamine complexe. To form this complexe, they suggest to react 0.52 g of nickel(actylacetonate)$_2$ with 2 mL of oleylamine. We failed to reproduce their experimental conditions as it was not possible to synthesize the complex due to the high amount of solid nickel(acac)$_2$ compared to the low amount of liquid oleylamine. Indeed, even heating at the desired temperature of 100 °C did not managed to soak all the solid phase. Thus, owing to our expertise on thermal decomposition of inorganic precursors, we decided to investigate a new pathway to synthesize NiO nanoparticles with controlled shape and narrow size distribution.

Chemical composition and ligands configuration of $NiSt_2$

Thanks to the preparation of a homemade iron (II) stearate as precursor, we managed to get well defined spherical iron oxide nanoparticles with tunable size ranging from 5 to 20 nm with a narrow size distribution, as shown in the previous chapters. Thus we first choose stearate as ligand in order to synthesize nickel stearate (NiSt) precursor. Nickel stearate has been synthesized in the same conditions as to synthesize iron (II) stearate by replacing $FeCl_2$ by $NiCl_2$. A light green solid was obtained which was then studied by FT-IR spectroscopy and thermogravimetric (TG) analysis. The FT-IR spectrum of NiSt in Figure 82 presents several peaks in the range between 4 000 and 450 cm^{-1} that were indexed according to the work of Abrahamson and Lukaski on iron stearate[33] and to the work of Xu and al. on nickel stearate.[34] Peaks located at 2 917 and 2 850 cm^{-1} are attributed to the symmetric (ν_sC-H) and antisymmetric (ν_{as}C-H) stretching vibrations of the fatty chain of stearate. Bands centered at 1 554 and 1 414 cm^{-1} arise from the antisymmetric ($\nu_{as}COO^-$) and symmetric (ν_sCOO^-) stretching vibrations of the carboxylic acid function which is at the end of the stearate's fatty chain. The bands at 1 689 and 1 115 cm^{-1} corresponds to the symmetric and antisymmetric stretching vibrations of ν_sC=O and ν_{as}C=O from free carboxylic acid group, evidencing the presence of free stearate. Indeed, when the stearate chain is coordinated to the metal, the νC=O split into the νCOO^- bands. The band located at 720 cm^{-1} is characteristics of the H-C-H scissoring from the fatty chain and the weak band at 679 cm^{-1} corresponds to O-C-O scissoring. Moreover, the distance Δ between the two νCOO^- bands is known to give information on the coordination mode of the ligand towards the metal. For Δ < 110 cm^{-1}, the coordination mode is chelating bidentate, for 140 < Δ < 190 cm^{-1}, it is bridging bidentate and for 200 < Δ < 320 cm^{-1}, it is monodentate.[35,36] Here, two different contributions were observed for (ν_sCOO^-) were observed. Hence two values of Δ of 90 and 153 cm^{-1} were calculated. They respectively correspond to a mixed chelating bidentate and a bridging bidentate coordination mode. It is similar to other synthesized iron (II) and cobalt (II) stearate. Hence, FT-IR analysis proved that the synthesis of nickel stearate has been successfully processed.

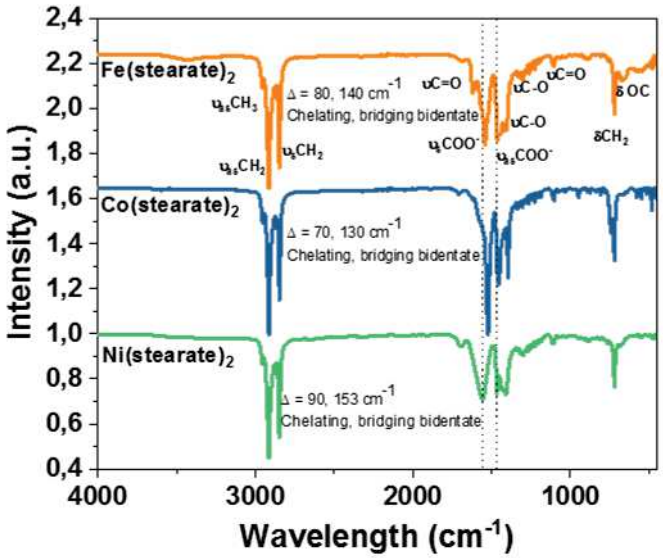

Figure 82. Comparison of FT-IR spectra of different metallic stearate precursors.

Thermal stability of $NiSt_2$

The thermal stability of nickel stearate precursor was investigated by thermogravimetric (TG) analysis (Figure 83). It evidences a start of weight loss around 200 °C, and a soft but constant decrease of the weight loss until 450 °C. Sleep decreases of weight loss were observed at 325 °C and at 365 °C. In order to have a better insight in the different episodes, the derivative of TG analysis (DTG) (Figure 83) evidences that no weight loss around 100 °C corresponding to water were found and that the weight starts to decrease at 200 °C, followed by two main episodes starting at 319 and 380 °C respectively.
In compliance with the literature on similar precursors,[15,37–39] we attributed the start of the weight loss at 200 °C to arise from the beginning of the decomposition of the precursor up to 370 °C which is generally attributed to the nucleation step. The growth step then starts at around 380 °C after which, the final weight loss at about 400 °C corresponds to the total decomposition of the organic ligands. Compared to the other stearates (Fe and Co stearates), $NiSt_2$ shows the most stable nucleation step while the growth step appears to be in between iron stearate and cobalt stearate. Thus, in order to synthesize the nanoparticles, we first tried to increase the reaction temperature.

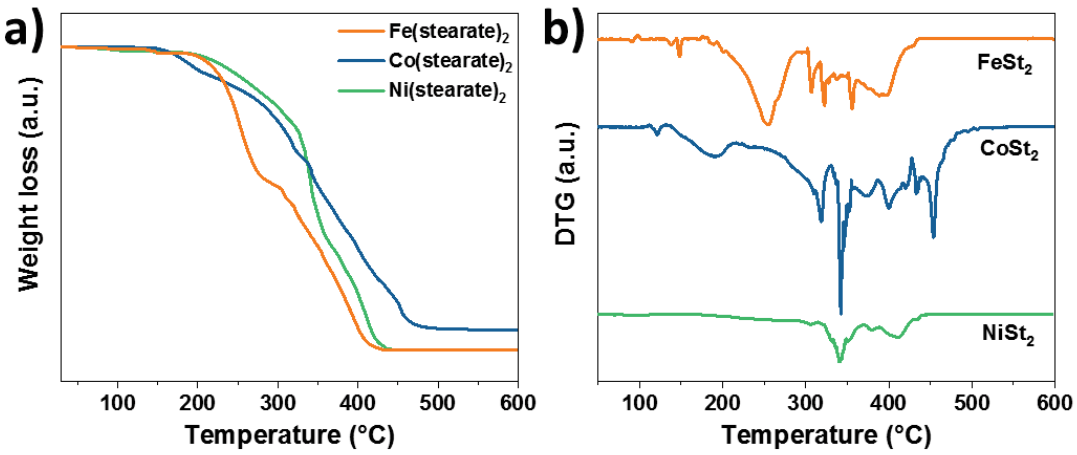

Figure 83. a) Thermogravimetric analysis of different metallic stearate based precursors with their corresponding derivative curves.

Preliminary study on the growth of NiO nanoparticles from the decomposition of $NiSt_2$

The first attempt consisted to decompose NiSt in a solvent displaying a boiling point (B_P) close to the growth temperature determined from TG analysis (around 380 °C). However, we did not find a suitable solvent with such a high boiling point and we finally used 1-docosene which displays a B_P of 367 °C. Hence, the mixture of $NiSt_2$ was heated at reflux for 2 h with a slow heating ramp of 2 °C/min without any oleic acid to avoid the enhancement of the thermal stability of the precursor. At the end, the nanoparticles were difficult to wash due to the fact that docosene is solid at room temperature, and TEM micrographs showed that the obtained nanoparticles displayed an extended shape with a 20 nm long and 5 nm thick size. The indexation of the corresponding XRD pattern agrees with the expected NiO phase and also evidence the presence of some impurities at small angles.

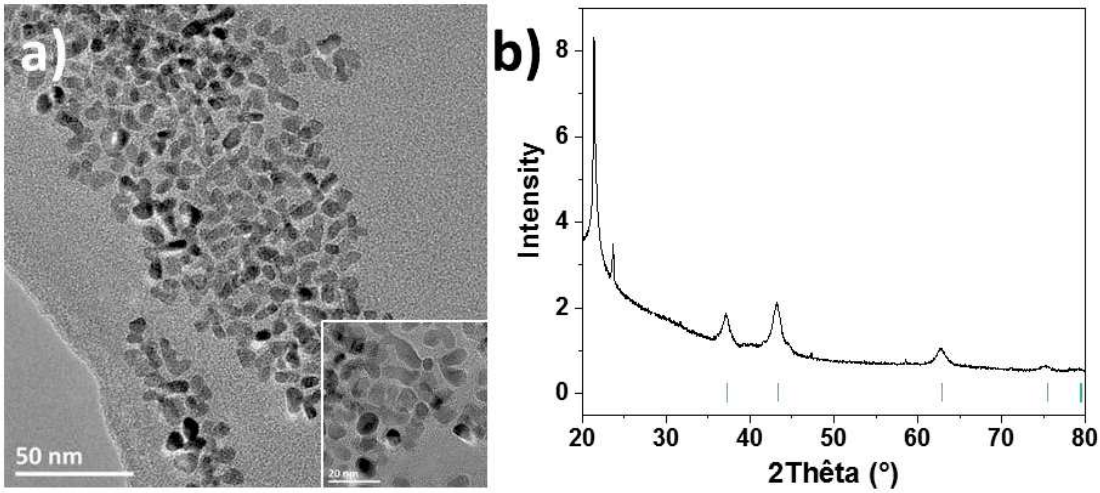

Figure 84. a) TEM micrographs of nanoparticles synthesized through the thermal decomposition of NiSt in 1-docosene. b) Corresponding XRD patterns indexed with a NiO phase (green bars, JCPDS card n°00-044-1159)

Then, we adaptated the protocol of Davar and al.[25] and used trioctylphosphine as solvent to decompose $NiSt_2$ in presence of oleylamine and oleic acid as capping agents. A temperature of 310 °C for 2 h was reached with a 2 °C/min heating ramp after a stage at 250 °C for 15 min reached thanks to a 5 °C/min heating ramp. The oleic acid was expected to stabilize the precursor while amine would destabilize it.[40] We expected to favor the nucleation step during the stage at 250 °C. Such conditions led to the synthesis of nanoparticles with a non-controlled size around 50-70 nm and the presence of non-crystalline particles (arrows) that seems to correspond to germs which were not removed during the washes. From the XRD pattern, it was possible to determine a Ni^0 composition for the crystalline nanoparticles. Hence the synthesis conditions were too rough and reduced the Ni^{2+} precursor in metallic nickel.

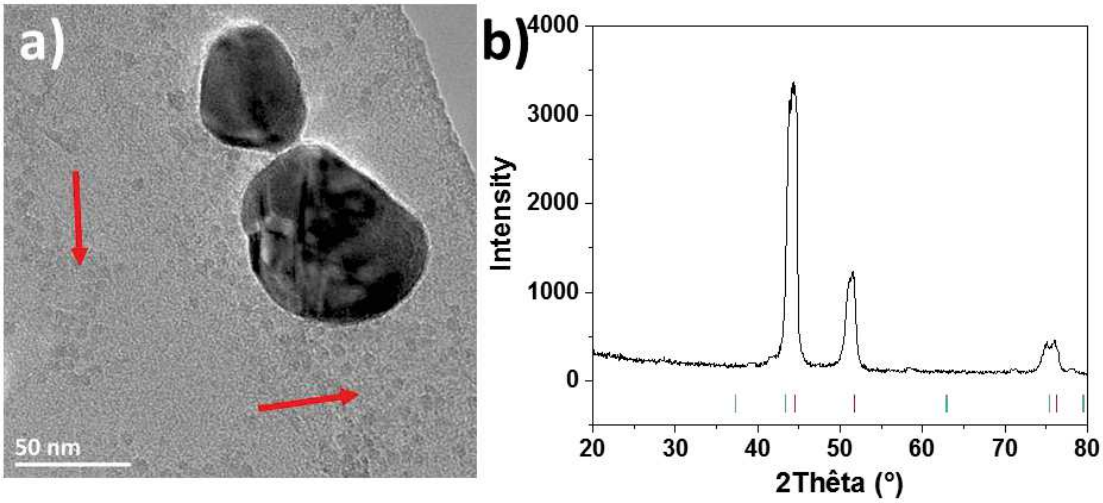

Figure 85. a) TEM micrograph of nanoparticles synthesized by the thermal decomposition of $NiSt_2$ in trioctylphosphine in presence of oleic acid and oleylamine. b) Corresponding XRD patterns, green and black bars correspond to NiO (JCPDS card n°00-044-1159) and Ni^0 references (JCPDS card n°04-010-6148).

A new trial was completed according to the results of Chen and al.[23] $NiSt_2$ was decomposed in the presence of oleic acid in octadecene (B_P = 320 °C) with a heating ramp of 2°C/min. TEM micrographs

show very small particles that seem to be non-crystalline and with a high content of organic phase. The XRD patterns however indicate that the small nanoparticles are actually crystalline according to a NiO chemical composition. Hence, the reaction conditions were too soft to increase the size of the nanoparticles.

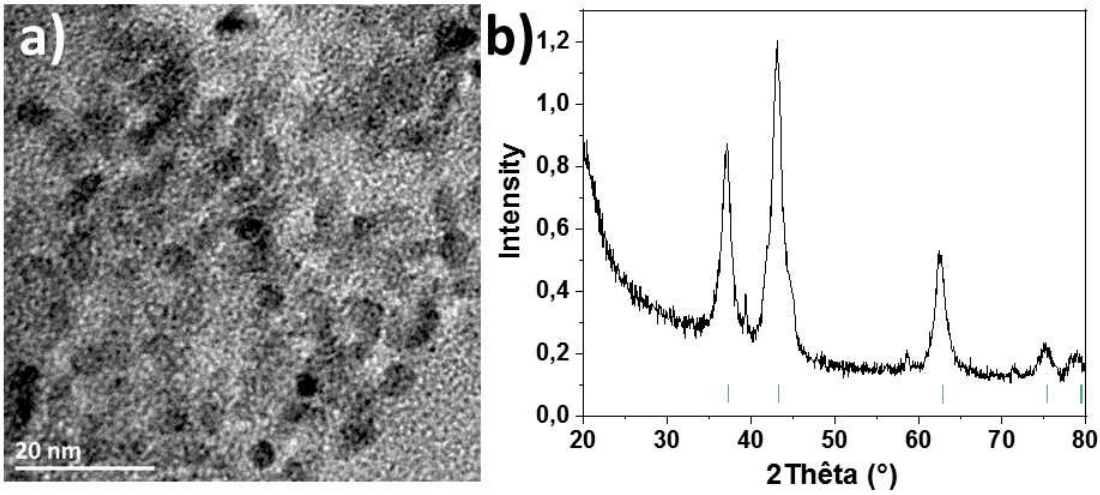

Figure 86. a) TEM micrograph of the product of the thermal decomposition of $NiSt_2$ in 1-octadecene in presence of oleic acid with b) the corresponding XRD patterns where the green bars correspond to NiO reference (JCPDS card n°00-044-1159).

Core@shell(@shell) nanoparticles synthesized from the thermal decomposition of $NiSt_2$

$Fe_{3-d}O_4$@NiO nanoparticles

Even though if the synthesis conditions of NiO nanoparticles were not satisfying, the synthesis of $Fe_{3-d}O_4$@NiO nanoparticles was proceeded as the presence of seeds is known to facilitate the deposition of monomers on the nanoparticles (see chapter I and ref.[41]). Hence, iron oxide nanoparticles were synthesized thanks to the thermal decomposition of $FeSt_2$ in dioctyl ether (B_P = 290 °C) with oleic acid. The $Fe_{3-d}O_4$ nanoparticles were washed and then used as seeds to decompose $NiSt_2$ at 310 °C for 2 h in a mixture of dioctyl ether : 1-octadecene (1 : 2) in presence of oleic acid after a heating ramp of 1°C/min. While the iron oxide core nanoparticles displayed a spherical shape with a size centered to 9.9 ± 1.1 nm, the $Fe_{3-d}O_4$@NiO core@shell nanoparticles displayed an octopod-like shape with extended corners and some small particles were observed. The XRD patter of $Fe_{3-d}O_4$@NiO nanoparticles show the presence of the iron oxide spinel structure and of the NiO phase. However, size measurements from TEM micrographs did not show any increase of the size compared to the core with an edge to edge size of 9.8 ± 0.9 nm. Thus, it is expected that the NiO phase has grown on specific surfaces of the spherical shell to form the octopod shape.

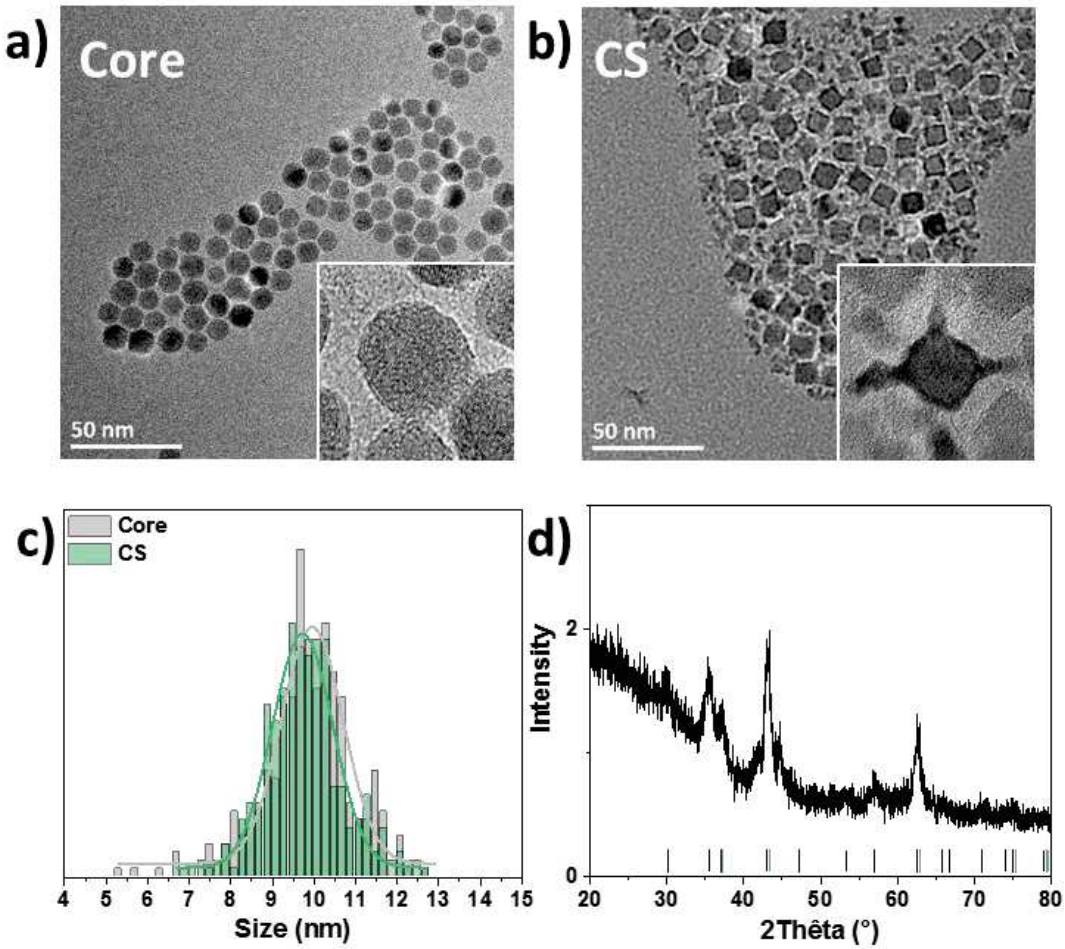

Figure 87. TEM micrographs of a) iron oxide core, b) core@shell $Fe_{3-d}O_4$@NiO nanoparticles with their c) corresponding size distributions and d) the XRD patterns of the $Fe_{3-d}O_4$@NiO nanoparticles where black and green bars correspond to Fe_3O_4 (JCPDS card n°04-005-4319) and NiO references (JCPDS card n°00-044-1159).

$Fe_{3-d}O_4$@CoO@NiO nanoparticles

Similar synthesis conditions were used in order to synthesize $Fe_{3-d}O_4$@CoO@NiO nanoparticles from $Fe_{3-d}O_4$@CoO nanoparticles that were synthesized following a previously published protocol.[17,42] Thus $NiSt_2$ was decomposed in presence of the $Fe_{3-d}O_4$@CoO nanoparticles used as. It was observed that the iron oxide core nanoparticles had a sphere-like shape, the $Fe_{3-d}O_4$@CoO nanoparticles displayed a cubic shape with truncated corners while $Fe_{3-d}O_4$@CoO@NiO nanoparticles showed a fine cubic shape.

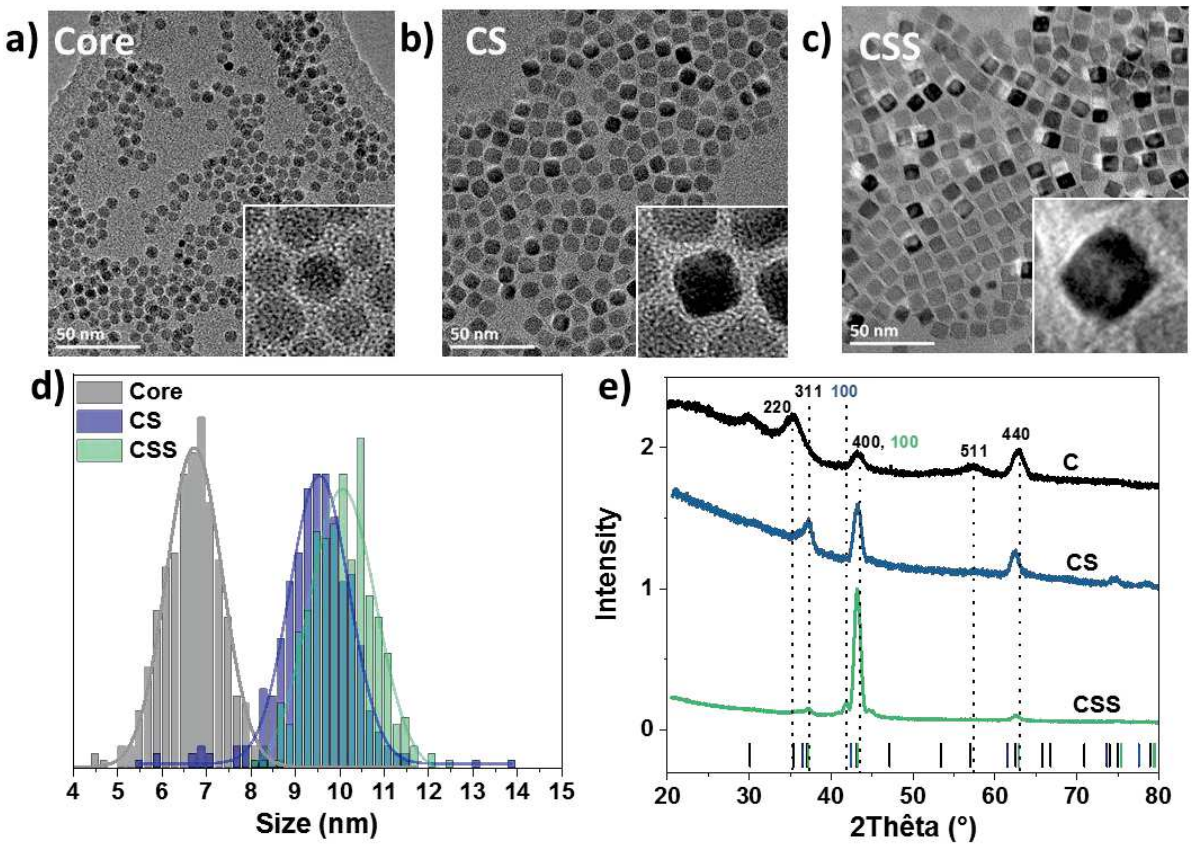

Figure 88. TEM micrographs of a) iron oxide core, b) core@shell and c) core@shell@shell of $Fe_{3-d}O_4$@CoO@NiO nanoparticles with in inset a zoom on a nanoparticle. d) is their corresponding size distribution and e) XRD patterns with black, blue and green bars the Fe_3O_4 (JCPDS card n°04-005-4319), CoO (JCPDS card n°00-048-1719) and NiO (JCPDS card n°00-044-1159) references.

Hence, both results indicate a preferential growth of nickel monomers on the faceted seeds nanoparticles which has also obviously been influenced by the preferential growth of the CoO shell on the iron oxide seed. Huang and al.[41] evidenced that during a seed-mediated growth synthesis, two nucleation steps are present. The first one consists in the formation of monomers in the solution while the second burst of nucleation allows to form monomers directly at the surface of the seeds which forms a new nucleation point that will ensure the growth of the nanoparticles. Xia and co-workers[43] studied the reactions kinetics of seed mediated-growth synthesis and evidenced that depending on the reaction conditions, different products are formed. Indeed, while there exists only one thermodynamic product, several kinetic products are possible. The thermodynamic product is the one that displays the lowest total free energy where sphere is the common thermodynamic shape for isotropic system. While kinetic products corresponds to a local minimal total free energy. Hence, thermodynamic products will be favored if the energy and time given to the system is high enough to overcome its energetic barrier.[43,44]

It is possible to modify the energetic barrier by tuning synthesis parameters such as the temperature and the precursor/capping agent ratio. Moreover, crystalline nanoparticles generally display some facets which have different surface free energies (γ). Their energy can be determined from the *broken bond symmetry approximation* where to create two new facets, the bounds between two neighboring atoms have to be broken and $\gamma = \frac{1}{2} N_B \varepsilon \rho_A$ with N_B the number of broken bounds, ε the bond strength and ρ_A the number of surface atoms per unit area. Thus, Xia and al.[43] has calculated that $\gamma_{(111)} < \gamma_{(100)} < \gamma_{(111)}$ for a face-centered cubic metal. Moreover, they have also shown that the monomers first deposit on the facets that display the highest surface free energies and then migrates on facets with the lowest energy. However, this mechanism depends on the kinetic reaction of $V_{deposition}$ and $V_{migration}$ where, for a cubic seed, the deposition of a shell if $V_{deposition} << V_{migration}$, creates a cuboctahedron, while if $V_{deposition} < V_{migration}$ it creates a cube with round corners. Hence, both products are thermodynamically controlled as the migration rate is higher than the deposition rate. However, if the migration rate is lower than the deposition rate, it leads to kinetic products where, if $V_{deposition} > V_{migration}$ the core@shell nanoparticle will display a concave cubic shape and if $V_{deposition} >> V_{migration}$, they will display an octopod shape.[43]

According to this, we can conclude that the shape of $Fe_{3-d}O_4$@NiO corresponds to a kinetic product while $Fe_{3-d}O_4$@CoO@NiO is a thermodynamic product. Hence, this evidence that the reaction kinetic is not the same between both systems and may differ from surface reactivity where iron oxide and CoO are expected to display different surface's reactivity.

$Fe_{3-d}O_4$@CoO@NiO nanoparticles synthesized with different concentration of $NiSt_2$

According to these results, different quantities of $NiSt_2$ were decomposed in presence of $Fe_{3-d}O_4$@CoO as seeds in order to investigate the kinetic effects.

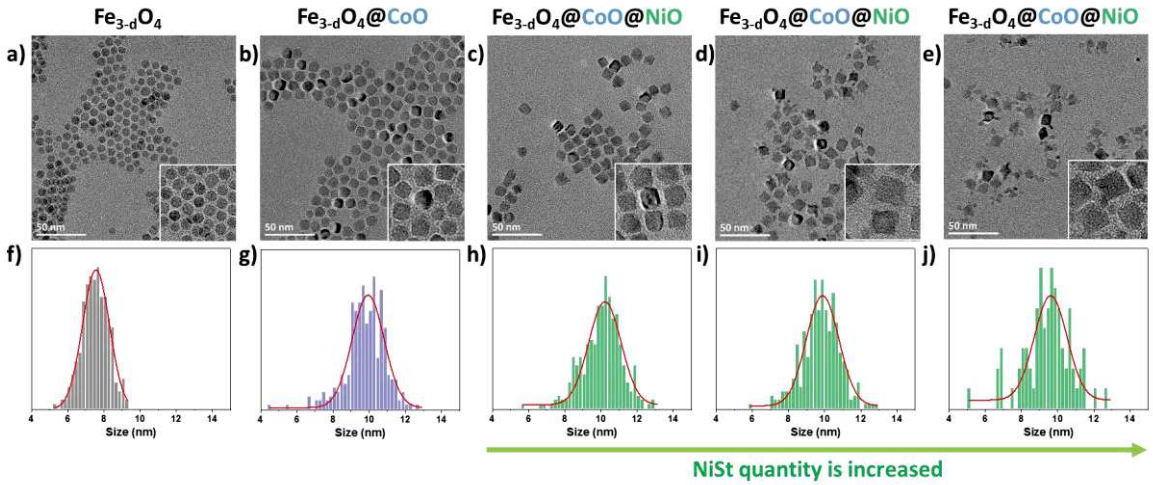

Figure 89. Synthesis of $Fe_{3-d}O_4$@CoO@NiO nanoparticles by using different amount of $NiSt_2$. TEM micrographs of a) $Fe_{3-d}O_4$ core nanoparticles, b) $Fe_{3-d}O_4$@CoO, c) $Fe_{3-d}O_4$@CoO@NiO with low NiSt quantity (R = 0.5), d) $Fe_{3-d}O_4$@CoO@NiO with medium NiSt quantity (R = 1.0), e) $Fe_{3-d}O_4$@CoO@NiO with high NiSt quantity (R = 1.5), where R is defined as $R = (n_{NiSt2})/(n_{FeSt2})$. f-j) Corresponding size-distributions.

Figure 89 shows that the iron oxide core nanoparticles display a close to sphere morphology with a mean size centered at 7.5 ± 0.7 nm. The $Fe_{3-d}O_4$@CoO core@shell nanoparticles show larger size which increases to 9.8 ± 1.1 nm corresponding to a shell thickness of 1.2 nm with a controlled morphology that deviates from the sphere morphology to cubes with rounded corners morphology. It evidences that there is a preferential growth of CoO on certain facets of the iron oxide core nanoparticles that are completely surrounded by the CoO shell according to the size increase.
Then, Ni monomers also deposit on preferential facets to grow as cubes for the lowest quantity of NiSt up to an octopod shape for the highest quantity of NiSt. The edge-to-edge distance corresponds to 10.1 ± 1.1, 9.8 ± 1.0 and 9.5 ± 1.3 nm respectively for an increase of the NiSt content. Hence, besides the preferential growth, one can also notice that the size of the nanoparticle tends to decrease as the amount of nickel precursor increases. Such a behavior is attributed to a preferential deposition rate compared to the migration rate: the quantity of Ni monomers in the solution increases with the increase of nickel precursor, then more Ni monomers deposit on the seeds for the highest concentration than for the lowest one. Hence, in the lowest NiSt content solution, the monomers have more time to migrate than for the highest concentration and so, the CoO edges of the seeds that are not being covered by nickel monomers undergo a partial solubilisation leading to an edge-to-edge size decrease (see chapter III).[14] Moreover, the increase of the $NiSt_2$ led to the synthesis of small nanoparticles that are attributed to the heteronucleation due to the high concentration of Ni monomers and the low concentration of seeds in the solution. According to the XRD pattern of the $Fe_{3-d}O_4$@CoO@NiO nanoparticles with the highest concentration of $NiSt_2$, we attributed the composition of the small particles to be NiO or $Co_{1-x}Ni_xO$ due to the possible partial solubilisation and recrystallization of the CoO shell.

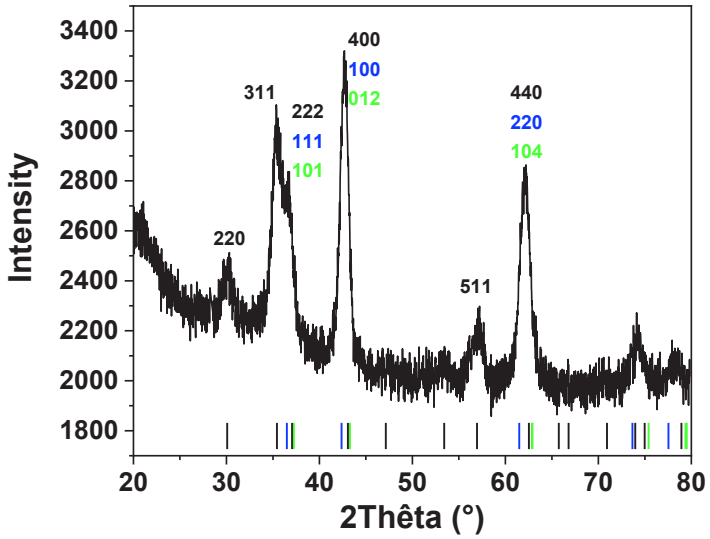

Figure 90. XRD pattern of $Fe_{3-d}O_4$@CoO@NiO with high NiSt quantity (R = 1.5) presented in Figure 89. Black, blue and green bars correspond to Fe_3O_4 (JCPDS card n°00-019-0629), CoO (JCPDS card n° 00-048-1719) and NiO (JCPDS card n°04-011-2340) references respectively.

Determination of a new Ni precursor to synthesize NiO nanoparticles

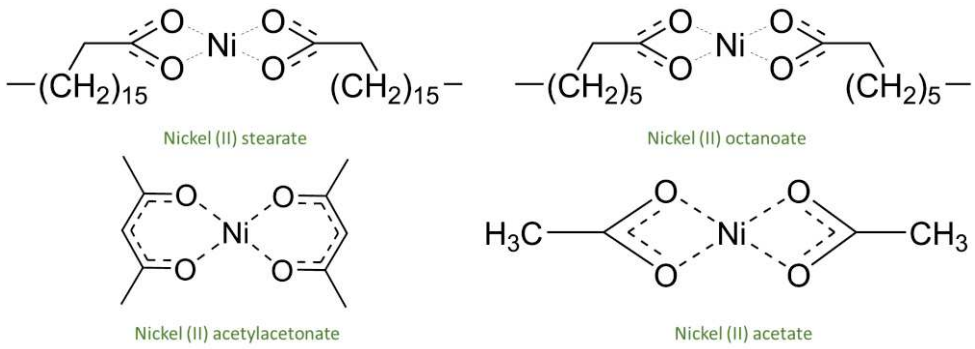

Figure 91. Developed chemical formula of nickel (II) stearate, nickel (II) octanoate, nickel (II) acetylacetonate, nickel (II) acetate all represented in chelating bidentate coordination.

As the decomposition of nickel precursor based on stearate was not satisfying, the stearate ligand was replaced by shorter organic chains in the aim to eventually reduce the decomposition temperature of the nickel precursor. Thus, Nickel octanoate (NiOct), nickel acetylacetonate (NiAcac) and nickel acetate (NiAc) were studied by FT-IR spectroscopy. It was observed that NiOct and NiSt infrared spectra display the same bands as for NiSt with $\Delta = 149$ cm^{-1} corresponding to a same bridging bidentate coordination mode.[35,36]

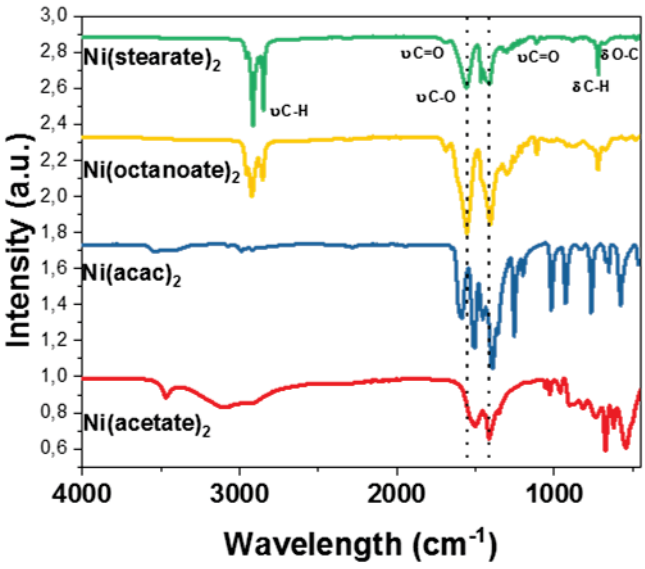

Figure 92. FT-IR spectra of different nickel precursors.

The FT-IR spectrum of NiAcac (Figure 92) is different from the two previous one, the band centered at 1 692 cm^{-1} corresponds to the vibration of ν(C=C) and ν(C=O) together, the band at 1 513 cm^{-1} arises from the vibration of ν(C=O), the bands at 1 388 and 1 257 cm^{-1} are attributed to the deformation of CH_3 and C-C bonds respectively and CH_3 display another band at 1 018 cm^{-1}. The bands at 925 and 763 cm^{-1} are attributed to CCH_3 bond and CH out of plane bending mode respectively. Finally, NiO vibration displays a band at 573 cm^{-1}.[45,46]

The FT-IR spectrum of NiAc displays a thin band at 3 468 and two broad bands at 3 106 and 2 917 cm^{-1} that are attributed to arise from ν(OH) stretching vibrations of adsorbed water. The bands centered at 1 504 and 1 411 cm^{-1} correspond respectively to the antisymmetric and symmetric ν(CO) vibration modes. Evidencing a chelating bidentate coordination mode of the acetate ligand according to a Δ of 93 cm^{-1}.[47,48]

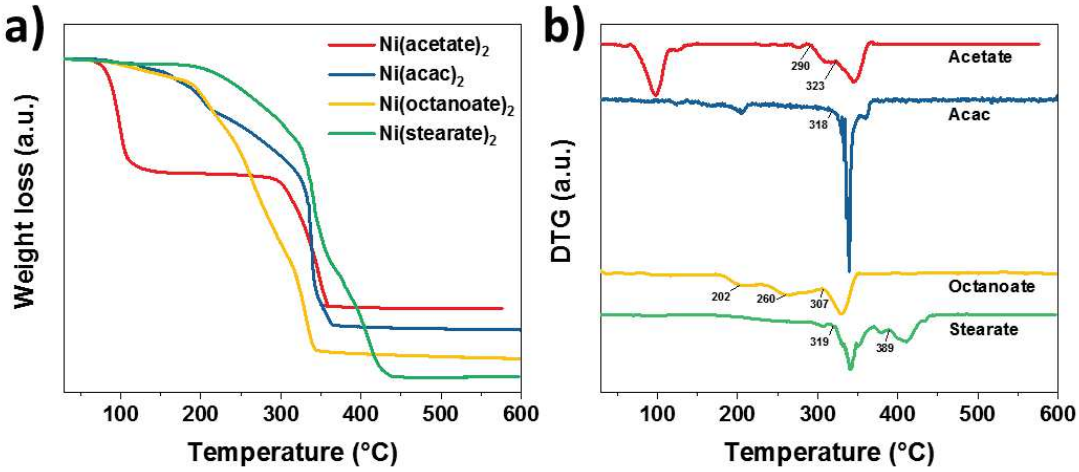

Figure 93. a) Thermogravimetric analysis of different nickel precursors with their corresponding derivative curves.

The decomposition of these precursors was also investigated by TG analysis (Figure 93) which shows that NiOct, NiAcac and NiAc display a first weight loss at 89, 118 and 70 °C, respectively followed by a continuous decrease of weight loss for NiOct and NiAcac and by a constant weight for NiAc before evidencing a second abrupt weight loss at 310 °C. The different slopes during the weight loss evidence

the presence of different regimes that are better shown by DTG curves. DTG curve of NiAc displays a first weight loss at 100 °C which corresponds to water, the second decomposition episode that starts at 290 °C is attributed to the nucleation step which does not show a very clear separation from the growth step that may starts around 323 °C. NiAcac displays a first small weight loss at 200 °C that is attributed to the nucleation step and the second weight loss starting at 318 °C corresponds to the growth step and to the final degradation of the alkyl chains where it is not possible to distinguish both episodes. Finally, the DTG curve of NiOct show three weight losses starting at 180, 240 and 307 °C corresponding to the nucleation step, growth step and final degradation of the alkyl chains respectively.

Hence, NiOct, NiAcac and NiAc are less stable than $NiSt_2$ against temperature. Moreover, as NiOct and NiAc display the clearer separation between their nucleation and growth steps compared to the other studied Ni based precursor, they are promising precursors to synthesize nickel-oxide based nanoparticles.

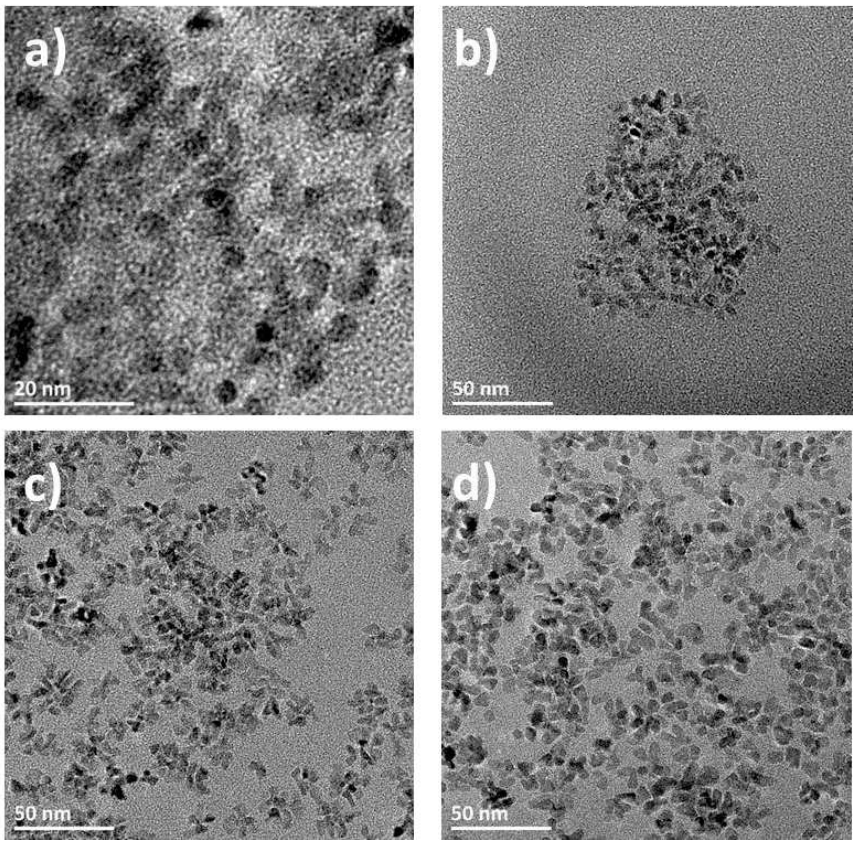

Figure 94. TEM micrographs of NiO nanoparticles synthesized by the thermal decomposition of a) NiSt, b) NiAc, c) NiOct, in presence of oleic acid d) NiOct in presence of oleylamine, in 1-octadecene with a heating ramp of 2 °C/min

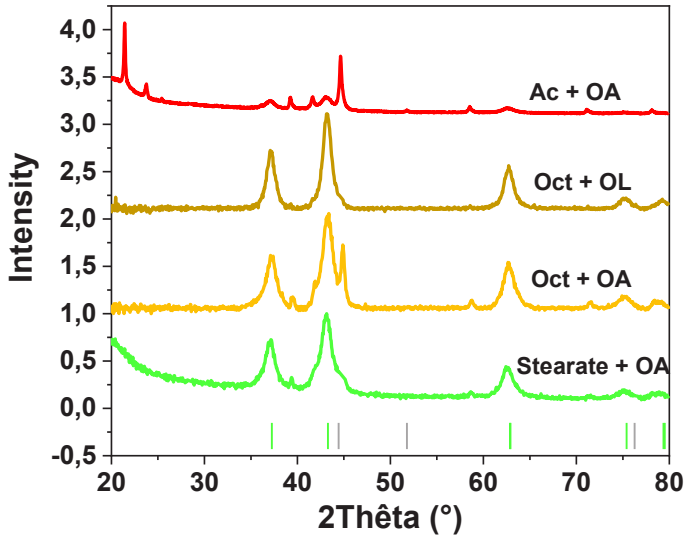

Figure 95. XRD pattern of NiO nanoparticles synthesized by the thermal decomposition of NiSt, NiAc, NiOct, in presence of oleic acid and NiOct in presence of oleylamine all in 1-octadecene with a heating ramp of 2 °C/min. Green and grey bars correspond to NiO (JCPDS card n°04-011-2340) and Ni^0 (JCPDS card n°04-010-6148) references.

NiOct and NiAc precursors were firstly decomposed in presence of oleic acid (OA) used as stabilizing agent.[15] According to the TG analysis experiments and to a better stabilization of the precursor due to the oleic acid, the decomposition was processed in 1-octadecene (B_P = 320 °C) with a slow heating ramp of 2 °C/min to give enough time to the nucleation step to proceed. In both cases, small NiO nanoparticles with a non-controlled shape were obtained. They have similar shapes to the NiO nanoparticles synthesized by the thermal decomposition of $NiSt_2$ in the same conditions but with a larger size and a better defined morphology according to TEM micrographs. It agrees with the fact that the replacement of $NiSt_2$ by NiAc or NiOct allowed to decrease the decomposition temperature of the precursor in order to synthesize better defined nanoparticles, while the nanoparticles obtained with $NiSt_2$ resemble more to germs than to nanoparticles due to their small size and the absence of periodic fringes on their high-resolution TEM micrographs. However XRD patterns showed that the nanoparticles are crystalline with a NiO chemical composition. An additional component in the XRD pattern of particles resulting from the decomposition of NiAc and NiOct with oleic acid could not be indexed and is attributed to a pollution.

As the decomposition of NiOct in presence of oleic acid gave the best results between NiOct, NiAc and NiSt due to its lower decomposition temperature, NiOct was decomposed in presence of oleylamine (OL). The amine group is expected to destabilize the precursor and facilitate its decomposition.[40] TEM micrographs show that the particles are similar to the one obtained in presence of OA. A similar XRD pattern was recorded for NiOct in presence of OA than in presence of OL however, no pollution are present in the last. Thus the presence of an amine group seem to favor the synthesis of NiO nanoparticles.

$Fe_{3-d}O_4$@NiO nanoparticles synthesized from the decomposition of NiOct

Solvent effect

According to the improvement on the decomposition of Ni-based metallic precursor, NiOct was decomposed in presence of iron oxide nanoparticles used as seeds which lowers the energy barrier of the nucleation steps as the seeds acts as nucleation sites. Moreover, during the synthesis of the

expected NiO shell, an equimolar content of oleic acid and hexadecylamine was used in order to stabilize the nanoparticles and to play on the stabilization/destabilisation of the organo-metallic precursors. $Fe_{3-d}O_4$@NiO nanoparticles were synthesized according to a seed-mediated growth process where the iron oxide core were firstly synthesized and washed. Then NiOct was decomposed in the presence of iron oxide nanoparticles used as seeds with an equimolar content of oleic acid and hexadecylamine as surfactant. A variety of solvent with different boiling point was used: dioctyl ether (B_P = 290 °C), 1-octadecene (B_P = 320 °C), squalane (B_P = 470 °C, operating temperature = 350 °C due to temperature limitations of the heating mantle), in order to study the effect of the reaction kinetics on the nanoparticles formation.

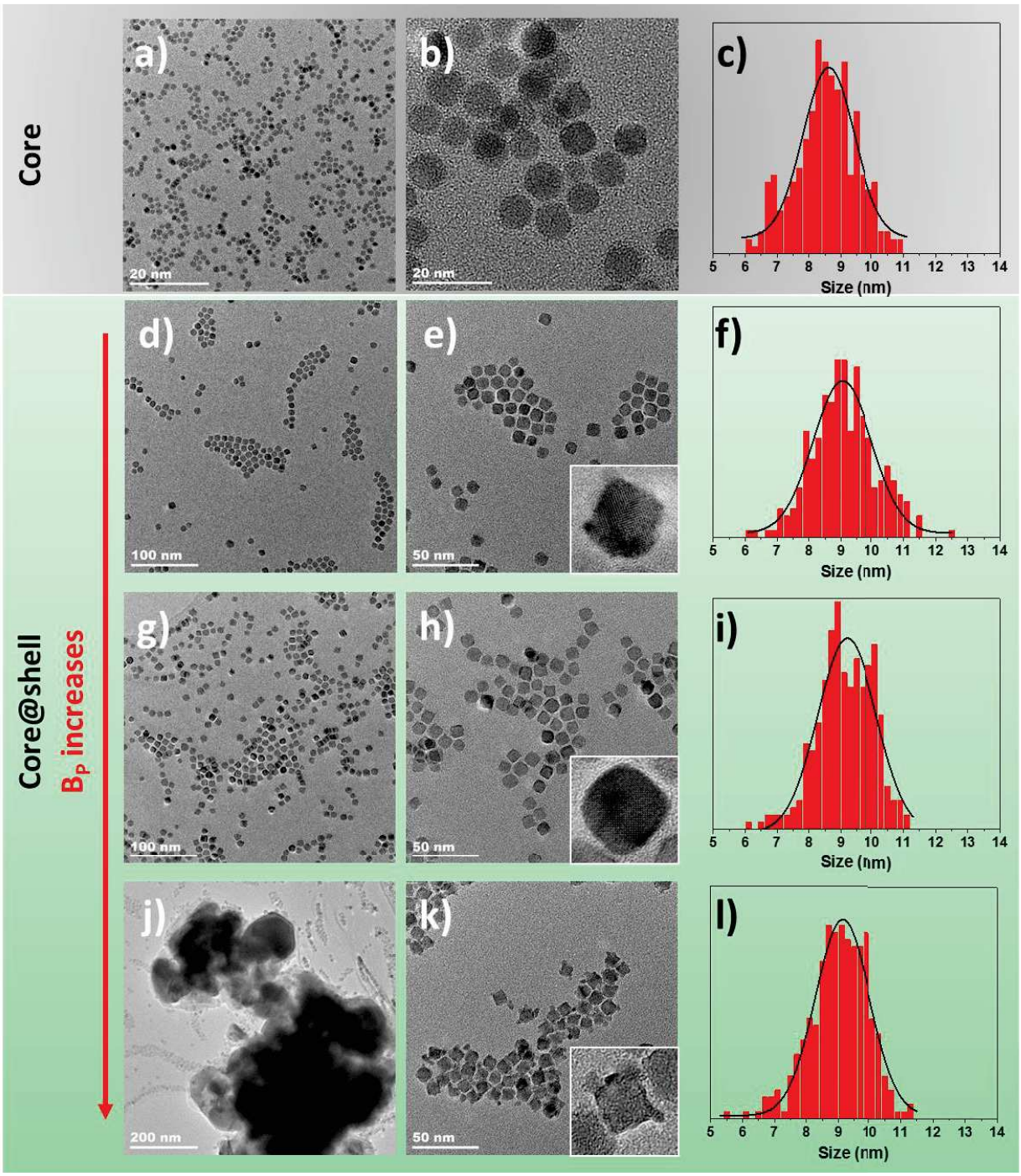

Figure 96. TEM micrographs of a, b) the $Fe_{3-d}O_4$ core and d, e, g, h, j and k) $Fe_{3-d}O_4$@NiO nanoparticles where the NiO shell was synthesized according to the thermal decomposition of NiOct in presence of the iron oxide seeds with an equimolar mixture of oleic acid and hexadecylamine in a, b) dioctyl ether, c, d) 1-octadecene, e, f) squalane with a heating ramp of 5

°C/min. Insets are HR-TEM micrographs evidencing the presence of lattice fringes. c, f, i, l) Are the corresponding size distributions.

For the synthesis of the three different core@shell nanoparticles of Figure 96, the same iron oxide core was used (Figure 96 a-c). One can observes that for the decomposition of NiOct in a low boiling point solvent i.e. in ether dioctyl (CS OE), the core@shell nanoparticles display a shape intermediate to a sphere and a cube. When the boiling point temperature is intermediate i.e. for 1-octadecene, the shape of the nanoparticles (CS 1-Oc) get closer to a truncated cube morphology and for high boiling point solvent i.e. squalane, the nanoparticles (CS Sq) display an octapodic shape. Moreover, increasing the decomposition temperature led to an increase of the Ni content within the final product, as shown by energy dispersive spectrometry (EDS) results where the proportion of Ni compared to Fe atoms increases from 24 to 40 and 43 % for CS OE, CS 1-Oc and CS Sq respectively. The iron oxide core displays a size of 8.5 ± 0.8 nm, and the three core@shell nanoparticles display an increase of this size with similar edge-to-edge distances of 9.1 ± 0.9 nm which, considering also the increase of nickel content from EDX analysis as B_P increases, proves that Ni atoms are located all around the core@shell nanoparticles with a higher concentration on the corners of the nanoparticles. EELS-SI and EELS profile should be perform to support this hypothesis. Hence, the increase of the nickel monomers content in the solution increases the deposition rate towards the migration rate. Thus Ni monomers deposit according to a preferential orientation favoring the octapodic shape for high deposition rate and high monomers content. As shown by Figure 96j, for high boiling point solvent, some big clusters are formed which are attributed to heteronucleation during the decomposition of NiOct, due to the very high concentration of nickel monomers in the solution compared to the concentration of iron oxide nanoparticles seeds.

Table 36. Structural characteristics of $Fe_{3-d}O_4$@NiO nanoparticles synthesized in different solvents (dioctyl ether, 1-octadecene and squalane).

	C	CS OE	CS 1-Oc	CS Sq
Size (nm)	8.5 ± 0.8	9.1 ± 0.9	9.2 ± 0.9	9.1 ± 0.9
Thickness (nm)	-	0.3	0.4	0.3
Fe : Ni at. Ratio (%)	-	76 : 24	60 : 40	52 : 43

Concentration effect

As shown previously, the [seeds]/[Ni precursor] ratio affects the reaction kinetic and resulted in different shape of the final core@shell nanoparticles. Moreover, as the decomposition of NiOct in dioctyl ether resulted in a shape close to sphere, we investigated the effect of the relative concentration of NiOct with respect to iron oxide seeds in the core@shell structure. In samples CSNi1 and CSNi3, the same molar ratio $R = [(n_{NiOct})/(n_{FeSt})]$ was used while the concentration of both iron oxide core and NiOct was increased in the solution. TEM micrographs in Figure 97 shows that the iron oxide cores are both spherical with a narrow size distributions centered at 8.5 ± 1.0 and 8.4 ± 0.7 nm for CSNi1 and CSNi3 respectively. Core@shell nanoparticles exhibit different shape: CSNi1 displays a cubic with rounded corners, CSNi3 displays an octapodic shape. Sizes corresponding to edge-to-edge distances of 9.0 ± 0.9 and 8.6 ± 0.7 nm were measured for CSNI& and CSNi3 respectively. Resulting in shell thicknesses of 0.3 and 0.1 nm for CSNi1 and CSNi3 respectively. Moreover, CSNi3 evidences a lower shell volume of 22.7 nm^3 than the 60.1 nm^3 for CSNi1 while CSNi3 shows a higher Fe : Ni ratio of 58 : 42 than the 76 : 24 for CSNi1, which evidences that the shell is not homogeneous on CSNi3 and agrees with the presence of nickel atoms on the corners of the octapod. Hence, the increase of the [seeds]/[Ni precursor] concentration ratio in solution facilitates the deposition of Ni monomers on the nanoparticles at the expense of the migration rate.

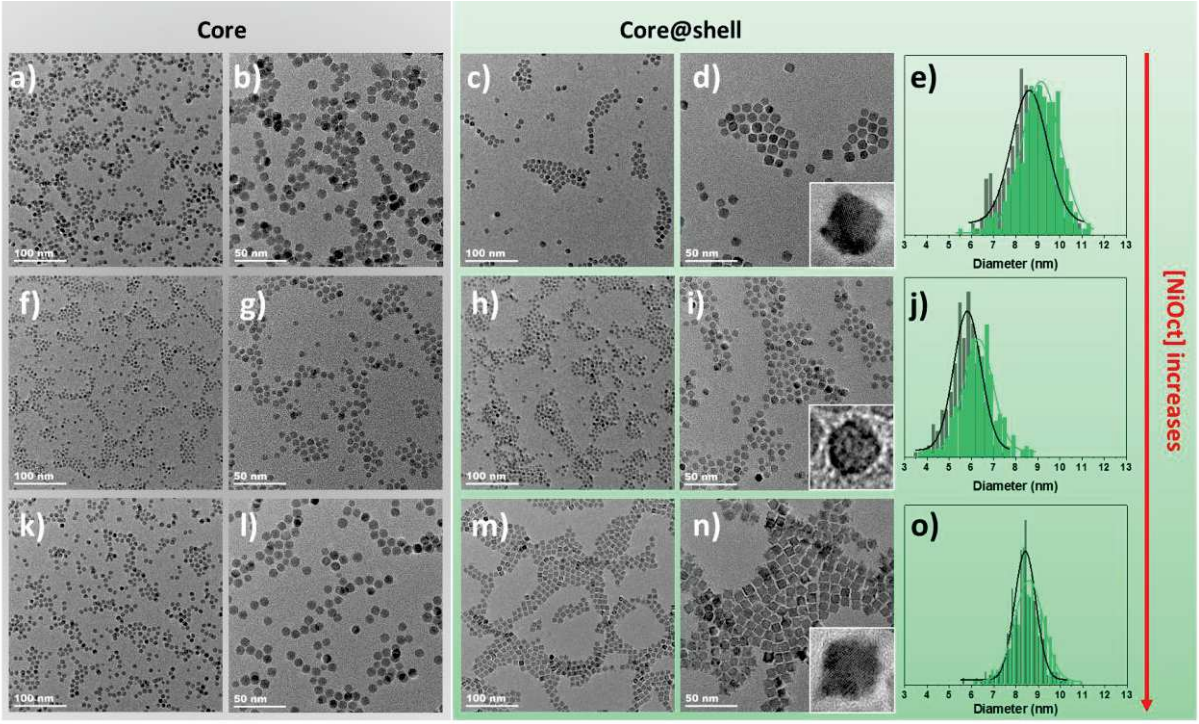

Figure 97. TEM micrographs of a, b, f, g, k, l) iron oxide seeds nanoparticles with $Fe_{3-d}O_4$@NiO nanoparticles with increasing NiOct concentrations: c, d) CSNi1, h, i) CSNi2, m, n) CSNi3, insets are an enlargement on 1 nanoparticle. Graphs e, j, o) are the corresponding size distributions with core size in black and core@shell size in green.

Table 37. Structural characteristics of $Fe_{3-d}O_4$@NiO nanoparticles synthesized with different concentrations of NiOct precursors.

	CSNi1	CSNi2	CSNi3
$\mathbf{R = [(n_{NiOct})/(n_{FeSt})]}$	1.0	1.5	1.0
C NiOct (10^{-5} mol/L)	2.8	5.5	9.9
C oleic acid (10^{-5} mol/L)	2.8	11.0	9.9
C hexadecylamine (10^{-5} mol/L)	2.8	11.0	9.9
Core size	8.5 ± 1.0	5.8 ± 0.7	8.4 ± 0.7
Core@shell size (nm)	9.0 ± 0.9	6.3 ± 0.8	8.6 ± 0.7
Shell thickness (nm)	0.3	0.3	0.1
Shell volume (nm^3)	60.1	28.8	22.7
Core@shell Fe : Ni at. Ratio (%)	76 : 24	65 : 35	58 : 42

The iron oxide core of CSNi1 and CSNi2 both display a spherical shape with a narrow size distribution centered at 8.5 ± 1.0 and 5.8 ± 0.7 nm respectively. The synthesis of the core@shell nanoparticles in CSNi1 led to a cubic with rounded corners shape while CSNi2 exhibits a close to sphere shape. In both cases, the measured shell thickness corresponds to 0.3 nm with a volume of 60.8 nm^3 for CSNi1 and 28.8 nm^3 for CSNi2 hence a lower shell volume for CSNi2 than for CSNi1. However, the atomic EDX ratio of CSNi1 and CSNi2 evidences a higher nickel atomic quantity in CSNi2 (35 % of nickel atoms) than in CSNi1 (24 % of nickel atoms). The lowest shell volume of CSNi2 than for CSNi1 can be attributed to size effect where the core of CSNi2 displays a smaller size (5.8 ± 0.7 nm) compared to the one of CSNi1 (8.5 ± 1.0 nm).

When the concentration of NiOct in solution is increased compared to the concentration of iron oxide seeds: R = 1.0 for CSNi1 while R = 1.5 for CSNi2, it should favor the kinetic product i.e. a more octapodic shape for CSNi2 than for CSNi1. However, TEM micrographs shows that CSNi2 displays a close to sphere shape. This was attributed to the doubling of the surfactant quantity in CSNi2 compared to CSNi1 which

changes the kinetic decomposition of the precursors and can also affect the deposition and migration rate of the nickel monomers on the seeds.[43,44]
Hence, the increase of surfactant concentration in the solution allows to favor the thermodynamic product as evidenced by Feld and al.[44]

Spherical $Fe_{3-d}O_4$@NiO nanoparticles

FT-IR spectroscopy

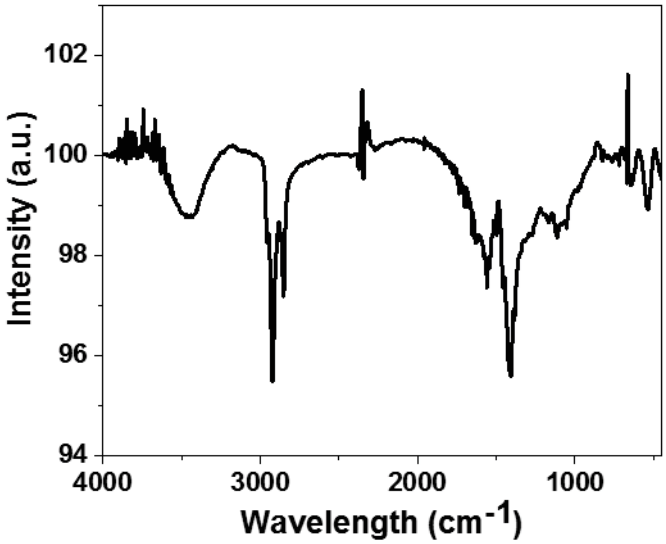

Figure 98. FT-IR spectrum of CSNi2 nanoparticles.

CSNi2 nanoparticles were investigated more deeply as its' spherical shape allow to get a simpler model than cubic nanoparticles due to the limitation of anisotropic shape effects.
The FT-IR spectrum of CSNi2 nanoparticles recorded in the range 4 000 to 450 cm^{-1} displays several bands. With a large band centered at 3 456 cm^{-1} that corresponds to the stretching vibration of O-H bonds from ambient water molecules, the bands at 2 923 and 2 852 cm^{-1} are attributed to the symmetric and antisymmetric stretching of C-H bonds of the alkyl chains respectively. The bands between 1 742 and 1 046 cm^{-1} arises from the symmetric and antisymmetric vibrations of the C-O bonds from the COO^- groups of oleic acid. The large basis of these two peaks suggest the presence of a high content of remaining ligands. Finally, the band centered at 536 cm^{-1} is attributed to the stretching vibration of the metal-oxygen bond. Thus the FT-IR spectrum of CSNi2 evidence the presence of ligands grafted at the surface of CSNi2 where, due to a similar chemical structure of the ligands, FT-IR experiments do not allow to discriminate the grafting between hexadecylamine and oleic acid.

X-ray diffraction

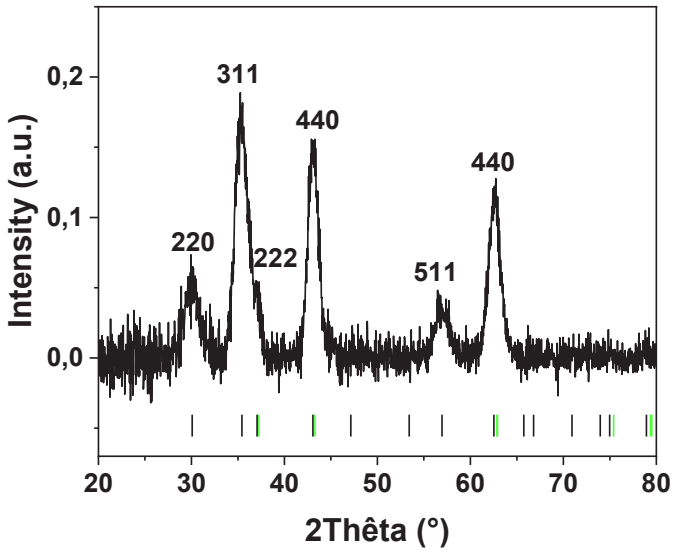

Figure 99. XRD pattern of CSNi2 nanoparticles. Black and green bars correspond to Fe_3O_4 (JCPDS card n° 19-062) and NiO (JCPDS card n° 47-1049) references respectively.

The XRD pattern of CSNi2 nanoparticle evidence the presence of an invert spinel structure which can be indexed according to a magnetite structure. An additional small contribution corresponding to the (222) reflection of the wüstite phase was ascribed to the NiO shell. Due to a crystallization in similar space group of Fe_3O_4 (Fd-3m) and NiO (Fm-3m) and to the concordance of their cell parameters (a_{Fe3O4}=8.396 Å JCPDS card n° 19-062, a_{NiO} = 4.1771 Å JCPDS card n° 47-1049) it is not possible to clearly separate the contribution of iron oxide and NiO. Moreover, the calculated cell parameter from the Debye-Scherrer method of CSNi2 XRD pattern display a value of 8.398 ± 0.001 Å. This is slightly higher than the cell parameter of magnetite and we attribute such discrepancy from the chemical reduction of the $Fe_{3-d}O_4$ core. Larger experimental values than the cell parameter of Fe_3O_4 were attributed to result from strains due to the lattice mismatching as already shown in previous chapters. The Debye-Scherrer formula allowed us to determine a crystal size of 6.3 ± 0.1 nm which is identical to the size of CSNi2 measured from TEM micrographs, showing the good epitaxial growth of the NiO shell on the iron oxide seeds.

XAS, XMCD spectroscopy

Table 38. XAS and XMCD characteristics of CSNi2 and its' corresponding iron oxide core C2.

Sample	Diameter (nm)	I1/I2	(S1+S2)/(S2+S3)	δ	S5 (%)
C2	5.8 ± 0.7	0.52	0.73	0.31	-
CSNi2	6.3 ± 0.8	0.70	1.09	0.07	0.1
Magnetite ref	-	0.71	1.14	0	-
Maghemite ref	-	0.35	0.69	0.33	-

In order to investigate separately the atomic environment of the nickel and iron atoms, soft XAS and XMCD experiments were performed on the DEIMOS beamline of synchrotron SOLEIL. In the isotropic XAS recorded at the Fe edge, the intensity of peak I_1 arises mostly from the contribution of Fe^{2+} in octahedral (Oh) sites while the intensity of peak I_2 arises from the contribution of Fe^{3+} in Oh sites. Hence, the ratio I_1/I_2 brings further information on the Fe^{2+} content in the sample where for example,

a pure magnetite displays a calculated I_1/I_2 ratio of 0.71 while a pure maghemite displays 0.35 for the same ratio according to ref.[49] This ratio is equivalent to 0.52 for the iron oxide core which is between magnetite and maghemite. Considering the small size of 5.8 nm of this magnetite based nanoparticles, the result is concordant with partially oxidized nanoparticles in surface.[15] The I_1/I_2 ratio increases then to 0.70 in CSNi2 being very close to the 0.71 for a pure magnetite, as observed for the synthesis of $Fe_{3-d}O_4$@CoO nanoparticles.[16] Hence, the increase of Fe^{2+} content in CSNi2 was attributed to arise from the chemical reduction of the iron oxide core during the synthesis of the NiO shell, in accordance with XRD results.

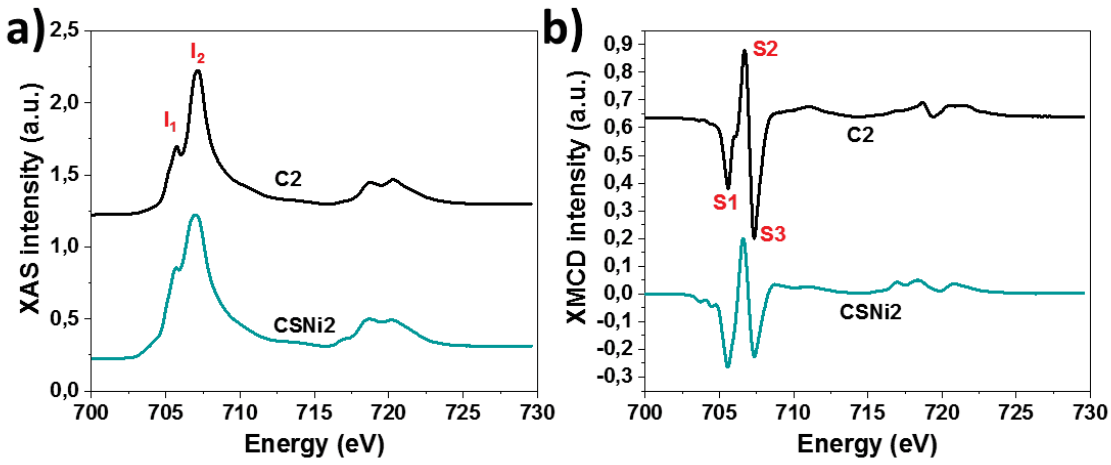

Figure 100. a) XAS and b) XMCD spectra of CSNi2 and its' corresponding iron oxide core C2, recorded at the Fe $L_{2,3}$ edges.

The XMCD spectra brings further information on the presence of Fe^{2+} within the nanoparticles. Indeed, they evidence three main peaks in the L_3 region where peak S1 is attributed to Fe^{2+} and Fe^{3+} in octahedral (Oh) sites, peak S3 corresponds to the solely absorption of Fe^{3+} in Oh sites. Fe^{3+} in Oh sites are coupled ferrimagnetically to Fe^{3+} in Td sites that are displayed by peak S2. Hence, for a pure magnetite, peak S1 displays a lower intensity than peak S3 while for a pure maghemite the intensities are at the opposite. Thus, the distance between IS1-S2I and IS2-S3I allows to investigate the Fe^{2+} content. According to the work of Pellegrin and al.[49] on magnetite based nanoparticles with several oxidation degrees: $Fe^{3+}_{2/3}Fe^{2+}_{1/3-\delta}O_4$ with δ ranging from 0 (magnetite) to 0.33 (maghemite), for a pure magnetite, the (S1+S2)/(S2+S3) ratio is equivalent to 0.71 while for a pure maghemite it is 0.35. Here this ratio is equivalent to 0.73 (δ = 0.31) for the iron oxide core which evidences a high oxidation rate of the core, as already observed in XAS experiments. This ratio increases to 1.09 (δ = 0.07) in CSNi2 which shows the chemical reduction of the iron oxide core as already discussed in isotropic XAS recorded at the Fe edge.

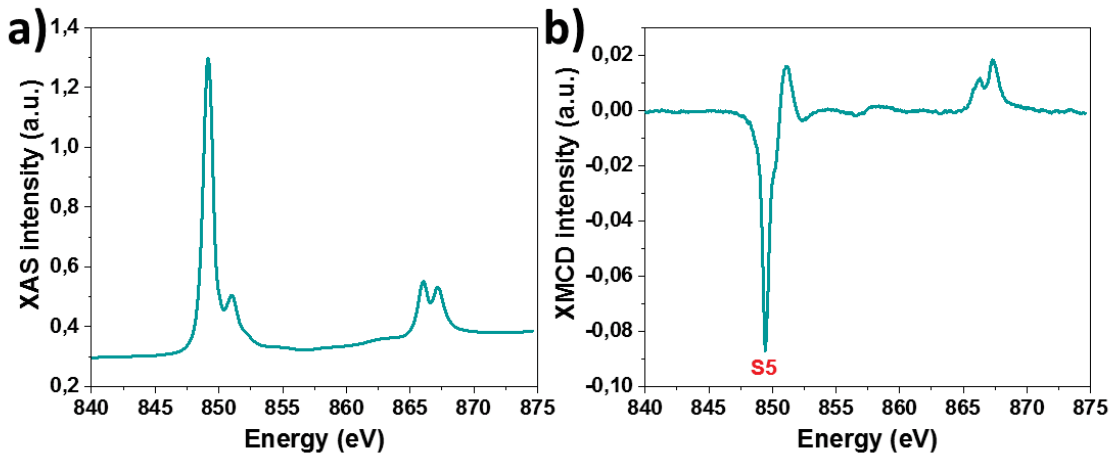

Figure 101. a) XAS and b) XMCD spectra of CSNi2 recorded at the Ni $L_{2,3}$ edges.

The same experiments were performed at the Ni $L_{2,3}$ edges where isotropic XAS and XMCD spectra are typical of Ni^{2+} in Oh sites.[50,51] XAS and XMCD spectra of Ni^{2+} in a nickel ferrite or in a NiO structure are similar. The intensity of the XMCD signal recorded at the Ni edge for CSNi2 is very weak with a maximum of 0.1 % at S5 which indicates that no nickel atoms are included in a nickel ferrite structure. Such a result is surprising as some nickel cations were expected to form an interfacial nickel ferrite by analogy with core@shell nanoparticles composed of iron oxide and CoO.[16,40] According to this, to XRD results and to the high Ni atomic ratio from EDX (35%) measurements, it shows that the nickel-composed shell displays a NiO structure. Thus, in this case, the kinetic formation of the NiO shell was faster than the solubilisation-recrystallisation process of the iron oxide core and the migration process of Ni^{2+} in the iron oxide core is not efficient. Skoropata and al.[51] obtained similar results for γ-Fe_2O_3@NiO nanoparticles of 6.5 nm sized. However they attributed their small XMCD signal at the Ni $L_{2,3}$ edges (<0.1 %) to the surface sensitivity of the TEY mode which according to them does not allow to probe the efficiently the γ-Fe_2O_3/NiO interface. They performed XMCD magnetization temperature dependent measurements in order to evidence that some interfacial nickel is indeed present. However, even if the TEY mode is mostly sensitive to the surface, it probes the 2 to 3 first nm[52,53] and is thus sensitive to the whole NiO shell of CSNi2 and to the eventually formed interfacial nickel ferrite. Hence, the low XMCD signal for CSNi2 disagree with the presence of interfacial nickel ferrite. According to this, the evolution of the XMCD magnetic moment as a function of the temperature probed by Skoropata and al.[51] in their γ-Fe_2O_3@NiO nanoparticles is better due to interfacial Fe-O-Ni interactions. And we can conclude that the low XMCD signal recorded at the Ni $L_{2,3}$ edge for CSNi2 arise from surface spin disorders (i.e. spin canting) or from interfacial Fe-O-Ni interactions.

Element specific hysteresis

Element specific hysteresis recorded at the iron S1 and at the Ni S5 edges for CSNi2 are presented in Figure 102. They both evidence closed hysteresis at 4K while at the Fe edge, the hysteresis cycle was expected to display a small coercive field, as observed for $Fe_{3-d}O_4$@CoO nanoparticles. Consequently, at the Fe S1 and at the Ni S5 edges, the M_R/M_S ratio is null. As the measure was performed on powders we attributed the absence of coercive field and the low reduced magnetization to arise from high dipolar interactions between the nanoparticles even though if the behavior (increase/decrease) of the coercive field and of the reduced magnetization towards the dipolar strength is still under debates.[54–58] Furthermore, according to the very low XMCD signal recorded at the Ni $L_{2,3}$ edges, the hysteresis recorded at the Ni S5 edge at 4K was expected to display an antiferromagnetic behavior. Nevertheless, the presence of a ferrimagnetic behavior is attributed to non-compensated Ni^{2+} cations from the iron oxide/NiO interface (Fe-O-Ni) but also from the spin canted surface.

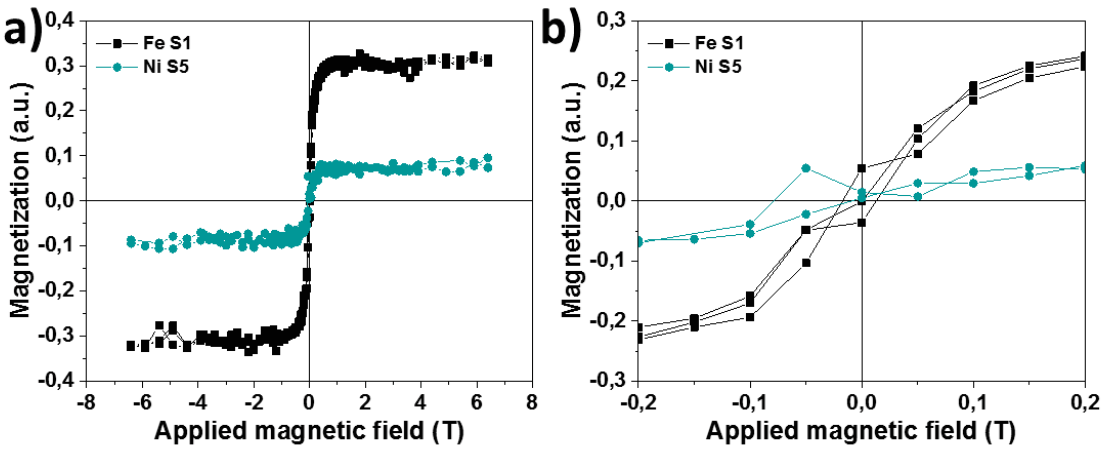

Figure 102. a) Element selective hysteresis of CSNi2 recorded at the Fe S1 and at the Ni S5 edges at 4 K with b) an enlargement.

SQUID magnetometry

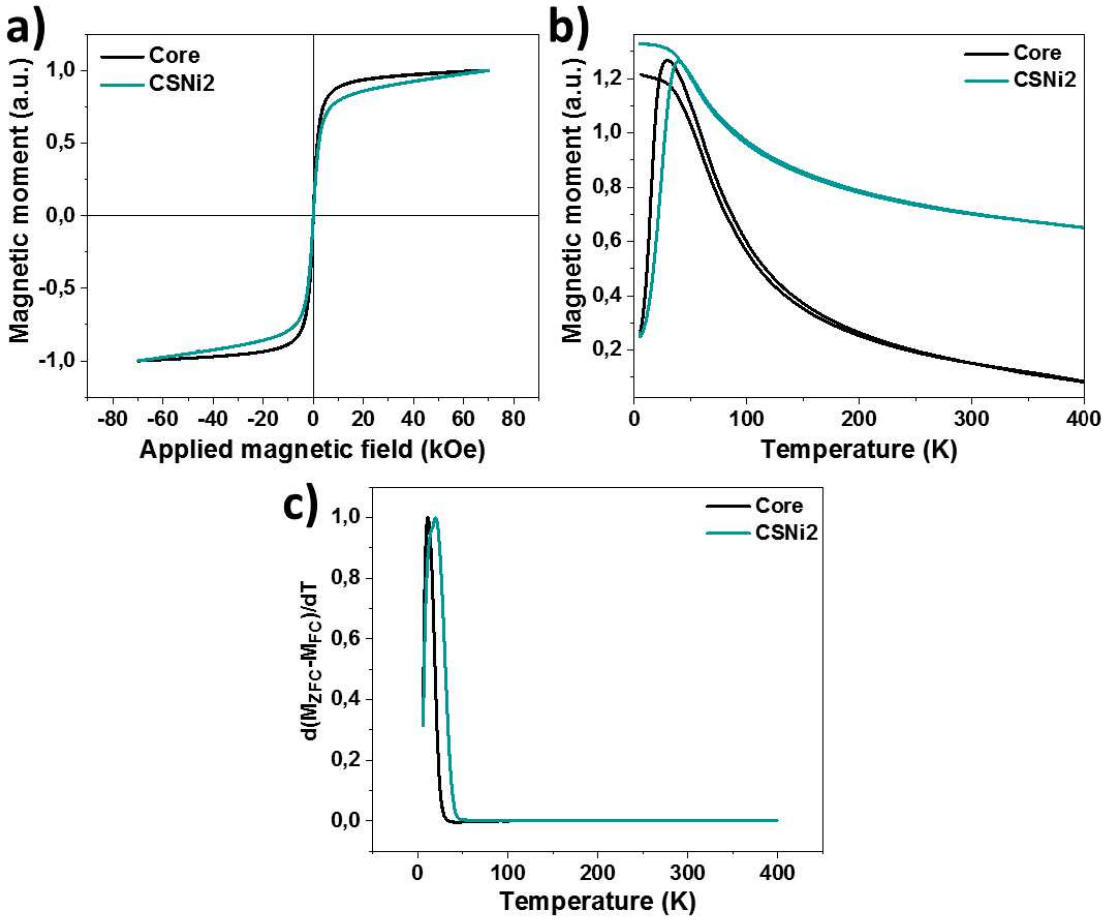

Figure 103. Magnetic properties of CSNi2: a) Magnetic moment versus an applied magnetic field recorded at 300 K, b) Magnetic moment versus an applied magnetic field after FC-ZFC, c) $d(M_{ZFC}-M_{FC})dT$.

Magnetic properties of CSNi2 and its' iron oxide core were investigated by SQUID magnetometry. Magnetization recorded against an applied magnetic field at 300 K evidenced unblocked magnetic moment i.e. superparamagnetic behavior for both samples (Figure 103a). Such an observation agrees with magnetic moment recorded against temperature after field cooling (FC) and zero field cooling (ZFC) (Figure 103b). In such measurements, the FC curve is generally above the ZFC curve. However in some cases as for the ZFC-FC curve of the iron oxide core, the FC curve is below the ZFC one. This arises from ferromagnetic and antiferromagnetic correlations, spin frustrations or irreversibility mechanisms.[59] The maximum of the ZFC curve, called T_{max}, corresponds to the thermodynamic equilibrium where the thermal energy is equivalent to the anisotropic energy ($kT \approx KV$). Hence, the iron oxide core display a T_{max} of 29 K which is in accordance with the literature for similar sizes of 5.3 nm (25 K).[15] This T_{max} increases to 40 K in CSNi2 which is far from the 525 K of the Neel temperature of the NiO phase that we expected to reach thanks to a strong magnetic coupling effects between the core and the NiO shell. Nevertheless, the small increase of T_{max} agrees with the size increase of the nanoparticles.[15]

The true blocking temperature that is a distribution of energetic barrier is more accurately determined from the inflection point of the ZFC curve which can easily be extracted by the maximum of the d(MZFC-MFC)/dT curve.[60] Hence, close T_B of 15 and 18 K were determined for the core and CSNi2. Thus, the growth of a NiO shell on an iron oxide core does not have a real impact on the blocking temperature where the increase is better due to volume effects. Indeed, small NiO nanoparticles display a lower T_{max} than the iron oxide core.[51,61]

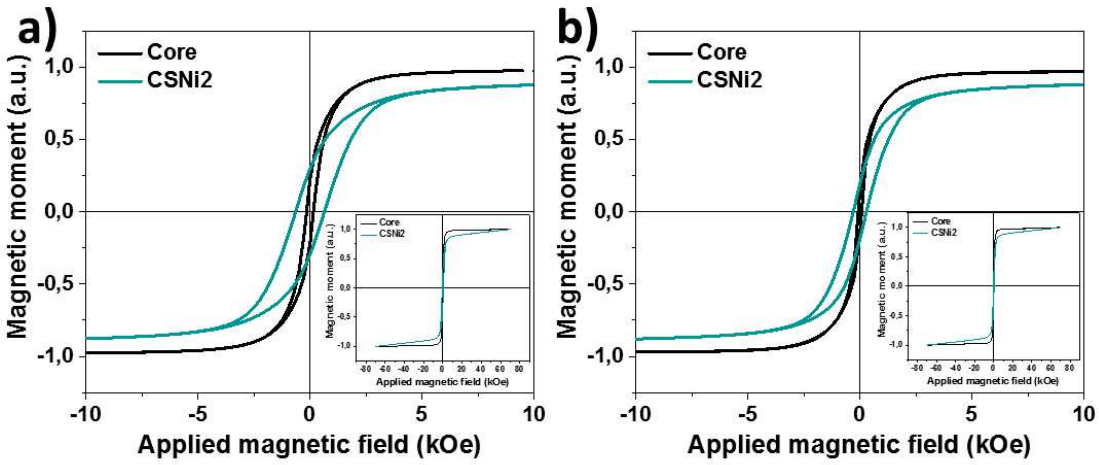

Figure 104. Magnetic properties of CSNi2. Magnetic moment versus an applied magnetic field recorded at a) 5K, b) 10 K after field cooling under a field of 7 T.

Magnetic moment versus an applied magnetic field recorded at 5 K evidence opened hysteresis cycles for both samples where the coercive field (H_C) of the core is equal to 151 Oe which is coherent with the 185 Oe of 5.0 nm sized iron oxide nanoparticles from the literature.[15] H_C increases to 643 Oe in CSNI2 which is higher than the 354 Oe for 8 nm sized iron oxide nanoparticles[15] and can be at first sight attributed to exchange-bias coupling as expected from a FiM-AFM system.

However, magnetization recorded against an applied magnetic field after cooling down to 10 K under a 7T field evidence no exchange field (H_E) in CSNi2 which shows that no exchange-bias coupling occurs in CSNi2. Therefore, the increase of H_C from the core to CSNi2 is not due to exchange-bias coupling. Skoropata and al.[51] have evidenced similar behavior for γ-Fe_2O_3@NiO nanoparticles featured by a γ-Fe_2O_3 core size of 6.6 nm and γ-Fe_2O_3@NiO nanoparticles of 6.5 nm with additional NiO crystallites of 3 nm sized. Indeed, they evidenced no increase of T_{max} with the growth of a NiO shell on the iron oxide seed but a high increase of H_C at 5 K. They attributed this behavior to a strong exchange coupling between the FiM core and the rotable AFM NiO shell. Indeed, in an exchange-biased system, the AFM

phase should pinned the magnetic moment of the FiM phase thanks to $K_{AFM}V_{AFM}>>K_{FiM}V_{FiM}$ where the spins of the AFM part do not rotate with the field, providing unidirectional anisotropy and de facto H_E. However, as $K_{NiO} < K_{magnetite/maghemite}$ and $V_{NiO} < V_{iron\ oxide\ core}$, it results that $K_{AFM}V_{AFM}$ ($2.3\ 10^{-22}$ J)<<$K_{FiM}V_{FiM}$ ($2.04\ 10^{-21}$ J) evidencing why no exchange-bias occurs in CSNi2.

The effective magnetic anisotropy was determined from T_B according to the Stoner-Wohlfarth model[62] $K_{eff} = \frac{25k_BT_B}{V}$. Hence K_{eff} of $5.1\ 10^4$ J/m^3 has been calculated for the iron oxide core which is lower than for bulk magnetite ($2.0\ 10^4$ J/m^3)[63] due to size reduction effect where K_{eff} depends on the volume and of the surface anisotropy constant: $K_{eff} = K_V+(6/d)K_s$. Moreover, K_{eff} of the iron oxide core agree with the K_{eff} of $5.5\ 10^4$ J/m^3 determined for 6 nm sized iron oxide nanoparticles[59] or with the $2.2\ 10^4$ J/m^3 for maghemite nanoparticles of 6.6 nm sized.[18] The growth of a NiO shell on the iron oxide core led to a decrease of K_{eff} to $4.7\ 10^4$ J/m^3 in CSNi2 contrary to Skoropata and al.[51] who evidenced an increase of K_{eff} from 2.5 to $5.3\ 10^4$ J/m^3 for the γ-Fe_2O_3 seeds and the γ-Fe_2O_3@NiO nanoparticles respectively. However, they did not noticed any change of size and their γ-Fe_2O_3@NiO nanoparticles displayed the presence of NiO crystallites of 3 nm on the seeds. Thus, we attributed our decrease of K_{eff} to the concomitant size increase of the nanoparticles and to the presence of the NiO shell that displays a lower anisotropy constant of $8\ 10^3$ J/m^3 [64] in bulk than bulk iron oxide.

Even if $K_{NiO}<K_{Fe3O4}$ and that there is no exchange bias coupling within the $Fe_{3-d}O_4$@NiO nanoparticles. The presence of the AFM NiO shell at the surface of the iron oxide core may decrease the effect of spin canting of the iron oxide core, resulting in a higher H_C. Furthermore, as shown by XRD and XAS, XMCD measurements, the iron oxide core in CSNi2 has more Fe^{2+} than its $Fe_{3-d}O_4$ core which may also participates to the increase of H_C in the core@shell nanoparticles.

Table 39. Magnetic characteristics of C2 and CSNi2.

	C2	**CSNi2**
Size (nm)	5.8 ± 0.7	6.3 ± 0.8
Shell thickness (nm)	-	0.3
Volume (nm^3)	102.2	28.8
H_C 5 K ZFC (Oe)	151	643
H_C 10 K FC (Oe)	76	294
H_E 10 K FC (Oe)	0	0
H_C 300K ZFC (Oe)	0	0
T_B FC-ZFC (K)	29	40
T_B d(MZFC-MFC)/dT (K)	15	18
K_{eff} (10^4 J/m3)	5.1	4.7

Summary

In the literature, the only reference found on NiO nanoparticles, smaller than 20 nm synthesized with controlled size and shape by the thermal decomposition method, evidence an aberration in the experimental protocol. Thus, we have firstly try to determine new synthesis conditions to synthesize the desired NiO nanoparticles. However, the synthesis by the thermal decomposition method is highly influenced by a wide range of parameters such as the nature of the precursor, precursor/capping agent ratio, heating ramp and boiling temperature. Hence a good control over all of them is required.[65]
Thus, the effect of the nature of the precursors and capping agents and of the solvent i.e. different B_P temperatures were studied. The decrease in length of the fatty chain of the nickel precursors evidenced a lowering of its' decomposition temperature that allow to work in more common organic solvent. The increase of the Ni precursor/iron oxide seeds nanoparticles show more cubic nanoparticles due to the increase of the deposition kinetic toward the migration one. The same observation was made with the increase of the solvent boiling point. The final use of a mixture of oleic acid and hexadecylamine allow to play on the stabilization and destabilization effects of the metallic precursors.

Once the synthesis conditions were improved, iron oxide nanoparticles were used as seeds in order to lower the germination steps' energetic barrier and facilitate the decomposition of NiOct. $Fe_{3-d}O_4$@NiO nanoparticles of controlled size and shape were successfully synthesized.
Then, the effect of the solvent, of the precursors and seeds concentration in solution were studied. Cubic, cubic with rounded corners and spherical $Fe_{3-d}O_4$@NiO nanoparticles were obtained depending on the synthesis conditions.

Due to simpler anisotropic shape effect, spherical $Fe_{3-d}O_4$@NiO nanoparticles were better studied than cubic ones. The spherical $Fe_{3-d}O_4$@NiO nanoparticles showed an increase of H_C but no improvement of T_{max} or T_B and exchange-bias properties did not exist. Such behavior was attributed to the smaller anisotropic constant of NiO compared to the iron oxide and to the low volume of NiO that could not afford exchange-bias coupling but allowed nevertheless to evidence a strong exchange coupling as evidenced by XAS and XMCD measurements.

Experimental section

Nickel precursors

Nickel stearate, nickel octanoate and nickel acetate, were synthesized by dissolving 32 mmol of sodium stearate, octanoate or acetate in 320 mL of water. The mixture was heated at reflux and under a magnetic stir until complete dissolution of the powders. Then 16 mmol of nickel (II) chloride hexahydrated dissolved in 160 mL of water were poured in the round-bottom flask. A green precipitate immediately formed. The mixture was further heated and stirred vigorously for another 15 min. At the end, the reactant middle was allowed to cool down to room temperature. The greenish solids were recovered by centrifugation methods (14 000 rpm, 5 min) and washed several times with water by filtration on a Buchner funnel. The product was finally dried in an oven at 65 °C for 15 h.

Iron and cobalt (II) stearate

Iron (II) stearate was synthesized according to an already published protocol[66] which has been adapted to synthesize cobalt (II) stearate.

In a two necked round-bottom flask, 9.8 g of sodium stearate and 320 mL of water were poured. The solution was heated at reflux under a constant magnetic stir until complete dissolution of the powder. Then a solution composed of 3.16 g of metal chloride ($FeCl_2.4H_2O$ or $CoCl_2.6H_2O$) dissolved in 160 mL of water was added to the solution. A precipitate immediately formed (brown with iron and blue with cobalt) and the mixture was kept at reflux under a vigorous stir. After 15 min the mixture was allowed to cool down. The precipitate was recovered by centrifugation (14 000 rpm, 5 min) and washed with water on a Buchner funnel. Finally the solid was placed in an oven at 65 °C for 15 h in order to remove water.

Iron oxide core nanoparticles

Iron oxide core nanoparticles were synthesized thanks to an already published protocol.[15] Briefly, 1.38 g (2.22 mmol) of a homemade iron (II) stearate was poured in a two-necked round-bottom flask. Afterwards, 1.254 g (4.44 mmol) of oleic acid and 20 mL of dioctyl ether (B_P = 290 °C) were added. The mixture was heated at 120 °C for 30 min under a magnetic stir in order to remove residual water and to homogenize the solution. Then the stir was stopped and the flask was connected to a reflux condenser in order to heat the brownish solution at reflux for 2 h with a heating ramp of 5 °C/min. At the end the black dark solution was allowed to cool down to 120 °C and the nanoparticles were precipitated by the addition of acetone and recovered by a centrifugation method (14 000 rpm, 5 min). The nanoparticles were then washed by a mixture of chloroform : acetone 1 : 7 with a centrifugation method (14 000 rpm, 5 min). The final nanoparticles were stored in chloroform.

$Fe_{3-d}O_4$@CoO core@shell nanoparticles

$Fe_{3-d}O_4$@CoO core@shell nanoparticles were synthesized according to an already published protocol.[42] 90 % of the solution of cleaned iron oxide nanoparticles were evaporated under vacuum in a two-necked round-bottom flask. Then 10 mL of ether dioctyl was poured in the flask which was then sonicated in order to redisperse the nanoparticles. Cobalt stearate was then poured in the flask according to a R ratio (R = 1 for CSCo2, R = 0.8 for CSCo4) where R=[n(CoSt)/n(FeSt)]. Then 2n(CoSt) of oleic acid and 20 mL of 1-octadecene was added. The dark mixture was heated at 120 °C under a magnetic stir for 30 min. Afterwards the stir was stopped and the flask was connected to a reflux condenser in order to heat the mixture at reflux for 2 h with a heating ramp of 1 °C/min. Then the black solution was allowed to cool down to 120 °C and the nanoparticles were washed by a mixture of chloroform : acetone 1 : 7 with a centrifugation method (14 000 rpm, 5 min). The final nanoparticles were stored in chloroform.

$Fe_{3-d}O_4$@NiO core@shell nanoparticles

$Fe_{3-d}O_4$@NiO core@shell nanoparticles were synthesized by the adaptation of the synthesis protocol of $Fe_{3-d}O_4$@CoO according to the experimental conditions described in the text.

$Fe_{3-d}O_4$@CoO@NiO spherical core@shell@shell nanoparticles (CSSNi4)

$Fe_{3-d}O_4$@CoO@NiO core@shell@shell nanoparticles were synthesized by an adaptation of the synthesis protocol of $Fe_{3-d}O_4$@CoO nanoparticles.

$Fe_{3-d}O_4$@CoO CSCo4 nanoparticles were used as seeds and 50 % of the solution of CSCo4 was evaporated under vacuum in a two-necked round-bottom flask. The nanoparticles were then redispersed by sonication in 10 mL of dioctyl ether. After that, 0.273 g of a homemade NiOct (0.8 mmol), 0.224 g (0.8 mmol) of oleic acid and 0.191 g (0.8 mmol) of hexadecylamine were poured in the flask before adding another 10 mL of dioctyl ether. The mixture was then heated at 120 °C under a magnetic stir for 30 min. Then the stir was stopped and the flask was connected to a reflux condenser in order to heat the solution at reflux for 2 h with a heating ramp of 5 °C/min. At the end, the black solution was allowed to cool down to 120 °C and the nanoparticles were washed by centrifugation (14 000 rpm, 5 min) with a mixture of chloroform : acetone 1 : 7. The final nanoparticles were stored in chloroform.

$Fe_{3-d}O_4$@CoO@NiO cubic core@shell@shell nanoparticles (CSSNi2A and CSSNi2C)

CSSNi2A and CSSNi2C were synthesized according to a seed-mediated growth method.

One third of $Fe_{3-d}O_4$@CoO CSCo2 nanoparticles were evaporated under vacuum in a two-necked round-bottom flask. Then 5 mL of dioctyl ether were poured and the solution was sonicated to redisperse the nanoparticles. After that, homemade NiOct, hexadecylamine, oleic acid and 8 mL of dioctyl ether were added. The dark solution was then heated at 120 °C under a magnetic stir for 30 min. Afterwards the stir was stopped and the solution was heated at reflux for 2 h with a 5 °C/min heating ramp. At the end the dark solution was cooled down to 120 °C and the nanoparticles wrer washed by a centrifugation method (14 000 rpm, 5 min) with a mixture of chloroform : acetone 1 : 7. The final nanoparticles were stored in chloroform.

The quantity of NiOct poured in the flask was defined according to R=[(nNiOct)/n(FeSt)] with R=0.5 or 1.5 in CSSNi2A or CSSNi2C. Hence 0.44 (CSSNi2A) or 1.32 mmol (CSSNi2C) of NiOct were poured. The poured quantity of hexadecylamine and oleic acid was half of the one of NiOct: 0.22 mmol for CSSNi2A or 0.66 mmol for CSSNi2C.

Transmission electron microscopy

Transmission electron microscopy (TEM) were performed on a JEOL 2100 LaB6 with a 0,2nm point to point resolution. EDX were performed with a JEOL Si(Li) detector. The nanoparticle sizes were calculated by measuring at least 300 nanoparticles from TEM micrographs by using the Image J software. The shell thickness corresponds to half of the difference between nanoparticle sizes which were measured before and after Co decomposition. The size distribution was calculated by fitting with a Gaussian function that fits well with our data.

X-ray diffraction

X-ray diffraction (XRD) using a Bruker D8 Advance equipped with a monochromatic copper radiation (Kα = 0.154056 nm) and a Sol-X detector in the 20− 70° 2θ range with a scan step of 0.02°. High purity silicon powder (a = 0.543082 nm) was systematically used as an internal standard.

Fourier transform infra-red spectroscopy

Fourier transform infrared (FTIR) spectroscopy was performed using a Perkin Elmer Spectrum spectrometer in the energy range 4000−400 cm^{-1} on samples diluted in KBr pellets.

Granulometric measurements

Granulometric measurements were performed using a nano-sizer Malvern (nano ZS) zetasizer at a scattering angle of 173° with 1 measure of 7 runs of 30 seconds.

X-ray magnetic circular dichroism

XAS and XMCD spectra were recorded at the $L_{2,3}$ edges of Fe and Co, on the DEIMOS beamline at SOLEIL synchrotron.[67] All spectra were recorded at 4.2 K under UHV conditions (10^{-10} mbar) and using total electron yield (TEY). The measurement protocol has previously been detailed by Daffé and al.[68] An external parallel magnetic field H^+ (respectively antiparallel H^-) was applied on the sample while a σ_+ polarized (σ_- polarized respectively) perpendicular beam was directed on the sample. Isotropic XAS signals were obtained by taking the mean of the $\sigma_+ + \sigma_-$ sum where $\sigma_+ = [\sigma_L(H^+) + \sigma_R(H^-)]/2$ and $\sigma_- = [\sigma_L(H^-) + \sigma_R(H^+)]/2$ with σ_L and σ_R the absorption cross section measured respectively with left and right circularly polarized X-rays. And XMCD spectra were obtained by taking the $\sigma_+ - \sigma_-$ dichroic signal with a ± 6.5 T applied magnetic field. The circularly polarized X-rays are provided by an Apple-II HU-52 undulator for both XAS and XMCD measurements while EMPHU65 with a polarization switching rate of 10 Hz was used to record hysteresis cycle at fixed energy.[67]

The samples consist of a silicon substrate where the colloidal suspension of the nanoparticles (ferrofluids) were previously drop casted to evaporate the solvent at room temperature. The substrates were then fixed on a cupper sample holder. Measurements were performed between 700 and 740 eV at the iron edge and between 770 and 800 eV at the cobalt edge with a resolution of 100 meV and a beam size of 800*800 µm. Both XMCD and isotropic XAS signals presented here are normalized by dividing the raw signal by the edge jump of the isotropic XAS.

Magnetometry

Magnetic measurements were performed on samples by using a Superconducting Quantum Interference Device (SQUID) magnetometer (Quantum Design MPMS-XL 5). Temperature dependent zero-field cooled (ZFC) and field cooled (FC) magnetization curves were recorded as follows: the sample was introduced in the SQUID at room temperature and cooled down to 5 K with no applied field after applying a careful degaussing procedure. A magnetic field of 7.5 mT was applied, and the ZFC magnetization curve was recorded upon heating from 5 to 400 K. The sample was then cooled down to 5 K under the same applied field, and the FC magnetization curve was recorded upon heating from 5 to 400 K. Magnetization curves as a function of a magnetic field (M(H) curves) applied in the plane of the substrate were measured at 5 and 400 K. The sample was also introduced in the SQUID at high temperature and cooled down to 5 K with no applied field (ZFC curve) after applying a subsequent degaussing procedure. The magnetization was then measured at constant temperature by sweeping the magnetic field from +7 T to −7 T, and then from −7 T to +7 T. To evidence exchange bias effect, FC M(H) curves have been further recorded after heating up at 400 K and cooling down to 5 K under a magnetic field of 7 T. The FC hysteresis loop was then measured by applying the same field sweep as for the ZFC curve. The coercive field (H_C) and the M_R/M_S ratio were measured from ZFC M(H) curves. The exchange bias field (H_E) was measured from FC M(H) curves. Magnetization saturation (M_S) was measured from hysteresis recorded at 5 K.

Themogravimetry

Thermogravimetry (TG) analysis was performed using a SDTQ600 from TA instrument. Measurements were performed on dried powders under air in the temperature range of 20 to 600 °C at a heating rate of 5 ° C/min.

References of annexes

(1) Synchrotron SOLEIL. Malette Pédagogique, Thème Lumière Synchrotron.

(2) Daffé, N. Anisotropies and magnetic couplings of texturable ferrofluids, Université Pierrre et Marie Curie.

(3) C. Noguera; J. Petiau; G. Krill; F. Gautier; J. P. Renard; J. Goulon; C. Vettier; P. Thiry; M. Taborelli; C. S. Fadley; et al. *Rayonnement Synchrotron Polarisé Électrons Polarisés et Magnétisme, Applications à l'étude Des Surfaces, Interfaces et Molécules.*; E. Beaurepaire, B. Carrière, J.P. Kappler: Mittelwihr (Haut-Rhin), 1989.

(4) M. Belakhovsky; M. Bessiere; D. Chandesris; P. Chevallier; R. Coisson; P. Dhez; B. Dorner; P. Elleaume; A. Fontaine; A. Freund; et al. *Rayonnement Synchrotron Dans Le Domaine Des Rayons X, Recueil Des Cours Dispensés à l'école d'été Rayonnement Synchrotron, Aussois Septembre 1986*; CNRS.

(5) Carlile, C. J. La production des neutrons. *J. Phys. IV Proc.* **2003**, *103*, 51–66. https://doi.org/10.1051/jp4:20030002.

(6) La source et les faisceaux sortis http://www-llb.cea.fr/presllb/Part_2.pdf.

(7) Schéma représentatif de la ligne PA-20 G5-1 http://www-llb.cea.fr/en/fr-en/pdf/PA20-description.pdf.

(8) Li, T.; Senesi, A. J.; Lee, B. Small Angle X-Ray Scattering for Nanoparticle Research. *Chem. Rev.* **2016**, *116* (18), 11128–11180. https://doi.org/10.1021/acs.chemrev.5b00690.

(9) Cousin, F. Small Angle Neutron Scattering. *EPJ Web Conf.* **2015**, *104*, 01004. https://doi.org/10.1051/epjconf/201510401004.

(10) Krycka, K. L.; Booth, R.; Borchers, J. A.; Chen, W. C.; Conlon, C.; Gentile, T. R.; Hogg, C.; Ijiri, Y.; Laver, M.; Maranville, B. B.; et al. Resolving 3D Magnetism in Nanoparticles Using Polarization Analyzed SANS. *Phys. B Condens. Matter* **2009**, *404* (17), 2561–2564. https://doi.org/10.1016/j.physb.2009.06.024.

(11) Chaboussant, G.; Désert, S.; Lavie, P.; Brûlet, A. PA20 : A New SANS and GISANS Project for Soft Matter, Materials and Magnetism. *J. Phys. Conf. Ser.* **2012**, *340*, 012002. https://doi.org/10.1088/1742-6596/340/1/012002.

(12) Sasview software http://www.sasview.org/.

(13) Gavrilov-Isaac, V. Synthèse de Nanoparticules Magnétiques à Énergie d'anisotropie Modulable, Pierre et Marie-Curie, 2015.

(14) Lentijo-Mozo, S.; Deiana, D.; Sogne, E.; Casu, A.; Falqui, A. Unexpected Insights about Cation-Exchange on Metal Oxide Nanoparticles and Its Effect on Their Magnetic Behavior. *Chem. Mater.* **2018**, *30* (21), 8099–8112. https://doi.org/10.1021/acs.chemmater.8b04331.

(15) Baaziz, W.; Pichon, B. P.; Fleutot, S.; Liu, Y.; Lefevre, C.; Greneche, J.-M.; Toumi, M.; Mhiri, T.; Begin-Colin, S. Magnetic Iron Oxide Nanoparticles: Reproducible Tuning of the Size and Nanosized-Dependent Composition, Defects, and Spin Canting. *J. Phys. Chem. C* **2014**, *118* (7), 3795–3810. https://doi.org/10.1021/jp411481p.

(16) Sartori, K.; Cotin, G.; Bouillet, C.; Halté, V.; Bégin-Colin, S.; Choueikani, F.; Pichon, B. P. Strong Interfacial Coupling through Exchange Interactions in Soft/Hard Core–Shell Nanoparticles as a Function of Cationic Distribution. *Nanoscale* **2019**, *11* (27), 12946–12958. https://doi.org/10.1039/C9NR02323B.

(17) Liu, X.; Pichon, B. P.; Ulhaq, C.; Lefèvre, C.; Grenèche, J.-M.; Bégin, D.; Bégin-Colin, S. Systematic Study of Exchange Coupling in Core–Shell $Fe_{3-\delta}O_4$@CoO Nanoparticles. *Chem. Mater.* **2015**, *27* (11), 4073–4081. https://doi.org/10.1021/acs.chemmater.5b01103.

(18) Skoropata, E.; Desautels, R. D.; Chi, C.-C.; Ouyang, H.; Freeland, J. W.; van Lierop, J. Magnetism of Iron Oxide Based Core-Shell Nanoparticles from Interface Mixing with Enhanced Spin-Orbit Coupling. *Phys. Rev. B* **2014**, *89* (2). https://doi.org/10.1103/PhysRevB.89.024410.
(19) Gilmore, K.; Idzerda, Y. U.; Klem, M. T.; Allen, M.; Douglas, T.; Young, M. Surface Contribution to the Anisotropy Energy of Spherical Magnetite Particles. *J. Appl. Phys.* **2005**, *97* (10), 10B301. https://doi.org/10.1063/1.1845973.
(20) Cao, C.; Tian, L.; Liu, Q.; Liu, W.; Chen, G.; Pan, Y. Magnetic Characterization of Noninteracting, Randomly Oriented, Nanometer-Scale Ferrimagnetic Particles. *J. Geophys. Res.* **2010**, *115* (B7), B07103. https://doi.org/10.1029/2009JB006855.
(21) Meiklejohn, W. H.; Bean, C. P. New Magnetic Anisotropy. *Phys. Rev.* **1956**, *102* (5), 1413–1414. https://doi.org/10.1103/PhysRev.102.1413.
(22) E. Stavitski, F.M.F. de Groot, Micron 41, 687 (2010).
(23) Chen, Z.; Xu, A.; Zhang, Y.; Gu, N. Preparation of NiO and CoO Nanoparticles Using M2+-Oleate (M=Ni, Co) as Precursor. *Curr. Appl. Phys.* **2010**, *10* (3), 967–970. https://doi.org/10.1016/j.cap.2009.11.083.
(24) Dharmaraj, N.; Prabu, P.; Nagarajan, S.; Kim, C. H.; Park, J. H.; Kim, H. Y. Synthesis of Nickel Oxide Nanoparticles Using Nickel Acetate and Poly(Vinyl Acetate) Precursor. *Mater. Sci. Eng. B* **2006**, *128* (1–3), 111–114. https://doi.org/10.1016/j.mseb.2005.11.021.
(25) Davar, F.; Fereshteh, Z.; Salavati-Niasari, M. Nanoparticles Ni and NiO: Synthesis, Characterization and Magnetic Properties. *J. Alloys Compd.* **2009**, *476* (1–2), 797–801. https://doi.org/10.1016/j.jallcom.2008.09.121.
(26) Park, J.; Kang, E.; Son, S. U.; Park, H. M.; Lee, M. K.; Kim, J.; Kim, K. W.; Noh, H.-J.; Park, J.-H.; Bae, C. J.; et al. Monodisperse Nanoparticles of Ni and NiO: Synthesis, Characterization, Self-Assembled Superlattices, and Catalytic Applications in the Suzuki Coupling Reaction. *Adv. Mater.* **2005**, *17* (4), 429–434. https://doi.org/10.1002/adma.200400611.
(27) Li, Y.; Afzaal, M.; O'Brien, P. The Synthesis of Amine-Capped Magnetic (Fe, Mn, Co, Ni) Oxide Nanocrystals and Their Surface Modification for Aqueous Dispersibility. *J. Mater. Chem.* **2006**, *16* (22), 2175. https://doi.org/10.1039/b517351e.
(28) Jana, N. R.; Chen, Y.; Peng, X. Size- and Shape-Controlled Magnetic (Cr, Mn, Fe, Co, Ni) Oxide Nanocrystals via a Simple and General Approach. *Chem. Mater.* **2004**, *16* (20), 3931–3935. https://doi.org/10.1021/cm049221k.
(29) Hosny, N. M. Synthesis, Characterization and Optical Band Gap of NiO Nanoparticles Derived from Anthranilic Acid Precursors via a Thermal Decomposition Route. *Polyhedron* **2011**, *30* (3), 470–476. https://doi.org/10.1016/j.poly.2010.11.020.
(30) Farhadi, S.; Roostaei-Zaniyani, Z. Simple and Low-Temperature Synthesis of NiO Nanoparticles through Solid-State Thermal Decomposition of the Hexa(Ammine)Ni(II) Nitrate, [Ni(NH3)6](NO3)2, Complex. *Polyhedron* **2011**, *30* (7), 1244–1249. https://doi.org/10.1016/j.poly.2011.01.028.
(31) Wang, Y.; Zhu, J.; Yang, X.; Lu, L.; Wang, X. Preparation of NiO Nanoparticles and Their Catalytic Activity in the Thermal Decomposition of Ammonium Perchlorate. *Thermochim. Acta* **2005**, *437* (1–2), 106–109. https://doi.org/10.1016/j.tca.2005.06.027.
(32) Nemati, Z.; Alonso, J.; Rodrigo, I.; Das, R.; Garaio, E.; García, J. Á.; Orue, I.; Phan, M.-H.; Srikanth, H. Improving the Heating Efficiency of Iron Oxide Nanoparticles by Tuning Their Shape and Size. *J. Phys. Chem. C* **2018**, *122* (4), 2367–2381. https://doi.org/10.1021/acs.jpcc.7b10528.

(33) Abrahamson, H. B.; Lukaski, H. C. Synthesis and Characterization of Iron Stearate Compounds. *J. Inorg. Biochem.* **1994**, *54* (2), 115–130. https://doi.org/10.1016/0162-0134(94)80025-1.
(34) Xu, N.; Sarkar, D. K.; Chen, X.-G.; Tong, W. P. Corrosion Performance of Superhydrophobic Nickel Stearate/Nickel Hydroxide Thin Films on Aluminum Alloy by a Simple One-Step Electrodeposition Process. *Surf. Coat. Technol.* **2016**, *302*, 173–184. https://doi.org/10.1016/j.surfcoat.2016.05.050.
(35) Nakamoto, K. *Infrared and Raman Spectra of Inorganic and Coordination Compounds*, 6th ed.; Wiley: Hoboken, N.J, 2009.
(36) Ren, Y.; Iimura, K.; Kato, T. Structure of Barium Stearate Films at the Air/Water Interface Investigated by Polarization Modulation Infrared Spectroscopy and Π− *A* Isotherms. *Langmuir* **2001**, *17* (9), 2688–2693. https://doi.org/10.1021/la000872e.
(37) Ding, X.; Bao, L.; Jiang, J.; Gu, H. Colloidal Synthesis of Ultrathin γ-Fe2O3 Nanoplates. *RSC Adv.* **2014**, *4* (18), 9314. https://doi.org/10.1039/c3ra46728g.
(38) Hyeon, T.; Lee, S. S.; Park, J.; Chung, Y.; Na, H. B. Synthesis of Highly Crystalline and Monodisperse Maghemite Nanocrystallites without a Size-Selection Process. *J. Am. Chem. Soc.* **2001**, *123* (51), 12798–12801. https://doi.org/10.1021/ja016812s.
(39) Kwon, S. G.; Piao, Y.; Park, J.; Angappane, S.; Jo, Y.; Hwang, N.-M.; Park, J.-G.; Hyeon, T. Kinetics of Monodisperse Iron Oxide Nanocrystal Formation by "Heating-Up" Process. *J. Am. Chem. Soc.* **2007**, *129* (41), 12571–12584. https://doi.org/10.1021/ja074633q.
(40) Baaziz, W.; Pichon, B. P.; Liu, Y.; Grenèche, J.-M.; Ulhaq-Bouillet, C.; Terrier, E.; Bergeard, N.; Halté, V.; Boeglin, C.; Choueikani, F.; et al. Tuning of Synthesis Conditions by Thermal Decomposition toward Core–Shell $Co_x Fe_{1-x} O$@$Co_y Fe_{3-y} O_4$ and $CoFe_2O_4$ Nanoparticles with Spherical and Cubic Shapes. *Chem. Mater.* **2014**, *26* (17), 5063–5073. https://doi.org/10.1021/cm502269s.
(41) Huang, J.-H.; Parab, H. J.; Liu, R.-S.; Lai, T.-C.; Hsiao, M.; Chen, C.-H.; Sheu, H.-S.; Chen, J.-M.; Tsai, D.-P.; Hwu, Y.-K. Investigation of the Growth Mechanism of Iron Oxide Nanoparticles via a Seed-Mediated Method and Its Cytotoxicity Studies. *J. Phys. Chem. C* **2008**, *112* (40), 15684–15690. https://doi.org/10.1021/jp803452j.
(42) Sartori, K.; Choueikani, F.; Gloter, A.; Begin-Colin, S.; Taverna, D.; Pichon, B. P. Room Temperature Blocked Magnetic Nanoparticles Based on Ferrite Promoted by a Three-Step Thermal Decomposition Process. *J. Am. Chem. Soc.* **2019**, *141* (25), 9783–9787. https://doi.org/10.1021/jacs.9b03965.
(43) Xia, Y.; Xia, X.; Peng, H.-C. Shape-Controlled Synthesis of Colloidal Metal Nanocrystals: Thermodynamic versus Kinetic Products. *J. Am. Chem. Soc.* **2015**, *137* (25), 7947–7966. https://doi.org/10.1021/jacs.5b04641.
(44) Feld, A.; Weimer, A.; Kornowski, A.; Winckelmans, N.; Merkl, J.-P.; Kloust, H.; Zierold, R.; Schmidtke, C.; Schotten, T.; Riedner, M.; et al. Chemistry of Shape-Controlled Iron Oxide Nanocrystal Formation. *ACS Nano* **2019**, *13* (1), 152–162. https://doi.org/10.1021/acsnano.8b05032.
(45) Nakamoto, K. Infrared Spectra of Metal Chelate Compounds III. *Infrared Spectra* **1961**, *83*, 1272.
(46) Lawson. The Infrared Absorption Spectra. *Spectrochim. Acta* **1961**, *17*, 248.
(47) Farzaneh et al. Green Synthesis and Characterization of Nickel. *J. Ceram. Process. Res.* **2013**, *14* (6), 673.
(48) Edwards et al. Transition Metal Acetates. *Can. J. Chem.* **1968**, No. 46.
(49) E. Pellegrin et al. Characterization of Nanocrystalline Y-Fe2O3 with Synchrotron Radiation Techniques. *Phys Stat Sol* **1999**, *215*, 797.

(50) Ikeno, H. First-Principles Analysis of X-Ray Magnetic Circular Dichroism for Transition Metal Complex Oxides. *J. Appl. Phys.* **2016**, *120* (14), 142104. https://doi.org/10.1063/1.4961713.
(51) Skoropata, E.; Su, T. T.; Ouyang, H.; Freeland, J. W.; van Lierop, J. Intermixing Enables Strong Exchange Coupling in Nanocomposites: Magnetism through the Interfacial Ferrite in γ − Fe 2 O 3 / NiO. *Phys. Rev. B* **2017**, *96* (2). https://doi.org/10.1103/PhysRevB.96.024447.
(52) Li, J.; Menguy, N.; Arrio, M.-A.; Sainctavit, P.; Juhin, A.; Wang, Y.; Chen, H.; Bunau, O.; Otero, E.; Ohresser, P.; et al. Controlled Cobalt Doping in the Spinel Structure of Magnetosome Magnetite: New Evidences from Element- and Site-Specific X-Ray Magnetic Circular Dichroism Analyses. *J. R. Soc. Interface* **2016**, *13* (121), 20160355. https://doi.org/10.1098/rsif.2016.0355.
(53) Manna, P. K.; Skoropata, E.; Ting, Y.-W.; Lin, K.-W.; Freeland, J. W.; van Lierop, J. Interface Mixing and Its Impact on Exchange Coupling in Exchange Biased Systems. *J. Phys. Condens. Matter* **2016**, *28* (48), 486004. https://doi.org/10.1088/0953-8984/28/48/486004.
(54) Tan, R. P.; Lee, J. S.; Cho, J. U.; Noh, S. J.; Kim, D. K.; Kim, Y. K. Numerical Simulations of Collective Magnetic Properties and Magnetoresistance in 2D Ferromagnetic Nanoparticle Arrays. *J. Phys. Appl. Phys.* **2010**, *43* (16), 165002. https://doi.org/10.1088/0022-3727/43/16/165002.
(55) Kechrakos, D.; Trohidou, K. N. Effects of Dipolar Interactions on the Magnetic Properties of Granular Solids. *J. Magn. Magn. Mater.* **1998**, *177–181*, 943–944. https://doi.org/10.1016/S0304-8853(97)00762-2.
(56) Kechrakos, D.; Trohidou, K. N. Dipolar Interaction Effects in the Magnetic and Magnetotransport Properties of Ordered Nanoparticle Arrays. *J. Nanosci. Nanotechnol.* **2008**, *8* (6), 2929–2943. https://www.ingentaconnect.com/content/asp/jnn/2008/00000008/00000006/art00019.
(57) Aslibeiki, B.; Kameli, P.; Salamati, H. The Effect of Dipole-Dipole Interactions on Coercivity, Anisotropy Constant, and Blocking Temperature of $MnFe_2O_4$ Nanoparticles. *J. Appl. Phys.* **2016**, *119* (6), 063901. https://doi.org/10.1063/1.4941388.
(58) Matthias, P. Structuration de nanoparticules magnétiques d'oxyde de fer en films et étude de leurs propriétés magnétiques et de magnétotransport, 2010.
(59) Espinosa, A.; Muñoz-Noval, A.; García-Hernández, M.; Serrano, A.; Jiménez de la Morena, J.; Figuerola, A.; Quarta, A.; Pellegrino, T.; Wilhelm, C.; García, M. A. Magnetic Properties of Iron Oxide Nanoparticles Prepared by Seeded-Growth Route. *J. Nanoparticle Res.* **2013**, *15* (4), 1514. https://doi.org/10.1007/s11051-013-1514-8.
(60) Bruvera, I. J.; Mendoza Zélis, P.; Pilar Calatayud, M.; Goya, G. F.; Sánchez, F. H. Determination of the Blocking Temperature of Magnetic Nanoparticles: The Good, the Bad, and the Ugly. *J. Appl. Phys.* **2015**, *118* (18), 184304. https://doi.org/10.1063/1.4935484.
(61) Winkler, E.; Zysler, R. D.; Vasquez Mansilla, M.; Fiorani, D.; Rinaldi, D.; Vasilakaki, M.; Trohidou, K. N. Surface Spin-Glass Freezing in Interacting Core–Shell NiO Nanoparticles. *Nanotechnology* **2008**, *19* (18), 185702. https://doi.org/10.1088/0957-4484/19/18/185702.
(62) Cullity, B. D.; Graham, C. D. *Introduction to Magnetic Materials*, 2nd ed.; IEEE/Wiley: Hoboken, N.J, 2009.
(63) O'Handley, R. C. *Modern Magnetic Materials: Principles and Applications*; Wiley: New York, 2000.

(64) Tadic, M.; Nikolic, D.; Panjan, M.; Blake, G. R. Magnetic Properties of NiO (Nickel Oxide) Nanoparticles: Blocking Temperature and Neel Temperature. *J. Alloys Compd.* **2015**, *647*, 1061–1068. https://doi.org/10.1016/j.jallcom.2015.06.027.

(65) van Embden, J.; Chesman, A. S. R.; Jasieniak, J. J. The Heat-Up Synthesis of Colloidal Nanocrystals. *Chem. Mater.* **2015**, *27* (7), 2246–2285. https://doi.org/10.1021/cm5028964.

(66) Cotin, G.; Kiefer, C.; Perton, F.; Boero, M.; Özdamar, B.; Bouzid, A.; Ori, G.; Massobrio, C.; Begin, D.; Pichon, B.; et al. Evaluating the Critical Roles of Precursor Nature and Water Content When Tailoring Magnetic Nanoparticles for Specific Applications. *ACS Appl. Nano Mater.* **2018**, *1* (8), 4306–4316. https://doi.org/10.1021/acsanm.8b01123.

(67) Ohresser, P.; Otero, E.; Choueikani, F.; Chen, K.; Stanescu, S.; Deschamps, F.; Moreno, T.; Polack, F.; Lagarde, B.; Daguerre, J.-P.; et al. DEIMOS: A Beamline Dedicated to Dichroism Measurements in the 350–2500 EV Energy Range. *Rev. Sci. Instrum.* **2014**, *85* (1), 013106.

(68) Daffé, N.; Choueikani, F.; Neveu, S.; Arrio, M.-A.; Juhin, A.; Ohresser, P.; Dupuis, V.; Sainctavit, P. Magnetic Anisotropies and Cationic Distribution in CoFe 2 O 4 Nanoparticles Prepared by Co-Precipitation Route: Influence of Particle Size and Stoichiometry. *J. Magn. Magn. Mater.* **2018**, *460*, 243–252. https://doi.org/10.1016/j.jmmm.2018.03.041.

Aknowledgements

Ces trois années de thèse ont été pour moi une expérience incroyable où j'ai pu être au cœur d'un projet interdisciplinaire multi-collaboratif. Ainsi, je tiens à remercier ici toutes les personnes qui ont pu contribuer de près ou de loin à l'aboutissement de cette thèse.

En tout premier lieu je tiens à remercier les personnes qui ont rendu cette thèse possible, mes deux directeurs de thèse, Benoît Pichon et Fadi Choueikani. Leur forte implication tout au long de ces trois années a permis de fournir un travail précis et détaillé. Il ne m'était pas forcément facile au début de réussir à bien comprendre tous les mécanismes de synthèses de nanoparticules, leurs propriétés magnétiques et leurs propriétés physique. Mais grâce à eux, tout est devenu plus clair.

Merci Benoît de m'avoir accordé de ton temps lors de ces longues réunions et corrections que nous avons eues et surtout merci de m'avoir poussé au bout des choses pour mieux les comprendre. En effet, au cours de cette thèse nous nous sommes arraché des cheveux plus d'une fois pour comprendre les mécanismes et les structures présente. Ce fut un plaisir de pouvoir travailler avec toi et d'apprendre de toi. Merci également de m'avoir fait découvrir le monde de la recherche scientifique ainsi que ses revers.

Fadi, j'ai particulièrement apprécié travailler avec toi du fait de ta bonne humeur et de ton sens du détail. Merci de m'avoir formé à la technique XAS, XMCD et de m'avoir donné l'opportunité de piloter la ligne DEIMOS lors de ton temps inhouse. Les expériences synchrotron sont particulièrement intéressantes du fait des analyses que l'on y réalise mais aussi de pouvoir observer que durant celles-ci, on perd toute notion du temps qui semble alors parfois suspendu. Merci à toi également pour nos discussions de physiques et pour celles qui l'étaient moins. Je te souhaite bonne chance pour la suite et surtout bon courage pour la rédaction de ton HDR ! Je tiens aussi à remercier Darine pour ses excellents petits plats lors de notre dernier run.

Au cours de cette thèse, j'ai aussi eu la chance de pouvoir réaliser des expériences sur la ligne PA 20 du laboratoire Léon Brillouin. Du fait de l'arrêt du réacteur Orphée le 29 octobre 2019 entre 14h30 et 15h, cette ligne sera transférée au PSI prochainement. Grâce aux expériences de diffusion des neutrons polarisés aux petits angles menées là-bas et aussi de diffusion des rayons X, j'ai eu la chance de travailler avec Grégory Chaboussant et Frédéric Ott. Merci à vous pour m'avoir formé sur ces techniques et sur l'exploitation de leurs données. N'étant pas physicien et les expériences de diffusion nécessitant la compréhension d'équations mathématiques à rallonge, je vous remercie aussi pour votre patience durant ma formation. Merci aussi à Nicolas Martin et Fabrice Cousin avec qui j'ai pu interagir durant mes séjours au LLB. Je remercie également Jean-Baptiste Moussy du SPEC d'avoir été disponible pour m'aider à faire quelques expériences SQUID au début de ma thèse.

Un des derniers « grands » instruments auquel j'ai été formé est le TEM. Ainsi je remercie ma mentor de microscopie, Corinne Bouillet de m'y avoir formé et d'avoir réparé certaines de mes bêtises. Merci aussi à Dris, Waalid, Mounir et Kassiogé de leurs disponibilités lorsque j'avais besoin d'aide pour calibrer le microscope.
Le TEM n'étant pas ma spécialité, les analyses de microscopies plus poussées ont été faites par des microscopistes de carrière. Merci donc à Corinne Bouillet pour les analyses apportées dans le second chapitre de cette thèse. Merci à Dario Taverna et Alexandre Gloter d'avoir réalisé les analyses du troisième chapitre. Et enfin merci à Raul Arenal et Simon Hettler d'avoir étudié en détails les nanoparticules du quatrième chapitre. Les images que vous avez réussi à produire sont absolument extraordinaire. Travailler avec vous fut très enrichissant pour moi et je reste impressionné par la puissance de ces techniques. Merci à vous, gracias a ustedes !

Durant ces trois ans, j'ai commencé à assembler des nanoparticules sur des substrats. Dans le but d'observer leur agencement, il a été nécessaire d'obtenir des images de microscopie MEB. Merci à toi Cédric Leuvrey d'avoir réalisé ces images. Aussi, des analyses AFM ont également été réalisées, merci à Mircea Rastei de m'avoir formé à l'AFM.

Des analyses des diffractions des rayons X ont été réalisées afin de déterminer la composition chimique des nanoparticules. Merci à toi, Marc Lenertz, de m'y avoir formé ainsi que pour nos discussions sur ce sujet. Merci également à Paula Dueñas Ramirez d'avoir réalisé les affinements de Rietveld des diffractogrammes des nanoparticules du premier chapitre. Merci à Christophe Lefèvre pour l'exploitation des analyses de diffractions résonantes réalisées sur la ligne Diffabs à SOLEIL. J'en profite aussi pour remercier Solenn Reguer qui était notre local contact sur Diffabs. Merci à toi pour ta bonne humeur et disponibilité au cours des manips et aussi et surtout d'avoir été aussi arrangeante.

Les analyses XMCD ont été essentiellement faites sur la ligne DEIMOS à SOLEIL, néanmoins, nous avons aussi pu bénéficier d'un run sur la ligne blade du synchrotron DIAMOND. Merci à Peter Bencok et Paul Steadman de nous y avoir accueilli aussi chaleureusement ! Merci également à Valérie Halté de l'IPCMS de nous avoir soutenus durant quelques runs XMCD et de m'avoir aidé à traiter les données de Diamond. Merci encore à toi et à Mario de votre accueil !

Afin de mieux comprendre la structure de mes nanoparticules, des expériences de spectroscopie Mössbauer ont été réalisée au Mans. Merci à toi Jean-Marc Greneche d'avoir fait ces analyses et de m'avoir formé à l'exploitation et à la compréhension de ces données.

Ce travail n'aurait pas été le même sans toutes les petites mains qui s'affairent en coulisse.
C'est pourquoi je suis reconnaissant envers les stagiaires que j'ai pu encadrer : Yuting, Diane et Alexandra. Merci du travail que vous avez fourni et qui a participé à la production de ce manuscrit. Je vous souhaite à toutes les trois un très bel avenir !

Toute ma gratitude va à l'ensemble des membres du jury qui m'a fait l'honneur de juger ces trois années de travail en ces quelques pages.

Je remercie également mes collègues du DCMI et plus particulièrement Sylvie Bégin-Colin pour nos discussions sur la synthèse des nanoparticules. Un grand merci aussi à Guillaume Rogez pour m'avoir formé au SQUID et qui a toujours pris le temps de discuter de sujet scientifiques et plus personnels.

Grâce au projet Hi-graphen, j'ai pu passer un mois à Brasilia au Brésil pour faire des mesures de magnétométrie SQUID. Je suis reconnaissant envers toute l'équipe du laboratoire de instituto de Fisica de l'université de Brasilia pour leur accueil et surtout envers Maria Soler, Coaquira, Camilia, Hermano, Antonia et Isis.

Toujours au DCMI, je remercie les anciens thésards pour leur accueil : Mathilde, Mathias, Quentin, Elodie et Ziyad. Je souhaite un bon courage à mes camarades thésards qui soutiennent juste après moi : Kübra, Florian et Francis (chez qui il n'y a pas de cédille). Bonne chance à vous pour la soutenance et pour la suite. C'était un plaisir d'avoir partagé trois années avec vous où nous avons passé de bons moments. Je souhaite également un bon courage aux thésards plus jeunes pour concrétiser leur travail : Paula, Nesrine, Suvi, Pier, Frédéric, Paschi, Wissal, Lisa, Guillaume, Laurianne et Barbara. Pensez à faire de la bibliographie dès le début et commencez à rédiger le plus tôt possible.

Je remercie plus particulièrement les services d'appuis à la recherche qui sont essentiels dans le but de pouvoir travailler dans les meilleures conditions possibles.
Je remercie ainsi l'ensemble des services administratifs de l'IPCMS, de SOLEIL et du LLB. Avec un merci tout particulier à Anne Touze (LLB), qui a géré mes arrivées au LLB et la communication avec le CEA, et

au bureau des missions de SOLEIL qui s'est occupé de toutes mes missions. Je remercie vivement Catherine Bonnin et Sylvie Maingé de l'IPCMS. Sans vous nous serions certainement bien perdus ici. Merci de m'avoir aidé dans les démarches administratives et merci à vous pour votre gentillesse. Sylvie, je te souhaite de passer une bonne retraite prochaine, tu l'auras vraiment bien méritée !

Didier Burger, merci pour tous les ATG que tu m'as fait. Et surtout, merci pour nos discussions, ton franc parlé et ton humour décalé qui ont rendu cette thèse un peu plus cocasse. A toi aussi je te souhaite une bonne retraite dans un futur plus ou moins proche, puisses tu attraper les plus gros poissons !
Merci également à Céline Kiefer de faire régner l'ordre au laboratoire. Merci à Gilles Versini pour nos bavardages et ton sourire qui égaye les couloirs de l'IPCMS. Je te souhaite encore un prompt rétablissement. Merci à Béatrice Masson de s'occuper de la bibliothèque et des imprimantes. Merci à José Radmacher pour la réception et l'envoi des colis et la réservation des salles. Merci aussi au service informatique : Xavier Ledoux, Christine Tugène et Fabien Muller.

Toujours à l'IPCMS mais extérieur au DCMI, je tiens à remercier Nathaly, Matias et Wenjia pour nos discussions, soirées, jeux de rôles et tests culinaires. Bonne chance à vous dans la réussite de vos thèses !

Enfin, à l'IPCMS, merci à l'ADDEPT et surtout à François, Marc et Anne pour organiser des soirées de retrouvailles entre collègues et, surtout, les soirées jeux de société.

Pendant ma thèse, j'ai eu la chance de pouvoir donner des cours à l'université de Strasbourg. Merci aux professeurs référents des cours : Matthias Pauly, Quentin Raffy, Marco Cecchini et Rachel Schurhammer. Merci aussi à Yannick Geiger pour son accompagnement lors des enseignements de TP et à Nicole Caccaveli et Aurélie Husser pour l'organisation de la salle et les produits chimiques.

Je remercie aussi mes encadrants de stage de M1 Rémy Barillon, Quentin Raffy et Nicolas Ludwig qui ont confirmé mon goût pour la physico-chimie et m'ont donné celui pour le monde des accélérateurs de particules.

Je tiens à remercier mes enseignants de la faculté de chimie de Strasbourg pour l'excellence de la formation. Et en particulier Sylvie Ferlay-Charitat, Thomas Ebbesen, Quentin Raffy, Rémi Barillon, Robert Vincent, Alain Chaumont, Burkhard Bechinger et Marc Henry, qui sont des enseignants passionnés et fournissent des cours exemplaires !

Merci à mes amis pour leur soutient et pour les bons moments que nous passons ensemble. Et en particulier à Robin, Marion, Maxime, Marina, Marie, Coralie, Olivier, Wenjia, Matias, Dany, Daniela et Mathieu. Merci aussi à Cyprien, David, Cédric et Coraline mes amis de la faculté et mes amis de galères. Je vous souhaite à tous de réussir dans vos entreprises professionnelles et personnelles !

Enfin, si j'ai pu réussir jusqu'ici c'est aussi grâce à l'ensemble de ma famille et surtout ma maman, ma mamie et ma sœur. Merci de m'avoir permis de réaliser cette thèse. Et surtout, merci pour votre soutient moral et financier.
Merci aussi à ma sœur pour l'aide apporté dans l'élaboration du premier schéma. Je te souhaite de pouvoir t'épanouir dans tes études et de les réussir pleinement ! Pense à aller boire quelques verres avec tes camarades plus souvent.

En tout dernier lieu, je tiens à remercier ma compagne, Paula, de me supporter chaque jour et de m'avoir épaulé lors de cette thèse et surtout lors de sa rédaction. J'attends avec impatience de pouvoir te rendre la pareil pour ta soutenance qui arrive à grands pas ! Bon courage à toi pour ta dernière année ! Bientôt nous pourront mettre Drs sur la boîte aux lettres =).

Résumé de la thèse en Français

Depuis le début de l'industrialisation mondiale, l'Homme n'a de cesse d'augmenter la pollution environnante à tel point que si aucune mesure n'est rapidement mise en place dans le but de diminuer notre impact écologique, les conséquences d'ici à cinquante ans pourraient en être dévastatrices. L'impact de la production des terres rares sur l'écologie, qui ont un enjeu économique crucial du fait de leur utilisation dans le domaine électronique, est aujourd'hui mal mesuré. En effet, des trous béants et des mines profondes sont creusés afin d'extraire ces terres rares. Elles sont ensuite séparées et purifiées en utilisant un large panel de solvant et d'acides puis en les rinçant finalement avec de l'eau. Parmi les terres rares, 90 % d'entre elles sont produites par la Chine qui bien souvent rejette simplement l'eau contaminée dans la nature sans la traiter. Aussi, afin de diminuer la pollution provenant de l'extraction de terre rare il est nécessaire de trouver des alternatives.

L'oxyde de fer et plus particulièrement la magnétite Fe_3O_4 est un matériau naturel, abondant, peu cher et ayant une très faible cytotoxicité. La magnétite adopte une structure AB_2O_4 dite spinelle inverse où A et B représentent des cations. Elle cristallise selon le groupe d'espace Fd-3m qui consiste en un empilement cubique à face centrée de 32 atomes d'oxygènes formant alors 64 sites tétraédriques (Td) et 32 sites octaédriques (Oh) où seulement un huitième des sites Td et la moitié des sites Oh sont occupés. Dans la structure spinelle inverse, les 16 cations trivalents occupent de façon équitablement réparties les sites Oh et Td tandis que les 8 cations Fe^{2+} occupent les sites Oh. Ainsi la formule chimique de la magnétite s'écrit $(Fe^{3+})_{Td}[Fe^{3+}Fe^{2+}]_{Oh}O_4$.
La magnétite s'oxyde spontanément en maghémite (γ-Fe_2O_3) par exposition à l'air. Celle-ci ne présente alors plus aucun Fe^{2+} dans sa maille qui laisse place à l'apparition de lacunes (□). Les lacunes peuvent s'agencer de trois manières différentes au sein de la structure :

- En conservant le groupe d'espace Fd-3m et sans modifier la maille avec une distribution aléatoire des lacunes selon la structure $(Fe^{3+})_{Td}\left[Fe^{3+}_{5/3}\square_{1/3}\right]_{Oh}O_4$
- Sans déformation de la maille mais avec un ordre partiel des sites Oh selon le groupe d'espace $P4_132$: $(Fe^{3+}_8)_{Td}\left[Fe^{3+}_{4/3}\square_{8/3}Fe^{3+}_{12}\right]_{Oh}O_4$
- De manière entièrement ordonnée dans une maille tétragonale selon le groupe d'espace $P4_32_12$.

Les Fe^{2+} et les Fe^{3+} possèdent un moment magnétique de 4 et 5 μ_B respectivement. La magnétite qui a une structure spinelle inverse voit ses moments magnétiques portés par les sites Oh opposés à ceux portés par les sites Td. Il en résulte la présence de propriétés dites ferrimagnétiques (FiM) qui lui confère un moment magnétique total uniquement dû aux cations Fe^{2+}, lui procurant une valeur de 4 μ_B par unité de formule soit 32 μ_B par maille.
Dans la maghémite en revanche, le moment magnétique total est plus faible puisque un Fe^{3+} est présent en site Td pour cinq tiers de Fe^{3+} en site Oh produisant un moment magnétique de 10/3 μ_B.

A l'état massif, l'oxyde de fer est divisé en plusieurs domaines magnétiques appelé domaines de Weiss qui sont séparés par les parois de Bloch. Ces domaines présentent tous une aimantation dans des directions aléatoires qui résultent en l'absence d'une aimantation spontanée pour le matériau massif.

Afin de remplacer les terres rares dans les dispositifs électroniques tels que l'enregistrement de données, il faut diminuer la taille de l'oxyde de fer. En réduisant la taille en-dessous d'un diamètre d_0, les parois de Bloch disparaissent laissant place à un seul domaine de Weiss pour l'ensemble du matériau. Il en résulte alors une aimantation spontanée maximale. Si la taille est réduite encore plus, en-dessous d'un diamètre critique d_c, typiquement en dessous de 20 nm pour l'oxyde de fer, il en résulte la perte de la stabilité magnétique. En effet, pour de si petites tailles, l'énergie thermique (kT) devient supérieure à l'énergie d'anisotropie magnétique de la nanoparticule (KV) résultant en la perte

de l'aimantation spontanée, c'est le domaine superparamagnétique. Cette propriété ne dépend pas seulement du volume de la particule mais également de la température, puisque si celle-ci est suffisamment basse, la nanoparticule retourne dans son état dit bloqué. La température de transition entre ces deux états est appelé température de blocage (T_B). T_B est obtenu en mesurant l'aimantation du matériau en fonction de la température (M(T)) où le maximum de cette courbe (T_{max}) est généralement attribué à la valeur de T_B. Le superparamagnétisme trouve des applications dans le domaine biomédical notamment mais rend impossible l'utilisation de petites nanoparticules d'oxyde de fer pour des applications de stockage de données.

Il a été rapporté dans la littérature qu'il est possible d'augmenter la température de blocage de matériau ferro(i)magnétique (F(i)M) en l'associant à un matériau antiferromagnétique (AFM) c-à-d un matériau où ses spins se compensent parfaitement. En effet, Skumryev et al.[1] ont démontré qu'en insérant des nanoparticules de cobalt (FM) dans une matrice de NiO (AFM), il est possible d'augmenter T_B jusqu'à 300 K environ alors que les mêmes nanoparticules insérés dans une matrice non magnétique d'Al_2O_3 démontrent une T_B de seulement une dizaine de kelvin.

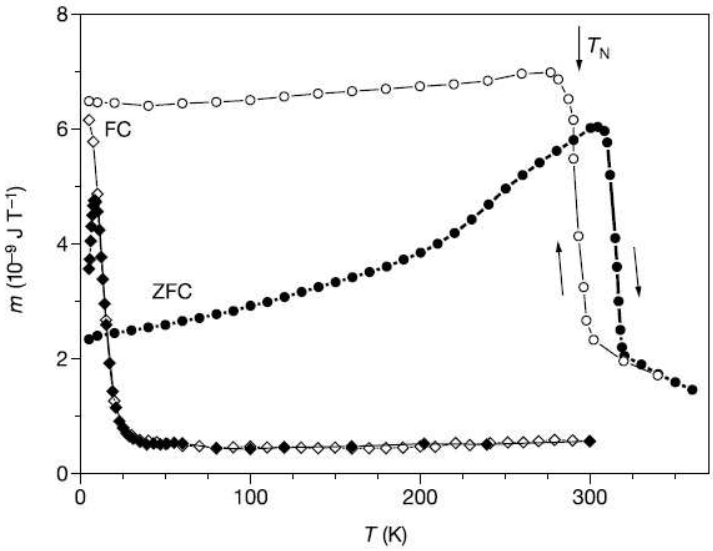

Figure 105. Mesure de l'aimantation de nanoparticules de 4 nm de Co@CoO insérées dans une matrice de Al_2O_3 (losange) ou de NiO (rond) en fonction de la température après refroidissement sous champ (symboles vides) ou sans refroidissement sous champ (symboles pleins).[1]

Cet effet de proximité, appelé exchange-bias est généré par un intime couplage magnétique entre la phase F(i)M et la phase AFM où, la phase AFM vient magnétiquement polariser les spins de la phase F(i)M. Pour ce faire, il est nécessaire que la phase AFM présente une énergie d'anisotropie magnétique ($K_{AFM}V_{AFM}$) supérieure à celle de la phase F(i)M ($K_{F(i)M}V_{F(i)M}$). Il faut également que $K_{AFM}V_{AFM}$ soit supérieur à l'énergie d'anisotropie interfaciale (J_{int}). La présence d'exchange-bias au sein d'un matériau est notamment démontrée par un décalage du cycle d'aimantation mesuré en fonction d'un champ appliqué après avoir refroidit le matériau sous champ (FC : field cooling). Cela est lié au fait que les spins magnétiques s'orientent selon le champ magnétique appliqué lors de la procédure de FC. Puis, lorsque l'aimantation est mesurée à basse température et que le champ magnétique est inversé, les spins de la phase F(i)M, qui sont magnétiquement polarisés par la phase AFM, se retournent difficilement. Puis si le champ est à nouveau inversé, les spins de la phase F(i)M vont cette fois se retourner beaucoup plus facilement pour retourner dans la configuration de plus basse énergie en permettant aux spins interfaciaux de la phase F(i)M de retrouver leur configuration parallèle aux spins interfaciaux de la phase AFM.

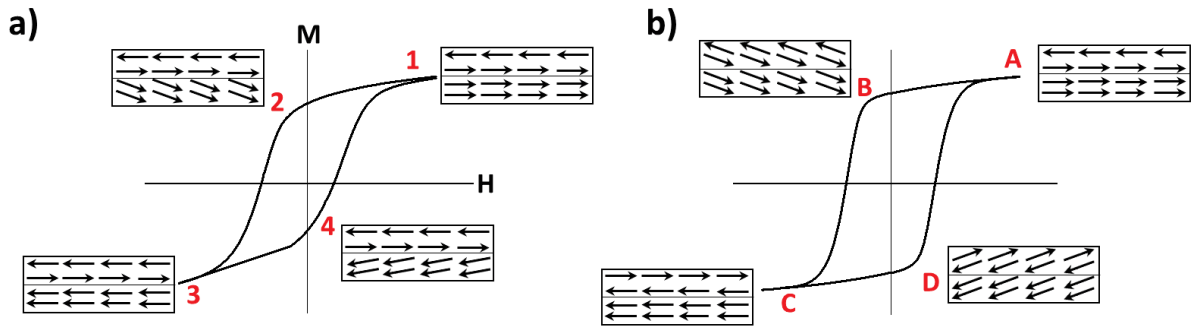

Figure 106. Représentation schématique de la configuration de spins pendant l'enregistrement du moment magnétique mesuré en fonction du moment magnétique appliqué après refroidissement sous champ à une interface FM/AFM avec a) $K_{AFM}V_{AFM}>K_{FM}V_{FM}$, b) $K_{AFM}V_{AFM}<K_{FM}V_{FM}$. Adapté de ref.[2]

Ainsi, il est possible d'augmenter l'énergie d'anisotropie magnétique de petites nanoparticules d'oxyde de fer grâce à un couplage d'exchange-bias avec un matériau AFM. Pour ce faire il est possible d'insérer les nanoparticules dans une matrice ou bien de synthétiser des nanoparticules de type coeur@coquille qui ont l'avantage d'être plus modulable. Afin de de synthétiser des nanoparticules de type coeur@coquille, avec l'oxyde de fer au centre et une coquille AFM, il faut que la phase AFM cristallise dans un système similaire avec un paramètre de maille le plus proche possible de celui de la magnétite ($a_{magnetite}$ = 8.396 Å fiche JCPDS n° 019-0629). Ce qui laisse comme candidats : MnO, CoO et NiO qui cristallisent dans le groupe d'espace Fm-3m (cubique face centré) et ont des paramètres de maille de 4.4460 Å (fiche JCPDS n° 04-005-4310), 4.2612 Å (fiche JCPDS n° 70-2856) et 4.1771 Å (fiche JCPDS n° 47-1049) respectivement. Cependant, MnO a une faible T_N (118 K) et une constante d'anisotropie (K_{MnO} = 2.8 10^{-2} J/m^3) plus faible que celle de la magnetite (K_{Fe3O4} = 2 10^4 J/m^3 [3,4]) qui fait qu'il n'arrivera pas à polariser les moments magnétiques de l'oxyde de fer. CoO est celui ayant la plus grande constante d'anisotropie de 5.0 10^2 J/m^3 pour une T_N de 290 K. Enfin, NiO a la plus grande T_N des trois avec 525 K mais sa constante d'anisotropie est faible, seulement 8 10^3 J/m^3.

Ainsi dans la littérature, la synthèse de nanoparticules de $Fe_{3-d}O_4$@MnO n'a pas de véritable impact sur la T_B comparé aux nanoparticules $Fe_{3-d}O_4$ de cœur restant donc vers 70 K [5,6] et le champ d'échange mesuré peut-être très faible (0.07 kOe [5]) ou bien très elevé (5.9 kOe [6]).

Comme NiO et Fe_3O_4 ont des constantes d'anisotropies relativement proches, les nanoparticules $Fe_{3-d}O_4$@NiO ne présentent qu'un petit champ d'échange qui témoigne d'un faible couplage d'exchange bias. Bien que la T_N de NiO soit élevée, la T_B des nanoparticules $Fe_{3-d}O_4$@NiO est peu différente de celle des nanoparticules de $Fe_{3-d}O_4$ de base.[5,7]

A contrario des deux systèmes précédents, les nanoparticules de $Fe_{3-d}O_4$@CoO présentent les plus grands champs d'échanges (4.3 kOe pour un cœur d'une taille de 9.6 nm et une coquille de 1.5 nm d'épaisseur[8]) accompagné par une grande ouverture du cycle d'hystérèse à 5 K : 0.4 à 12.7 kOe dans le meilleur des cas[8] (cœur d'une taille de 8.2 nm et coquille d'une épaisseur de 1.0 nm). Une telle structure a ainsi permis d'augmenter la T_B de nanoparticules d'oxyde de fer de 150 à 290 K.[5,9] Cette augmentation est possible grâce à la grande énergie d'anisotropie magnétique de la coquille de CoO qui permet d'augmenter l'énergie d'anisotropie magnétique globale de la nanoparticule core@coquille.

Cependant, de tels systèmes sont limités par la T_N de la phase AFM au-delà de laquelle, l'AFM perd son ordre magnétique et sa faculté à polariser magnétiquement la phase FiM.

Il a été rapporté dans la littérature que la synthèse de nanoparticules de type oignon (coeur@(coquille)$_n$) permet elle aussi d'augmenter l'énergie d'anisotropie magnétique des nanoparticules.
En effet, Salazar-Alvarez et al.[10] ont rapporté la synthèse de nanoparticules de FeO@Fe_3O_4@MnO@Mn_3O_4 avec trois interfaces FiM/AFM (AFM/FiM/AFM/FiM) pour une taille finale de 34 nm. La mesure de leur aimantation en fonction de la température a montré la présence de trois T_B distinctes de 40, 120 et 130 K, qui correspondent aux températures d'ordre de transition de MnO, Mn_3O_4 et FeO@Fe_3O_4 respectivement. A l'opposé, la synthèse de nanoparticules de FeO@Fe_3O_4@Mn_3O_4 où l'ensemble du MnO a été oxydé en Mn_3O_4 démontre la présence d'une seule T_B à 200 K qui est lié au fort couplage d'échange interfacial entre l'oxyde de fer et le Mn_3O_4. De plus, les nanoparticules FeO@Fe_3O_4@MnO@Mn_3O_4 ont montrées avoir un champ d'échange plus important que celles de FeO@Fe_3O_4@Mn_3O_4. Ainsi, tandis que les propriétés magnétiques des nanoparticules FeO@Fe_3O_4@MnO@Mn_3O_4 sont dominées par la couche de MnO, celles des FeO@Fe_3O_4@Mn_3O_4 sont dominées par les effets interfaciaux.

Krycka et al.[11] ont synthétisés des nanoparticules de structure Fe_3O_4@MnO@γ-Mn_2O_3 (FiM/AFM/FiM) d'un cœur d'une taille de 6 nm, d'une coquille de MnO de 30 nm qui a été oxydée sur les cinq premiers nanomètres. Ils comparent leurs propriétés magnétiques à celles des nanoparticules Fe_3O_4@γ-Mn_2O_3 ayant un cœur d'une taille de 3 nm et une coquille d'une épaisseur de 2.5 nm. En analysant ces deux structures à l'aide de la diffusion des neutrons polarisés aux petits angles, ils ont démontré que les spins du cœur et de la coquille se retournent de manière concerté dans Fe_3O_4@γ-Mn_2O_3 alors que dans la structure Fe_3O_4@MnO@γ-Mn_2O_3, il existe un effet de proximité magnétique entre MnO et γ-Mn_2O_3 qui permet aux spins de la phase γ-Mn_2O_3 de rester ordonné au-delà de leur température de Curie.

Le dernier système reporté consiste en des nanoparticules d'un cœur de $MnFe_2O_4$ d'une taille de 5.5 nm, d'une première coquille de $CoFe_2O_4$ épaisse de 1.2 nm et une seconde coquille de $NiFe_2O_4$ épaisse de 2.0 nm formant une structure $MnFe_2O_4$@$CoFe_2O_4$@$NiFe_2O_4$.[12] Grâce à cette structure, la T_B a pu être augmentée de 20 à 190 K.

Cette thèse propose une étude détaillée de la relation structure propriété au sein de nanoparticules hybrides de type oignon.
Le premier volet a consisté en l'étude de la croissance de nanoparticules d'oxyde de fer par une méthode de croissance sur germe selon une succession de synthèses par décomposition thermique. Cette étude a su montrer que la synthèse de croissance sur germe permet d'obtenir des nanoparticules avec une taille et une forme contrôlée même après une succession de cinq synthèses. En outre, les effets d'oxydation interfaciaux ont pu être étudié en ayant recours à l'utilisation de plusieurs techniques analytiques telles que la diffraction des rayons X, la transmission infrarouge et la spectroscopie Mössbauer.

Dans la seconde partie, nous avons étudié les phénomènes de diffusion interfaciaux présent dans des nanoparticules de $Fe_{3-d}O_4$@CoO qui ont été reporté plus tôt.[13] Ainsi, nous avons synthétisé des nanoparticules de $Fe_{3-d}O_4$@CoO, $Fe_{3-d}O_4$@$CoFe_2O_4$ et d'oxyde de fer dopées au cobalt dans le but de comparer leurs propriétés magnétiques. Nous avons alors démontré que la présence de ferrite de cobalt influe beaucoup sur ces dernières.

Puis, grâce à la connaissance et à la maîtrise des deux chapitres précédents, nous avons doublés l'interface $Fe_{3-d}O_4$/CoO présente dans des nanoparticules $Fe_{3-d}O_4$@CoO afin de synthétiser des nanoparticules coeur@coquille@coquille $Fe_{3-d}O_4$@CoO@$Fe_{3-d}O_4$ dans le but d'augmenter l'anisotropie magnétique des nanoparticules $Fe_{3-d}O_4$@CoO. Les nouveaux objets synthétisés ont été analysé dans les moindres détails en utilisant une batterie de techniques analytique. En effet, du fait de la présence

de diffusion atomique interfaciale prouvé dans les nanoparticules $Fe_{3-d}O_4$@CoO, nous avons étudié la distribution atomique spatiale grâce à des analyses de microscopie électronique. L'environnement des atomes de Fe a pu être étudié par spectroscopie Mössbauer et par absorption des rayons X (XAS, XMCD). De même pour l'environnement des atomes de Co qui a été analysés par spectroscopie XAS, XMCD. Des mesures de diffusion des neutrons polarisés aux petits angles (p-SANS) ont permis de vérifier la composition chimique des nanoparticules et notamment d'estimer une épaisseur de couche interfaciale de ferrite de cobalt qui peut être confrontée aux résultats obtenus en spectroscopie Mössbauer. Les analyses des propriétés magnétiques mesurées grâce au SQUID ont démontrées que l'ajout d'une seconde couche sur la nanoparticule de $Fe_{3-d}O_4$@CoO augmente fortement les propriétés magnétiques comparées aux nanoparticules natives de $Fe_{3-d}O_4$@CoO et ce grâce à de forts couplages magnétiques au sein des nanoparticules $Fe_{3-d}O_4$@CoO@$Fe_{3-d}O_4$.

Pour s'affranchir des effets de diffusion interfaciale sur les couplages d'échanges magnétiques, des nanoparticules de $Fe_{3-d}O_4$@$CoFe_2O_4$@$Fe_{3-d}O_4$ ont également été synthétisées. Il est attendu que la présence de la phase dure de ferrite de cobalt augmente fortement l'anisotropie magnétique globale de la nanoparticule grâce à de forts couplage d'échange dur-doux. La structure de ces nanoparticules a été précisément étudiée selon les mêmes analyses que pour le chapitre précédent (microscopie électronique, XAS, XMCD, DRX, Mössbauer). Il a alors été possible de déterminer un modèle théorique qui permet de confronter la structure aux propriétés magnétiques enregistrées. Enfin, les propriétés magnétiques de ces nanoparticules ont été comparées à celles des nanoparticules de $Fe_{3-d}O_4$@CoO@$Fe_{3-d}O_4$.

Une dernière piste étudiée a consisté à bénéficier cette fois de la haute température de Néel du NiO (525 K) dans des nanoparticules de $Fe_{3-d}O_4$@CoO grâce à un effet de proximité antiferromagnétique. De toro et al.[14] ont déjà prouvé le potentiel de ce phénomène en augmentant la température d'ordre magnétique de nanoparticules de Co@CoO en les déposant dans une matrice de NiO. Des nanoparticules de $Fe_{3-d}O_4$@CoO@NiO ont alors été synthétisées. Seulement, la synthèse de nanoparticules de NiO par décomposition thermique n'est que très peu reportée dans la littérature. Il a donc fallu dans un premier temps étudié la décomposition de précurseurs organométalliques à base de nickel puis déterminer des conditions de synthèses optimales pour produire les nanoparticules désirées. Deux séries de nanoparticules de $Fe_{3-d}O_4$@CoO@NiO ont alors été synthétisées : une cubique et une sphérique. Leur structure ainsi que les phénomènes de croissance sur faces et leurs propriétés magnétiques ont été étudiées.

Chapitre I
Nanoparticules $Fe_{3-d}O_4(@Fe_{3-d}O_4)_n$

Des nanoparticules d'oxyde de fer ont été synthétisé en décomposant du stéarate de fer dans du dioctyl éther ($T_{éb}$ = 290 °C) en présence d'acide oléique en tant qu'agent stabilisant. La moitié de ces nanoparticules sont conservées pour des analyses ultérieures tandis que l'autre moitié est utilisée en tant que germe pour déposer par-dessus une couche d'oxyde de fer selon le même mode opératoire que pour synthétiser les nanoparticules de cœur. Il a ainsi été possible de déposer quatre couches successives d'oxyde de fer sur les nanoparticules de cœur.

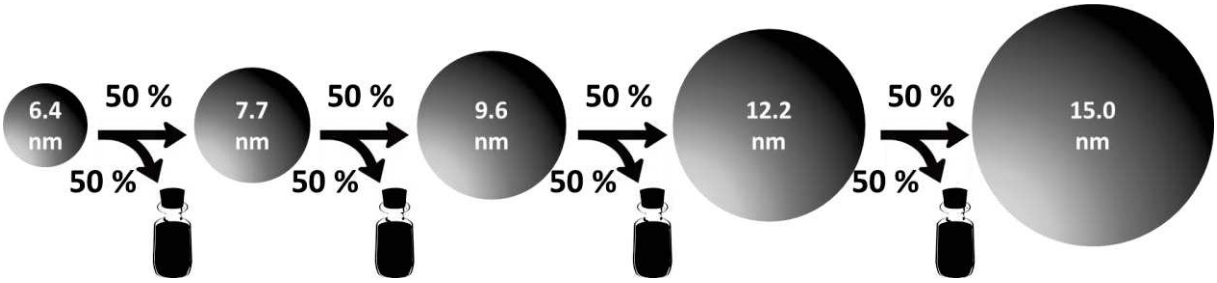

Figure 107. Stratégie de synthèses des nanoparticules $Fe_{3-d}O_4(@Fe_{3-d}O_4)_n$

Les images de microscopie électronique en transmission montrent que les nanoparticules de cœur sont sphériques avec une distribution en taille étroite centrée à 6.4 nm. L'augmentation régulière de la taille mesurée d'après les images de microscopie électronique en transmission à mesure que les couches sont déposées démontre la bonne croissance de chaque couche où après quatre couches, la taille est augmentée à 15.0 nm. L'ajout de couche de $Fe_{3-d}O_4$ altère peu à peu la forme sphérique et élargit la distribution en taille qui restent tout de même raisonnable après la synthèse de la dernière couche d'oxyde de fer.

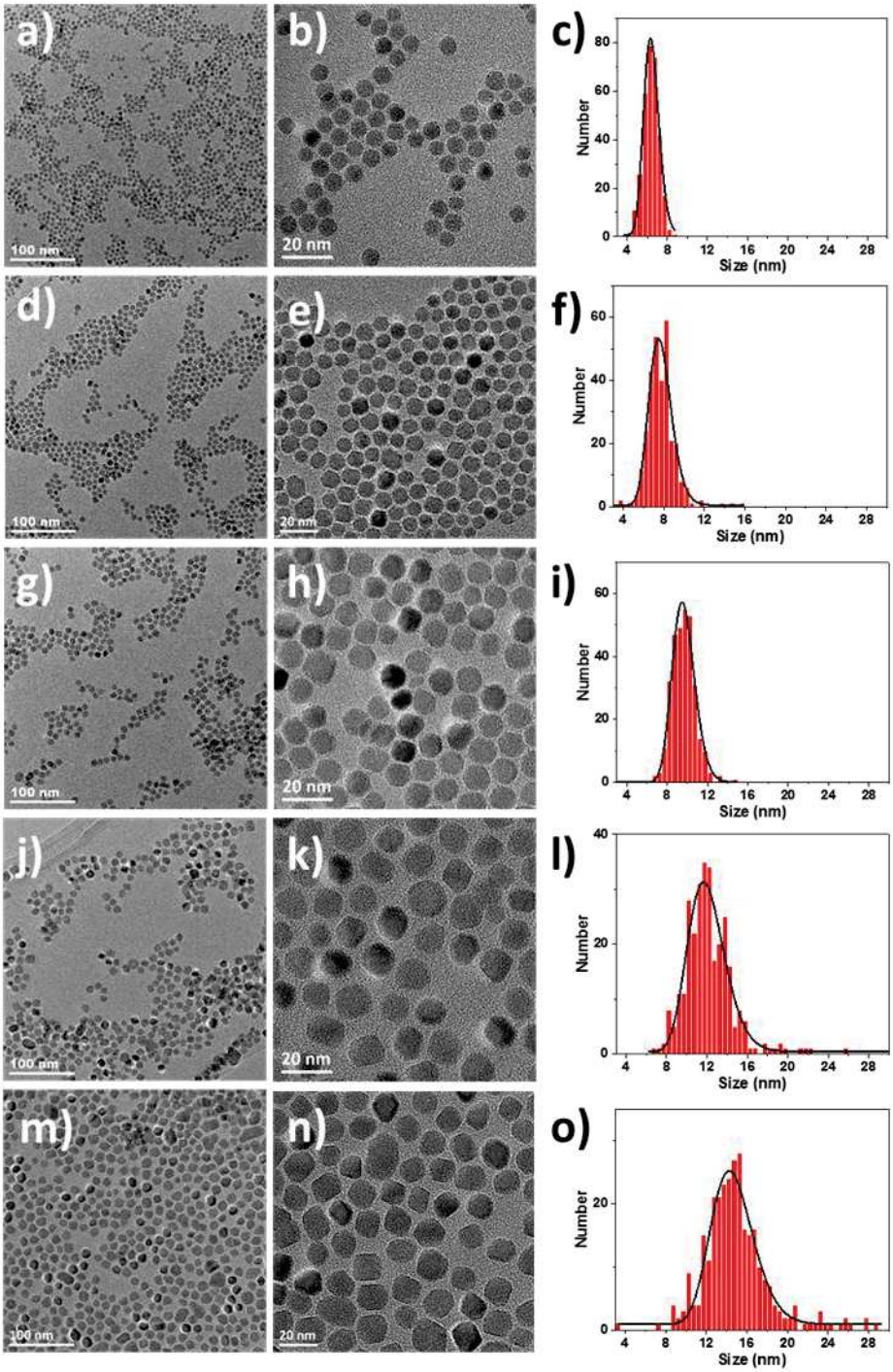

Figure 108. a, b, d, e, g, h, j, k, m, n) Images de microscopie électronique en transmission de a, b) IOC, d,e) IOCS1, g, h) IOCS2, j, k) IOCS3 et m, n) IOCS4 et c, f, i, l, o) leur distribution en taille correspondante.

Les analyses de spectroscopie infrarouge à transformée de Fourier (FT-IR) ont démontrées que les ligands acides oléiques sont bien présents à la surface des nanoparticules synthétisées. En outre, en observant la bande Fe-O centrée vers 570 – 638 cm^{-1} il a été démontré que toutes les nanoparticules contiennent une portion de magnétite et de maghémite.

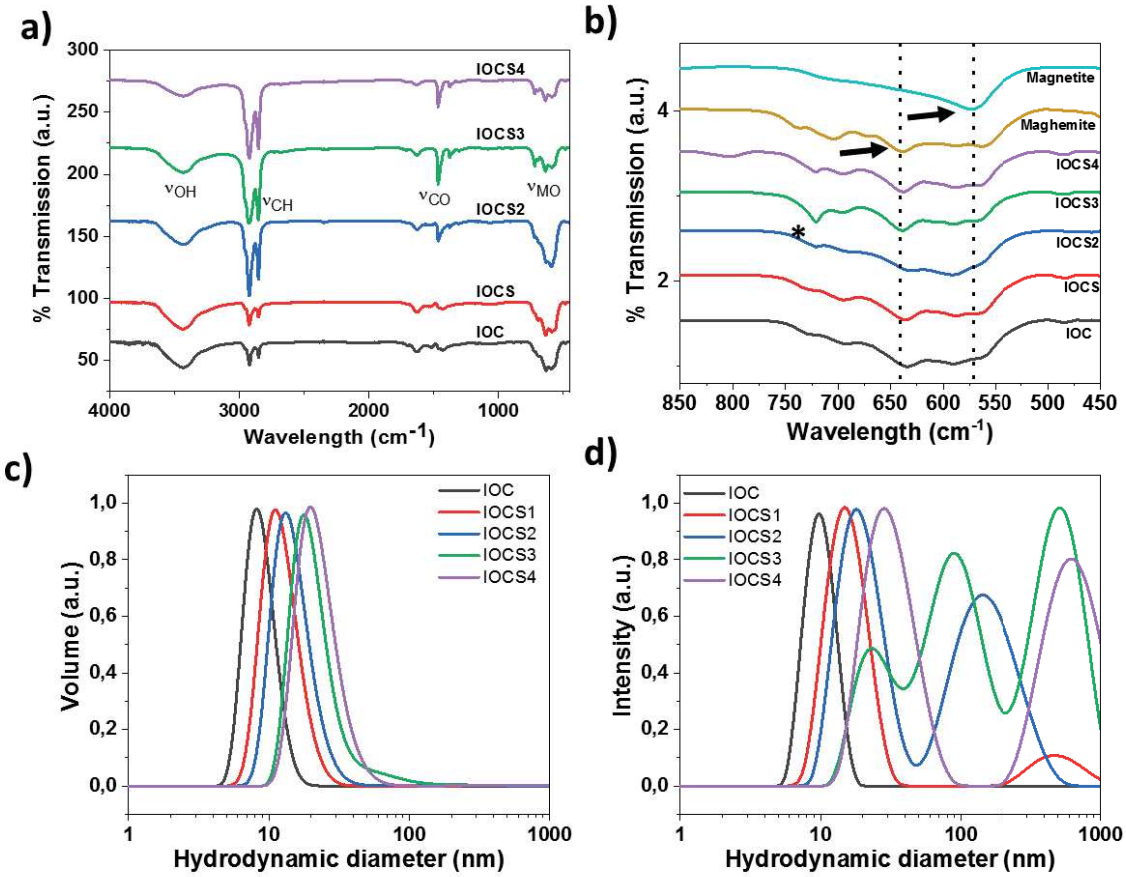

Figure 109. Spectre infrarouge à transformée de Fourier réalisées sur les nanoparticules IOCSn a) dans la gamme de 400 à 4000 cm^{-1} et b) avec un agrandissement de 450 à 850 cm^{-1}. Mesures de granulométrie c) en volume et d) en intensité.

La présence de ligands organique à la surface des nanoparticules leur permet d'être stable en suspension dans les solvants organiques commun tels que le chloroforme, le THF, le cyclohexane. Cela est démontré par des mesures de diffusion dynamique de la lumière qui montrent la présence d'une seule distribution en taille pour chaque nanoparticule. Aussi, l'évolution des diamètres hydrodynamique est en accord avec l'évolution des tailles mesurées à partir des images TEM. Ils apparaissent cependant plus grand que ceux des images TEM car le diamètre hydrodynamique tient compte de la taille du matériau entouré des ligands organiques.

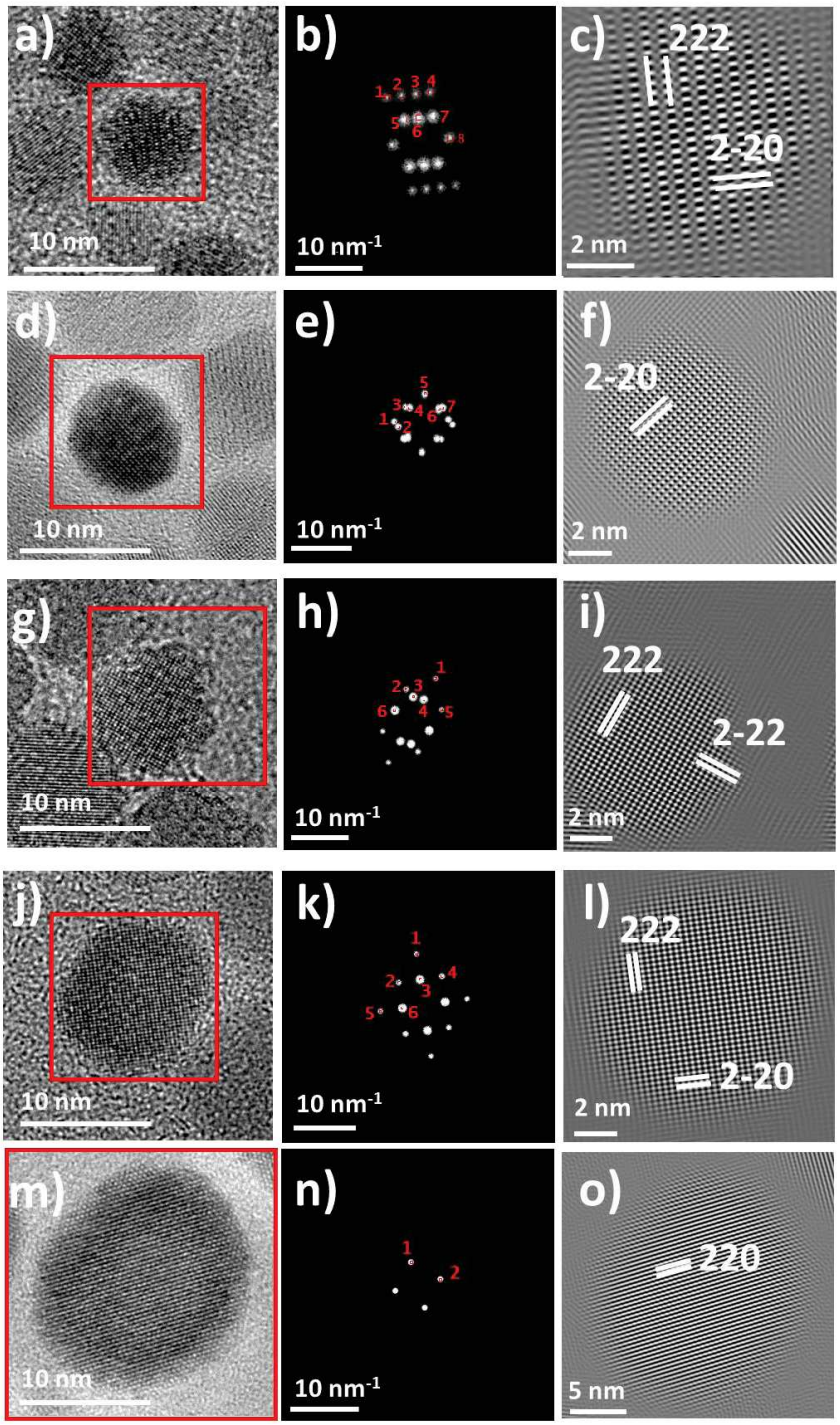

Figure 110. a, d, g, j, m) Images de microscopie électronique en transmission avec b, e, h, k, n) les FFT après application d'un filtre de Bragg et c, f, i, l, o) les FFT inverses des FFT filtrées pour les nanoparticules a, b, c) IOC, d, e, f) IOCS1, g, h, i) IOCS2, j, k, l) IOCS3, m, n, o) IOCS4.

Les mesures de microscopie électronique en transmission à haute résolution révèlent la présence de franges périodiques qui témoignent d'un comportement similaire à celui de monocristaux. Cela démontre la bonne épitaxie de chaque couche sur la précédente. La distance entre les franges peut être indexée selon les plans de hkl de la magnétite/maghémite.

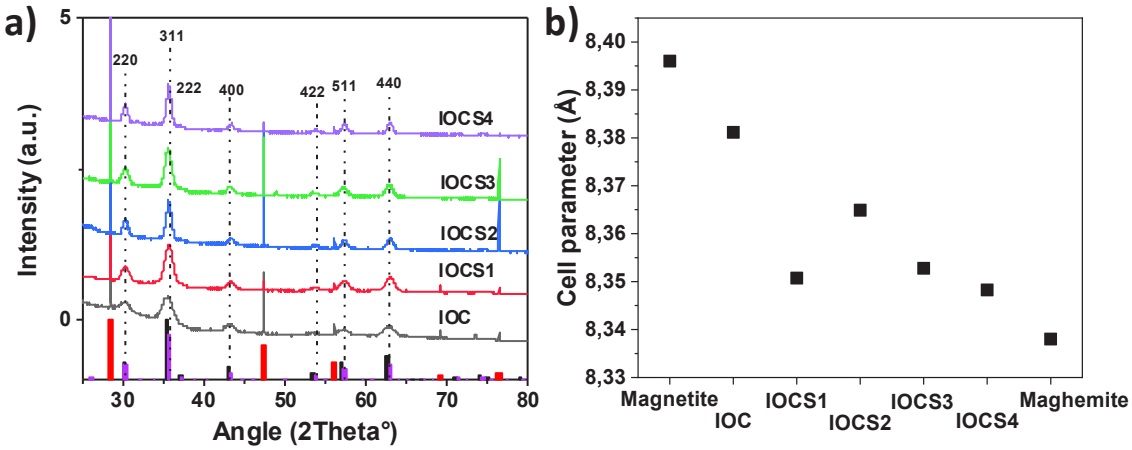

Figure 111. a) Diffractogrammes par rayons X et b) paramètres de mailles calculés à partir des diffractogrammes des nanoparticules IOCSn.

Les diffractogrammes enregistrés pour chaque nanoparticule montrent qu'elles cristallisent toute sous forme d'oxyde de fer magnétite/maghémite. La taille des cristallites est calculée à partir de la largeur à mi-hauteur des pics grâce à la formule de Debye-Scherrer. La taille évolue de façon cohérente avec l'ajout des couches, en accord avec les tailles mesurées à partir des images TEM. Enfin, il a aussi été possible de déterminer les paramètres de maille pour chaque nanoparticule. Il a été démontré que plus la taille de la nanoparticule est augmentée, plus sa structure s'éloigne de la magnétite pour s'approcher de la maghémite. Ces observations sont confortées par des analyses de spectroscopie Mössbauer qui ont permis de conclure que les couches déposées sont oxydées en maghémite. Il a été démontré plus tôt[15] que des nanoparticules d'une taille inférieure à 8 nm sont entièrement oxydée en maghémite. Ainsi la faible épaisseur des couches (0.7 à 1.4 nm) est en accord avec cette étude.

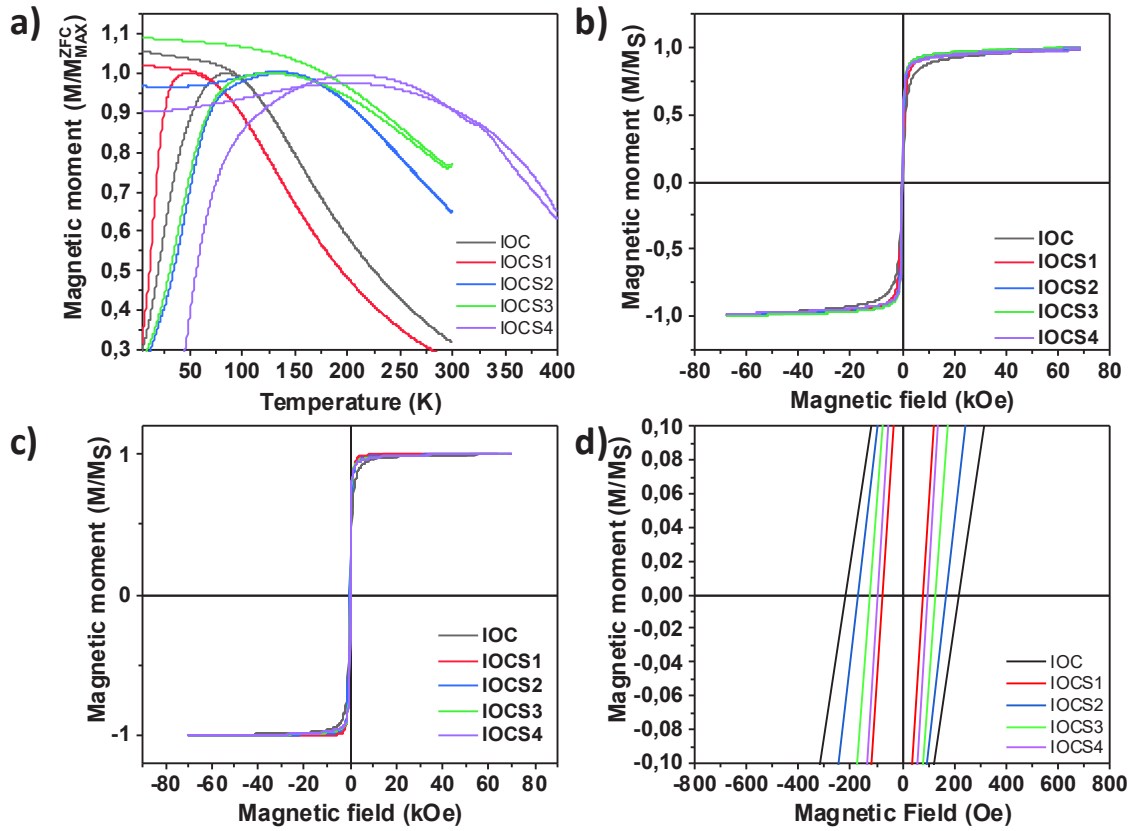

Figure 112. a) Aimantation mesurée en fonction de la température. Champ magnétique enregistré en fonction d'un champ magnétique externe appliqué à b) 300 K, c) 5 K avec d) un agrandissement de la courbe M(H) mesurée à 5 K.

Enfin, les propriétés magnétiques des nanoparticules ont été étudiées par magnétométrie SQUID. La température de transition magnétique (T_{max}) ainsi que la température de blocage augmentent généralement de façon cohérente en augmentant la taille des nanoparticules. Elle passe alors de 84 K pour IOC à 203 K pour IOCS4. Les incohérences mesurées peuvent être attribuées à de forts moments dipolaires puisque l'aimantation des nanoparticules est mesurée à l'état de poudre. A température ambiante (300 K) toutes les nanoparticules présentent des propriétés superparamagnétiques sauf pour IOCS4 qui démontrent l'existence d'un faible champ coercitif de 43 Oe à 300 K. L'augmentation de la taille des nanoparticules a ainsi permis d'augmenter l'énergie d'anisotropie magnétique effective des nanoparticules. Le ratio M_R/M_S montre une tendance à augmenter de IOC à IOCS4, en accord avec un comportement verre de spin qui provient d'interactions dipolaires plus fortes. Les aimantations à saturation mesurées ont cependant un comportement incohérent puisque les M_S de IOC, IOCS1 et IOCS4 sont très élevé comparés aux M_S mesurés dans la littérature pour des nanoparticules d'oxyde de fer de tailles similaires. Ces observations sont néanmoins attribuées à des effets de surface mais aussi à des effets de frustration magnétique interfaciaux résultant de défauts structurels.

Chapitre II
Nanoparticules $Fe_{3-d}O_4$@CoO, $Fe_{3-d}O_4$@$CoFe_2O_4$ et $Fe_{3-d}O_4$ dopées au Co

Dans la seconde partie de ce manuscrit, nous avons étudié en détail le phénomène de diffusion interfacial d'atomes de Co dans une nanoparticule d'oxyde de fer au sein de différentes structures.

Des nanoparticules de $Fe_{3-d}O_4$@CoO (CS_CoO), $Fe_{3-d}O_4$@$CoFe_2O_4$ (CS_CoFe2) et $Fe_{3-d}O_4$ dopées au Co (CS_CoFe1) ont alors été synthétisées par des synthèses de croissance sur germe grâce à une succession de deux synthèses de décomposition thermique.

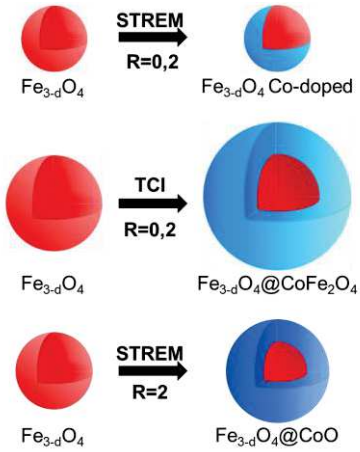

Figure 113. Stratégie de synthèse des nanoparticules $Fe_{3-d}O_4$@CoO (CS_CoO), $Fe_{3-d}O_4$@$CoFe_2O_4$ (CS_CoFe2) et $Fe_{3-d}O_4$ dopées au Co (CS_CoFe1).

Les images MET montrent que les nanoparticules d'oxyde de fer de cœur sont toutes sphériques avec une distribution en taille étroite centrée à 7.2, 10.3 et 8.8 nm pour CS_CoFe1, CS_CoFe2 et CS_CoO. La croissance d'une coquille a augmenté la taille des nanoparticules à 12.3 et 10.2 nm pour CS_CoFe2 et CS_CoO alors que la taille des nanoparticules dopées au Co n'a pas été modifiée. Les nanoparticules cœur@coquille ont une morphologie finale contrôlée, proche de la forme de sphère.

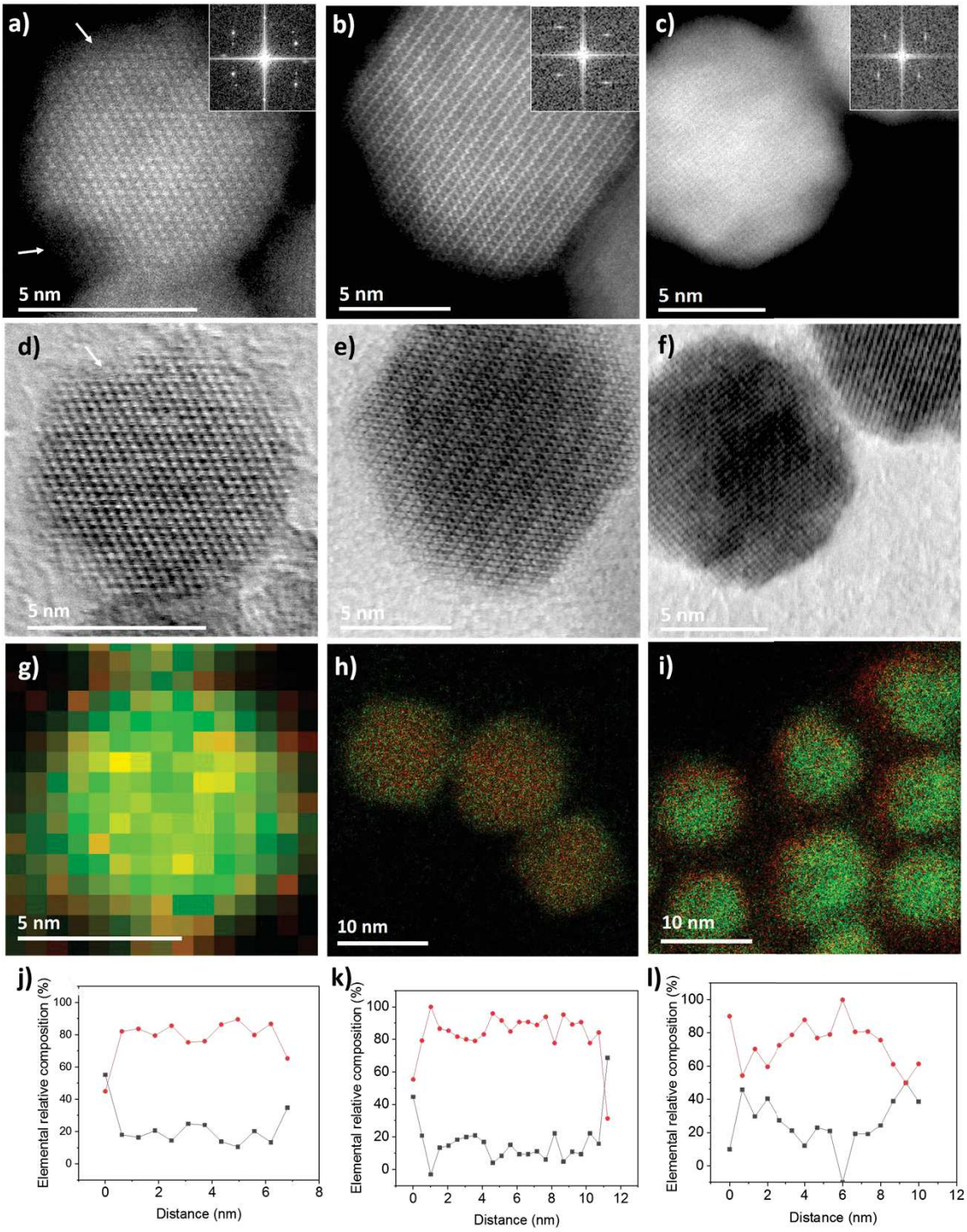

Figure 114. a, b, c, d, e, f) Images STEM haute résolution, g, h, i) distribution spatiale atomique (EELS-SI) des atomes de fer (vert) et de cobalt (rouge) et j, k, l) Profil EELS des nanoparticules a, d, g, j) CS_CoF1, b, e, h, k) CS_CoF2 et c, f, i, l) CS_CoO.

Les mesures d'analyse dispersive en énergie montrent la présence de Fe et de Co pour chaque structure coeur@coquille ce qui démontre le bon dopage des nanoparticules CS_CoFe1.

Les images STEM présentent des franges continues et périodiques sur l'ensemble des nanoparticules coeur@coquille, démontrant les bonnes relations d'épitaxies entre le cœur et la coquille. Les analyses de spectres images de perte d'énergie des électrons (EELS-SI) permettent de dresser une cartographie en deux dimensions de la distribution atomiques des atomes de Fe et de Co. On observe que les

nanoparticules CS_CoFe1 possèdent quelques atomes de Co localisés en surface, en accord avec leur structure dopée. Les nanoparticules CS_CoF2 présentent une distribution homogène des atomes de Fe et de Co sur l'ensemble des nanoparticules, conformément à une structure $Fe_{3-d}O_4$@$CoFe_2O_4$. Enfin, les atomes de Co sont présents surtout sur les bords des nanoparticules avec au centre une forte concentration d'atomes de Fe pour CS_CoO, en accord avec une structure $Fe_{3-d}O_4$@CoO. Des profils de perte d'énergie électronique (EELS) viennent compléter cette étude. Leurs résultats appuient ceux obtenus en EELS-SI.

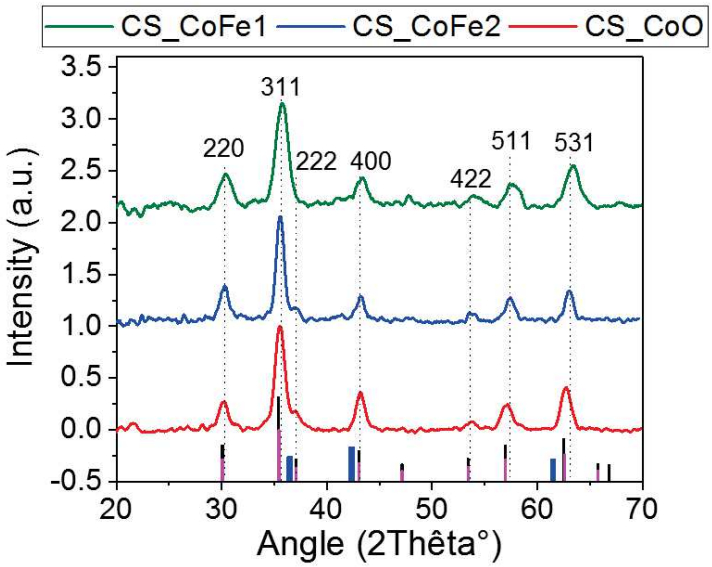

Figure 115. Diffractogrammes des nanoparticules CS_CoF1, CS_CoF2 et CS_CoO par les rayons X.

Les diffractogrammes de CS_CoFe1 et CSCoFe_2 montrent la présence d'une seule phase cristalline en accord avec une structure spinelle inverse telle que $Fe_{3-d}O_4$ ou $CoFe_2O_4$. Du fait de paramètre de maille très proches, il n'est pas possible de distinguer $Fe_{3-d}O_4$ (a_{Fe3O4} = 8.396 Å, carte JCPDS n° 19-062, $a_{\gamma\text{-}Fe2O3}$ = 8.338 Å, carte JCPDS n° 39-1346) de $CoFe_2O_4$ ($a_{CoFe2O4}$ = 8.3919 Å, carte JCPDS n° 22-1086). En revanche, une contribution supplémentaire de phase wüstite apparaît dans le diffractogramme de CS_CoO. En utilisant la formule de Debye-Scherrer, des tailles de cristallite de 5.4, 9.7 et 8.4 nm ont été calculées pour CS_CoFe1, CS-CoFe2 et CS_CoO respectivement. Ces tailles sont inférieures aux tailles TEM mesurées du fait de la projection 2D des nanoparticules. Des paramètres de mailles de 8.401, 8.398 et 8.372 Å ont été calculés pour CS_CoFe1, CS-CoFe2 et CS_CoO respectivement. Ces paramètres de taille sont intermédiaires entre ceux de la maghémite et de la ferrite de Co pour CS-CoFe1 et CS-CoFe2 et entre la maghémite et CoO pour CS_CoO ce qui démontrent également les bonnes relations d'épitaxie entre le cœur et la coquille.

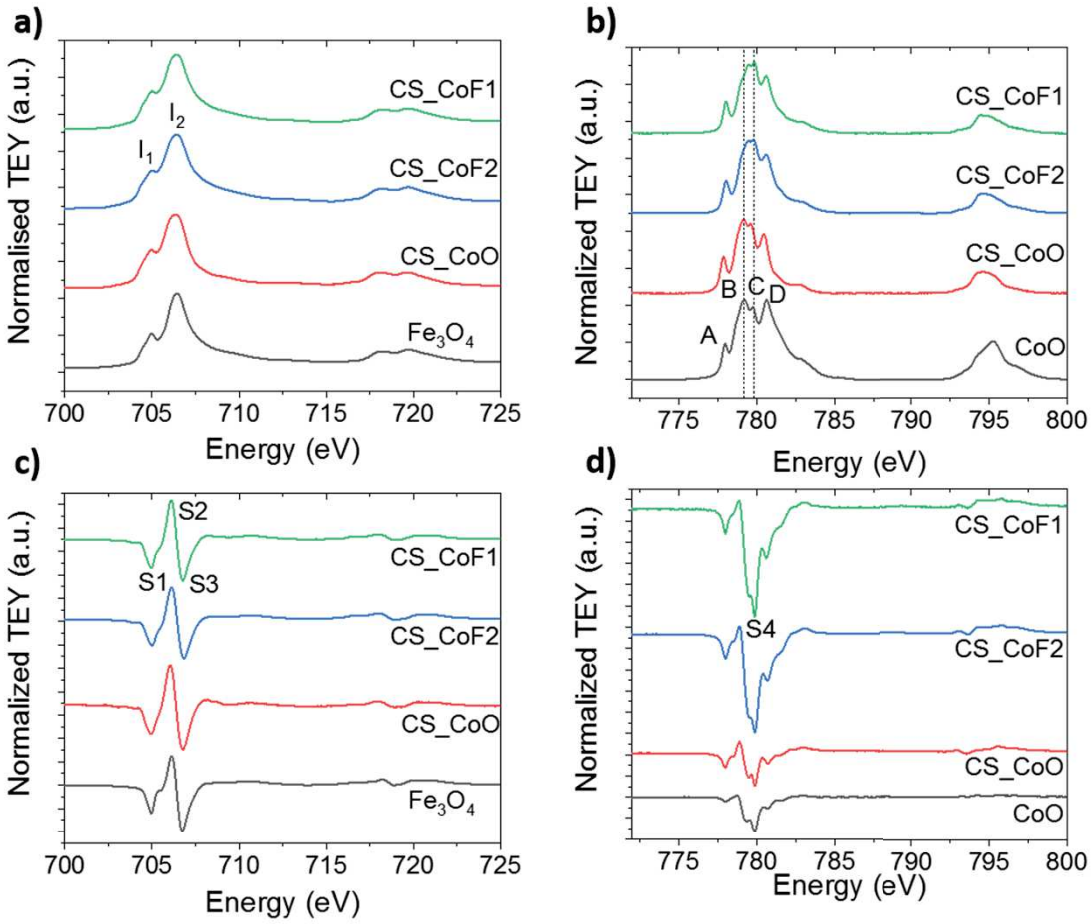

Figure 116. Spectres a, c) XAS et b, d) XMCD réalisés aux seuils $L_{2,3}$ du a, b) fer et c, d) cobalt à 4,2 K et 6,5 T.

Afin de déterminer les environnements atomiques du fer et du cobalt, des expériences de spectroscopie d'absorption des rayons X ont été menée sur la ligne DEIMOS du synchrotron SOLEIL. La technique XAS/XMCD est ici très utile car elle est sélective de spin et d'orbite. Elle permet ainsi de sonder séparément les atomes de Fe et de Co et d'étudier leur état de valence.

Les spectres XAS et XMCD enregistrés au seuil $L_{2,3}$ du fer sont en accord avec une structure spinelle inverse de type $Co_{1-x}Fe_{2+x}O_4$ ($0<x<1$). Ces expériences ont démontré que les nanoparticules d'oxyde de fer de cœur sont partiellement oxydées, comme attendu d'après la littérature.[15] La proportion de Fe^{2+} est néanmoins plus importante dans les cœur@coquille, ce qui est attribué à la présence de la coquille dopée au Co, de ferrite de cobalt ou de CoO qui protège le cœur d'oxyde de fer contre une oxydation spontanée suite à l'exposition des nanoparticules à l'air. Le calcul des ratios I1/I2 et (S1+S2)/(S2+S3) a démontré que la composition des nanoparticules coeur@coquille diffèrent de ceux de la magnétite du fait de la présence de ferrite de cobalt dans les nanoparticules ou le Co^{2+} remplacent les Fe^{2+} en site Oh.

Ces observations sont supportées par la présence d'un signal XMCD au seuil du Co pour toutes les nanoparticules. De plus, les spectres sont tous normalisés par rapport au saut au seuil du XAS. Donc l'intensité des spectres XMCD est directement proportionnel au nombre de spins non compensés. Ainsi, un matériau purement antiferromagnétique ne possède pas de signal XMCD. L'intensité du spectre XMCD est très important pour les nanoparticules CS_CoFe1 et CS_CoFe2 du fait de la présence de ferrite de cobalt, en accord avec les structures $Fe_{3-d}O_4$ dopé au Co et $Fe_{3-d}O_4$@$CoFe_2O_4$. Le spectre XMCD de CS_CoO est moins intense du fait de la présence de CoO antiferromagnétique et donc son intensité démontre la faible quantité de Co^{2+} présent dans le cœur d'oxyde de fer suite à leur diffusion.

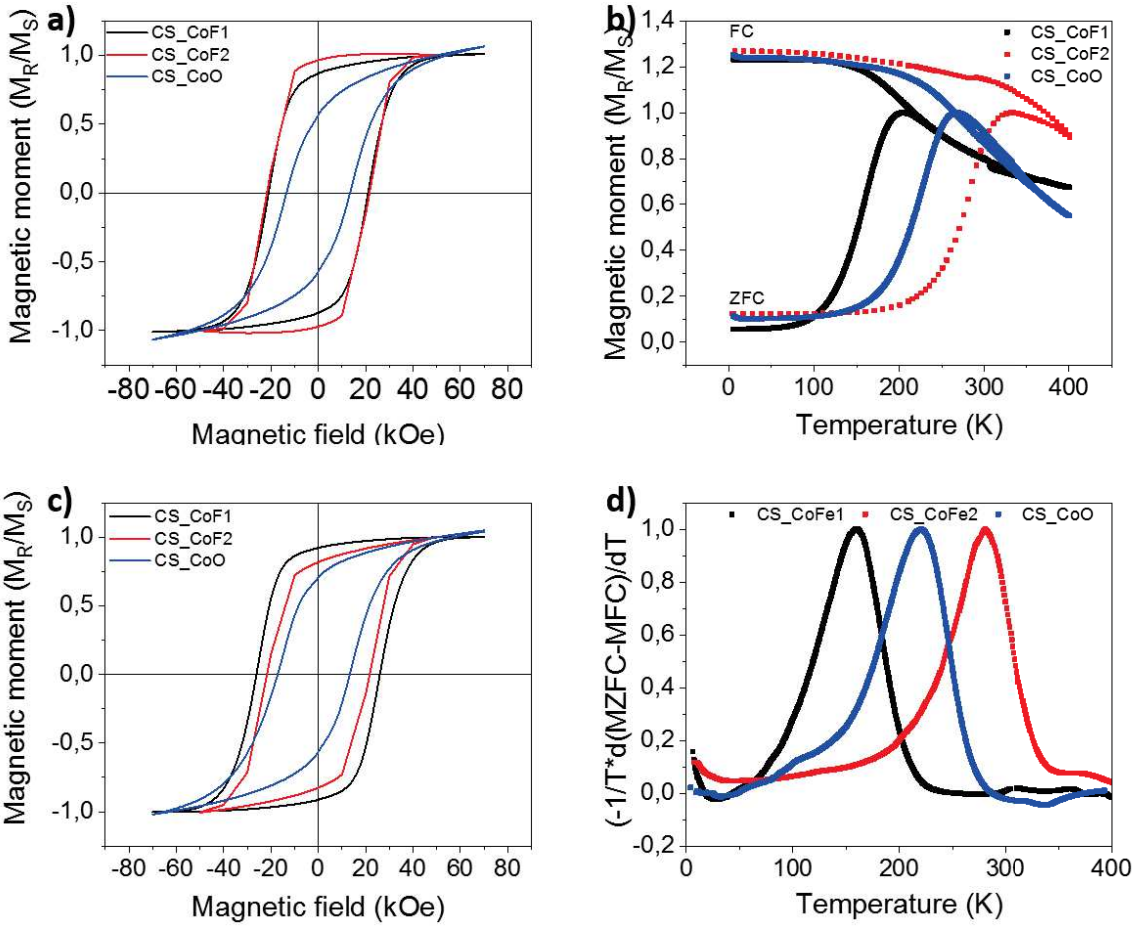

Figure 117. Propriétés magnétiques des nanoparticules coeur@coquille mesurées en SQUID. Courbes M(H) mesurée à a) 5 K sans refroidissement sous champ et c) 5 K après refroidissement sous champ. b) Mesure de l'aimantation en fonction de la température. D) Distribution des températures de blocage calculée à partir de b).

Les propriétés magnétiques de ces nanoparticules ont été étudiées par magnétométrie SQUID. Il en ressort que toutes les nanoparticules ont un comportement superparamagnétiques à 300 K. Cela est en accord avec leur T_B respectives de 159, 284 et 220 K pour CS_CoFe1, CS_CoFe2 et CS_CoO. Néanmoins, l'ajout d'une coquille de ferrite de cobalt ou de CoO a permis d'augmenter T_B comparé au cœur comme attendu. De plus, cela a permis d'obtenir des grands champs coercitifs de 21, 21.7 kOe pour CS_CoFe1 et CS_CoFe2 mesuré à 10 K sans refroidissement sous champ. Tandis que CS_CoO a un plus petit H_C de 13.4 kOe qui est dû à une plus faible proportion de ferrite de cobalt.

Les mesures d'aimantation à 10 K après refroidissement sous un champ de 7 T montrent que le cycle d'hystérèse de CS_CoO est décalé avec un champ d'échange de 2.0 kOe tandis que celui des autres échantillons ne l'est pas. Cela démontre que les propriétés magnétiques de CS_CoO résultent essentiellement de la présence d'exchange-bias tandis que celles de CS_CoFe1 et CS_CoFe2 résultent d'un couplage d'échange dur-mou.
Du fait de la présence de CoO à la surface de CS_CoO voit son aimantation à saturation réduite : seulement 46 emu/g alors que CS_CoFe1 et CS_CoFe2 possèdent des M_S de 67 et 63 emu/g qui sont en accord avec la présence de $Fe_{3-d}O_4$ (le M_S nanoparticules d'oxyde de fer de 7 nm est de 55 emu/g[15]) et de $CoFe_2O_4$ (le M_S de nanoparticules de ferrite de cobalt de 12 nm est de 66 emu/g).

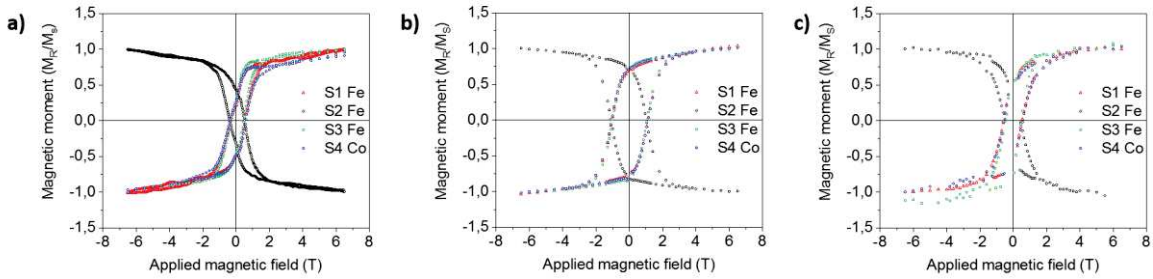

Figure 118. Hystérèse XMCD spécifique de l'élément enregistrées aux seuils du fer et du cobalt à 4 K pour a) CS_CoF1, b) CS_CoF2, c) CS_CoO.

L'enregistrement d'hystérèse sélective montrent que chaque nanoparticule a des champs coercitifs similaires au seuil S1, S2 et S3 du fer et au seuil S4 du cobalt. Ce qui démontre que les phases d'une nanoparticule sont fortement couplées entre elles.

La diffusion des atomes de Co dans le cœur d'oxyde de fer dans CS_CoFe1 est attribuée à une faible stabilité du précurseur commercial utilisé. En outre, l'absence de surfactant tel que l'acide oléique lors de la synthèse de la coquille a permis de décomposer encore plus rapidement le précurseur, favorisant ainsi les effets de diffusion. A l'opposé, le précurseur utilisé pour CS_CoFe2 était plus stable et l'utilisation d'acide oléique a également permis de le stabiliser. Il en résulte alors la croissance d'une coquille de ferrite de cobalt. Pour CS_CoO, la quantité de stéarate de cobalt a été multipliée par dix comparée à celle utilisée pour CS_CoFe1 et CS_CoFe2. Ainsi, seule une petite partie des atomes de Co ont diffusés dans le cœur et la majeure partie des monomères de Co ont formé la coquille de CoO. Les propriétés magnétiques enregistrées dépendent directement de la structure des nanoparticules. Les propriétés magnétiques ont été augmentées comparée à celle des cœurs respectifs qui est favorisée grâce à de bonnes relations d'épitaxie entre les phases. La T_B des nanoparticules de CS_CoFe2 est la plus grande car elle est la nanoparticule qui possède le cœur le plus large. En revanche le H_C de CS_CoFe1 est le plus grand car cette nanoparticule possède le cœur le plus petit et donc la plus grande anisotropie magnétique effective d'après le modèle de Stoner-Wohlfarth. Enfin, ce chapitre a démontré que le couplage d'échange dur-mou entre deux phases ferrimagnétiques est plus efficace que le couplage exchange bias entre une phase ferrimagnétique et une phase antiferromagnétique.

Chapitre III
Nanoparticules $Fe_{3-d}O_4$@CoO@$Fe_{3-d}O_4$

Le but de ce chapitre est de combiner l'expertise obtenue dans les deux chapitres précédents en synthétisant des nanoparticules coeur@coquille@coquille. Ainsi, en doublant l'interface ferrimagnétique antiferromagnétique dans des nanoparticules de base de $Fe_{3-d}O_4$@CoO, nous espérons pouvoir multiplier le couplage d'exchange-bias et donc augmenter l'anisotropie magnétique effective en synthétisant des nanoparticules $Fe_{3-d}O_4$@CoO@$Fe_{3-d}O_4$.

Ces nanoparticules sont synthétisées par une succession de trois décompositions thermiques. Tout d'abord le cœur d'oxyde de fer (C) est synthétisé suivant le même protocole que celui utilisé pour les deux chapitres précédents. Ces nanoparticules sont ensuite lavées avant d'être utilisées en tant que germes pour décomposer du stéarate de cobalt selon R = ($n_{précurseur\ coquille}$)/($n_{précurseur\ coeur}$) = 2 en présence d'acide oléique. Les nanoparticules de $Fe_{3-d}O_4$@CoO (CS) sont elles aussi lavées et utilisées en tant que germes pour décomposer du stéarate de fer dans les mêmes conditions que pour synthétiser le cœur en faisant varier la concentration de précurseur de fer avec un ratio R de 0.5 (CSSA), 1.0 (CSSB) et 1.5 (CSSC). Les nanoparticules finales de $Fe_{3-d}O_4$@CoO@$Fe_{3-d}O_4$ sont enfin elles aussi lavées.

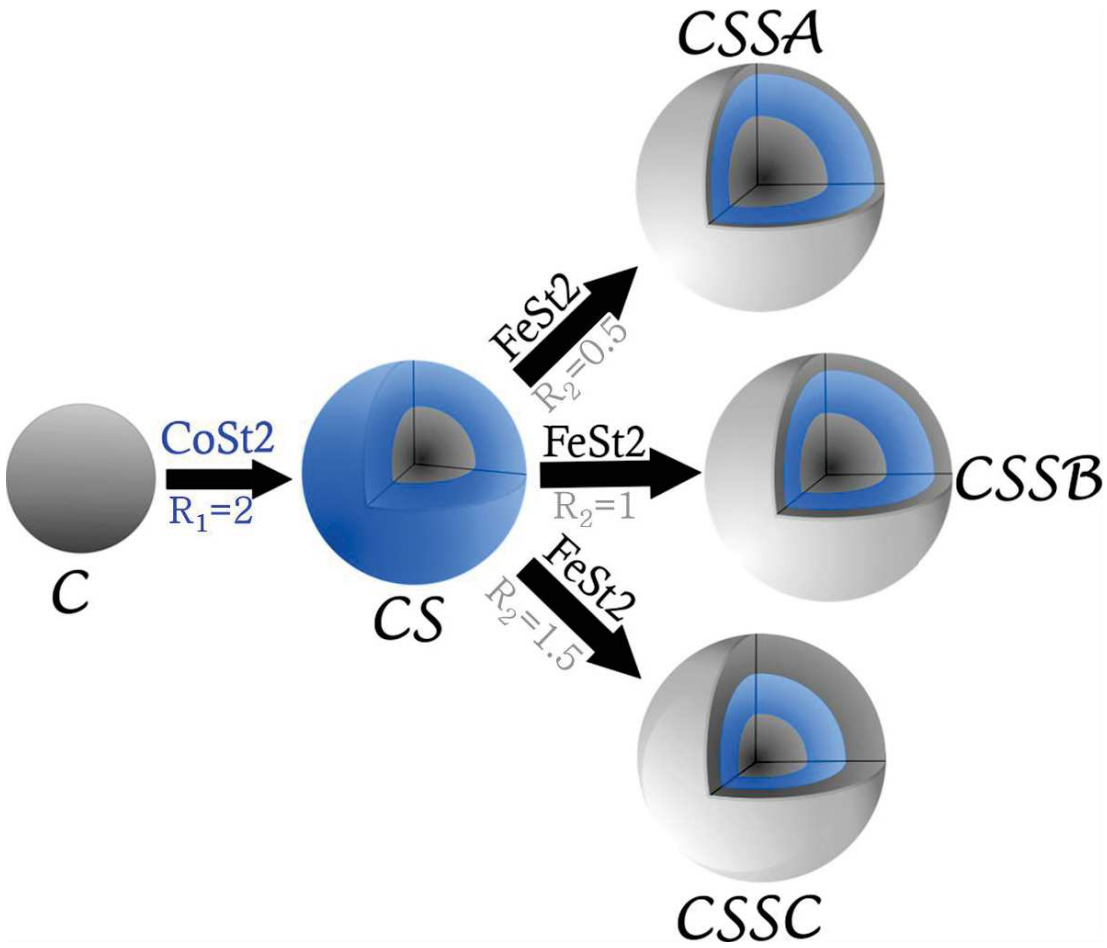

Figure 119. Illustration schématique de la succession de trois décompositions thermiques utilisée pour synthétiser les nanoparticules de $Fe_{3-d}O_4$@CoO@$Fe_{3-d}O_4$.

Les images MET montrent que les nanoparticules de cœur ont une forme proche des sphères avec une distribution en taille étroite centrée à 10.1 nm. La taille des objets augmente au fur et à mesure que

les coquilles croissent et passe à 14.0, 14.5, 15.1 et 15.6 nm pour CS, CSSA, CSSB et CSSC qui correspondent à des épaisseurs moyennes de 2.0, 0.3, 0.6 et 0.8 nm pour chaque coquille. La distribution en taille s'élargit et la morphologie s'éloigne peu à peu de la forme d'une sphère mais restent tout de même contrôlées.

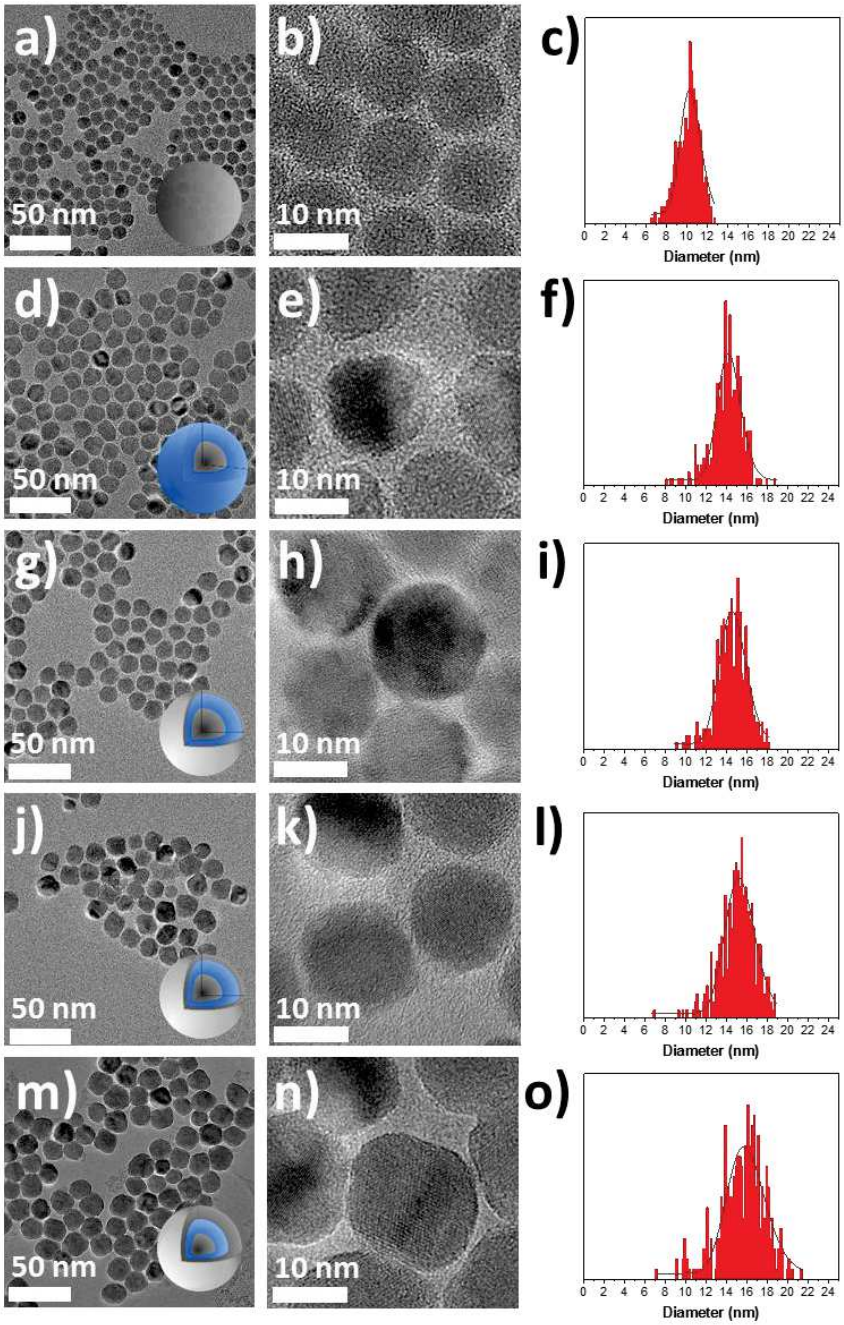

Figure 120. Images TEM avec la représentation schématique pour les nanoparticules de a, b) cœur, d, e) CS, g, h) CSSA, j, k) CSSB et m, n) CSSC avec c, f, i, l, o) leur distribution en taille correspondante.

Les analyses EDX montrent que CS contient à la fois du fer et du cobalt pour un ratio atomique Fe : Co de 45 : 55. Le fer augmente en proportion lorsque la deuxième coquille d'oxyde de fer croit avec des ratios de 57 : 43, 68 : 32 et 73 : 27. Cela démontre la bonne croissance de chaque phase.

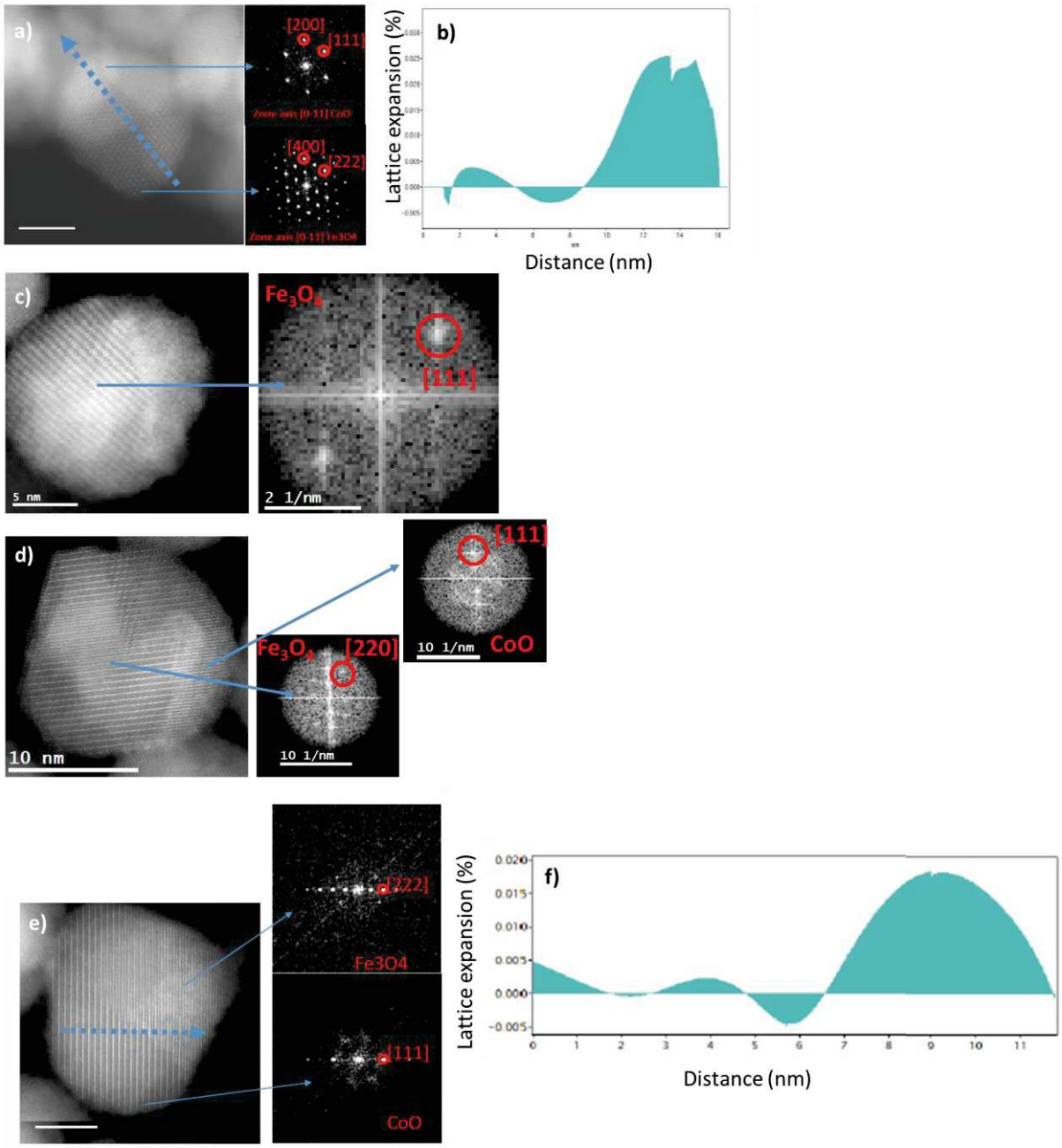

Figure 121. Images STEM haute résolution avec les FFT réalisées sur des axes de zone spécifiques des nanoparticules pour a) CS, c) CSSA, d) CSSB et e) CSSC. Analyse de phase géométrique pour b) CS et f) CSSC.

Sur les images TEM haute résolution, des franges continuent et périodiques sur l'ensemble de chaque nanoparticule sont perceptibles. Elles témoignent de la bonne épitaxie de chaque phase qui est favorisée par une cristallisation des phases dans des groupes d'espace similaires et parce qu'elles ont des paramètres de maille proche. L'analyse de phase géométrique (GPA) démontre tout de même la présence de contraintes cristalline de l'ordre de 2 % au sein des nanoparticules CS et CSSC. En effet, même si les paramètres de maille de Fe_3O_4 (8.396 Å, carte JCPDS n° 19-062) et CoO (4.26 Å, carte JCPDS n° 048-1719) sont très proches, elles ne sont pas identiques, ce qui mène à l'apparition de faibles contraintes cristallines pour faire concorder les mailles.

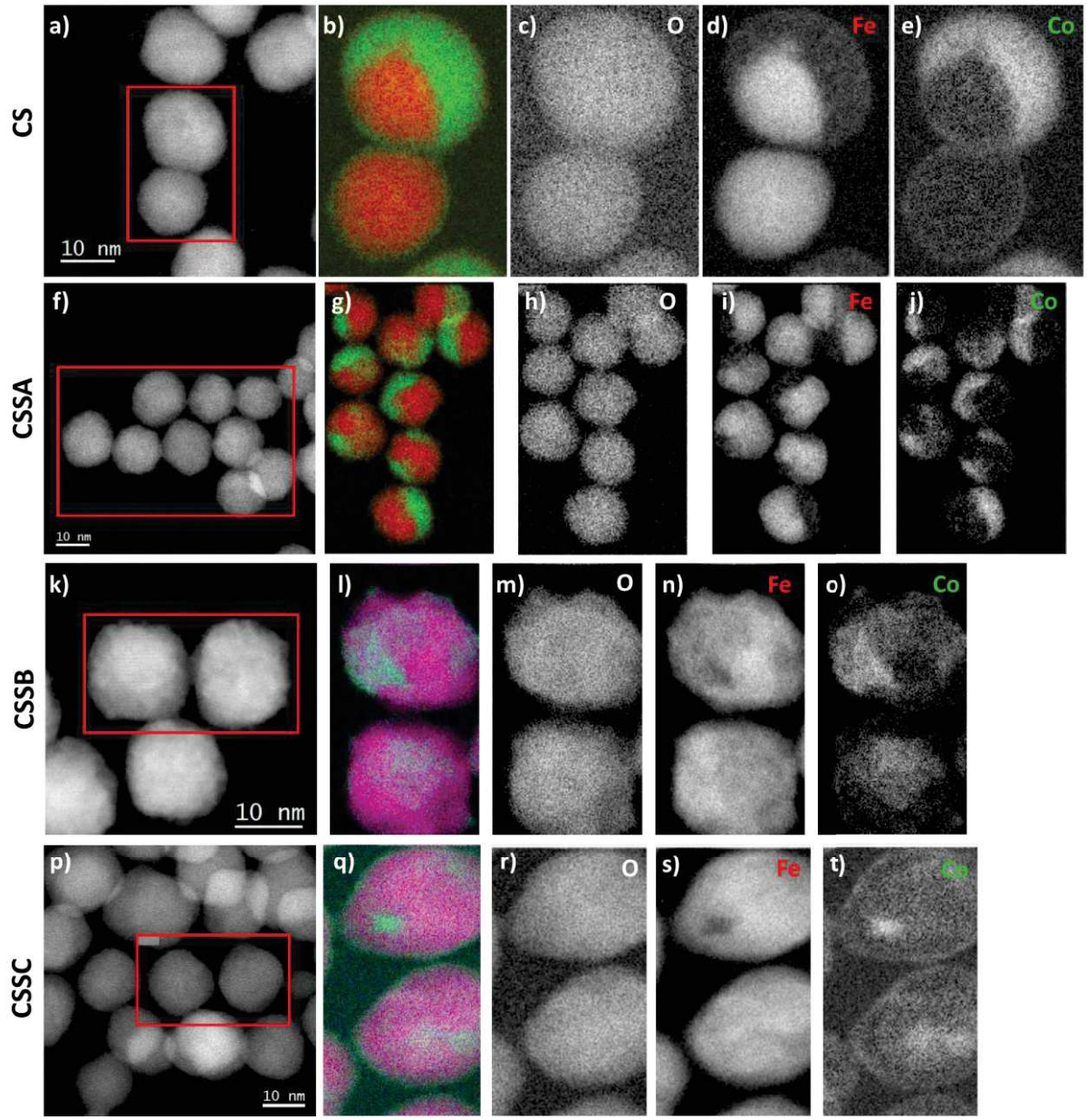

Figure 122. a, f, k, p) Image haute-résolution en champ sombre avec b, g, l, q) les cartographies EELS-SI composite correspondantes et les cartographies EELS-SI au seuil c, h, m, r) de l'oxygène, d, i, n, s) du fer et e, j, o, t) du cobalt pour les nanoparticules a-e) CS, f-j) CSSA, k-o) CSSB et p-t) CSSC.

Les analyses EELS-SI montrent la bonne formation de chaque coquille et la croissance de la dernière coquille. Cependant, les coquilles ne croissent pas de façon homogène. En effet, les nanoparticules présentent des facettes qui ont chacune des énergies différentes. Ainsi, les coquilles croissent à partir de facettes spécifiques puis s'étalent sur le reste de la nanoparticule.[16] Ces deux phénomènes sont gouvernés par des effets cinétiques de croissance qui dépendent de la concentration de monomères en solution et du temps de synthèse.

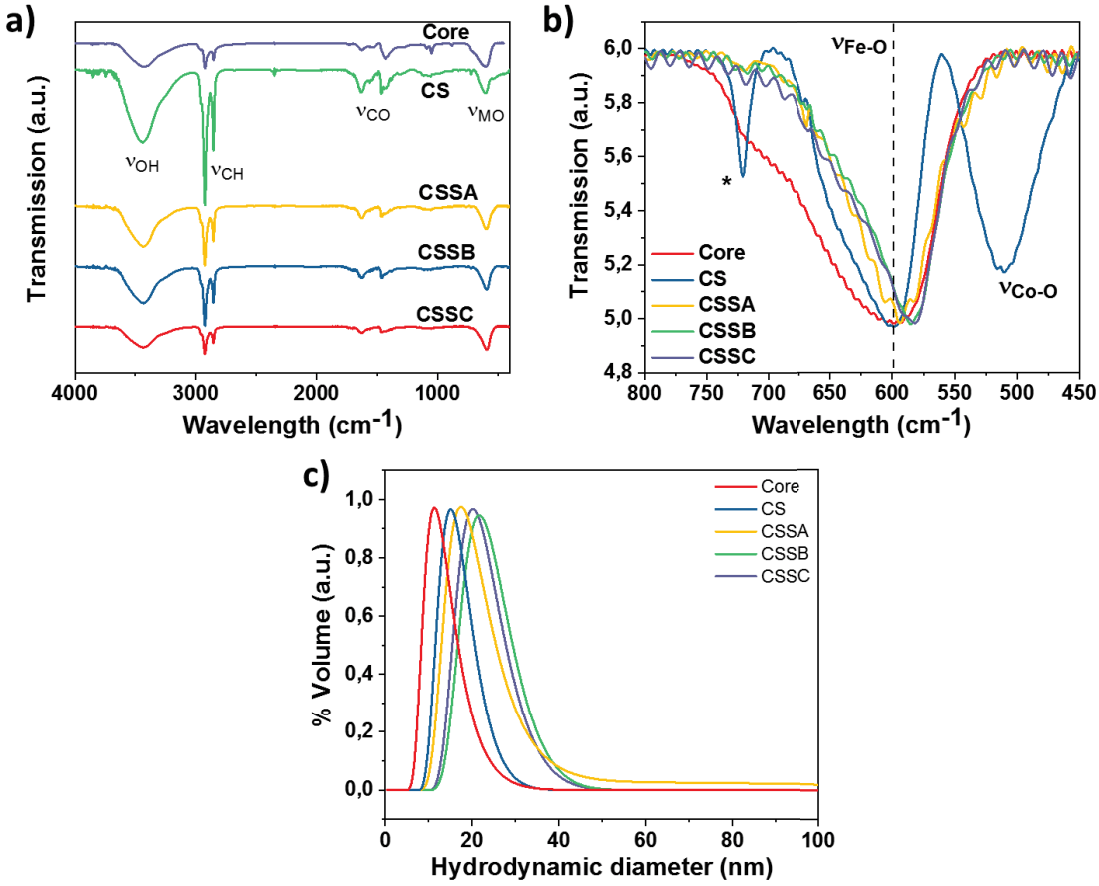

Figure 123. Spectres infrarouges des nanoparticules C, CS, CSSA, CSSB et CSSC de a) 400 à 4000 cm^{-1} avec b) un agrandissement entre 450 et 800 cm^{-1}. c) Granulométrie des nanoparticules C, CS, CSSA, CSSB et CSSC en volume.

La présence de ligands acide oléique à la surface des nanoparticules a été analysé par spectroscopie infrarouge à transformée de fourrier. En outre, en observant plus précisément la bande Fe-O centrée autour de 600 cm^{-1}, on observe que le cœur est partiellement oxydé, comme attendu. La bande se décale vers de plus faible longueur d'onde pour CS ce qui démontre une plus grande quantité de Fe^{2+} liée à la réduction chimique du cœur lors de la synthèse de la coquille qui ensuite protège le cœur contre les phénomènes futurs d'oxydation par exposition des nanoparticules à l'air. De façon surprenante, la bande évolue encore vers les longueurs d'ondes plus basses CSSA, CSSB et CSSC, témoignant de l'augmentation de la proportion de Fe^{2+}. Du fait de la fine couche d'oxyde de fer déposée, il aurait été normal que cette couche soit entièrement oxydée. Des analyses complémentaires sont ici nécessaires pour mieux étudier cette observation.

La présence de ligands organiques à la surface des nanoparticules leur permet d'être stable en solution tel que démontré par les analyses de granulométrie qui montrent une seule distribution de diamètre hydrodynamique centré à 11, 15, 17 22 et 20 nm pour C, CS, CSSA, CSSB et CSSC. Ces diamètres hydrodynamiques évoluent de façon cohérente avec les tailles mesurées à partir des images TEM mais sont cependant plus grand du fait que les ligands organiques participent eux aussi à la diffusion de la lumière dans les mesures de granulométrie.

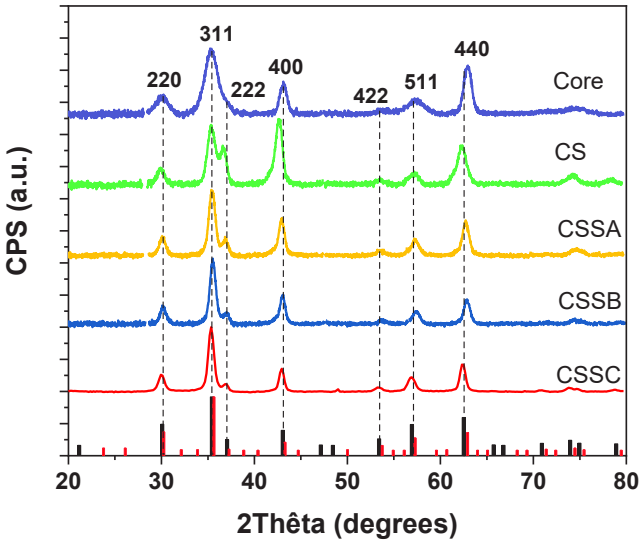

Figure 124. Diffractogrammes des nanoparticules C, CS, CSSA, CSSB et CSSC.

La structure cristalline des nanoparticules a été étudiée par diffraction des rayons X qui montrent que toutes les nanoparticules cristallisent comportent une phase de ferrite. Une contribution additionnelle de CoO est présente pour les nanoparticules CS, CSSA, CSSB et CSSC. Proportionnellement à la contribution de la ferrite, celle de CoO est très importante pour CS et sa quantité diminue à mesure que la deuxième coquille d'oxyde de fer croît. Les tailles de cristallites calculées à partir de la formule de Debye-Scherrer sont de 8.0, 9.1, 11.4, 12.2 et 12.7 nm, ainsi elles augmentent avec la croissance des coquilles, en accord avec les analyses TEM et de granulométrie.
Le paramètre de maille du cœur est de 8.379 Å, et est intermédiaire à celui de la magnétite et de la maghémite, en accord avec une nanoparticule partiellement oxydée, comme attendu de par sa taille. Le paramètre de maille augmente à 8.409 Å pour CS ce qui est plus haut que le paramètre de maille de la magnétite. Cela provient du fait que le cœur contient plus de Fe^{2+} que dans C mais aussi de la présence de contraintes cristallines. Enfin, ce paramètre de maille diminue un peu à 8.391 Å pour CSSA puis réaugmente à 8.401 puis 8.412 Å pour CSSB et CSSC ce qui démontre la présence de Fe^{2+} et de contraintes cristallines.

Afin d'étudier la structure interne plus en détails, des analyses de diffusion des rayons X aux petits angles (SAXS) ont été menées. Le SAXS permet de sonder un grand volume de nanoparticule en suspension dans un solvant organique transparent aux rayons X, ici le toluène. A partir de cela, il est possible de déterminer la taille des nanoparticules, leur polydispersité et facteur de forme. Comme le CoO et la magnétite ont des longueurs de diffusion différente ($\Delta\eta = 5.18\ 10^{-6}$ Å^{-2} pour Fe_3O_4 et $6.44\ 10^{-6}$ Å^{-2} pour CoO), leur contraste sera différent et donc il serait possible de les discriminer en SAXS. A contrario, comme la magnétite et la ferrite de cobalt ($\Delta\eta = 5.30\ 10^{-6}$ Å^{-2}) ont des longueurs de diffusion très proches, il ne sera pas possible de les discriminer. Les courbes log(I)=f(Q) remontent doucement à petits Q et forment presque un plateau ce qui prouve l'absence d'agrégats en solution. A grands Q, plusieurs oscillations sont présentes ce qui démontrent que la polydispersité des nanoparticules est très limitée. Enfin, il est possible de fitter ces courbes avec un modèle de sphère simple ou un modèle de sphère coeur@coquille. Cependant, ces analyses n'ont pas été concluantes et ont données des tailles et épaisseurs bien différentes de ce qui a été mesuré à partir des images TEM ou en RX.

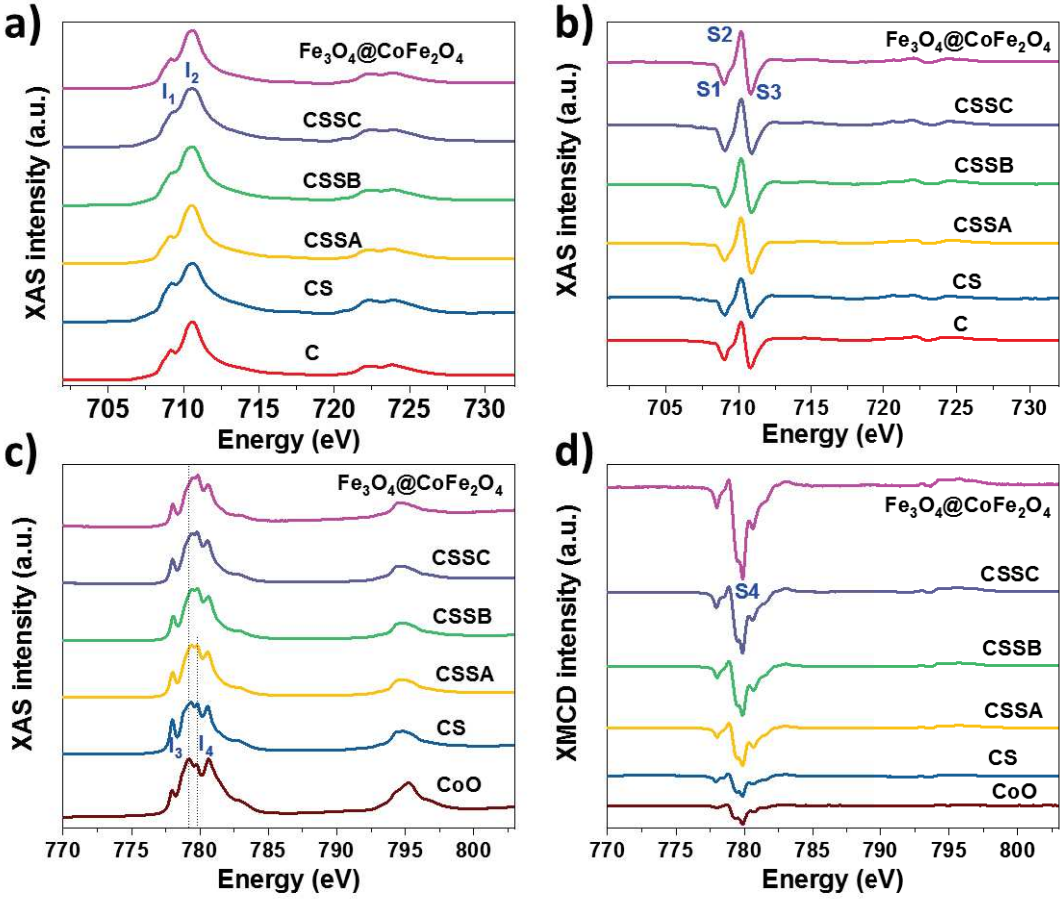

Figure 125. Spectres a, c) XAS et b, d) XMCD enregistrées aux seuils $L_{2,3}$ du a, b) fer et c, d) cobalt à 4 K sous un champ de 6,5 T.

L'environnement des atomes de Fe et de Co a pu être étudié séparément avec des analyses XAS et XMCD. Les spectres XAS et XMCD enregistrés au seuil $L_{2,3}$ du fer sont en accord avec une structure de ferrite pour chaque échantillon. Le calcul des ratios I1/I2 et (S1+S2)/(S2+S3) montrent que le cœur est effectivement partiellement oxydé et que CS contient plus de Fe^{2+} que C, en accord avec les analyses RX et FT-IR.

Au seuil $L_{2,3}$ du cobalt, les spectres XAS et XMCD sont typiques de Co^{2+} en sites Oh. Sur les spectres XAS du Co, les pic I3 et I4 sont particulièrement intéressants. Pour une structure CoO, le pic I4 est de plus faible intensité que le pic I3. En revanche, pour une structure $Fe_{3-d}O_4$@$CoFe_2O_4$, leurs intensités sont inversées et le pic I4 est de plus grande intensité que le pic I3. On observe que dans le cas de CS, le pic I4 est plus bas que le pic I3. Puis plus la seconde coquille d'oxyde de fer croit, plus la pic I4 augmente en comparaison du pic I3. Cela traduit une augmentation de la proportion de ferrite de cobalt au sein des nanoparticules coeur@coquille@coquille. Sur les spectres XMCD, les nanoparticules de CoO présentent une faible intensité du signal qui est produit par des phénomènes importants de canting de spin de surface du fait de la grande taille de la nanoparticule et de sa morphologie particulière. La nanoparticule CS présente aussi une faible intensité du signal XMCD dont une partie provient de possible phénomènes de canting de spin, l'autre provenant de la présence de spins de Co^{2+} non compensés où les Co^{2+} sont dans les sites Oh d'une structure de ferrite de cobalt. La croissance de la seconde coquille d'oxyde de fer augmente l'intensité du signal XMCD ce qui traduit une augmentation de la quantité de ferrite de cobalt au sein des nanoparticules. Celle-ci augmente par des phénomènes de diffusion tel qu'évoqué dans le chapitre II. Afin d'étudier si la diffusion des cations Co^{2+} de la première coquille de CoO diffusent plus lors de la synthèse à haute température de la seconde coquille, un échantillon de $Fe_{3-d}O_4$@CoO (CS2) a été rechauffé à haute température (CS2r) dans des conditions

similaires aux CSS mais sans ajout de précurseur. Il en résulte que la taille mesurée de CS2r à partir des images TEM est plus petite que celle de CS2. Cela est lié à un phénomène de resolubilisation partielle du germe[17] favorisé par la haute température du solvant. Les analyses XAS et XMCD ont ici montrés que la diffusion des cations Co^{2+} existe bien mais que celle-ci est vraiment très limitée.
Ainsi, l'augmentation de la proportion de ferrite de Co pour CSSA, CSSB et CSSC est lié à un phénomène de resolubilisation partielle du germe suivi par sa recristallisation avec les nouveaux monomères[17] pour former de la ferrite de cobalt.

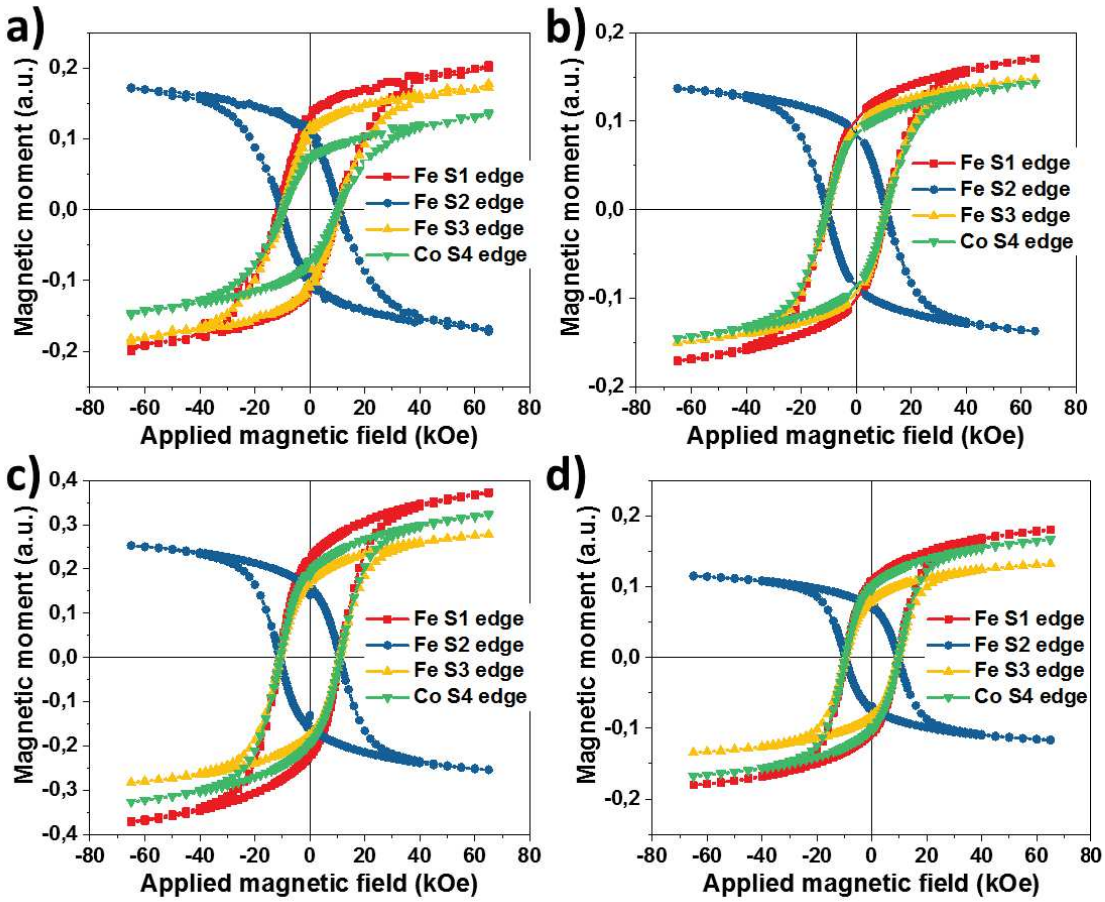

Figure 126. Hystérèse sélectives enregistrées à 4 K par spectroscopie XMCD aux seuils $L_{2,3}$ du fer et du cobalt pour a) CS, b) CSSA, c) CSSB et d) CSSC.

L'enregistrement d'hystérèse sélective aux seuils S1, S2, S3 du fer et S4 du cobalt pour CS, CSSA, CSSB et CSSC met en évidence que les champs coercitifs mesuré pour un échantillon sont tous similaires. Cela démontre que les phases d'oxyde de fer et de ferrite de cobalt sont magnétiquement couplées. L'approche lente et douce de la saturation pour toutes les hystérèses témoigne à la fois de ce fort couplage[18] et de la présence de CoO antiferromagnétique. Enfin, le ratio M_R/M_S est de 67 % pour CS et diminue vers 60 à 62 % pour CSSA, CSSB et CSSC. Cela démontre le comportement plus doux des nanoparticules CSSA, CSSB et CSSC qui est lié à l'ajout d'oxyde de fer magnétiquement doux comparé au CoO qui lui est magnétiquement plus dur.

Des spectres Mössbauer ont été enregistré hors champ et à 77 K pour chaque échantillon. Ils montrent que le cœur est partiellement oxydé et que la quantité de Fe^{2+} augmente dans CS, à l'instar de ce qui a été observé avec les analyses FT-IR, DRX et XAS. La spectroscopie Mössbauer montre également la présence de ferrite de cobalt au sein de CS puisque les hauts champs hyperfins calculés témoignent de la proximité d'atomes de fer avec ceux de cobalt. La quantité de ferrite de cobalt augmente

graduellement de CSSA à CSSC, de même que la coquille d'oxyde de fer. Seulement, l'augmentation de la ferrite de cobalt est proportionnellement plus grande que celle d'oxyde de fer ce qui affecte quelque peu les valeurs calculées. Grâce a cette étude, il est possible de déterminer une cartographie des nanoparticules qui sont composées d'un cœur de 6.8 nm de diamètre entouré d'une coquille de $CoFe_2O_4$ de 1.7 nm d'épaisseur avec 1.3 nm d'épaisseur de CoO puis 0.6, 0.5 et 0.6 nm d'épaisseur d'oxyde de fer pour CSSA, CSSB et CSSC respectivement.

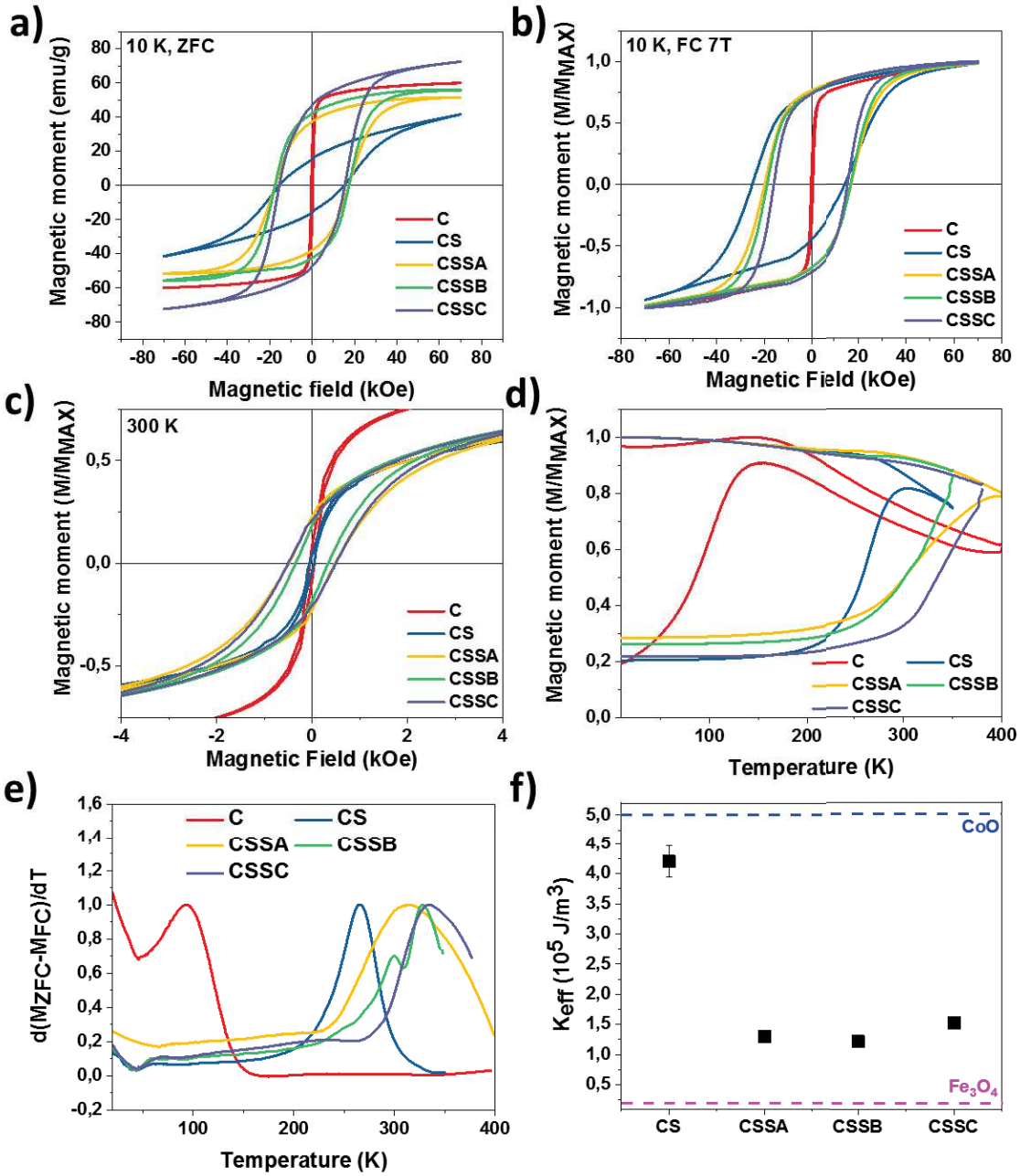

Figure 127. Propriétés magnétiques des nanoparticules C, CS, CSSA, CSSB et CSSC enregistrées par magnétométrie SQUID. Mesure de l'aimantation en fonction d'un champ appliqué à a) 10 K sans refroidissement sous champ, b) 10 K après refroidissement sous champ, c) 300 K. d) Mesure de l'aimantation en fonction de la température. e) Distribution de la température de blocage calculée à partir des mesures M(T) d). f) Constante d'anisotropie effective en fonction des différentes nanoparticules calculée à partir des fit de $H_C=f(T)$ d'après le modèle de Stoner-Wohlfarth.

Les propriétés magnétiques des nanoparticules ont été analysées par magnétométrie SQUID. L'aimantation enregistrée en fonction de la température (FC-ZFC) présente des T_{max} de 150, 290, 400

K pour C, CS, CSSA et au-delà de 400 K pour CSSB et CSSC. Ainsi T_{max} a été augmentée de C à CS grâce à la propriété d'exchange bias jusqu'à la T_N de CoO (290 K). Puis T_{max} augmente à nouveau avec l'ajout d'une seconde coquille d'oxyde de fer et augmente encore quand l'épaisseur de cette coquille augmente. A partir des courbes FC-ZFC, T_B sont determinées par la formule $d(M_{ZFC}-M_{FC})/dT$. Ainsi des T_B de 93, 266, 310, 298 et 335 K sont obtenues pour C, CS, CSSA, CSSB et CSSC respectivement. Grâce à l'ajout d'une coquille supplémentaire, T_B a été augmentée au-delà de la température ambiante.
A 10 K, le champ coercitif des nanoparticules C est de 0.4 kOe et augmente à 16.4 kOe pour CS grâce à la présence de ferrite de cobalt interfaciale mais aussi grâce à un fort couplage d'exchange bias. H_C augmente à 17.5 kOe pour CSSA, reste stable à 17.2 kOe pour CSSB puis diminue à 15.0 kOe pour CSSC. Le grand H_C pour CSSA et CSSB peut s'expliquer par l'augmentation de la phase de ferrite de cobalt. Puis la diminution de ce H_C dans CSSC est attribuée à la croissance de la phase douce d'oxyde de fer.

Pour mieux étudier les effets dur/doux, les champs coercitifs des échantillons CS, CSSA, CSSB et CSSC ont été mesuré à différentes températures. En appliquant la formule de Stoner-Wohlfarth au modèle obtenu, il est possible d'extraire les anisotropies magnétiques effectives de chaque échantillon. CS a un K_{eff} de 42.1 10^4 J/m^3 qui diminue à 13.0 puis 12.2 10^4 J/m^3 pour CSSA et CSSB. Cela est attribué à l'augmentation de la ferrite de cobalt qui augmente J_{int} et diminue $K_{AFM}V_{AFM}$. Puis, K_{eff} augmente à 15.3 10^4 J/m^3 dans CSSC qui est attribué à la présence d'une très grande quantité de ferrite de cobalt.

Les mesures d'aimantation en fonction d'un champ appliqué après refroidissement sous un champ de 7 T montre que CS a un grand H_E de 5.3 kOe. Ce H_E diminue à 2.8, 0.9 et 0.5 pour CSSA, CSSB et CSSC, ce qui conforte les hypothèses précédentes concernant la diminution de $K_{AFM}V_{AFM}$ et l'augmentation de J_{int} qui petit à petit tue l'exchange bias.
La quantité de ferrite de cobalt augmente ainsi aux dépends de la quantité de CoO comme montré par les analyses RX même s'il reste encore du CoO dans CSSC tel que mis en évidence par les analyses EELS. CoO n'est alors plus suffisant pour régir seul les propriétés magnétiques des nanoparticules.

L'aimantation à saturation de CS est faible (41 emu/g) du fait de la présence de CoO AFM à la surface des NPs. Le M_S augmente ensuite à 51, 55 puis 72 emu/g pour CSSA, CSSB et CSSC du fait de la diminution de la phase antiferromagnétique de CoO et de l'augmentation des phases d'oxyde de fer et de ferrite de cobalt.
Le ratio M_R/M_S traduit la forme carrée de l'hystérèse. Il est de 38 % pour CS ce qui est inférieur aux 50 % attendus pour des nanoparticules magnétiques orientées de façon aléatoire. Ainsi l'hystérèse de CS est quelque peu penchée du fait du fort couplage d'exchange bias et aussi de la forte contribution antiferromagnétique du CoO. Ce ratio augmente à 59, 68 et 66 % pour CSSA, CSSB et CSSC traduisant une augmentation de la proportion de phase ferrimagnétique dure donc de ferrite de cobalt.

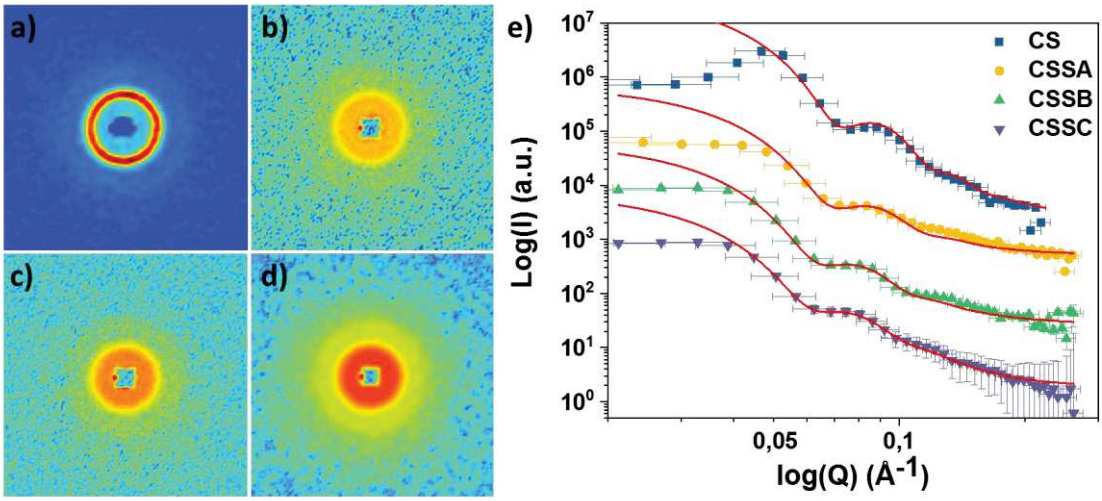

Figure 128. Carte 2D de diffusion des neutrons aux petits angle pour a) CS, b) CSSA, c) CSSB, d) CSSC avec e) leurs intégrations circulaires moyenne en fonction du vecteur de diffusion Q, les courbes en rouge correspondent aux courbes affinées.

La diffusion des neutrons aux petits angles (SANS) est une technique très complémentaire au SAXS et à l'absorption des rayons X. En effet, les neutrons ne vont plus interagir avec l'environnement électronique des atomes mais directement avec leur noyau. Cela permet de déterminer la composition chimique des nanoparticules, leur taille, leur polydispersité et leur forme.

L'image 2D des nanoparticules CS présente un bel anneau de corrélation qui provient d'agrégats présent dans l'échantillon. Les nanoparticules ayant été mesurée sous forme de poudre, il est normal que le séchage des solutions ait provoqué leur agrégation. A l'opposé, les images 2D de CSSA, CSSB et CSSC montrent de belles tâches circulaires. L'intégration de ces images en 1D produit des courbes de log(I)=f(Q). A des faibles valeurs du vecteur de diffusion Q, un pic de structure apparaît pour CS, il provient des agrégats. Ce pic n'est pas présent dans les courbes 1D des autres nanoparticules qui présentent un beau plateau aux petites valeurs du vecteur Q, témoignant de l'absence d'agrégats. Au moins deux oscillations sont perceptibles dans chaque courbe, elles montrent la faible polydispersité des nanoparticules.

Ces courbes sont ensuite affinées avec un modèle mathématique de sphère coeur@coquille où la coquille est considérée comme étant CoO (CS) ou CoO@$Fe_{3-d}O_4$ (CSSA, CSSB et CSSC). Ainsi, un rayon de cœur de 4.5 (CS) et 4.3 (CSSA, CSSB et CSSC) nm est déterminé. Sa valeur correspond à celle mesurée à partir des images TEM (5.05 nm) ou en DRX (4.0 nm). L'épaisseur de la coquille augmente de 2.2, 2.3, 2.8 à 3.0 nm pour CS, CSSA, CSSB et CSSC selon des épaisseurs qui sont en accord avec les données TEM et RX. Tout comme dans le cas du SAXS, du fait de longueur de diffusion très proche entre la magnétite ($6.9\ 10^{-6}$ Å^{-2}) et la ferrite de cobalt ($6.1\ 10^{-6}$ Å^{-2}), il n'est pas possible de discriminer ces deux éléments. En revanche, celle de CoO ($4.3\ 10^{-6}$ Å^{-2}) est suffisamment différente de la magnétite pour estimer la composition de chaque phase en termes de ferrite / CoO. On aperçoit alors que la quantité de CoO est très importante dans le cas de CS et diminue au profit de la quantité de ferrite pour CSSA, CSSB et CSSC, en accord avec les données EDX, EELS, DRX et XAS XMCD.

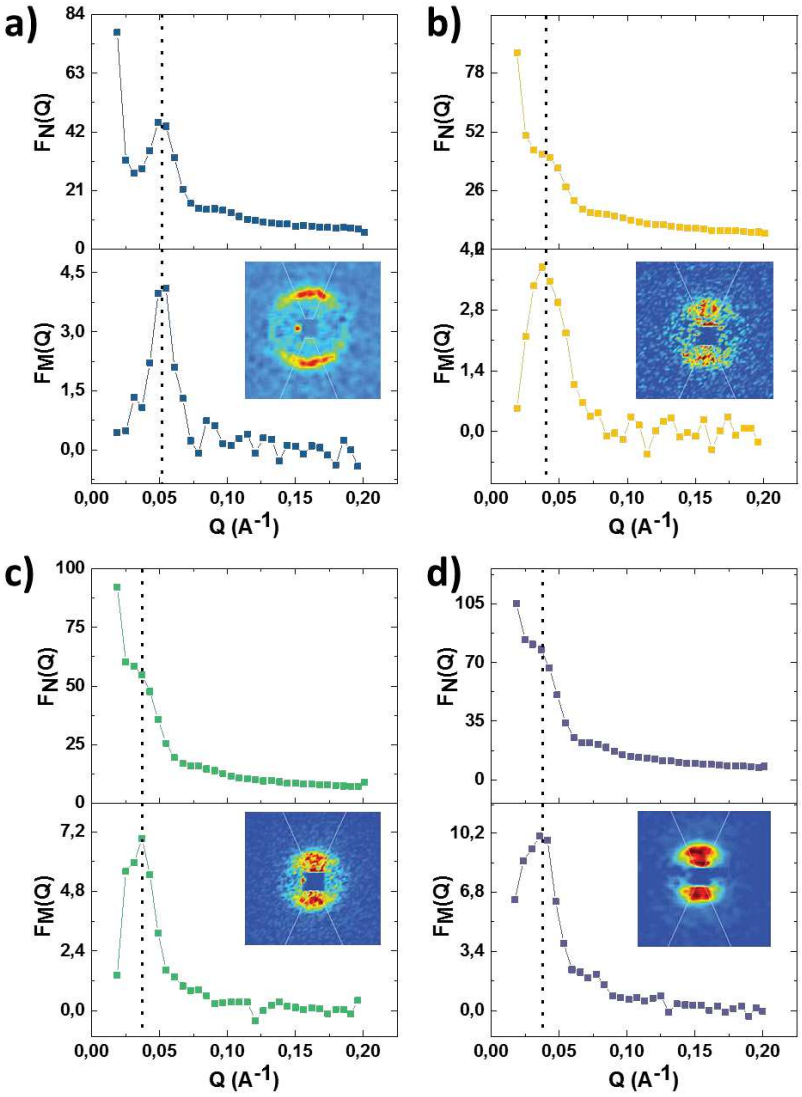

Figure 129. Courbes 1D de $[I^+(Q)+I^-(Q)]/2$ avec les facteurs nucléaires au-dessus et les facteurs magnétiques perpendiculaires $I^+(Q)-I^-(Q)$ en-dessous avec les courbes 2D correspondantes en encart où les secteurs angulaires (lignes blanches) montrent les aire d'intégration utilisées pour générer les courbes 1D pour a) CS, b) CSSA, c) CSSB et d) CSSC. Les lignes servent de guide pour les yeux et les pointillées noirs montrent la correspondance des maximums entre les facteurs nucléaires et magnétiques.

En utilisant des neutrons polarisés, le p-SANS permet d'étudier la structure magnétique interne des nanoparticules et de la comparer à sa structure nucléaire. En plaçant l'échantillon sous un champ de 3 T à 150 K, on voit apparaître des tâches asymétriques sur le signal 2D. Toutes les nanoparticules ne présentent aucun contraste perpendiculaire au champ tandis qu'un contraste parallèle au champ est visible. Cela témoigne d'une anisotropie magnétique au sein de l'échantillon dont les moments magnétiques sont orientés parallèlement au champ magnétique appliqué. En intégrant les contrastes verticaux observé, on aperçoit que les pics des courbes 1D sont aux mêmes positions que les oscillations des courbes de facteur nucléaire, ce qui démontre l'absence de canting de spin au sein des nanoparticules. De plus, l'intensité des courbes $F_M(Q)$ est directement reliée au moment magnétique des nanoparticules qui passe de 8.8 % pour CS à 12.9 % pour CSSC et démontre alors la bonne augmentation du moment magnétique à mesure que la nanoparticule croît.

De ces faits, la décomposition de stéarate de cobalt en présence de nanoparticules d'oxyde de fer en tant que germes a permis de faire croître une coquille de CoO avec une phase interfaciale de ferrite de cobalt produite par diffusion et par effets de solubilisation partielle-recristallisation. Grâce à un fort

couplage d'exchange bias, qui est démontré avec notamment la présence d'un grand champ d'échange mesuré sur les cycles M(H) à 10 K après refroidissement sous champ, la stabilité magnétique des nanoparticules d'oxyde de fer de base a pu être augmenté jusqu'à 266 K. Au-delà de cette température, la coquille antiferromagnétique de CoO perd son ordre magnétique et sa faculté de polariser magnétiquement le cœur d'oxyde de fer. La décomposition de stéarate de fer en présence des nanoparticules de $Fe_{3-d}O_4$@CoO mène à la synthèse de ferrite de cobalt interfaciale aux dépends de la phase de CoO. La phase de ferrite de cobalt augmente plus la quantité de précurseur de fer ajoutée est importante. Dans le même temps, une coquille d'oxyde de fer croît également avec une épaisseur de plus en plus importante lorsque la quantité de précurseur de fer ajoutée augmente. L'oxyde de fer en surface n'est pas oxydé contrairement à ce que nous attendions. Les raisons de sa stabilisation sont pour le moment inconnues et nécessitent de plus amples analyses.
Grâce à cette démarche, les propriétés magnétiques ont encore été augmentées et la T_B passe même au-delà de la température ambiante. En effet, des champs coercitifs de 300 à 500 Oe ont été mesurés à 300 K pour CSSA, CSSB et CSSC. Cependant, la propriété d'exchange bias diminue à mesure que la nanoparticule croît. Cela est lié à l'augmentation volumique de la phase dure de ferrite de cobalt aux dépends de la phase de CoO. Néanmoins, un faible H_E est toujours présent même pour CSSC. Ainsi, on ne peut encore déterminer si l'augmentation des propriétés magnétiques est lié à un fort couplage d'échange dur/doux entre les phases d'oxyde de fer et de ferrite de cobalt ou à un phénomène d'exchange bias.

Chapitre IV
Nanoparticules $Fe_{3-d}O_4@CoFe_2O_4@Fe_{3-d}O_4$

Dans ce chapitre, l'influence de la propriété de couplage d'échange dur/doux sur des nanoparticules est étudié. En effet, la présence d'une phase dure de $CoFe_2O_4$ sur une phase douce de magnétite permet d'augmenter significativement l'anisotropie magnétique effective. En doublant ainsi l'interface par la synthèse de nanoparticules $Fe_{3-d}O_4@CoFe_2O_4@Fe_{3-d}O_4$ dur/doux, on espère également pouvoir augmenter encore cette anisotropie. L'étude de ces nanoparticules permettra également de déterminer l'origine des propriétés magnétiques observée dans les nanoparticules de $Fe_{3-d}O_4@CoO@Fe_{3-d}O_4$.

Le cœur (C) est synthétisé tel que décrit dans les chapitres précédents. A la fin de sa synthèse, le milieu réactionnel est laissé à refroidir à 100 °C puis un mélange de stéarate de cobalt : stéarate de fer (1 :2) dans de l'octadécène est ajouté selon R = 0.8. Le milieu est alors rechauffé à ébullition. A la fin les nanoparticules de $Fe_{3-d}O_4@CoFe_2O_4$ (CS) sont lavées puis la moitié est utilisée en tant que germes pour décomposer du stéarate de fer dans du dioctyl éther. Le milieu est à nouveau chauffé et les nanoparticules de $Fe_{3-d}O_4@CoFe_2O_4@Fe_{3-d}O_4$ (CSS) sont enfin lavées également.

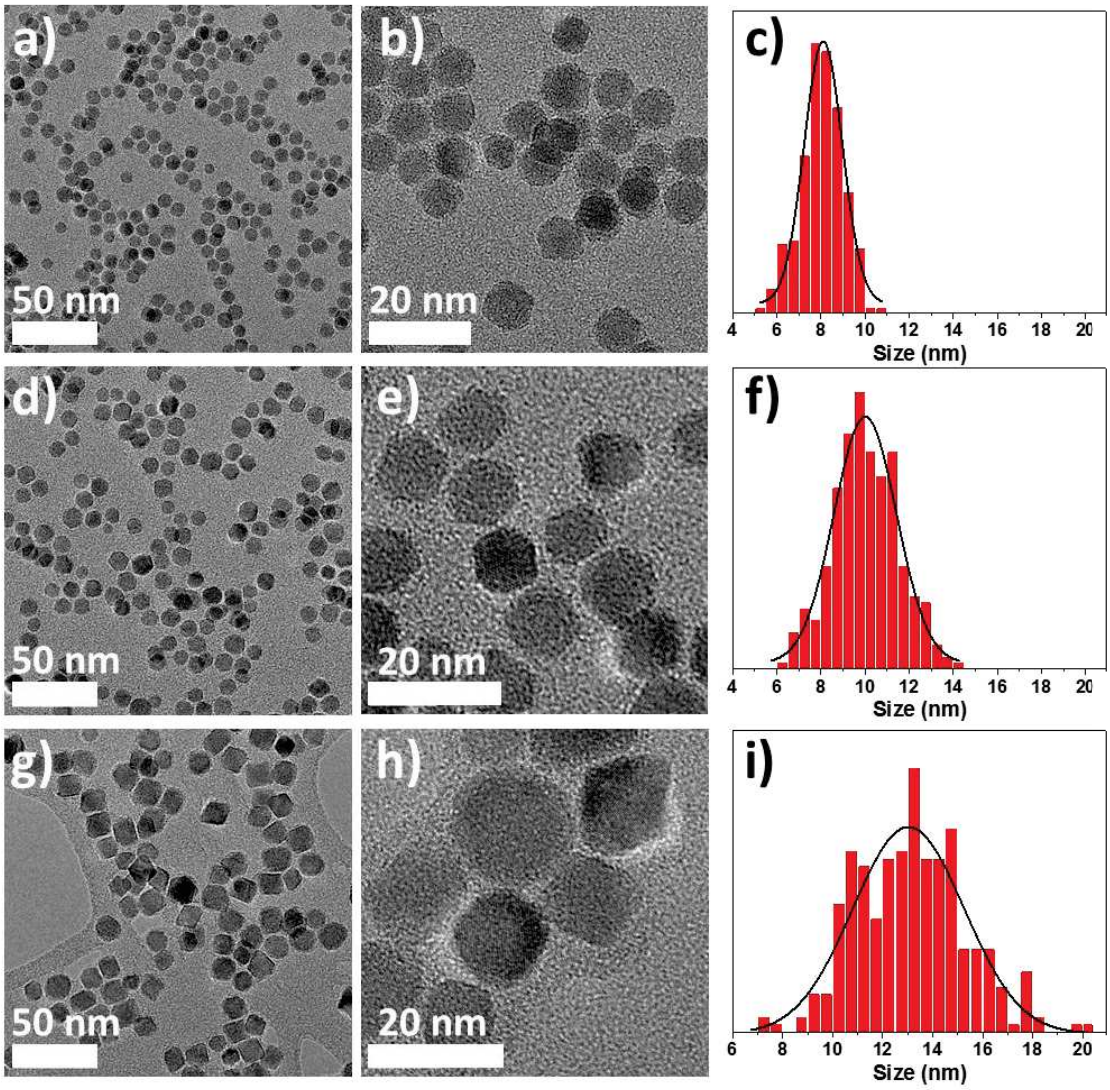

Figure 130. Images MET des nanoparticules a, b) C, d, e) CS et g, h) CSS avec c, f, i) leur distribution de taille correspondante.

Les images TEM montrent que les nanoparticules ont toutes des formes proches de sphères avec une distribution en taille étroite centrée à 8.0, 10.0 et 13.1 nm pour C, CS et CSS. Correspondant à des épaisseurs de coquille de 1.0 et 1.6 nm pour CS et CSS.

L'analyse EDX montre la présence d'atome de cobalt pour CS en proportion 86 : 14 (Fe : Co). Ce ratio augmente à 94 : 6 dans CSS démontrant l'augmentation de la phase d'oxyde de fer.

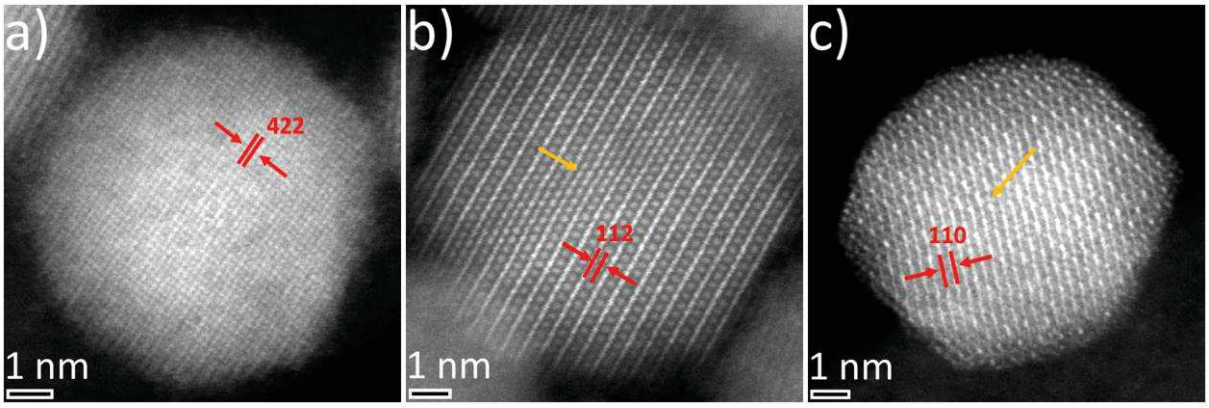

Figure 131. Images STEM des nanoparticules a) C, b) CS et c) CSS montrant leur microstructures. Les indications en rouge montrent les axes de zone respectifs. Les flèches jaune indiquent des défauts cristallins.

Sur les images STEM haute résolution, on aperçoit des franges périodiques et continuent sur l'ensemble des nanoparticules. Les distances interréticulaires peuvent être indexées selon une structure de magnétite. Cependant, certains défauts apparaissent sur les images de CS et CSS qui sont attribués à la présence de défauts d'empilements qui provient certainement de la discordance des réseaux. Cela est démontré avec des analyses de phase géométrique où la présence de contraintes cristalline est perceptible. Néanmoins, les coquilles ont crû de manière épitaxiée sur les germes.
La distribution spatiale des atomes Fe et Co est analysée à l'aide de la technique EELS-SI. Les atomes de Fe et de Co ont une distribution similaire dans chaque nanoparticule qui est en accord avec une structure $Fe_{3-d}O_4$@$CoFe_2O_4$ pour CS. En revanche, la seconde coquille de $Fe_{3-d}O_4$ n'est ici pas perceptible pour CSS.
Les spectres EELS enregistrés à différents endroits sur une même nanoparticule de chaque échantillon (bords et centre) sont en accord avec les données EELS-SI. Ils montrent en plus la forme sphérique des nanoparticules puisque les spectres sont moins intenses sur les bords qu'au centre.

La présence de ligands à la surface des nanoparticules est démontrée par spectroscopie infrarouge à transformée de Fourier. Ils permettent aux nanoparticules d'être stable en suspensions dans les solvants organiques communs avec des diamètres hydrodynamiques de 8.7, 13.5 et 18.2 nm pour C, CS et CSS.

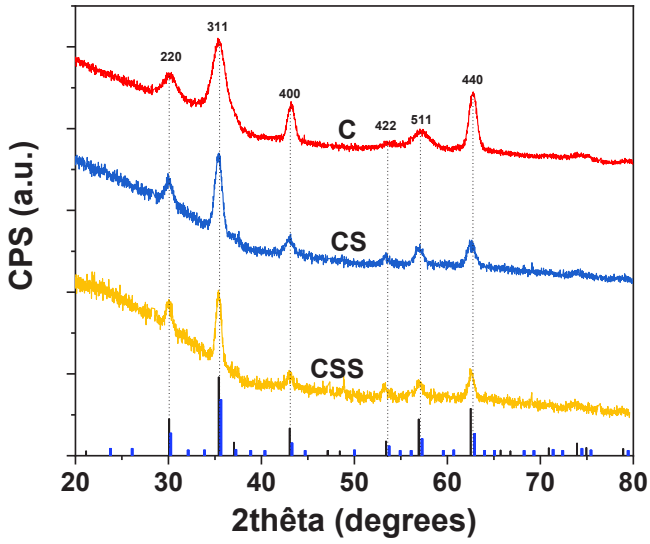

Figure 132. diffractogrammes des nanoparticules C, CS et CSS. Les barres noire et bleue correspondent aux phases Fe_3O_4 (JCPDS card n° 19-062) et $CoFe_2O_4$ (JCPDS card n°00-022-1086) respectivement.

Les diffractogrammes RX montrent que les nanoparticules ont toutes une structure spinelle inverse. En effet, la magnétite et la ferrite de cobalt cristallisant dans un même groupe d'espace (Fd-3m) avec des paramètres de maille très proche, il n'est pas possible de les distinguer. A mesure que la nanoparticule croit, les pics du diffractogramme s'affinent, il en résulte des tailles de cristallite de 7.4, 10.1 et 12.0 nm pour C, CS et CSS. Ces tailles augmentent de façon cohérente à ce qui a été observé au TEM.

Le paramètre de maille de C (8.370 Å) est en accord avec une nanoparticule partiellement oxydée. Le paramètre de maille augmente à 8.412 Å pour CS du fait d'une plus grande quantité de Fe^{2+} que dans C, de la présence de ferrite de cobalt et aussi de par la présence de contrainte cristalline. Il reste identique à CS dans le cas de CSS (8.410 Å).

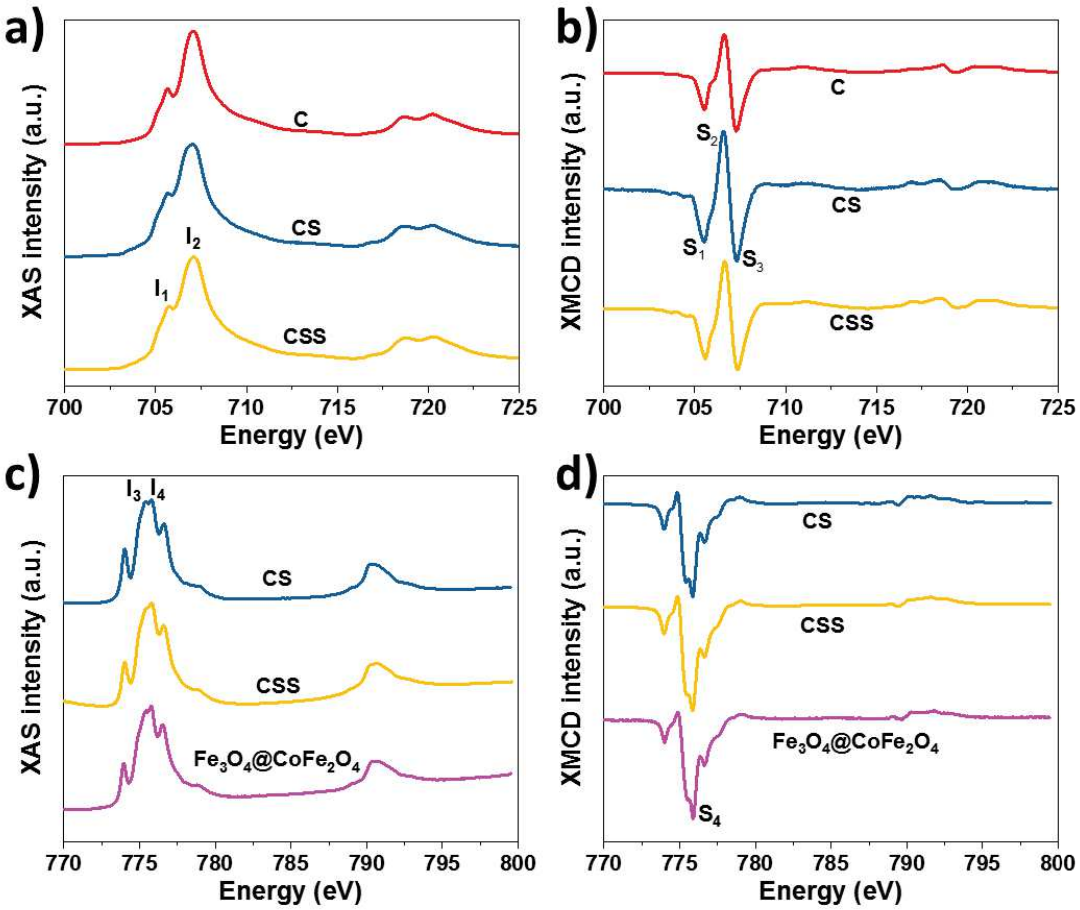

Figure 133. Spectres a, c) XAS et c, d) XMCD des nanoparticules C, CS et CSS enregistrés aux seuils $L_{2,3}$ du a, b) fer et c, d) cobalt à 4 K et sous un champ de 6,5 T.

Les spectres XAS et XMCD enregistrés au seuils $L_{2,3}$ du fer sont typique d'une structure ferrite. Les ratios I1/I2 et (S1+S2)/(S2+S3) montrent que CS contient plus de Fe^{2+} que C et que la proportion de Fe^{2+} augmente encore dans CSS. Ils démontrent également que la seconde coquille a en réalité une composition chimique similaire à celle de CS donc que la proportion de ferrite de cobalt a augmentée dans CSS, ce qui explique les paramètres de maille similaire calculés pour CS et CSS. Cela est lié à la présence de précurseur de cobalt résiduel lors de la décomposition du stéarate de fer pour la synthèse de la dernière coquille. Ces analyses sont en accord avec les spectres XAS et XMCD enregistrés au seuil $L_{2,3}$ du cobalt où l'on observe que le pic I4 augmente encore plus dans CSS en comparaison à CS et que le signal XMCD est plus intense pour CSS que pour CS.

L'oxydation partielle de C est démontrée avec les analyses Mössbauer qui montrent également que la quantité de Fe^{2+} est plus importante dans CS que dans C du fait de la préservation de la magnétite par la coquille de ferrite de cobalt. La quantité de Fe^{2+} diminue ensuite dans CSS en comparaison à C. Et les valeurs moyennes de déplacement isomérique permettent de déterminer la composition des nanoparticules qui résultent en un cœur d'oxyde de fer de 6.8 nm de diamètre entouré d'une coquille de ferrite de cobalt de 1.6 nm d'épaisseur pour CS.
Dans le cas de CSS, le cœur reste stable tandis que l'épaisseur de la coquille de ferrite de cobalt augmente à 2.9 nm avec à sa surface une coquille d'oxyde de fer de 0.3 nm d'épaisseur.
Cette fine épaisseur est inférieure à la résolution de 0.5 nm du TEM, c'est pourquoi il n'était pas possible de la voir dans les analyses EELS-SI.

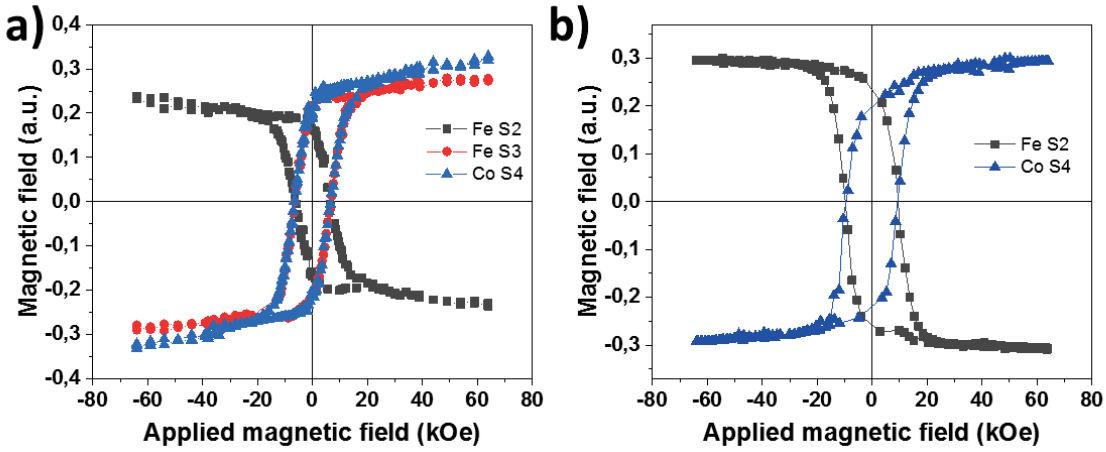

Figure 134. Hystérèse sélective enregistrés en XMCD à 4 K aux seuils $L_{2,3}$ du fer et du cobalt pour a) CS et b) CSS.

Les hystérèses sélectives enregistrées aux seuils S2 du fer et S4 du cobalt pour CS et CSS montrent que les champs coercitifs sont identiques entre les seuils pour chaque échantillon. Cela témoigne d'un fort couplage d'échange entre les phases d'oxyde de fer et de ferrite de cobalt. De plus, leur rapport M_R/M_S sont haut et similaire (69 et 67 % pour CS et CSS) ce qui démontre la présence de la phase dure de ferrite de cobalt et la composition chimique similaire de la deuxième coquille dans CSS vis-à-vis de CS.

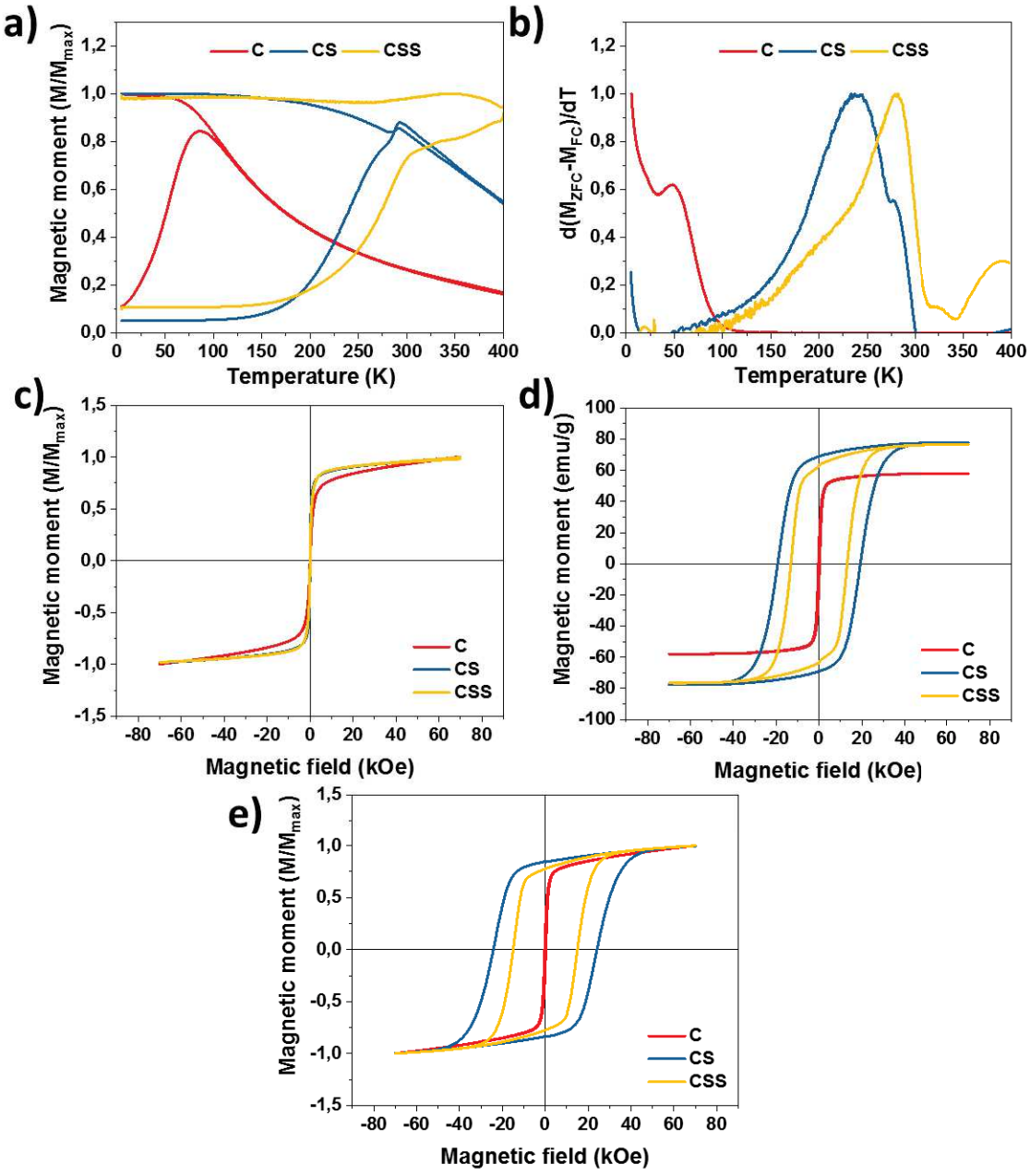

Figure 135. Propriétés magnétiques des nanoparticules C, CS et CSS mesurées par magnétométrie SQUID. a) Mesure de l'aimantation en fonction de la température. b) Distribution de T_B calculée à partir de a). Mesure de l'aimantation en fonction d'un champ appliqué à c) 300 K, d) 5 K sans refroidissement sous champ, e) 5 K après refroidissement sous champ.

Cette structure permet alors d'augmenter la T_{max} de 86 K (C) à 290 (CS) puis 301 K (CSS) et les cycles M(H) enregistrés à 300 K montrent que toutes les nanoparticules ont un comportement superparamagnétique à température ambiante.

La croissance de la première coquille a permis d'augmenter le champ coercitif mesuré à 5 K de 0.3 à 19.2 kOe grâce à un fort couplage d'échange dur/doux entre les phases. En revanche, l'ajout de la seconde coquille diminue H_C à 13.1 kOe. Cela était au départ attribué à la croissance de la phase magnétite. Seulement, il apparaît que C a un K_{eff} de 6.2 10^4 J/m^3 qui augmente à 15.8 10^4 J/m^3 pour CS et qui diminue ensuite à 8.2 10^4 J/m^3 pour CSS. Or, il était attendu que la présence d'une double interface dur/doux augmente encore l'anisotropie magnétique effective. Cela plus le fait que la variation de T_B soit moins importante avec l'ajout de la seconde coquille qu'avec l'ajout de la première

montre que l'ajout de la seconde coquille ne produit pas un couplage d'échange supplémentaire. En effet, son effet sur les propriétés magnétiques est seulement lié à des effets de volume.

De même, le ratio M_R/M_S est de 26 % pour C puis augmente à 89 % pour CS et reste quasiment similaire pour CSS (82 %). Cela démontre une augmentation de la dureté magnétique de la nanoparticule avec la croissance de ferrite de cobalt en première coquille. Puis comme la seconde coquille a une composition chimique similaire à celle de la nanoparticule CS, le ratio M_R/M_S n'évolue pas.
De la même manière, l'aimantation à saturation augmente de 58 à 78 emu/g de C à CS puis reste similaire à CS pour CSS (77 emu/g).

Ainsi, les nanoparticules synthétisées ont bien une structure $Fe_{3-d}O_4$, $Fe_{3-d}O_4@CoFe_2O_4$ et $Fe_{3-d}O_4@CoFe_2O_4@Fe_{3-d}O_4$ qui ont été démontré à l'aide des techniques DRX, XAS, Mössbauer et TEM. Cependant lors de la croissance de la seconde coquille, de la ferrite de cobalt a également crû du fait des résidus de précurseur de cobalt. La coquille de ferrite de cobalt est passée de 1.3 à 2.9 nm d'épaisseur. Et une coquille de 0.3 nm d'épaisseur a été ajoutée dans la deuxième coquille.
La première coquille permet d'augmenter significativement les propriétés magnétiques de la nanoparticule d'oxyde de fer de base grâce à un fort couplage d'échange dur/mou. Cependant, bien que fine et présente, la seconde coquille d'oxyde de fer ne participe pas à un couplage d'échange supplémentaire et la faible augmentation de T_B de CSS (en comparaison à CS) est uniquement liée à un effet de volume.
Cette étude a donc démontré que les propriétés magnétiques enregistrées pour les nanoparticules $Fe_{3-d}O_4@CoO@Fe_{3-d}O_4$ ne sont pas uniquement liée à la présence d'un couplage d'échange dur/doux mais à la présence des couplages d'échange dur/mou et d'exchange-bias qui agissent en synergie permettant alors la présence d'un champ coercitif à température ambiante pour une taille de nanoparticule inférieure à 16.0 nm.

Chapitre V
Nanoparticules de $Fe_{3-d}O_4$@CoO@NiO

Le but de ce dernier chapitre est de synthétiser des nanoparticules de $Fe_{3-d}O_4$@CoO@NiO afin de bénéficier des propriétés magnétiques des nanoparticules de $Fe_{3-d}O_4$@CoO et de la proximité antiferromagnétique du NiO qui grâce à sa haute T_N de 525 K pourrait permettre d'augmenter la T_B des nanoparticules coeur@coquille@coquille.
La synthèse de nanoparticules de NiO par décomposition thermique est très peu reportée dans la littérature et les nanoparticules obtenues n'ont pas une forme et une taille contrôlée. C'est pourquoi en premier lieu une étude de la décomposition de différents précurseurs organométallique de nickel a été menée. Après avoir déterminé un précurseur satisfaisant, sa décomposition a été faite seule et en présence de nanoparticules servant en tant que germes.

Les précurseurs de fer et de cobalt utilisés durant cette thèse sont composés de stéarate. Le premier précurseur étudié en vue de former des nanoparticules de NiO est donc le stéarate de nickel. Il est synthétisé par co-précipitation entre du stéarate de sodium et du chlorure de nickel. Le produit vert obtenu est ensuite séché.

Son spectre infrarouge est similaire à celui des précurseurs de stéarate de cobalt et de fer et démontre une coordination mixte chélate et bidentate pontant à l'instar des autres précurseurs susnommés. Les mesures de DTG montrent qu'il est cependant bien plus stable thermiquement que les deux autres précurseurs. Sa décomposition dans du docosène (T_{eb} = 367 °C) a permis de synthétiser de petites nanoparticules de NiO dont le lavage s'est avéré extrêmement difficile du fait que le docosène est solide à température ambiante. Lorsque le précurseur est décomposé dans la trioctylphosphine (T_{eb} = 310 °C), les mêmes nanoparticules sont obtenues avec des plus grosses. Les analyses DRX montrent la présence de phases de NiO et de Ni^0. Et lorsque le stéarate de nickel est décomposé dans de l'octadécène (T_{eb} = 320 °C), de très petites nanoparticules de NiO sont obtenues.

Comme la présence de germes évite aux monomères de former des nucleus, leur présence facilite la décomposition du précurseur. Le stéarate de nickel a donc été décomposé en présence de nanoparticules d'oxyde de fer. Le NiO ainsi crû sur des facettes spécifiques formant des octopodes à partir des sphères d'oxyde de fer. Sa décomposition sur des nanoparticules de $Fe_{3-d}O_4$@CoO produit elle des cubes.

Dans le but de diminuer la stabilité thermique du précurseur de nickel, la chaîne organique a été raccourcie et des précurseurs d'octanoate, d'acetylacetonate et d'acétate de nickel ont été synthétisés. Un précurseur d'acétate de nickel aura aussi été testé mais a été acheté dans le commerce. Leur stabilité a été étudiée par DTG. D'après cette étude, l'octanoate de nickel présente une assez bonne séparation de ses étapes de nucléations et de croissance. Il se décompose à partir de 200 °C. Ainsi il est le meilleur candidat des précurseurs étudiés. Sa décomposition dans de l'octadécène forme néanmoins des nanoparticules similaires à celles obtenus avec le stéarate.

L'octanoate de nickel a été décomposé en présence de nanoparticules d'oxyde de fer sphérique dans des solvants avec des températures d'ébullition croissante. La morphologie passe de cubique à octopadique lorsque la température d'ébullition du solvant augmente. Cela est lié à la cinétique de croissance. En effet, lors de croissance sur germe, deux cinétiques sont à prendre en compte : la cinétique de déposition des monomères et la cinétique de migration. Les monomères se déposent d'abords sur les faces de plus hautes énergies des nanoparticules présentes puis ils migrent ensuite vers les faces de plus basses énergies. Ainsi, pour des hautes températures, les monomères ont une cinétique de déposition à la surface plus rapide que la cinétique de migration.

Aussi, l'augmentation de la concentration d'octanoate de nickel pour une concentration fixe de nanoparticules d'oxyde de fer favorise la cinétique de déposition et forme des cubes tandis que pour des faibles concentrations, la cinétique de migration est favorisée, formant plutôt des sphères.

La croissance de NiO à la surface des nanoparticules d'oxyde de fer permet aussi de préserver le cœur contre son oxydation à l'air. Les mesures XAS, XMCD montrent que de la ferrite de nickel interfaciale n'est pas formée. La croissance de NiO à la surface des nanoparticules d'oxyde de fer ne permet pas d'augmenter T_{max} ni T_B puisque NiO est un matériau plus doux que l'oxyde de fer. Mais, les mesures M(H) à basse température montrent que le champ coercitif est faiblement augmenté du fait d'un fort couplage d'échange entre le cœur ferrimagnétique et la coquille antiferromagnétique.[7]

Ces études préliminaires ont permis de synthétiser deux séries de nanoparticules de $Fe_{3-d}O_4$@CoO@NiO, une sphérique et une cubique.

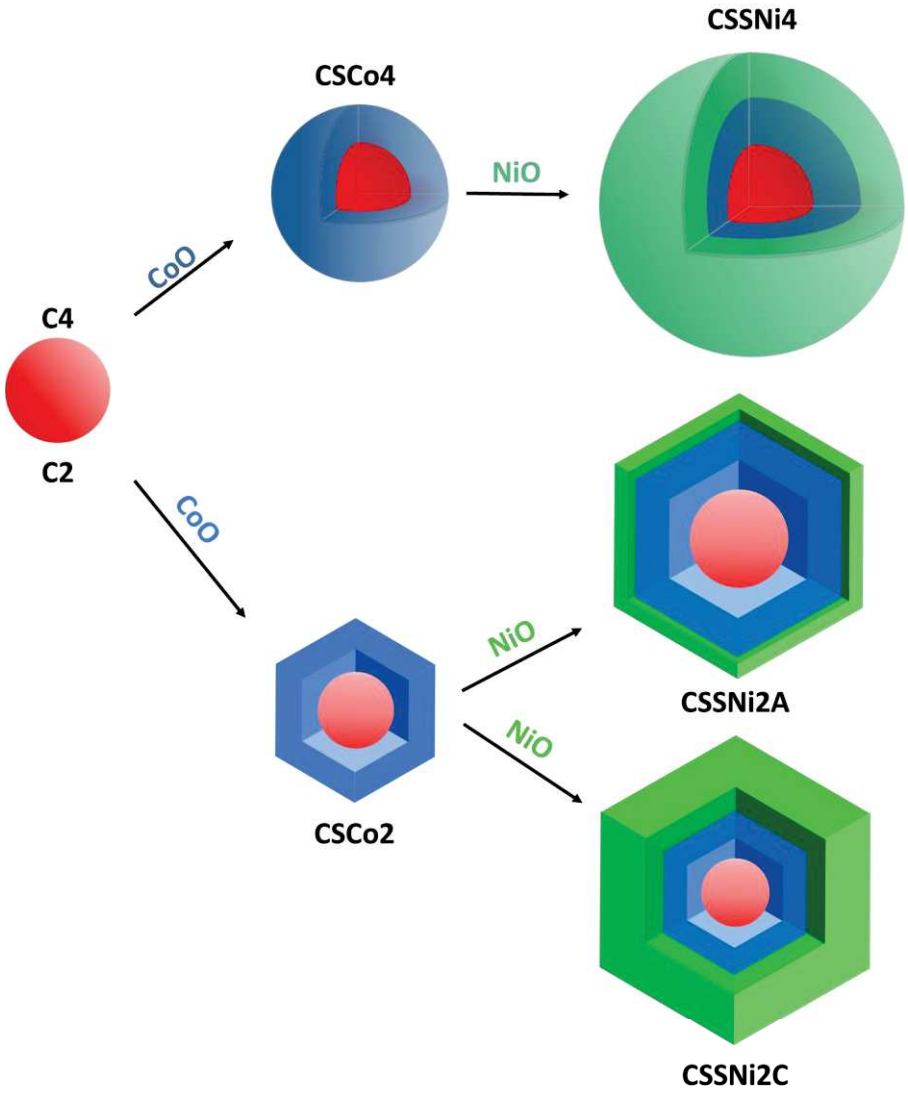

Figure 136. Représentation schématique de la croissance d'une coquille de NiO sur des nanoparticules de $Fe_{3-d}O_4$@CoO sous forme sphérique et cubique.

La croissance du NiO sous forme de cube est influencée par la croissance de la coquille de CoO en forme cubique à la surface de la nanoparticule sphérique d'oxyde de fer. Cette croissance spécifique est favorisée de par l'utilisation d'un précurseur de CoO moins hydraté que pour les sphères. En effet,

un précurseur moins hydraté se décompose plus vite et favorise donc une cinétique de déposition. Le NiO croit ensuite préférentiellement sur le CoO plutôt que sur l'oxyde de fer puisque les contraintes cristalline finales y sont moins élevées.

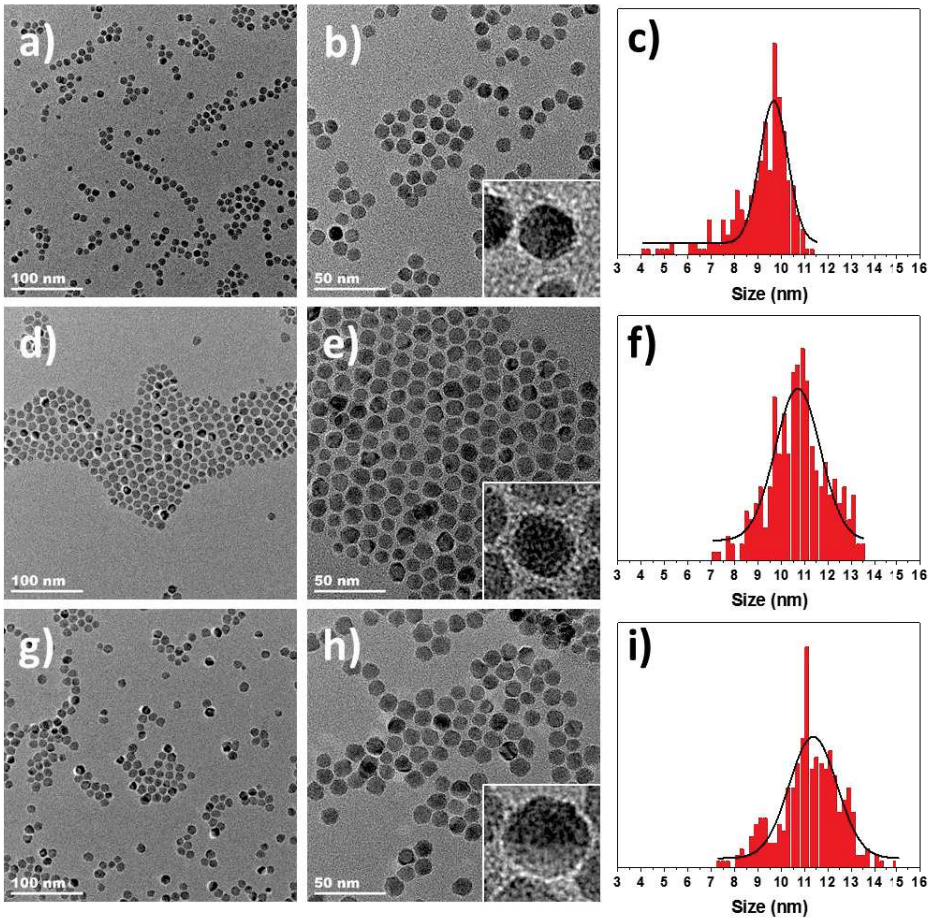

Figure 137. Images MET des nanoparticules a, b) C4, d, e) CSCo4, g, h) CSSNi4 avec d, f, i) leur distribution de taille correspondante.

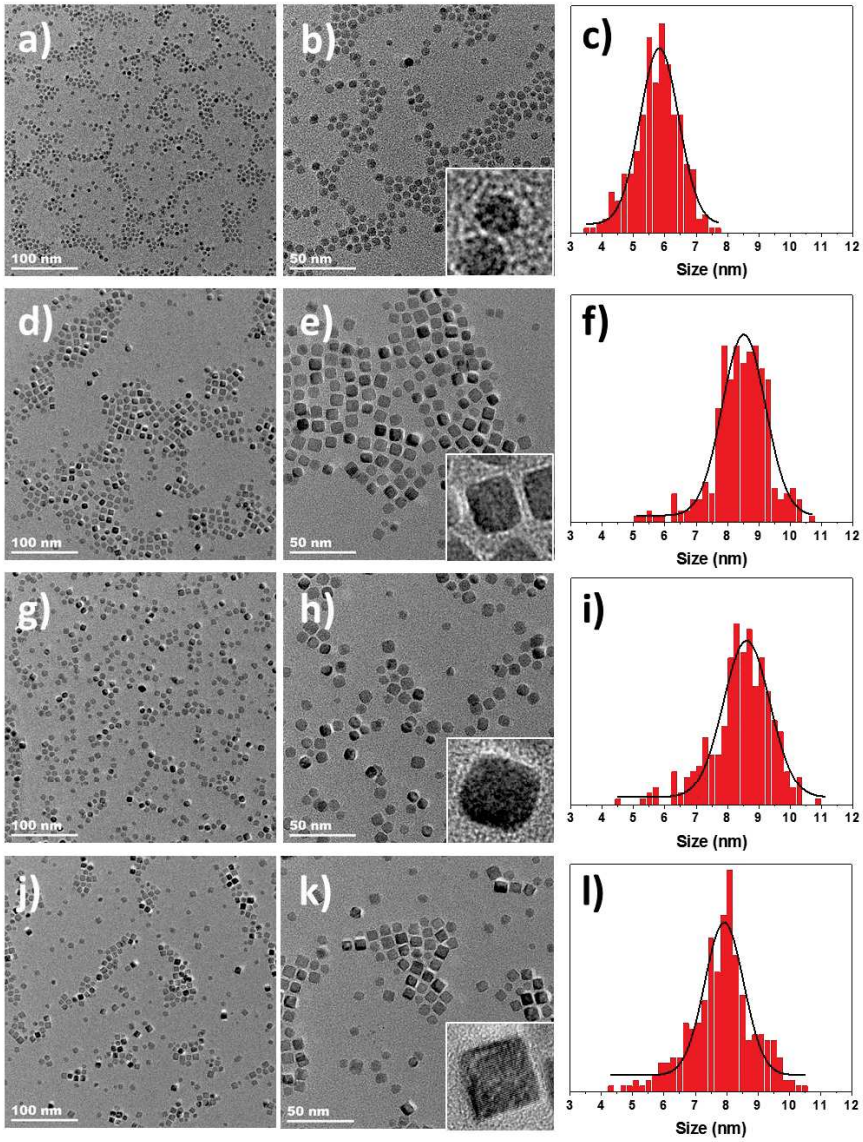

Figure 138. Images MET des nanoparticules a, b) C2, d, e) CSSNi2A, j, k) CSSNi2C avec c, f, i, l) leur distribution de taille correspondante.

Les nanoparticules de cœurs apparaissent toutes sphériques avec des distributions en taille étroite centrée à 9.2 et 5.8 nm pour la série sphérique et cubique respectivement.
Ensuite, une coquille de CoO de 0.8 et 1.3 nm d'épaisseur est déposée dans la série sphérique et cubique. Suivi par la croissance d'une coquille de NiO de 0.3 nm d'épaisseur pour la série sphérique. Tandis que la taille ne bouge pas dans la série cubique pour une faible concentration en précurseur de nickel alors qu'avec une grande concentration de nickel, la taille globale diminue de 0.6 nm (-0.3 nm d'épaisseur).
Les analyses EDX montrent la présence de fer et de cobalt pour les nanoparticules coeur@coquille et de fer, cobalt et nickel pour les nanoparticules coeur@coquille@coquille avec une quantité de nickel plus faible pour la série sphérique que pour la série cubique.
Ainsi, la diminution de la taille dans la série cubique avec la présence d'atomes de Ni montre qu'une partie de la nanoparticule coeur@coquille s'est resolubilisée et que le NiO a cru sur les coins du cube de $Fe_{3-d}O_4$@CoO.

Les mesures de spectroscopie infrarouge à transformée de Fourier montrent que la présence de ligands organiques greffés à la surface de chacune des nanoparticules qui sont stable en suspension.

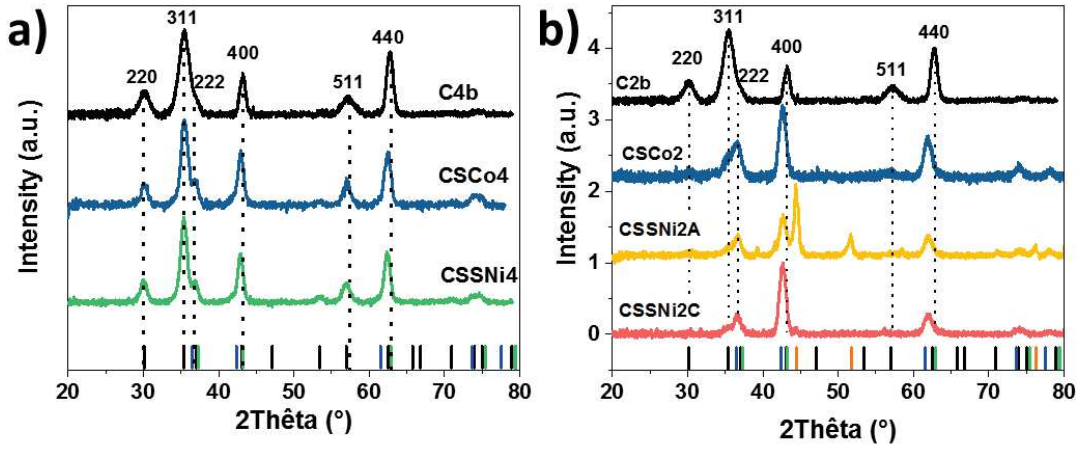

Figure 139. Diffractogrammes des nanoparticules a) C4, CSCo4, CSSNi4 et b) C2, CSCo2, CSSNi2A et CSSNi2C. Les barres noire, bleue, verte et orange correspondent aux structures Fe_3O_4 (JCPDS card n° 19-062), CoO (JCPDS card n° 70-2856), NiO (JCPDS card n° 47-1049) and Ni^0 (JCPDS card n° 04-010-6148) respectivement.

Les diffractogrammes enregistrées montrent que les nanoparticules de cœur ont bien une structure magnétite/maghémite. Dans la série sphérique, une contribution additionnelle de phase wüstite de CoO apparaît pour les nanoparticules $Fe_{3-d}O_4$@CoO et $Fe_{3-d}O_4$@CoO@NiO. Dans la série cubique en revanche, les diffractogrammes des nanoparticules $Fe_{3-d}O_4$@CoO et $Fe_{3-d}O_4$@CoO@NiO présentent essentiellement des contributions d'une phase wüstite (CoO et NiO). Cela est attribué au fait que la croissance de CoO et NiO sous forme de cube à la surface des sphères d'oxyde de fer a un volume beaucoup plus important que pour une croissance homogène en sphère.
Les paramètres de maille de la série sphérique sont en accord avec celles mesurées pour des nanoparticules coeur@coquille@coquille dans les chapitres précédents. En revanche, ils sont très faibles pour la série cubique et sont attribués à la grande quantité de CoO et NiO qui écrasent la contribution du cœur de $Fe_{3-d}O_4$.

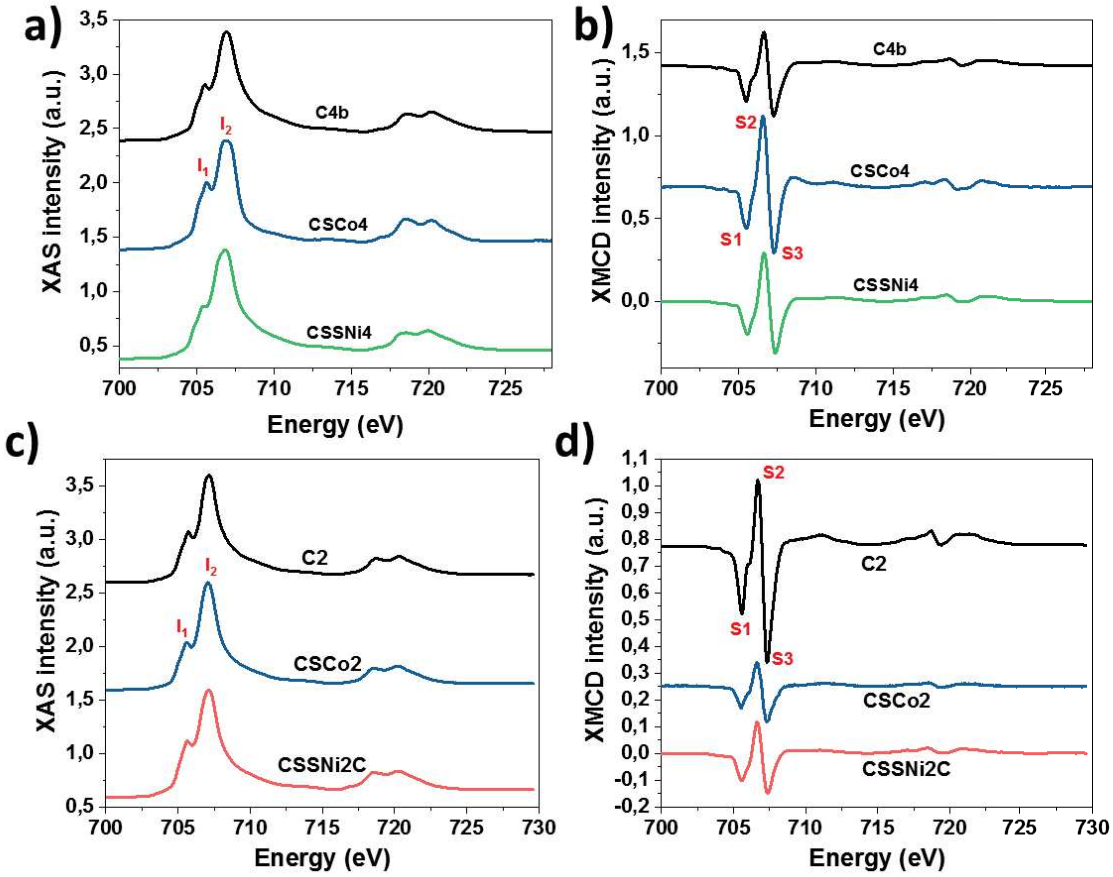

Figure 140. Spectres a, c) XAS et b, d) XMCD enregistrés au seuil $L_{2,3}$ du fer pour les nanoparticules a, b) C4b, CSCo4, CSSNi4 et c, d) C2, CSCo2 et CSSNi2C.

Les spectres XAS et XMCD enregistrés au seuil $L_{2,3}$ du fer montrent l'augmentation de la quantité de Fe^{2+} entre les cœurs et les coeur@coquille, conformément aux observations effectuées dans les chapitres II et III. De manière surprenante, ils montrent que la quantité de Fe^{2+} augmente encore dans la série cubique de $Fe_{3-d}O_4$@CoO@NiO où des analyses complémentaires sont nécessaires pour comprendre ce phénomène.

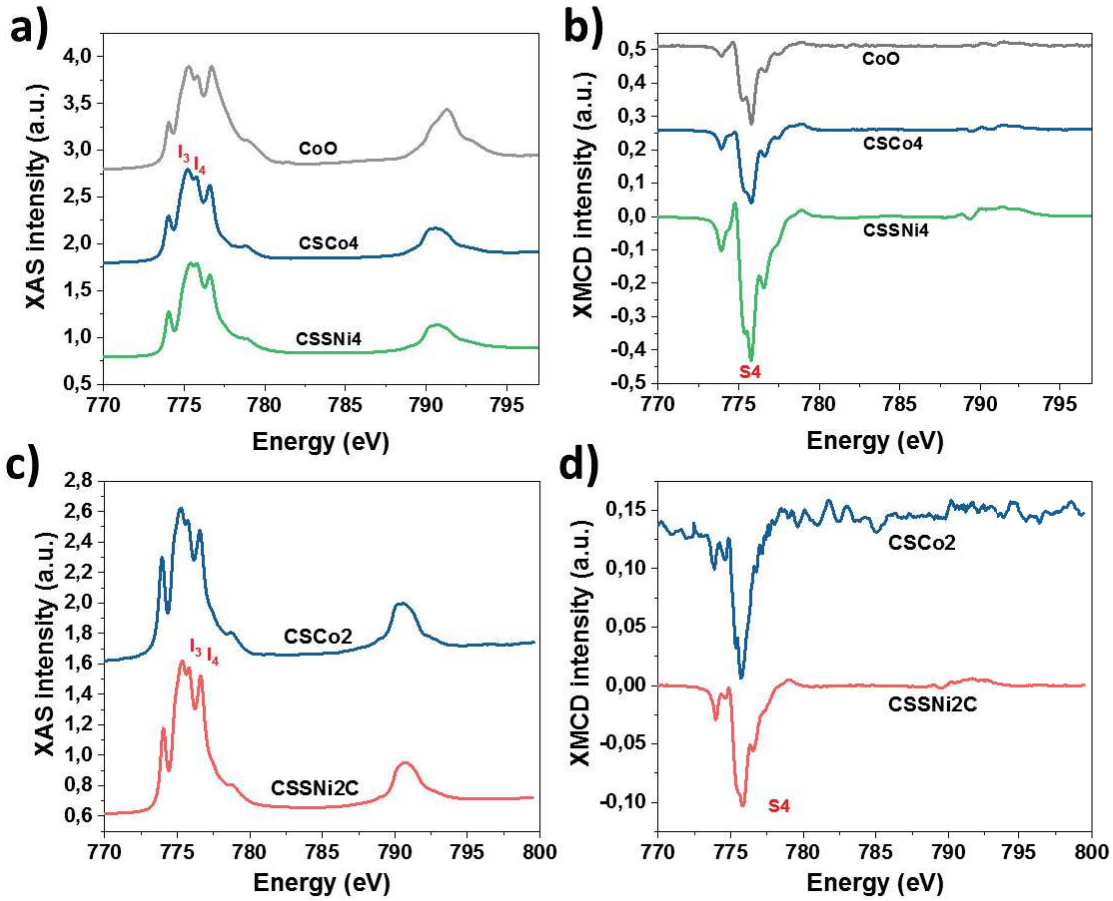

Figure 141. Spectres a, c) XAS et b, d) XMCD enregistrés au seuil $L_{2,3}$ du cobalt pour les nanoparticules a, b) CoO, CSCo4, CSSNi4 et c, d) CSCo2 et CSSNi2C.

Les spectres XAS et XMCD enregistrés au seuil $L_{2,3}$ du cobalt démontrent la présence de ferrite de cobalt interfaciale dans les nanoparticules $Fe_{3-d}O_4$@CoO cubiques et sphériques, en accord avec les chapitres II et III. Dans la série sphérique, l'intensité du signal XMCD enregistré au seuil du Co augmente entre $Fe_{3-d}O_4$@CoO et $Fe_{3-d}O_4$@CoO@NiO, ce qui est attribué à la présence de spins de Co^{2+} non compensés qui peut être attribué à des interactions Co-O-Ni dans une structure $Co_{1-x}Ni_xO$ ou à la création de ferrite de nickel interfaciale. A l'opposé, l'intensité de ce signal dans la série cubique diminue du fait de la croissance de la deuxième coquille et que le mode TEY est sensible à la surface.

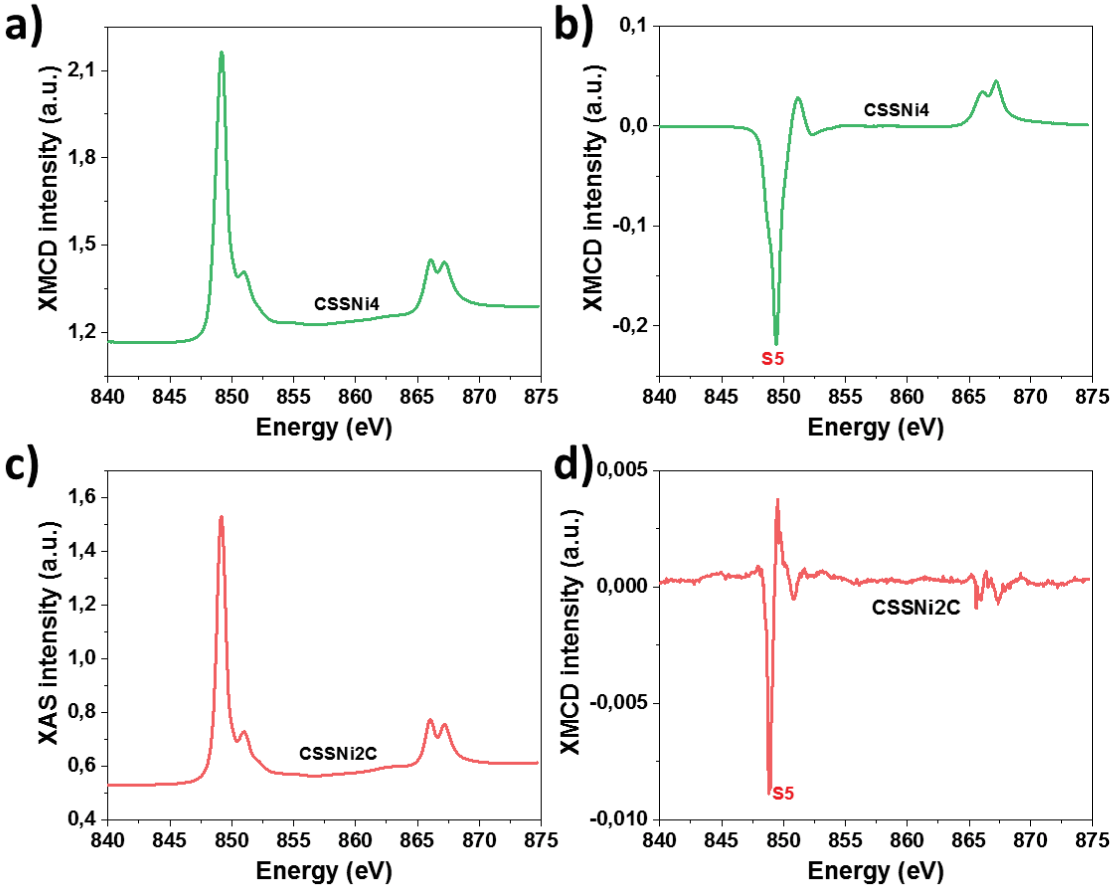

Figure 142. Spectres a, c) XAS et b, d) XMCD enregistrés au seuil $L_{2,3}$ du nickel pour les nanoparticules a, b) CSSNi4 et c, d) CSSNi2C.

Enfin, des spectres XAS et XMCD ont aussi été enregistrés au seuil $L_{2,3}$ du nickel et montrent une grande intensité du signal XMCD pour la série sphérique qui peut être attribué à des Ni^{2+} dans une structure $Co_{1-x}Ni_xO$ ou à la création de ferrite de nickel. A l'inverse, dans la série cubique, le spectre XMCD est en accord avec la seule présence de NiO antiferromagnétique.

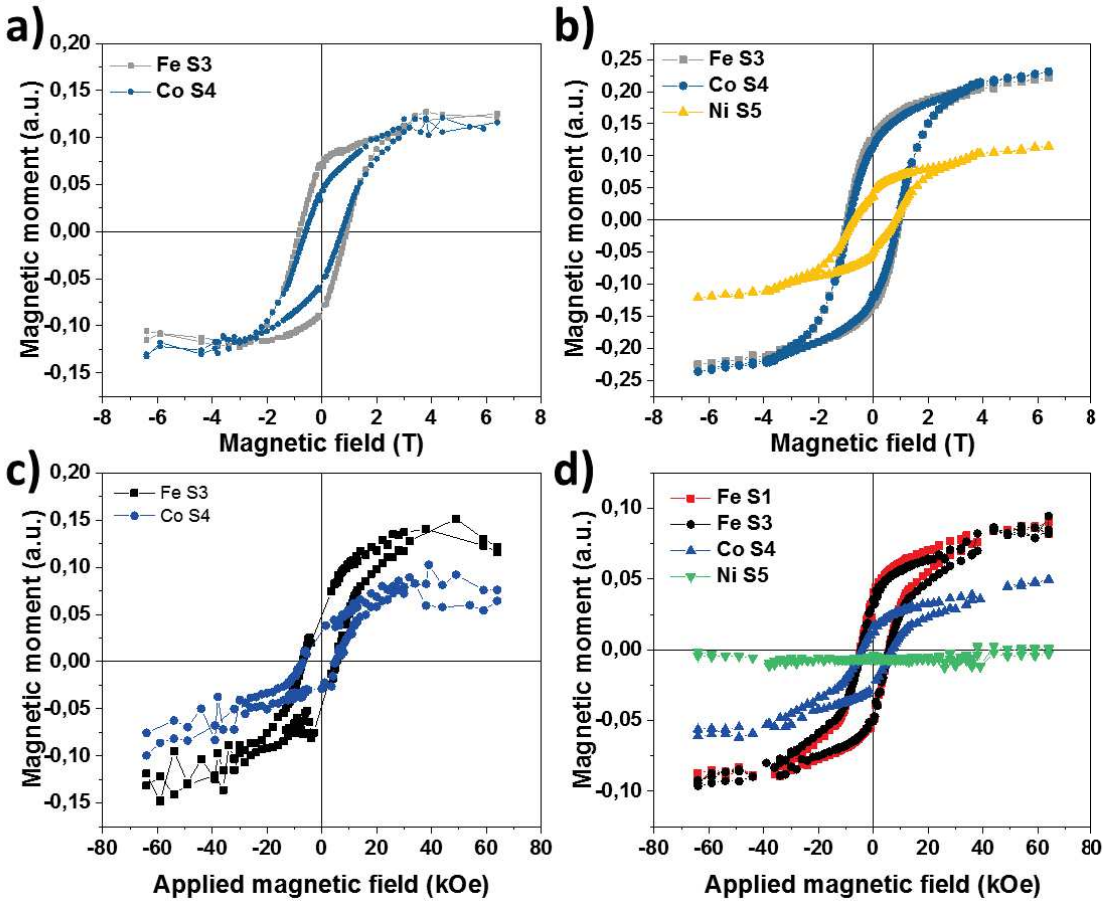

Figure 143. Hystérèses sélectives XMCD enregistrées aux seuils du fer S3, du cobalt S4 et du nickel S5 at 4 K pour les nanoparticules a) CSCo4, b) CSSNi4, c) CSCo2, d) CSSNi2C.

Les hystérèses sélectives enregistrées aux seuils du fer, cobalt et nickel sont en accord avec ces conclusions. Elles montrent également la présence d'un fort couplage magnétique entre les phases contenant du fer, cobalt et nickel. La forme penchée des hystérèses montre la contribution antiferromagnétique de CoO et NiO et leur approche lente et douce de la saturation témoigne du fort couplage magnétique. La croissance d'une coquille de NiO à la surface des nanoparticules de $Fe_{3-d}O_4$@CoO permet de diminuer les effets de canting de spin et d'augmenter leur ratio M_R/M_S.

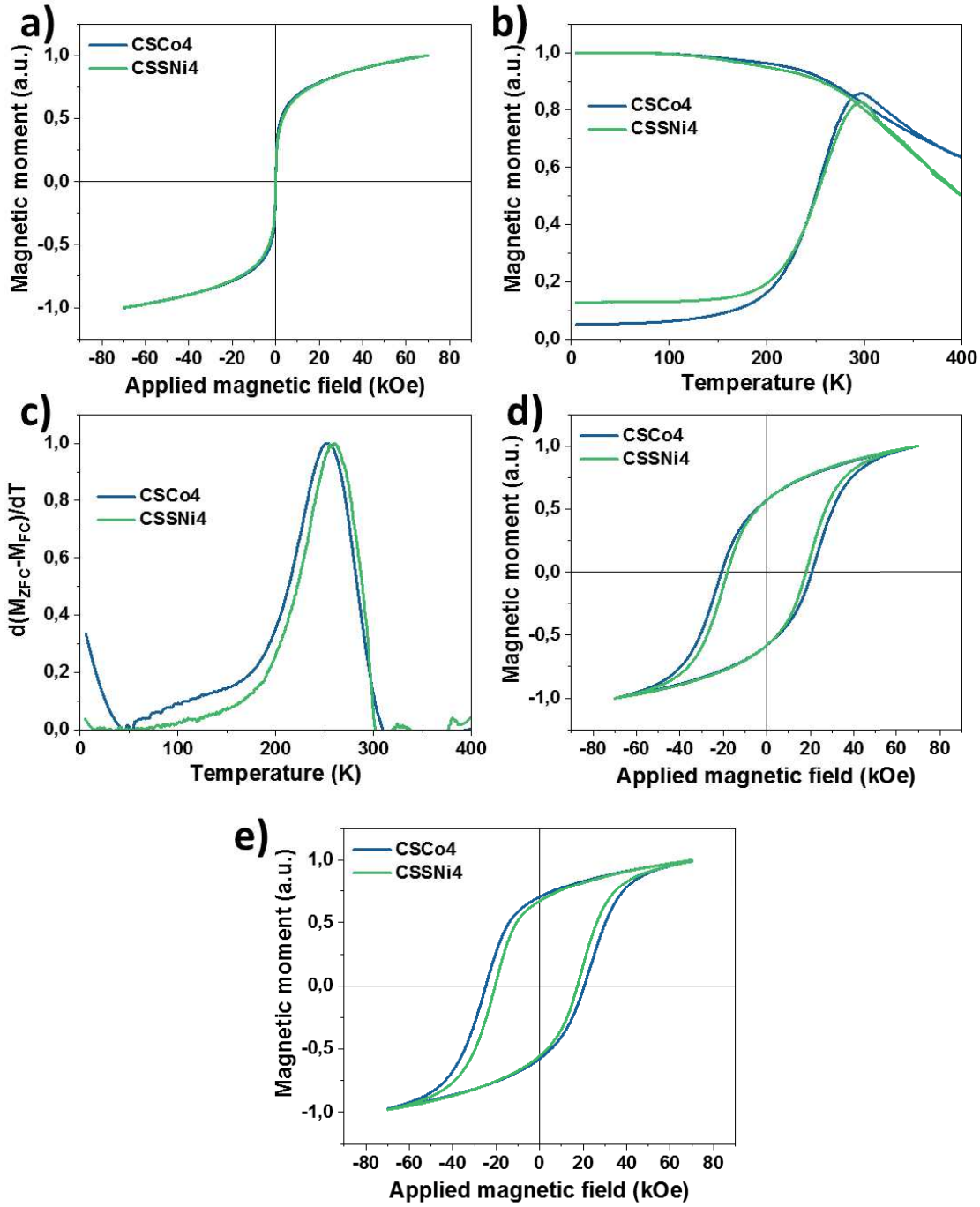

Figure 144. Propriétés magnétiques des nanoparticules CSCo4 et CSSNi4 mesurées par magnétométrie SQUID. Mesure de l'aimantation en fonction d'un champ appliqué à a) 300 K, d) 5 K sans refroidissement sous champ, e) 10 K après refroidissement sous champ. b) Mesure de l'aimantation en fonction de la température. c) Distribution des températures de blocages déterminée à partir de b).

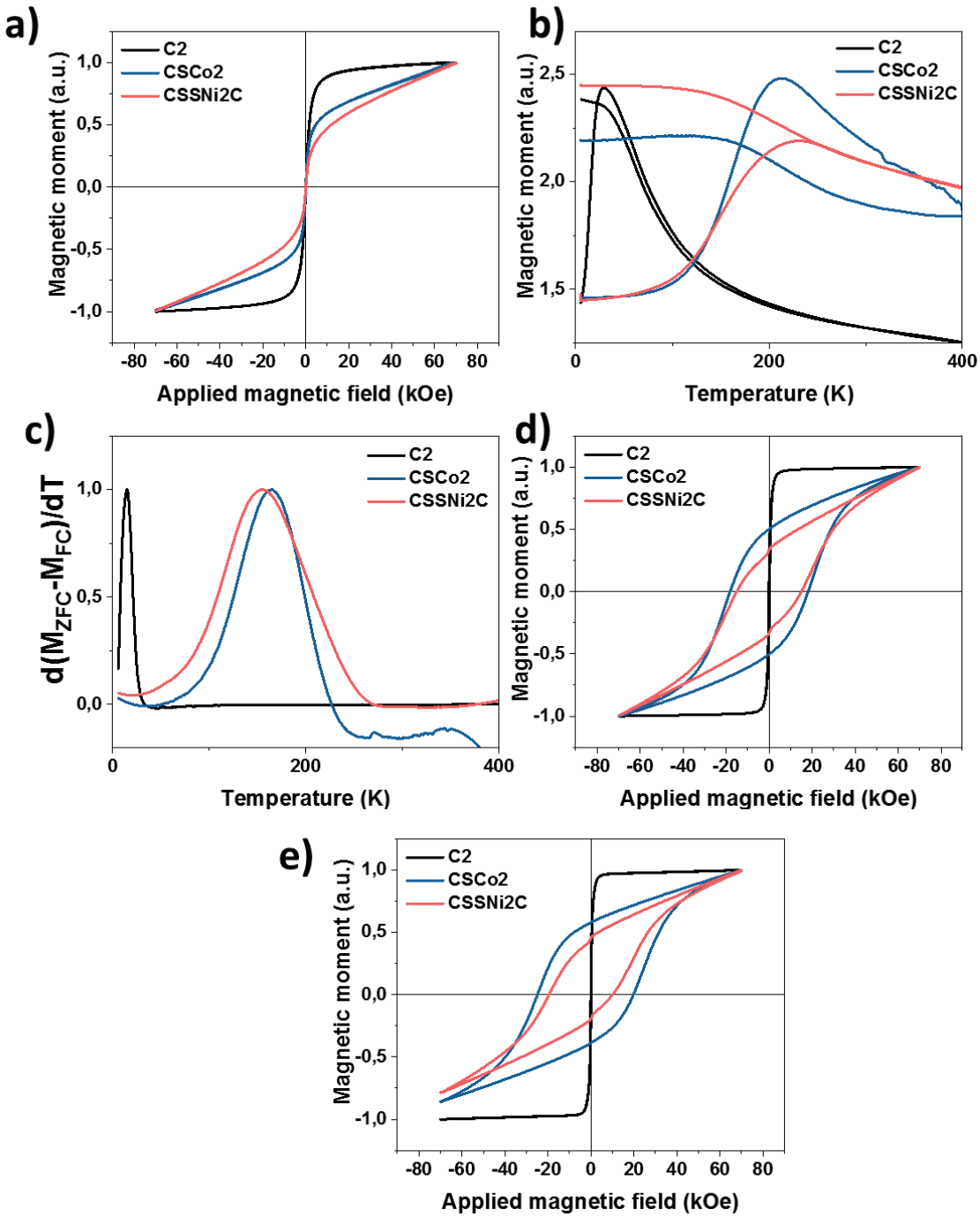

Figure 145. Propriétés magnétiques des nanoparticules C2, CSCo2 et CSSNi2C mesurées par magnétométrie SQUID. Mesure de l'aimantation en fonction d'un champ appliqué à a) 300 K, d) 5 K sans refroidissement sous champ, e) 10 K après refroidissement sous champ. b) Mesure de l'aimantation en fonction de la température. c) Distribution des températures de blocages déterminée à partir de b).

La présence d'une coquille de NiO à la surface de $Fe_{3-d}O_4$@CoO n'influence pas T_{max} ni T_B aussi bien pour une croissance cubique que sphérique. Et, dans les deux cas, la présence de NiO diminue le champ coercitif. La croissance d'une coquille de NiO à la surface de nanoparticules de $Fe_{3-d}O_4$@CoO a augmenté le H_E pour la série cubique et l'a diminué pour la série sphérique. La diminution du H_E est en accord avec la présence de NiO doux tandis que l'augmentation est un accord avec une restructuration de la nanoparticule cubique. De plus, la forme cubique des $Fe_{3-d}O_4$@CoO montre la présence de spins non compensés dans la phase antiferromagnétique qui sont situés dans les coins du cube. Leur nombre

diminue avec la croissance d'une coquille de NiO dans la série cubique. K_{eff} diminue avec la croissance de NiO dans la série sphérique tandis qu'il augmente dans la série cubique du fait de la croissance ultérieure de CoO tel que démontrée par les analyses XAS, XMCD. Ainsi, le volume de NiO présent à la surface des nanoparticules de $Fe_{3-d}O_4$@CoO est trop faible pour pouvoir influer plus sur leurs propriétés magnétiques.

Ce chapitre a permis d'améliorer les conditions de synthèses de nanoparticules de NiO et plus particulièrement de nanoparticules de $Fe_{3-d}O_4$@NiO et $Fe_{3-d}O_4$@CoO@NiO. Dans ce but, une première étude préliminaire sur le choix et la décomposition de précurseurs de nickel a été menée.
Deux types de nanoparticules de $Fe_{3-d}O_4$@CoO@NiO ont été synthétisés : une série sphérique et une cubique toutes deux à partir de nanoparticules de $Fe_{3-d}O_4$ sphériques. La croissance sous forme de cube ou de sphère dépend des cinétiques de déposition et migration des monomères à la surface des germes. Il a été démontré que la forme des nanoparticules influe sur leurs propriétés magnétiques et que la croissance de NiO à la surface des nanoparticules de $Fe_{3-d}O_4$@CoO n'a pas permis d'améliorer leurs propriétés magnétiques et surtout leur T_B du fait que le volume de NiO ajouté est trop faible.

Conclusion

En conclusion, le premier chapitre reprend les bases de la synthèse de croissance sur germes en faisant croître des nanoparticules d'oxyde de fer par une succession de cinq décompositions thermiques. Ce chapitre a ainsi su montrer que même avec une succession de plusieurs synthèses, la taille et la forme des nanoparticules résultantes restent contrôlées. Des études de spectroscopie Mössbauer ont démontré que les fines couches d'oxyde de fer déposées sur les germes sont en fait oxydées du fait de leur faible épaisseur et de leur oxydation à l'air en maghémite.

Dans le second chapitre, des nanoparticules de $Fe_{3-d}O_4$@CoO, $Fe_{3-d}O_4$@$CoFe_2O_4$ et $Fe_{3-d}O_4$ dopées au cobalt ont été synthétisées dans le but d'étudier les phénomènes de diffusion interfaciale présent dans les nanoparticules de $Fe_{3-d}O_4$@CoO. Ainsi, les analyses Mössbauer et XAS XMCD s'entendent pour montrer qu'une couche interfaciale de ferrite de cobalt est bien présente dans ces dernières. Cette couche interfaciale favorise ainsi un fort couplage d'échange entre le cœur et la coquille.

Dans le troisième chapitre, des nanoparticules de $Fe_{3-d}O_4$@CoO ont été rechauffées pour mimer la synthèse d'une seconde coquille (CS2r). Il apparaît que l'échantillon rechauffé a une taille plus petite que les $Fe_{3-d}O_4$@CoO natives. Cela a été attribué à un phénomène de resolubilisation partielle de la coquille du fait de la haute température du solvant utilisé.
Les études précédentes ont été nécessaires dans le but de synthétiser des nanoparticules de composition espérée $Fe_{3-d}O_4$@CoO@$Fe_{3-d}O_4$. Il était attendu qu'un tel objet puisse bénéficier d'un double couplage d'exchange bias du fait de deux interfaces FiM/AFM. L'étude de la composition chimique grâce aux rayons X, spectroscopie Mössbauer, XAS-XMCD et SANS ont démontrées qu'une grande quantité de ferrite de cobalt a cru à la seconde interface. La croissance de la coquille de ferrite de cobalt se fait aux dépends de la coquille de CoO qui malgré une épaisseur nominale de 2.0 nm disparaît quasiment avec une épaisseur finale de 0.3 nm (CSSC). La nanoparticule finale comporte encore à sa surface une couche d'oxyde de fer où du Fe^{2+} est stabilisé de façon surprenante. Les mesures magnétiques montrent que la température de blocage est augmentée de 93 à 266 à 335 K à mesure que les coquilles croissent à la surface de la nanoparticule. Ainsi les nanoparticules cœur@coquille@coquille possèdent un champ coercitif de 500 Oe à 300 K et l'anisotropie magnétique des nanoparticules de bases d'oxyde de fer a pu être drastiquement augmentée !
Des analyses d'hystérèses sélectives aux seuils du fer et du cobalt réalisées sur ces nanoparticules ont démontrées que l'ensemble des atomes de Fe et de Co ont un fort couplage magnétique entre eux. Cependant, au vu de la disparition de la phase de CoO au profit de la phase de ferrite de cobalt, il n'est pas possible de dire si le CoO restant participe toujours à l'augmentation de l'anisotropie magnétique des nanoparticules.

Dans le quatrième chapitre, la synthèse de nanoparticules de $Fe_{3-d}O_4$@$CoFe_2O_4$@$Fe_{3-d}O_4$ permet de répondre à la question précédente. En effet, il a été démontré que la température de blocage augmente fortement du cœur au coeur@coquille. A contrario, l'augmentation de T_B de $Fe_{3-d}O_4$@$CoFe_2O_4$ à $Fe_{3-d}O_4$@$CoFe_2O_4$@$Fe_{3-d}O_4$ est beaucoup plus faible que précédemment et provient d'un effet de volume plutôt que d'un double couplage d'échange de type dur-mou. Ainsi, la grande anisotropie des nanoparticules de $Fe_{3-d}O_4$@$(CoFe_2O_4@)_{1-x}CoO_{1+x+y}$@$(CoFe_2O_4@)_{1-y}Fe_{3-d}O_4$ est liée à un couplage synergique entre les couplages d'échange dur/mou et d'exchange bias.

Le NiO possède une très haute T_N de 525 K et pourrait donc augmenter la T_B de nanoparticules de $Fe_{3-d}O_4$@CoO en synthétisant des nanoparticules de $Fe_{3-d}O_4$@CoO@NiO. La synthèse de NiO est très peu rapportée dans la littérature. Donc pour synthétiser les coquilles de NiO, une étude sur la décomposition de précurseurs organométallique à base de Ni a d'abord été menée. Celle-ci est présentée en annexe. Puis, une fois les conditions de synthèses déterminées, des nanoparticules de $Fe_{3-d}O_4$@NiO et $Fe_{3-d}O_4$@CoO@NiO ont été synthétisées avec une série sphérique et une série cubique

de $Fe_{3-d}O_4$@CoO@NiO. Il apparaît que la présence de NiO à la surface des nanoparticules n'a pas de réelle influence sur les propriétés magnétiques des nanoparticules. Cela est lié au fait que sa constante d'anisotropie est proche de celle de l'oxyde de fer et que son volume est faible. Ainsi son énergie d'anisotropie magnétique est inférieure à celle de l'oxyde de fer et des nanoparticules $Fe_{3-d}O_4$@CoO et aussi à celle de l'énergie d'échange interfaciale.
Dans ce chapitre, nous avons également démontré que la forme des nanoparticules a un impact sur ses propriétés. En effet, les nanoparticules cubiques ont beaucoup plus de phases wüstite (CoO et NiO) comparé à la phase de ferrite que les nanoparticules sphériques. Aussi, la croissance de NiO sur les coins du cube permet d'avoir un vrai comportement AFM du NiO tandis que sur la sphère, un comportement FiM de la dernière coquille a été observé. Des analyses de microscopie avancée (EELS, EELS-SI) vont permettre de déterminer si cela est lié à la présence d'interaction Co-O-Ni ou de ferrite de Ni synthétisée par solubilisation partielle et recrystallisation.

Finalement, au cours de cette thèse, nous avons montrées qu'il est possible d'avoir des nanoparticules à base d'oxyde de fer d'une taille inférieure à 16 nm qui sont bloquées à température ambiante. Il conviendra par la suite de maîtriser les distances entre les nanoparticules pour étudier les effets collectifs et pouvoir éventuellement plus tard les utiliser en tant que dispositif d'enregistrement de données.

(1) Skumryev, V.; Stoyanov; Zhang; Hadjipanayis; Givord; Nogués. Beating the Superparamagnetic Limit with Exchange Bias. *Nature* **2003**, *423* (6942), 847–850. https://doi.org/10.1038/nature01750.

(2) Nogués, J.; Sort, J.; Langlais, V.; Skumryev, V.; Suriñach, S.; Muñoz, J. S.; Baró, M. D. Exchange Bias in Nanostructures. *Phys. Rep.* **2005**, *422* (3), 65–117. https://doi.org/10.1016/j.physrep.2005.08.004.

(3) Gilmore, K.; Idzerda, Y. U.; Klem, M. T.; Allen, M.; Douglas, T.; Young, M. Surface Contribution to the Anisotropy Energy of Spherical Magnetite Particles. *J. Appl. Phys.* **2005**, *97* (10), 10B301. https://doi.org/10.1063/1.1845973.

(4) Cao, C.; Tian, L.; Liu, Q.; Liu, W.; Chen, G.; Pan, Y. Magnetic Characterization of Noninteracting, Randomly Oriented, Nanometer-Scale Ferrimagnetic Particles. *J. Geophys. Res.* **2010**, *115* (B7), B07103. https://doi.org/10.1029/2009JB006855.

(5) Skoropata, E.; Desautels, R. D.; Chi, C.-C.; Ouyang, H.; Freeland, J. W.; van Lierop, J. Magnetism of Iron Oxide Based Core-Shell Nanoparticles from Interface Mixing with Enhanced Spin-Orbit Coupling. *Phys. Rev. B* **2014**, *89* (2). https://doi.org/10.1103/PhysRevB.89.024410.

(6) Walter, A. Elaboration de nano-objets magnétiques dendronisés à vocation théranostic, Université de Strasbourg, 2014.

(7) Skoropata, E.; Su, T. T.; Ouyang, H.; Freeland, J. W.; van Lierop, J. Intermixing Enables Strong Exchange Coupling in Nanocomposites: Magnetism through the Interfacial Ferrite in γ − Fe 2 O 3 / NiO. *Phys. Rev. B* **2017**, *96* (2). https://doi.org/10.1103/PhysRevB.96.024447.

(8) Liu, X.; Pichon, B. P.; Ulhaq, C.; Lefèvre, C.; Grenèche, J.-M.; Bégin, D.; Bégin-Colin, S. Systematic Study of Exchange Coupling in Core–Shell Fe $_{3-\delta}$ O $_4$ @CoO Nanoparticles. *Chem. Mater.* **2015**, *27* (11), 4073–4081. https://doi.org/10.1021/acs.chemmater.5b01103.

(9) Baaziz, W.; Pichon, B. P.; Lefevre, C.; Ulhaq-Bouillet, C.; Greneche, J.-M.; Toumi, M.; Mhiri, T.; Bégin-Colin, S. High Exchange Bias in Fe $_{3-\delta}$ O $_4$ @CoO Core Shell Nanoparticles Synthesized by a One-Pot Seed-Mediated Growth Method. *J. Phys. Chem. C* **2013**, *117* (21), 11436–11443. https://doi.org/10.1021/jp402823h.

(10) Salazar-Alvarez, G.; Lidbaum, H.; López-Ortega, A.; Estrader, M.; Leifer, K.; Sort, J.; Surinach, S.; Baró, M. D.; Nogués, J. Two-, Three-, and Four-Component Magnetic Multilayer Onion Nanoparticles Based on Iron Oxides and Manganese Oxides. *J. Am. Chem. Soc.* **2011**, *133* (42), 16738–16741.

(11) Krycka, K. L.; Borchers, J. A.; Laver, M.; Salazar-Alvarez, G.; L?pez-Ortega, A.; Estrader, M.; Suri?ach, S.; Bar?, M. D.; Sort, J.; Nogu?s, J. Correlating Material-Specific Layers and Magnetic Distributions within Onion-like Fe3O4/MnO/?-Mn2O3 Core/Shell Nanoparticles. *J. Appl. Phys.* **2013**, *113* (17), 17B531. https://doi.org/10.1063/1.4801423.

(12) Gavrilov-Isaac, V.; Neveu, S.; Dupuis, V.; Taverna, D.; Gloter, A.; Cabuil, V. Synthesis of Trimagnetic Multishell MnFe $_2$ O $_4$ @CoFe $_2$ O $_4$ @NiFe $_2$ O $_4$ Nanoparticles. *Small* **2015**, *11* (22), 2614–2618. https://doi.org/10.1002/smll.201402845.

(13) Baaziz, W.; Pichon, B. P.; Liu, Y.; Grenèche, J.-M.; Ulhaq-Bouillet, C.; Terrier, E.; Bergeard, N.; Halté, V.; Boeglin, C.; Choueikani, F.; et al. Tuning of Synthesis Conditions by Thermal Decomposition toward Core–Shell Co $_x$ Fe $_{1-x}$ O@Co $_y$ Fe $_{3-y}$ O $_4$ and CoFe $_2$ O $_4$ Nanoparticles with Spherical and Cubic Shapes. *Chem. Mater.* **2014**, *26* (17), 5063–5073. https://doi.org/10.1021/cm502269s.

(14) De Toro, J. A.; Marques, D. P.; Muñiz, P.; Skumryev, V.; Sort, J.; Givord, D.; Nogués, J. High Temperature Magnetic Stabilization of Cobalt Nanoparticles by an Antiferromagnetic Proximity Effect. *Phys. Rev. Lett.* **2015**, *115* (5). https://doi.org/10.1103/PhysRevLett.115.057201.

(15) Baaziz, W.; Pichon, B. P.; Fleutot, S.; Liu, Y.; Lefevre, C.; Greneche, J.-M.; Toumi, M.; Mhiri, T.; Begin-Colin, S. Magnetic Iron Oxide Nanoparticles: Reproducible Tuning of the Size and Nanosized-Dependent Composition, Defects, and Spin Canting. *J. Phys. Chem. C* **2014**, *118* (7), 3795–3810. https://doi.org/10.1021/jp411481p.

(16) Xia, Y.; Xia, X.; Peng, H.-C. Shape-Controlled Synthesis of Colloidal Metal Nanocrystals: Thermodynamic versus Kinetic Products. *J. Am. Chem. Soc.* **2015**, *137* (25), 7947–7966. https://doi.org/10.1021/jacs.5b04641.

(17) Lentijo-Mozo, S.; Deiana, D.; Sogne, E.; Casu, A.; Falqui, A. Unexpected Insights about Cation-Exchange on Metal Oxide Nanoparticles and Its Effect on Their Magnetic Behavior. *Chem. Mater.* **2018**, *30* (21), 8099–8112. https://doi.org/10.1021/acs.chemmater.8b04331.

(18) Estrader, M.; López-Ortega, A.; Estradé, S.; Golosovsky, I. V.; Salazar-Alvarez, G.; Vasilakaki, M.; Trohidou, K. N.; Varela, M.; Stanley, D. C.; Sinko, M.; et al. Robust Antiferromagnetic Coupling in Hard-Soft Bi-Magnetic Core/Shell Nanoparticles. *Nat. Commun.* **2013**, *4*. https://doi.org/10.1038/ncomms3960.

Kevin SARTORI

Etude du couplage d'échange interfacial de nanoparticules magnétiques à base de ferrite préparées via une succession de synthèses par décomposition thermique

Résumé

L'utilisation de terres rares dans des dispositifs d'enregistrement de données est très coûteux et polluant. Leur remplacement par de l'oxyde de fer permettrait de s'affranchir de cela. En-dessous d'une taille de 20 nm, les nanoparticules d'oxyde de fer ne peuvent pas être considérées comme des aimants permanents. Une alternative consiste à les combiner à une autre phase magnétique pour permettre d'augmenter leur anisotropie magnétique via un couplage d'échange interfacial au sein de nanoparticules de type coeur@coquille. En revanche la stabilité magnétique de ces dernières reste insuffisante.

L'objectif de cette thèse est de concevoir un nouveau type de nanoparticules magnétiques de type coeur@coquille@coquille avec un cœur de $Fe_{3-d}O_4$ et des coquilles de $CoFe_2O_4$, CoO ou NiO qui a permis d'augmenter encore les propriétés magnétiques tout en conservant une taille inférieure à 18 nm. L'étude approfondie de leur relation structure-propriété a été réalisée au moyen d'un large éventail de techniques.

Mots-Clefs : Nanoparticules magnétiques, couplage d'échange, exchange-bias, anisotropie magnétique, diffusion atomique, XAS, XMCD, p-SANS, Mössbauer.

Résumé en anglais

The use of rare earths in data storage devices is expensive and polluting. Their replacement with iron oxide would make it possible to avoid this. Below a size of 20 nm, iron oxide nanoparticles cannot be considered as permanent magnet. An alternative is to combine them with another magnetic phase to enhance their magnetic anisotropy via interfacial exchange coupling within core@shell nanoparticles. However, the magnetic stability of the latter remains insufficient.

The scope of this thesis is to design a new type of magnetic nanoparticles of core@shell@shell structure with a $Fe_{3-d}O_4$ core and $CoFe_2O_4$, CoO or NiO as shells which has further enhance the magnetic properties while maintaining a size below 18 nm. The in-depth study of their structure-properties relationship was carried out using a wide set of analytical techniques.

Keywords: Magnetic nanoparticles, exchange coupling, exchange-bias, magnetic anisotropy, atomic diffusion, XMCD, p-SANS, Mössbauer.